

# COORDINATION CHEMISTRY OF PTERIDINE LIGANDS WITH TRANSITION AND $d^{10}$ METALS

A Thesis submitted to the  
UNIVERSITY OF NORTH BENGAL

For the Award of  
Doctor of Philosophy (Ph.D.)

In  
Chemistry

By  
**Siddhartha Sankar Baisya,**  
M.Sc. In Chemistry

Guide  
Prof. PARAG SINCHAN ROY  
Professor of Chemistry

DEPARTMENT OF CHEMISTRY  
UNIVERSITY OF NORTH BENGAL  
DARJEELING - 734013  
December, 2016

## DECLARATION

I declare that the thesis entitled “**Coordination chemistry of pteridine ligands with transition and d<sup>10</sup> metals**” has been prepared by me under the guidance of Professor Parag Sinchan Roy, Professor of Chemistry, Department of Chemistry, University of North Bengal. The research data represented in the thesis are new and original based on experiments in our research laboratory. I would like to mention that my work or any part of it has not previously been submitted for any degree whatsoever by me or by anyone else.

*Siddhartha Sankar Baisya*

(Siddhartha Sankar Baisya)

Department of Chemistry,  
University of North Bengal,  
Siliguri – 734013,  
Dist. – Darjeeling,  
INDIA.

DATE: 28/11/16

UNIVERSITY OF NORTH BENGAL

Professor PARAG. S. ROY  
DEPARTMENT OF  
CHEMISTRY  
University of North Bengal  
Email: psrnbu@gmail.com



Ph: ( 0353 )2776381  
Fax: (0353 ) 2699001  
P.O. North Bengal  
University,  
Raja Rammohunpur,  
Siliguri.PIN – 734 013

This is to certify that Shri Siddhartha Sankar Baisya has carried out the work described in the dissertation entitled “**Coordination chemistry of pteridine ligands with transition and d<sup>10</sup> metals**” under my supervision. It is further to certify that the said thesis incorporates the results of original investigation made by Shri Baisya in the Department of Chemistry, University of North Bengal, Siliguri 734013, India. In this context, I would like to mention that this work or any part of it has not previously been submitted for any degree whatsoever by him or by anyone else.

Date: 28-11-2016

*Parag Sinchan Roy*

(Parag Sinchan Roy)  
Supervisor  
Professor of Chemistry  
University of North Bengal

**PROFESSOR OF CHEMISTRY**  
University of North Bengal

*I have dedicated my little work to my  
parents and family.*

# *Acknowledgement*

At the moment of accomplishment first of all I would like to convey my special appreciation and hearty thanks to my supervisor Prof. Parag Sinchan Roy, Department of Chemistry, University of North Bengal for providing me the opportunity to my doctoral program under his guidance and to learn from his research expertise. This work would not have been possible without his constant steering, continuous assistance and genuine encouragement.

I am indebted to all the teachers of the Chemistry department for their kind help and advice. I am grateful to Prof. M. N. Roy, Head, Department of Chemistry, University of North Bengal for his kind cooperation and valuable suggestion throughout my doctoral program. I am thankful to Dr. A. K. Nanda, Dr. Sajal Das and Dr. B. Sinha, Department of Chemistry, University of North Bengal for NMR spectroscopic investigation and different instrumental measurements. I am obliged to Prof. J. P. Naskar, Department of Chemistry, Jadavpur University, Kolkata, India for most of the cyclic voltammetric data.

I express my gratitude also to UGC, New Delhi for financial support (SAP - DRS); DST, New Delhi for a FIST programme, providing a Bruker 300 MHz NMR instrument; CSMCRI, Bhavnagar, India for X-ray structural data, microanalytical data, CD spectral data and some ESIMS data ; SAIF, CDRI, Lucknow for ESIMS data of few samples; SAIF, IIT, Bombay for EPR data; IICB, Kolkata for some fluorescence data; University of North Bengal for infrastructural facility; Professor Junhua Yan for Isotope Pattern Calculator (v, 4.0).

I extend my thanks to all the staff members and research scholars of this department for their kind cooperation in academic, official and laboratory work related to this thesis. Day to day helps on computational works by Suranjan Shil and Tamal Goswami deserve special mention.

I appreciate my research team members Dr. Md. Afsar Ali, Samir Sen and Baidyanath Ghosh for their outstanding discussions and co-operation. We have studied, correlated the theoretical background and the experimental data in the best possible way. I also acknowledge the institute, Valmiki Vidyapith (H.S.), Surya Sen Colony, Siliguri Town, Jalpaiguri, where I am presently teaching, for their permission to complete this work.

I am very much indebted to my family too. I would like to thank to my cousins, aunts, and uncles for their good wishes, helps and cooperation. Words cannot express how grateful I am to my wife, Rituparna for her support, generous care and all the sacrifices made on my behalf. Cute smile of my little girl, Sharannya makes always me happy and gives energy. I owe a lot to my parents and my brother Rabi who always encouraged and helped me at every stage of my life, and longed to see this achievement come true.

Last but not the least, valuable technical supports have been received from M/S. Lab Instruments and Chemical Works, Siliguri – 734001, who promptly supplied the glass apparatus as par design and repaired equipments reliably.

I will gratefully receive comments concerning errors of typography, omissions which might have crept in inadvertently.

(Siddhartha Sankar Baisya)  
Department of Chemistry,  
University of North Bengal,  
Siliguri – 734013, India.

## **Abstract**

Pterins (2-amino-4-oxidopteridines) are ubiquitous in nature and their reduced forms act as essential components of different classes of metalloenzymes containing molybdenum or tungsten or iron (non heme or heme type). This treatise explores new coordination compounds of cobalt, nickel copper and zinc. The discussions include the current status of chemical approaches, the impact of X-ray structural data on enzymes, spectroscopic techniques and molecular modeling methods in giving clear descriptions of pterin coordination compounds in terms of molecular structures, electronic structures as well as correlation of structures with reactivity.

The basic purpose of this work is stated below.

1. To study the redox reactivities of well-characterized pterin coordination compounds which will be relevant to the reactions catalysed by the above metalloenzymes as well as new reaction pathways evolving out of such attempts.
2. To study the ability of new compounds as above, in transferring reducing equivalents to relevant reaction sites, e.g., for modeling a catalytic reaction pathway at least on a modest scale.

Abstracts of different chapters are presented below.

### **Chapter I.**

It stresses the importance of pterin chemistry, pterin-containing metalloenzymes and spells out the aims and objectives of the work.

## Chapter II.

A 6-substituted pterin ligand 2-amino-7-methyl-4-oxidopterin-6-carboxylic acid (**1**, H<sub>2</sub>L) plays a pivotal role for the present study; it is complemented by a  $\pi$ -acid ligand like 1, 10-phenanthroline (phen). Solubility of **1** in aqueous alkali permits the synthesis of a mononuclear copper(II) complex [Cu<sup>II</sup>(L)(phen)(H<sub>2</sub>O)]. 3H<sub>2</sub>O (**2**) from this medium in the crystalline form and its x-ray structural characterization [CCDC deposition no. 985054; R[F<sup>2</sup>>2 $\sigma$ (F<sup>2</sup>)] = 0.113; wR(F<sup>2</sup>) = 0.279]. Alternatively, the green crystals of **2** can also be obtained through a redox cycle involving the NaBH<sub>4</sub> reduction of **2** and the aerial reoxidation of the resulting dark-brown compound. Such crystals provide x-ray structural data of better accuracy [R[F<sup>2</sup>>2 $\sigma$ (F<sup>2</sup>)] = 0.051; wR(F<sup>2</sup>) = 0.136; Baisya, S. S.; Roy, P. S. *Acta Cryst.* **2014**, E70, 348 – 351]. The above-mentioned dark-brown compound Na<sub>2</sub>[Cu<sup>I</sup>(L')(H<sub>2</sub>O)<sub>2</sub>]- $\mu$ -(phen)-Cu<sup>I</sup>(L')(H<sub>2</sub>O)<sub>2</sub>]. 2H<sub>2</sub>O (**3**), can be isolated in the solid state, where (L')<sup>2-</sup> is the 7,8-dihydro form of (L)<sup>2-</sup>. Characterization data (elemental analysis, spectroscopic and electrochemical studies) of both **2** and **3** are presented here. Reactivity of **2** towards both imidazole and NaBH<sub>4</sub> have been followed kinetically; the relevant negative  $\Delta S^\ddagger$  values indicate the associative nature of the reaction pathways. The reaction of **2** with NaBH<sub>4</sub> turned out to be a two-step process, which can be rationalized from the thermodynamic considerations. Reaction of **3** with bromobenzene in presence of dioxygen has been followed both kinetically and stoichiometrically; isolation and characterization of 4-bromophenol as a product of this reaction, point towards aromatic ring activation. Attempts have been made to correlate some of the above reactivities with the electronic structures of **2** and **3**, obtained by DFT calculations. The exceptionally small band gaps ( $\Delta E = 0.22 - 0.5$  eV) between the LUMO and LUMO+1 levels of **2** and that between the HOMO - 2 and HOMO - 1 levels of

**3** respectively, are noteworthy. Such a situation is beneficial for accommodating the reducing equivalents transferred by NaBH<sub>4</sub> towards **2** leading to the formation of **3**; the latter responds to a reaction mixture consisting of bromobenzene and dioxygen or aerial oxidation, with the recovery of **2** as one of the products. This facile interconversion of **2** and **3**, is believed to be associated with the structural stability (both molecular and electronic) of **2**; the combined role of the redox non-innocent pterin ligand and the dual oxidation states (II, I) of the copper ion, in this process cannot be ruled out.

### Chapter III.

A new mixed ligand cobalt(II) complex of the title ligands has been synthesized and characterized using elemental analysis, ESIMS and x-ray structural data as well as different physico-chemical studies. X-ray data of this compound [Co(L)(phen)(H<sub>2</sub>O)].3H<sub>2</sub>O reveals tridentate pterin coordination towards a mononuclear Co(II) atom. The neutral bidentate ancillary ligand [1, 10-phenanthroline (phen)] and the aqua group complete the distorted octahedron around the metal center. Near perpendicular disposition of the two chelate rings involving pterin and phen, respectively is indicated. The crystal forces are further augmented by two types of  $\pi$ - $\pi$  stacking involving the pterin ring and phen. The cyclic voltamogram is characterized by several irreversible reduction peaks (-0.6, -1.1V, -1.3V and -1.6V respectively) of which the one at -0.6 V can be assigned to a metal-centered reduction process, e.g. Co (II)  $\rightarrow$  Co(I). The group transfer reaction involving replacement of the aquo group of this complex by imidazole has been followed kinetically, giving a  $k_{\text{obs}}$  value of  $2.6 \times 10^{-2} \text{ s}^{-1}$  and  $\Delta S^\ddagger = -256.0 \text{ J mol}^{-1} \text{ deg}^{-1}$  respectively; the negative  $\Delta S^\ddagger$  value indicates an associative pathway. Reactivity of this Co(II) complex towards NaBH<sub>4</sub> as well as that of the NaBH<sub>4</sub> reduction product towards bromobenzene have been followed spectrophotometrically in presence of O<sub>2</sub>; activation of the aromatic ring of

bromobenzene towards hydroxylation could be inferred from the associated stoichiometric studies. Gaussian DFT calculations throw lights on the frontier orbital energies as well as their percentage compositions and help to rationalize the above reaction.

#### Chapter IV.

A 6-substituted pterin ligand 7-methylpterin-6-carboxylic acid ( $H_2L$ ) plays a pivotal role for the present study; it is complemented by a typical  $\sigma$ - donor ancillary ligand like 1,2-diaminoethane(en). Solubility of  $H_2L$  in aqueous alkali permits the synthesis of a mononuclear nickel(II) complex  $[Ni^{II}(L)(en)(H_2O)] \cdot 2H_2O$  (**1**) from this medium in the crystalline form and its x-ray structural characterization. Again, the use of imidazole (Im) as an additional supporting ligand, permits the synthesis and x-ray structural characterization of another new complex  $[Ni(L)(en)(Im)] \cdot 2H_2O$  (**2**). Their microanalytical, spectroscopic, magnetic susceptibility, cyclic voltammetric and reactivity data are quite valuable for characterization purpose. Both of them are chiral; their longer wavelength (755 -769 nm) positive cotton effect may be correlated with the  $\delta$ -conformation of the 'en' chelate ring. Reactivity of **1** towards imidazole (Im) is characterized by substrate saturation kinetics as well as a negative  $\Delta S^\ddagger$  value ( $-178.5 \text{ J mol}^{-1} \text{ deg}^{-1}$ ), indicating an associative pathway. The  $\mu_{\text{eff}}$  values (BM) are consistent with the presence of Ni(II) centres in these complexes, while cyclic voltammetric data point towards a metal-centred  $[Ni(II) \rightarrow Ni(I)]$  reduction process around -0.7 V. Their response towards redox reagents is almost unique. While the reactivity of **1** towards  $NaBH_4$  is characterized by a substrate saturation process [ $k_{\text{obs}} = 9.0 \times 10^{-3} \text{ s}^{-1}$ ;  $\Delta S^\ddagger = -186.0 \text{ J mol}^{-1} \text{ deg}^{-1}$ ], that of **2** is an one-step process with three isosbestic points. The corresponding  $NaBH_4$  reduced complexes [**1R** and **2R**] could be isolated in the solid state as dark-colored, hygroscopic compounds and characterized to

be Ni(I) complexes with 7, 8-dihydro form of the pterin ligand residue. **1R** and **2R** respond differently towards a reaction mixture of bromobenzene/O<sub>2</sub>; reaction profile of the latter is characterized by two isosbestic points. Their  $k_{\text{obs}}$  and  $\Delta S^\ddagger$  values are in the range  $1.4 \times 10^{-2}$  to  $8.8 \times 10^{-3} \text{ s}^{-1}$  and  $-191.6$  to  $-178.0 \text{ J mol}^{-1} \text{ deg}^{-1}$ , respectively, consistent with a group transfer process, involving associative pathway. Stoichiometric studies could establish the isolation of 4-bromophenol in each case, indicating activation of the aromatic ring. The above reactivity data highlight the change over in reaction profile brought about by substituting the aquo group of **1** with an imidazole group in **2**, that is, the fine tuning of both metal and pterin-centred redox reactivities. No less interesting is the oxidation of **2R** by K<sub>3</sub>[Fe(CN)<sub>6</sub>], where the relatively better resolved reaction profile is marked by three isosbestic points [ $k_{\text{obs}} = 3.6 \times 10^{-2}$ ;  $\Delta S^\ddagger = -184.0 \text{ J mol}^{-1} \text{ deg}^{-1}$ ]. The above ability of facile reactions with either a reducing agent (NaBH<sub>4</sub>) or an oxidizing agent [bromobenzene/O<sub>2</sub> mixture or K<sub>3</sub>[Fe(CN)<sub>6</sub>]], may be considered as redox amphoteric behavior; electronic structures (DFT) provide with the necessary frame work for rationalizing this property.

## Chapter V.

Two new nickel(II) complexes having the identical chemical composition [Ni(L)(pn)(H<sub>2</sub>O)] · 5H<sub>2</sub>O have been synthesized and characterized, where L<sup>2-</sup> is the anion of 7-methylpterin-6-carboxylic acid and ‘pn’ represents R-(+)-pn or S-(-)-pn. Circular dichroism spectroscopy establish their chiral nature which can be traced to the conformation of their ‘pn’ chelate rings. Reactivities of these two complex have been studied using both group and group/electron transfer reagents. For group and group/electron transfer reagents (imidazole, NaBH<sub>4</sub>, bromobenzene/O<sub>2</sub>) the  $k_{\text{obs}}$  values are of the order of  $10^{-3} \text{ s}^{-1}$ ; for an electron transfer agent like K<sub>3</sub>[Fe(CN)<sub>6</sub>], the  $k_{\text{obs}}$  value has an order of  $10^{-2} \text{ s}^{-1}$ . In all these cases, the  $\Delta S^\ddagger$  value is

negative, indicating the associative nature of such reactions. The reaction profiles of these two chiral complexes towards each of the above reagents, are different highlighting the conformational control of the 'pn' chelate ring in such cases. The small band gaps between some of the frontier orbitals of these complexes, are partly responsible for such unique redox activities.

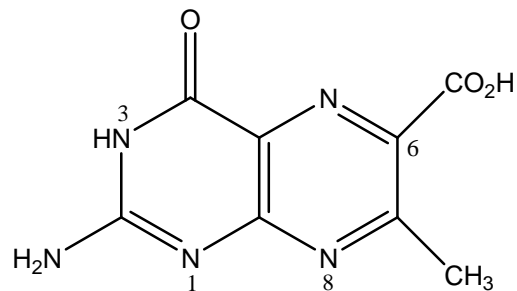
## Chapter VI.

Four new mononuclear mixed ligand complexes  $[M(L)(B)(H_2O)] \cdot xH_2O$  [ $M = Co(II), Ni(II), Cu(II)$  and  $Zn(II)$ ;  $B = bipy, phen$ ;  $x = 2$  or  $3$ ] have been synthesized using 7-methylpterin-6-carboxylic acid ( $H_2L$ ). They have been characterized by elemental analysis, electrospray ionization mass spectrometry, different spectroscopic techniques and cyclic voltammetry. For the  $Zn(II)$  complex (**1**), x-ray structural data could be recorded. The DFT optimized molecular structures and related geometric parameters of all these complexes are consistent with the x-ray structural data of **1**. The EPR spectral data for **2** and **4** are of the axial type, indicating elongation along the z-axis. The UV-VIS MLCT bands are observed in the longer wavelength region, most of which could be assigned to pterin  $\rightarrow$  phen/bipy charge transfer across the metal centre, on the basis of the electronic structures.  $^1H$  NMR spectrum of **1** verify such charge transfer in terms of shielding of the phen proton signals. Redox reactivities with  $NaBH_4$  and  $K_3[Fe(CN)_6]$  further highlight the redox non-innocent property of the pterin ligand residue here.

## PREFACE

The research work embodied in this thesis entitled, “*Coordination chemistry of pteridine ligands with transition and  $d^{10}$  metals*”, has been carried out in the laboratory of Professor Parag S. Roy, Department of Chemistry, University of North Bengal. The thesis consists of six chapters, followed by concluding remarks. In Chapter I, a general introduction stresses the importance of the works reported here, along with the highlights of the available knowledge in these fields and the necessary references (indicated by superscript numbers), which are collected together at the end of this treatise. The aims and objectives of this work as described in Chapter I (Introduction), point out the scope of the present work, research goals to be achieved and the outlines of the experimental techniques used for realizing them. Chapter II and Chapter III are concerned with the investigations on two mixed ligand coordination compounds of copper(II) and cobalt (II) with a pterin ligand [H<sub>2</sub>L.1.5H<sub>2</sub>O] [Scheme-1] and 1,10-phenanthroline (phen). Chapter IV deals with the mixed ligand coordination compounds of nickel(II) and the pterin ligand [H<sub>2</sub>L.1.5H<sub>2</sub>O]; the ancillary ligand being 1,2-diaminoethane (en) . Chapter V is concerned with the study of mixed ligand coordination compounds of nickel(II) with the pterin ligand (H<sub>2</sub>L. 1.5H<sub>2</sub>O) along with optically active R-(+)-diaminopropane[R-(+)-pn]/ S(-)-diaminopropan [S(-)-pn] as ancillary ligands. Chapter VI deals with four mixed ligand complexes, e.g., of zinc(II), cobalt (II), nickel(II) and copper (II), with a pterin ligand [H<sub>2</sub>L.1.5H<sub>2</sub>O], where the ancillary ligands are 1,10-phenanthroline (phen) and 1,2-bipyridile (bipy). The highlights of observations of the entire thesis, are grouped together at the end of the thesis in the form of concluding remarks. Schematic structures of the tautomeric forms, IUPAC and trivial nomenclature of the pterin ligand (H<sub>2</sub>L) used in this thesis, along with their abbreviations, are indicated below. The ancillary ligands are also indicated here (Scheme -1 to Scheme-9).

Tables, Figures and Schemes in each chapter have been numbered using a combination of Roman and Arabic numerals; for example, the first Table of Chapter I is numbered I-1, the second Table is numbered I-2, whereas the first Table of Chapter II is numbered II -1, the second Table as II-2 and so on. In each Chapter the compounds have been assigned serial numbers (in bold letters ) and referred to them by these numbers during discussion.



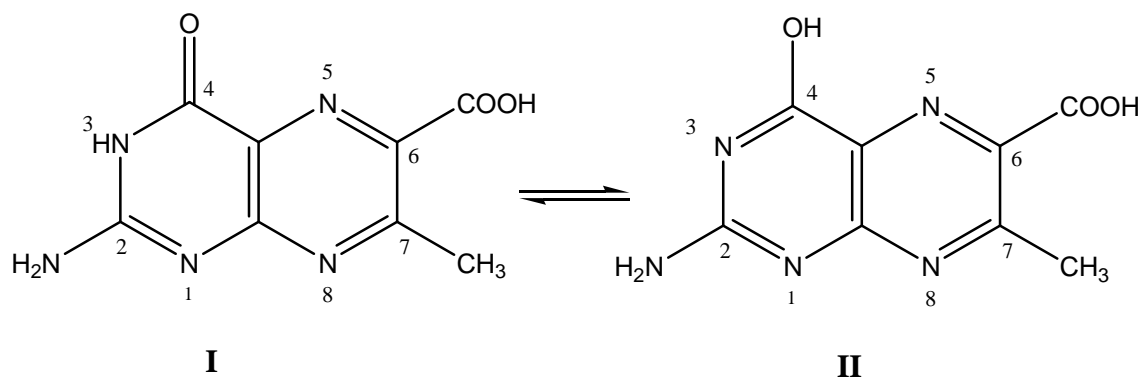
**Scheme -1**

2 - Amino -7- methyl - 4- oxidopterinidone – 6- carboxylic acid (IUPAC)

7 - Methylpterin - 6 - carboxylic acid (Trivial)

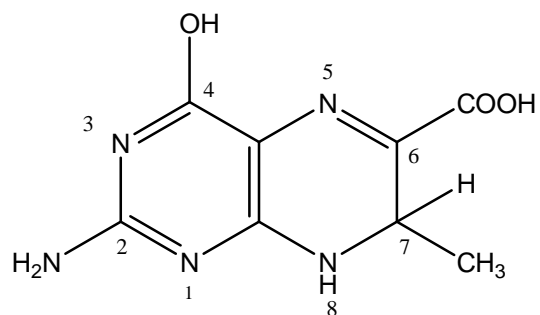
[H<sub>2</sub>L]

(abbreviation)



**I** **II**  
Tautomeric forms (amido-imidol system) of the pterin ligand [H<sub>2</sub>L]

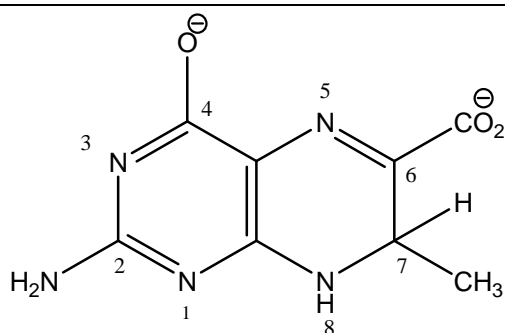
**Scheme -2**



7, 8-dihydro pterin

**Scheme-3**

---

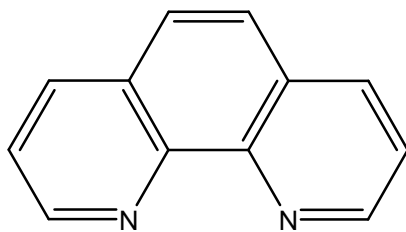


7, 8-dihydro pterin anion L' 2<sup>-</sup>

**Scheme-4**

---

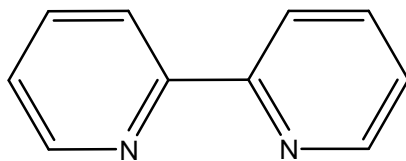
### Ancillary ligands



1, 10 - phenanthroline (Trivial)  
phen (Abbreviation)

**Scheme-5**

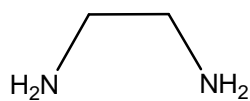
---



2, 2' - bipyridine (Trivial)  
bipy (Abbreviation)

**Scheme -6**

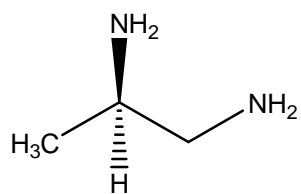
---



1,2-diaminoethane (Trivial)  
en (Abbreviation)

**Scheme-7**

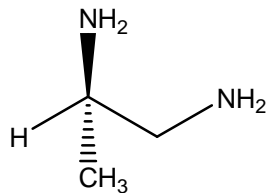
---



R-(+)- 1, 2- diaminopropane (Trivial)  
[R-(+)-pn] (Abbreviation)

**Scheme-8**

---



S-(-)- 1, 2- diaminopropane (Trivial)  
[S-(-)-pn] (Abbreviation)

### Scheme-9

---

The multiplicities of NMR spectral signals are indicated by the usual abbreviations, e.g., ‘s’ for singlet ; ‘bs’ for broad singlet, ‘ss’ for sharp singlet, ‘d’ for doublet, ‘dd’ for doublet of doublet, ‘t’ for triplet, ‘o’ for octet, ‘m’ for multiplet, ‘br’ for broad and ‘wb’ for weak broad.

The pterin ring numbering system has been used for the schemes related to the schematic structures and utilized in the discussion part. Most of the compounds have been x-ray structurally characterized, as reported here. Few of the complexes reported in Chapter II and Chapter VI could not be characterized x-ray structurally for those cases DFT optimized molecular structures are reported and the corresponding geometric parameters are incorporated in the relevant tables.

References are mentioned at the end of this thesis following standard international conventions. In spite of taking utmost care, some of the references are repeated and the author expresses regret for this.

Preliminary reports involving parts of this work have been submitted to UGC, New Delhi as annual progress reports as well as final technical report. Five papers have already been published out of the subject matters of this thesis.. Such publications on coordination compounds of pterin ligands reflect the continuing interest of this laboratory on this subject.

## TABLE OF CONTENTS

	Page No.
<b>Declaration</b>	ii
<b>Supervisor's certificate</b>	iii
<b>Dedication</b>	iv
<b>Acknowledgement</b>	v-vi
<b>Abstract</b>	vii-xii
<b>Preface</b>	xiii – xvii
<b>List of Tables</b>	xx - xxi
<b>List of Figures</b>	xxii - xxix
<b>Chapter I:</b> General Introduction, aims and objectives of the work.	1 – 56
<b>Chapter II:</b> Copper (II,I)-pterin coordination chemistry with a 6-substituted pterin ligand: synthetic, characterization and reactivity studies including utilization of molecular oxygen (O <sub>2</sub> ) for organic substrate conversion.	57-123
<b>Chapter III:</b> A new cobalt(II) complex of 7-methylpterin-6-carboxylic acid with 1, 10- phenanthroline as the ancillary ligand: synthesis, x-ray structural, physic-chemical, kinetic studies and DFT calculations.	125 - 182
<b>Chapter IV:</b> Nickel (II)-pterin coordination chemistry in presence of 1, 2-diaminoethane as the ancillary ligand: synthesis, structural and comparative reactivity studies for aqua and imidazole substituted complexes in the light of DFT.	183-264
<b>Chapter V:</b> Conformational control of pterin- and nickel- centred redox reactions of mixed ligand nickel-pterin complexes: synthesis, structural, chiroptical and reactivity studies.	265-321

<b>Chapter VI:</b> Internal redox process in metal-pterin complexes: synthesis, characterization, physico-chemical and DFT studies on new pterin complexes of $d^7 - d^{10}$ bivalent transition metal ions.	323-384
<b>Concluding Remarks</b>	385 - 392
<b>References</b>	393-406

## LIST OF TABLES

Chapter II	<b>Table II-1.</b> Crystal data of <b>2</b>
	<b>Table II-2.</b> Geometric parameters ( $\text{\AA}$ , $^\circ$ ) of <b>2</b>
	<b>Table II-3.</b> Hydrogen-bond geometry ( $\text{\AA}$ , $^\circ$ ) of <b>2</b> , Cg is the centroid of the N3/N4/C13–C16 ring.
	<b>Table II – 4.</b> Selected optimized geometric parameters ( $\text{\AA}$ , $^\circ$ ) of <b>3</b> <sup>155-160</sup> and their comparison with the related x-ray structural data of <b>2</b> .
	<b>Table II-5.</b> Electronic spectral data of the copper-pterin-phen mixed ligand complexes
	<b>Table II-6.</b> Comparison of characteristic <sup>1</sup> H NMR signals ( $\delta$ , ppm) of <b>1</b> (Scheme II-1) and <b>3</b> (Scheme II-5) along with the corresponding $\Delta$ ( $\delta$ , ppm) Values
	<b>Table II-7.</b> Cyclic voltammetry data <sup>a</sup> of the copper complexes <b>2</b> and <b>3</b> characterizing the process $\text{Cu}^{2+} + e' \rightleftharpoons \text{Cu}^+$ .
Chapter III	<b>Table III-1.</b> Crystal data and structure refinement for ( <b>2</b> ).
	<b>Table III-2.</b> Geometric parameters of ( <b>2</b> )
	<b>Table III-3.</b> Selected hydrogen bonds of <b>2</b>
	<b>Table III-4.</b> Electronic spectral data of <b>2</b> in CH <sub>3</sub> OH
Chapter IV	<b>Table IV-1.</b> Crystallographic data and structure refinement for <b>1</b> and <b>2</b> .
	<b>Table IV- 2.</b> Geometric parameters for <b>1</b> .
	<b>Table IV- 3.</b> Hydrogen Bonds Geometry for <b>1</b> .
	<b>Table IV- 4.</b> Geometric parameters for <b>2</b>
	<b>Table IV- 5</b> Hydrogen Bonds Geometry for <b>2</b> .
	<b>Table IV- 6.</b> Effect of imidazole substitution on selected bond length data.
	<b>Table IV-7.</b> Electronic spectral data of <b>1</b> in H <sub>2</sub> O and <b>2</b> in CH <sub>3</sub> OH
	<b>Table IV-8.</b> Some outer-sphere electron-exchange reactions.
Chapter V	<b>Table: V-1.</b> Crystal data and structure refinement for <b>2</b> and <b>3</b>
	<b>Table V – 2.</b> Geometric parameters of <b>2</b> .
	<b>Table V – 3.</b> Hydrogen Atom Coordinates ( $\text{\AA} \times 10^4$ ) and Isotropic Displacement Parameters ( $\text{\AA}^2 \times 10^3$ ) for <b>2</b> .
	<b>Table V – 4:</b> Geometric parameters of <b>3</b> .
	<b>Table V- 5:</b> Hydrogen Atom Coordinates ( $\text{\AA} \times 10^4$ ) and Isotropic Displacement Parameters ( $\text{\AA}^2 \times 10^3$ ) for <b>3</b> .
	<b>Table V-6.</b> Comparison of kinetic parameters for the reactions of ( <b>2</b> ), & ( <b>3</b> ) with different Substrates.
Chapter VI	<b>Table VI-1.</b> Crystallographic data and structure refinement for <b>1</b> .
	<b>Table VI-2.</b> Selected geometric parameters for <b>1</b> ( $\text{\AA}$ , $^\circ$ ).
	<b>Table VI-3.</b> Selected optimized geometric parameters ( $\text{\AA}$ , $^\circ$ ) of <b>1</b> <sup>155-160</sup> and their comparison with the related x-ray structural data (Table VI-2) <sup>17a</sup> .
	<b>Table VI-4.</b> Selected optimized geometric parameters ( $\text{\AA}$ , $^\circ$ ) of <b>2</b> <sup>155-160</sup> and their comparison with the related x-ray structural data (Table III-2) <sup>17e</sup> .
	<b>Table VI-5.</b> Selected optimized geometric parameters ( $\text{\AA}$ , $^\circ$ ) of <b>3</b> and their comparison with the x-ray structural data of a related compound (Table IV-2) <sup>17d</sup> .

	<b>Table VI-6.</b> Selected optimized geometric parameters ( $\text{\AA}, ^\circ$ ) of <b>4</b> and their comparison with the x-ray structural data of a related compound (Table II-2) <sup>17b</sup> .
	<b>Table VI-7.</b> Electronic spectral data of <b>1</b> , <b>2</b> , <b>3</b> and <b>4</b> in CH <sub>3</sub> OH.
	<b>Table VI-8.</b> <sup>1</sup> H NMR signals ( $\delta$ , ppm) of <b>1</b> , 10-phenanthroline monohydrate (ancillary ligand) and the 'phen' moiety in <b>1</b> , along with $\Delta(\delta_{\text{complex}} - \delta_{\text{ligand}})$ values (ppm).

## LIST OF FIGURES

Chapter II	<p><b>Figure II-1.</b> The blue mother liquor (a) and the green crystals (b) as per method A<sup>17b</sup>; (c) the dark-brown compound formed on treatment of <b>2</b> with equimolar amount of NaBH<sub>4</sub> in aqueous medium as described in method B<sup>17b</sup></p>
	<p><b>Figure II-2.</b> (a) The 300 MHz <sup>1</sup>H NMR spectrum of bromobenzene in CDCl<sub>3</sub> over the region δ10 – 6.5. The inset shows the expanded view of the aromatic proton signals. (b) The 300 MHz <sup>1</sup>H – <sup>1</sup>H cosy spectrum (symmetrized) of the recovered white compound (mp. 337K) (Scheme 7) in CDCl<sub>3</sub> over the region δ9.5 – 7.0. The inset shows a new signal ( - OH) at δ9.26 for this compound, as compared to the starting material bromobenzene.</p>
	<p><b>Figure II- 3.</b> The molecular structure of <b>2</b>, with the displacement ellipsoids drawn at the 30% probability level.</p>
	<p><b>Figure II-4.</b> The crystal packing diagram of the title compound, viewed along the a axis. Hydrogen bonds (dotted lines) assist the formation of a layer structure parallel to (001).</p>
	<p><b>Figure II-5.</b> A molecular packing diagram highlighting π-π stacking interactions between neighbouring phen–phen and pterin–pterin rings.</p>
	<p><b>Figure II-6.</b> (a) ESIMS data of <b>2</b>; (b) the calculated isotope pattern for the base peak at m/z = 459.2 corresponding to the fragment [M – 4H<sub>2</sub>O – 3H<sup>+</sup>]<sup>+</sup>, where M is the molecular formula of <b>2</b>.</p>
	<p><b>Figure II-7.</b> (a) ESIMS data (m/z = 463.36) of <b>2</b> recovered from a reaction mixture, as indicated in Scheme 8(b); (b) the corresponding calculated isotope pattern for the fragment [M – 4H<sub>2</sub>O]<sup>+</sup>, where M is the molecular formula of <b>2</b>.</p>
	<p><b>Figure II-8.</b> (a) ESIMS data (m/z = 705.0 and 808.9) of <b>3</b>; the corresponding calculated isotope patterns are shown in (b) and (c).</p>
	<p><b>Figure II-9.</b> IR spectra (KBr) (characteristic region) of <b>1</b> (a), <b>2</b> (b) and <b>3</b>(c), with Figures II-10 showing their total spectrum of <b>3</b>.</p>
	<p><b>Figure II-10.</b> IR spectrum (KBr) of <b>1</b></p>
	<p><b>Figure II-11.</b> IR spectrum (KBr) of <b>2</b>(a), Scheme II-3 and <b>3</b> (b), Scheme II-4 to II-6'</p>
	<p><b>Figure II-12.</b> Fluorescence emission spectrum of the pterin ligand (<b>1</b>) in aqueous NaOH solution.</p>
	<p><b>Figure II-13.</b> Fluorescence emission spectra of <b>2</b> (CH<sub>3</sub>OH, 1.4 x 10<sup>-4</sup> M), <b>3</b> (CH<sub>3</sub>OH, 1.4 x 10<sup>-4</sup> M) and the blue aqueous mother liquor from which <b>2</b> was isolated (3.4 x 10<sup>-3</sup> M).</p>
	<p><b>Figure II-14.</b> X- band EPR spectrum of <b>2</b> in DMSO at 77K with a probe frequency of 9144.756 MHz and a field centre of 303.338 mT.</p>
	<p><b>Figure II-15.</b> The 500 MHz <sup>1</sup>H NMR spectrum of <b>3</b> in DMSO-d<sub>6</sub>, with expansion of a few specific regions.</p>
<p><b>Figure II-16.</b> The 300 MHz <sup>1</sup>H NMR spectrum of <b>1</b> in NaOD/D<sub>2</sub>O(a) ; (b) and (c)</p>	

	represent selected parts of <b>3</b> (DMSO- $d_6$ ), from Figure II-14.
	<b>Figure II-17.</b> The 500 MHz 2-D NMR spectrum of <b>3</b> (DMSO- $d_6$ ); (a) represents the region $\delta 4.0 - 0.5$ ; (b) represents the phen protons along with assignments.
	<b>Figure II-18.</b> (a) The 300 MHz $^1\text{H}$ NMR spectrum of <b>1</b> , 10-phenanthroline monohydrate in DMSO- $d_6$ . The inset shows the expanded view of the spectrum as well as the corresponding 2-D $^1\text{H}$ - $^1\text{H}$ cosy spectrum (partly symmetrized). (b) The expanded 2-D $^1\text{H}$ - $^1\text{H}$ cosy spectrum (symmetrized) indicates the assignment of the phen proton signals on the basis of spin-spin interaction and arguments <sup>39,43</sup> .
	<b>Figure II-19.</b> CD spectral response in $\text{CH}_3\text{OH}$ of (a) <b>2</b> ( $9.3 \times 10^{-4} \text{M}$ ); (b) <b>3</b> ( $1.1 \times 10^{-3} \text{M}$ ).
	<b>Figure II-20.</b> Cyclic voltammetry data of <b>2</b> in DMSO (0.1M TBAP; scan rate, $100 \text{mV s}^{-1}$ ).
	<b>Figure II-21.</b> Cyclic voltammetry data of <b>3</b> in DMSO (0.1M TBAP) (a) the potential scan starts from 0 mV and terminates here; scan rate, $300 \text{mV s}^{-1}$ ; (b) the potential scan starts from $-1800 \text{mV}$ and terminates here; scan rate, $150 \text{mV s}^{-1}$ .
	<b>Figure II-22.</b> Absorption spectral changes recorded at 2 min interval during the reaction of <b>1</b> ( $1.34 \times 10^{-3} \text{M}$ ) in aqueous NaOH solution ( $1.25 \times 10^{-2} \text{M}$ ) with $\text{NaBH}_4$ ( $1.35 \times 10^{-2} \text{M}$ ) at 303K.
	<b>Figure II-23.</b> Absorption spectral changes recorded at 5 min interval during the reaction of <b>2</b> ( $8.9 \times 10^{-5} \text{M}$ ) with imidazole (Im) ( $3.6 \times 10^{-2} \text{M}$ ) in $\text{CH}_3\text{OH}$ at 318K; (a) expanded view (300 – 450nm) of the spectral changes is shown in the inset; (b) the absorbance versus time curve at 375 nm, 318K.
	<b>Figure II-24.</b> Absorption spectral changes recorded at 2 min interval during the reaction of <b>2</b> ( $8.9 \times 10^{-5} \text{M}$ ) with $\text{NaBH}_4$ ( $6.9 \times 10^{-2} \text{M}$ ) in $\text{CH}_3\text{OH}$ at 298K indicating a composite process which can be separated into two consecutive steps [inset, (a) and (b) respectively]; the step (a) is complete within 35 min; this is followed by step (b) showing three isosbestic points (at 314, 383 and 410 nm) and levelling off after another 25min. The figures (c) and (d) represent the absorbance versus time curves corresponding to steps (a) and (b) respectively.
	<b>Figure II-25.</b> Absorption spectral changes recorded at 2 min interval during the reaction of <b>1</b> , 10-phenanthroline monohydrate (phen) ( $1.25 \times 10^{-3} \text{M}$ ) in $\text{CH}_3\text{OH}$ at 303K with $\text{NaBH}_4$ ( $1.35 \times 10^{-2} \text{M}$ ).
	<b>Figure II-26.</b> Absorption spectral changes recorded at 5 min interval during the reaction of <b>3</b> ( $1.0 \times 10^{-4} \text{M}$ ) with bromobenzene ( $1.9 \times 10^{-2} \text{M}$ ) in $\text{CH}_3\text{OH}$ saturated with $\text{O}_2$ at 300K; (a) the absorption versus time curve at 372 nm, 303K.
	<b>Figure II-27.</b> Frontier molecular orbitals of <b>2</b> and <b>3</b> , showing their energies (eV) and compositions (%). The notations $L_L$ and $L_R$ represent the two pterin ligand residues of <b>3</b> (Scheme II-5).
	<b>Figure II-28.</b> A summary of the chemical and electrochemical reactivities of <b>2</b> and <b>3</b> .
Chapter III	<b>Figure III- 1</b> ORTEP diagram of ( <b>2</b> ) with atom numbering scheme (50% probability factor for the thermal ellipsoids). Lattice water molecules are omitted for clarity.
	<b>Figure III-2.</b> The crystal packing diagram of ( <b>2</b> ), viewed along the $a$ axis. Dotted lines indicate hydrogen bonds.
	<b>Figure III- 3.</b> A molecular packing diagram highlighting $\pi$ - $\pi$ stacking interactions between two neighboring pterin-pterin rings of ( <b>2</b> ).

	<b>Figure III-4(a).</b> ESIMS data of <b>(2)</b>
	<b>Figure III-4(b).</b> ESIMS data of <b>(3)</b>
	<b>Figure III-5.</b> The calculated isotope patterns for <b>(2)</b> ; (a) the base peak at $m/z = 450.9$ corresponding to the fragment $[M - 3H_2O - CO + 2H]^+$ , where M is the molecular formula of <b>2</b> ; (b) and (c) correspond to the fragments $[M - 4H_2O - CO_2 + 5H]^+$ and $[M - 3H_2O - 4H]^+$ respectively.
	<b>Figure III-6:</b> FTIR spectrum (KBr) of the pterin ligand ( $H_2L$ )( <b>1</b> ).
	<b>Figure III-7.</b> IR spectra of compound <b>2</b> on KBr pellets
	<b>Figure III-8(a)</b> Absorbance spectrum of <b>2</b> in $CH_3OH$ ( $4.15 \times 10^{-5} M$ )
	<b>Figure III-8(b)</b>
	<b>Figure III-8(c)</b>
	<b>Figure III-8(d)</b>
	<b>Figure III-9.</b> CD spectral response in $CH_3OH$ of (a) <b>2</b> ( $4.7 \times 10^{-4} M$ ).
	<b>Figure III-10.</b> Cyclic voltammetry data of <b>2</b> in DMSO ( $0.1 mM$ ; $0.1 M$ TBAP; GCE) at a scan rate, $100 mVs^{-1}$ ; the potential scan starts from $-1900 mV$ and terminates here.
	<b>Figure III-11.</b> Fluorescence emission spectra of <b>2</b> ( $CH_3OH$ , $1.4 \times 10^{-4} M$ ), <b>3</b> ( $CH_3OH$ , $4.6 \times 10^{-5} M$ ).
	<b>Figure III-12.</b> Absorption spectral changes recorded at 6 minute interval during the reaction of <b>2</b> ( $1.42 \times 10^{-5} M$ ) with imidazole (Im) ( $3.6 \times 10^{-2} M$ ) in $CH_3OH$ at 328K; (a) over the range 230- 325 nm; (b) over the range 300-425 nm.
	<b>Figure III-13.</b> Absorption spectral changes recorded at 2 min interval during the reaction of <b>2</b> ( $8.9 \times 10^{-5} M$ ) with $NaBH_4$ ( $6.9 \times 10^{-2} M$ ) in $CH_3OH$ at 298K showing three isosbestic points (at 277, 350 and 450 nm).The inset (a) shows the kinetic trace at 367 nm.
	<b>Figure III-14.</b> Absorption spectral changes recorded at 5 min interval during the reaction of <b>3</b> ( $1.0 \times 10^{-4} M$ ) with bromobenzene ( $1.9 \times 10^{-2} M$ ) in $CH_3OH$ saturated with $O_2$ at 300K.
	<b>Figure III-15.</b> Absorption spectral changes recorded at 2 min interval during the reaction of 1, 10-phenanthroline monohydrate (phen) ( $1.25 \times 10^{-3} M$ ) in $CH_3OH$ at 303K with $NaBH_4$ ( $1.35 \times 10^{-2} M$ ).
	<b>Figure III-16.</b> absorption spectral changes recorded at 2 min interval during the reaction of <b>1</b> ( $1.34 \times 10^{-3} M$ ) in aqueous $NaOH$ solution ( $1.25 \times 10^{-2} M$ ) with $NaBH_4$ ( $1.35 \times 10^{-2} M$ ) at 303K.
	<b>Figure III-17.</b> Frontier molecular orbitals of <b>2</b> and <b>3</b> , showing their energies (eV) and compositions (%).
Chapter IV	<b>Figure IV-1.</b> ORTEP diagram of the complex <b>1</b> with atom numbering scheme ( 40% probability factor for the thermal ellipsoids); lattice water molecules are omitted for clarity.
	<b>Figure IV-2.</b> ORTEP diagram of the complex <b>2</b> with atom numbering scheme( 40% probability factor for the thermal ellipsoids).
	<b>Figure IV-3:</b> Crystal packing diagram of <b>1</b> and H-bonding network viewed along c axis.
	<b>Figure.IV- 4</b> Crystal packing diagram of <b>2</b> with H-bonding network viewed along a

axis
<b>Figure IV-5.</b> (a) ESIMS data of <b>1</b> ; (b) the calculated isotope pattern for the base peak at $m/z = 338$ corresponding to the fragment $[\text{Ni}(\text{L})(\text{en})]^+$
<b>Figure IV- 6.</b> (a) ESIMS data of <b>1</b> ; (b) the calculated isotope pattern for the base peak at $m/z = 278$ corresponding to the fragment $[\text{Ni}(\text{L})]^+$ .
<b>Figure IV- 6a.</b> (a) ESIMS data of <b>1R</b> ; the calculated isotope pattern for the base peak at $m/z = 447.27$ and $397.21$ .
<b>Figure IV-7.</b> (a) ESIMS data of <b>2</b> ; (b) the calculated isotope pattern for the base peak at $m/z = 371$ corresponding to the fragment $[\text{M}-\text{Im}-3\text{H}^+]^+$ , where M is the molecular formula of <b>2</b> .
<b>Figure IV-8</b> IR spectrum of <b>1</b> (KBr pellet)
<b>Figure IV-9.</b> IR spectrum of compound <b>2</b> (KBr pellet)
<b>Figure IV-10</b> IR spectrum of (en)
<b>Figure IV-11</b> Spectrum of imidazole (Im) (KBr pellet)
<b>Figure IV-12.</b> Electronic spectra of <b>1</b> in $\text{H}_2\text{O}$ ( $1.48 \times 10^{-4} \text{ mol dm}^{-3}$ )
<b>Figure IV-13.</b> Electronic spectra of <b>2</b> in $\text{CH}_3\text{OH}$
<b>Figure IV-14.</b> CD spectra in $\text{H}_2\text{O}$ : (a) <b>1</b> ( $2.55 \times 10^{-3} \text{ M}$ ); (b) <b>2</b> ( $2.26 \times 10^{-3} \text{ M}$ ).
<b>Figure IV-15.</b> $\delta$ – conformation of the ethelenediamine chelate ring for <b>1</b> and <b>2</b> , as obtained from their x-ray structural data; other donor atoms [Figure IV-1 and IV-2] are omitted for enhancing the effect chelate ring puckering.
<b>Figure IV-16.</b> Fluorescence emission spectra of <b>1</b> ( $\text{CH}_3\text{OH}$ , $1.4 \times 10^{-4} \text{ M}$ ), <b>1R</b> ( $\text{CH}_3\text{OH}$ , $1.4 \times 10^{-4} \text{ M}$ ).
<b>Figure IV-17.</b> Fluorescence emission spectra of <b>2</b> ( $\text{CH}_3\text{OH}$ , $1.4 \times 10^{-4} \text{ M}$ ), <b>2R</b> ( $\text{CH}_3\text{OH}$ , $1.4 \times 10^{-4} \text{ M}$ ).
<b>Figure IV-18.</b> X-band EPR spectrum of <b>2</b> in DMSO at 77K.
<b>Figure IV-19.</b> Cyclic voltammogram of <b>2</b> in DMSO (0.1 mM, 0.1M TBAP, GCE, $100 \text{ mVs}^{-1}$ )
<b>Figure IV-20.</b> Cyclic voltammogram of <b>1</b> in $\text{H}_2\text{O}$ (1 mM, 0.1 M $\text{KNO}_3$ , GCE, $250 \text{ mVs}^{-1}$ ).
<b>Figure IV -21.</b> Cyclic voltammetry data of <b>1</b> in DMSO ( 1mM, 0.1M TBAP, GCE, $100 \text{ mVs}^{-1}$ ).
<b>Figure IV-22.</b> Absorption spectral changes recorded at 2 min interval during the reaction of ( <b>1</b> ) ( $5.8 \times 10^{-5} \text{ M}$ ) with imidazole (Im) ( $4.8 \times 10^{-3} \text{ M}$ ) in $\text{CH}_3\text{OH}$ at 311K. The break at 340 nm in the spectral curve is due to lamp change over inside the instrument.
<b>Figure. IV-23.</b> (a)Dependence of the rate of reaction of ( <b>1</b> ) ( $5.8 \times 10^{-5} \text{ M}$ ) with 20-100 times Im in $\text{CH}_3\text{OH}$ at 334K on Im; (b) the corresponding double reciprocal plot.
<b>Figure IV-24.</b> Absorption spectral changes recorded at 1.5 min interval during the reaction of <b>1</b> ( $5.8 \times 10^{-5} \text{ M}$ ) with $\text{NaBH}_4$ ( $4.59 \times 10^{-3} \text{ M}$ ) in $\text{CH}_3\text{OH}$ ; (a) absorption spectral changes recorded at 257 nm represent the absorbance versus time curve at 311K.
<b>Figure IV-25:</b> (a) Dependence of the rate of reaction of <b>1</b> ( $5.8 \times 10^{-5} \text{ M}$ ) and 20-100

	times of NaBH <sub>4</sub> in CH <sub>3</sub> OH at 311K on NaBH <sub>4</sub> ; (b) the corresponding double reciprocal plot.
	<b>Figure IV-26:</b> (a) Colour of the Ni(II) complex <b>1</b> : it is dark brown in the solid state but is yellow-green in aqueous solution; (b) colour of the corresponding NaBH <sub>4</sub> reduced compound, <b>1R</b> which is dark coloured.
	<b>Figure IV-27.</b> Absorption spectral changes recorded at 1.5 min interval during the reaction of <b>1R</b> (5.8x10 <sup>-5</sup> M) with bromobenzene (4.59x10 <sup>-3</sup> M) in CH <sub>3</sub> OH, saturated with O <sub>2</sub> (a) Absorption spectral changes recorded at 365 nm represent the absorbance versus time curve at 311K.
	<b>Figure IV-28.</b> Absorption spectral changes recorded at 1.5 min interval during the reaction of ( <b>2</b> ) (5.8x10 <sup>-5</sup> M) with NaBH <sub>4</sub> (4.59x10 <sup>-3</sup> M) in CH <sub>3</sub> OH at 311K.
	<b>Figure IV-29.</b> Absorption spectral changes recorded at 1 min interval during the reaction of ( <b>2R</b> ) (5.8x10 <sup>-5</sup> M) with bromobenzene (4.59x10 <sup>-3</sup> M) in CH <sub>3</sub> OH saturated with dioxygen (O <sub>2</sub> ) at 311K.
	<b>Figure IV-30.</b> Absorption spectral changes recorded at 15 second interval during the reaction of ( <b>2R</b> ) (5.8x10 <sup>-5</sup> M) with K <sub>3</sub> [Fe(CN) <sub>6</sub> ] (4.59x10 <sup>-3</sup> M) in CH <sub>3</sub> OH -H <sub>2</sub> O (3:1 v/v) at 298K.
	<b>Figure IV-31:</b> Absorption spectral data recorded at 10 min interval for exploring the reactivity between NaBH <sub>4</sub> (1.2x10 <sup>-4</sup> M) and K <sub>3</sub> [Fe(CN) <sub>6</sub> ] (1.2x10 <sup>-4</sup> M) in CH <sub>3</sub> OH-H <sub>2</sub> O (3:1 v/v) at 320 K.
	<b>Figure IV-32.</b> Frontier molecular orbitals of <b>1</b> and <b>2</b> , showing their energies (eV) and compositions (%).
Chapter V	<b>Figure V-1:-</b> ORTEP diagram of <b>2</b> probability at 50% thermal ellipsoide; lattice water molecules are omitted for clarity
	<b>Figure V-2:-</b> ORTEP diagram of <b>3</b> probability at 50% thermal ellipsoide; lattice water molecules are omitted for clarity.
	<b>Figure V-3.</b> Crystal packing diagram of <b>2</b> and H-bonding network viewed along b axis.
	<b>Figure V – 4.</b> Unit cell of the complex <b>2</b> along c axis
	<b>Figure V – 5.</b> Crystal packing diagram of <b>3</b> and H-bonding network viewed along a axis.
	<b>Figure V – 6.</b> Unit cell of the complex <b>3</b> along c axis.
	<b>Figure V-7:</b> Projections of x-ray structural data of <b>2</b> and <b>3</b> for viewing the puckering of R-(+)-pn/S-(-)-pn [pn = 1,2-diaminopropane] chelate rings respectively, from different angles. <sup>79,90</sup> For <b>2</b> [with R-(+)-pn] a δ-conformation is observed, while in case of <b>3</b> [with S-(-)-pn], the chelate ring approach planarity for achieving the equatorial disposition of the CH <sub>3</sub> group.
	<b>Figure V-8:</b> ESIMS data of <b>2</b> : (a) for the peak at m/z = 352 corresponding to the fragment [M-6H <sub>2</sub> O] <sup>+</sup> , relative abundance=65%; (b) m/z = 458 for the peak corresponding to the fragment [M-2H] <sup>+</sup> , relative abundance=20%; (c) m/z = 702 for the peak corresponding to the fragment 2[M-6H <sub>2</sub> O-H] <sup>+</sup> , relative abundance=100%. Here M is the molecular formula of <b>2</b> .
	<b>Figure V-9.</b> ESIMS data of <b>3</b> : (a) for the peak at m/z = 352 corresponding to the fragment [M-6H <sub>2</sub> O] <sup>+</sup> , relative abundance= 100%; (b) m/z = 458 for the peak corresponding to the fragment [M-2H] <sup>+</sup> , relative abundance= 83%; (c) m/z = 702 for

	<p>the peak corresponding to the fragment <math>2[M-6H_2O-H]^+</math>, relative abundance= 62%. Here M represents the formula of <b>3</b>.</p> <p><b>Figure V-10.</b> The calculated isotope patterns of <b>2</b> &amp; <b>3</b>: (a) for the peak at <math>m/z = 352</math> corresponding to the fragment <math>[M-6H_2O]^+</math>; (b) <math>m/z = 458</math> for the peak corresponding to the fragment <math>[M-2H]^+</math>; (c) <math>m/z = 702</math> for the peak corresponding to the fragment <math>2[M-6H_2O-H]^+</math>. Here M has the usual meaning.</p> <p><b>Figure V-11.</b> IR spectrum (KBr) of <math>H_2L \cdot 1.5H_2O</math> (<b>1</b>)</p> <p><b>Figure V-12.</b> IR spectrum (KBr) of <b>2</b></p> <p><b>Figure V-13.</b> IR spectrum (KBr) of <b>3</b></p> <p><b>Figure V-14.</b> Fluorescence emission spectra of <b>2</b> (<math>CH_3OH</math>, <math>1.1 \times 10^{-3} M</math>), <b>2R</b> (<math>CH_3OH</math>, <math>1.4 \times 10^{-3} M</math>).</p> <p><b>Figure V-15.</b> Fluorescence emission spectra of <b>3</b> (<math>CH_3OH</math>, <math>5.8 \times 10^{-4} M</math>), <b>3R</b> (<math>CH_3OH</math>, <math>5.8 \times 10^{-4} M</math>).</p> <p><b>Figure IV-16.</b> CD spectral data in <math>CH_3OH</math> of (a) <b>2</b> (<math>1.3 \times 10^{-3} M</math>); (b) <b>3</b> (<math>1.1 \times 10^{-3} M</math>).</p> <p><b>Figure V-17.</b> Cyclic voltammetry data of <b>2</b> in DMSO (0.1M TBAP; scan rate, <math>100 mV s^{-1}</math>).</p> <p><b>Figure V-18.</b> Cyclic voltammetry data of <b>3</b> in DMSO (0.1M TBAP; scan rate, <math>100 mV s^{-1}</math>).</p> <p><b>Figure V-19.</b> Absorption spectral changes recorded at 2 min interval during the reaction of (<b>2</b>) (<math>5.8 \times 10^{-5} M</math>) with Im (<math>4.8 \times 10^{-3} M</math>) in <math>CH_3OH</math> at 311K</p> <p><b>Figure V-20.</b> Absorption spectral changes recorded at 4.5 min interval during the reaction of (<b>3</b>) (<math>4.8 \times 10^{-5} M</math>) with Im (<math>4.68 \times 10^{-3} M</math>) in <math>CH_3OH</math> at 313K</p> <p><b>Figure V-21.</b> Absorption spectral changes recorded at 1.5 min interval during the reaction of (<b>2</b>) (<math>3.5 \times 10^{-5} M</math>) with <math>NaBH_4</math> (<math>2.35 \times 10^{-3} M</math>) in <math>CH_3OH</math></p> <p><b>Figure V-22.</b> Absorption spectral changes recorded at 1.5 min interval during the reaction of <b>3</b> (<math>4.8 \times 10^{-5} M</math>) with <math>NaBH_4</math> (<math>2.55 \times 10^{-3} M</math>) in <math>CH_3OH</math>.</p> <p><b>Figure V-23.</b> Absorption spectral changes recorded at 15 second interval during the reaction of <b>2R</b> (<math>3.5 \times 10^{-5} M</math>) with <math>K_3Fe(CN)_6</math> (<math>3.68 \times 10^{-3} M</math>) in <math>CH_3OH</math> at 298K.</p> <p><b>Figure V-24.</b> Absorption spectral changes recorded at 15 second interval during the reaction of <b>3R</b> (<math>4.8 \times 10^{-5} M</math>) with <math>K_3Fe(CN)_6</math> (<math>2.68 \times 10^{-3} M</math>) in <math>CH_3OH</math> at 298K.</p> <p><b>Figure V-25.</b> Absorption spectral changes recorded at 2 min interval at 303K during the reaction of (<b>2R</b>) (<math>3.5 \times 10^{-5} M</math>) with bromobenzene (<math>3.54 \times 10^{-3} M</math>) in <math>CH_3OH</math> saturated with <math>O_2</math>.</p> <p><b>Figure V-26.</b> Frontier molecular orbitals of <b>2</b> and <b>3</b>, showing their energies (eV) and compositions (%).</p>
Chapter VI	<p><b>Figure VI-1.</b> ORTEP diagram of the complex <b>1</b> with atom numbering scheme (40% probability factor for the thermal ellipsoids); lattice water molecules are omitted for clarity.</p> <p><b>Figure VI-2.</b> Unit cell packing diagram of <b>1</b> viewed along plane 1 0 0.</p> <p><b>Figure VI-3.</b> DFT optimized molecular structure of the compound <b>1</b>.</p> <p><b>Figure VI-4.</b> DFT optimized molecular structure of the compound <b>2</b></p> <p><b>Figure VI-5.</b> DFT optimized molecular structure of the compound <b>3</b>.</p> <p><b>Figure VI-6.</b> DFT optimized molecular structure of the compound <b>4</b>.</p>

<p><b>Figure VI-7.</b> (a) ESIMS data of <b>2</b>; (b) the calculated isotope pattern for the base peak at <math>m/z = 435</math> corresponding to the fragment <math>[\text{Co}(\text{L})(\text{bipy})]^+</math> and (c) for the peak <math>m/z = 391</math> corresponding to the fragment <math>[\text{Co}(\text{L})(\text{bipy}) - \text{CO}_2]^+</math>.</p>
<p><b>Figure VI-8.</b> (a) and (b) ESIMS data of <b>3</b>; (c) the calculated isotope pattern for the base peak at <math>m/z = 434</math> corresponds to the fragment <math>[\text{Ni}(\text{L})(\text{bipy})]^+</math> and (d) for the calculated peak <math>m/z = 390</math> corresponding the fragment <math>[\text{Ni}(\text{L})(\text{bipy}) - \text{CO}_2]^+</math>.</p>
<p><b>Figure VI-9.</b> (a) ESIMS data of <b>4</b>; (b) the calculated isotope pattern for the base peak at <math>m/z = 438.9</math> corresponding to the fragment <math>[\text{Cu}(\text{L})(\text{bipy})]^+</math>.</p>
<p><b>Figure VI-10.</b> IR spectrum of compound <b>1</b> (KBr pellet).</p>
<p><b>Figure VI-11.</b> IR spectrum of compound <b>2</b> (KBr pellet).</p>
<p><b>Figure VI-12.</b> IR spectrum of compound <b>3</b> (KBr pellet).</p>
<p><b>Figure VI-13.</b> IR spectrum of compound <b>4</b> (KBr pellet).</p>
<p><b>Figure VI-14.</b> Electronic spectra of <b>1</b> in <math>\text{H}_2\text{O}</math> (<math>1.58 \times 10^{-5} \text{ mol dm}^{-3}</math>).</p>
<p><b>Figure VI-15.</b> Electronic spectra of <b>2</b> in DMSO (<math>0.62 \times 10^{-4} \text{ mol dm}^{-3}</math>).</p>
<p><b>Figure VI-16.</b> Electronic spectra of <b>3</b> in DMSO (<math>3.6 \times 10^{-5} \text{ mol dm}^{-3}</math>).</p>
<p><b>Figure VI-17.</b> Electronic spectra of <b>4</b> in <math>\text{H}_2\text{O}</math> (<math>2.78 \times 10^{-5} \text{ mol dm}^{-3}</math>).</p>
<p><b>Figure VI-18.</b> Fluorescence emission spectra of <b>2</b> in DMSO.</p>
<p><b>Figure VI-19.</b> Fluorescence emission spectra of <b>3</b> in DMSO.</p>
<p><b>Figure VI-20.</b> Fluorescence emission spectra of <b>4</b> and <b>4R</b> in <math>\text{H}_2\text{O}</math>.</p>
<p><b>Figure VI-21.</b> X-band EPR spectrum of <b>2</b> in DMSO at 77K versus TCNE marker. The lower curve is a repetition of the upper one, showing the scan result on the higher field (H) side. This spectrum has been recorded by SAIF, IIT Bombay, using a Varian E-112 ESR spectrometer.</p>
<p><b>Figure VI-22.</b> X-band EPR spectrum of <b>4</b> in DMSO at 77K. This spectrum has been recorded by SAIF, IIT Bombay using a Jeol JES-FA200 ESR spectrometer.</p>
<p><b>Figure VI-23.</b> 300MHz <math>^1\text{H}</math> NMR spectrum of <b>1</b> in DMSO-<math>d_6</math>. The expanded regions are shown in the inset. Expansion of the region <math>\delta 2.5-0.7</math> is shown in Figure VI-24. Figure VI-25 shows the corresponding 2D NMR spectrum.</p>
<p><b>Figure VI-24.</b> 300 MHz <math>^1\text{H}</math> NMR spectrum of <b>1</b> in DMSO-<math>d_6</math>. Expansion of the region <math>\delta 2.5-0.7</math> of Figure VI - 23 is shown pterin ligand and a coordinated DMSO molecule.</p>
<p><b>Figure VI-25.</b> 300MHz <math>^1\text{H} - ^1\text{H}</math> cosy spectrum of <b>1</b> in DMSO-<math>d_6</math>.</p>
<p><b>Figure VI -26.</b> Cyclic voltammetry data of <b>1</b> in DMSO ( 1mM, 0.1M TBAP, GCE, <math>100 \text{ mVs}^{-1}</math>).</p>
<p><b>Figure VI -27.</b> Cyclic voltammetry data of <b>2</b> in DMSO ( 1mM, 0.1M TBAP, GCE, <math>100 \text{ mVs}^{-1}</math>).</p>
<p><b>Figure VI-28.</b> Absorption spectral changes recorded at 2 min interval during the reaction of (<b>4</b>) (<math>2.76 \times 10^{-5} \text{M}</math>) with Im (<math>3.78 \times 10^{-3} \text{M}</math>) in <math>\text{CH}_3\text{OH}</math> at 300K.</p>
<p><b>Figure VI-29:</b> Absorption spectral changes recorded at 1.0 min interval during the reaction of (<b>4</b>) (<math>2.78 \times 10^{-5} \text{M}</math>) with <math>\text{NaBH}_4</math> (<math>3.56 \times 10^{-3} \text{M}</math>) in <math>\text{CH}_3\text{OH}</math>.</p>
<p><b>Figure VI-30:</b> Absorption spectral changes recorded at 20 second interval during the reaction of (<b>4R</b>) (<math>3.86 \times 10^{-5} \text{M}</math>) with <math>\text{K}_3\text{Fe}(\text{CN})_6</math> (<math>4.68 \times 10^{-3} \text{M}</math>) in <math>\text{CH}_3\text{OH}</math> at 298K.</p>
<p><b>Figure VI-31.</b> Frontier molecular orbitals of <b>1</b> and <b>2</b>, showing their energies (eV) and</p>

	compositions (%); the $ \Delta E $ (ev) values ( $\leq 0.5$ ev) are also indicated. <sup>64-66</sup>
	<b>Figure VI-32.</b> Frontier molecular orbitals of <b>3</b> and <b>4</b> , showing their energies (eV) and compositions (%); the $ \Delta E $ values ( $\leq 0.5$ ev) are also indicated. <sup>64-66</sup>

## **LIST OF APPENDICES**

- Appendix A:** List of Publications
- Appendix B:** List of Seminars/Symposium participated
- Appendix C:** Published papers

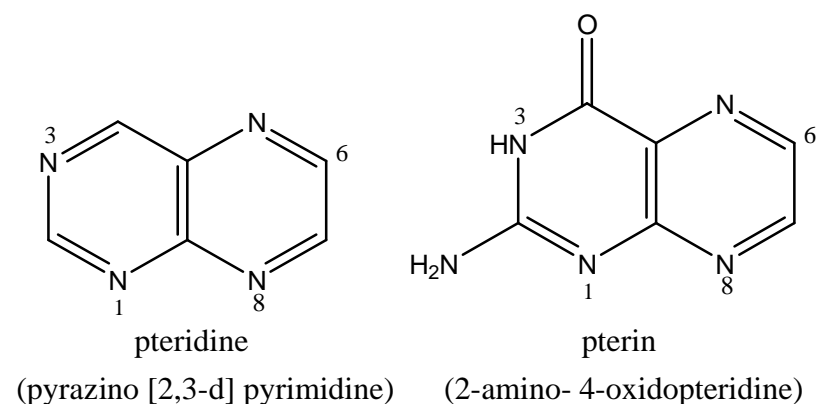
# **CHAPTER I**

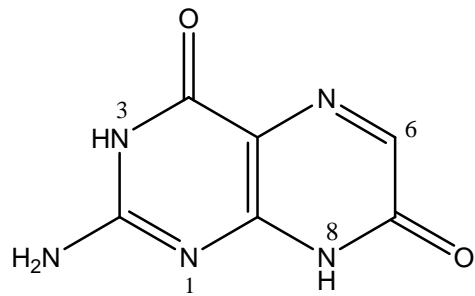
**General Introduction**  
**Aims and objectives of the work**

## General Introduction

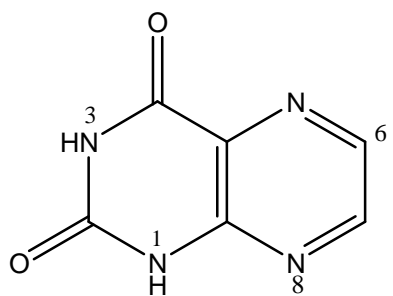
An outline about pterin-containing metalloenzymes is presented here, with the next section indicating the scope of research work on new pterin coordination compounds of cobalt, nickel, copper and zinc. The discussions include the current status of chemical approaches, the impact of X-ray structural data on enzymes, spectroscopic techniques and molecular modeling methods in giving clear descriptions of pterin coordination compounds in terms of molecular structures, electronic structures as well as correlation of structures with reactivity.

Pterins (2-amino-4-oxidopteridines) are ubiquitous in nature and their reduced forms act as essential components of different classes of metalloenzymes containing molybdenum or tungsten or iron (non heme or heme type).<sup>5-35</sup> Pterin is structurally related to guanine; isoalloxazine is another biomolecule possessing the pteridine core and this is present in flavin.<sup>5</sup>

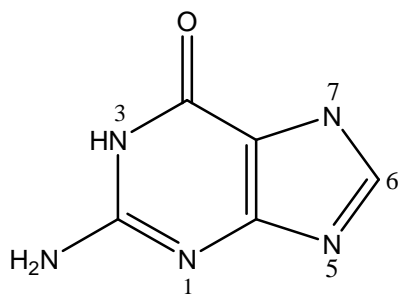




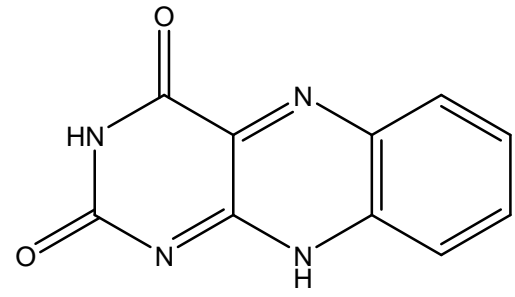
isoxanthopterin  
(2-amino-4,7-dioxidopterin)



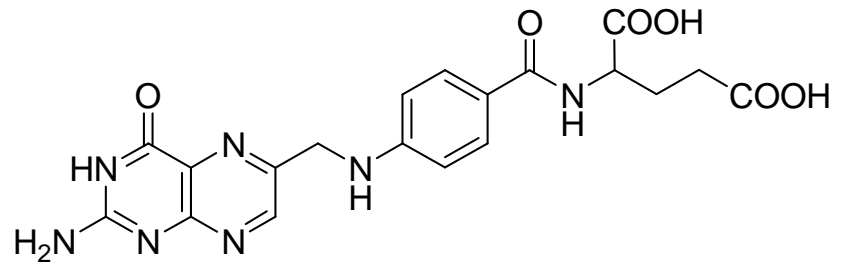
lumazine  
(2,4-dioxidopterin)



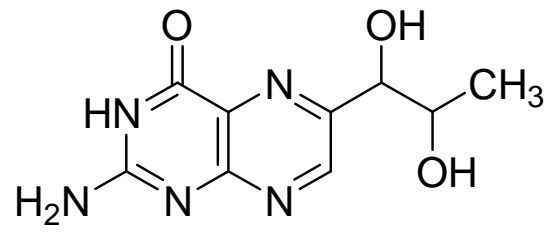
guanine



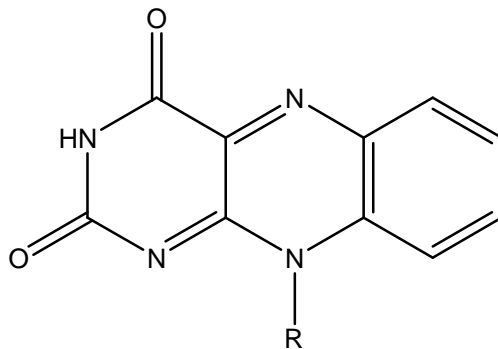
isoalloxazine



Folic acid



Biopterin



R =  $-\text{CH}_2(\text{CHOH})_3\text{CH}_2\text{OPO}_3^{2\ominus}$  in FMN

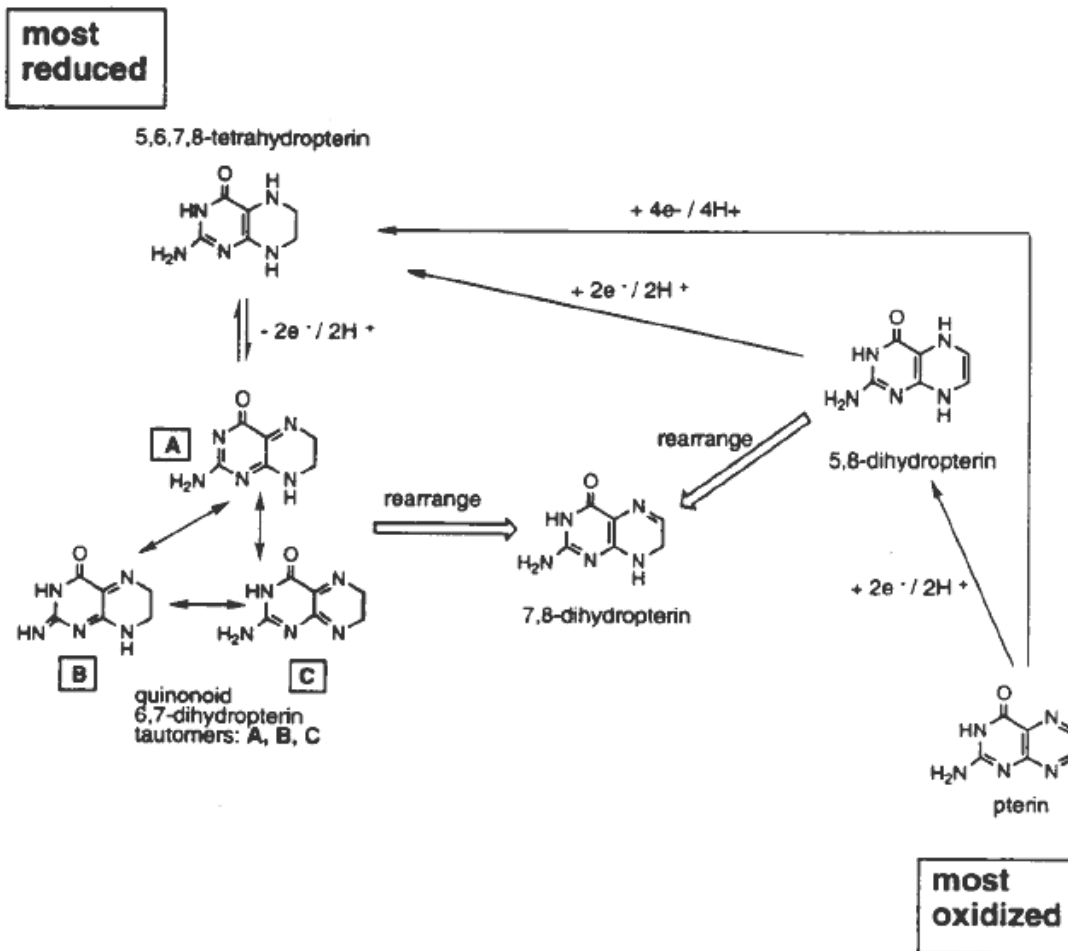
R =  $-\text{CH}_2(\text{CHOH})_3\text{CH}_2-$  ADP in FAD

Biopterin (Scheme I -11) and folic acid are two important biomolecules with the pterin core. **6-substituted pterins dominate the biological forms of pterin.** The polar C=N bonds impart reactivity to pterin. The electron deficiency of the pteridine structure is compensated by the conjugation with the electron rich groups like amine, carbonyl, etc.<sup>10</sup>

The above redox enzymes catalyze rich chemistries, ranging from oxygen atom transfer reactions using water as its source to and from a variety of biologically important substrates by oxomolybdoenzymes and tungstopterin enzymes,<sup>1-6,10,99-104,106-109,133</sup> activation of aromatic rings (of aromatic amino acids) towards hydroxylation by phenylalanine hydroxylases (PAH) containing non-heme iron<sup>7-10,52-55,105,117-121</sup> and finally heme iron- containing mammalian nitric oxide synthases (NOSs) converting L-arginine to L-citrulline and nitric oxide, an important second – messenger molecule in neutral and cardiovascular systems; it is a overall five-electron oxidation process.<sup>122-125</sup>

Pterin has the unique ability of displaying multi-electron redox reactivity; this redox non-innocent nature of pterin is reciprocated by the ability of the associated transition metal ion in displaying multiple oxidation states, in the above enzymes. Their functional aspects require that



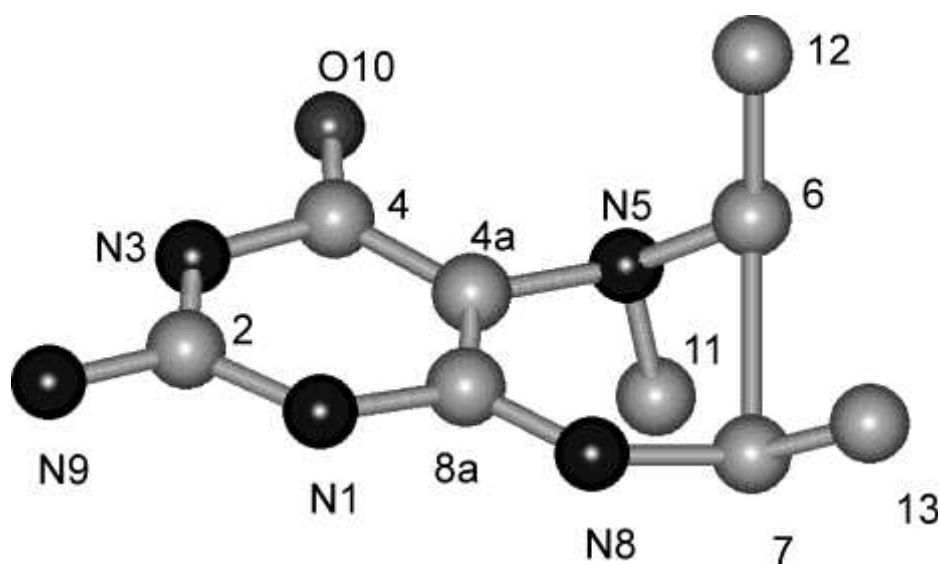


**Scheme I-1**

oxidized and fully reduced forms of pterin are also accessible. They mostly occur at the dihydro-level of reduction and are inter-related by tautomerism or proton rearrangement. The initial product of biopterin reduction is the 2-electron/2-proton product 5, 8- dihydropterin which is unstable and undergoes conversion to 7, 8- dihydropterin. The other dihydropterins such as the 2-electron/ 2-proton product of tetrahydropterin oxidation, exhibits tautomerism among different kinds of so-called quinonoid – dihydropterin (or 6, 7-dihydropterin), including one containing a C-N double bond at the 2-amino group. Like the 5, 8-dihydropterin, the 6,7-dihydropterin is also unstable and rearranges to 7,8-dihydropterin. Since this rearrangement involves H-transfer from

C6 position of the pterin ring, the quinonoid form can be isolated if C6 bears two methyl substituents to block this H6 loss.<sup>124</sup>

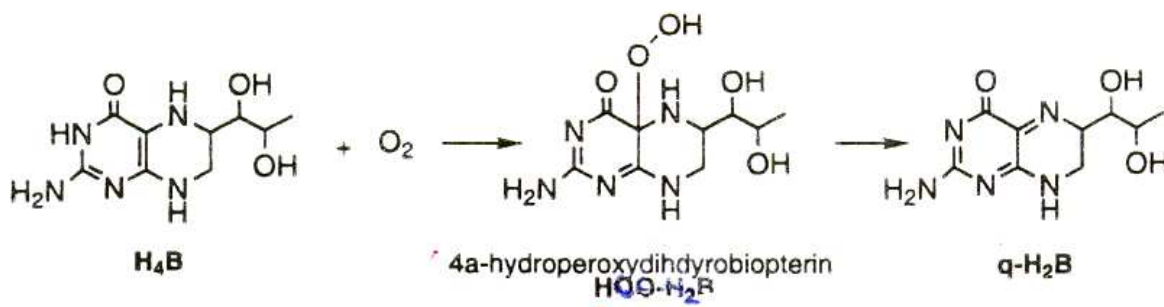
X-ray structural data on a few di- and tetrahydropterins throw light on their relative stabilities through  $\pi$ -electron delocalization. The tetrahydropyrazine ring of 5, 6, 7-trimethyl-5, 6, 7, 8-tetrahydropterin dihydrochloride-mono-hydrate, exists in a conformation in which the C6 ( $sp^3$ ) atom deviates markedly from the mean plane of the other five atoms; the pyrazine ring is planar with N8 and C7 coplanar to this ring.



On the other hand, for 6-methyl-7,8-dihydropterin-mono-hydrochloride-mono-hydrate, the 7,8-dihydropyrazine ring is essentially planar with  $\pi$ -electron delocalisation into both pyrazine and pyrimidine rings. This aspect decides the greater stability of the 7,8-dihydro form among the three above-mentioned possibilities<sup>124</sup>.

Formation of a pterin radical in the reaction of the heme domain of inducible nitric oxide synthase with oxygen, could be detected by EPR spectroscopy. Here the bound cofactor tetrahydrobiopterin ( $BH_4$ ) undergoes one-electron oxidation to the radical ( $BH_3^\bullet$ ) where the unpaired electron localizes mainly at the N5 position of the pterin ring<sup>115,122</sup>

In connection with the intimate mechanism for phenylalanine hydroxylase (PAH) catalysis, formation of a 4a-hydroperoxydihydrobiopterin has been identified involving the addition of O<sub>2</sub> at the C4a bridgehead site of pterin (Scheme I-2). This reaction has precedence

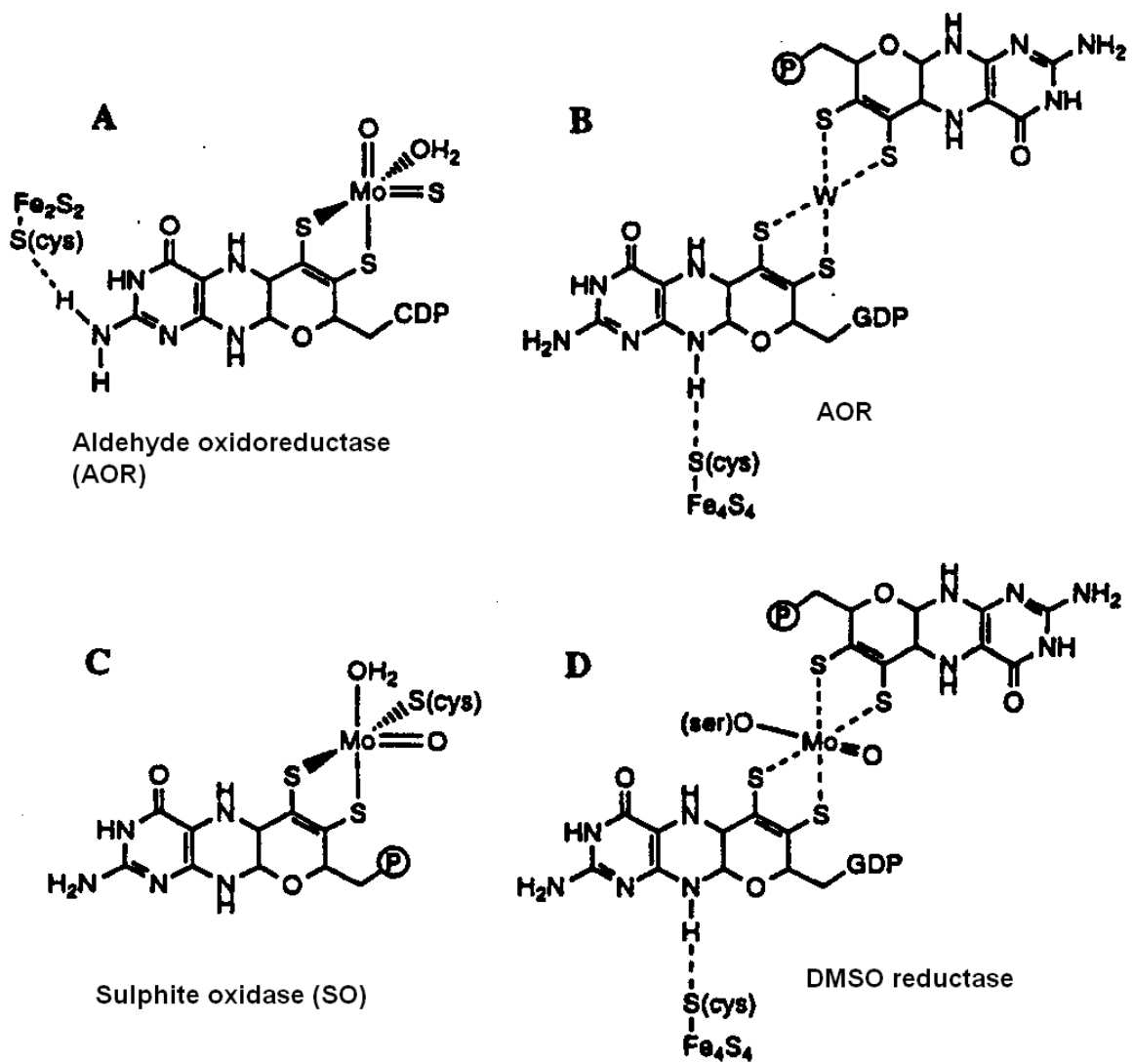


### Scheme I-2

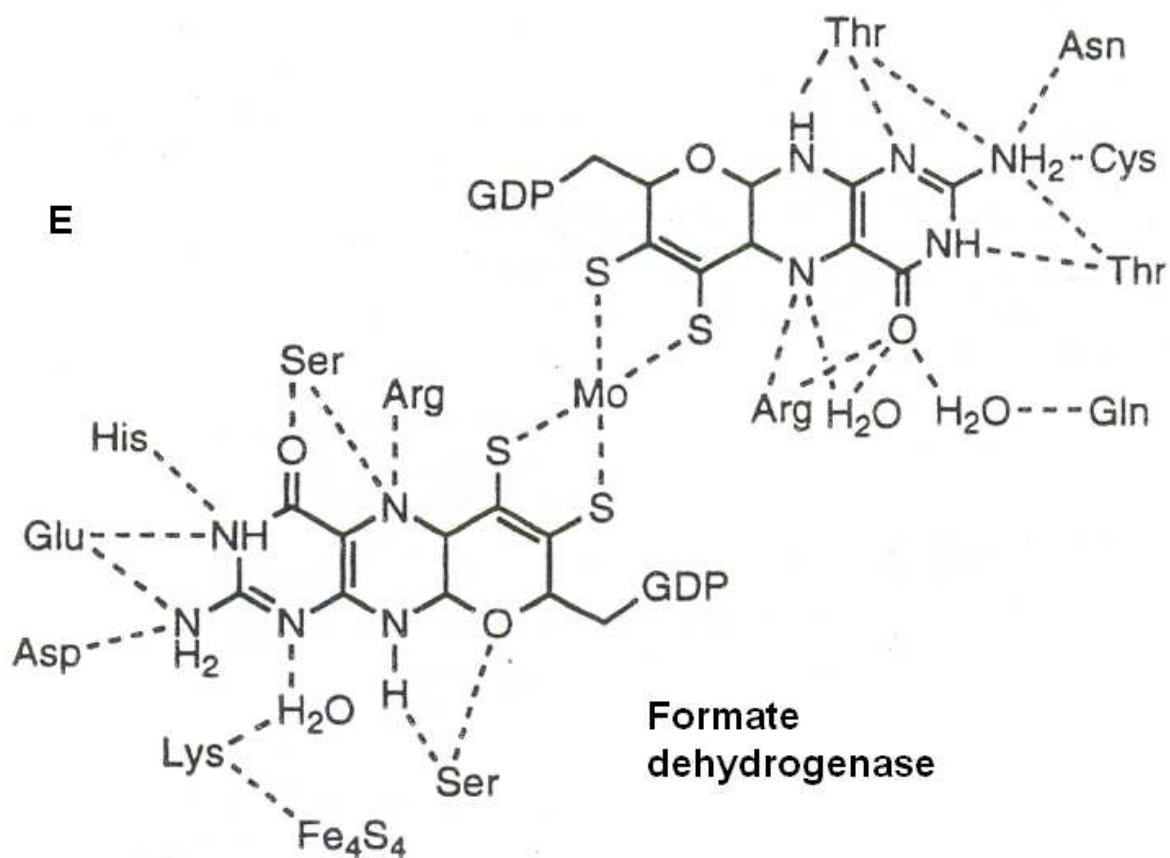
in flavin chemistry. Most likely O<sub>2</sub> activated in this manner, generates a reactive species capable of hydroxylating the unactivated aromatic rings.<sup>10</sup> Theoretical calculations in vacuo predicted that C4a of tetrahydropterin has the maximum electron density and that the adjacent nitrogen (N5) enhanced the reactivity of C4a. The low energy  $\pi^*$  orbital of biopterin and large orbital coefficient of C4a, are suggested to be responsible for the above observations<sup>124</sup>.

The various reactivities of pterin-containing enzymes originate from the regulation of redox potentials of pterin cofactors by noncovalent interactions between pterins and functional groups of protein backbones. The noncovalent interactions include multiple hydrogen bonding towards pterin cofactors at the active sites and  $\pi$ - $\pi$  interactions in the vicinity of the metal centres.<sup>126,127</sup>

The extensive hydrogen bonding interactions as revealed by x-ray crystallography, around the active sites of Mo or W-containing oxotransferases are shown below schematically (Scheme I-3 & I-4).

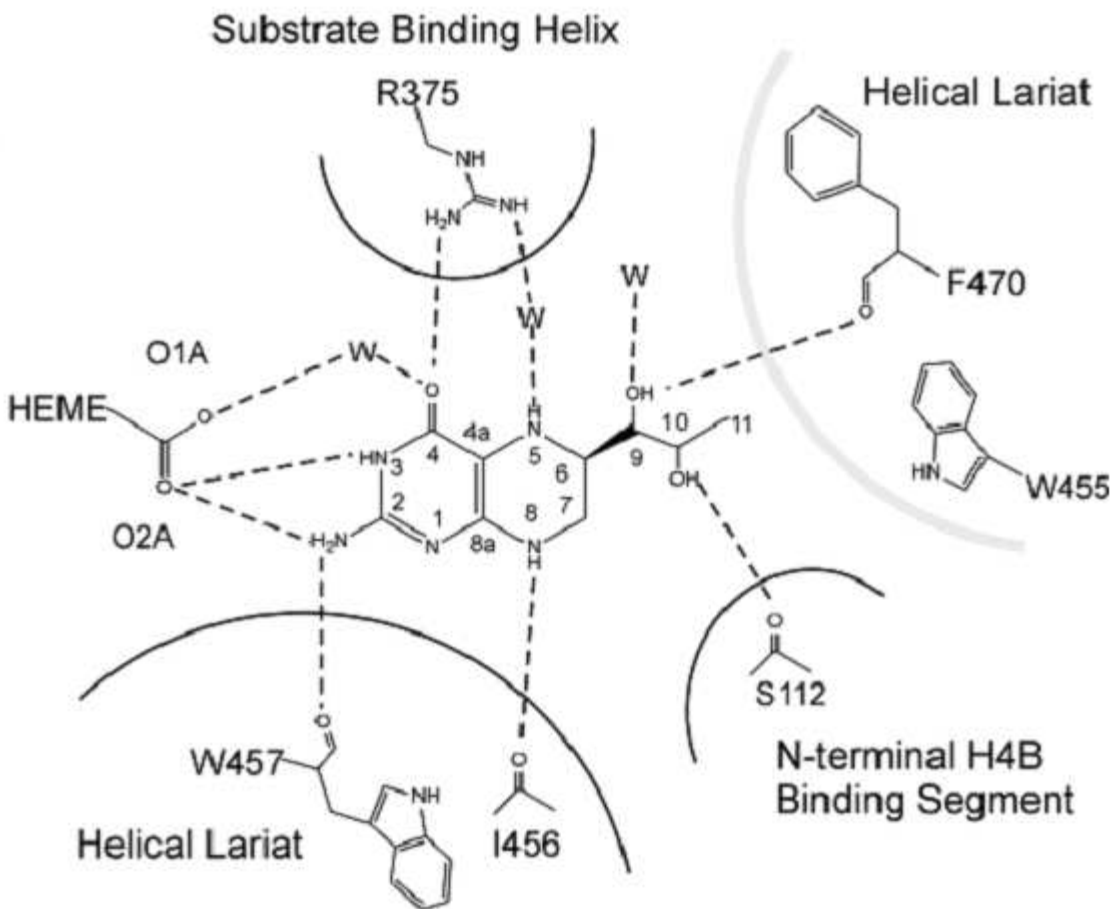


Scheme I-3



#### Scheme I-4

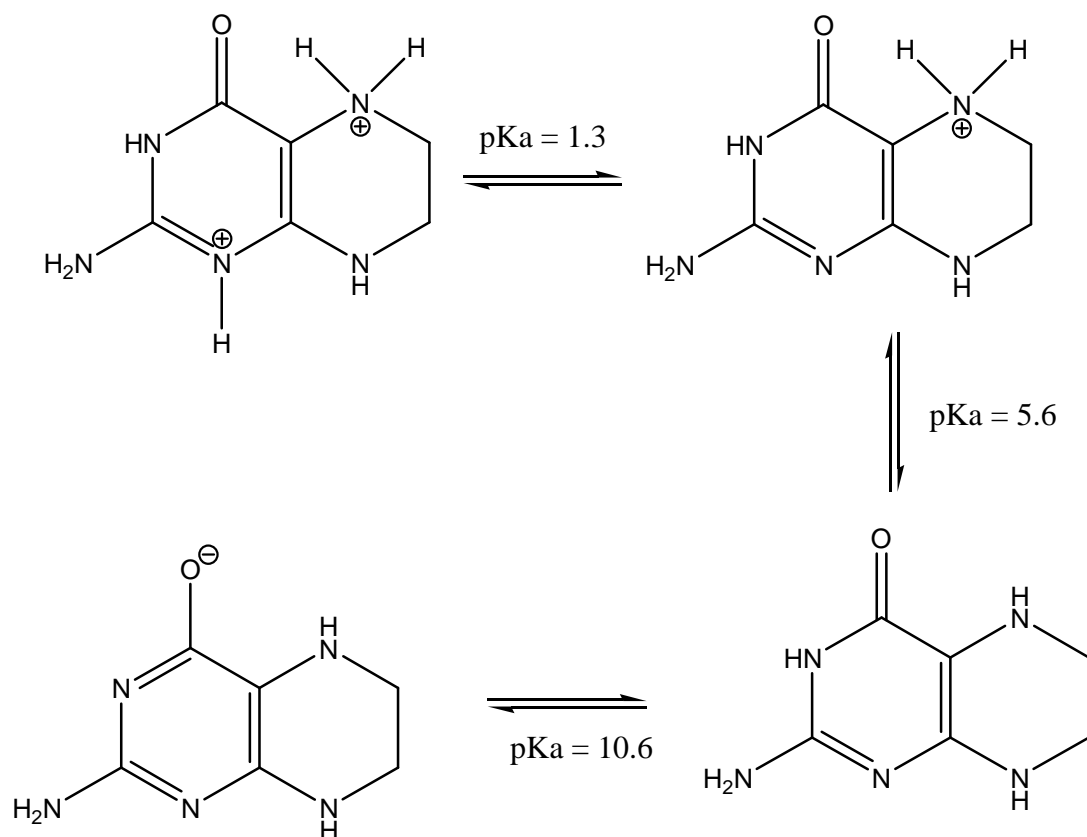
The 2-amino group and the 8-NH group are the points of the pterin structure involved in the majority of the hydrogen bonding interactions that include other electron-transfer groups such as iron-sulphur clusters as observed in oxotransferases. For nitric oxide synthases (NOSs) the tetrahydrobiopterin cofactor (BH<sub>4</sub>) uses three additional positions of the pterin ring (e.g., 3-NH, 4-O and 5-NH) for hydrogen bonding interactions. Scheme I-5 highlights this aspect.



### Scheme I-5

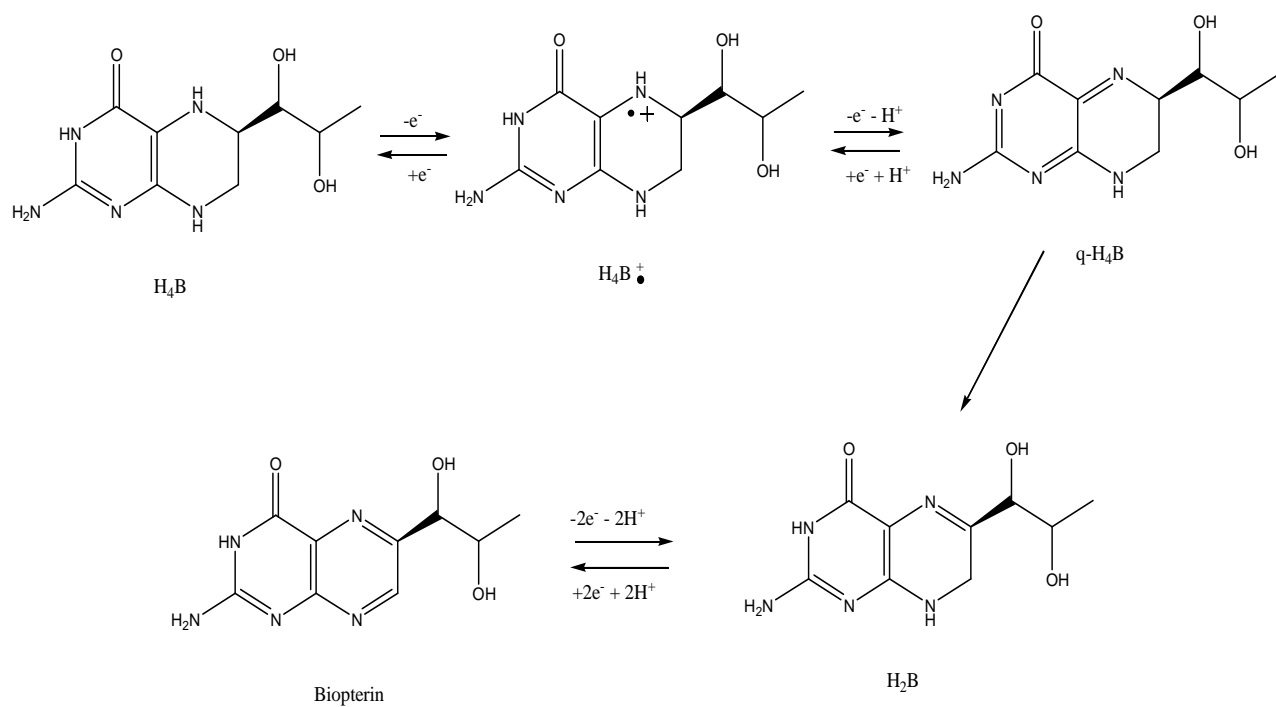
The pterin site is well designed to facilitate electronic interaction between heme and BH<sub>4</sub> by virtue of direct hydrogen bonds between a heme carboxylate and pterin N2 and N3. The same heme carboxylate group integrates BH<sub>4</sub> binding with substrate binding by also forming hydrogen bonds to the substrate amino group.<sup>115,122-125</sup> Furthermore,  $\pi$ -stacking interactions, an overall negative potential at the pterin site and interaction of an Arg residue with pterin O4 may all facilitate BH<sub>4</sub> radical formation in NOS.

Scheme I-6 shows protonation of the pterin nitrogen (amide group) and phenolate groups as a function of pH. The pK<sub>a</sub> of N1 and N5 are 1.3 and 5.6 respectively, such that at physiological pH, biopterin exists essentially as an uncharged species.



**Scheme I-6** Protonation states of pterin

Biopterin can pass through different oxidation states including a free radical one where the electron density is localized mainly on the N5 atom. As indicated in Scheme I-7, heteroatom



### Scheme I-7 Redox states of $\text{H}_4\text{B}$

protonation follows the same order in both the dihydro and tetrahydro forms of pterin. Here  $\text{BH}_2$  stands for the most stable dihydro form, i.e., 7, 8- dihydropterin due to essentially planarity of the partly reduced pyrazine ring, as elucidated earlier<sup>124</sup>. The pterin ring protonation state is a vital parameter that regulates biopterin binding and function in enzymes.

Tetrahydropterins like  $\text{BH}_4$  are labile in solution and can react with  $\text{O}_2$ , superoxide,  $\text{H}_2\text{O}_2$  etc. (Scheme I-2). Oxidations under anaerobic conditions have been studied using chemical oxidants like ferricyanide or by electrochemical means.

Evolutionary process has endowed nature with sufficient maturity for utilizing the intricate properties of pterin derivatives as above, to the optimum limit in different classes of redox metalloenzymes. Folic acid, an essential nutrient for mammalian organism, is a vital pterin derivative. Riboflavin and flavin enzymes are based on a common structural motif called lumazine; the latter possesses a pteridine core. Flavoenzyme oxidases are unique in the sense that they are the only class of such oxidases in which a metal ion is not essential for the activation of O<sub>2</sub>.<sup>124</sup>

Essential aspects of the relevant metalloenzymes are presented below.

### 1. **Oxo-transferases containing molybdenum or tungsten**

This class of enzymes catalyse hydroxylations and net oxygen atom transfer reaction (OAT) to and from a variety of biologically important substrates.<sup>1-6,10,99-104,106-109,133</sup>

Hydroxylation:



Net oxygen atom transfer:



The above reactions mostly involve two-electron redox chemistry coupled to the transfer of an oxygen atom to or from water. During the catalytic cycle the Mo/W centre cycles between VI and IV oxidation states. These redox enzymes catalyse key reactions in the metabolism of carbon, nitrogen and sulphur; while molybdenum is essential for almost every life form, tungsten is proved to be essential for microorganisms, the hyperthermophilic archaea, which thrive near 100<sup>0</sup>C (hydrothermal vents on the ocean floor). From 1995 onwards many of such enzymes have been characterized x-ray structurally. Molybdenum is available in natural waters as molybdate, exceeding in concentrations such essential trace elements as Mn, Fe, Co, Cu and Zn. This

availability and a remarkable chemical versatility make Mo a crucial component of enzymes.

Few typical examples are shown below.

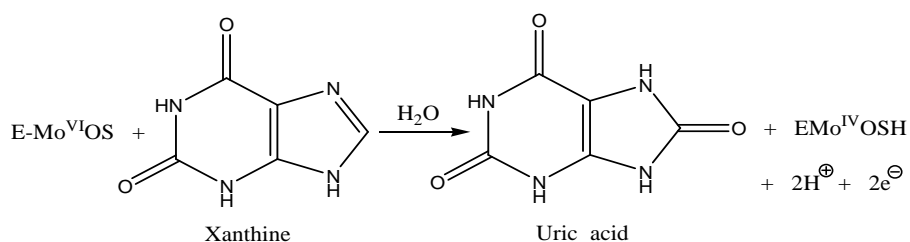
### Nitrate reductase



### Sulphite oxidase

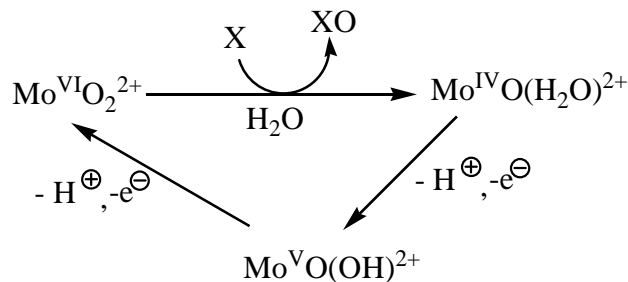


### Xanthine oxidase



E = enzyme without the metal centre

A typical enzyme cycle for net oxygen atom transfer is shown below.



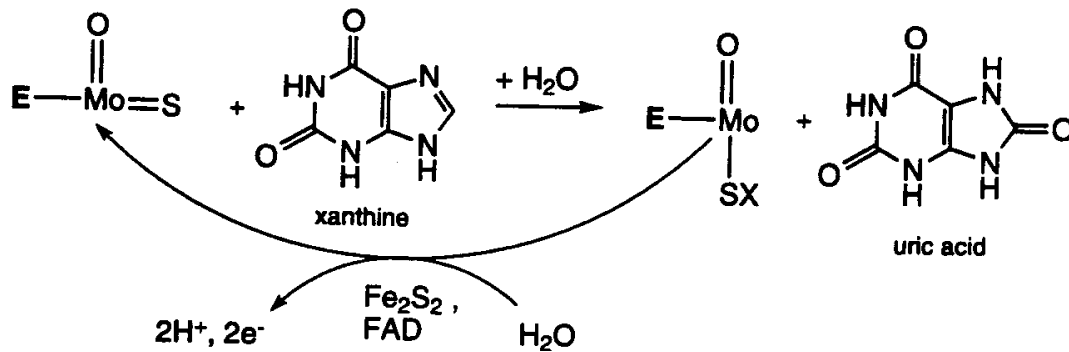
This cycle can operate in either direction. For sulphite oxidase ( $\text{X} = \text{SO}_3^{2-}$ ) it is valid as shown above; in case of nitrate reductase ( $\text{XO} = \text{NO}_3^-$ ) the cycle operates in the reverse direction. The above scheme is based on x-ray structural data of Mo- or W- containing enzymes, supported by spectroscopic (e.g., EXAFS, EPR) kinetic methods as well as computational approaches.<sup>1,2,</sup>

<sup>108,109,133</sup> The intimate catalytic mechanism involves coupled electron- proton transfer (CEPT) and the oxygen atom transferred to the substrate is derived from the solvent (e.g.,  $\text{H}_2\text{O}$ ). The

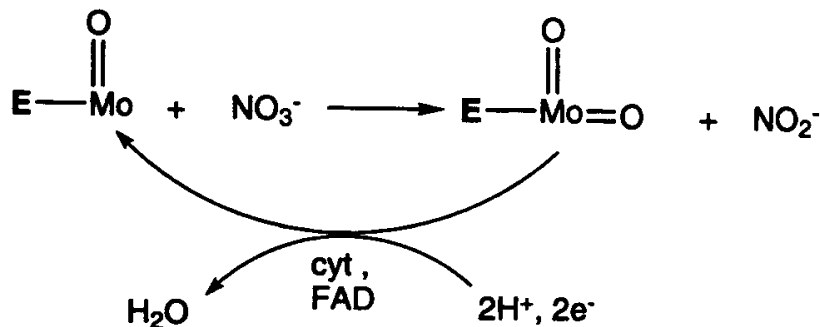
metal oxidation states (VI/V/IV) control the level of protonation of the water-based ligand ( $\text{H}_2\text{O}/\text{OH}/\text{O}^{2-}$ ).

As indicated above, both Mo and W are redox active under physiological conditions (ranging between oxidation states VI and IV); since the V oxidation state is also accessible, they can act as transducers between obligatory two-electron and one-electron redox systems; they can catalyse reactions such as hydroxylation of carbon centers (e.g., xanthine  $\rightarrow$  uric acid conversion) under more moderate conditions than are required by other systems, using  $\text{H}_2\text{O}$  as the source of the oxygen atom transferred. The oxidations of more resistant substrates, such as alkyl chains and aromatics, do not appear to be catalysed by Mo or W enzymes. Such reactions are catalysed by cytochrome P-450 and methane monooxygenase with the iron – containing aggressive active sites like  $\text{Fe}^{\text{IV}}=\text{O}$  (cyt P-450) or  $\text{Fe}_2^{\text{IV}}=\text{O}$  (methane monooxygenase) group, attacking the substrates. Such intermediates are derived from dioxygen rather than water and higher operating redox potentials are needed here.

### xanthine oxidase



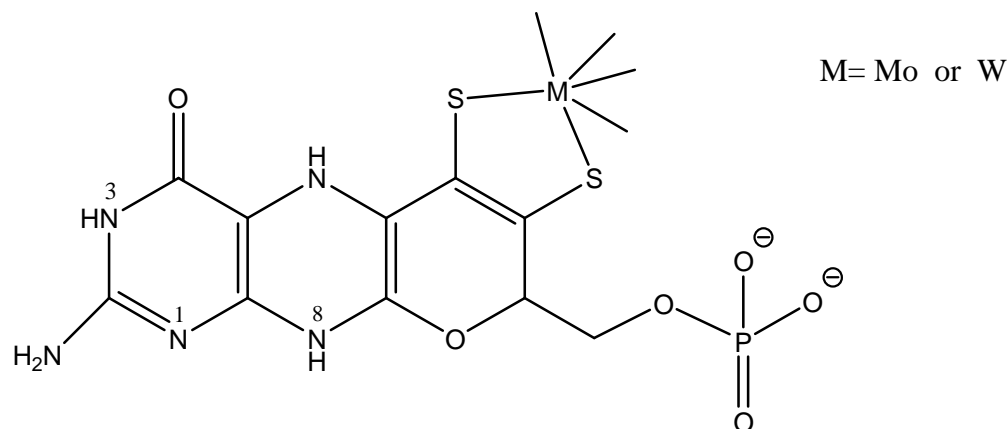
### nitrate reductase



Presence of prosthetic groups (FAD, cyt, Fe-S centres) are essential for mediating the reducing equivalents [ $2H^+$ ,  $2e^-$ ] or [ $2H$ ] involved in each enzyme turnover cycle.

The stoichiometry of the reaction  $RH + H_2O \rightarrow ROH + 2H^+ + 2e^-$  associated with the xanthine oxidase family is unique among biological systems catalyzing hydroxylation reactions in that reducing equivalent are generated rather than consumed in the course of the reaction and water rather than dioxygen is utilized as the ultimate source of the oxygen atom incorporated into the substrate.<sup>1</sup> As outlined above, the overall reaction mechanism of all such enzymes can be broken down into reductive and oxidative half- reactions of the catalytic cycle. For xanthine oxidase the reductive half-reaction is associated with the hydroxylation process, coupled with the reduction  $Mo(VI) \rightarrow Mo(IV)$ .

Protein x-ray crystallography has revealed the structures of the active sites of many of these enzymes, in each of them the active site consists of either a molybdenum or tungsten atom coordinated by two sulphur atoms of one (or two) ene-dithiolate group (Scheme I-8)

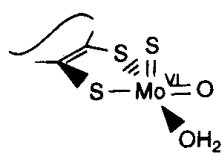


### Scheme I-8

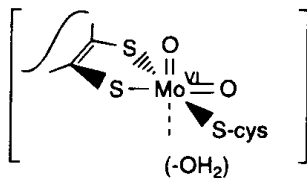
The ene-dithiolate group located on the pyran ring which is fused to the pterin, has the name pyranopterin. Schemes I-3& I-4 reveal few additional aspects of x-ray data.

The active sites of such enzymes are further differentiated from one another by the number of terminal oxo and / or sulphide groups, OH and /or H<sub>2</sub>O and by coordinated amino acid residues, e.g., a cysteine sulphur in sulphite oxidase, serine oxygen in DMSO reductase or selenocysteine selenium in formate dehydrogenase from the polypeptide backbone of the protein.<sup>104</sup>

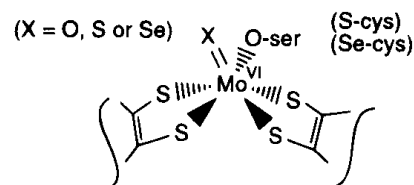
Hille has classified the oxo-molybdenum enzymes into three families based on their protein sequences and the structures of their oxidized active sites; each family is named in terms of its most prominent member (Scheme I-9).<sup>1,103,133</sup>



*The Xanthine Oxidase Family*  
(true hydroxylases)



*The Sulfite Oxidase Family*



*The DMSO Reductase Family*

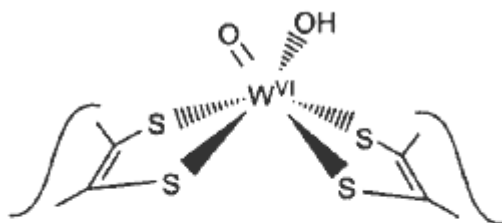
### Scheme I-9

The tungstopterin enzymes are classified into three families according to their active sites, determined by x-ray crystallography.<sup>2</sup>

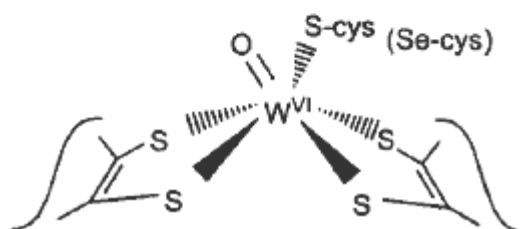
1. The aldehyde-ferredoxin oxidoreductase family (AOR).
2. The formate dehydrogenase family (FDH).
3. The acetylene hydratase family (AH)

The active site structures are shown for two cases (Scheme I-10).

*The aldehyde:ferredoxin oxidoreductase family*



*The formate dehydrogenase family*



### Scheme I-10

Presence of a relatively large number of both ion-pairs and buried atoms may contribute to the extreme thermostability of these enzymes (approx. 100°C).

A third family, exemplified by acetylene hydratase, might be similar to that of aldehyde-ferredoxin oxidoreductase.

Their functional aspects are stated below briefly.

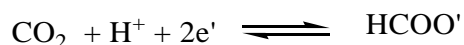
### **AOR family**



Aldehyde oxidation is a two-electron process but ferredoxin (Fd) contains a single [4Fe-4S] cluster and undergoes only a one-electron redox reaction; for maintaining electron stoichiometry one catalytic turnover requires the reduction of two molecules of Fd.

### **FDH family**

They utilise  $\text{CO}_2$  as the substrate.



Here NADPH acts as the physiological electron donor.

### **Acetylene hydratase (AH)**

The enzyme catalyses the hydration of acetylene to acetaldehyde:

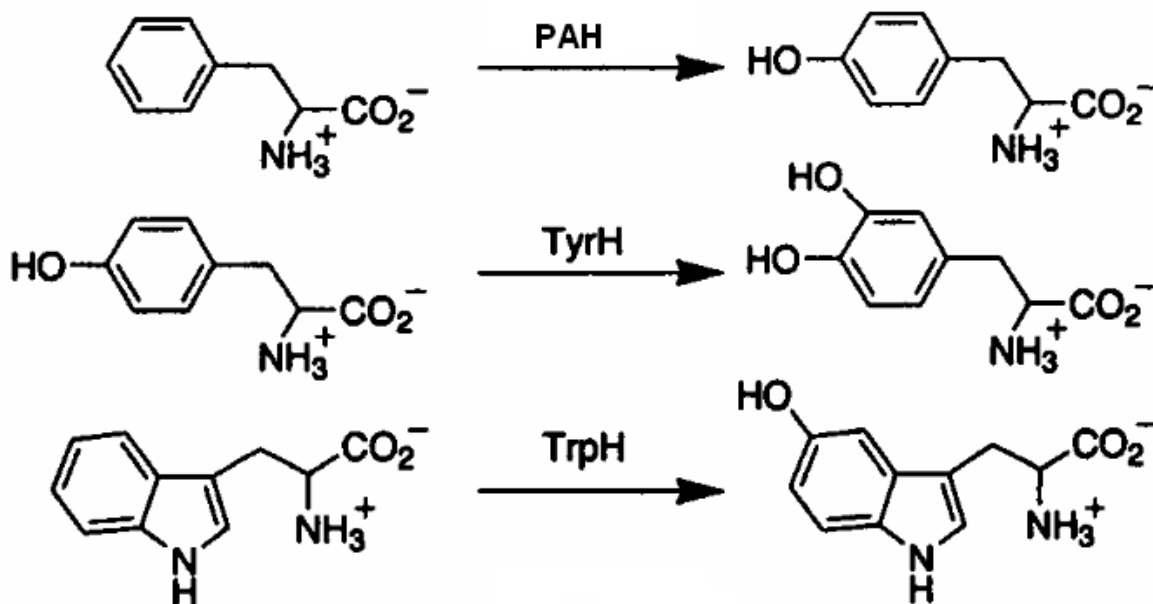


## **2. Aromatic amino acid hydroxylases**

The aromatic amino acid hydroxylases (AAHs) constitute a family of mononuclear non-heme iron(II)-containing enzymes – phenylalanine hydroxylases (PAH), tyrosine hydroxylases (TryH) and the tryptophan hydroxylase (TrpH) – which all catalyse the hydroxylation of aromatic amino acids like phenylalanine, tyrosine and tryptophan respectively (Scheme I-11).

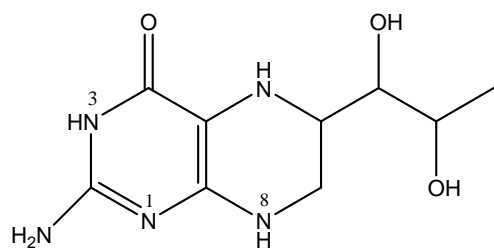
The conversion of phenylalanine to tyrosine by phenylalanine hydroxylase is believed to play an obligatory role in the catabolism of phenylalanine for energy production. One of the products of tyrosine breakdown, fumarate, can be oxidized to  $\text{CO}_2$  and water or it can lead to the formation

of glucose. Since gluconeogenesis takes place mainly in the liver, it seems appropriate that phenylalanine hydroxylase is present in highest concentration in that tissue. The only other organ capable of significant glyconeogenesis, the kidney, has also been shown to contain significant phenylalanine hydroxylase activity.<sup>139,146,147</sup>

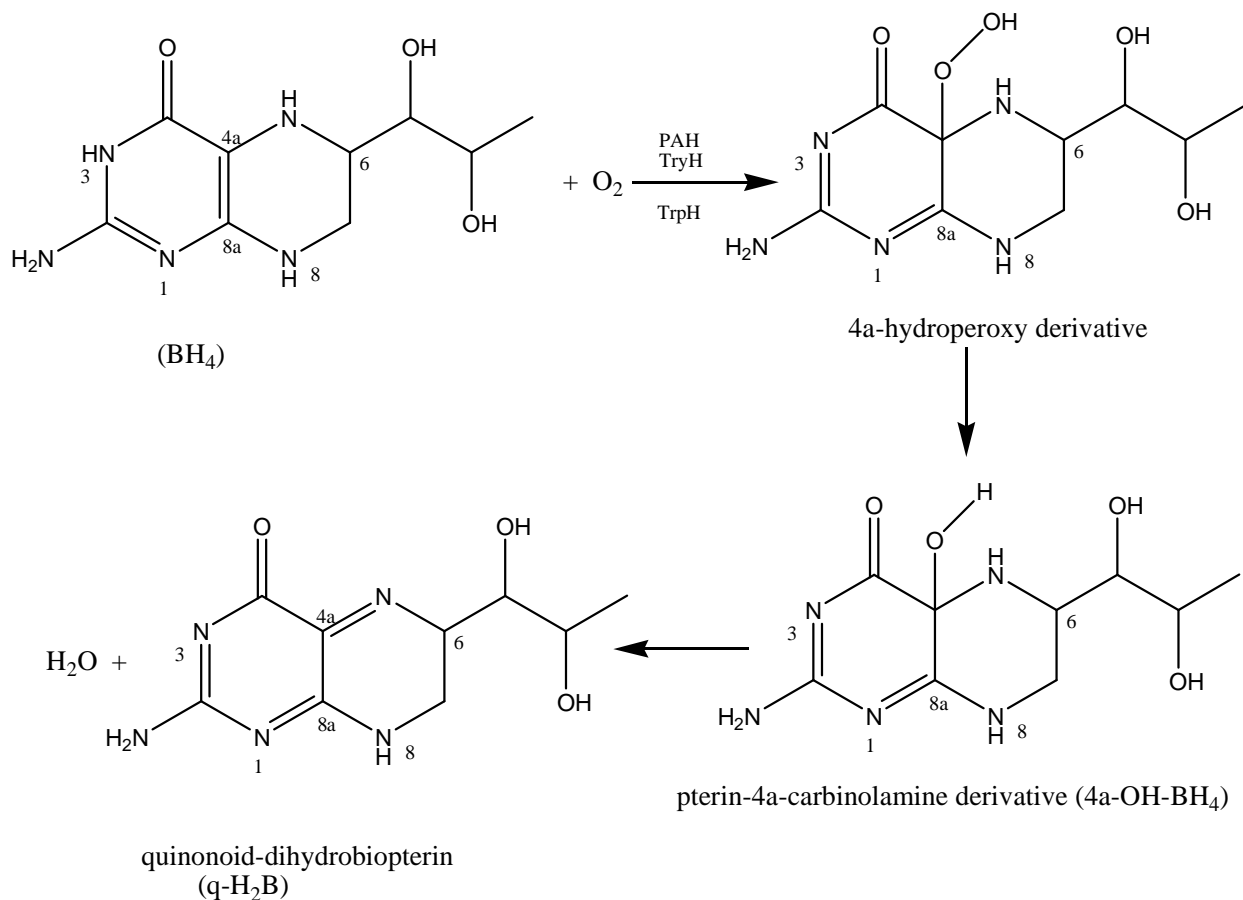


### Scheme I-11

The common features within the AAH family are the dependence on the tetrahydrobiopterin cofactor,  $\text{BH}_4$  which is oxidized to pterin-4a-carbinolamine (4a-OH- $\text{BH}_4$ ) during the catalytic cycle and the use of molecular oxygen, the atoms of which are incorporated into the amino acid and the cofactor (Scheme I-12).<sup>53,55,105,117,119-121</sup>

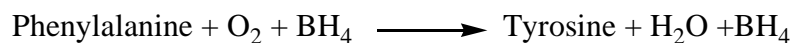


Tetrahydrobiopterin



**Scheme I-12** Role of BH<sub>4</sub> cofactor in activation/splitting of the dioxygen molecule.

One molecule of O<sub>2</sub> is consumed in the reaction; one oxygen atom is inserted as an hydroxyl group into the substrate (Scheme I-11), while the second oxygen atom is reduced to water (Scheme I-12).

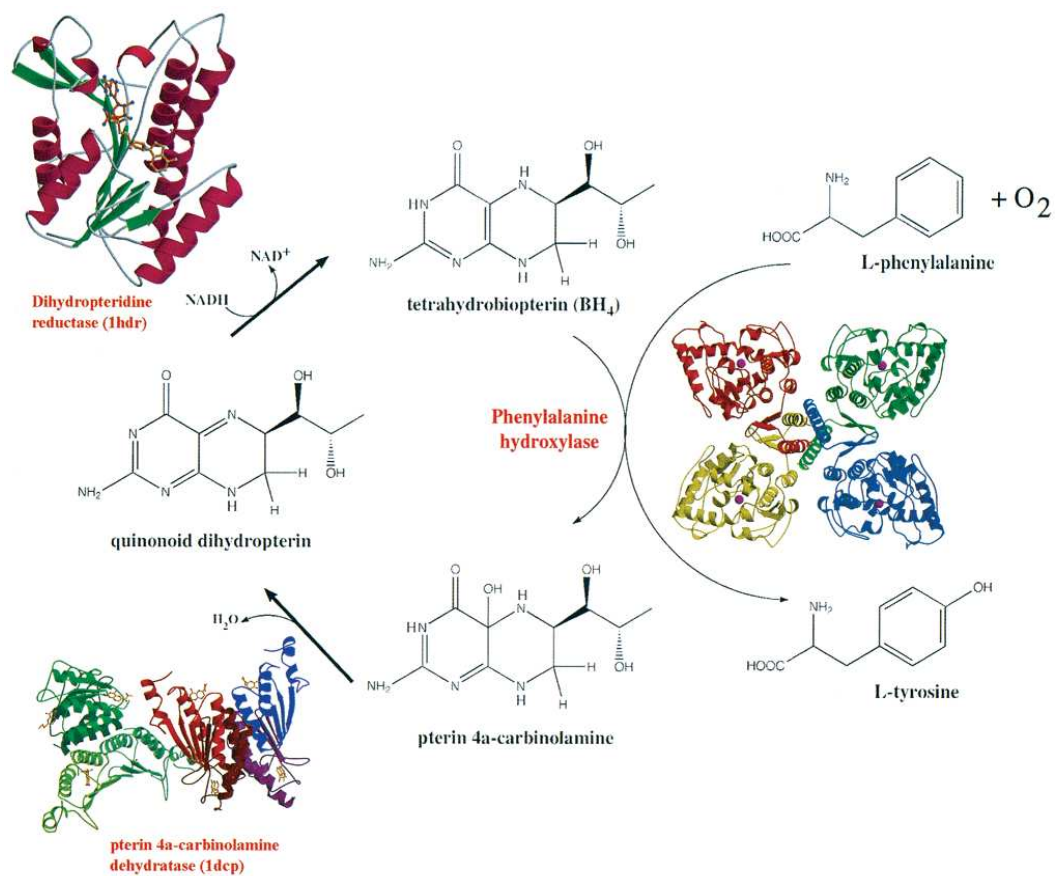


or



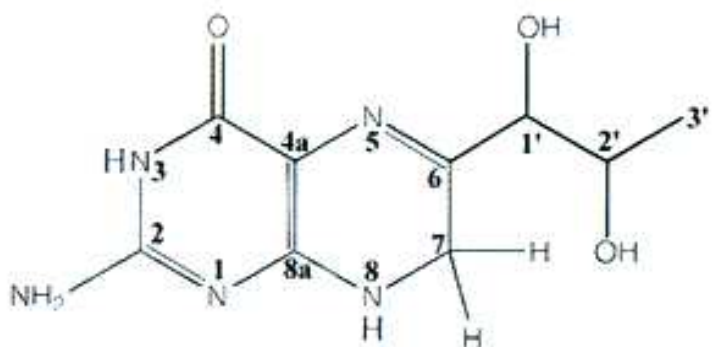
The four-electron reduction of oxygen thermodynamically drives the hydroxylation of the substrate, namely, phenylalanine (a formal two electron oxidation) in tandem with the two electron oxidation of tetrahydrobiopterin ( $\text{BH}_4$ ) to its quinonoid dihydropterin state ( $\text{q-BH}_2$ ). NADH most likely reconverts  $\text{BH}_2$  to  $\text{BH}_4$  (Scheme I-13). The mixed function oxygenase nature of the enzyme (PAH) was demonstrated by  $^{18}\text{O}$  incorporation into [ $^{18}\text{O}$ ] tyrosine and  $\text{H}_2\text{O}^{18}$ .

Although the primary product of PAH activity is the quinonoid isomer of dihydrobiopterin ( $\text{q-H}_2\text{B}$ , Scheme I-12) the cofactor isolated from rat liver, however, was 7,8-dihydrobiopterin (Scheme I-1). In the presence of the 7, 8-dihydro isomer, another enzyme (e.g., dihydrofolate reductase) was shown to be an essential component of the hydroxylation system.<sup>139,146,147</sup>



**Scheme I-13.** Reaction of phenylalanine hydroxylase (PAH) and regeneration of tetrahydropterin cofactor (BH<sub>4</sub>).<sup>53</sup>

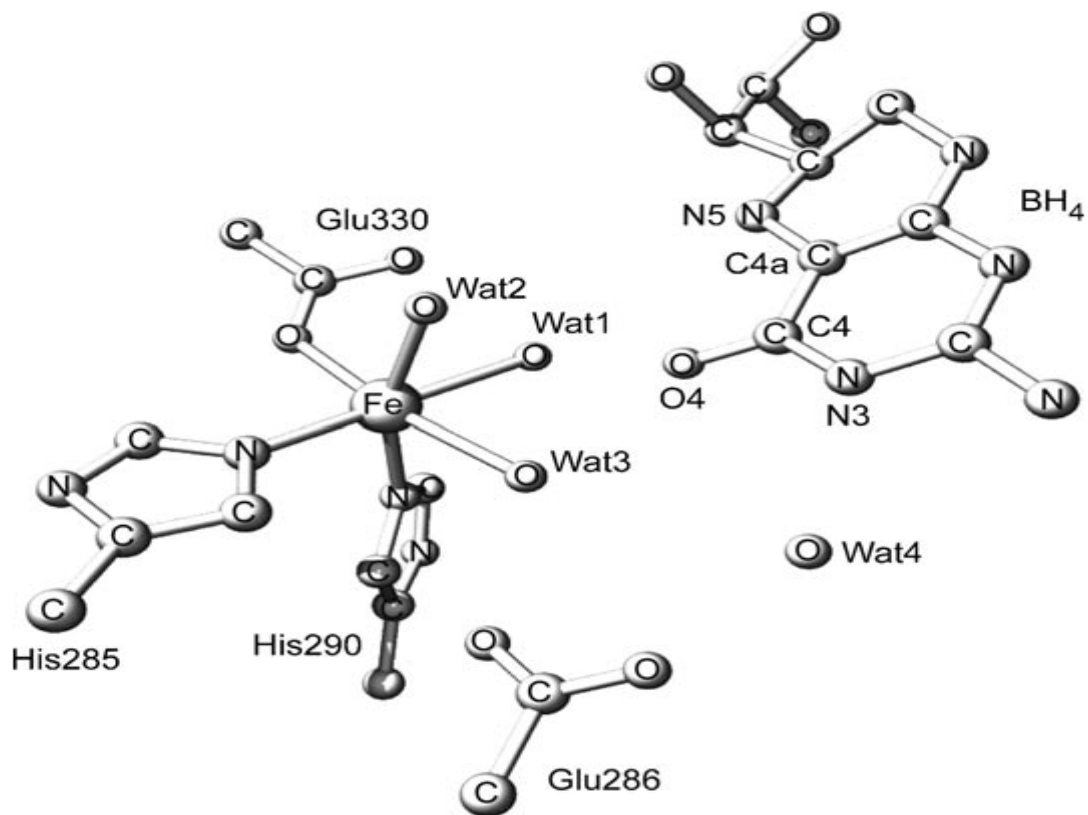
The quinonoid dihydropterin (q-BH<sub>2</sub>) can isomerise to 7, 8-dihydro-L-biopterin (BH<sub>2</sub>) (Scheme I-14), stressing the stability of the 7, 8-dihydro form among different possible dihydropterins.<sup>9,10</sup>



**7,8-dihydro-L-biopterin**

**Scheme I-14**

As an example, the x-ray crystal structure of the active iron centre in the catalytic domain of the human (h) PAH in a binary complex with the cofactor  $\text{BH}_4$ , e.g., ( $\text{hPAH-Fe}^{\text{II}}\text{-BH}_4$ ) is shown in Scheme I-15. In the binary complex, two His, one Glu and three water molecules



**Scheme I-15** The x-ray crystal structure of the active iron centre in the catalytic domain of the hPAH – Fe<sup>II</sup> – BH<sub>4</sub> binary complex.<sup>120</sup>

coordinate to the metal, which results in a hexacoordinate complex with essentially octahedral geometry. The cofactor (BH<sub>4</sub>) is located in the second coordination sphere of iron<sup>120</sup>.

### 3. Nitric oxide syntheses (NOSs)

Mammalian nitric oxide syntheses (NOSs) require the tetrahydrobiopterin (BH<sub>4</sub> Scheme I-7) to convert L-arginine to L-citrulline and nitric oxide, an important second-messenger molecule in neutral and cardiovascular systems.<sup>122-125</sup> NOS catalyses the reaction:

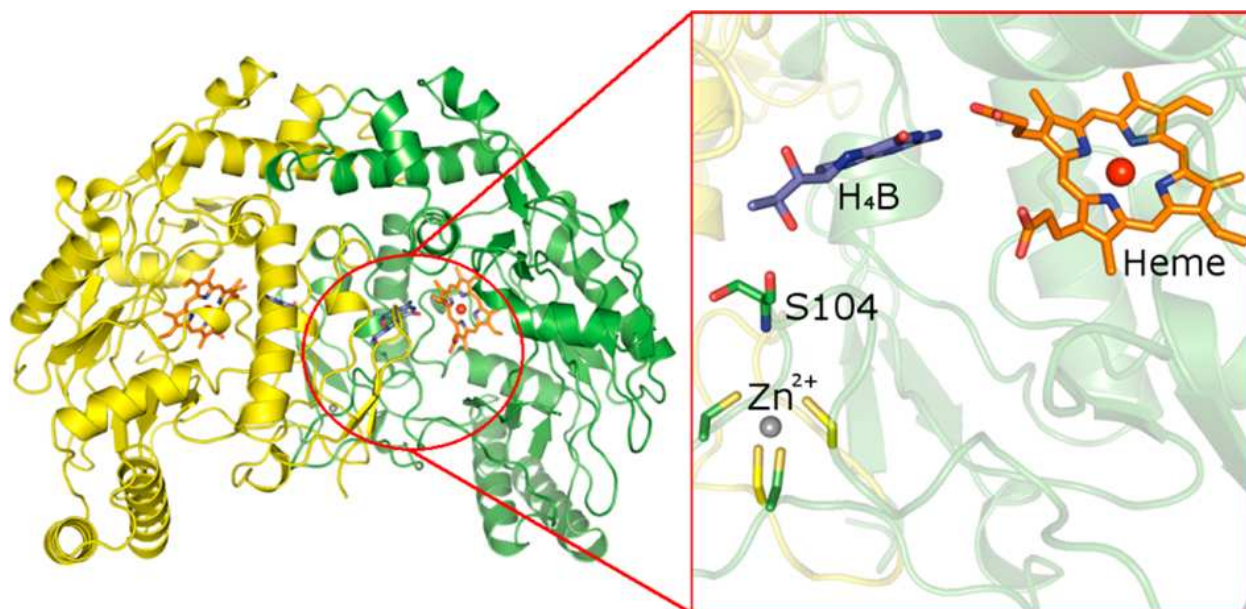


The electron flow in the NOS reaction is :



Tetrahydrobiopterin (BH<sub>4</sub>) provides an additional electron during the catalytic cycle which is replaced during turnover.

A relevant x-ray structure is shown in Scheme I-16 indicating the heme and pterin (BH<sub>4</sub>)



**Scheme I-16** Overall structure of the bovine eNOS dimer in complex with H<sub>4</sub>B. The Zn<sup>2+</sup> binding site is located at the dimer interface and ~ 15Å from the centre of the pterin binding pocket in both molecules A and B of the dimer.<sup>125</sup>

---

sites, along with other sites of the bovine e NOS dimer in complex with BH<sub>4</sub>. The dimer surface is formed between two N-terminal heme binding oxygenase domains that is further stabilized by the coordination of a Zn<sup>2+</sup> ion ligated to two cysteine thiols from each subunit (ZnS<sub>4</sub>)<sup>125</sup>.

The above characterization data about NOSs highlight several aspects having bioinorganic relevance

- i. The catalytic reaction itself with unique stoichiometry;
- ii. The electron transfer pathway from NADPH to the electron sink O<sub>2</sub>;
- iii. The need of class of heme-thiolate proteins for oxygenase type activity;
- iv. Achievement of stability of the homodimer through Zn<sup>2+</sup> coordination;
- v. The role of BH<sub>4</sub> in the catalytic reaction.

### **Aims and objectives of the work**

The primary motivation for pursuing the coordination chemistry of pterins (and also related heterocycles possessing the pteridine ring system, like isoxanthopterin, lumazine, etc.) is the presence of this heterocyclic system in a substantial number of metalloenzymes, as outlined above. Important bioinorganic chemistry has grown up, centred around this structural motif. The general features of the active site of pterin-containing metalloenzymes, are unprecedented in coordination chemistry. Apart from the intellectual attractiveness of this subject, a considerable

experimental challenge is posed by the redox non-innocent nature of pterin, coupled with its poor solubility.

The aforesaid information about the structural and functional aspect of pterin-containing redox metalloenzymes have catalysed symbiotic developments of coordination chemistry of pterin ligands in particular and pteridine ligands in general. References 10-18, 25-28, 76, 83, 84, 101, 110-116, 118, 129, 143 give a good overview of the available literature on the coordination chemistry of such ligands. They cover complex compounds of mainly molybdenum, first transition metals and a few later transition metals like ruthenium, rhenium, silver and cadmium. The relevant data cover a significant number of x-ray structurally characterized compounds, throwing light on the metal-pterin/pteridine bonding interactions.

However, continued efforts are needed on the synthetic and reactivity aspects of pterin coordination chemistry, for improving our understanding about the above redox metalloenzymes, especially their functional aspects and their mechanism of action. The associated modeling studies may throw up new pathway/ideas for studying the redox non-innocent pterin ligands their coordination compound and correlating their properties with molecular and electronic structures. Few basic guidelines may be stated here.

1. The synthetic chemist is to assemble minimal active site representations and to determine intrinsic geometric, electronic and reactivity properties of the resulting new compounds.
2. To define function in terms of structure (both geometric and electronic)- a basic goal of bioinorganic research.
3. For the above-mentioned pterin-containing redox metalloenzymes, the electron transfer pathway to or from the metal centre is to be understood along with the possible cooperativity between formally metal-based and pterin-based redox processes as well as the maintenance of

stoichiometric compatibility of the electron transfer activity of the metal site with the redox process/oxidation state change at the substrate active site (e.g.,  $S^{IV}O_3^{2-} \rightarrow S^{VI}O_4^{2-}$ ,  $N^V O_3' \rightarrow N^{III}O_2'$ , etc;



4. The above aspect immediately raises the question about the formal oxidation states of both the metal-and pterin-ligand centres in the new synthetic models.

5. Bench-mark data (spectroscopic, electrochemical/cyclic voltammetric and kinetic data on group/electron transfer reactions, etc.) are to be gathered on such synthetic model compounds where the oxidation states of both the metal and pterin ligand centres are to be carefully controlled, together with the donor atoms from the ancillary ligands; development of such coordination chemistry will also enable chemical and electrochemical studies to be accomplished which are relevant and complementary for studying the functional aspects of the enzyme catalytic centres, including the exact role of the metal and pterin ligand centres in oxygen atom transfer or  $O_2$  activation, etc.

6. Even the source of the oxygen atom transferred to or from the substrate by different pterin-containing enzymes, need attention. For example, water is the ultimate source of the oxygen atom transferred to the substrate by the Mo/W-containing oxotransferases. On the other hand, dioxygen is the source of the oxygen atom involved in the phenylalanine  $\rightarrow$  tyrosine conversion, with the other oxygen atom being reduced to the level of water. For a couple of other classes of monooxygenases, the iron-containing aggressive active sites attack the substrates, e.g.,  $Fe^{IV}=O$  (cytochrom P450) or  $Fe_2^{IV}=O$  (methane monooxygenase) and such intermediates are derived from dioxygen rather than from water as in case of the Mo and W enzymes.

**Answers to such fundamental problems are to be found** from the stand point of basic parameters of inorganic chemistry, e.g., the operating reduction potentials of the enzyme active sites,  $O_2/H_2O$  systems and the associated free energy relationships in terms of the Frost diagrams. **Such interpretations are to be carefully tested on the synthetic model compounds.** These studies will also bring to the focus a few other fundamental aspects like kinetics and thermodynamics of long-range electron transfer, multielectron reduction and ultimately the pathways adopted by nature to harness the redox non-innocent nature of pterin for fruitful purposes in diversified metalloenzymes.

7. **Information about the frontier orbitals of the synthetic models** are to be obtained using theoretical methods (e.g., DFT calculations) and their basic properties (e.g., energy in eV, percentage compositions, energy gaps, etc.) are to be **correlated with the reactivities and different physico-chemical properties.** Ligand fields at the metal centres are to be interpreted carefully for a correct description of the associated chemical bonding and their role in controlling reactivity/functional aspects.

For a better conceptual frame work of this proposed synthetic study aimed apart from anything else, at modeling the PAH type activity, a closer look is needed into the  $NADH/NAD^+$  as well as the dioxygen systems, as they are intimately connected with the PAH catalytic cycle (Scheme I-13).<sup>53</sup> There are four major classes of redox enzymes based on the nature of the associated electron mediators.<sup>94,145</sup> (1) the pyridine-linked dehydrogenases catalyzed reversible transfer of electrons from substrates to the loosely bound coenzymes  $NAD^+/NADP^+$  to/ from  $NADH/NADPH$ , respectively; the reduction of the pyridine ring is stereospecific and is accompanied by a spectral change. (2) The flavin-linked dehydrogenase contain tightly bound FMN or FAD as prosthetic groups and often a metal; their intensely colored oxidized forms are

bleached on reduction. (3) The iron-sulfur protein containing enzymes. (4) The redox systems utilizing the cytochromes, acting in series, transferring electrons from flavoproteins to oxygen. Their reversible Fe(II) – Fe(III) transition can be followed spectrophotometrically.<sup>94</sup>

Few relevant potentials are indicated here:

<b>Couple</b>	<b>E<sup>0</sup>(V)</b>
$1/2\text{O}_2 + 2\text{H}^+ + 2\text{e}' \rightleftharpoons \text{H}_2\text{O}$	+ 0.816
$[\text{Fe}(\text{CN})_6]^{3-} + \text{e}' \rightleftharpoons [\text{Fe}(\text{CN})_6]^{4-}$	+0.36
$\text{NAD}^+ + 2\text{H}^+ + 2\text{e}' \rightleftharpoons \text{NADH} + \text{H}^+$	-0.320
$\text{NADP}^+ + 2\text{H}^+ + 2\text{e}' \rightleftharpoons \text{NADPH} + \text{H}^+$	-0.324
Ferredoxin ox/red (algal)	-0.41
Flavodoxin ox/red (clostridial)	-0.31
$2\text{Cyt } b_k(\text{ox}) + 2\text{e}' \rightleftharpoons 2\text{Cyt } b_k(\text{red})$	+0.030
$2\text{Cyt } C_{\text{ox}} + 2\text{e}' \rightleftharpoons 2\text{Cyt } C_{\text{red}}$	+0.254
$2\text{Cyt } a_3(\text{ox}) + 2\text{e}' \rightleftharpoons 2\text{Cyt } a_3(\text{red})$	+0.385

---

It may be added that  $\text{NAD}^+/\text{NADP}^+$  can be reduced nonenzymatically by sodium dithionite or  $\text{NaBH}_4$ .  $\text{NADH}/\text{NADPH}$  can in turn be nonenzymatically reoxidized with  $\text{K}_3[\text{Fe}(\text{CN})_6]$ , but they are not oxidized directly by dioxygen at pH 7.0<sup>94</sup>

---

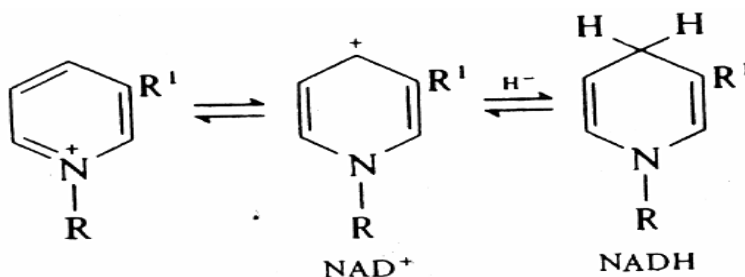
### **Coenzyme of electron transport: $\text{NAD}^+$**

The coenzyme most frequently employed as acceptor of electrons from the substrate is nicotinamide adinine dinucleotide ( $\text{NAD}^+$ ). When bound to the appropriate site on a dehydrogenase protein, a hydride ion is liberated from the substrate to the nicotinamide moiety and a proton is liberated into the medium.

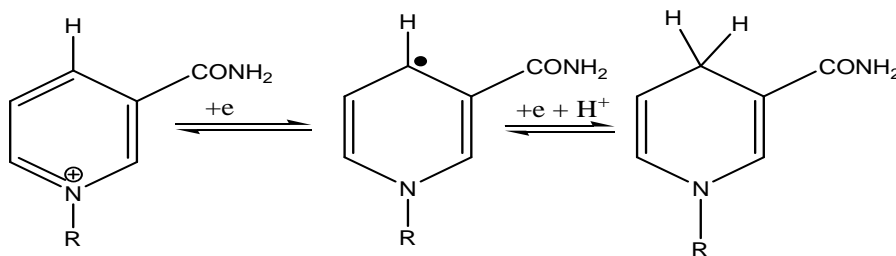


Nicotinamide adenine dinucleotide phosphate ( $\text{NADP}^+$ ) also functions in the same manner. The reduced coenzyme is not metabolized further on the same enzyme surface, but after dissociation from the original location, it transfers its electrons to an acceptor on the surface of a second enzyme.

It is known in organic chemistry that pyridinium compounds react as if the para carbon were positively charged; thus they can add hydride ions.  $\text{NAD}^+$  carries out this reaction in biological system.



Alternatively, the above transformation can be represented as a two electron transfer step along with a proton ( $\text{H}^- \equiv \text{e}' + \text{e}' + \text{H}^+$ ), since the one electron reduced intermediate radical is not stable.



In the mitochondrial system, no enzyme catalyzes a reaction in which the metabolite ( $\text{MH}_2$ ) reacts directly with  $\text{O}_2$ .

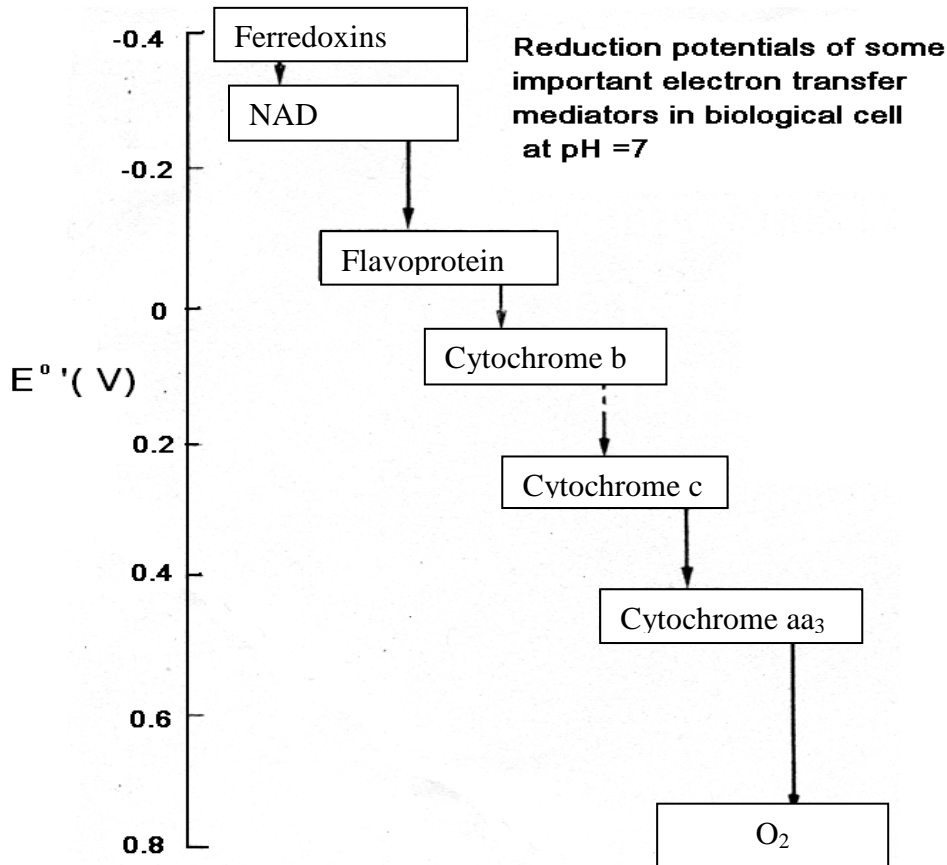


Rather, a transfer of electrons occurs from substrate to coenzyme (coenz),



with subsequent oxidation of the reduced coenzyme in an independent process.

The arrays of electron carriers that convey electrons from the dehydrogenated substrates to  $O_2$ , are shown below schematically.



These series of mediators, which act like a series of locks on a canal, allowing oxidation to occur in stages. Here control is of paramount importance, for uncontrolled oxidation by oxygen is combustion. Such mediators include the heme-containing cytochromes and flavoproteins, which also mediate the reaction that invest oxygen into the organic molecules.

The energetics of electron transport from NADH ( $E^{0'} = -0.32V$ ) to dioxygen ( $E^{0'} = +0.82V$ ), that is, along the entire length of the respiratory chain, can be calculated using the relation:

$$\Delta G^{0'} = -nF\Delta E^{0'}$$

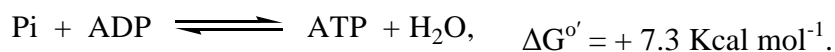
where n is the number of electrons transferred, F is the faraday (23,062 cal), and  $\Delta E^{0'}$  is the  $E^{0'}$  of the electron-accepting couple minus the  $E^{0'}$  of the electron donating couple.

$$\Delta G^{0'} = -2 \times 23062 \times [0.82 - (-0.32)]$$

$$= -52,700 \text{ cal mol}^{-1}$$

$$= -52.7 \text{ Kcal mol}^{-1}.$$

This value may be compared with the standard free energy of formation of ATP at pH 7.0 from ADP and phosphate:



Thus the formation of many ATP molecules, is needed to absorb the energy released during the passage of a pair of electrons down the respiratory from NADH to oxygen as above.<sup>59,94</sup> Two striking characteristics of the electron-transport process are relevant to the mechanism of energy conservation during electron transport: (i) the fact that a large number of sequential electron – transferring steps is involved, which suggests stepwise release of energy, and (ii) the fact that  $\text{H}^+$  ions are absorbed and released at some of these steps, suggesting that proton exchanges are involved in energy conservation.<sup>94</sup>

### **Alcohol dehydrogenase**

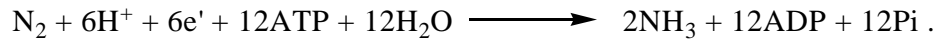
This enzyme catalyzes the  $\text{NAD}^+$ -dependent conversion of primary alcohols to aldehydes:



Although the reaction involves redox chemistry, the enzyme contains zinc, which serves to bind and activate the substrate molecule prior to a hydride-transfer step; it does so much as it does in carboxypeptidase and carbonic anhydrase. Conclusive evidence indicates that zinc promotes hydride transfer to  $\text{NAD}^+$  via the formation of a  $\text{Zn(II)}$ -alcoholate complex.<sup>137,144</sup>

## The nitrogenase system

Here the overall reaction is :



Reduced ferredoxin serves as the immediate electron donor. Regeneration of reduced ferredoxin occurs through the enzyme NADH-ferredoxin reductase:

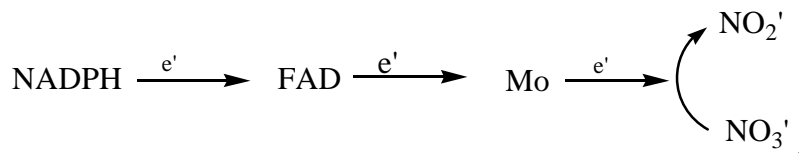


or by the pyruvate dehydrogenase system.<sup>94</sup> The active site of nitrogenase containing a MoFeS cluster has been characterized x-ray structurally.

## Nitrate reductase

Nitrate is the principal form of nitrogen available to higher plants from the soil. This metabolic assimilation of nitrate into the form of ammonia proceeds in two major steps: (i) reduction of nitrates to nitrite and (ii) reduction of nitrite to ammonia.

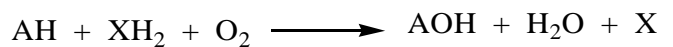
The first reaction in nitrate utilization is catalyzed by nitrate reductase, which is widely distributed in plants and fungi.<sup>94</sup> This enzyme is a flavoprotein containing both a molybdenum cofactor and cytochrome b; it employs NADPH as electron donor. The overall process of electron flow to nitrate can be shown schematically:



At the active site, the molybdenum centre shuttles between the Mo(VI) and Mo(IV) oxidation states through Mo(V).

## NADPH or NADH dependent monooxygenases

The monooxygenases or hydroxylases, catalyze insertion of one oxygen atom of molecular oxygen into the organic substrate; the other oxygen atom is reduced to water:



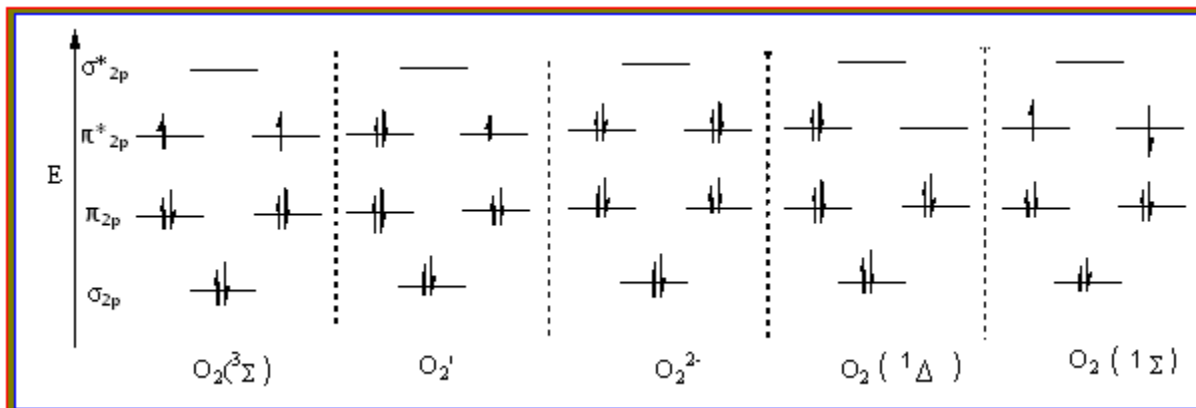
Monooxygenases require a second substrate to donate electrons for the reduction of the second oxygen atom in the oxygen molecule, the one reduced to water. Hence the monooxygenases are also called mixed-function monooxygenases; this was established by using  $^{18}\text{O}$  as tracer.

In most monooxygenases reactions the second substrate that furnishes electrons to reduce one atom of oxygen to water is ultimately NADH or NADPH; however, different electron carriers are employed to transfer electron from NADPH or NADH to the oxygen.

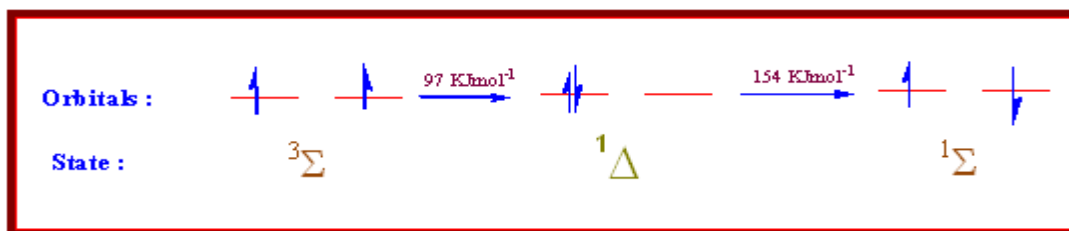
In the reaction catalyzed by the liver enzyme **phenylalanine hydroxylase, the reducing equivalents are transferred via the tetrahydrobiopterin cofactor.**

### **Dioxygen: thermodynamic and kinetic aspects of its behavior as an oxidant**

Dioxygen is a powerful oxidant, but it is kinetically inert. This paradox has allowed life, in evolution to come to terms with dioxygen in the atmosphere and to make its controlled use in biosynthesis, biodegradation and respiration. Thus the two problems of survival are to activate dioxygen sufficiently for reaction, while ensuring that dangerous by products are not allowed to damage the organism<sup>137,138</sup>. Flavin is the only organic cofactor known to interact enzymatically with dioxygen. Otherwise in the biological systems metal-containing biomolecules (almost exclusively Fe and Cu) are used to deal with dioxygen, superoxide and peroxide.<sup>139</sup> Their electronic structure are shown below; here x axis is the internuclear axis and the  $\pi_{2p}/\pi^*_{2p}$  levels have two components along with y and z axis respectively.



The paramagnetism (with two unpaired electrons) of the dioxygen molecule is easily explained in terms of MOT with its degenerate  $\pi^*_{2p}$  orbitals. The MO designations of the superoxide ( $O_2'$ ) and peroxide ( $O_2^{2-}$ ) are shown above along with the excited-state configurations of  $O_2$ , that is,  $O_2(^1\Delta)$  and  $O_2(^1\Sigma)$  which are 97 and 154.5  $\text{KJmol}^{-1}$  above the ground state ( $^3\Sigma$ ) respectively.



The characterization data of  $O_2$ ,  $O_2'$  and  $O_2^{2-}$  are shown below, indicating the extent of electron transfer (e.g. from metal) to dioxygen (or specifically its antibonding MOs).

	$O_2$	$O_2'$	$O_2^{2-}$
Bond order	2	1.5	1
Bond length(Å)	1.21	1.28	1.49

$\nu_{O-O}(cm^{-1})$	1560	1150-1100	850-740
----------------------	------	-----------	---------

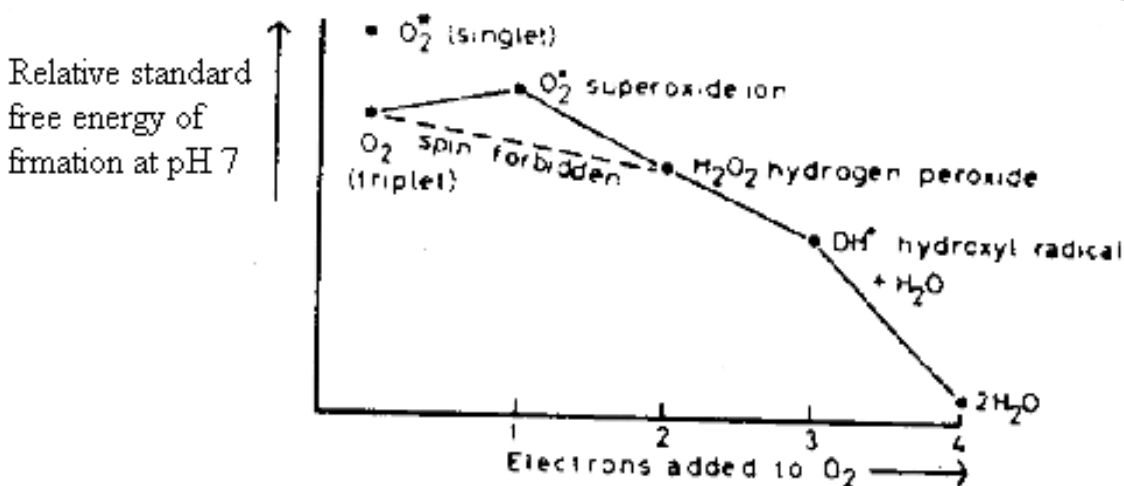
The overall geometry of the  $M(O_2)$  or  $M(O_2)M$  group is also a useful guide on this matter, e.g. peroxo complexes  $M(O_2)M$  are usually non-planar.

### The kinetic inertness of $O_2$ and its activation

The kinetic inertness of oxygen is emphasized by the fact that autooxidation of organic compounds (that is, reaction of  $O_2$ ) at room temperature usually takes place through metal-ion catalysis, by photochemical activation (for example, of butadienes) or by chain reactions promoted by an extraneous radical (for example, of ethers). Simple bimolecular reactions between  $O_2$  and organic compounds are unusual. Two factors are responsible for the above observations:

- (i) the high energy of formation of superoxide;
- (ii) the stability of triplet  $O_2$  ground state.

The thermodynamic aspect dioxygen reduction is shown below schematically.<sup>138</sup>

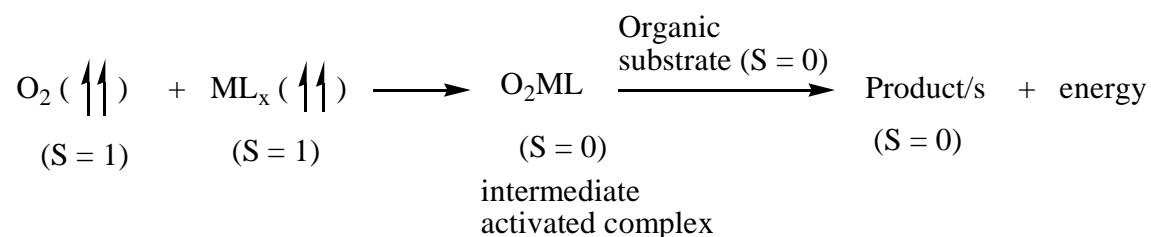


Thermodynamics of dioxygen reduction.  $E^0$  for a couple is represented by the slope of the line joining the two species. An intermediate can only disproportionate to the two species if it lies above such line.

---

One-electron reduction of  $O_2$  to superoxide ion ( $O_2^-$ ) is thermodynamically unfavorable, requiring a reducing couple of -0.33 V. Reaction to any other species is exothermic, but now we encounter a spin restriction.  $O_2$  has a triplet ground state ( $S=1$ ), with two unpaired electrons. Quantum mechanical laws require that if it is to be rapidly reduced to peroxide, a diamagnetic (singlet) molecule, then the reductant supplying the two electrons must be a free radical or must change from a singlet to a triplet state, or  $O_2$  itself must be excited to its singlet state ( $^1\Delta$ ,  $S=0$ ). This rules out most stable organic substrates ( $S=0$ ), since free radicals are generally unstable. Two-electron reduction of  $O_2$  ( $S=1$ ) by singlet molecules ( $S=0$ ), being spin forbidden, will not take place in the lifetime of a simple collision complex (ca.  $10^{-13}$ s). This is due to the fact that spin is weakly coupled with molecular vibration. Molecular vibration is about  $10^4$  times faster than spin inversion.<sup>137,138</sup>

The activation energy of dioxygen ( $97 \text{ KJ mol}^{-1}$ ) is too high for biological systems, but nature has designed suitable pathways requiring low activation energy for achieving fast reactions with  $O_2$ . One typical example is the quenching of  $O_2$  spin ( $^3\Sigma$ ) by the unquenched spin (e.g., a triplet) of a transition metal complex—a process involved in the action of  $O_2$  as the terminal oxidant in the respiratory chain.



Transition metal reacts with O<sub>2</sub> in various ways by virtue of their labile d-electron configurations. Favin, by contrast, probably activates O<sub>2</sub> by adopting a semiquinone radical state. If Cu or Fe salts are added to tissue slices or cultures, they promote O<sub>2</sub>-toxicity, while in vivo they are pressed into service as cofactors to control its reactions, and destroy its dangerous by-products.<sup>138</sup>

For the above spin quenching interaction, the geometry of the  $\pi$ -antibonding MOs of the O<sub>2</sub> molecule will impose limitations on the feasibility of different redox reactions occurring. Reduction will involve the transfer of electrons from the valence shell of the metal ion to the oxygen molecule and therefore there will be a symmetry requirement on the orbital of the metal ion. The implications of the Franck-Condon principle will also hold here. For example, metal t<sub>2g</sub> orbitals can overlap with ligand orbitals having  $\pi$  symmetry, whereas metal e<sub>g</sub> orbitals are suitable for overlap with ligand  $\sigma$  orbitals.<sup>137</sup>

Oxygen donor ligands will particularly affect the rate of electron transfer as these bases have  $\pi$ -donor properties and hence will enhance the transfer of electron density from the appropriate metal d orbital into the oxygen molecule. In contrast  $\sigma$  donors, such as nitrogen ligands, trans to the oxygen molecule will have little influence.

Molecular oxygen is a strong oxidizing agent and the full reduction potential will be realized only when the oxidation process involves an essentially synchronous four-electron transfer reaction.

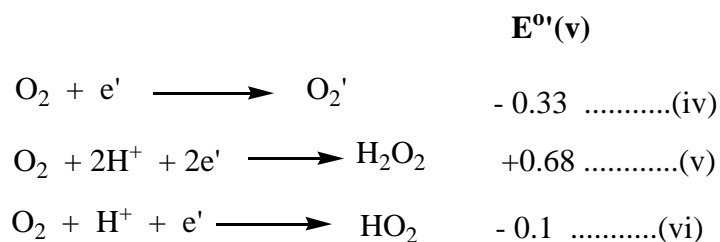


To derive the pH dependence from the Nernst equation, it is assumed that the partial pressure of oxygen is 1 bar and setting  $\nu = 4$ .<sup>63</sup> from the above equation we get

in 1N acidic medium,  $E^0 = 1.23\text{V}$  .....(ii) and

in neutral medium (pH =7),  $E^0 = 0.817\text{V}$  .....(iii).

Few other reduction reactions of oxygen in the neutral medium (pH =7, 25<sup>0</sup>C) have been suggested for biological oxidations, involving one-or two- electron steps.



Evidently, the atmospheric oxygen is innocent to us, but not the singlet oxygen. However, the ordinary oxygen can react through hydrogen atom abstraction which generates free radicals to initiates chain reaction.

Finally, the ligating property of singlet- $\text{O}_2$  may be compared with that of triplet  $\text{O}_2$ . Singlet- $\text{O}_2$  with the distinguishing electronic configuration  $(\pi^*_{2p})^2(\pi^*_{2p})^0$  can use the  $\pi^*$ -pair for  $\sigma$ - donation and the vacant  $\pi^*$ -MO for  $\pi$ -acceptance. Thus, singlet- $\text{O}_2$  ( $^1\text{O}_2$ ) can act as a better  $\pi$ -acid ligand and consequently with higher crystal field splitting property.

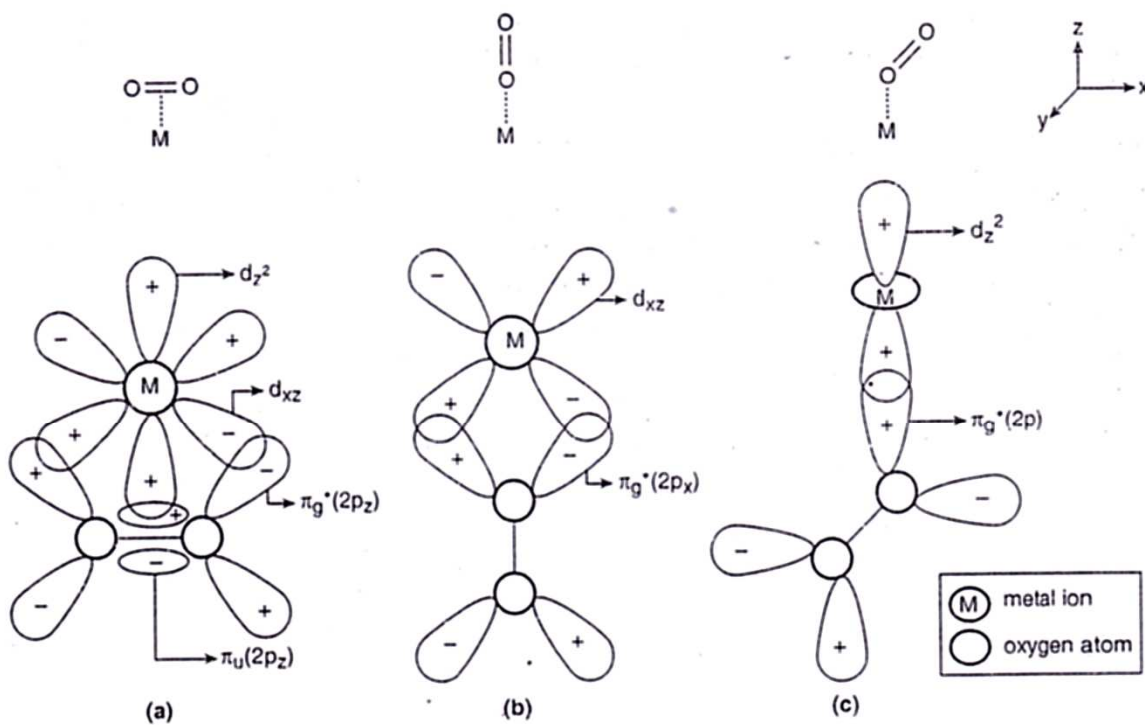
### **Activation of dioxygen through complex formation with transition metal ion**

Nature has developed different energetically favorable pathways to convert the triplet oxygen to singlet oxygen which is utilized in biochemical redox reactions. Complex formation of triplet oxygen ( $^3\text{O}_2$ ,  $S = 1$ ) with transition metal ion (possessing d orbitals with unpaired electrons ) produces singlet oxygen ( $^1\text{O}_2$ ,  $S = 0$ ) in the resulting complex. The common modes of binding of  $\text{O}_2$  with a metal centre are:

- (a) perpendicular (i.e., edge-on-overlap)
- (b) linear (i.e., end-on-overlap) and

(c) angular (i.e., bent end-on-overlap).

These possibilities are shown below schematically. They are based on the Dewar-Chatt-Duncanson bonding model of alkene complexes as well as the bonding considerations about the dioxygen-carrying Co(II)-Schiff base complexes.<sup>134-141</sup>



**Different modes of bonding in  $M-O_2$  complexes. (a) Perpendicular mode (edge-on overlap); (b) Linear mode (end-on overlap) (c) Bent end-on overlap**

As delineated below the perpendicular and angular modes of  $O_2$  binding to a suitable transition metal centre can remove the degeneracy of the  $\pi^*_{2p}$  orbitals of  $O_2$ , but the linear mode of binding cannot remove the said degeneracy.<sup>140</sup>

In the linear mode (b), both the  $\pi^*_{2p}$  orbitals of  $O_2$  overlap ( $\pi$ -interaction) equally with  $d_{xz}$  and  $d_{yz}$  orbitals of the metal centre and consequently the said degeneracy of the  $\pi^*_{2p}$

orbitals is retained even after complex formation [the  $\pi$ -interaction are ( $\pi^*_{2px} + d_{xz}$ ) and ( $\pi^*_{2py} + d_{yz}$ ) respectively]. Here the M – O bond direction is assumed to lie along the z-axis.

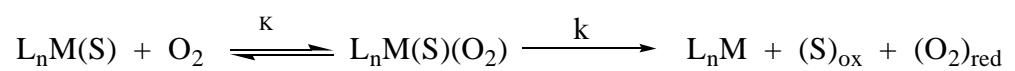
The following overlapping interactions can be considered for the perpendicular mode of bonding (a). The filled  $\pi_{2pz}$  orbital of  $O_2$  forms a  $\sigma$ -bond with the  $d_z^2$  orbital of the metal centre. The  $\pi^*_{2pz}$  orbital of  $O_2$  can overlap with the metal  $d_{xz}$  orbital; but only a weak overlap is possible between the  $\pi^*_{2py}$  (perpendicular to the plane of the paper) orbital of  $O_2$  with the metal  $d_{yz}$  orbital. After the above complex formation process  $\pi^*_{2pz}$  will have lower energy, while  $\pi^*_{2py}$  will be of relatively higher energy. Since their degeneracy is now lost, the original two unpaired electrons of the  $\pi^*_{2p}$  level of  $O_2$  ( $^3O_2$ ), will now be accommodated in the lower energy orbital (that is,  $\pi^*_{2pz}$ ). Here the metal  $d_{xy}$  and  $d_{x^2-y^2}$  orbitals remain nonbonding.

For the bent manner of bonding (c), one  $\pi^*_{2p}$  orbital of  $O_2$  is oriented to overlap with the metal  $d_z^2$  orbital to form a  $\sigma$ -bond, while the other  $\pi^*_{2p}$  orbital combines with the metal  $d_{yz}$  orbital to form a  $\pi$ -bond. This mode of bonding removes the degeneracy of the  $\pi^*_{2p}$  orbitals of  $O_2$  through complex formation. In this mode of coordination, the metal  $d_z^2$  orbital is stabilized; the  $d_{xy}$ ,  $d_{x^2-y^2}$  and  $d_{xz}$  orbitals remain nonbonding.

Actually for the  $ML_5O_2$  complexes of  $Co(II)(d^7)$  and  $Fe(II)(d^6)$ ,  $O_2$  binds strongly in a bent manner and the metal  $d_z^2$  orbital electrons are located in the resulting MO where the  $\pi^*_{2p}$  orbital character of  $O_2$  is significant. The net result is the flow of electron density from the metal to the  $\pi^*_{2p}$  orbital of  $O_2$ , implying oxidation of the metal centre as well as reduction of  $O_2$ . In other words,  $^3O_2$  is activated through an intermediate complex,  $O_2ML_5$  ( $S = 0$ ) for reaction with the substrate X ( $S = 0$ ), leading to the product as pointed out earlier. The basic requirements of the above bonding interaction are:

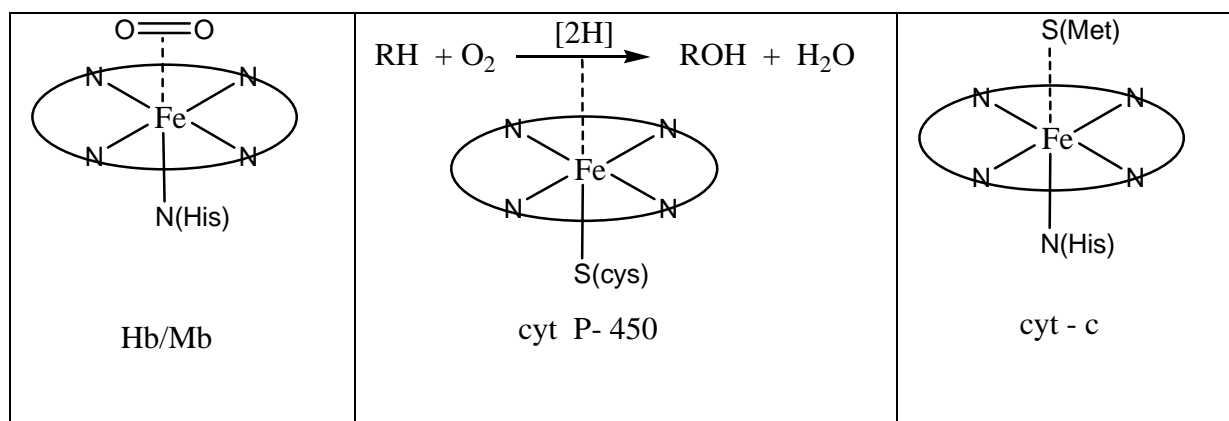
- (i) the transition metal complex must have an active site to accommodate O<sub>2</sub>, e.g. the formation of a 5-coordinate ML<sub>5</sub> intermediate through the loss of a ligand from the z-axis;
- (ii) for the bent bond formation by O<sub>2</sub> in the adduct, the HOMO (acting as the donor orbital) of the metal centre should be d<sub>z</sub><sup>2</sup>, assuming M – O bond formation in the z-direction;
- (iii) the metal centre should be able to display multiple oxidation states;
- (iv) the deoxygenated and oxygenated forms should have the comparable stability.<sup>137,140</sup>

The above discussions throw lights on the attributes of both an oxidase enzyme (e.g., cytochrome O-450 enzyme) and an oxygen carrying protein (Mb/Hb); the thermodynamic stability constant (K) and the electron transfer rate constant (k) of the intermediate complex L<sub>n</sub>M(S)O<sub>2</sub> (where S is an oxidizable substrate) decide the issue .



The oxygen carrying property is favoured when K is large and k is small; a large value of k favours the oxidase activity.

The above situations may be represented schematically, using the iron (II)-prophyrin system as an example. When the sixth coordination position is blocked (e.g., by a

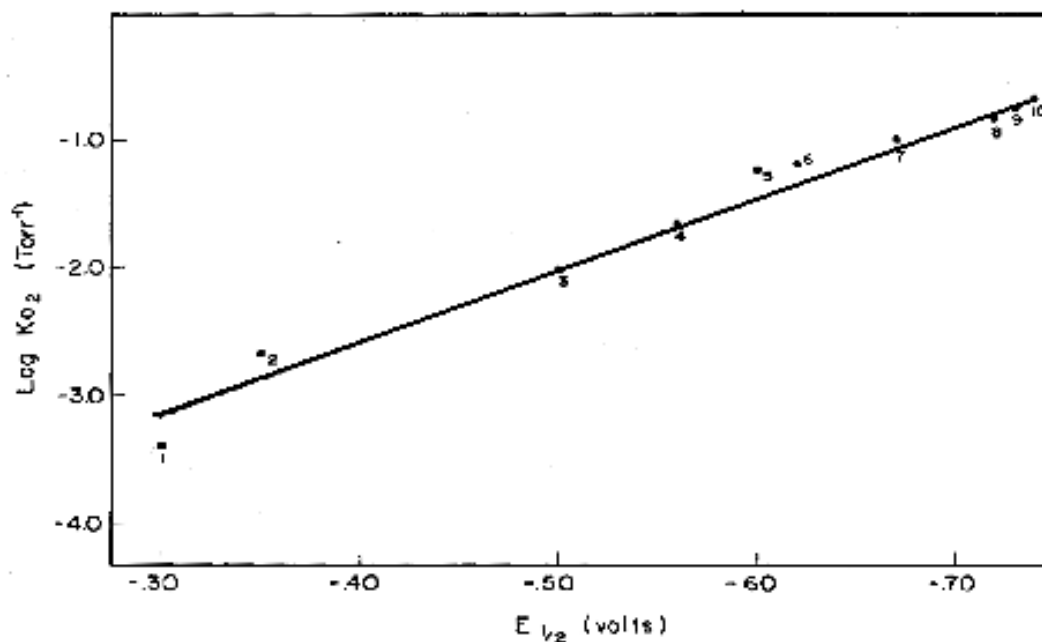


methionine sulphur ligand), an electron carrier (cyt-c) property is manifested.

The above well-characterized metalloproteins/metalloenzymes illustrate how the same cofactor (iron-prophyrin) unit can be made to perform drastically different functions by the donor atoms from the protein chain.

In oxyhemoglobin, the stretching frequency for the O – O bond is  $1106\text{ cm}^{-1}$  which is closer to the value of  $1150 - 1100\text{ cm}^{-1}$  for  $\text{O}_2^-$ . X-ray structural studies indicate that oxy-Hb is a bent superoxo complex of Fe(III) with a Fe – O – O angle of about  $120^\circ$ .

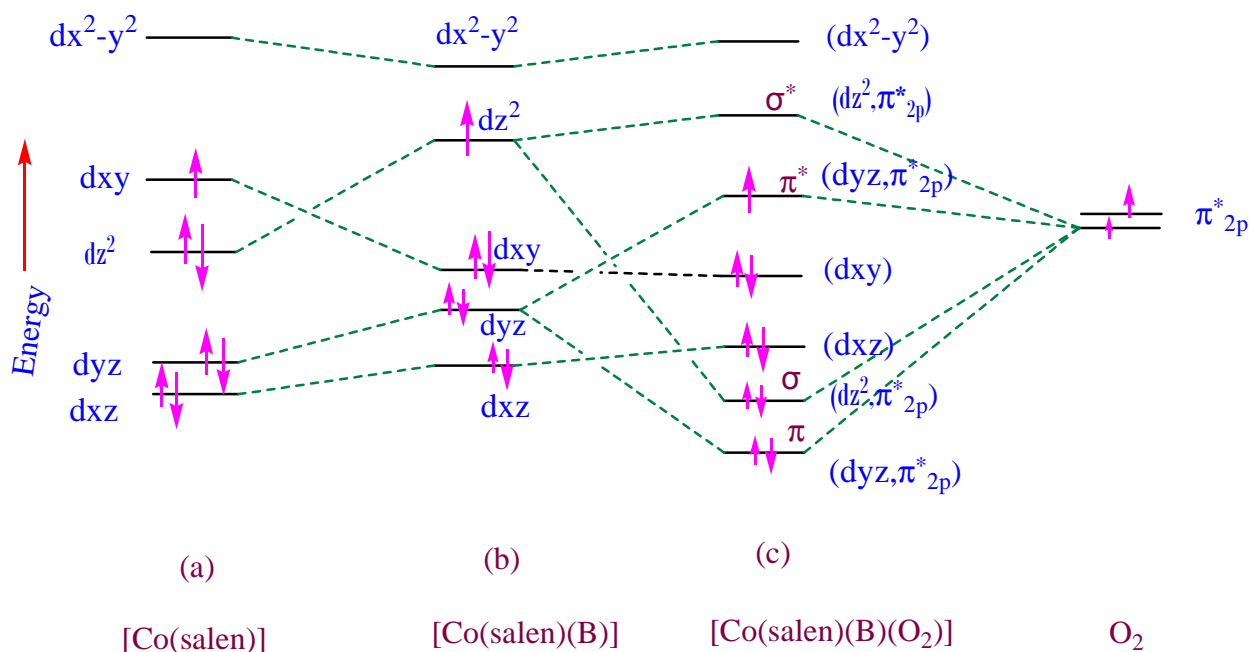
Model (synthetic) oxygen carriers have received considerable attention including the Co(II)-Schiff base complex like salcomine,  $[\text{Co}(\text{salen})]$  which reversibly binds  $\text{O}_2$  in solution containing a base, e.g., pyridine (py) to give the superoxo complex  $[\text{Co}(\text{salen})(\text{B})(\text{O}_2)]$ . It supports the  $\text{O}_2$  binding model leading to oxidation of the metal centre, i.e.,  $\text{M}^{n+} + \text{O}_2 \rightarrow \text{M}^{(n+1)+} - \text{O}_2^-$ . Studies indicate that  $\log K$  (K is the  $\text{O}_2$  – binding constant) increases linearly with the reduction potential ( $E_{1/2}$ ) for the



Comparison of oxygen uptake ( $\log K_{O_2}$ ,  $-21^\circ\text{C}$ ) with  $E_{1/2}$  values for  $\text{Co(II)} \rightarrow \text{Co(III)}$  of  $\text{Co}(\text{benacen})(\text{B})$ : (1)  $\text{PPh}_3$ ; (2) 4-CNpy; (3) py; (4) 3,4-Me<sub>2</sub>py; (5) pip; (6) sec-BuNH<sub>2</sub>; (10) n-BuNH<sub>2</sub>.

$\text{Co(III)/Co(II)}$  complexes. It is reasonable to infer that electron transfer from cobalt(II) (and reduction of  $\text{O}_2$  e.g.,  $\text{O}_2 \rightarrow \text{O}_2^-$ ) is involved in  $\text{O}_2$  binding. However, an increase of 0.4v (40  $\text{KJmol}^{-1}$  in terms of  $\Delta G^0 = -nFE^0$ ) in  $E^0$  leads to an increase in  $\log K$  of only about 2.1 (12  $\text{KJmol}^{-1}$  in terms of  $\Delta G^0 = -RT \ln K$ ). The difference suggests that electron transfer to  $\text{O}_2$  is incomplete and that  $\text{Co(II)} - \text{O}_2$  and  $\text{Co(III)} - \text{O}_2^-$  are idealized extremes<sup>134-136</sup>. The above data also indicate that greater the  $\sigma$ -donor property of B, higher is the  $\text{O}_2$  binding constant, favouring the step  $\text{Co(II)} - \text{O}_2 \rightarrow \text{Co(III)} - \text{O}_2^-$ . If the base (B) is a good  $\pi$ -acid ligand, then formation of the  $\text{O}_2$  - adduct will not be favored (where  $\text{O}_2$  acts as a  $\pi$ -acid ligand at the trans-position of B). The importance of the trans-axial ligand B in imparting the  $\text{O}_2$  carrying properties of  $[\text{Co(II)}-(\text{salen})]$  compound can

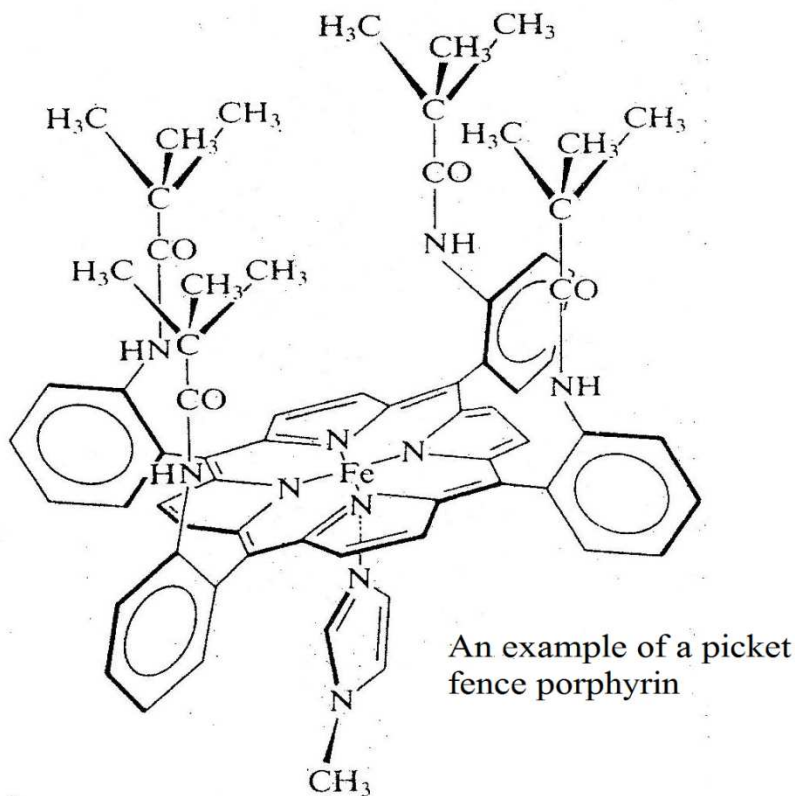
be explained as follows in terms of bent – on bonding (c) stated earlier; here the  $d_z^2$  orbital is used for  $\pi$ -bonding, with the  $dx^2-y^2$ ,  $d_{xy}$  and  $d_{xz}$  orbitals remain nonbonding.<sup>135,140,141</sup>



Energy level diagram (qualitative) for the d orbitals of Co(II) in (a) square -planar and (b) square-pyramidal fields in  $CoL_4$  and  $CoL_4B$ ; (c) MO diagram (qualitative) for Co - O<sub>2</sub> bond in  $CoL_4B(O_2)$  involving the d orbitals of Co(II) in  $CoL_4B$  with the antibonding  $\pi$  MO-s of O<sub>2</sub>.<sup>135</sup>

The net result of the above bonding interaction between [Co(salen)(B)] and O<sub>2</sub> is that the unpaired electron of the metal is located in a  $\pi^*$  MO which is energetically close to the  $\pi^*_{2p}(O_2)$  orbital. This is equivalent to the electron transfer  $Co(II) - O_2 \rightarrow Co(III) - O_2^-$ , forming the superoxide ion. EPR spectral data indicate that about 80% of the odd electron resides in the superoxide ion, while x-ray structural data provide with an ‘O – O’ bond distance of 1.26Å. This can be compared with the corresponding distance of 1.28Å (in the O<sub>2</sub><sup>-</sup>) in KO<sub>2</sub> and 1.21Å in O<sub>2</sub>,

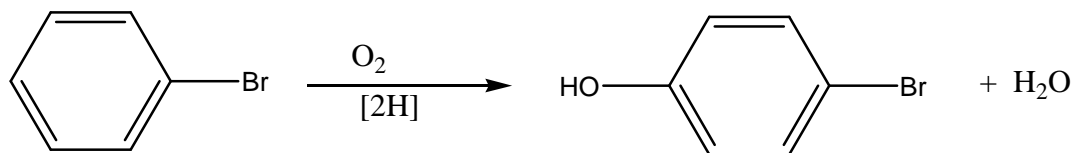
respectively. It is comparable to the formulation  $\text{Fe(III)} - \text{O}_2^-$  frequently used for oxy-Hb, with bent Fe - O - O bond.



In this connection it is worthwhile to refer to the picket fence model of the oxygen carrying protein myoglobin (Mb).<sup>136</sup> Here imidazole (Im) is an effective  $\sigma$ -base that favors coordination of a  $\pi$ -acid lying trans to itself. The blocking substituents create a pocket for  $\text{O}_2$  coordination and prevent the formation of a  $\mu\text{-O}_2$  species through reaction with a second Fe centre. It reacts with  $\text{O}_2$  giving a structure with an Fe - O - O angle of  $136^\circ$  and O - O distance of  $1.25\text{\AA}$ . The O - O stretching frequency lies at  $1107\text{ cm}^{-1}$ , which is closer to the  $\text{O}_2^{2-}$  value of  $1145\text{ cm}^{-1}$  than the  $\text{O}_2$  value of  $1550\text{ cm}^{-1}$ . In the light of the above MO model, this diamagnetic (low spin) compound may be considered to be a low - spin  $d^6\text{ Fe(II)}$  complex of singlet  $\text{O}_2$ ; this would mean that  $\text{Fe(II)} \rightarrow \text{O}_2$  reduction is less important than in the above  $\text{Co(II)}$  complex.<sup>136</sup>

Alternatively, the above low – spin character could arise as the result of spin pairing of Fe(III) and  $O_2^-$ , in which case the complex would be similar to the cobalt model compound. That such a possibility is quite real is underlined by the observation that a  $d^3$  Cr(III) porphyrin complex of oxygen has been synthesized which has only two unpaired electrons. Since  $d^3$  Cr(III) must be high-spin, the only explanation for the spin observation is spin-pairing with an electron from  $O_2^-$ .

The above bonding consideration are **pertinent in the present context** because dioxygen ( $O_2$ ) has been used here extensively for modeling the phenylalanine hydroxylase (PAH) activity using bromobenzene as a model substrate and a reduced metal-pterin complex as the source of reducing equivalents:<sup>7,52-55</sup>



Scheme I-13 represents the phenylalanine hydroxylase (PAH) catalytic cycle including the regeneration of tetrahydrobiopterin cofactor ( $BH_4$ ) through the action of NADH on quinonoid dihydropterin.<sup>53</sup> As detailed out in this treatise **NaBH<sub>4</sub> been used here as the source of reducing equivalents (instead of NADH)** towards the oxidized form of a suitable metal-pterin complex; the reduced form of the corresponding complex is able to drive the above reaction, that is, hydroxylation of the aromatic ring (of bromobenzene). Experimental data indicate **that direct transfer of reducing equivalent from NaBH<sub>4</sub> to the above reaction system is not possible**. But the presence of a suitable mediator is essential for this purpose, e.g., a metal-pterin complex as above. As per the above MO diagram, the reduced metal centre initially activates  $O_2$  through electron transfer (involving the  $\pi^*_{2p}$  orbital) and the reduced pterin ring completes the process of reducing equivalent transfer to the above reaction system.<sup>139</sup>

Scheme I-15 shows the x-ray structural data of the active iron centre in the catalytic domain of the hPAH-Fe-BH<sub>4</sub> binary complex.<sup>120</sup>

### **Developing functional models of PAH type activity**

To achieve the above objectives using the later members of the 3d transition series, is a major research goal of this study. The synthetic and characterization aspects of the proposed new compounds pose considerable challenge due to the presence of redox non-innocent pterin ligand.<sup>9,10</sup> Possible understanding of the mechanism of action of the PAH type enzymes, will be a gratifying result of such an endeavour.<sup>55,120</sup>

Preface of this thesis indicates the pterin ligand (H<sub>2</sub>L) and the ancillary ligands (Schemes 1 to 6) used for the present research work. H<sub>2</sub>L plays a pivotal role for entire study, including highlighting the role of its redox non-innocent nature in imparting unique redox properties to its new coordination compounds.

Chapter II presents the synthetic, characterization and reactivity aspects of two new copper (I, II) complexes of H<sub>2</sub>L, with 1, 10-phenanthroline (phen) as the ancillary ligand. Reactivity studies of the copper(II) complex towards NaBH<sub>4</sub> and that of the copper (I) complex towards a mixture of bromobenzene – O<sub>2</sub>, elicit unique redox properties which can be rationalized in the light of the electronic structures (DFT). The diamagnetic copper(I) complex presents itself here as an excellent candidate for 2D NMR study.

Chapter III is concerned with the synthesis, characterization and reactivity studies of a new cobalt(II) complex with 1, 10-phenanthroline as the ancillary ligand. The corresponding cobalt(I) complex can be accessed on the time scale of cyclic voltammetry as well as isolated through NaBH<sub>4</sub> reduction and characterized (ESIMS,  $\mu_{\text{eff}}$ , etc., data). Reactivity of the latter

compound with a mixture of bromobenzene and O<sub>2</sub>, affords 4-bromophenol. Significance of such reactivity data has been analyzed on the basis of frontier orbitals/electronic structures (DFT).

Chapter IV reports the synthesis of a new mixed ligand nickel(II) complex with 1,2-diaminoethane (en) as the ancillary ligand. The corresponding quaternary complex, obtained through substitution of its aquo group with imidazole (Im), could also be synthesized. Both of them have been characterized x-ray structurally. Their group transfer and redox reactivity studies elicit an important aspect, e.g. a considerable change over in property is associated with the substitution of the aquo group with imidazole. The corresponding nickel(I) complex could be isolated using NaBH<sub>4</sub> as the reducing agent and characterized (ESIMS data). Properties of their frontier orbitals (DFT) throw light on their redox properties.

In chapter V two new chiral mixed nickel(II) complexes are reported, using the ancillary ligand like R-(+)-propylene diamine and S-(-)-propylene diamine. Both of them have been characterized x-ray structurally and different physico-chemical data including CD spectroscopy. X-ray structural data point towards  $\delta$ -conformation of the ancillary ligands in both these cases. These two chemically identical compounds show unique difference among their reactivity properties; their electronic structures (DFT) throw light on such reactivity differences.

Synthesis of several new copper(II), cobalt(II) and nickel(II) mixed ligand complexes are reported in chapter VI; the ancillary ligands include 2, 2' – bipyridyl (bipy) and 1, 10-phenanthroline (phen) . Their chemical compositions have been established on the basis of elemental analysis (C-H-N data), ESIMS data as well as different physico-chemical studies; such data include those of a new zinc(II) complex whose x-ray data have been presented elsewhere. In all these cases, optimized molecular structures have been obtained through DFT calculations; the computed bond length/bond angle data tally with those reported in chapters II-V. The

diamagnetic zinc(II) complex is helpful in recording the 2D NMR data. Their reactivities and considerations about electronic structures complete this chapter.

References are grouped together at the end of this thesis.

## **Chapter II**

**Copper (II,I)-pterin coordination chemistry with a 6-substituted pterin ligand: synthetic, characterization and reactivity studies including utilization of molecular oxygen (O<sub>2</sub>) for organic substrate conversion.**

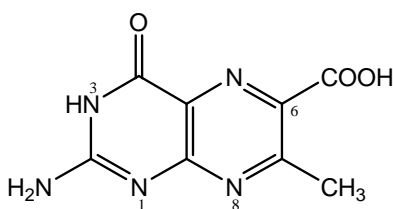
**Abstract**

A 6-substituted pterin ligand 2-amino-7-methyl-4-oxidopteridine-6-carboxylic acid (**1**, H<sub>2</sub>L) plays a pivotal role for the present study; it is complemented by a  $\pi$ -acid ligand like 1, 10-phenanthroline (phen). Solubility of **1** in aqueous alkali permits the synthesis of a mononuclear copper(II) complex [Cu<sup>II</sup>(L)(phen)(H<sub>2</sub>O)]. 3H<sub>2</sub>O (**2**) from this medium in the crystalline form and its x-ray structural characterization (CCDC deposition no. 985054; R[F<sup>2</sup>>2 $\sigma$ (F<sup>2</sup>)] = 0.113; wR(F<sup>2</sup>) = 0.279). Alternatively, the green crystals of **2** can also be obtained through a redox cycle involving the NaBH<sub>4</sub> reduction of **2** and the aerial reoxidation of the resulting dark-brown

compound. Such crystals provide x-ray structural data of better accuracy ( $R[F^2 > 2\sigma(F^2)] = 0.051$ ;  $wR(F^2) = 0.136$ ; Baisya, S. S.; Roy, P. S. *Acta Cryst.* **2014**, E70, 348 – 351)<sup>17b</sup>. The above-mentioned dark-brown compound  $\text{Na}_2[\text{Cu}^{\text{I}}(\text{L}')(\text{H}_2\text{O})_2 - \mu\text{-(phen)-Cu}^{\text{I}}(\text{L}')(\text{H}_2\text{O})_2] \cdot 2\text{H}_2\text{O}$  (**3**), can be isolated in the solid state, where  $(\text{L}')^{2-}$  is the 7,8-dihydro form of  $(\text{L})^{2-}$ . Characterization data (elemental analysis, spectroscopy and electrochemical studies) of both **2** and **3** are presented here. The DFT optimized molecular structure of **3** affords realistic geometry parameters and helps to rationalize its physico-chemical/spectroscopic data. Reactivity of **2** towards both imidazole and  $\text{NaBH}_4$  have been followed kinetically; the relevant negative  $\Delta S^\ddagger$  values indicate the associative nature of the reaction pathways. The reaction of **2** with  $\text{NaBH}_4$  turned out to be a two-step process, which can be rationalized from the thermodynamic considerations. Reaction of **3** with bromobenzene in presence of dioxygen has been followed both kinetically and stoichiometrically; isolation and characterization of 4-bromophenol as a product of this reaction, point towards aromatic ring activation. Attempts have been made to correlate some of the above reactivities with the electronic structures of **2** and **3**, obtained by DFT calculations. The exceptionally small band gaps ( $\Delta E = 0.22 - 0.5$  eV) between the LUMO and LUMO+1 levels of **2** and that between the HOMO – 1 and HOMO – 2 levels of **3** respectively, are noteworthy. Such a situation is beneficial for accommodating the reducing equivalents transferred by  $\text{NaBH}_4$  towards **2** leading to the formation of **3**; the latter responds either to a reaction mixture of bromobenzene and dioxygen or aerial oxidation, with the recovery of **2** as one of the products. This facile interconversion of **2** and **3**, is believed to be associated with the stability (both molecular and electronic structures) of **2**; the combined role of the redox non-innocent pterin ligand and the dual oxidation states (II, I) of the copper ion, in this process is highlighted.

## Introduction

Pterins (2-amino-4-oxopteridines) are ubiquitous in nature including different classes of metalloenzymes containing molybdenum or tungsten or iron (nonheme or heme).<sup>1-8,133</sup> For such enzymes the redox non-innocent nature of pterin is reciprocated by the ability of the associated transition metal ion in displaying multiple oxidation states. Their functional aspects need the tacit assumption that the redox process at the metal centre should be linked to the changes in the pterin/pyrazine ring oxidation level.<sup>9-11,13</sup> Such information have fostered a remarkable growth of pterin coordination chemistry.<sup>10-18,142</sup>



The pterin ligand (**1**, H<sub>2</sub>L)

The phenylalanine hydroxylase (PAH) catalysed reaction is concerned with the insertion of one oxygen atom from molecular oxygen (O<sub>2</sub>) into an aromatic ring, involving the C – H bond activation / hydroxylation<sup>7</sup>. On the other hand, copper-mediated oxidations cover a diverse array of reactions in both biology and chemistry<sup>153</sup>. Here the possibility of developing a biomimic of the PAH enzyme is explored, utilizing the above versatility of copper-oxygen chemistry. Two new copper complexes of the 6-substituted pterin ligand, 2-amino-7-methyl-4-oxidopteridine-6-carboxylic acid (**1**, H<sub>2</sub>L) assist this endeavour<sup>17b</sup>. The experimental designs involve their interfacing with the oxidized and reduced (dihydro) forms of the pterin ring, for developing the copper-pterin-O<sub>2</sub> chemistry.<sup>10, 14, 18,137,139,153</sup>

## Experimental Section

**General.** All starting materials and solvents were purchased from reliable commercial sources and used without further purification. Electronic spectra and kinetic data were recorded on a

Jasco V-530 UV-vis spectrophotometer, with thermostatic conditions ( $\pm 0.5\text{K}$ ) being maintained using a Shimadzu (TB-85) thermostat. Infrared spectra were recorded on a Perkin Elmer model RXI infrared spectrophotometer. Some of the  $^1\text{H}$  NMR spectral measurements were done on a Bruker, Avance 300 MHz NMR spectrometer. Fluorescence spectra were recorded on a Photon Technology International spectrofluorometer (model Fluorescence Master System). Magnetic susceptibility measurements were performed on a Sherwood instrument (model MSB mk1), using  $\text{HgCo}(\text{SCN})_4$  as the calibrant. Cyclic voltammetric experiments were performed with a Bioanalytical Systems Epsilon electrochemical workstation (model CV-50) using 1.0mM analyte in DMSO (0.1 M TBAP; glassy carbon working electrode). Elemental analysis data, some of the mass spectra, 500 MHz  $^1\text{H}$  NMR spectral data, CD spectral data and X-ray diffraction data were obtained from CSMCRI, Bhavnagar. EPR and rest of the mass spectral data were recorded by SAIF, IIT, Bombay and SAIF, CDRI, Lucknow, respectively.

**Computational Details.** DFT calculations were done using the GAUSSIAN 09 and GAUSS VIEW 5 program packages. For **2** the XRD structure was used as the starting point. Geometry optimizations were done with the DFT-B3LYP approach using the 6-31G\* basis set<sup>155-159</sup>. For **3** the optimized structure based on elemental analysis, ESIMS, IR, CD and  $^1\text{H}$  NMR data was used for electronic structure calculation.

**Synthesis of 2-amino-4-hydroxy-7-methylpteridine-6-carboxylic acid sesquihydrate( $\text{H}_2\text{L} \cdot 1.5\text{H}_2\text{O}$ ) (1).**

It was obtained by a published procedure<sup>19</sup>. Yield : moderate. Anal. Calcd for  $\text{C}_8\text{H}_7\text{N}_5\text{O}_3 \cdot 1.5\text{H}_2\text{O}$  : C, 38.71; H, 4.03; N, 28.22. Found : C, 38.96; H, 3.18; N, 28.0.

**Synthesis of  $[\text{Cu}^{\text{II}}(\text{L})(\text{phen})(\text{H}_2\text{O})] \cdot 3\text{H}_2\text{O}$  (2).** This compound could be prepared by alternative methods, e.g., **method A** and **method B** respectively, as described by Baisya and Roy<sup>17b</sup>. Brief outlines of such procedures are presented below.

**Method A.** This procedure involves a reaction on the 0.125mmol scale in aqueous alkaline medium (50mL, pH10.5) among  $\text{Cu}(\text{NO}_3)_2 \cdot 3\text{H}_2\text{O}$ , 1, 10-phenanthroline monohydrate (phen) and the pterin ligand **1** dissolved in NaOH (0.275mmol); a steady flow of dixxygen is to be maintained for 60h at 301-303K under subdued light. The final blue solution yielded green crystals within a week [ Figure II- 1(a) and (b)]. Their x-ray structural data are available from the Cambridge Crystallographic Data Centre (CCDC deposition No. 985054). (Anal. Calcd for  $\text{CuC}_{20}\text{H}_{21}\text{N}_7\text{O}_7$ : C, 44.89; H, 3.93; N, 18.33. Found C, 43.38; H, 4.06; N, 17.65).

**Method B.** Treatment of **2** (obtained by **Method A**) with equimolar amount (0.125mmol scale) of  $\text{NaBH}_4$  in aqueous medium (50mL) at 301-303K, produced a dark-brown compound [Figure II-1(c) ]. Subsequent aerial exposure reoxidized this reduced complex affording the above-mentioned green crystals (**2**) again [Scheme II- 8(a)], which were also characterized x-ray structurally<sup>17b</sup>. This dark-brown compound could be isolated in the solid state, by repeating this reaction in  $\text{CH}_3\text{OH}$  medium, using an excess of  $\text{NaBH}_4$ , as described below.

**Synthesis of  $\text{Na}_2[\text{Cu}^{\text{I}}(\text{L}')(\text{H}_2\text{O})_2-\mu-(\text{phen})-\text{Cu}^{\text{I}}(\text{L}')(\text{H}_2\text{O})_2] \cdot 2\text{H}_2\text{O}$  (**3**),** where  $(\text{L}')^{2-}$  is the 7,8-dihydro form (Scheme II-4) of the pterin ligand anion (Scheme II-1); chemical composition of **3** was established on the basis of microanalytical and spectroscopic data (vide infra). A methanolic solution (50 mL) of **2** (26.7 mg, 0.05 mmol) was treated with  $\text{NaBH}_4$  (11.3 mg, 0.3 mmol) and the reaction was allowed to continue for 45 min at 301-303K under subdued light in a Schlenk flask attached to a paraffin oil bubbler. The reaction mixture passed through a sequence of color changes e.g., bright green→pink→deep orange-brown. It was then rotavapped and a dark brown solid was recovered (Schemes II-5 and II-6). It was washed quickly (decantation ) with dinitrogen purged  $\text{CH}_3\text{OH}$  ( 3 X 4 mL) and dried in vacuo over silica gel for 48h. Yield: 35%.

Anal. Calcd for  $\text{Na}_2\text{Cu}_2\text{C}_{28}\text{H}_{34}\text{N}_{12}\text{O}_{12}$ : C, 37.21; H, 3.80; N, 18.60. Found: C, 36.98; H, 3.49; N, 17.58.

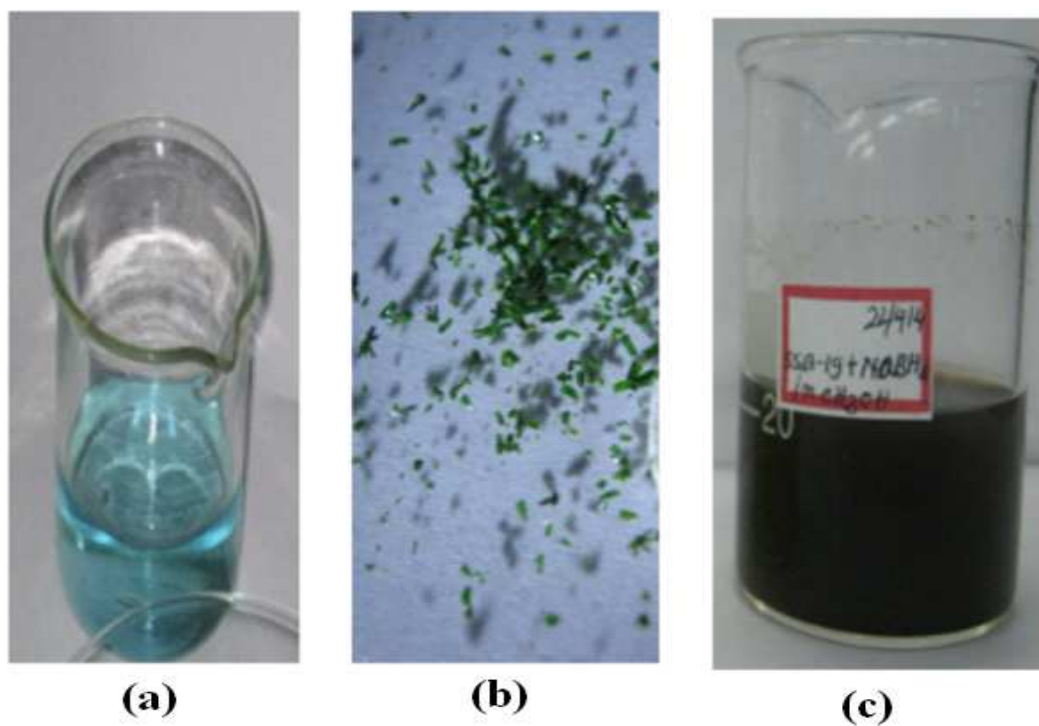
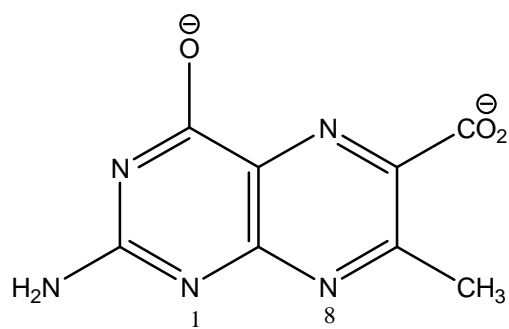
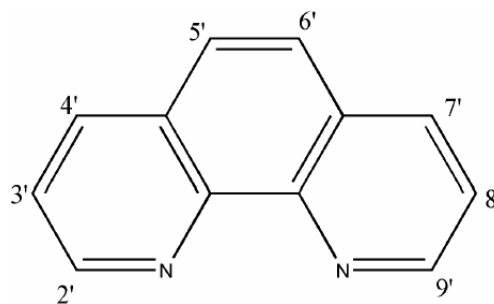


**Figure II-1.** The blue mother liquor (a) and the green crystals (b) as per method A<sup>17b</sup>; (c) the dark-brown compound formed on treatment of **2** with equimolar amount of  $\text{NaBH}_4$  in aqueous medium as described in method B<sup>17b</sup>.



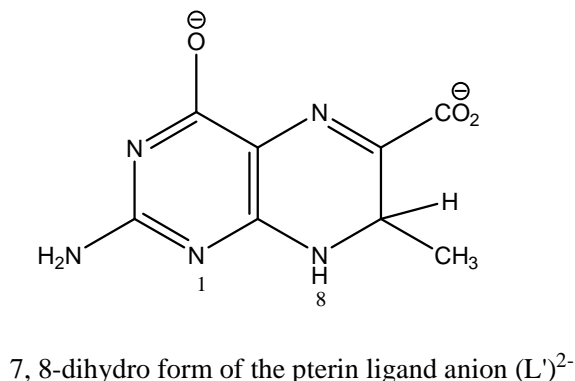
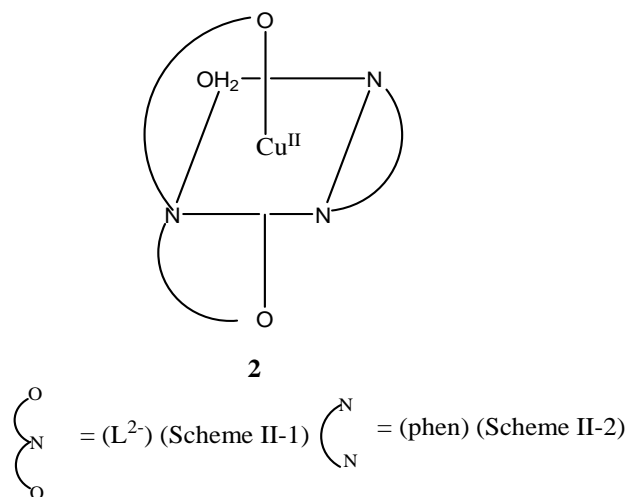
The pterin ligand (**1**,  $\text{H}_2\text{L}$ )  
anion ( $\text{L}^{2-}$ )

**Scheme II-1**



(phen)

**Scheme II-2**



**Scheme II-3**

**Scheme II-4**

**Reaction of bromobenzene with 3 and the recovery of 4-bromophenol as well as 2 from the reaction medium [Scheme II- 8(b)].** For this purpose **3** was generated in situ from **2** and NaBH<sub>4</sub> and then reacted with bromobenzene, for completing the reaction sequence as outlined in Scheme II-8(b). Initially a methanolic solution (50 mL) of **2** (67 mg, 0.125 mmol) was reacted with NaBH<sub>4</sub> (47 mg, 1.25 mmol) under the aforesaid conditions. Next a methanolic solution ( 10 mL) of bromobenzene (196 mg, 1.25 mmol) saturated with dioxygen was added to the above reaction mixture, dioxygen was bubbled in for 2.5h and then left aside for 72h. After that the reaction mixture was rotavapped to dryness and extracted with pet ether (bp.313-333K). The pet ether extract was rotavapped to dryness yielding a white solid which was dried in vacuo over silica gel for 48h; m.p. 335K (literature data show a melting point of 337K for 4-bromophenol)<sup>20</sup>. IR data (nujol, cm<sup>-1</sup>): new vibrational modes (with respect to bromobenzene) appear at 3350 [ν(OH)], 1333[δ(OH)] and 1285[ν(C-O) +δ(OH)] respectively, for the above white product, assignable to the phenolic – OH group<sup>21</sup>. In the <sup>1</sup>H NMR data [δ, CDCl<sub>3</sub>, Me<sub>4</sub>Si; Figure II-2] for bromobenzene over the region δ10.0 – 6.5, only two multiplet singnals (2:3 ratio) appear at δ7.48

and  $\delta 7.24$  respectively, assignable to its aromatic protons [Figure II-2(a)]; for the above white product a new broad singlet signal appears at  $\delta 9.26$  [phenolic – OH proton; Figure II-2(b)], in addition to the two multiplet signals (1:1 ratio) connected by cross peaks at  $\delta 8.32$  and  $\delta 7.73$  respectively (aromatic protons), verifying the hydroxylation of the aromatic ring of bromobenzene.

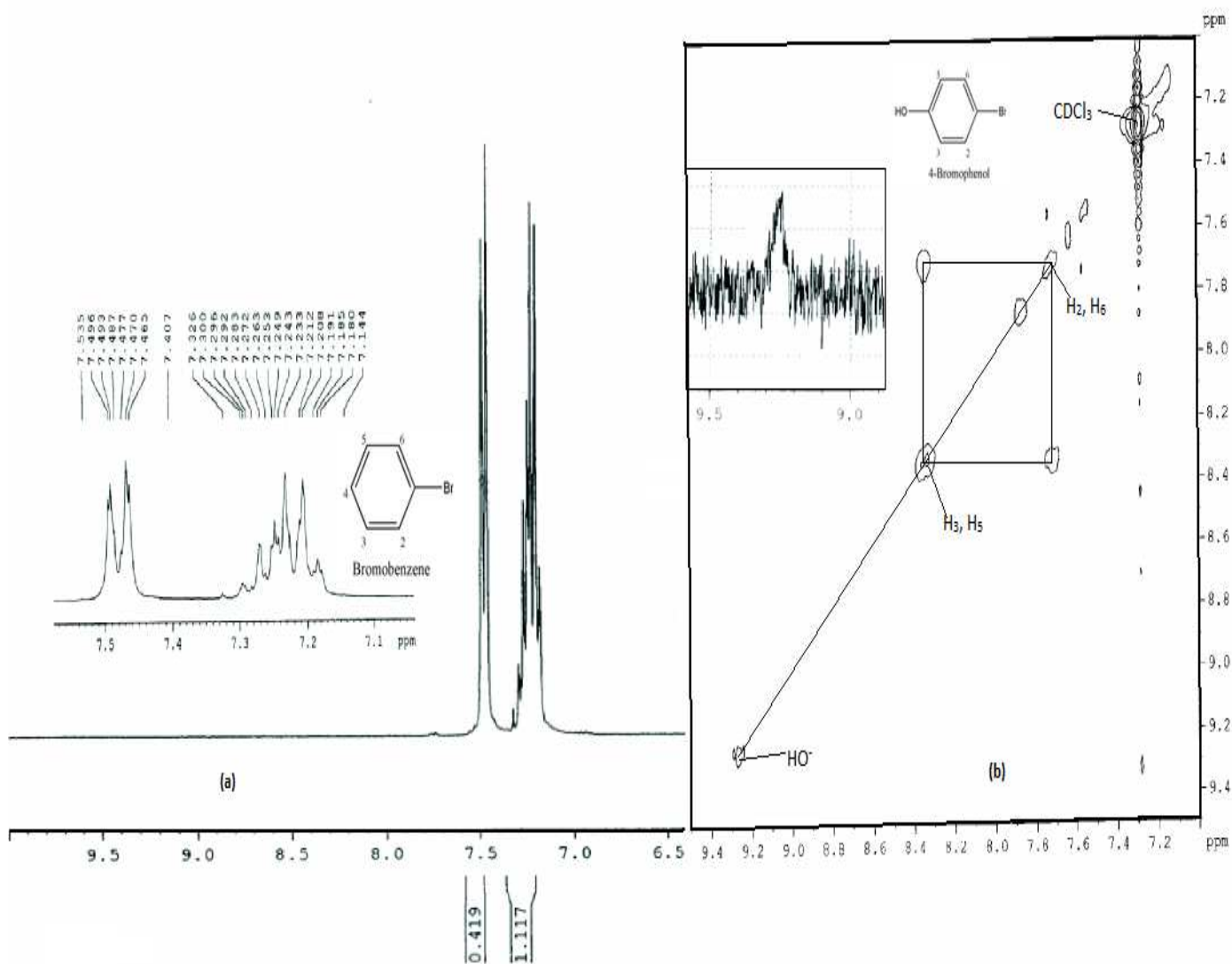


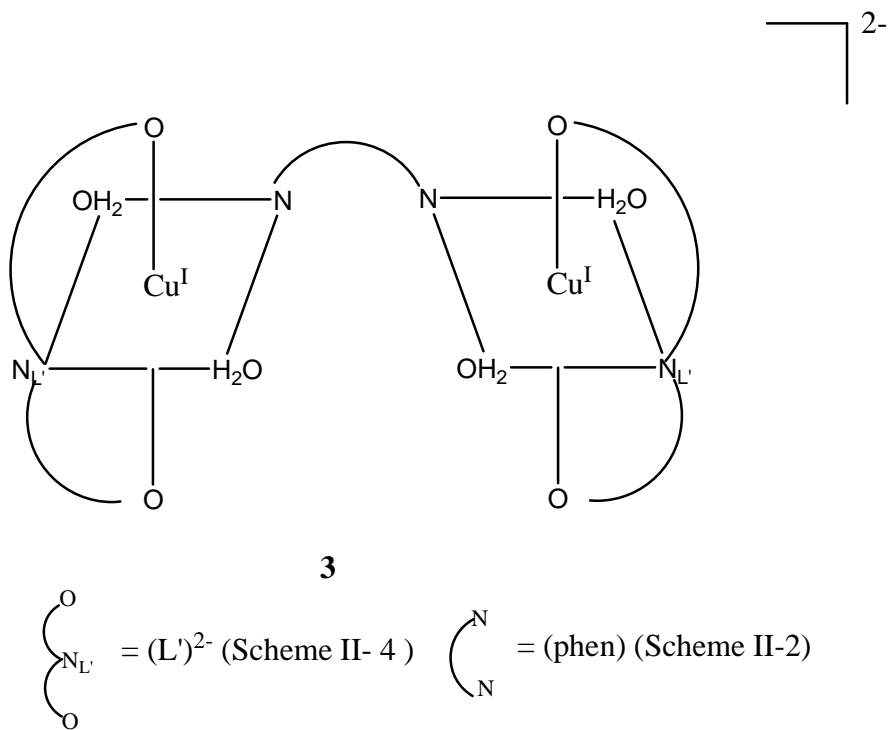
**Figure II-2.** (a) The 300 MHz <sup>1</sup>H NMR spectrum of bromobenzene in CDCl<sub>3</sub> over the region  $\delta 10 - 6.5$ . The inset shows the expanded view of the aromatic proton signals. (b) The 300 MHz

$^1\text{H} - ^1\text{H}$  cosy spectrum (symmetrized) of the recovered white compound (mp. 337K) (Schemes II-7, II-8) in  $\text{CDCl}_3$  over the region  $\delta 9.5 - 7.0$ . The inset shows a new signal (-OH) at  $\delta 9.26$  for this compound, as compared to the starting material bromobenzene.

---

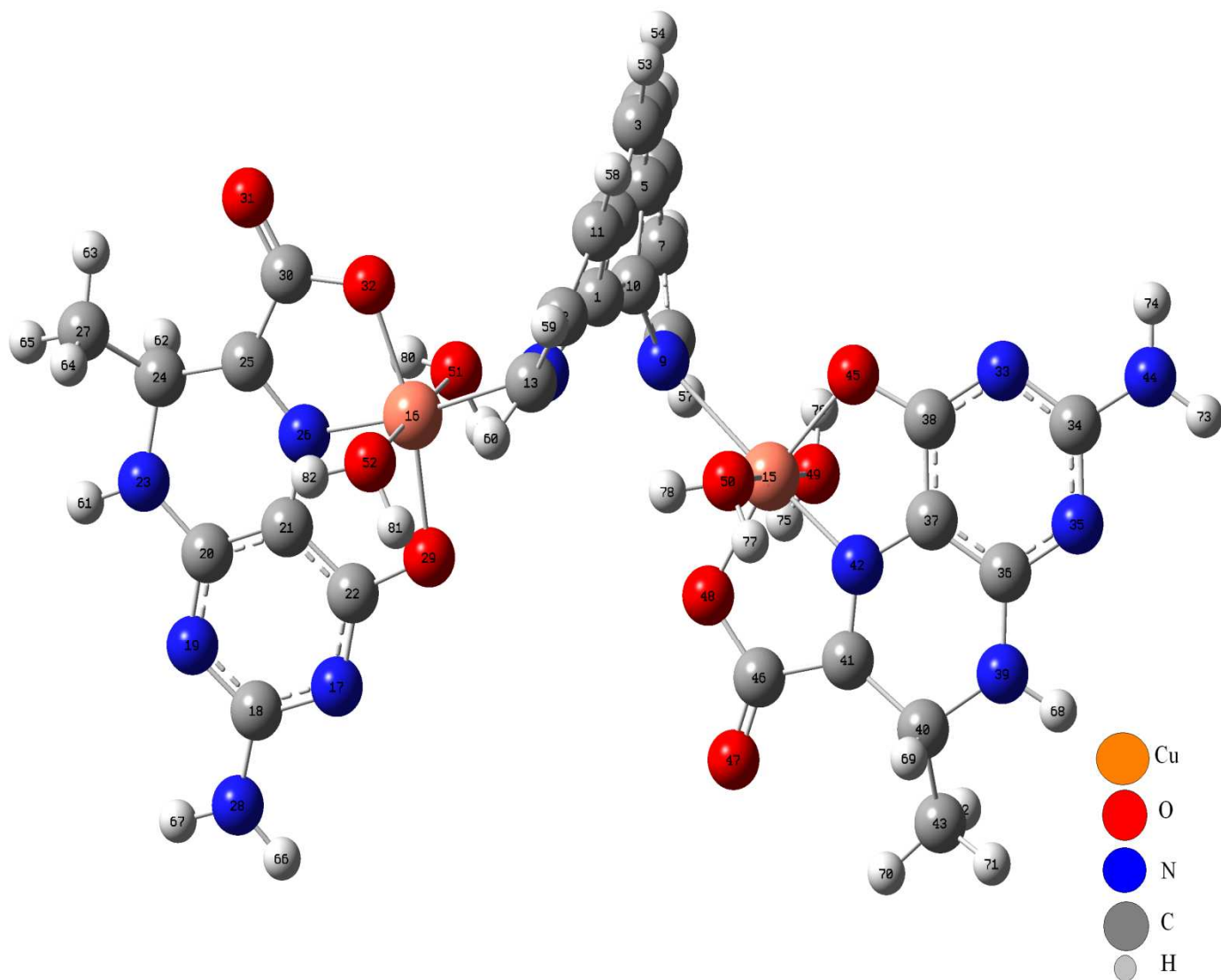
The residual part of the above reaction mixture left behind after pet ether extraction, yielded a green product which could be purified (extraction with  $\text{CH}_3\text{OH}$  and recrystallization from the same solvent) and characterized. Its microanalytical data are similar to those of **2** (Anal. Calcd for  $\text{CuC}_{20}\text{H}_{21}\text{N}_7\text{O}_7$ : C, 44.89; H, 3.96; N, 18.33. Found C, 43.5; H, 3.4; N, 17.85). Further verification of its chemical composition is achieved from the mass spectral data (vide infra).

---



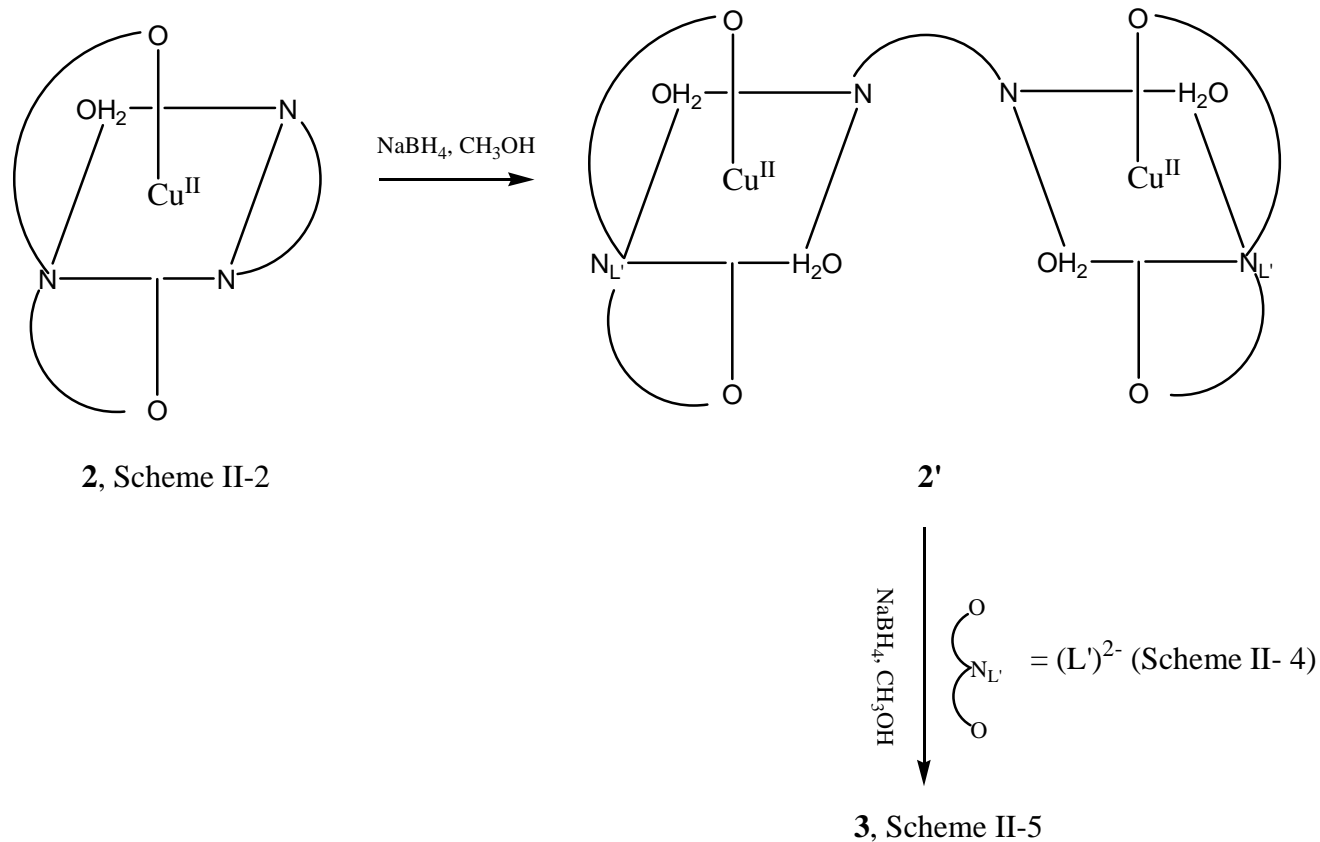
**Scheme II-5**

---



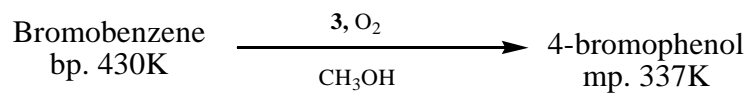
**Scheme II-5(a)** DFT optimized molecular structure of compound **3**; the  $\text{Na}^+$  ions are omitted for simplicity.

---



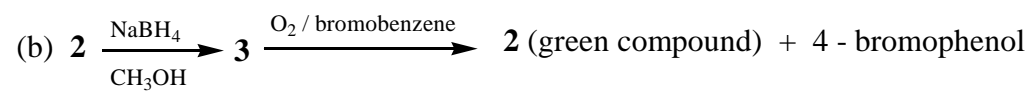
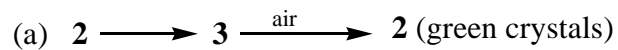
### Scheme II-6

---



### Scheme II-7

---



vide Schemes II-6 and II-7 for details

## Scheme II-8

---

### Results and Discussion

**Synthesis of the complexes.** It can be inferred from the experimental section that **2** can be synthesized by alternative routes, e.g., direct synthesis from a Cu(II) salt and the relevant ligands (method A), a redox reaction involving NaBH<sub>4</sub> reduction of **2** and its subsequent aerial reoxidation (method B) and finally its recovery from a reaction medium involving the interaction between **3** and bromobenzene [Scheme II-8(b)]. The above steps highlight the facile interconversion between **2** and **3** as well as the stability of the coordination geometry around the Cu(II) ion in **2**. Two of the above crops of **2** could be characterized x-ray structurally and the structural data of the one obtained using NaBH<sub>4</sub> reduction – aerial reoxidation cycle [method B, Scheme II-8(a)] are of better accuracy and summarized below<sup>17b</sup>.

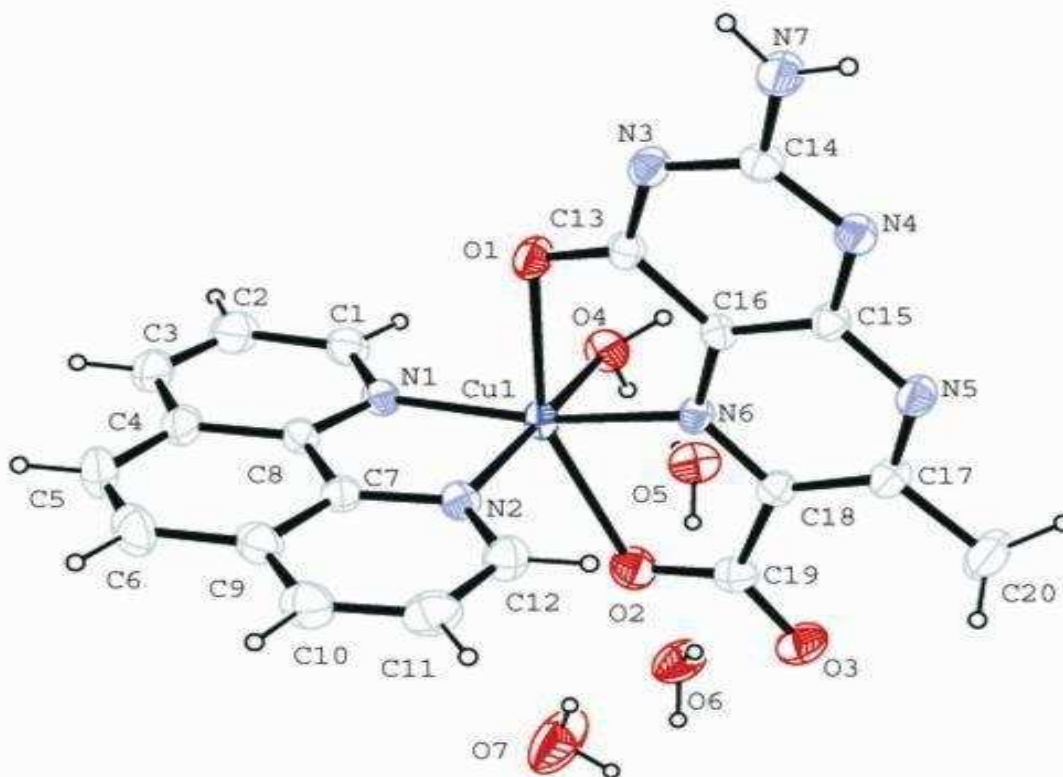


**Figure II- 3.** The molecular structure of **2**, with the displacement ellipsoids drawn at the 30% probability level. Few relevant bond lengths (Å) and angles (deg) are shown here : Cu1-N1=2.002(3), Cu1 – N2= 2.037(3), Cu1 – N6= 1.999(3), Cu1 – O1= 2.384(3), Cu1 – O2= 2.304(3), Cu1 – O4= 2.019(3), O1 – C13= 1.237(5), N7 – C14=1.327(5); O2 – Cu1 – O1=151.17(10), N6 – Cu1 – N1=165.66(13), O4 – Cu1 – N2=174.45(13), N6 –Cu1 – O1=76.47(10), N6 – Cu1- O2= 74.66(11)<sup>17b</sup>.

**Molecular structure of [Cu<sup>II</sup>(L)(phen)(H<sub>2</sub>O)]. 3H<sub>2</sub>O (**2**).** Figure II-3 shows a mononuclear Cu(II) centre in an axially elongated distorted octahedron, with two N atoms (N1 and N2) of the phen ligand, a pyrazine ring N atom (N6) of the pterin ligand and the aqua O atom (O4), forming the equatorial plane. The two pterin O atoms (O1 and O2) occupy the longer axial positions, with

the phenolate O1 forming the longest axial bond [2.384(3)Å]. In addition to the characteristic Jahn-Teller effect, another factor causing deviation from a regular octahedral geometry is that the pterin ligand forms two five-membered chelate rings with small bite angles [76.47(10) and 74.66(11)<sup>0</sup>]. In terms of the charge balance of this complex, the pterin ligand (**1**) acts as a binategative tridentate O,N,O - donor (Schemes II-1 and II-3). The phen ligand and pterin chelate ring are disposed almost orthogonally [ dihedral angle = 85.97(3)<sup>0</sup> ], thereby minimizing the steric repulsion. Of the three axes, the least deviation from linearity is observed along the O4-Cu1-N2 direction [174.45(13)<sup>0</sup>]. The pyrazine ring N atom (N6) forms the shortest Cu1-N6 bond [1.999(3)Å] here and is located in the equatorial plane, maintaining parity with the earlier observations on related copper and cobalt complexes<sup>17e,18c</sup>. The multiple bond character of the O1-C13 bond [1.237(4)Å] merits attention, as it throws light on the electron-shuffling ability of the pterin ring as well as its donor groups. According to Joule's hypothesis, electron-density is withdrawn from the pyrazine ring N5 by the pyrimidine ring C13 carbonyl group through mesomeric interaction.<sup>22,23</sup> Formation of the O1-Cu1 bond helps this electron migration towards the O1 atom, with possible participation of the electron- rich N7-C14[1.327(5)Å] bond in this process. This view is substantiated by similar observations on related Co(II), Ni(II) and Zn(II) complexes.<sup>17a,17c-17e</sup> Table II-I shows the crystal data of **2**, while its geometric parameters and hydrogen-bond geometry data are shown in Tables II-2 and II-3 respectively.

**Table II-1.** Crystal data of **2**

Chemical formula	[Cu(C <sub>8</sub> H <sub>5</sub> N <sub>5</sub> O <sub>3</sub> )(C <sub>12</sub> H <sub>8</sub> N <sub>2</sub> )(H <sub>2</sub> O)]·3H <sub>2</sub> O
$M_r$	534.98
Crystal system, space group	Triclinic, $P\bar{1}$
Temperature (K)	273
$a, b, c$ (Å)	8.5399 (17), 10.038 (2), 13.601 (3)
$\alpha, \beta, \gamma$ (°)	97.292 (3), 94.587 (3), 110.999 (3)
$V$ (Å <sup>3</sup> )	1069.8 (4)
$Z$	2
Radiation type	Mo $K\alpha$
$\mu$ (mm <sup>-1</sup> )	1.08
Crystal size (mm)	0.20 × 0.05 × 0.03
Data collection	
Diffractometer	Bruker Kappa APEXII
Absorption correction	Multi-scan (SADABS; Bruker, 2001)
$T_{\min}, T_{\max}$	0.813, 0.968
No. of measured, independent and observed [ $I > 2\sigma(I)$ ] reflections	8227, 4134, 3590

$R_{\text{int}}$	0.024
$(\sin \theta/\lambda)_{\text{max}} (\text{\AA}^{-1})$	0.617
Refinement	
$R[F^2 > 2\sigma(F^2)], wR(F^2), S$	0.051, 0.136, 1.15
No. of reflections	4134
No. of parameters	349
No. of restraints	10
H-atom treatment	H atoms treated by a mixture of independent and constrained refinement
$\Delta\rho_{\text{max}}, \Delta\rho_{\text{min}} (e \text{\AA}^{-3})$	0.66, -0.31

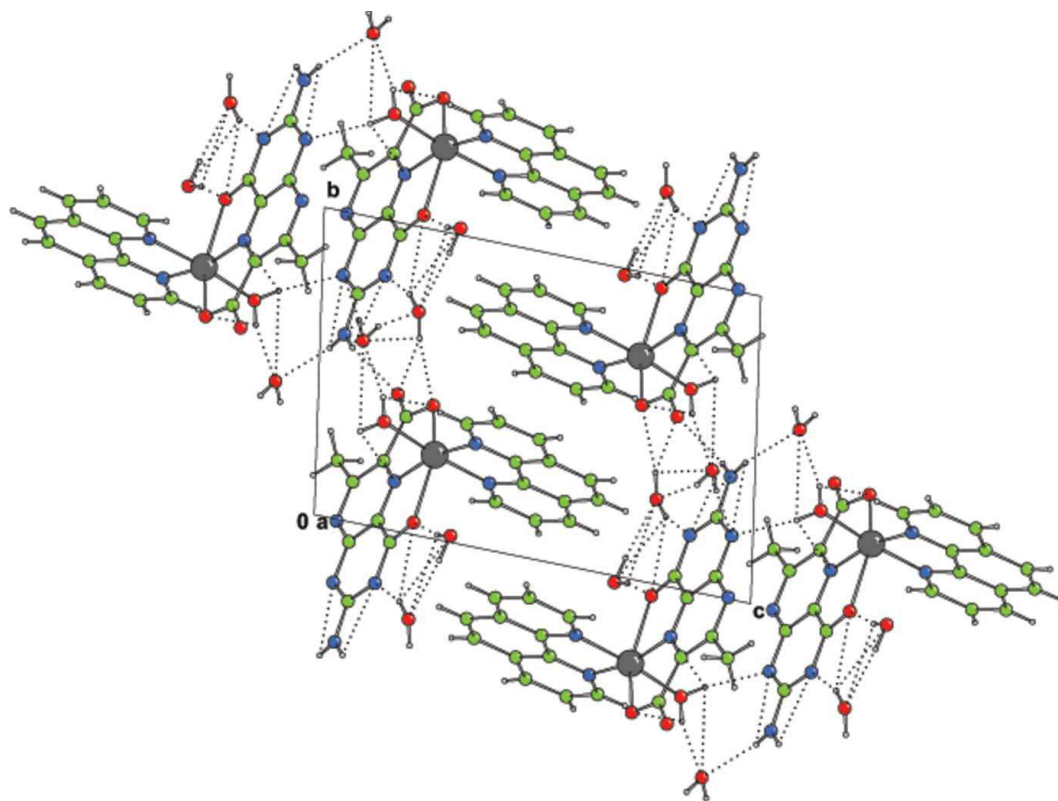


**Figure II-4.** The crystal packing diagram of the title compound, viewed along the a axis. Hydrogen bonds (dotted lines) assist the formation of a layer structure parallel to (001).

**Table II-2.** Geometric parameters (Å, °) of **2**

Cu1—O3	2.400 (7)	C15—C14	1.448 (13)
Cu1—N3	2.002 (7)	C15—C20	1.476 (14)
Cu1—N1	2.034 (8)	N6—H61	0.859
Cu1—O1	2.303 (7)	N6—H62	0.859
Cu1—N2	1.995 (8)	N6—C17	1.322 (13)

Cu1—O4	2.024 (7)	C9—C8	1.407 (13)
O3—C18	1.248 (11)	C8—C10	1.400 (16)
N3—C19	1.313 (12)	C8—C7	1.407 (16)
N3—C14	1.328 (12)	C4—C6	1.438 (15)
N1—C5	1.355 (12)	C4—C3	1.403 (16)
N1—C1	1.324 (12)	C12—H121	0.930
O1—C13	1.270 (12)	C12—C11	1.385 (14)
N2—C9	1.372 (12)	C1—H11	0.932
N2—C12	1.313 (12)	C1—C2	1.401 (15)
N4—C16	1.350 (12)	C10—H101	0.928
N4—C15	1.318 (13)	C10—C11	1.375 (17)
N7—C18	1.332 (13)	C20—H201	0.969
N7—C17	1.368 (12)	C20—H202	0.954
C16—C19	1.416 (11)	C20—H203	0.955
C16—N5	1.326 (12)	C6—H61	0.934
C19—C18	1.451 (13)	C6—C7	1.340 (18)
O2—C13	1.246 (12)	C3—H31	0.926

N5—C17	1.355 (12)	C3—C2	1.357 (17)
C13—C14	1.505 (14)	C7—H71	0.930
C5—C9	1.414 (13)	C2—H21	0.929
C5—C4	1.399 (13)	C11—H111	0.930
O3—Cu1—N3	76.4 (3)	H61—N6—C17	120.0
O3—Cu1—N1	91.0 (3)	H62—N6—C17	119.8
N3—Cu1—N1	93.9 (3)	C5—C9—N2	117.5 (8)
O3—Cu1—O1	151.3 (2)	C5—C9—C8	120.0 (9)
N3—Cu1—O1	75.0 (3)	N2—C9—C8	122.5 (9)
N1—Cu1—O1	89.8 (3)	N7—C17—N5	126.0 (9)
O3—Cu1—N2	89.6 (3)	N7—C17—N6	115.8 (8)
N3—Cu1—N2	165.4 (3)	N5—C17—N6	118.3 (9)
N1—Cu1—N2	82.2 (3)	C13—C14—C15	127.3 (9)
O1—Cu1—N2	118.9 (3)	C13—C14—N3	115.2 (8)
O3—Cu1—O4	92.9 (3)	C15—C14—N3	117.5 (9)
N3—Cu1—O4	90.7 (3)	C9—C8—C10	116.7 (10)
N1—Cu1—O4	174.6 (3)	C9—C8—C7	118.5 (10)

O1—Cu1—O4	88.7 (3)	C10—C8—C7	124.8 (10)
N2—Cu1—O4	94.0 (3)	C5—C4—C6	118.7 (10)
Cu1—O3—C18	106.3 (6)	C5—C4—C3	116.7 (10)
Cu1—N3—C19	116.8 (6)	C6—C4—C3	124.6 (10)
Cu1—N3—C14	121.1 (7)	N2—C12—H121	118.5
C19—N3—C14	122.1 (8)	N2—C12—C11	123.4 (10)
Cu1—N1—C5	111.8 (6)	H121—C12—C11	118.1
Cu1—N1—C1	130.0 (7)	N1—C1—H11	118.8
C5—N1—C1	118.2 (9)	N1—C1—C2	122.0 (10)
Cu1—O1—C13	112.3 (6)	H11—C1—C2	119.2
Cu1—N2—C9	111.8 (6)	C8—C10—H101	120.2
Cu1—N2—C12	129.7 (7)	C8—C10—C11	120.1 (9)
C9—N2—C12	118.2 (8)	H101—C10—C11	119.7
C16—N4—C15	120.8 (8)	C15—C20—H201	109.5
C18—N7—C17	118.6 (8)	C15—C20—H202	109.2
N4—C16—C19	118.4 (8)	H201—C20—H202	109.1
N4—C16—N5	120.6 (8)	C15—C20—H203	109.4

C19—C16—N5	121.0 (8)	H201—C20—H203	109.1
C16—C19—N3	120.7 (8)	H202—C20—H203	110.4
C16—C19—C18	118.8 (8)	C4—C6—H61	120.1
N3—C19—C18	120.5 (8)	C4—C6—C7	120.2 (10)
C19—C18—N7	118.3 (9)	H61—C6—C7	119.7
C19—C18—O3	119.8 (9)	C4—C3—H31	120.5
N7—C18—O3	121.9 (8)	C4—C3—C2	119.7 (10)
C16—N5—C17	117.2 (8)	H31—C3—C2	119.7
O1—C13—O2	124.1 (10)	C8—C7—C6	122.5 (10)
O1—C13—C14	116.1 (9)	C8—C7—H71	118.6
O2—C13—C14	119.7 (9)	C6—C7—H71	118.9
N1—C5—C9	116.4 (8)	C1—C2—C3	119.9 (10)
N1—C5—C4	123.5 (9)	C1—C2—H21	120.0
C9—C5—C4	120.1 (9)	C3—C2—H21	120.1
N4—C15—C14	120.4 (8)	C12—C11—C10	119.0 (10)
N4—C15—C20	117.9 (9)	C12—C11—H111	120.4
C14—C15—C20	121.7 (10)	C10—C11—H111	120.6

H61—N6—H62	120.2		
------------	-------	--	--

**Supramolecular features.** In the crystal, intermolecular N—H···O, O—H···N and O—H···O hydrogen bonds (Table II-3) link the complex molecules and lattice water molecules into a layer parallel to (001) (Figure II- 4). Intermolecular weak C—H···O hydrogen bonds and C—H··· $\pi$  interactions are also observed in the crystal. In addition,  $\pi$ - $\pi$  stacking between nearly parallel pterin ring systems of adjacent molecules occurs in the crystal structure, the centroid–centroid distance being 3.352 (2) Å (Figure II- 5). Again, the nearly parallel phen rings of adjacent molecules also display  $\pi$ - $\pi$  stacking interactions with centroids distances of 3.546 (3), 3.706 (3) and 3.744 (3) Å. These intermolecular interactions link the molecules into a three-dimensional supramolecular architecture.

**Table II-3.** Hydrogen-bond geometry (Å, °) of **2**, *Cg* is the centroid of the N3/N4/C13–C16 ring.

<i>D—H···A</i>	<i>D—H</i>	<i>H···A</i>	<i>D···A</i>	<i>D—H···A</i>
O4—H4C···O5	0.82 (3)	1.92 (3)	2.722 (4)	169 (5)
O4—H4D···N4 <sup>i</sup>	0.81 (3)	2.26 (3)	3.038 (4)	161 (5)
O5—H5C···O6	0.82 (3)	1.96 (4)	2.748 (5)	162 (4)
O5—H5D···N4 <sup>ii</sup>	0.82 (5)	2.07 (5)	2.891 (5)	176 (3)

<b><i>D—H…A</i></b>	<b><i>D—H</i></b>	<b><i>H…A</i></b>	<b><i>D…A</i></b>	<b><i>D—H…A</i></b>
O6—H6C…O2	0.82 (3)	2.23 (3)	2.921 (4)	141 (5)
O6—H6C…O3	0.82 (3)	2.25 (4)	3.029 (4)	158 (5)
O7—H7C…O6	0.82 (2)	2.24 (3)	2.965 (6)	148 (5)
O7—H7D…O1 <sup>iii</sup>	0.81 (5)	2.16 (4)	2.943 (6)	162 (5)
N7—H7E…O5 <sup>i</sup>	0.85 (5)	2.17 (4)	2.998 (6)	162 (4)
N7—H7F…O3 <sup>iv</sup>	0.86 (4)	2.14 (5)	2.908 (5)	148 (4)
C1—H1…O3 <sup>v</sup>	0.93	2.47	3.175 (6)	133
C10—H10…O1 <sup>vi</sup>	0.93	2.54	3.406 (5)	155
C12—H12…O7 <sup>vii</sup>	0.93	2.57	3.343 (7)	140
C6—H6…Cg <sup>vi</sup>	0.93	2.82	3.740 (5)	173

Symmetry codes: (i)  $-x+2, -y+2, -z+2$ ; (ii)  $x, y-1, z$ ; (iii)  $x-1, y-1, z$ ; (iv)  $x+1, y+1, z$ ; (v)  $x+1, y, z$ ;  
(vi)  $-x+2, -y+2, -z+1$ ; (vii)  $x, y+1, z$ .

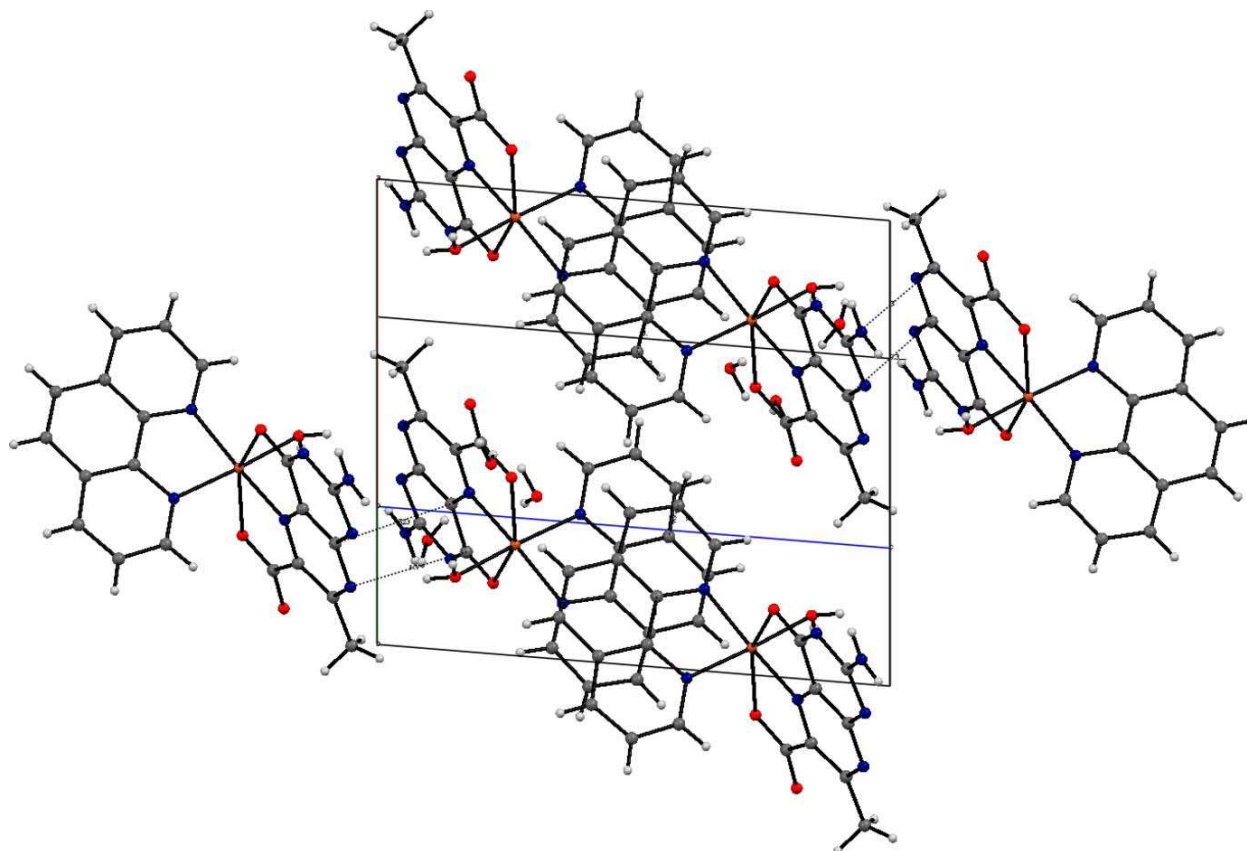


**Figure II-5.** A molecular packing diagram highlighting  $\pi$ - $\pi$  stacking interactions between neighbouring phen-phen and pterin-pterin rings.

**Table II – 4.** Selected optimized geometric parameters ( $\text{\AA}$ ,  $^\circ$ ) of **3**<sup>155-160</sup> and their comparison with the related x-ray structural data of **2**.

Bonds ( $\text{\AA}$ )	DFT optimized data of <b>3</b> (Gaussian 09)	x-ray structural data of <b>2</b> ( Table II-2 ) <sup>17b</sup>	MM2 optimized ( CHEM 3D ) data of <b>3</b>
Cu(15) – N(9)	2.3782	2.002(3)	2.378
Cu(16) – N(14)	2.3881	2.037(3)	2.388
Cu(15) – O(45)	1.9871	2.384(3)	1.987

Cu(15) – O(48)	1.9469	2.304(3)	1.947
Cu(15) – O(49)	1.9138	2.019(3)	1.914
Cu(15) – O(50)	1.922	2.019(3)	1.922
Cu(15) – N(42)	1.8902	1.999(3)	1.890
Cu(16) – N(26)	1.8959	1.999(3)	1.896
Cu(16) – O(51)	1.9314	2.019(3)	1.931
Cu(16) – O(52)	1.9144	2.019(3)	1.914
Cu(16) – O(32)	1.9501	2.384(3)	1.950
Cu(16) – O(29)	2.0335	2.304(3)	2.033

Bond angles ( ° )	DFT optimized data of <b>3</b> (Gaussian 09)	x-ray structural data of <b>2</b> ( Table II-2 ) <sup>17b</sup>	MM2 optimized ( CHEM 3D ) data of <b>3</b>
O(45) – Cu(15) – O(48)	168.1866	151.17(10)	168.187
N(9) – Cu(15) – N(42)	177.3987	165.66(13)	177.399
N(9) – Cu(15) – O(45)	93.6388	89.79(11)	93.639
N(9) – Cu(15) – O(48)	98.157	118.84(12)	98.157
N(9) – Cu(15) – O(50)	90.2632	82.20(13)	90.263
N(9) – Cu(15) – O(49)	92.5509	93.79(13)	92.551
N(42) – Cu(15) – O(45)	83.828	76.45(11)	83.828
N(42) – Cu(15) – O(48)	84.37	74.74(11)	84.370
N(42) – Cu(15) – O(49)	86.8199	91.01(12)	86.820
N(42) – Cu(15) – O(50)	90.3314	93.79(13)	90.331

O(45) – Cu(15) – O(50)	90.0711	90.74(12)	90.071
O(45) – Cu(15) – O(49)	88.9062	93.07(12)	88.906
O(50) – Cu(15) – O(48)	90.5147	88.62(12)	90.515
O(49) – Cu(15) – O(48)	89.924	89.98(12)	89.924
O(49)-Cu(15)-O(50)	177.0611	174.45(13)	177.061
N(26) – Cu(16) – N(14)	173.5472	165.66(13)	173.547
O(29) – Cu(16) – O(32)	166.3806	151.17(10)	166.381
N(14) - Cu(16) – O(29)	103.4795	118.84(12)	103.479
N(14) - Cu(16) – O(51)	89.9923	89.79(11)	89.992
N(14) - Cu(16) – O(52)	91.2396	93.79(13)	91.240
N(14) - Cu(16) – O(32)	90.1385	82.20(13)	90.138
N(26) – Cu(16) – O(29)	82.9732	76.45(11)	82.973
N(26) – Cu(16) – O(32)	83.4088	74.74(11)	83.409
N(26) – Cu(16) – O(51)	90.01	91.01(12)	90.010
N(26) – Cu(16) – O(52)	88.7801	93.79(13)	88.780
O(29) – Cu(16) – O(51)	90.3224	88.62(12)	90.322
O(29) – Cu(16) – O(52)	89.2679	89.98(12)	89.268
O(51) – Cu(16) – O(32)	89.8661	89.79(11)	89.866
O(52) – Cu(16) – O(32)	90.257	93.79(13)	90.257
O(51)-Cu(16)-O(52)	178.7621	174.45(13)	178.762

### DFT optimized molecular structure of **3**

Scheme II-5(a) shows the relevant optimized molecular structure of **3**<sup>155-159</sup>. It takes into account the 7, 8-dihydro form of the pterin ring (  $L^{2-}$ , Scheme II-4 ) as well as the bridging ‘phen’ ligand; it is consistent with its microanalytical, ESIMS, physico-chemical (cyclic voltammetry) and spectroscopic (UV-VIS, IR, fluorescence and <sup>1</sup>H NMR ) data. In short an effective frame work is obtained for further discussion (vide later). Here **3** consists of two octahedrally coordinated Cu(I) centres linked by a bridging ‘phen’ ligand; the latter is disposed almost orthogonally to the two pterin rings for minimizing the steric repulsions and it is puckered to a certain extent. Along with tridentate ONO coordination from the pterin ligand, the two aquo ligands complete the coordination octahedron around each copper (I) atom. The MM2 calculations (CHEM 3D model) provide with an almost identical optimized structure.<sup>160</sup> Table II-4 shows a few selected optimized geometric parameters (Å, °) of **3** obtained by either DFT (Gaussian 09) method or MM2 calculations (Chem 3D); they are compared with the x-ray structural data of **2**.<sup>17b</sup> The tally of computed/optimized data with the x-ray structural data is reasonable, in view of the fact that **3** possesses two Cu(I) centres linked by a μ-phen group and two 7, 8-dihydro pterin ligands instead of a mononuclear Cu(II) centre of **2** with aromatic/oxidized pterin.

**Chemical composition and mass spectrometry.** For all the compounds mentioned in the experimental section (**1**, **2** and **3**) as well as the green compound recovered from the methanolic reaction medium involving **3** and bromobenzene, identified here as **2** [Scheme II- 8(b)], satisfactory elemental analysis data and electrospray ionization mass spectra (ESIMS) have been obtained. For **1** a peak at m/z 222 (rel. inten.15%) corresponds to the dehydrated species  $[M - 1.5H_2O + H]^+$  where  $M(C_8H_7N_5O_3 \cdot 1.5H_2O)$  is the relevant molecular formula; the associated

isotope pattern could be calculated.<sup>21,24</sup> For **2** the intact molecular ion peak ( $[M + H]^+$ ) is observed at  $m/z$  536.4 (rel. inten. 40%), where  $M = \text{CuC}_{20}\text{H}_{13}\text{N}_7\text{O}_3 \cdot 4\text{H}_2\text{O}$ ; the base peak at  $m/z$  459.2 represents the corresponding dehydrated species  $[M - 4\text{H}_2\text{O} - 3\text{H}]^+$  and its isotope distribution pattern

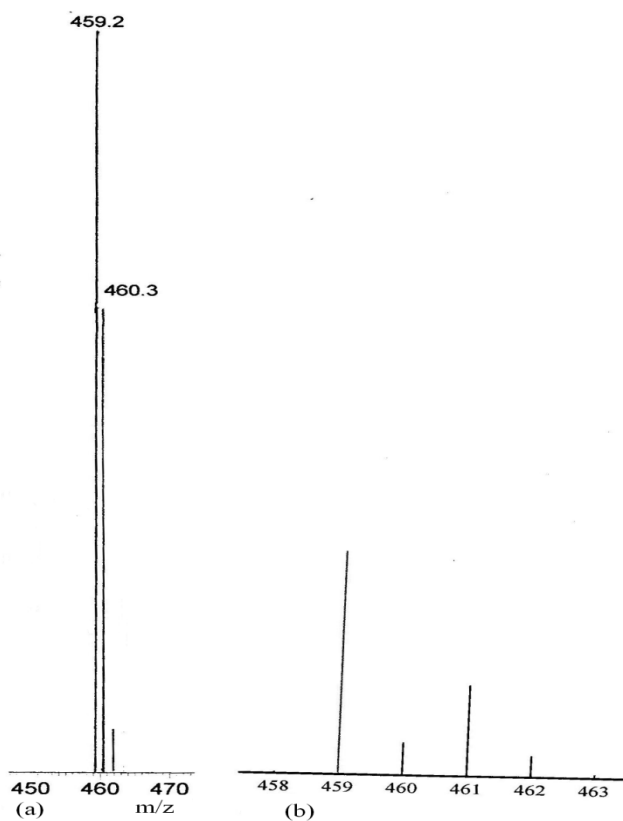


**Figure II-6.** (a) ESIMS data of **2**,  $m/z = 459.2$ ; (b) the calculated isotope pattern for the base peak at  $m/z = 459.2$  corresponding to the fragment  $[M - 4\text{H}_2\text{O} - 3\text{H}]^+$ , where  $M$  is the molecular formula of **2**.

---

could be simulated (Figure II-6). For the green compound recovered from the reaction sequence summarized in Scheme II-8(b), the base peak at  $m/z$  463.36 could be assigned to the desolvated

molecular ion  $[M - 4H_2O]^+$  where M is identified to be **2**, i.e.,  $M = CuC_{20}H_{13}N_7O_3 \cdot 4H_2O$ ; the relevant simulated isotope pattern is shown in Figure II-7. Finally, the ESIMS

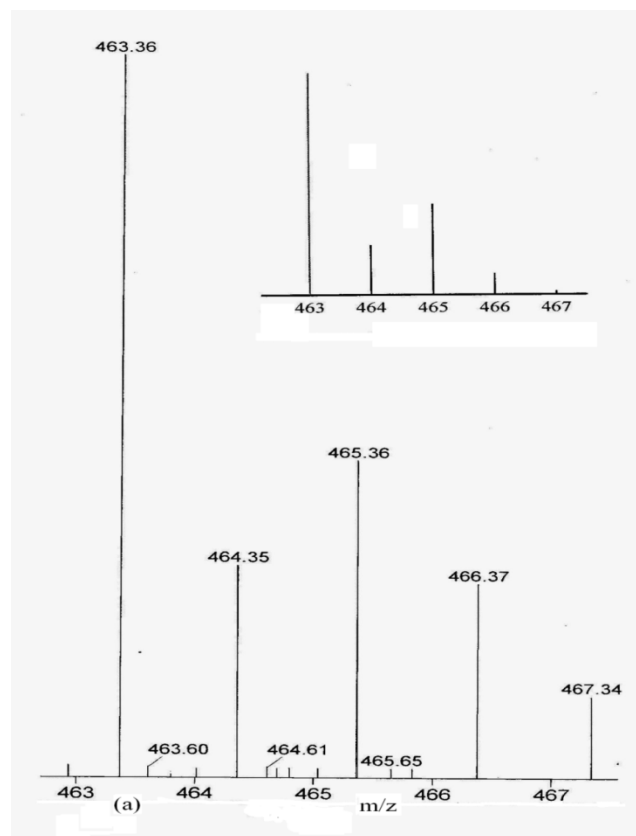


**Figure II-7.** (a) ESIMS data ( $m/z = 463.36$ ) of **2** recovered from a reaction mixture, as indicated in Scheme II-8(b); (b) the corresponding calculated isotope pattern for the fragment  $[M - 4H_2O]^+$ , where M is the molecular formula of **2**.

data [Figure II- 8(a)] are able to substantiate the composition of **3**, that is, its binuclear formulation. The peak at  $m/z$  808.9 (rel. inten. 20%) is assigned to the fragment  $[M - 5H_2O - 5H]^+$  where M is **3** ( $M = Na_2Cu_2C_{28}H_{22}N_{12}O_6 \cdot 6H_2O$ ); the loss of five H atoms is justified for a fragment ion peak.<sup>21</sup> The peak at  $m/z$  705.0 (rel. inten. 32%) corresponds to the fragment  $[M - 6H_2O - 2CO_2 - 2H]^+$ . The isotope distribution patterns of both these peaks could be simulated

[Figure II-8(b), (c)], verifying the overall stability of the parent binuclear species (**3**, Scheme II-5) as well as its chemical composition.

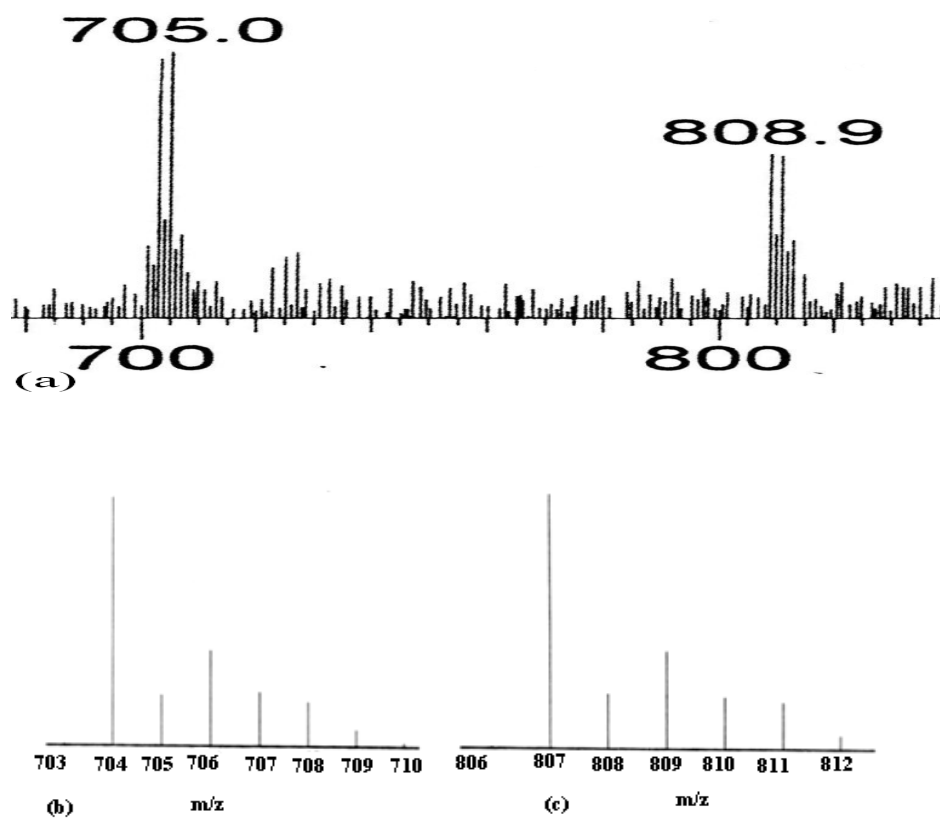


**Figure II-8.** (a) ESIMS data ( $m/z = 705.0$  and  $808.9$ ) of **3**; the corresponding calculated isotope patterns are shown in (b) and (c).

---

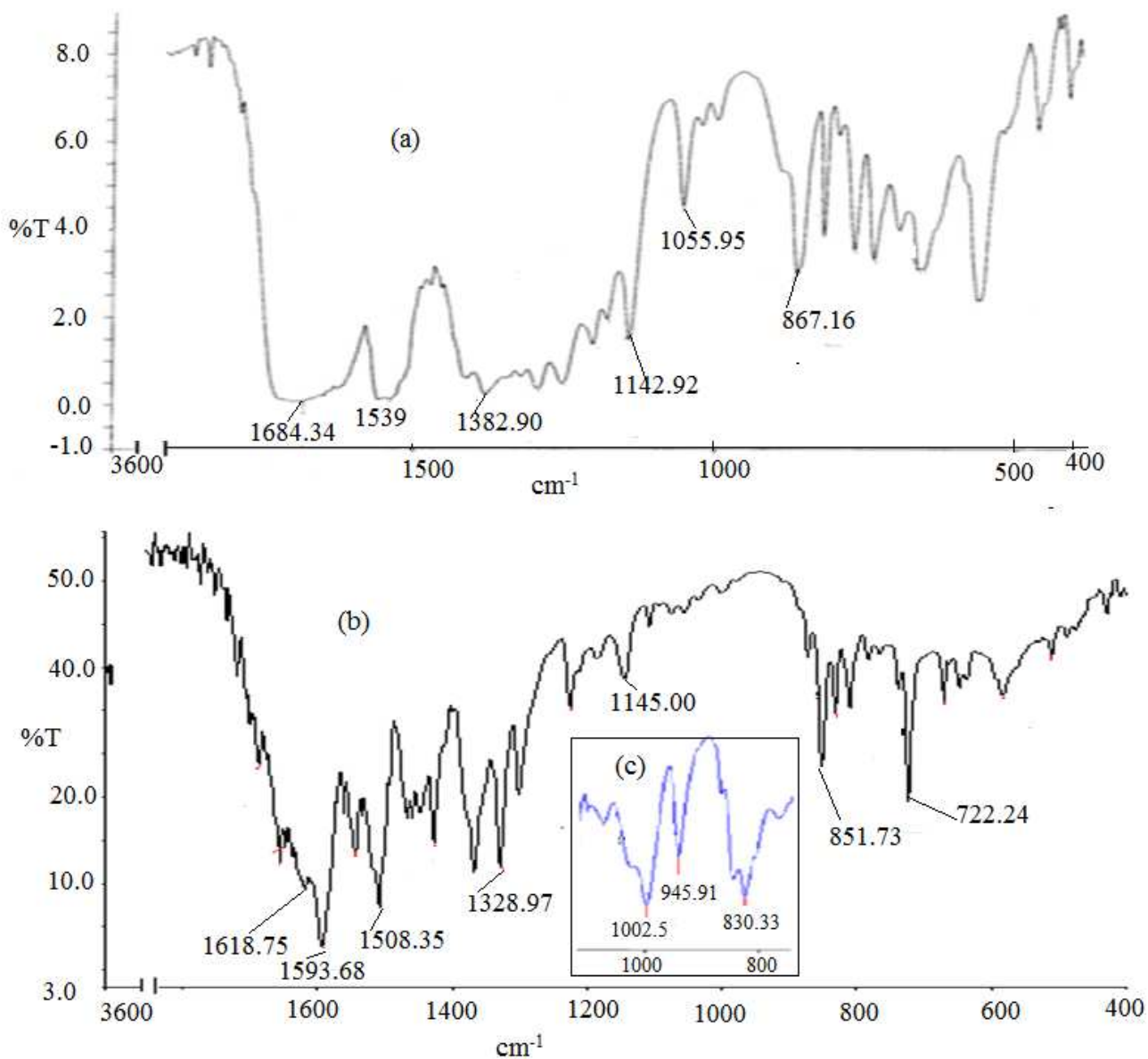


**Figure II-9.** IR spectra (KBr) (characteristic region) of **1** (a), **2** (b) with that of **3**(c) being included for visualizing the NaBH<sub>4</sub> reduction of **2** (Scheme II-4, II-8); Figures II-10 and II-11 show their complete spectra (3600-400 cm<sup>-1</sup>).

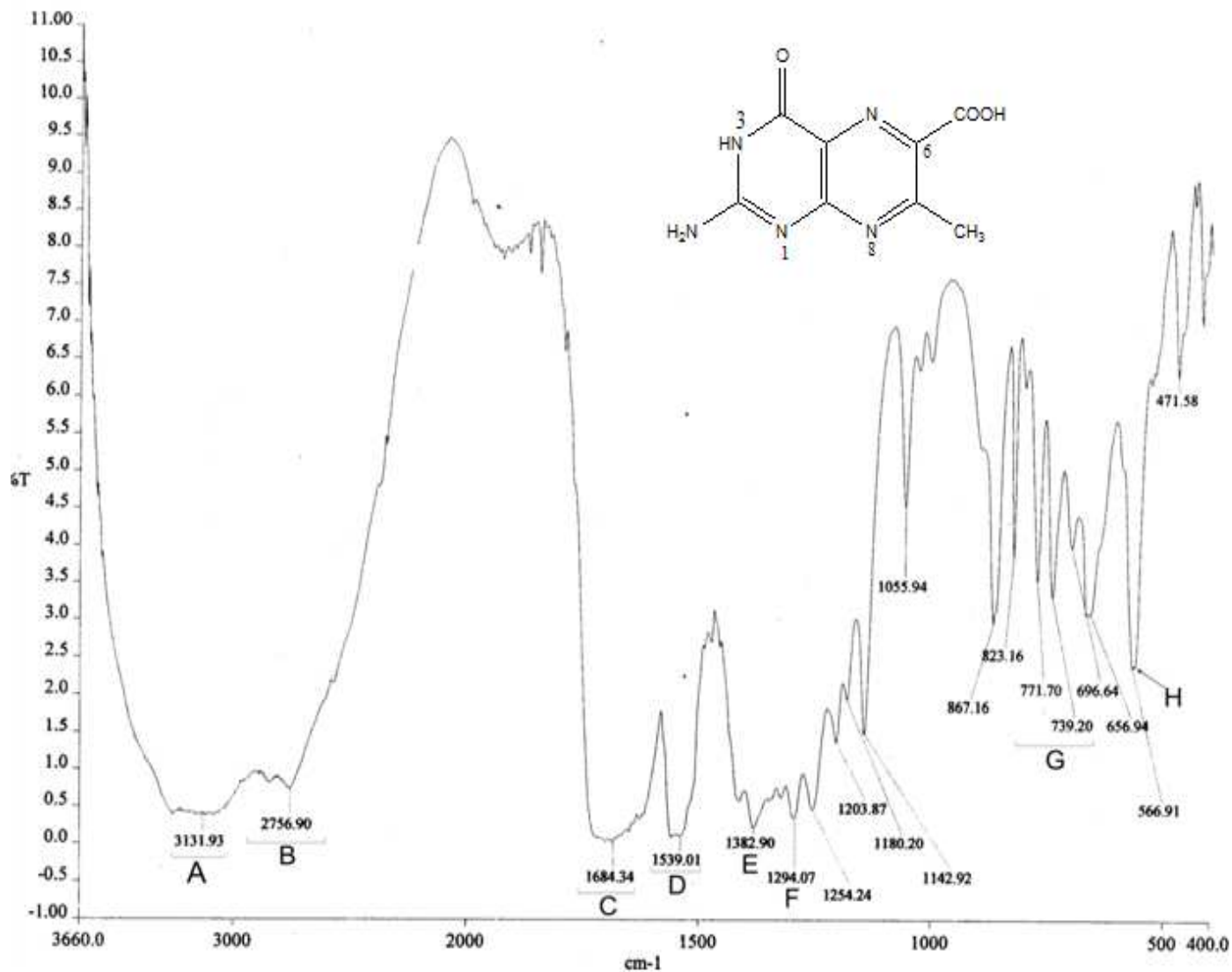


**Figure II-10.** IR spectrum (KBr) of **1**

- A: the broad band over the region  $3250\text{-}3050\text{ cm}^{-1}$  due to the  $\nu(\text{OH})$  and  $\nu(\text{NH})$  stretching vibrations of the hydrogen bonded  $\text{H}_2\text{O}$ ,  $-\text{COOH}(6)$ ,  $\text{NH}(3)$  and  $\text{NH}_2(2)$  groups, Scheme III-1;
- B: the  $\nu(\text{CH})$  stretching vibrations of the  $\text{CH}_3(7)$  group are observed at  $2851\text{ cm}^{-1}$  and  $2757\text{ cm}^{-1}$  respectively;

- C: an intense broad band centred at  $1684\text{ cm}^{-1}$  and spread over the region  $1718\text{-}1636\text{ cm}^{-1}$  is due to the  $\nu(\text{C}=\text{O})$  modes of the  $\text{C}=\text{O}(4)$  and  $\text{COOH}(6)$  groups, (Scheme III-1); the N-H bending vibrations at the  $\text{NH}_2(2)$  group are occluded under this band;
- D: the  $\nu(\text{C}=\text{C})$  and  $\nu(\text{C}=\text{N})$  modes at the pterin ring appears around  $1560\text{-}1539\text{ cm}^{-1}$ ;
- E&F: the  $\delta(\text{O-H})$  and  $\nu(\text{C-O}) + \delta(\text{O-H})$  modes of the  $\text{COOH}(6)$  group appear at  $1382\text{ cm}^{-1}$  and  $1294\text{ cm}^{-1}$  respectively;
- G: different types of skeletal bending vibrations of the pterin ring appear over the region  $860\text{-}650\text{ cm}^{-1}$ ;
- H: rocking vibrations of the  $\text{NH}_2(2)$  group appears around  $567\text{ cm}^{-1}$ .

---

**IR Spectroscopy.** The comparative IR spectra (KBr pellets) of **1** and **2** are shown in Figure II-9.

For **1** [Figure II- 10] an intense broad band extending over the region  $3250 - 3050\text{ cm}^{-1}$  along with a shoulder at  $3367\text{ cm}^{-1}$  corresponds to the  $\nu(\text{OH})$  and  $\nu(\text{NH})$  stretching vibrations of the hydrogen bonded lattice water molecules, the  $\text{COOH}(6)$ ,  $\text{NH}(3)$  and  $\text{NH}_2(2)$  groups. The  $\nu(\text{CH})$  stretching vibrations of the  $\text{CH}_3(7)$  group appear at  $2851$  and  $2757\text{ cm}^{-1}$  respectively.<sup>21</sup> Another intense broad band centred around  $1684\text{ cm}^{-1}$  and spread over the region  $1718$  to  $1636\text{ cm}^{-1}$ , characterizes the  $\nu(\text{C}=\text{O})$  modes of the  $\text{C}=\text{O}(4)$  group as well as that of the  $\text{COOH}(6)$  group. Some of the  $\nu(\text{C}=\text{C})$  and  $\nu(\text{C}=\text{N})$  modes of the pterin ring could be identified around  $1560\text{-}1539\text{ cm}^{-1}$ .<sup>25-28</sup> Two other broad bands at  $1383\text{ cm}^{-1}$  and  $1294\text{ cm}^{-1}$  characterize the  $\delta(\text{O-H})$  and  $\nu(\text{C-O}) + \delta(\text{O-H})$  modes of the  $\text{COOH}(6)$  group.<sup>21</sup> Most of the above-mentioned broad bands of **1** undergo considerable modification through complex formation with the  $\text{Cu(II)}$  ion, as evident from the IR spectrum of **2** [Figure II- 11(a)] (Schemes II-1to II-3). The  $\nu(\text{OH})$  and  $\nu(\text{NH})$  modes of the hydrogen bonded intra- and extra spheric water molecules and the  $\text{NH}_2(2)$  group appear at  $3401\text{ cm}^{-1}$  and  $3336\text{ cm}^{-1}$  respectively. The  $\nu(\text{CH})$  modes of the phen moiety appear at  $3158\text{ cm}^{-1}$

and  $3077\text{ cm}^{-1}$  respectively. The  $\nu_{\text{as}}$  and  $\nu_{\text{s}}$   $\text{C}(\dots\text{O})_2$  stretching vibrations of the carboxylate group(6) appear at  $1594\text{ cm}^{-1}$  and  $1368\text{ cm}^{-1}$  respectively.<sup>21</sup> The  $\nu(\text{C}=\text{O})$  mode of the coordinated  $\text{C}=\text{O}(4)$  group (Schemes II- 1, II-3) could be assigned at  $1619\text{ cm}^{-1}$ ; this is consistent with the multiple bond character of the O1-C13 bond with a bond length of  $1.237(4)\text{Å}$  (Figure II-3).<sup>17b</sup> Several sharp peaks over the region  $1545\text{-}1426\text{ cm}^{-1}$  as well as the one at  $1329\text{ cm}^{-1}$  correspond to the  $\nu(\text{C} = \text{C})$  and  $\nu(\text{C} = \text{N})$  vibrations of the pterin ring.<sup>25-28</sup> The C-H out- of- plane bending vibrations of the phen moiety appear at  $852\text{ cm}^{-1}$  and  $722\text{ cm}^{-1}$  respectively; for 1, 10-phenanthroline monohydrate such vibration appear at  $850\text{ cm}^{-1}$  and  $740\text{ cm}^{-1}$  respectively.<sup>21</sup> Evidently, the IR spectral data of the different functional groups of **2** are consistent with its chemical composition and the x-ray structural data.<sup>17b</sup> IR spectrum of **3** [Figure II-11(b)] (Schemes II-4 to II-6) possesses an intense broad band centered around  $3357\text{ cm}^{-1}$  associated with shoulders over the region  $3461\text{-}3052\text{ cm}^{-1}$ , representing the above-mentioned  $\nu(\text{OH})$ ,  $\nu(\text{NH})$ ,  $\nu(\text{CH})$  modes. The  $\nu_{\text{as}}$  and  $\nu_{\text{s}}$   $\text{C}(\dots\text{O})_2$  stretching vibrations of the carboxylate group(6)(Scheme II-1) are observed at  $1606\text{ cm}^{-1}$  and  $1369\text{ cm}^{-1}$  respectively. The  $\nu(\text{C} = \text{O})$  mode of the  $\text{C} = \text{O} (4)$  group appears at  $1632\text{ cm}^{-1}$ . The characteristic vibrations of the pterin ring (over the region  $1518\text{-}1428\text{ cm}^{-1}$ ) and the phen moiety ( at  $830\text{ cm}^{-1}$  and  $723\text{ cm}^{-1}$ ) are observed as well. An interesting feature of this spectrum [ Figure II-9(c )] is the appearance of two new sharp peaks at  $1002\text{ cm}^{-1}$  and  $946\text{ cm}^{-1}$  assignable to the N – H (8) and C – H (7) out-of-plane bending vibrations respectively, of the 7,8-dihydro form of the pterin moiety of **3** (Schemes II-4 and II-6).<sup>29-30</sup> This view is supported by the  $^1\text{H}$  NMR spectrum of **3** (vide later).

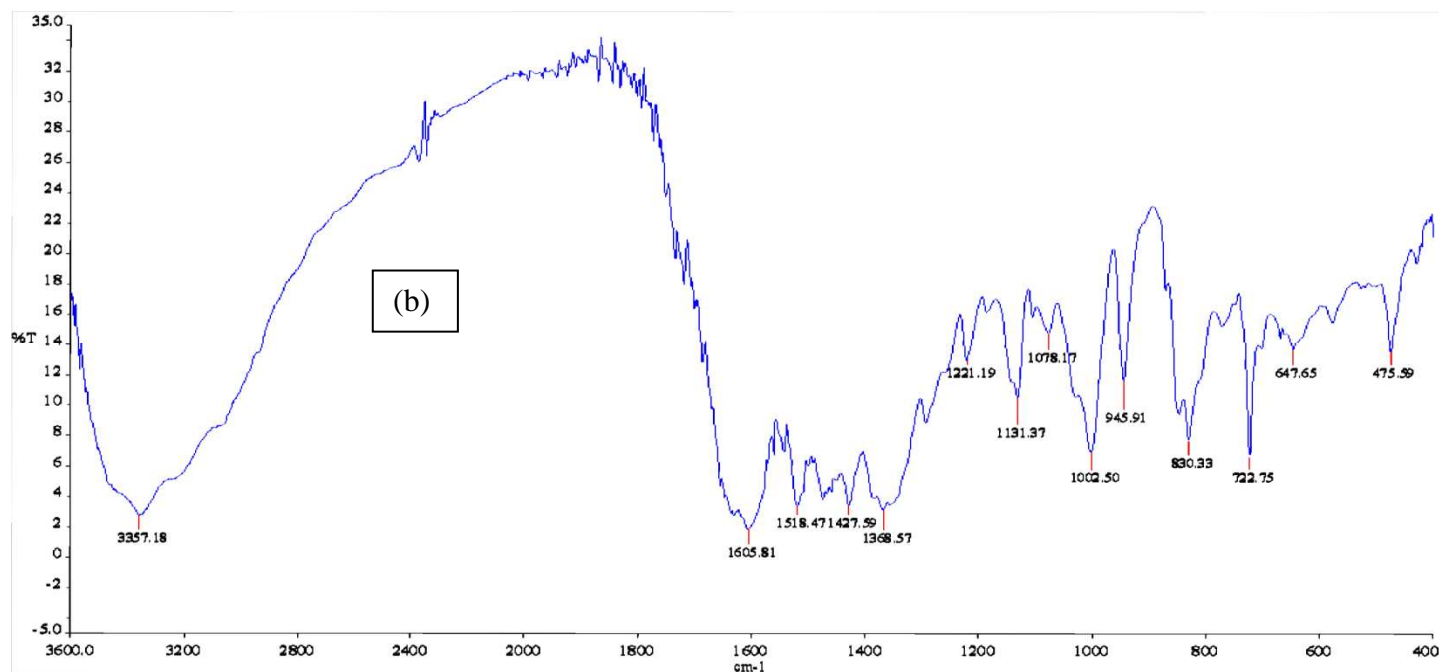
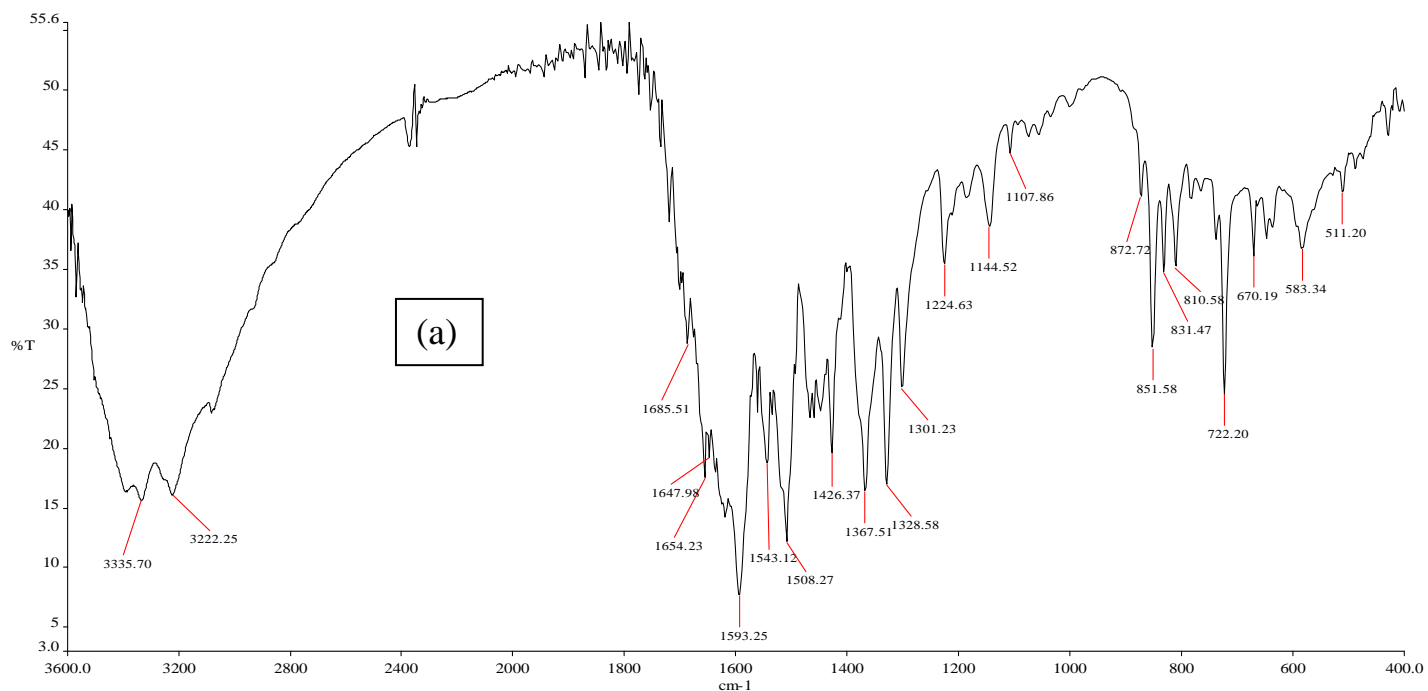


**Figure II-11.** IR spectra (KBr) of **2(a)**, Scheme II-3 and **3(b)**, Scheme II-4 to II-6.

**Electronic spectroscopy.** The electronic spectral data of the present copper complexes are presented in Table II- 5. For the green coloured complex **2**, the prominent band at 375 nm could

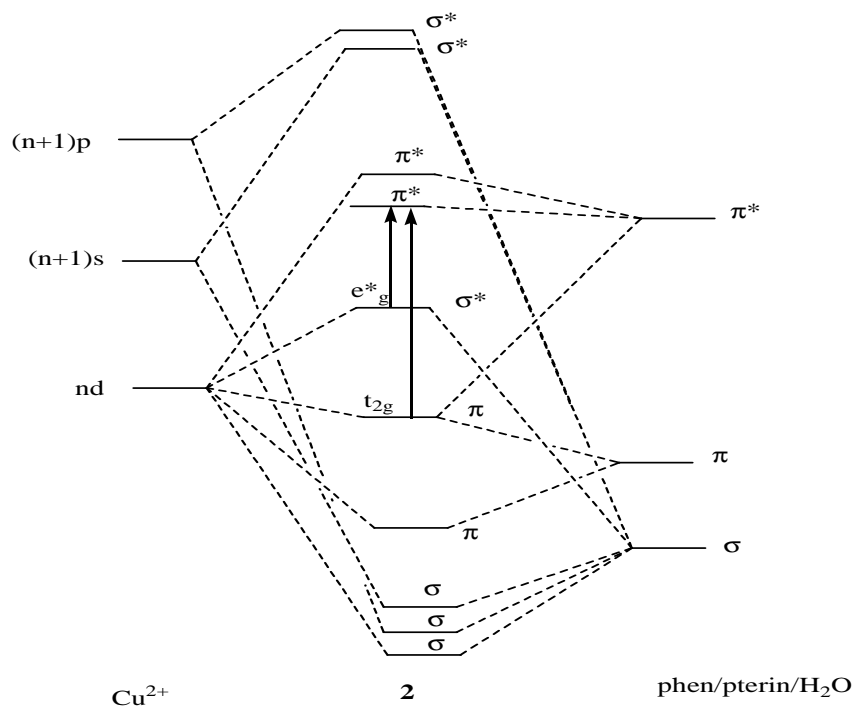
be assigned to a LMCT band. Its other absorption bands in the longer wavelength region (900 – 1100nm), possess much higher log  $\epsilon$  values as compared to the usual ligand field(LF) transitions of the Cu(II) ion ; such high intensities could not be ascribed to even intensity stealing from the distant 375 nm band .<sup>31</sup> A closer look at the frontier MO diagram of **2** (Figure II-27) reveals that the phen and pterin ligand residues make major contributions to the SOMO, LUMO and LUMO+1 levels and there is a small band gap (0.22eV) between the last two levels conferring unique redox property.<sup>64–66</sup> The large log  $\epsilon$  values (2.05 – 1.97) of the above longer wavelength bands (Table II-5), may be ascribed to MLCT transitions from occupied metal-centred orbitals (e.g.,  $t_{2g}$ ,  $e_g^*$ ) to vacant low lying ligand-centred orbitals (e.g.,  $\pi^*$  orbitals of pterin and phen). Such transitions are quite likely for **2** , a  $d^9$  system with three electrons in the  $e_g^*$  level (Scheme II-9). A Cu(II)-pteridine-phen mixed ligand complex possessing such a large log  $\epsilon$  value (2.21) at 705 nm has been reported earlier by Burgmayer and coworkers.<sup>26</sup> For the blue aqueous mother liquor (Table II-5), an intraligand  $\pi \rightarrow \pi^*$  transition and a LMCT transition are observed at 284 nm and 360 nm respectively; the broad band at 610 nm ( $\epsilon = 51.56$ ) may be assigned to a LF transition with intensity stealing.<sup>31</sup>

Electronic spectral data of **3** are characterized by more numerous bands of higher intensity as compared to those of **2** (Table II-5) and this observation may be traced to the following factors:

- (i) **2** is a mononuclear Cu(II) ( $d^9$ ) species (Scheme II-3), whereas **3** is a binuclear Cu(I) ( $d^{10}$ ) species (Scheme II- 5) of lower symmetry, with attendant additional splitting of energy levels;
- (ii) there is possibility of additional MLCT transitions of the type Cu(I) ( $d^{10}$ )  $\rightarrow$  phen in **3** as well as increased electronic circulation in its [Cu(I) (phen)Cu(I)] core.<sup>32</sup>

Besides this, the frontier orbitals (Figure II-27) of **3** are also composed of mainly pterin and phen orbitals, with a small band gap (0.5 eV) between the HOMO-1 and HOMO-2 levels, thereby retaining the unique redox property.<sup>64-66</sup>

Further verification of such assignments of MLCT transitions is provided by the corresponding Zn(II) complex (chapter VI)<sup>17a</sup>, showing an intense MLCT broad band ( $\log \epsilon = 4.086$ ) at 733 nm which is responsible for its light brown color.



**Scheme II-9** Simplified MO diagram for **2** indicating the possible metal-to-ligand charge transfer (MLCT) transition when both the  $e_g^*$  and  $t_{2g}$  are nearly occupied and the ligands have empty  $\pi^*$  orbitals; the metal-centred MOs of the former type are fully occupied for  $d^{10}$  ions like Cu(I) and Zn(II).<sup>32</sup>

**Table II-5.** Electronic spectral data of **2**, **3** and a related system.

Sl.No	Compound (solvent)	$\lambda_{\max}$ nm (log $\epsilon$ )
1.	<b>2</b> (CH <sub>3</sub> OH)	375(3.65), 905(2.05), 943(2.04),1015sh(1.97),1051br(1.98)
2.	Blue mother liquor(H <sub>2</sub> O) *	284 (2.84), 360(2.26), 610br(1.71)
3.	<b>3</b> (CH <sub>3</sub> OH)	360(3.84),366(3.82),830br(2.27),856sh(2.26),916sh(2.22),1034br(2.04), 1054sh(2.03),1071br(2.02)

\*This mother liquor[Figure II-1(a)] refers to the synthesis of **2** by method A as described in reference 17b.

**Fluorescence emission spectra.** The fluorescence emission spectra of **2**, **3** and the aforesaid blue mother liquor are shown in Figure II-13 ; their emission maxima appear at 445 nm,442 nm and 456 nm respectively. Such emission maximum of the pterin ligand (**1**) (in aqueous NaOH solution) appears at 449 nm (Figure II-12). Fluorescence data constitute an important property of pterin compounds, e.g., such data provided with the initial evidence about the pterin component of the molybdenum cofactor.<sup>33 - 34</sup>

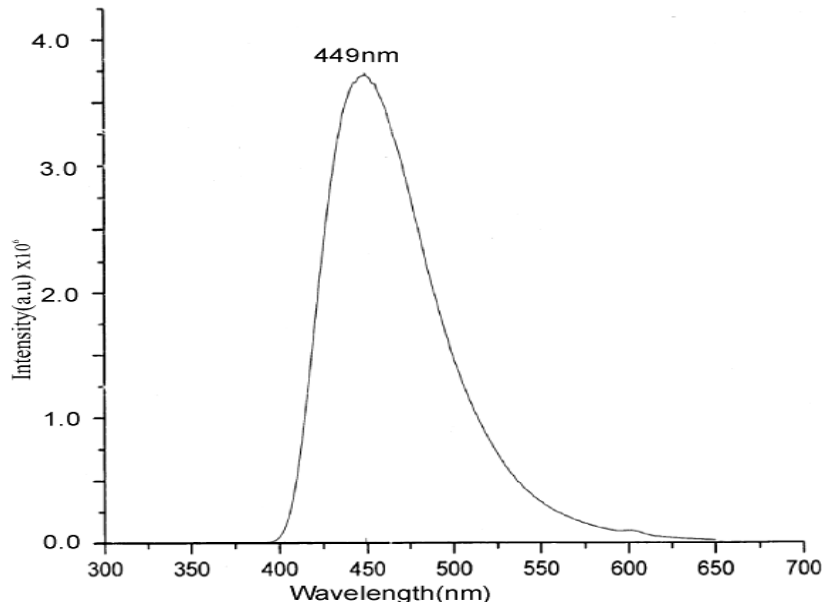


**Figure II-12.** Fluorescence emission spectrum of the pterin ligand (**1**) in aqueous NaOH solution.

The pH dependence of fluorescence property is also interesting, e.g., no fluorescence is observed for the protonated form of biopterin but the anion is strongly fluorescent.<sup>35</sup> Most organic fluorescent molecules contain conjugated system of double bonds with extended  $\pi$ -orbitals in a planar cyclic/rigid structure and not many loosely coupled substituents through which the vibronic energy can dissipate.<sup>36</sup> The common fluorophores include aromatic / heteroaromatic rings as well as functional groups like C = C, C = O, C = N, etc., while fluorochromes (usually electron donors) like - OH, - NH<sub>2</sub>, etc., enhance the transition probability or fluorescence intensity. The fluorescence property of **1**, **2** and the blue mother liquor may be correlated with the aromatic / oxidized nature of the associated pterin ring. The enhanced fluorescence intensity of **3** (Figure II-13) which is obtained by the NaBH<sub>4</sub> reduction of **2** in CH<sub>3</sub>OH, may be understood in the light of greater electronic circulation in its bridging unit [Cu(I) (phen) Cu (I)] (Scheme II-5) involving the Cu(I)(d<sup>10</sup>)  $\rightarrow$  phen type CT transition.<sup>32</sup>

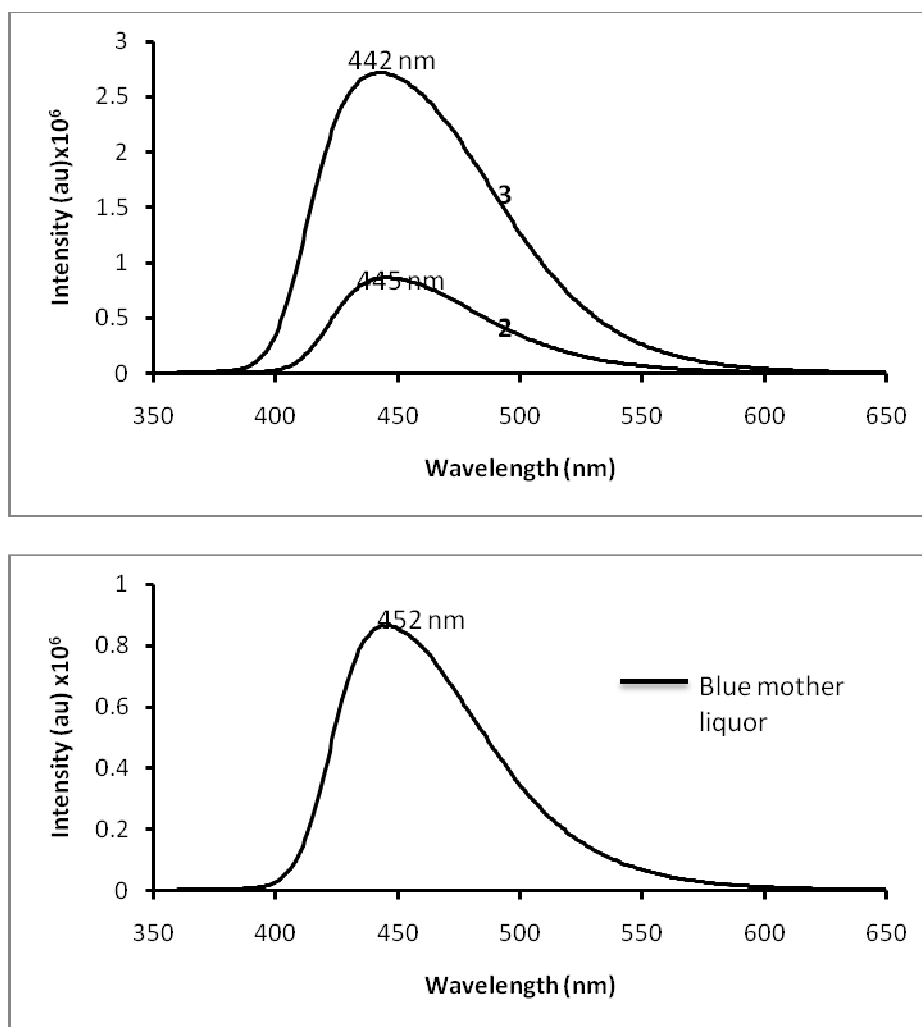


**Figure II-13.** Fluorescence emission spectra of **2** (CH<sub>3</sub>OH, 1.4 × 10<sup>-4</sup> M), **3** (CH<sub>3</sub>OH, 1.4 × 10<sup>-4</sup> M) and the blue aqueous mother liquor from which **2** was isolated (3.4 × 10<sup>-3</sup> M).

**EPR spectroscopy and magnetic susceptibility of 2.** The EPR spectrum (DMSO, 77K) of **2** is shown in Figure II-14, which indicates axial symmetry.<sup>37</sup> This is consistent with its elongated distorted octahedral coordination geometry around the Cu(II) ion (Figure II-3).<sup>17b</sup> In a tetragonally elongated octahedron, the energy of the  $d_{z^2}$  orbital will be lower than that of the  $d_{x^2-y^2}$

$y^2$  orbital and the unpaired electron of this  $d^9$  system will be located in the latter orbital. For this case, theoretical arguments indicate  $g_{\parallel} > g_{\perp} > 2$  and the relevant EPR parameters are assigned in Figure II-14.<sup>38</sup> According to magnetic susceptibility measurement data (298K), **2** exhibits a  $\mu_{\text{eff}}$  value of 1.32 B.M. It is lower than the expected spin-only value ( $\mu_s$ ) of 1.73 B.M. This lowering of  $\mu_{\text{eff}}$  value is possibly due to superexchange interaction between two complex molecules sharing each unit cell, as per the relevant crystal packing diagram of **2** (Figure II-5); the corresponding molecular packing diagram (Figure II-5) highlights the  $\pi$ - $\pi$  stacking interactions between neighbouring phen-phen and pterin-pterin rings.<sup>17b</sup>

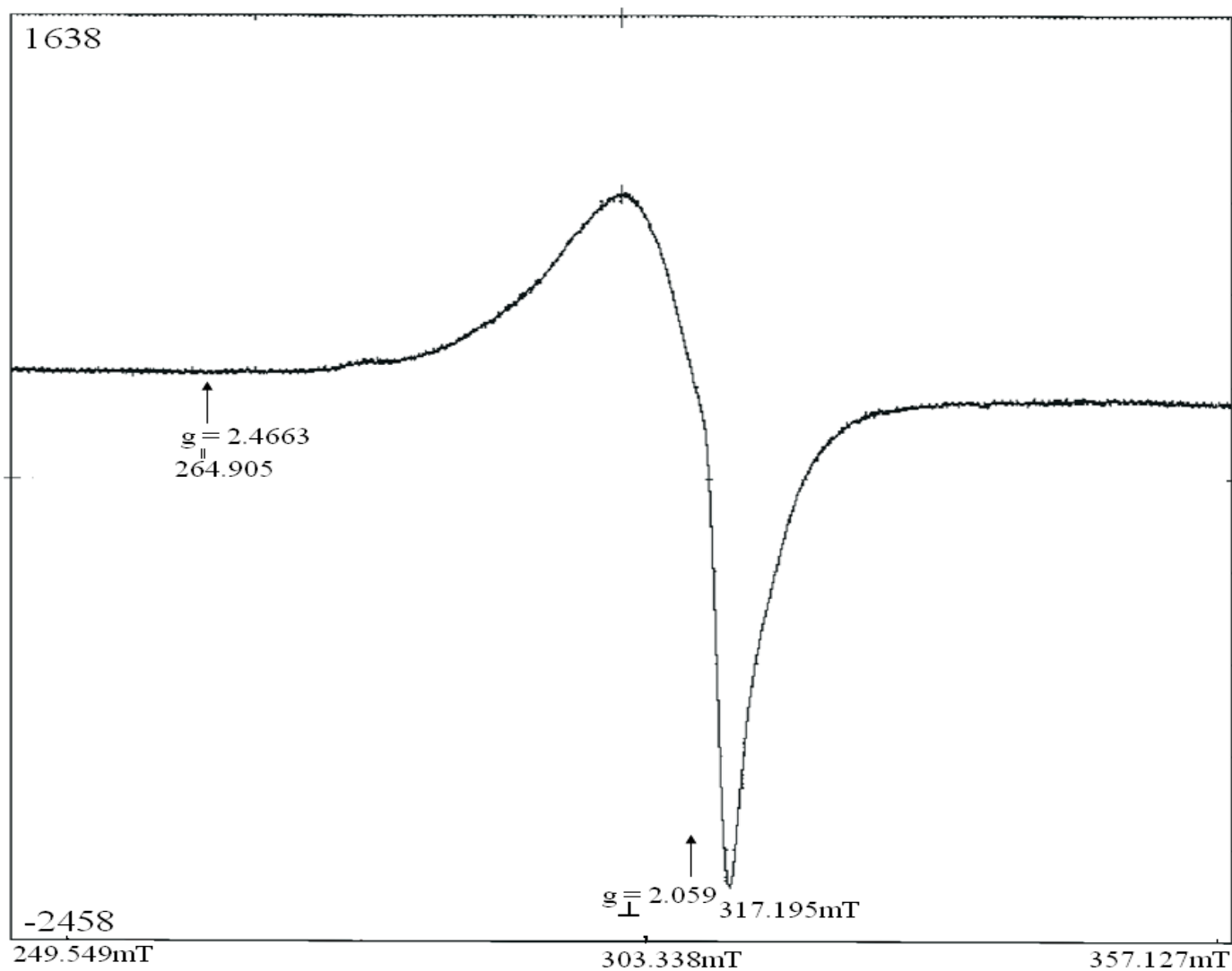
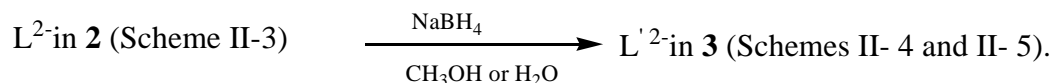


**Figure II-14.** X-band EPR spectrum of **2** in DMSO at 77K with a probe frequency of 9144.756 MHz and a field centre of 303.338 mT.

**<sup>1</sup>H NMR spectroscopy of 1 and 3.** The <sup>1</sup>H NMR spectrum of **3** [Scheme II-5, II-5(a)] in DMSO-d<sub>6</sub> is shown in Figure II-15, with the NH(8) and CH(7) proton signals (Scheme II-4) being depicted on an expanded scale, which appear at δ 6.81 (w,br) and δ 8.32 (s,s) respectively; such signals are absent in case of **1** in NaOD/D<sub>2</sub>O [L<sup>2-</sup> in Scheme II-1, Figure II-16(a)]. These

two new signals for **3** result from the transfer of reducing equivalents from NaBH<sub>4</sub> to the double bond at the 7,8-position of the L<sup>2-</sup> residue (Scheme II-1) of **2** (Scheme II-3, Figure II-3)(vide the experimental section for the synthesis of **3**; Scheme II-6):



This is consistent with the Joule's hypothesis of preferential hydride ion attack at the N(8) position of the pterin ring (Scheme II-1), as compared to the N(5) position; x-ray structural studies have verified that the pyrazine ring is the reaction locant of such a reduction process.<sup>22, 23</sup> Actually, several authors have pointed out the greater stability of the 7,8- dihydro pterin among other possibilities.<sup>9-11,13,146,147</sup> Figures II-16(a) and 16(b) represent the NH<sub>2</sub>(2) and CH<sub>3</sub>(7) signals of **1** (Scheme II-1) and **3** (Schemes II-4 and II-5) respectively. The two separate CH<sub>3</sub>(7) signals of **3** at  $\delta$  2.639 and  $\delta$  2.365 respectively [Figure II-16(b)], indicate the presence of two forms of this compound in solution on the NMR time scale. Table II-6 shows a comparison of the two above types of <sup>1</sup>H NMR signals, along with the  $\delta$  (ppm) values. The higher  $\Delta$  ( $\delta$ , ppm) value for the NH<sub>2</sub>(2) signal with respect to that of the CH<sub>3</sub>(7) signal (average value), indicates better electron withdrawal from the pyrimidine ring through complex formation; this inference is consistent with the x-ray structural data of **2** as well as those of a few other complexes of **1**.<sup>17a-</sup>

17e

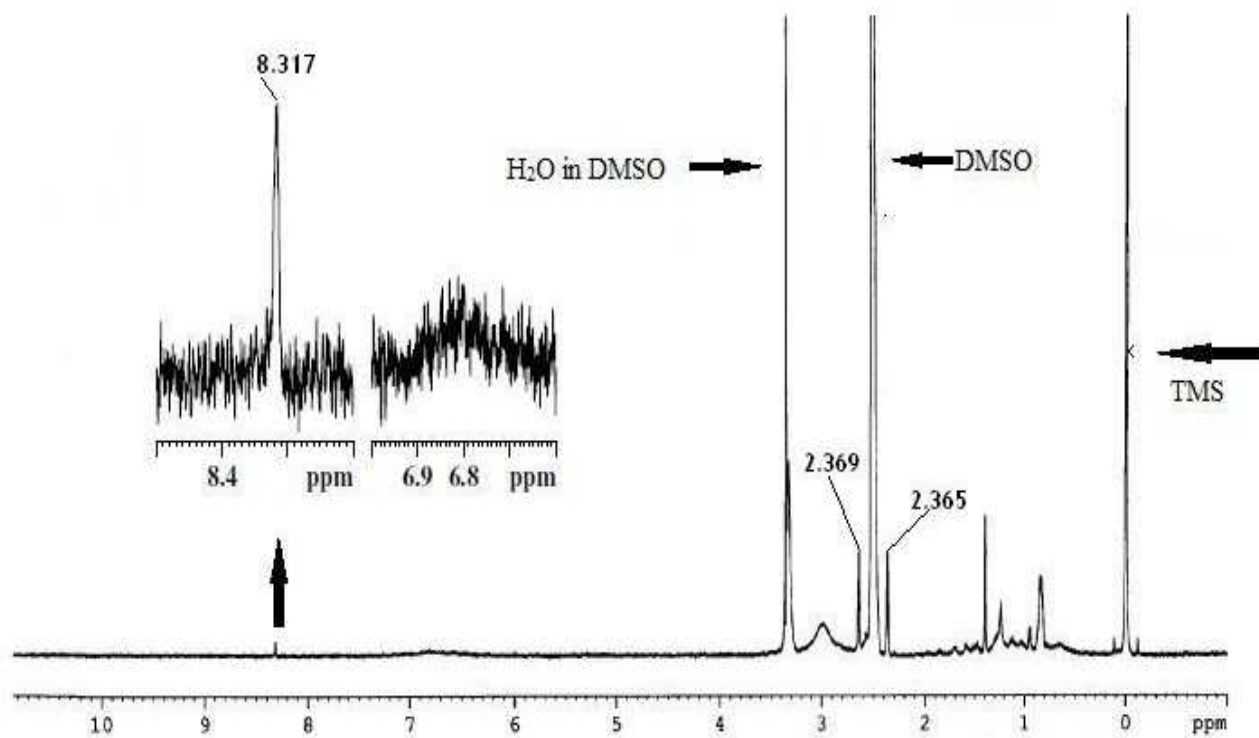


**Figure II-15.** The 500 MHz  $^1\text{H}$  NMR spectrum of **3** in  $\text{DMSO-d}_6$ , with expansion of a few specific regions.

---

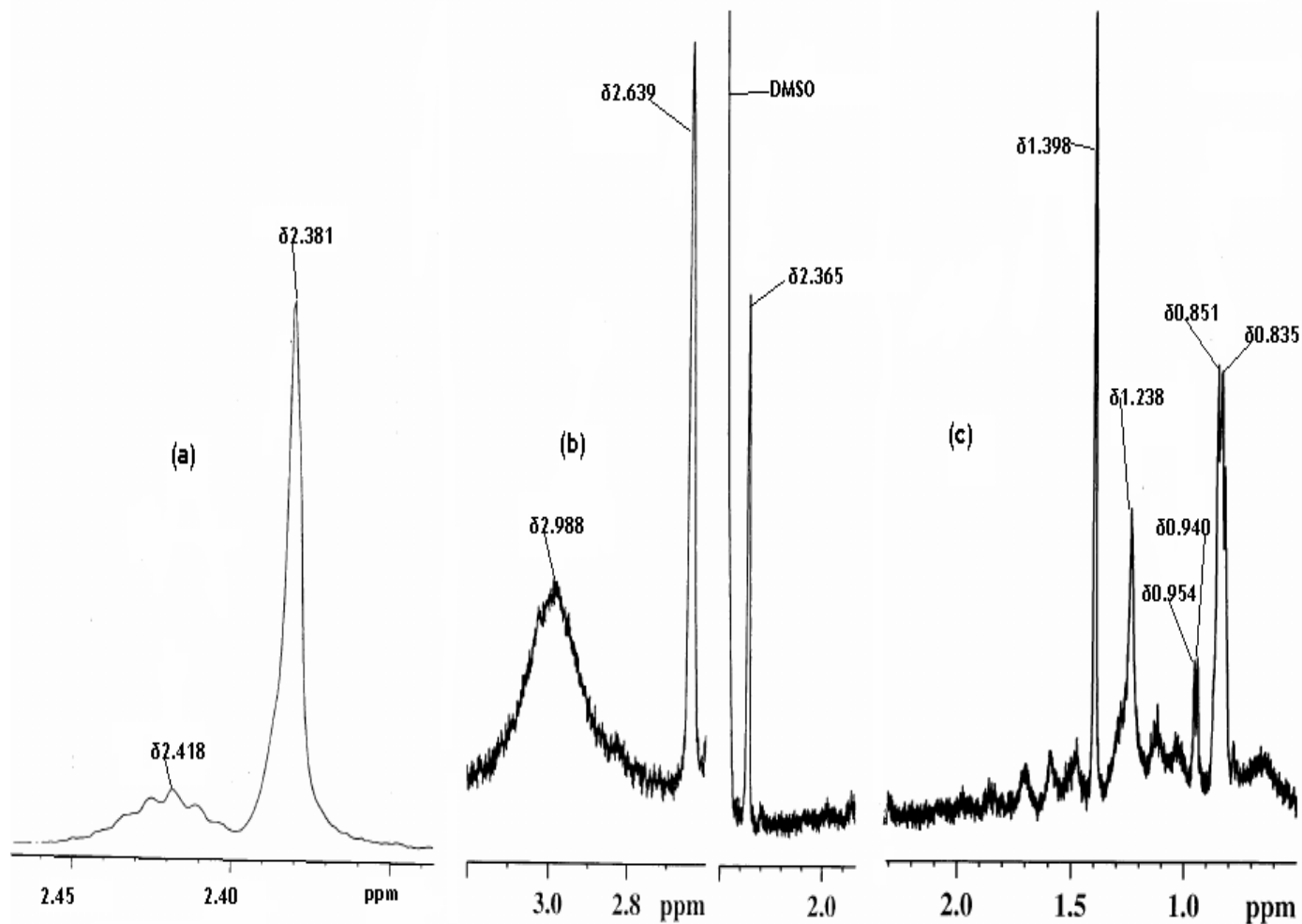


**Figure II-16.** The 300 MHz  $^1\text{H}$  NMR spectrum of **1** in  $\text{NaOD}/\text{D}_2\text{O}$ (a) ; (b) and (c) represent selected parts of Figure II-15 on expanded scale, highlighting the  $^1\text{H}$  NMR spectral features of **3**.

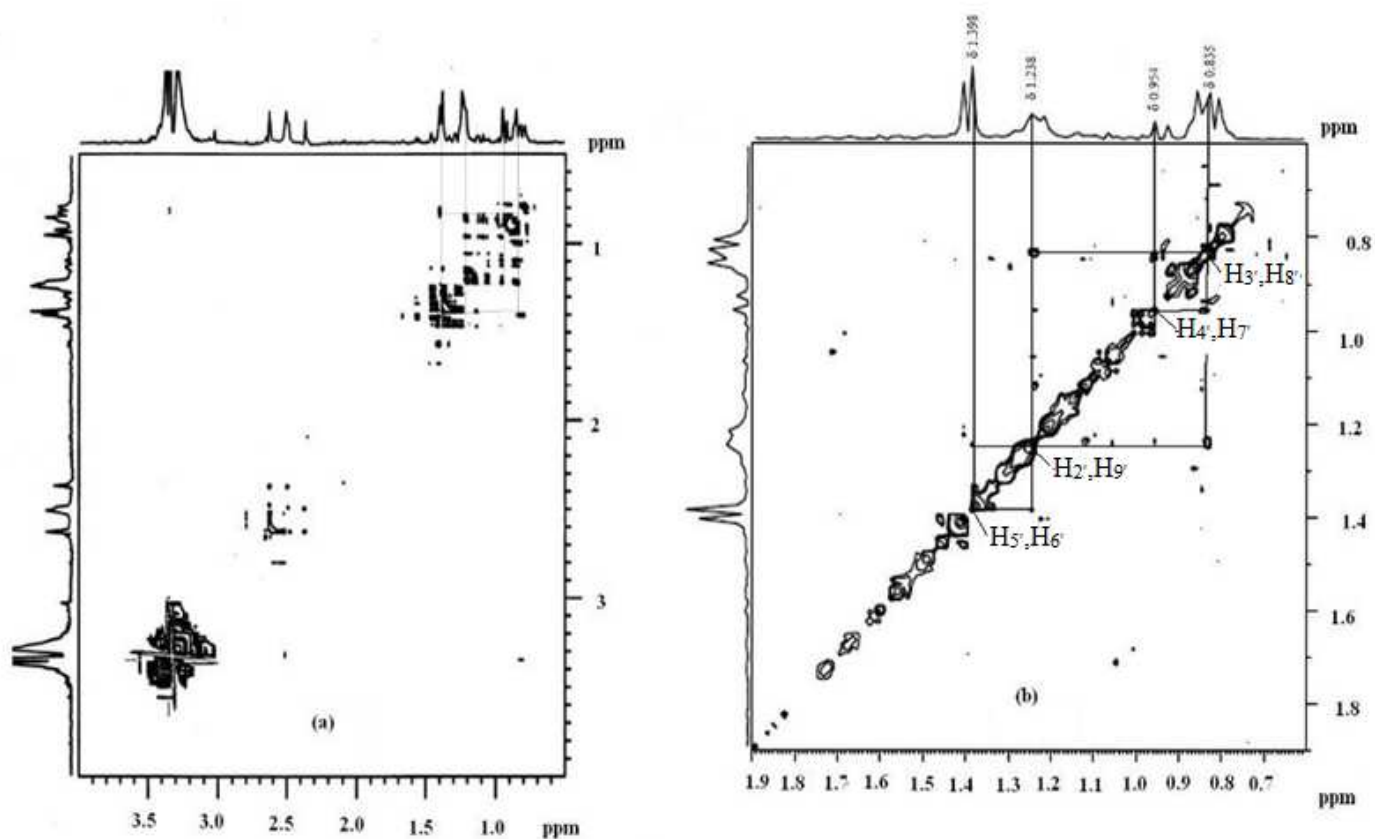


**Figure II-17.** The 500 MHz 2-D NMR spectrum of **3** (DMSO- $d_6$ ); (a) represents the region  $\delta 4.0$  – 0.5; (b) represents the phen (Scheme II-2) protons signals along with assignments.

**Table II-6.** Comparison of characteristic  $^1\text{H}$  NMR signals ( $\delta$ , ppm) of **1**(Scheme II-1) and **3**(Scheme II-5) along with the corresponding  $\Delta$  ( $\delta$ ,ppm) values.

Compound	NH <sub>2</sub> (2)	CH <sub>3</sub> (7)
<b>1</b>	2.418(w,br)	2.381(s,s)
<b>3</b>	2.988(br,s)	2.365(s,s)* 2.639(s,s)*
$\Delta(\delta\mathbf{3} - \delta\mathbf{1})$	0.57	0.121

\* Two separate CH<sub>3</sub>(7) signals correspond to the two separate forms of **3** in solution on the NMR time scale. w, br = weak, broad; s,s = sharp, singlet; br, s = broad, singlet.

The  $^1\text{H}$  NMR signals of the intra- and extraspheric aquo groups of **3** (Figure II-15), nearly merge with that of the dissolved water ( $\delta$  3.35) of DMSO-d<sub>6</sub>.<sup>21</sup> The  $^1\text{H}$  NMR signals appearing in the region  $\delta$  2.0 – 0.5 for **3**(Scheme II-5) [Figure II-15, shown on an expanded scale in Figure II-16(c), together with the 2-D NMR data in Figure II-17], are caused by the protons of its phen residue (Scheme II-2), as elucidated below. Figure II-18 shows the  $^1\text{H}$  NMR spectral data (both 1-D and 2-D) of 1, 10-phenanthroline monohydrate (phen) in DMSO-d<sub>6</sub>, along with the assignments.<sup>39</sup> The phen ligand (Scheme II-2) consists of four magnetically equivalent pairs of protons, e.g., H<sub>2'</sub> and H<sub>9'</sub>; H<sub>3'</sub> and H<sub>8'</sub>; H<sub>4'</sub> and H<sub>7'</sub> as well as H<sub>5'</sub> and H<sub>6'</sub>. Among them, H<sub>2'</sub>, H<sub>3'</sub> and H<sub>4'</sub> [or H<sub>9'</sub>, H<sub>8'</sub> and H<sub>7'</sub>] form an ABX or better an ABC system, with the chemically equivalent H<sub>5'</sub> and H<sub>6'</sub> protons showing no spin-spin splitting, like those of hydrogen, methane or benzene.<sup>40</sup> For **3** this singlet signal [of H<sub>5'</sub> and H<sub>6'</sub>] appearing at  $\delta$  1.398 [Figure II-16(c)], has

been used here as a point of entry into the present  $^1\text{H}$ - $^1\text{H}$  COSY spectra [Figure II-17 (a) and (b)], so that the correct information could be gleaned from them.<sup>21</sup>

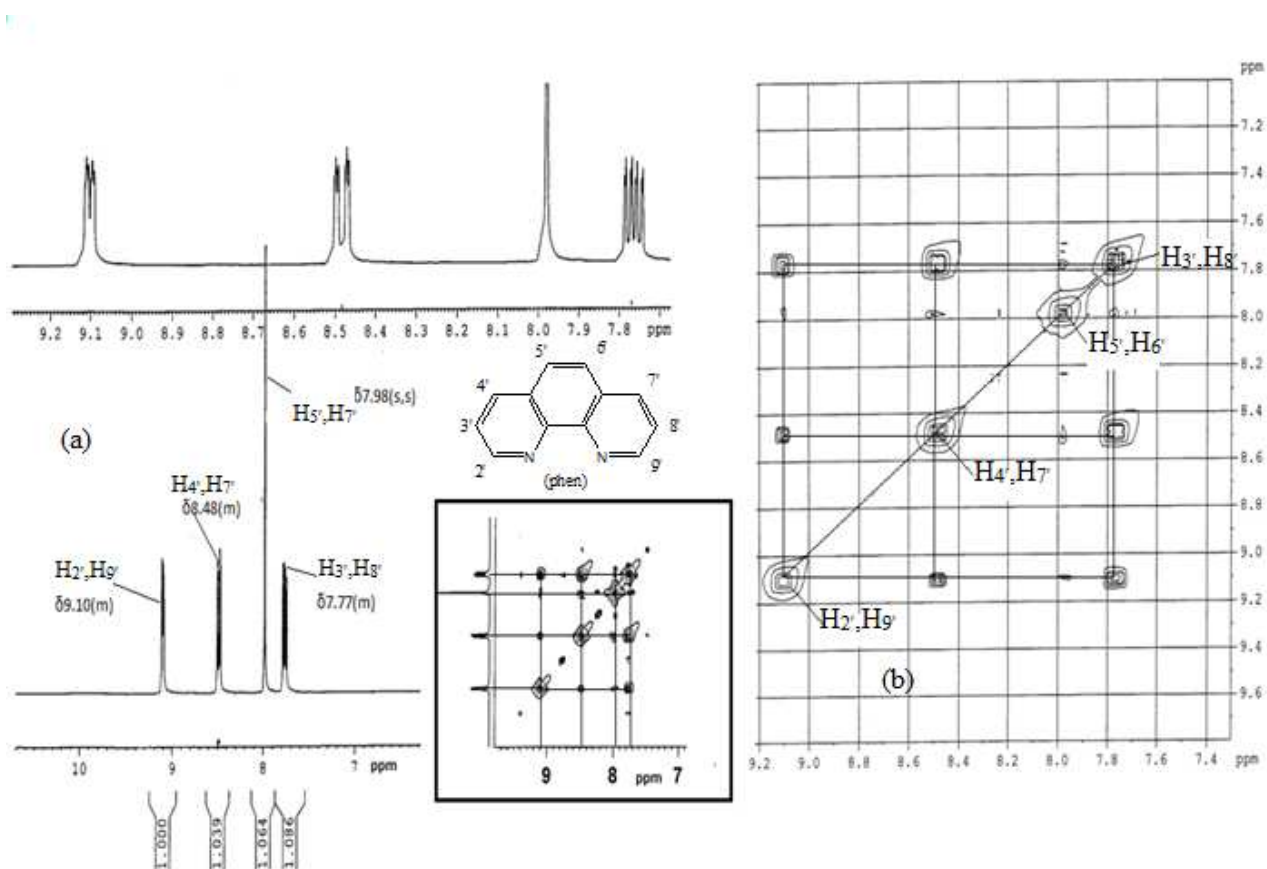


**Figure II-18.** (a) The 300 MHz  $^1\text{H}$  NMR spectrum of 1, 10-phenanthroline monohydrate in DMSO- $d_6$ . The inset shows the expanded view of the spectrum as well as the corresponding 2-D  $^1\text{H}$ - $^1\text{H}$  cosy spectrum (partly symmetrized). (b) The expanded 2-D  $^1\text{H}$ - $^1\text{H}$  cosy spectrum (symmetrized) indicates the assignment of the phen proton signals on the basis of spin-spin interaction and arguments<sup>39,43</sup>.

On comparing the 2-D NMR data of **3** in Figure II-17, especially that in Figure II-17(b) with that of phen (Figure II-18), it is evident that apart from the above-mentioned singlet signal at  $\delta$  1.398, the spin – spin interactions (in terms of cross peaks) among the three remaining proton pairs help

their unambiguous assignments at  $\delta$  1.238 [H<sub>2</sub>, H<sub>9</sub>'],  $\delta$  0.954 [H<sub>4</sub>, H<sub>7</sub>'] and  $\delta$  0.835 [H<sub>3</sub>, H<sub>8</sub>'] respectively. Just like the CH<sub>3</sub>(7) proton signals [ Figure II-16 (b)], some of the phen protons are characterized by two sets of signals [ Figure II-16 (c) and Figure II-17 (b)], thereby augmenting the inference about the existence of **3** in two forms in solution.

Finally, the chemical shift region ( $\delta$ 2.0-0.5) of the phen proton signals of **3** needs a special mention. Either for the free phen ligand or in complexes where this ligand exhibits different coordination modes, the relevant proton signals appear in the regions  $\delta$ 9.2-7.7 (Figure II-18) and  $\delta$ 10.5-7.7 respectively<sup>39,42,43</sup>. Such exceptionally large lower frequency shift (i.e., shielding by  $\delta$  7.8-6.5) in **3**, could be interpreted only in terms of the ring current effect of its two pterin ligand residues which are disposed orthogonally [Schemes II-5, II-5(a)] with respect to the bridging phen ligand<sup>20,40</sup>. X-ray structural data of **2** (Figure II-3) supports such a mutually perpendicular disposition of the phen and pterin ligand residues here.

### **Circular dichroism spectroscopy**

The above aspect about the asymmetry of the coordination environment, could be further rationalized in terms of the CD spectra [Figure II-19(a) and (b)] of **2** and **3**. **2** shows only weak CD spectral response over the region 300-850 nm. On the other hand, the CD spectrum of **3** consists of a negative Cotton effect at 382 nm associated with a LMCT band; besides this, two broad CD bands associated with shoulders at 460 nm and 732 nm respectively, characterize the MLCT transitions (Scheme II-9). The latter type of transitions could not be located in the UV-VIS spectral data (Table II-5). It can be inferred that the distinct CD spectral features of **3** reflect greater asymmetry of its binuclear  $\mu$ -phen type coordination environment.<sup>41</sup>

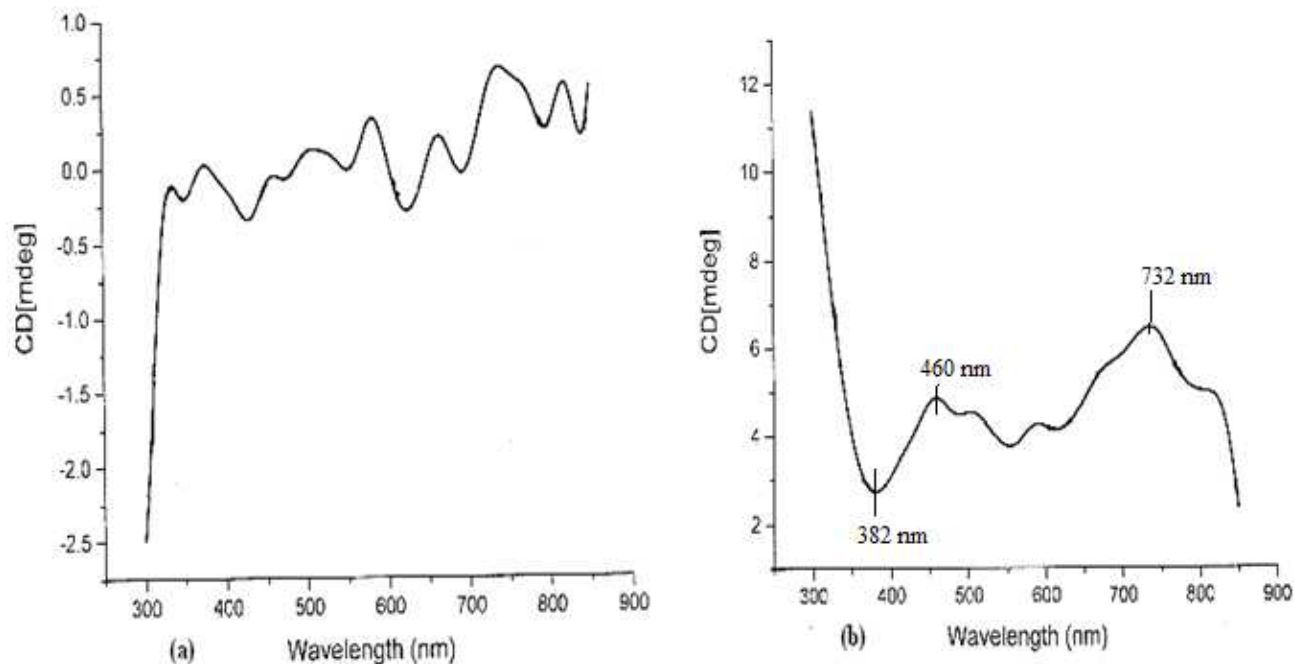
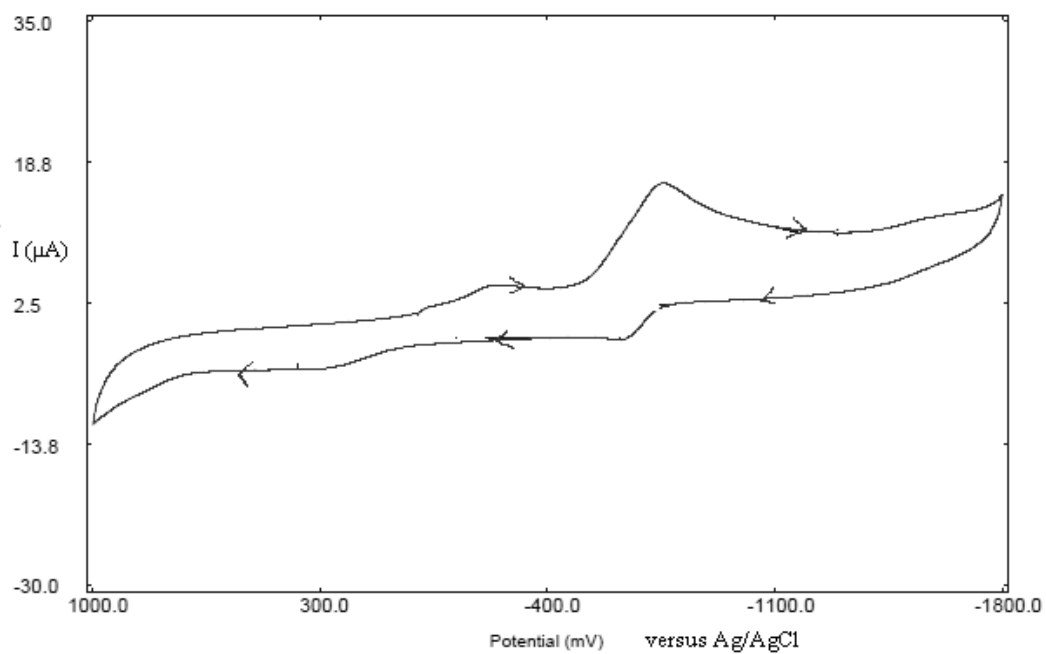


**Figure II-19.** CD spectral response in CH<sub>3</sub>OH of (a) **2** ( $9.3 \times 10^{-4}$  M); (b) **3** ( $1.1 \times 10^{-3}$  M).

**Cyclic Voltammetric Studies.** Cyclic voltammetry data of **2** and **3** are presented in Table II-7 as well as in Figures II-20 and II-21. Although the present pterin ligand (**1**) is characterized by a single irreversible reduction peak ( $E_{pc}$ ) at -418 mV (ca.  $1 \times 10^{-3}$  mol dm<sup>-3</sup> in aqueous NaOH medium, pH ca.10 with 0.1M mol dm<sup>-3</sup> KNO<sub>3</sub>; scan rate, 100 mVs<sup>-1</sup>), the relevant complexes (**2**, **3**) display metal-centred quasi-reversible electrochemical behavior, throwing light on their structure –electrochemical response correlation. Redox reactivities of these complexes studied using UV-Vis spectroscopy as discussed later, corroborate this aspect; for example, the time-dependent spectral curves (Figure II-22) for the NaBH<sub>4</sub> reduction of the aqueous alkaline solution

of the pterin ligand (**1**) are devoid of any isosbestic point, while such responses of both **2** and **3** towards different redox reagents, do possess such an attribute (Figure II-24 and Figure II-26).



**FigureII-20.** Cyclic voltammetry data of **2** in DMSO ( 0.1M TBAP; scan rate,  $100\text{mV s}^{-1}$ ).

---

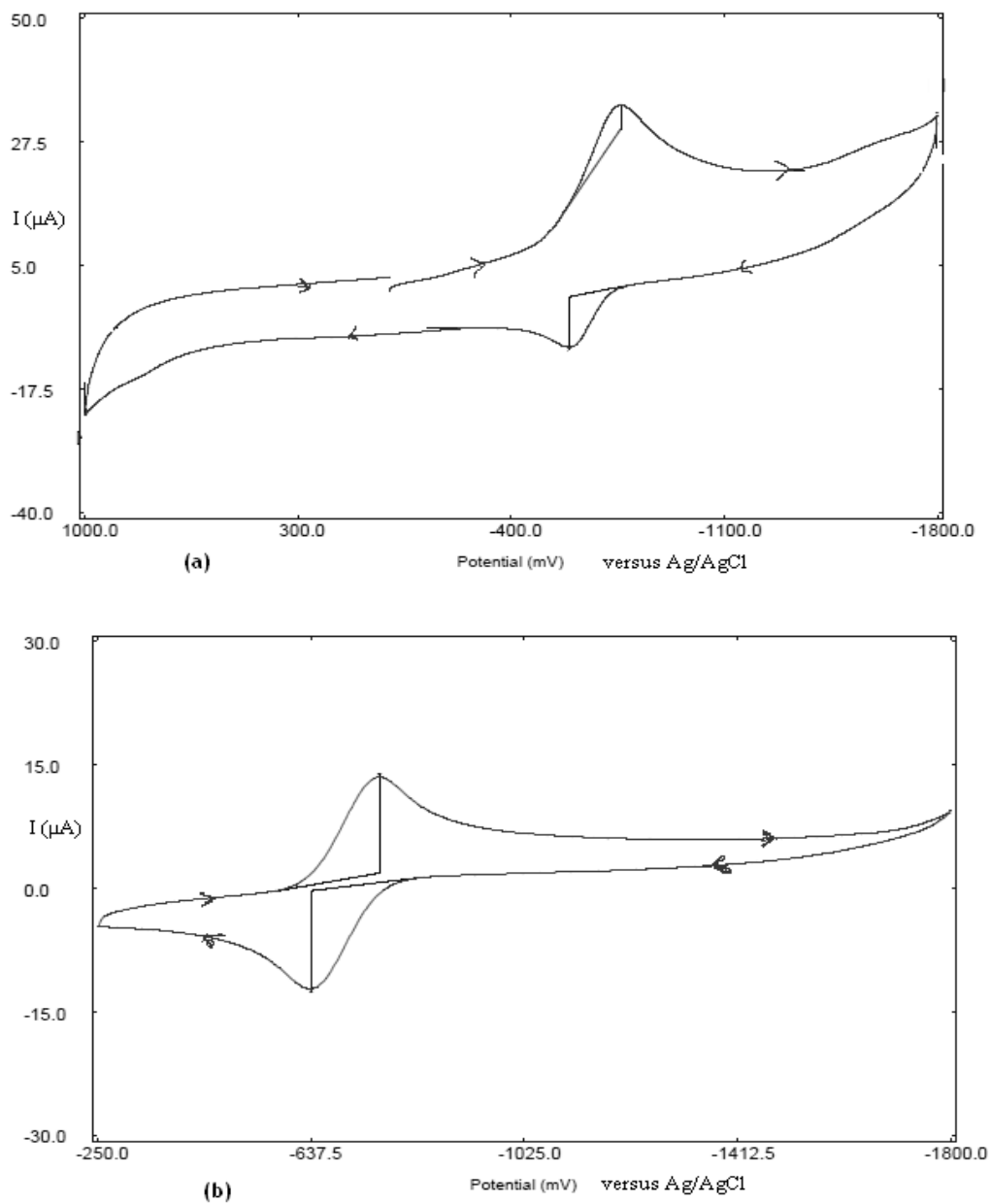


**Figure II-21.** Cyclic voltammetry data of **3** in DMSO (0.1M TBAP) (a) the potential scan starts from 0 mV and terminates here; scan rate,  $300\text{mVs}^{-1}$ ; (b) the potential scan starts from -1800 mV and terminates here; scan rate,  $150\text{mVs}^{-1}$ .

**Table II-7.** Cyclic voltammetry data<sup>a</sup> of the copper complexes **2** and **3** characterizing the process



Complex	$E_{pc}$ (mV)	$E_{pa}$ (mV)	$E_0$ (V) <sup>b</sup>	$\Delta E_p$ (mV)	$i_{pc}/i_{pa}$
<b>2</b> <sup>d</sup>	-760	-623	-0.691	137	1.2
<b>3</b> <sup>e</sup>	-750	-597	-0.673	153	0.92
<b>3</b> <sup>f</sup>	-762	-637	-0.699	125	0.97

<sup>a</sup> Cyclic voltammetry versus Ag/AgCl using glassy carbon working electrode in DMSO/0.1 mol dm<sup>-3</sup> TBAP.

<sup>b</sup>  $E_0' = 0.5 (E_{pc} + E_{pa})$ , where  $E_{pc}$  and  $E_{pa}$  are the cathodic and anodic peak potentials respectively.

<sup>c</sup>  $\Delta E_p = E_{pc} - E_{pa}$ .

<sup>d</sup> The potential scan starts from 0(mV) at a rate of 100 mVs<sup>-1</sup>.

<sup>e</sup> The potential scan starts from 0 (mV) at a rate of 300 mVs<sup>-1</sup>.

<sup>f</sup> The potential scan starts from -1800(mV) at a rate of 150 mVs<sup>-1</sup>.

---

In addition to the characteristic metal-centred peaks (Table II-7), few ligand – centred peaks may also be identified in Figures II-20 and II-21. For **2** two irreversible ligand reduction peaks ( $E_{pc}$ ) could be detected at -223 mV and -1589 mV respectively, followed by one ligand reoxidation peak ( $E_{pa}$ ) at 263 mV. In case of **3** weak signals representing ligand reduction and reoxidation could be detected at -1569 mV ( $E_{pc}$ ) and 777 mV ( $E_{pa}$ ) respectively, when the

potential scan starts from and terminates at 0 mV as well as extending from -1800 mV to 1000 mV on either side [Figure II-21(a)]. The above- mentioned ligand-centred peaks in Figures. II-20 and II-21(a) are interdependent, as inferred by Gorren and coworkers, from cyclic voltammetry studies on tetrahydrobiopterin <sup>44</sup>. However, close approach to electrochemical reversibility for the Cu(II)/Cu(I) couple could be achieved for **3** [Figure II-21(b)] without any other signal on the wings over the region -250 to -1800 mV, when -1800 mV is selected as the starting point and terminus of the potential scan. As evident from the <sup>1</sup>H NMR data of **3**, this situation corresponds to its assigned form [Scheme II-5, II-5(a)], with Cu(I) centers and the pterin ligand residues in their 7,8-dihydro state. The above metal-centred electrochemical reversibility [Figure II-21(b)] could be realized as chemical reversibility in transferring the reducing equivalents from **3** towards the model substrate bromobenzene (Figure II-26) in presence of O<sub>2</sub>, converting it into 4-bromophenol, as established through stoichiometric study (vide the experimental section).

From electrochemical studies on Cu(II) chelate complexes Patterson and Holm inferred that electrochemical reversibility ( $i_{pc}/i_{pa} \approx 1$ ) and thermodynamic driving force ( $\Delta G^0 = -nFE^0$ ) for the Cu(II)/Cu(I) couple are controlled by different ligand parameters, e.g., rigidity favours the Cu(II) state, while flexibility makes the Cu(I) state more accessible; N,O donor ligands shift the  $E_0'$ (V) value towards the negative region (-0.70 to -2.26V), whereas a  $\pi$ -acid ligand like phen helps to achieve a positive  $E_0'$  value (e.g., +0.64V), with respect to the Cu(II)(aq)/Cu(I)(aq) couple ( $E_0' = +0.17V$ ) <sup>45-47</sup>. The present  $E_0'$  values (Table II-7) represent a possible combination of the two above opposite controlling factors. The relevant  $E_{pc}$  or  $E_{pa}$  values correspond to one-electron transfer step for **2** and two-electron transfer step for the binuclear species **3** respectively

45, 48.

The close approach to electrochemical reversibility for **3** [Figure II-21(b)] may be ascribed to the ability of the ligand environment to adjust with the stereochemical change accompanying the electron transfer:

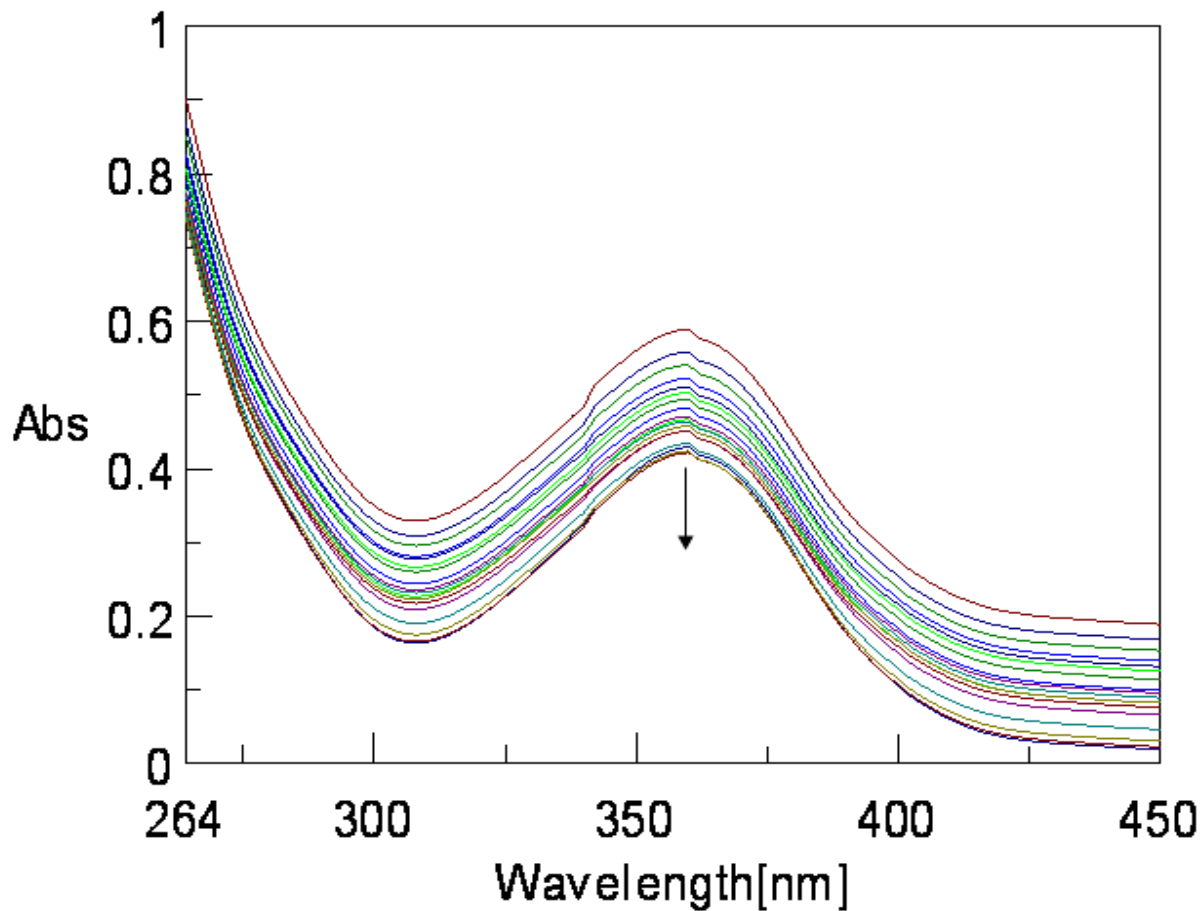
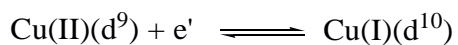


**Figure II-22.** Absorption spectral changes recorded at 2 min interval during the reaction of **1** ( $1.34 \times 10^{-3} \text{M}$ ) in aqueous NaOH solution ( $1.25 \times 10^{-2} \text{M}$ ) with  $\text{NaBH}_4$  ( $1.35 \times 10^{-2} \text{M}$ ) at 303K.

Besides this, the (M→L)π bonding ability of the phen moiety (Scheme II-9) also assists this steric adjustments through delocalizing the higher electron density on the Cu(I)(d<sup>10</sup>) core<sup>32</sup>.

**Reactivity of 2.** 2 possesses an aquo group as well as two redox centres, e.g., the Cu(II) ion and the redox non-innocent pterin ligand residue; thus it provides with an opportunity for exploring its reactivity towards carefully selected group transfer and redox reagents.

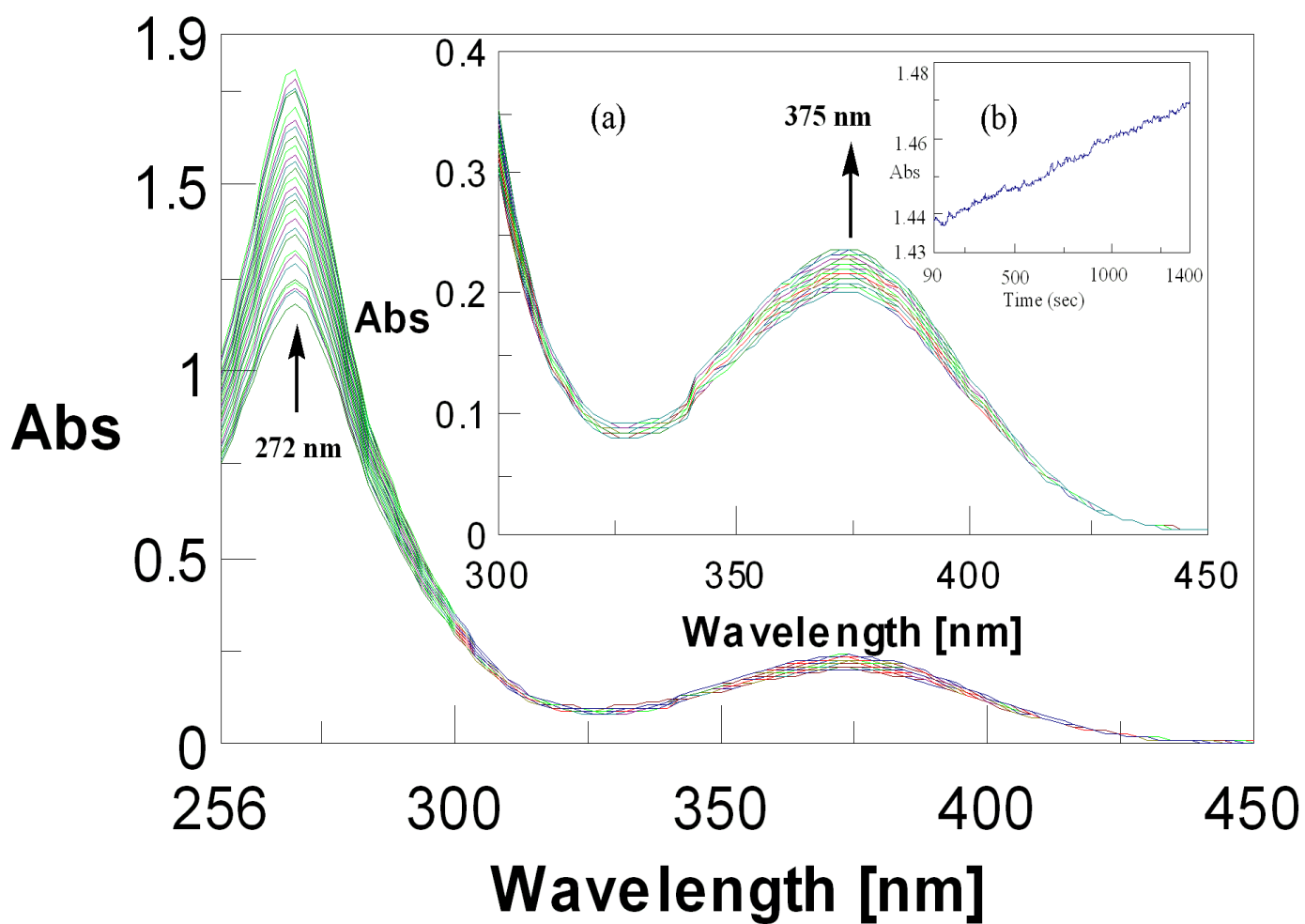


**Figure II-23.** Absorption spectral changes recorded at 5 min interval during the reaction of 2 ( $8.9 \times 10^{-5}\text{M}$ ) with imidazole (Im) ( $3.6 \times 10^{-2}\text{M}$ ) in  $\text{CH}_3\text{OH}$  at 318K; (a) expanded view (300 –

450nm) of the spectral changes is shown in the inset; (b) the absorbance versus time curve at 375 nm, 318K.

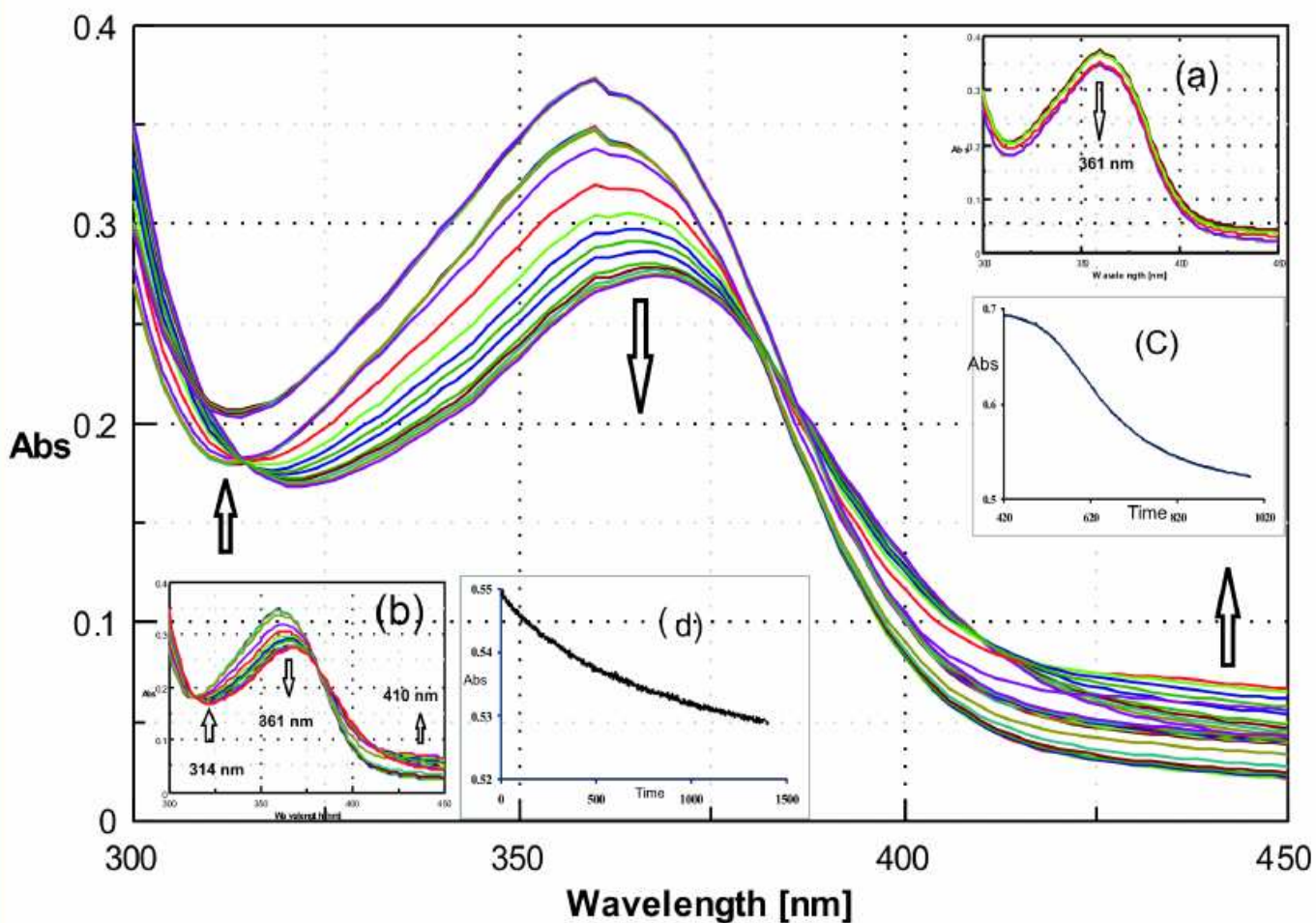
---

Figure II-23 depicts the absorption spectral changes associated with the reaction of **2** with imidazole in CH<sub>3</sub>OH medium at 315K. Imidazole is associated with the histidine residue which is well-known for its avidity towards the first transition metals in the biological system. Stoichiometry of this reaction could be established x-ray crystallographically in the corresponding Ni(II) system<sup>17c</sup>. Kinetics of this reaction was followed at 375nm and four different temperatures in the range 308 – 328 K under pseudo-first-order conditions (keeping ca. 100 times excess of imidazole ligand). Observed rate constants were determined by least square method from the plots of log(A<sub>t</sub> - A<sub>∞</sub>) versus time, which were linear for 3 half- lives<sup>49,50</sup>. The relevant data are k<sub>obs</sub> = 1.4x10<sup>-2</sup> s<sup>-1</sup> and ΔS<sup>‡</sup> = -227.0 J mol<sup>-1</sup>deg<sup>-1</sup>; they are commensurable with a ligand substitution process involving an associative pathway<sup>92,97,98</sup>.

Phenylalanine hydroxylase (PAH) is able to activate/hydroxylate the aromatic ring of phenylalanine, converting it into tyrosine, in presence of the cofactor tetrahydrobiopterin (BH<sub>4</sub>)<sup>52-55</sup>. One molecule of O<sub>2</sub> is utilized in the reaction; one oxygen atom is inserted into the substrate as an hydroxyl group, while BH<sub>4</sub> supplies the two electrons needed for reducing the other oxygen atom to the level of water. The resulting dihydrobiopterin (BH<sub>2</sub>) is restored to its tetrahydro state (BH<sub>4</sub>) once again by NADH<sup>10, 51-53</sup>. Although a non- heme iron atom is essential for the functioning of PAH, copper is not needed for this purpose<sup>54</sup>.

It is worthwhile to explore the ability of **2** to assimilate reducing equivalents from NaBH<sub>4</sub> and the onwards transmission of the same by the reduced compound (**3**), to a model substrate/substrate analogue like bromobenzene in presence of dioxygen<sup>55</sup>. Choice of

bromobenzene for the present study is guided by the fact that the corresponding hydroxylated product (along with any residual portion of the starting material) could be extracted from the reaction medium using pet ether and characterized (vide the experimental section).



**Figure II-24.** Absorption spectral changes recorded at 2 min interval during the reaction of **2** ( $8.9 \times 10^{-5} \text{M}$ ) with  $\text{NaBH}_4$  ( $6.9 \times 10^{-2} \text{M}$ ) in  $\text{CH}_3\text{OH}$  at 298K indicating a composite process which can be separated into two consecutive steps [inset, (a) and (b) respectively]; the step (a) is complete within 35 min; this is followed by step (b) showing three isosbestic points (at 314, 383 and 410 nm) and levelling off after another 25min. The figures (c) and (d) represent the absorbance versus time curves corresponding to steps (a) and (b) respectively.

---

The reaction of **2** with NaBH<sub>4</sub> in CH<sub>3</sub>OH (Figure II-24), is essentially a composite process which could be separated electronically into two consecutive steps [Figure II-24( a) and II-24 (b)], in terms of absorption spectral curves. Absence of any isosbestic point in Figure II-24(a) and the presence of such an attribute (at 314 nm, 383 nm and 410 nm) in Figure II-24(b), indicate that the corresponding reaction stages occur with and without structural changes respectively. First stage [ Figure II-24(a)] of the reaction continues for ca. 35 min and this is followed by the second stage [ Figure II-24(b)], which levels off after 25min; these two stages also differ in terms of their absorbance versus time curves [ Figure II-24(c) and II-24(d)] as well. Kinetics of these two consecutive steps of the reaction with NaBH<sub>4</sub>, were followed at 361 nm and four different temperatures in the range 300 – 330K in CH<sub>3</sub>OH under pseudo-first order conditions ( with a **2** : NaBH<sub>4</sub> ratio of 1 : 140) and the relevant kinetic parameters are stated below:

**1<sup>st</sup> stage** [Figures II-24(a) and II-24(c)]:  $k_{\text{obs}} = 3.8 \times 10^{-3} \text{ s}^{-1}$  ;  $\Delta S^{\ddagger} = -158.0 \text{ J mol}^{-1} \text{ deg}^{-1}$ ;

**2<sup>nd</sup> stage** [Figures II-24(b) and II-24(d)]:  $k_{\text{obs}} = 1.3 \times 10^{-2} \text{ s}^{-1}$ ;  $\Delta S^{\ddagger} = -149.0 \text{ J mol}^{-1} \text{ deg}^{-1}$ .

As par the negative  $\Delta S^{\ddagger}$  values, the transfer of reducing equivalents from NaBH<sub>4</sub> to **2** , is an associative process. Figures II-22 and II-25 represent the absorption spectral changes undergone by **1** and phen respectively, on addition of NaBH<sub>4</sub> in CH<sub>3</sub>OH medium over the relevant spectral region; while phen is essentially insensitive to reduction, the pterin ligand undergoes a definite reaction, with its pyrazine ring being responsible for the reduction<sup>22,23</sup>.

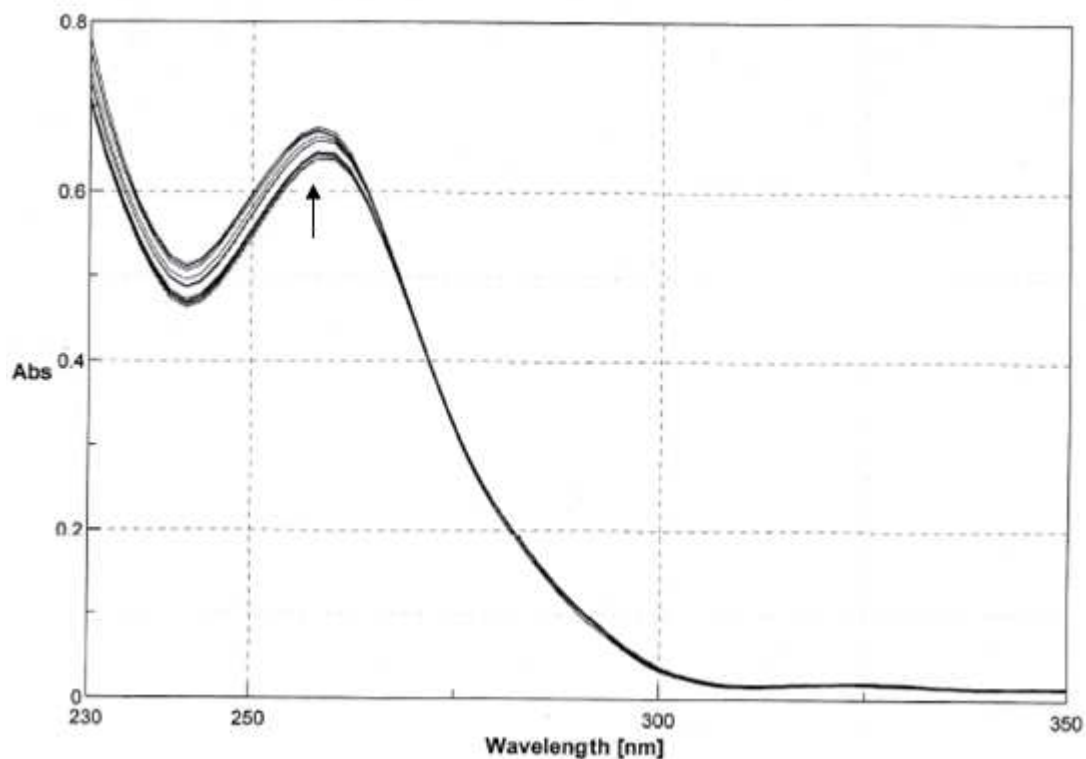


**Figure II-25.** Absorption spectral changes recorded at 2 min interval during the reaction of **1**, 10-phenanthroline monohydrate (phen) ( $1.25 \times 10^{-3} \text{M}$ ) in  $\text{CH}_3\text{OH}$  at 303K with  $\text{NaBH}_4$  ( $1.35 \times 10^{-2} \text{M}$ ).

Stoichiometry of the above reaction (Figure II-24) could be established through isolation of the  $\text{NaBH}_4$  reduction product of **2**, i.e., **3** (vide the experimental section for details) and characterizing it. As already pointed out, it is a binuclear Cu(I) complex with the pterin ligand residues in the 7,8-dihydro state [Schemes II-4 and II-5, II-5(a)] and is able to display near reversible electrochemical behavior [Figure II-21(b)] under controlled conditions. Steps leading to the formation of **3** are elucidated below.

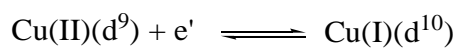
**Thermodynamic aspects of the reactions of **2** with  $\text{NaBH}_4$ .** Cyclic voltammetry data of **2** (Table II-7) indicate an  $E_0'$  value of  $-0.69 \text{V}$  for the Cu (II)/Cu(I) couple. The possible  $E_0'$  value

for NaBH<sub>4</sub> at different pH ranges has received much attention; close to the neutral medium an E<sub>0</sub>' value of -0.75V would be a reasonable choice<sup>56-58,161</sup>. Using the above data, an E<sub>cell</sub> value (E<sub>cell</sub> = E<sub>1</sub> - E<sub>2</sub>) of 0.06V is obtained for the Cu(II) + e' → Cu(I) reduction step in **2**<sup>59</sup>. Again in the light of the ligand reduction peak (E<sub>pc</sub>) at -0.223V for **2** (Figure II-20), an E<sub>cell</sub> value of 0.527V is indicated for the reduction of the pterin ligand residue; thus the latter reduction step is thermodynamically more feasible ( $\Delta G^0 = -nFE_0'$ ).

Now utilizing the reducing equivalent flow scheme in the PAH system by Chen and Frey as well as the E<sub>0</sub>' values of 0.207V and 0.174V for the iron centre in PAH and the BH<sub>4</sub>/BH<sub>2</sub> couple respectively (B = biopterin) by Martinez and coworkers, an E<sub>cell</sub> value of 0.033V may be calculated for the conversion: phenylalanine + BH<sub>4</sub> + O<sub>2</sub> → tyrosine + BH<sub>2</sub> + H<sub>2</sub>O<sup>60-62</sup>. In nature the pterin cofactor is regenerated (BH<sub>2</sub> → BH<sub>4</sub>) by NADH (E<sub>0</sub>' = -0.32V), suggesting an E<sub>cell</sub> value of 0.494V for the regeneration step<sup>53</sup>. Such estimated E<sub>cell</sub> values for the PAH system fall within a range, comparable to those of the **2** - NaBH<sub>4</sub> reaction system as above.

A closer look may be taken at Figure II-24 in the light of the above guidelines and Schemes II-4, II-5 and II-6 for understanding this reduction reaction. In terms of the aforesaid thermodynamic driving forces ( $\Delta G^0 = -nFE_0'$ ), the relevant time - dependent absorption spectral changes could be differentiated into two distinct types [ Figures II-24(a) and II-24(b)], e.g., without and with isosbestic points. In other words, the transfer of reducing equivalents to two different redox centres covalently linked within the same molecule (**2**), may be visualized on the time scale of electronic spectroscopy. As par the above thermodynamic driving forces the first step [Figure II-24(a)] without any isosbestic point represents the transfer of reducing equivalents to the pterin ring, followed by the formation of a putative Cu(II) intermediate **2'** (Scheme II-6) ; the next step [Figure II-24(b)] characterized by isosbestic points reflects the reduction of the

metal centres of **2'**, associated with the transformation, **2'** → **3**. As evident from the  $k_{\text{obs}}(\text{s}^{-1})$  data stated earlier, the second step is ca. 3 times faster than the first one. This is consistent with the cyclic voltammetry data of **3** [Figure II-20(b)], indicating a close approach to electrochemical reversibility for the corresponding metal-centred redox process



**Reactivity of 3 with bromobenzene and dioxygen.** For exploring the redox ability of **3** in transferring reducing equivalents, its reactivity towards bromobenzene (a model substrate for exploring PAH type activity) in presence of dioxygen has been studied<sup>55</sup>. Figure II-26 shows a clean reaction with two isosbestic points (314 nm and 396 nm) and the arrows indicating movements of the absorption spectral curves, represent opposite behavior as compared to those in Figure. II-24(b). Taken together, the two figures [Figure. II-24(b) and Figure. II-26], represent the response of **2** towards a reducing agent like  $\text{NaBH}_4$ , leading to the formation of **3** and the ability of **3** in transferring the reducing equivalents to bromobenzene in presence of  $\text{O}_2$ , respectively. Kinetics of the latter reaction (Figure II-26) was followed at 372 nm and four different temperatures (range 300-330K) in  $\text{CH}_3\text{OH}$  saturated with  $\text{O}_2$  under pseudo-first-order conditions (with a **3**: bromobenzene ratio of 1:140) and the relevant data are indicated below:

$$k_{\text{obs}} = 2.9 \times 10^{-2} \text{ s}^{-1}; \Delta S^\ddagger = -196.0 \text{ J mol}^{-1} \text{ deg}^{-1}.$$

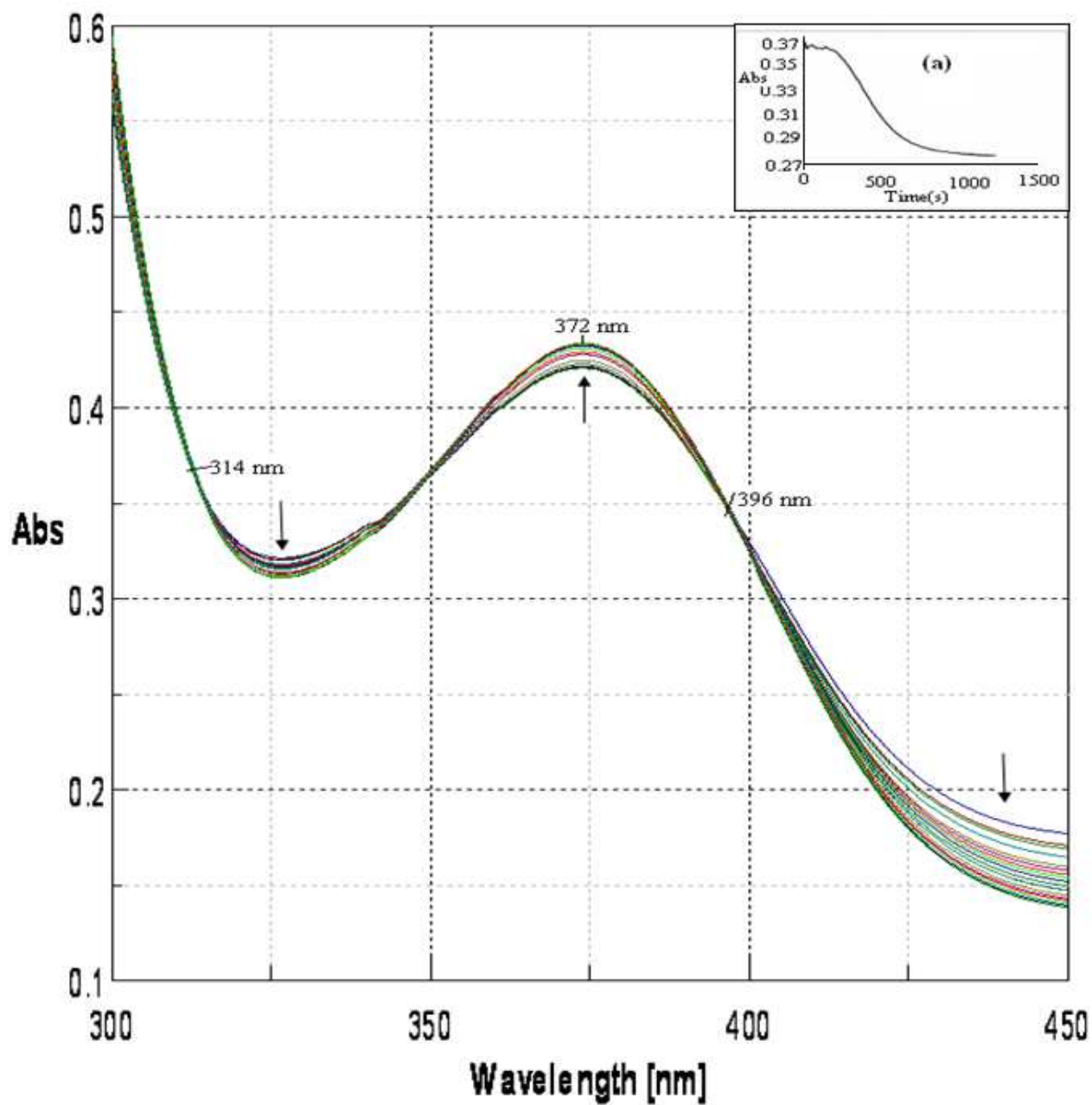


**Figure II-26.** Absorption spectral changes recorded at 5 min interval during the reaction of **3** ( $1.0 \times 10^{-4}\text{M}$ ) with bromobenzene ( $1.9 \times 10^{-2}\text{M}$ ) in  $\text{CH}_3\text{OH}$  saturated with  $\text{O}_2$  at 300K; (a) the absorption versus time curve at 372 nm, 303K.

They indicate an associative (Scheme II-7) process with a rate constant comparable to that of the reaction represented by Figure II-24(b). Stoichiometry of this reaction [Figure II-26; Scheme II-8(b)] was checked through its repetition on the preparative scale and isolating / characterizing 4-bromophenol and **2** as the products (vide the experimental section)<sup>55</sup>.

**Aerial Oxidation of 3.** Again, when **3** is left exposed to air in the absence of a substrate (e.g., bromobenzene), it is reconverted to **2** [Scheme II-8 (a)], as already established x-ray structurally<sup>17b</sup>. Most likely H<sub>2</sub>O<sub>2</sub> evolution accompanies this transformation, associated with one two-electron transfer step from the binuclear Cu<sub>2</sub>(I) centre of **3**, as indicated below<sup>48,63</sup>:



It helps to overcome the barriers associated with dioxygen reaction; the corresponding one-electron reduction is difficult ( $E_0' = -0.16\text{V}$ ) due to the exchange stabilization of the high-spin configuration ( $^3\Sigma_g^-$ )<sup>67</sup>.

**Reactivity and Electronic Structures of 2 and 3.** Viewed in the perspective of Scheme II-8 (a composite of Schemes II-6 and II-7), it is evident that the transfer of reducing equivalents (from NaBH<sub>4</sub>) to **2** converts it to the binuclear species **3** and further transfer of the same to the O<sub>2</sub>/bromobenzene reaction system [Scheme II-8 (b)] restores the original mononuclear species **2**. These steps are associated with structural rearrangements involving the copper centres and an important role is played by the phen residue of **3** during the conversion:



Recent x-ray structural study of the coupled binuclear copper enzyme tyrosinase reveals apparent mobility in copper binding modes, assisting the substrate binding orientation. But here six conserved histidine residues are able to preserve the binuclear active site of this enzyme<sup>68-71</sup>.

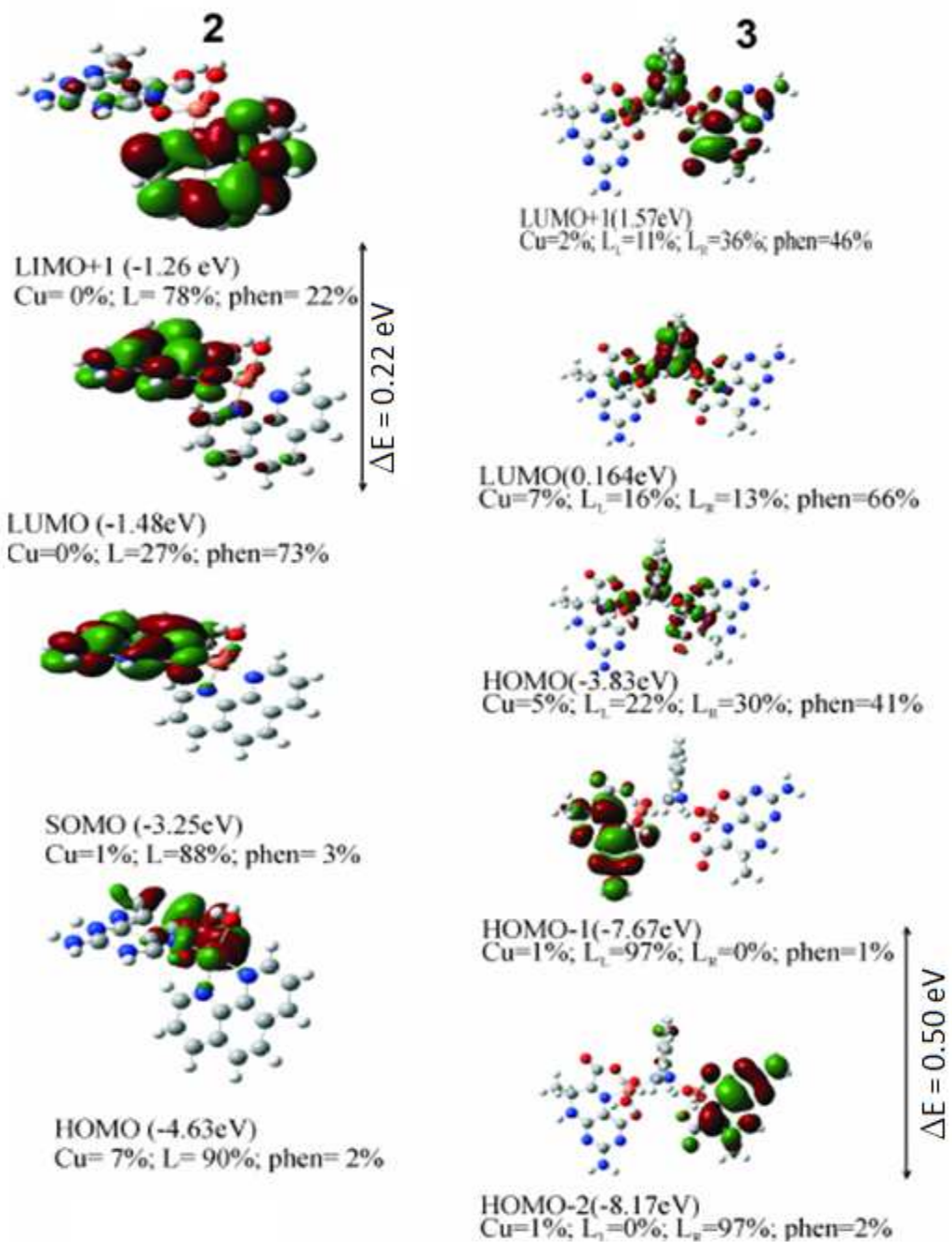


**Figure II-27.** Frontier molecular orbitals of **2** and **3**, showing their energies (eV) and compositions (%). The notations L<sub>L</sub> and L<sub>R</sub> represent the two pterin ligand residues of **3** [Scheme II-5, II-5(a)].

Further insight into the electron transfer process of **2** and **3** could be obtained from the frontier MO energy levels and their compositions (Figure II-27 ) obtained by DFT calculations<sup>154-159</sup>. Reliability of such a theoretical model is evident from its ability to interpret the chirality of **3** [Figure II-19(b)] in terms of unequal occupancies of the two pterin residues ( $L_L$  and  $L_R$ ) at the HOMO-1 and HOMO-2 levels respectively (Figure II-27); this creates an asymmetry about the phen residue (of **3**), which survives to a lesser extent even upto the HOMO level. The small band gap (0.5eV) between the HOMO-1 and HOMO-2 levels of **3** possibly facilitates its one-step reaction with the  $O_2$ /bromobenzene mixture [Figure II-26 and Scheme II-8(b)]; this step involves oxidations of both the metal [Cu(I)] and pterin ligand (7,8-dihydro form) centres of **3**, leading to the recovery of **2**. On the other hand, **2** is characterized by a even smaller band gap (0.22eV) between its LUMO and LUMO+1 levels (Figure II-27), which can accommodate the reducing equivalents transferred by  $NaBH_4$  (Figure II-24; Schemes II- 6,7 and 8).Such transfer of reducing equivalents in the opposite directions for **2** and **3** affects the oxidation states of their metal and pterin centers. Now-a-days synthetic molecules with exceptionally small (<0.5eV) HOMO –LUMO gaps (HLG) are receiving considerable attention due to their interesting electrochemical/redox amphoteric behavior<sup>64-66</sup>. Usually in such cases the HOMO – LUMO orbitals are located in different covalently linked centres in a single molecule. Thermo-excited intramolecular electron transfer may occur between two such centres in solution. Perhaps the combination of the redox non-innocent pterin ligand residue with the redox active metal centre [ Cu(II)/Cu(I)] in complexes **2** and **3**, helps to achieve such a situation here, associated with the distinct redox activities [ Figures II-24 and II-26]<sup>9-11,53</sup>.

## Conclusion

A structurally characterized copper (II) complex (**2**) of a 6-substituted pterin ligand (**1**, Scheme II-1) is able to retain reducing equivalents from  $\text{NaBH}_4$ , leading to the formation of a bimolecular copper (I) complex **3**. The latter is able to convert a model substrate like bromobenzene to 4-bromophenol in presence of  $\text{O}_2$  and affording back the original complex **2**. Again, **3** is able to display near reversible electrochemical behavior under a special condition [Figure II-21(b)]. These aspects are summarized in Scheme II-8 and Figure II-28. Such reactivities have been elucidated on the basis of physico-chemical studies and further rationalized in the light of electronic structures (DFT methods).

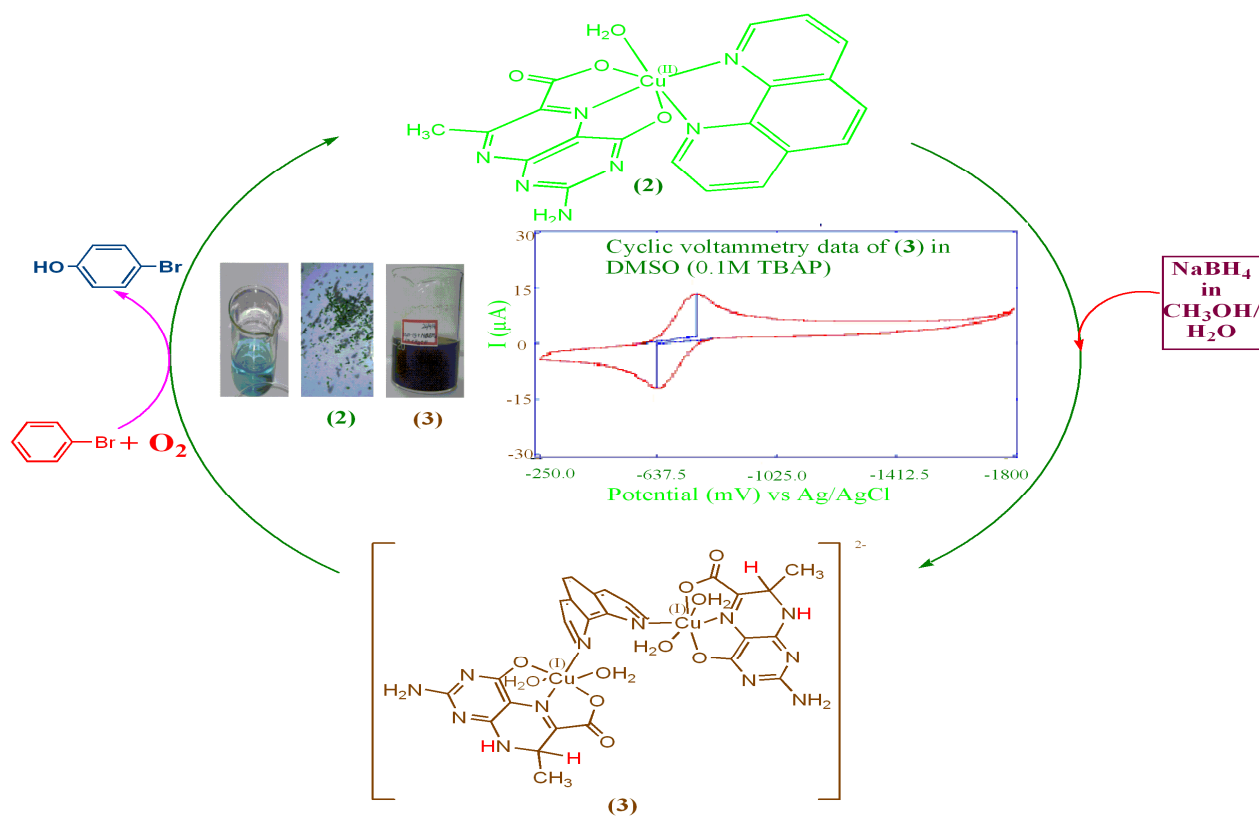


**Figure II-28.** A summary of the chemical and electrochemical reactivities of **2** and **3**.

That is, small band gaps ( $<0.5$  eV) between the relevant frontier orbitals are responsible for the transfer of reducing equivalents to **2** and their facile release from **3**. Exceptional stability of the coordination geometry around the Cu (II) ion in **2** is indicated, which allows it to survive through different chemical transformation (Scheme II-8). A combination of the redox non-innocent tridentate pterin ligand (**1**) and the  $\pi$ -acceptor ancillary ligand phen around the copper centre with its two closely related oxidation states [Cu (II)/ Cu (I)], possibly confers this unique redox flexibility.

## **CHAPTER III**

**A new cobalt(II) complex of 7-methylpterin-6-carboxylic acid with 1, 10- phenanthroline as the ancillary ligand: synthesis, x-ray structural, physico-chemical, kinetic studies and DFT calculations.**

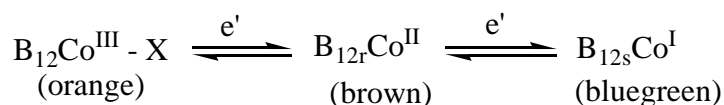
## Abstract

A new mixed ligand cobalt(II) complex of the title ligands has been synthesized and characterized using elemental analysis, ESIMS and x-ray structural data as well as different physico-chemical studies. X-ray data of this compound  $[\text{Co}(\text{L})(\text{phen})(\text{H}_2\text{O})]\cdot 3\text{H}_2\text{O}$  reveals tridentate pterin coordination towards a mononuclear Co(II) atom. The neutral bidentate ancillary ligand [1, 10-phenanthroline (phen)] and the aqua group complete the distorted octahedron around the metal center. Near perpendicular disposition of the two chelate rings involving pterin and phen, respectively is indicated. The crystal forces are further augmented by two types of  $\pi$ - $\pi$  stacking involving the pterin ring and phen. The cyclic voltamogram is characterized by several irreversible reduction peaks (-0.6, -1.1V, -1.3V and -1.6V respectively) of which the one at -0.6 V can be assigned to a metal-centered reduction process, e.g.  $\text{Co}(\text{II}) \rightarrow \text{Co}(\text{I})$ . The group transfer reaction involving replacement of the aquo group of this complex by imidazole has been followed kinetically giving a  $k_{\text{obs}}$  value of  $2.6 \times 10^{-2} \text{ s}^{-1}$  and  $\Delta S^\ddagger = -256.0 \text{ J mol}^{-1} \text{ deg}^{-1}$  respectively; the negative  $\Delta S^\ddagger$  value indicates an associative pathway. Reactivity of this Co(II) complex towards  $\text{NaBH}_4$  as well as that of the  $\text{NaBH}_4$  reduction product towards bromobenzene have been followed spectrophotometrically in presence of  $\text{O}_2$ ; activation of the aromatic ring of bromobenzene towards hydroxylation could be inferred from the associated stoichiometric studies. Gaussian DFT calculations throw lights on the frontier orbital energies as well as their percentage compositions and help to rationalize the above reactivities.

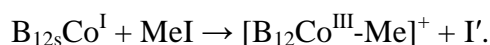
## Introduction

The most important biochemical role of cobalt is associated with vitamin B<sub>12</sub>, which is the only vitamin known to contain a metal. Vitamin B<sub>12</sub> is involved in a number of biochemical processes, the most important being the formation of red blood cells (erythrocytes). Reaction of vitamin B<sub>12</sub> with ATP leads to the formation of vitamin B<sub>12</sub>-coenzyme, which is involved in effecting many unusual rearrangement reactions.

Vitamin B<sub>12</sub>, cobalamin (orange) can be reduced in two successive one electron steps into vitamin B<sub>12r</sub> (brown) and vitamin B<sub>12s</sub>, with the cobalt centres existing in the +3, +2 and +1 oxidation states respectively.



In biological systems, these reductions are carried out by NADH and FADH<sub>2</sub>. Reduced vitamin B<sub>12</sub> species (the B<sub>12s</sub>) is a powerful reducing agent which reduces ClO<sub>3</sub>' to Cl' and at pH 1.5 – 2.5 NO<sub>3</sub>' to NH<sub>4</sub><sup>+</sup>. The vitamin B<sub>12s</sub> (blue-green) species is also strongly nucleophilic and undergoes ready alkylation leading to the formation of a Co-C bond:



Cobalt is also biologically important in some enzymes. Glutamic mutase is involved in the metabolism of amino acids and ribonucleotide reductase in the biosynthesis of DNA.

In the light of the aims and objectives of this treatise, the coordination chemistry of the cobalt (II) ion (d<sup>7</sup>) is explored here using the pterin ligand 7-methylpterin-6-carboxylic acid (H<sub>2</sub>L). A couple factors have guided the choice of Co (II) for this work e. g. the avidity of Co (II) complexes for molecular oxygen as well as the ability of this d<sup>7</sup> system to balance the extent of M→L π bonding (with molecular oxygen) with the transmission of reducing property of the

pterin ligand to the reaction site, using bromobenzene as a model substrate for PAH activity.

NaBH<sub>4</sub> is used here as the source of reducing equivalents.

Choice of 1, 10-phenanthroline (phen) as the ancillary ligand here depends solely on its ability to provide with x-ray quality crystals of the resulting Co (II) mixed ligand complex. 2, 2'-bipyridine (bipy) is unable to achieve this objective. Ability of such  $\pi$ -acid ligands to form Co(I) (d<sup>8</sup>) complexes . e g. [Co(bipy)<sub>3</sub>]<sup>+</sup> is well-known<sup>79</sup>. There is scope for accessing the Co(I) state chemically/electrochemically using the Co(II) complex. Gaussian DFT calculations on present system have been used to obtain information about the electronic structures which help to rationalize the reactivity aspects.

## Experimental

**Materials.** Reagent grade chemicals were used as received. Solvents were purified, prior to use, following literature procedure<sup>20</sup>. CoSO<sub>4</sub> · 7H<sub>2</sub>O was obtained from BDH, E. Merck, Mumbai. NaOH was obtained from SRL, Mumbai and 1, 10-phenanthroline was obtained from E. Merck, Mumbai. Kinetic and electrochemical measurements were performed in spectroscopic grade DMSO (SRL, Mumbai). Bu<sub>4</sub>NClO<sub>4</sub> (TBAP) for CV measurements was obtained by published methods<sup>72</sup>.

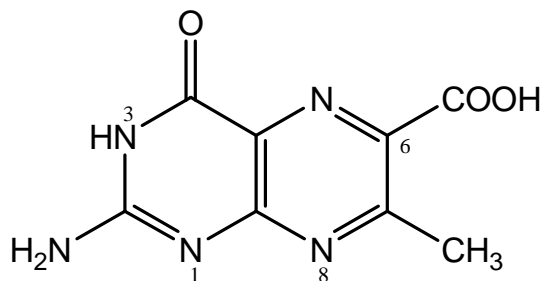
**Methods.** X-ray (Bruker Smart Apex CCD), elemental analysis (Elementor, Vario Micro Cube-C,H,N) and CD (Jasco J-815) data were obtained from the CSMCRI, Bhavnagar, Gujarat. The basic CD data were smoothed using the Origin Pro 8 software. The electrospray mass spectra in CH<sub>3</sub>OH were obtained from RSIC, Lucknow (Agilent 6520 Q-TOF mass spectrometer). Room temperature magnetic moment data were obtained by using a Sherwood magnetic susceptibility balance (model MSB Mk1). IR spectra (KBr pellet) were recorded on a Perkin Elmer IR

spectrometer (model RX 1). Cyclic voltammetric experiments were performed with a Bioanalytical Systems Epsilon electrochemical workstation (model CV-50) using 1.0mM analyte in DMSO (0.1M TBAP; glassy carbon working electrode). Electronic spectra and kinetic data (under N<sub>2</sub>- atmosphere) were recorded on a Jasco (UV-530) spectrophotometer, with thermostatic conditions ( $\pm 0.5$  K) being maintained using a Shimadzu (TB-85) thermostat. Pseudo-first-order rate constants ( $k_{\text{obs}}$ , s<sup>-1</sup>) were determined by the least square method from the plots of  $\log(A_{\infty} - A_t)$  vs. time, which were linear for at least three half-lives. These rate constants measured at four different temperatures, were used to determine activation parameters by means of an Eyring plot [ $\ln(k_{\text{obs}}/T)$  vs.  $(1/T)$ ]. The frontier orbitals diagrams were obtained by Gaussian 09 and Gauss View 05 computer softwares.

## Synthesis .

### **2-Amino-4-hydroxy-7-methylpteridine-6-carboxylic acid sesquihydrate (C<sub>8</sub>H<sub>7</sub>N<sub>5</sub>O<sub>3</sub>. 1.5H<sub>2</sub>O) (1)**

The pterin ligand 2-amino-4-hydroxy-7-methylpteridine-6-carboxylic acid sesquihydrate (C<sub>8</sub>H<sub>7</sub>N<sub>5</sub>O<sub>3</sub>. 1.5H<sub>2</sub>O) was obtained by published procedure. (Wittle et.al., 1947)<sup>19</sup>. Ligand (1) was prepared in 75 % yield by modifying the original method of synthesis in the light of later developments (e.g., darkness, N<sub>2</sub> – atmosphere)<sup>73</sup>. The product decomposed without melting above 573 K. It is soluble in aqueous/methanolic NaOH/KOH and Bu<sub>4</sub>NOH. Found : C, 44.0; H, 4.4; N, 28.4 %. Calc. for C<sub>8</sub>H<sub>7</sub>N<sub>5</sub>O<sub>3</sub>. 1.5H<sub>2</sub>O : C, 44.3; H, 4.1; N, 28.7 %. UV – VIS absorption bands [NaOH,  $\lambda_{\text{max}}^{\text{nm}}(\log\epsilon)$ ]: 293 (3.68), 341 (3.86), 400 (3.28), 422 (3.27), 456 sh (3.00).



The pterin ligand ( $H_2L$ )

### Scheme III-1

---

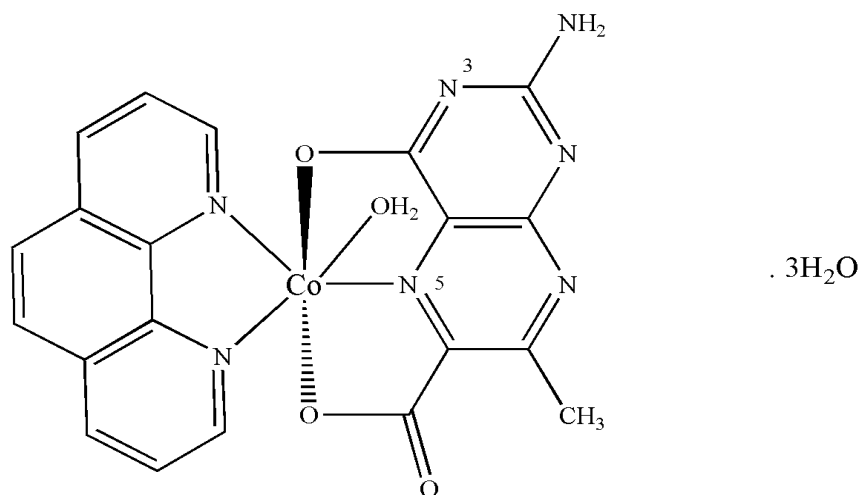
#### $[Co(C_8H_5N_5O_3)(C_{12}H_8N_2)(H_2O)] \cdot 3H_2O$ (2)

The title complex was prepared by the dropwise addition of an aqueous alkaline solution (NaOH : 11 mg, 0.275mmol) of the pterin ligand (35 mg, 0.125 mmol) to a warm (311K) aqueous reaction medium containing  $CoSO_4 \cdot 7H_2O$  (35 mg, 0.125 mmol) and 1, 10-phenanthroline monohydrate (25 mg, 0.125 mmol) in a total volume of 60 ml. The pH value was adjusted to 10.8 using aqueous NaOH solution and dioxygen was bubbled in for 48h; final pH was 10.3. Initially a small amount of yellow-white precipitate came out and the reaction mixture ultimately assumed as a reddish-pink tinge. It was transferred to a 100 ml beaker, requisite quantity of water was added to make up for the evaporation loss and allowed to stand at room temperature. Pink crystals suitable for single crystal x-ray diffraction appeared after 15 days (yield : 30%). Found: C, 43.0; H, 3.69; N, 17.81%. Calc. for  $[Co(C_8H_5N_5O_3)(C_{12}H_8N_2)(H_2O)] \cdot 3H_2O$ : C, 45.25; H, 3.96; N, 18.47%. UV-VIS absorption bands [ $CH_3OH$ ,  $\lambda_{max}nm$  ( $\log\epsilon$ ): 268(4.35), 372(3.65), 540br(2.22), 620br(2.19), 678(2.20), 712sh(2.17), 744(2.18), 807(2.18), 924sh(2.00), 970sh(1.9), 1056br(1.83)



### Scheme III-2

---



### Scheme III-3 (compound 2)

---



**Synthesis of  $\text{Na}[\text{Co}^{\text{I}}(\text{L}')(\text{phen})(\text{H}_2\text{O})] \cdot 2\text{H}_2\text{O} \cdot \text{CH}_3\text{OH}$  (3),** where  $(\text{L}')^{2-}$  is the 7,8-dihydro form (Scheme II-4) of the pterin ligand anion (Scheme II-1), as established on the basis of microanalytical and spectroscopic data (vide infra). A methanolic solution (50 mL) of **2** (26.51 mg, 0.05 mmol) was treated with  $\text{NaBH}_4$  (11.3 mg, 0.3 mmol) and the reaction was allowed to continue for 45 min at 301-303K under subdued light in a Schlenk flask attached to a paraffin oil bubbler. The reaction mixture passed through a sequence of color changes e.g., bright orange  $\rightarrow$  snuff colour . It was then rotavapped and a dark brown solid was recovered (Scheme II-6). It was washed quickly (decantation ) with dinitrogen purged  $\text{CH}_3\text{OH}$  ( 3 X 4 mL) and dried in vacuo

over silica gel for 48h. Yield: 35%. Anal. Calcd for  $\text{NaCoC}_{21}\text{H}_{25}\text{N}_7\text{O}_7$ : C, 44.29; H, 4.39; N, 17.22. Found: C, 43.24; H, 3.89; N, 17.58.

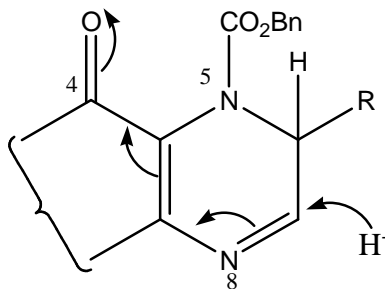
## Results and Discussion

Synthesis of the present Co(II) mixed ligand complex (**2**) is not straight forward. Initially a small quantity of yellow-white precipitate of unknown composition came out and only after prolonged exposure to dioxygen at  $38^\circ\text{C}$ , it could be redissolved and the desired crystals could be obtained. The crystals have to be dried in vacuo for at least 48 hours for getting analytically pure samples, suitable for elemental analysis (C-H-N) and mass spectral data (ESIMS).

The elegance of the synthetic procedure is that the complex compound of a pterin ligand could be crystallized out of the aqueous medium, whereas pterin compounds usually suffers from low solubility problems<sup>74</sup>. Most likely the presence of hydrophilic groups like –COOH and –OH in the pterin ligand contributes to the enhanced solubility of (**2**) in aqueous alkaline medium (ca.  $\text{pH} \approx 10.5$ ).

**Molecular Structure of  $[\text{Co}(\text{C}_8\text{H}_5\text{N}_5\text{O}_3)(\text{C}_{12}\text{H}_8\text{N}_2)(\text{H}_2\text{O})] \cdot 3\text{H}_2\text{O}$  (**2**).** In the title compound (**2**) (Figure III-1), the stereochemistry around the Co(II) atom is essentially distorted octahedral with two N atoms of phen, a pyrazine ring N atom (N3) of the pterin ligand and an aqua O atom forming the equatorial plane; two pterin O atoms (O1 and O3) define the longer axial positions, with the phenolate O3 forming the longest axial bond [2.270 (2) Å]. Extent of distortion of this coordination octahedron is much more pronounced as compared to that of the Co(II)-pteridine complexes reported earlier (Acuna-Cueva *et al.*, 2003; Burgmayer & Stiefel, 1988; Funahashi *et al.*, 1997)<sup>15,25,76</sup>. A major cause of this departure from regular geometry is that the pterin ligand forms two five-membered chelate rings having small bite angles [75.10 (10) and 76.26 (9)°], instead of only one per pteridine ligand for the earlier cases. Location of the short

Co1—N3 bond [2.016 (3) Å] in the equatorial plane is consistent with the literature, which suggests a strong cobalt-pterin interaction (Odani *et al.*, 1992)<sup>18c</sup>. The pterin ligand is coordinated here as a binegative tridentate ONO donor, as evident from the charge balance of this complex. The phen and pterin rings are nearly perpendicular to each other for minimizing the steric repulsion. The Co1—N1 [2.079 (3) Å] and Co1—N2 [2.123 (3) Å] bond lengths are at par with that of the Co1—N3 bond [2.016 (3) Å] and indicate receipt of  $\pi$ -back donation to both phen and pterin rings from the Co(II) centre ( $d^7$ ) through  $d\pi$ - $p\pi$  interactions. This process is further strengthened by the presence of  $\pi$ -donating phenolate and carboxylate O atoms around the metal centre (Kohzuma *et al.*, 1988)<sup>18a</sup>. For rationalizing the near double bond nature of the O3—C18 [1.265 (4) Å] bond, a hypothesis of Joule (Scheme III-4) (Beddoes *et al.*, 1993; Russell *et al.*, 1992)<sup>22,23</sup> may be invoked, which suggests withdrawal of electron density from the pyrazine ring N6 by the pyrimidine ring C18-carbonyl group through mesomeric interaction. Formation of the O3—Co1 bond accentuates this electron withdrawal towards O3. The electron-rich N7—C17 [1.337 (4) Å] bond may also participate in this electron transfer (Figure III-1). The presence of hydrogen-bonded electron transfer proteins (iron-sulphur proteins) at the pterin ring NH<sub>2</sub>(2) position (Scheme III-1, III-2, III-4) as revealed by x-ray crystallography for oxomolybdoenzymes, may bear instructive relation with the above-mentioned electron transfer process from N7 to O3 (bonded to the metal centre)<sup>10</sup>. The pyrimidine ring is fairly planar and deviations of the C16/N5/C17 and C17/N4/C18 segments with respect to the N7—C17 multiple bonds are 2.6 and 0.7°, respectively. The crystal data and geometric parameters of (**2**) are shown in Tables (III-1) and (III-2) respectively.



**Scheme III-4**

---

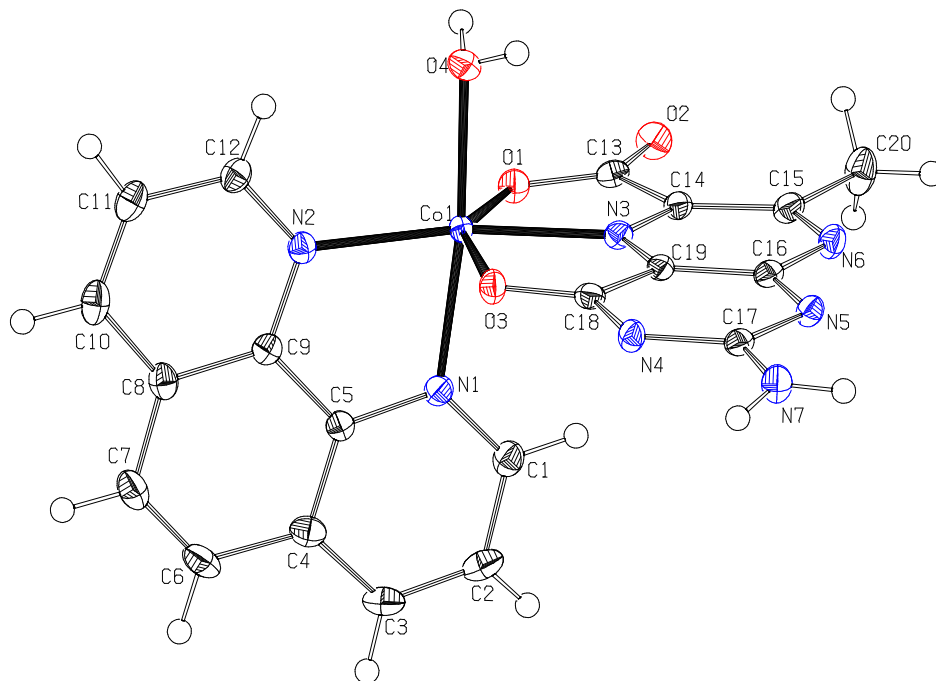


**Figure III- 1** ORTEP diagram of **(2)** with atom numbering scheme (50% probability factor for the thermal ellipsoids). Lattice water molecules are omitted for clarity.

---

**Table III-1. Crystal data and structure refinement for (2).**

Identification code	2
Empirical formula	C <sub>20</sub> H <sub>21</sub> CoN <sub>7</sub> O <sub>7</sub>
Formula weight	530.36
Temperature/K	110
Crystal system	Triclinic
Space group	P-1
a/Å	8.454(2)
b/Å	9.934(3)
c/Å	13.778(4)
α/°	97.534(4)
β/°	95.281(4)
γ/°	110.603(4)
Volume/Å <sup>3</sup>	1061.8(5)
Z	2
ρ <sub>calc</sub> /cm <sup>3</sup>	1.659
μ/mm <sup>-1</sup>	0.870
F(000)	546.0
Crystal size/mm <sup>3</sup>	0.230 × 0.110 × 0.040
Radiation	Mo Kα (λ = 0.71073)
2θ range for data collection/°	3.016 to 56.398

Index ranges	-11 ≤ h ≤ 11, -12 ≤ k ≤ 13, -18 ≤ l ≤ 18
Reflections collected	8945
Independent reflections	4744 [R <sub>int</sub> = 0.030, R <sub>sigma</sub> = 0.665]
Data/restraints/parameters	4744/0/316
Goodness-of-fit on F <sup>2</sup>	1.029
Final R indexes [I ≥ 2σ (I)]	R <sub>1</sub> = 0.0567, wR <sub>2</sub> = 0.1257
Final R indexes [all data]	R <sub>1</sub> = 0.0626, wR <sub>2</sub> = 0.1290
Largest diff. peak/hole / e Å <sup>-3</sup>	0.99/-0.88

**Table III-2. Geometric parameters of (2)**

Atoms 1,2	d 1,2 [Å]	Atoms 1,2	d 1,2 [Å]
Co1—O1	2.140(2)	N2—C12	1.333(4)
Co1—N3	2.016(3)	N2—C9	1.355(4)
Co1—O3	2.270(2)	C12—C11	1.402(5)
Co1—O4	2.120(2)	C12—H12	0.9230
Co1—N2	2.123(3)	C11—C10	1.363(5)
Co1—N1	2.079(3)	C11—H11	0.9140
O1—C13	1.279(4)	C10—C8	1.414(5)
C13—O2	1.244(4)	C10—H10	0.9260
C13—C14	1.519(4)	C8—C9	1.408(4)
C14—N3	1.319(4)	C8—C7	1.435(5)

C14—C15	1.426(4)	C9—C5	1.439(4)
N3—C19	1.319(4)	C5—N1	1.359(4)
C19—C16	1.397(4)	C5—C4	1.411(4)
C19—C18	1.450(4)	N1—C1	1.333(4)
C16—N5	1.354(4)	C1—C2	1.406(5)
C16—N6	1.360(4)	C1—H1	0.9300
N5—C17	1.360(4)	C2—C3	1.363(5)
C17—N4	1.378(4)	C2—H2	0.9280
C17—N7	1.337(4)	C3—C4	1.412(5)
N4—C18	1.335(4)	C3—H3	0.9280
C18—O3	1.265(4)	C4—C6	1.439(5)
N7—H7a	0.8520	C6—C7	1.349(5)
N7—H7b	0.8430	C6—H6	0.9250
N6—C15	1.342(4)	C7—H7	0.9260
C15—C20	1.491(4)	O7—H7c	0.8010
C20—H20a	0.9470	O7—H7d	0.8090
C20—H20b	0.9600	O5—H5a	0.8180
C20—H20c	0.9300	O5—H5b	0.8170
O4—H4a	0.8100	O6—H6a	0.8250
O4—H4b	0.8010	O6—H6b	0.8180

Atoms 1,2,3	Angle 1,2,3 [°]	Atoms 1,2,3	Angle 1,2,3 [°]
-------------	-----------------	-------------	-----------------

O1—Co1—N3	75.1(1)	H20a—C20—H20c	106.600
O1—Co1—O3	151.22(8)	H20b—C20—H20c	109.700
O1—Co1—O4	90.13(9)	Co1—O4—H4a	116.600
O1—Co1—N2	90.99(10)	Co1—O4—H4b	109.700
O1—Co1—N1	119.55(10)	H4a—O4—H4b	95.300
N3—Co1—O3	76.26(9)	Co1—N2—C12	128.8(2)
N3—Co1—O4	90.23(10)	Co1—N2—C9	112.7(2)
N3—Co1—N2	96.45(10)	C12—N2—C9	118.5(3)
N3—Co1—N1	164.48(10)	N2—C12—C11	122.3(3)
O3—Co1—O4	92.74(9)	N2—C12—H12	119.100
O3—Co1—N2	89.46(9)	C11—C12—H12	118.600
O3—Co1—N1	88.76(9)	C12—C11—C10	119.6(3)
O4—Co1—N2	173.29(10)	C12—C11—H11	120.200
O4—Co1—N1	94.58(10)	C10—C11—H11	120.200
N2—Co1—N1	79.12(10)	C11—C10—C8	119.9(3)
Co1—O1—C13	116.8(2)	C11—C10—H10	120.100
O1—C13—O2	124.1(3)	C8—C10—H10	120.000
O1—C13—C14	114.6(3)	C10—C8—C9	116.7(3)
O2—C13—C14	121.2(3)	C10—C8—C7	124.4(3)
C13—C14—N3	111.4(3)	C9—C8—C7	118.9(3)
C13—C14—C15	129.9(3)	N2—C9—C5	116.8(3)
N3—C14—C15	118.8(3)	C8—C9—N2	123.1(3)

Co1—N3—C14	121.6(2)	C8—C9—C5	120.1(3)
Co1—N3—C19	117.6(2)	C9—C5—N1	117.5(3)
C14—N3—C19	120.8(3)	C9—C5—C4	119.5(3)
N3—C19—C16	121.8(3)	N1—C5—C4	123.0(3)
N3—C19—C18	117.4(3)	Co1—N1—C5	113.6(2)
C16—C19—C18	120.7(3)	Co1—N1—C1	127.6(2)
C19—C16—N5	120.8(3)	C5—N1—C1	118.5(3)
C19—C16—N6	118.7(3)	N1—C1—C2	122.0(3)
N5—C16—N6	120.4(3)	N1—C1—H1	118.000
C16—N5—C17	115.1(3)	C2—C1—H1	120.000
N5—C17—N4	127.9(3)	C1—C2—C3	119.8(3)
N5—C17—N7	117.0(3)	C1—C2—H2	119.300
N4—C17—N7	115.1(3)	C3—C2—H2	120.900
C17—N4—C18	117.6(3)	C2—C3—C4	119.9(3)
C19—C18—N4	117.7(3)	C2—C3—H3	120.700
C19—C18—O3	118.1(3)	C4—C3—H3	119.400
N4—C18—O3	124.2(3)	C5—C4—C6	119.0(3)
Co1—O3—C18	110.63(19)	C3—C4—C5	116.8(3)
C17—N7—H7a	119.800	C3—C4—C6	124.2(3)
C17—N7—H7b	119.900	C4—C6—C7	121.2(3)
H7a—N7—H7b	117.600	C4—C6—H6	119.500
C16—N6—C15	119.0(3)	C7—C6—H6	119.200

C14—C15—N6	120.8(3)	C8—C7—C6	121.3(3)
C14—C15—C20	121.7(3)	C8—C7—H7	118.400
N6—C15—C20	117.4(3)	C6—C7—H7	120.300
C15—C20—H20a	111.500	H7c—O7—H7d	86.200
C15—C20—H20b	110.100	H5a—O5—H5b	108.700
C15—C20—H20c	110.700	H6a—O6—H6b	105.500
H20a—C20—H20b	108.200		

---

In the crystal, intermolecular N—H · · · O, O—H · · · N and O—H · · · O hydrogen bonds link the complex molecules and lattice water molecules into a layer parallel to (001) (Figure III-2). The lattice water molecules are decisive for the crystal packing. Table (III-3) shows a few hydrogen bond data. Figure III-3 reveals  $\pi$ - $\pi$  stacking interactions involving two parallel, inversion-related pterin rings within the same unit cell and showing face-to-face distance of 3.283 (4) and 3.366 (4) Å. Again the phen rings display two types of  $\pi$ - $\pi$  stacking on either side of the unit cell. In one case, the adjacent phen rings are essentially parallel to each other with an average interplanar distance of 3.496 (4) Å; on the other side of the unit cell, the face-to-face separations between parallel phen rings are 3.578 (4) and 3.629 (5) Å.

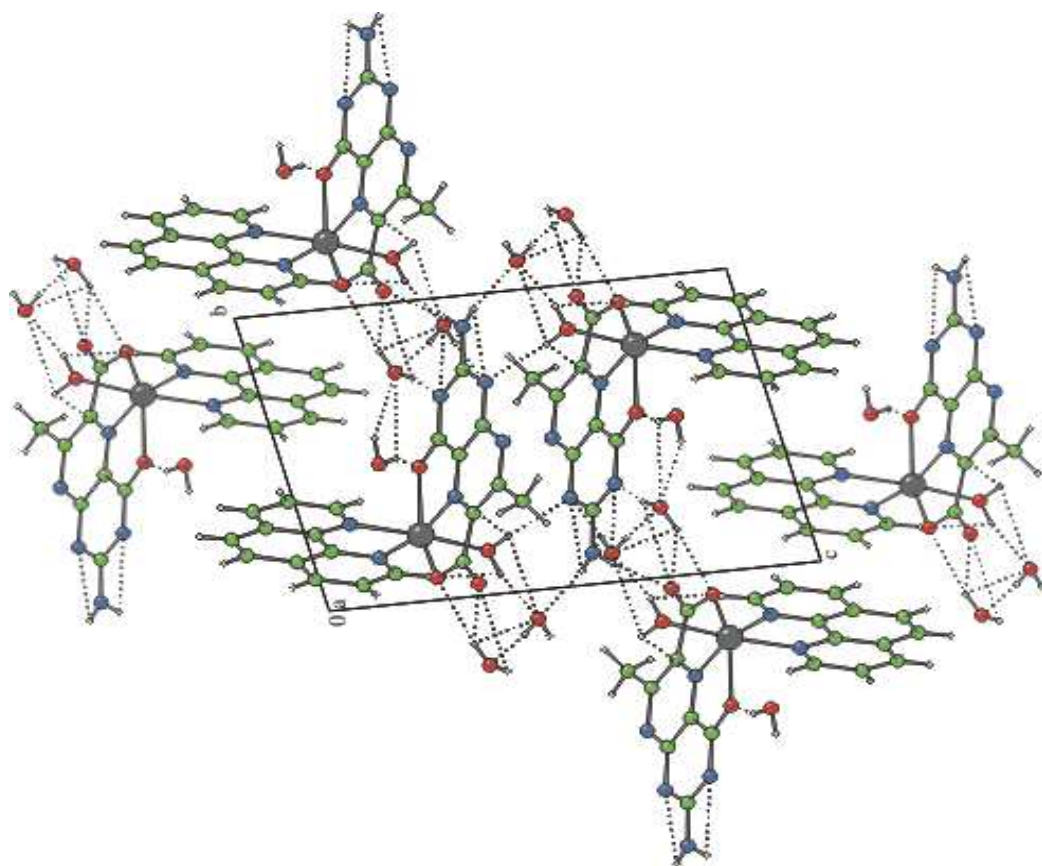


**Figure III-2.** The crystal packing diagram of (2), viewed along the *a* axis. Dotted lines indicate hydrogen bonds.

---

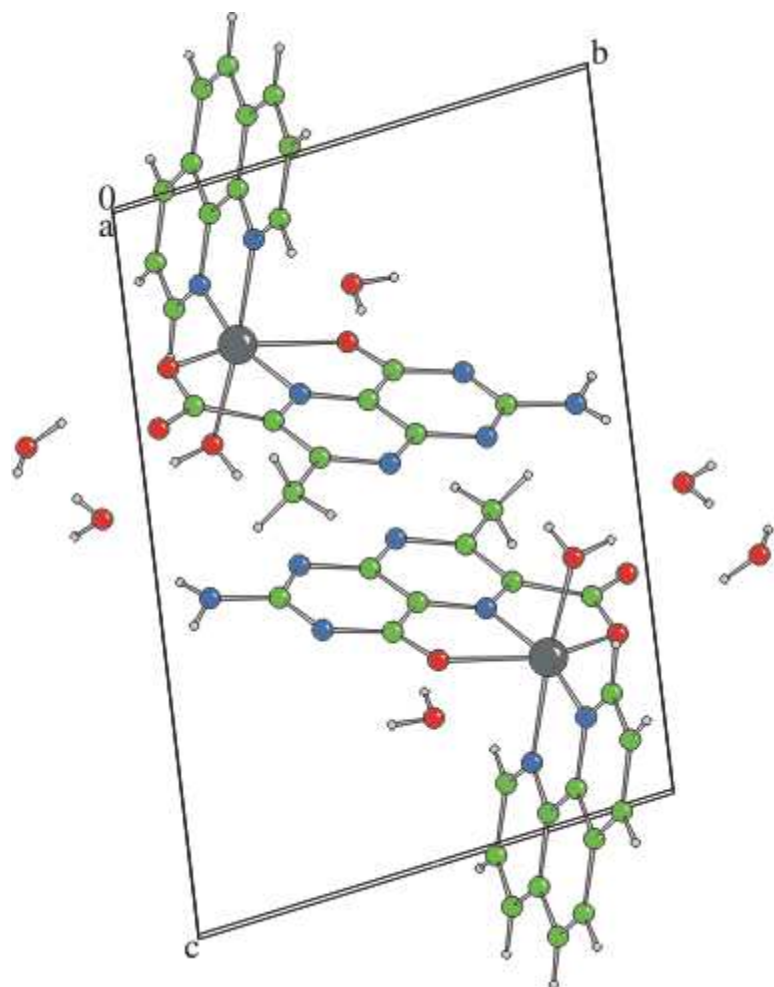


**Figure III- 3.** A molecular packing diagram highlighting  $\pi$ - $\pi$  stacking interactions between two neighboring pterin-pterin rings of (2).

---

**Table III-3. Selected hydrogen bonds of 2**

Atoms D,H,A	Dist. D,H [Å]	Dist. H,A [Å]	Dist. D,A [Å]	Angle D,H,A [°]
N7—H7a—O2 <sup>i</sup>	0.8520	2.1150	2.941(5)	163.12(10)
N7—H7b—O6 <sup>ii</sup>	0.8430	2.1480	2.970(5)	164.91(10)
O4—H4a—O6	0.8100	1.9290	2.717(5)	164.33(10)
O4—H4b—N5 <sup>ii</sup>	0.8010	2.2510	3.050(5)	176.15(9)
O5—H5a—O1	0.8180	2.3390	3.079(5)	150.86(8)
O5—H5a—O2	0.8180	2.2320	2.896(5)	138.60(9)
O5—H5b— N4 <sup>vi</sup>	0.8170	2.0430	2.843(5)	166.42(10)
O6—H6a—O5	0.8250	1.9180	2.740(5)	174.33(10)
O6—H6b— N5 <sup>vii</sup>	0.8180	2.0530	2.870(5)	176.04(10)

(i) 1+x, 1+y, z; (ii) 1-x, 1-y, 1-z; (iii) 1+x, y, z; (iv) 1-x, 1-y, -z;

(v) -1+x, y, z; (vi) -1+x, -1+y, z; (vii) x, -1+y, z.

---

### Mass spectrometry

Electrospray Ionization Mass Spectroscopy (ESIMS) involving soft ionization technique, has proved to be a valuable tool for characterizing wide variety of compounds including inorganic and coordination types<sup>21,77,78</sup>. This technique helps in assigning the molecular mass of this type of synthetic compounds. As true for different types of mass spectrometry, the assignment of

molecular formula (or any definite fragment originating from it) is confirmed by the experimental value of  $m/z$  (most abundant isotopic mass) as well as matching between the experimental and calculated (simulated) isotopic distribution profile<sup>24</sup>. As far as organic compounds containing O, F, P and I are concerned, the relative intensities of M, M+1 and M+2 isotope peaks are of great value in recognizing the molecular ion ( $M^+$ ) peak or any well-defined fragment containing it<sup>21</sup>. For **1** a peak at  $m/z$  222 (rel. inten.15%) corresponds to the dehydrated species  $[M - 1.5H_2O + H]^+$  where  $M(C_8H_7N_5O_3 \cdot 1.5H_2O)$  is the relevant molecular formula; the associated isotope pattern could be calculated<sup>21,24</sup>

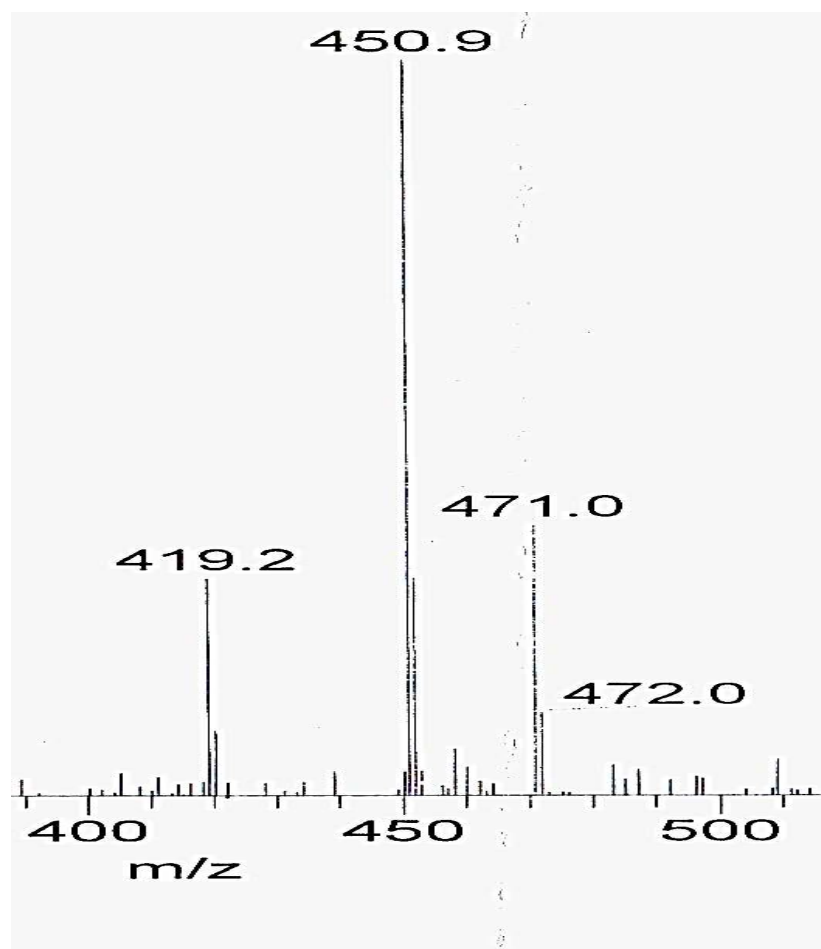


**Figure III-4(a).** ESIMS data of (**2**)

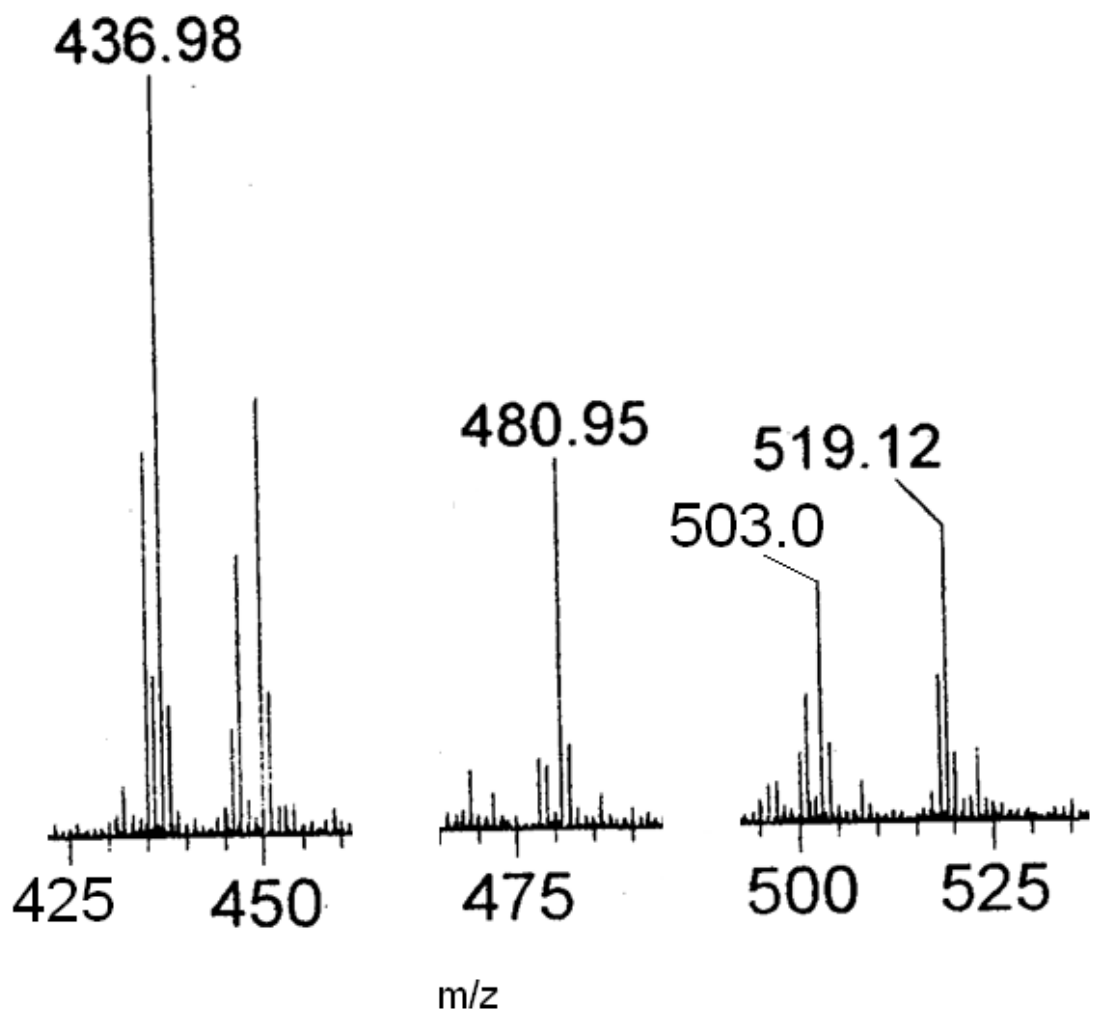


**Figure III-4(b).** ESIMS data of (3)

---

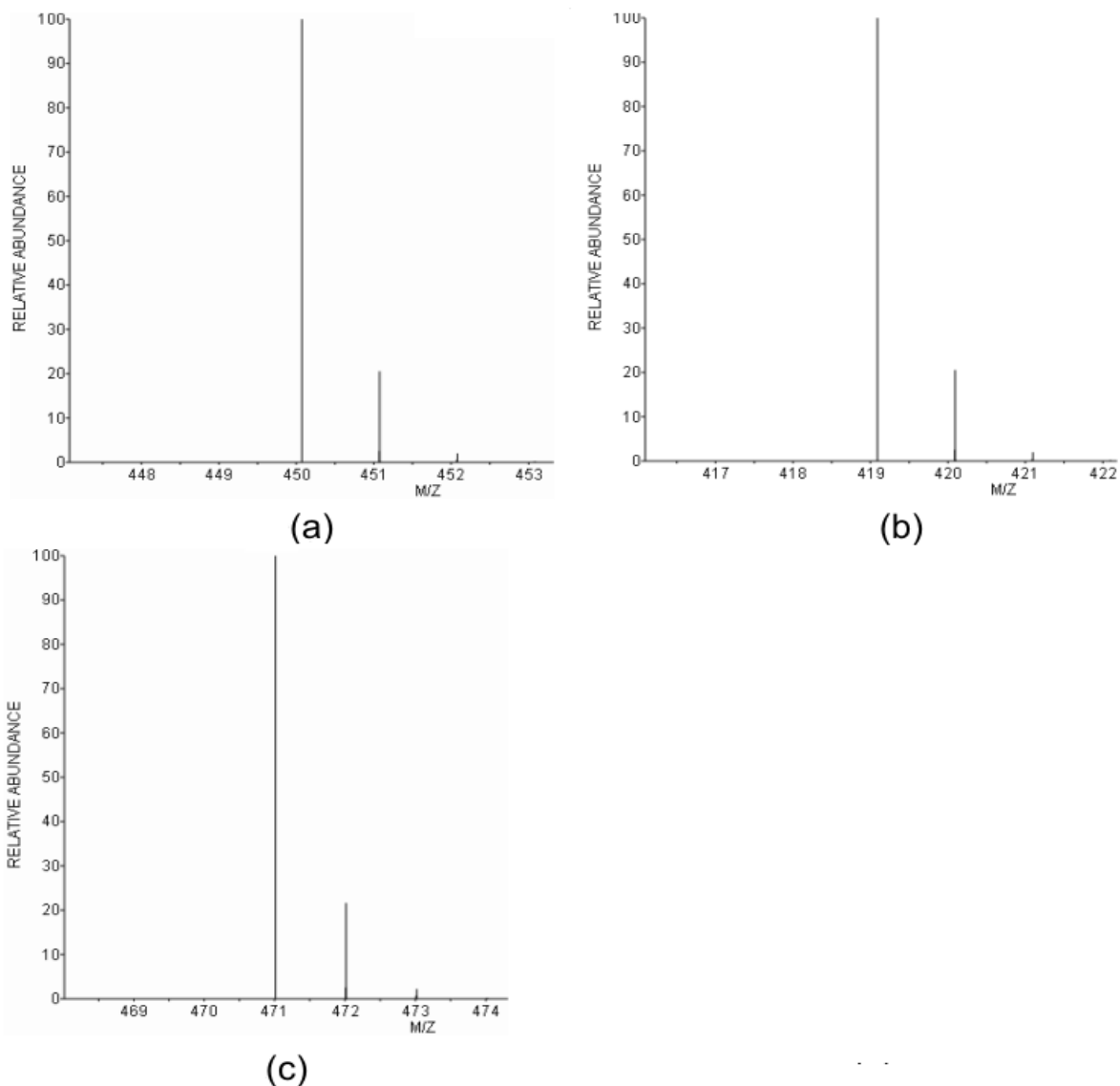


**Figure III-5.** The calculated isotope patterns for (**2**) ; (a) the base peak at  $m/z = 450.9$  corresponding to the fragment  $[M - 3H_2O - CO + 2H]^+$ , where M is the molecular formula of **2**; (b) and (c) correspond to the fragments  $[M - 4H_2O - CO_2 + 5H]^+$  and  $[M - 3H_2O - 4H]^+$  respectively.

ESIMS data of **2** help to assign a few important fragments through comparison of experimental and simulated isotope distribution patterns. For example, the fragment  $[M - 3H_2O - 4H]^+$  at

$m/z=471.0$  indicates removal of the extra spheric water molecules (Figure III-4a). The base peak at  $m/z = 450.0$  can be assigned to the fragment  $[M-3H_2O-CO+2H]^+$ . Finally, the completely dehydrated species  $[M-4H_2O-CO_2+5H]^+$  could be observed at  $m/z = 419.2$ . All these assignments could be verified through simulation experiments as indicated in Figure III-5. The fragments involving the gain or loss of 4 or 5 H atoms may apparently look unusual for molecular ion peaks, but they are justified for fragment ion peaks<sup>21</sup>. Sometimes, isotope peaks may be more instance than the calculated value because of ion-molecule interactions that vary with the sample concentration or with the class of compound involved e.g., the transfer of a hydrogen atom from the excess of the compound to the molecular ion in some cases<sup>21</sup>.

The ESIMS data of **3** is shown in Figure III-4b. The peaks at  $m/z$  519.12 , $m/z$  503 and  $m/z$  480.95 correspond to the fragmentants  $[M-CH_3OH - H_2O]^+$ ,  $[M-CH_3OH -2H_2O]^+$  and  $[M-CH_3OH -3H_2O - 2H]^+$ , respectively, where M is the molecular formula of **3**. These peaks arise as a result of the stepwise loss of solvent molecules from the parent compound with the complex core remaining essentially intact. This aspect verifies the architectural stability of the coordination sphere around the Co(I) centre with the reduced pterin ligand ( $L'^{2-}$ , Scheme II-4 ).

Besides this, the peak at  $m/z$  436.98 can be correlated with the fragment  $[M-CH_3OH - 3H_2O - CO_2 - 2H]^+$ . Most of the isotopic distribution patterns can be simulated.

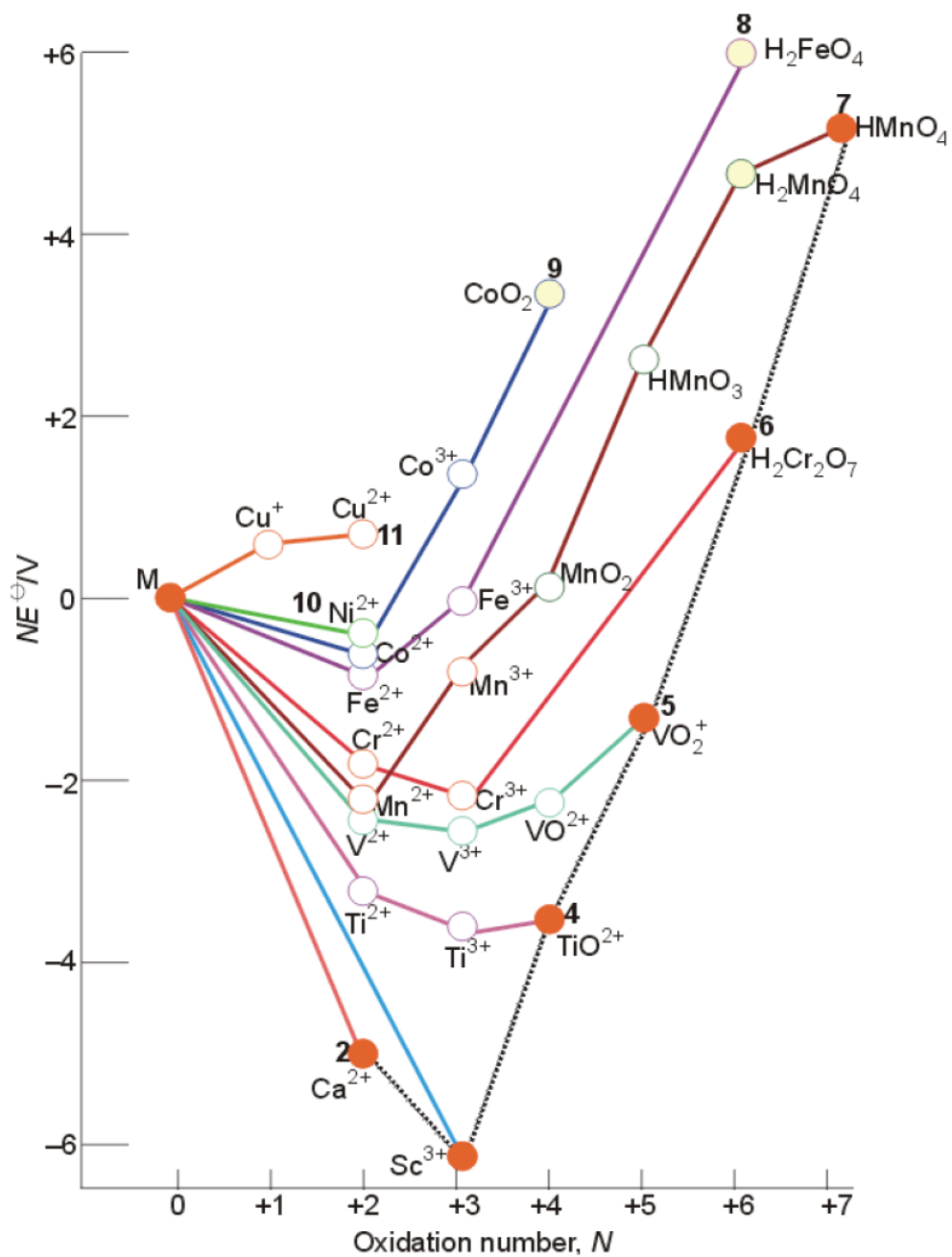
### **Magnetic susceptibility data of 2 and 3**

Compound **2** shows an effective magnetic moment of 4.41BM at room temperature. For a high spin octahedral configuration of this Co(II) complex, the spin-only formula gives a moment of 3.88BM, corresponding to three unpaired electrons. Due to the intrinsic orbital angular

momentum in the octahedral ground state ( ${}^4F/{}^4T_{1g}$ ), there is a considerable orbital contribution, leading to the observed higher value of the effective magnetic moment.<sup>31,79</sup> As discussed in the experimental section that **2** can be reduced with  $\text{NaBH}_4$  in  $\text{CH}_3\text{OH}$  medium to a snuff coloured compound, isolated in the solid state and characterized to be **3**. Magnetic susceptibility data of this snuff coloured, non hygroscopic compound (**3**) was measured at room temperature (297K) and found to be 3.42BM. Spin-only formula predicts a  $\mu_{\text{eff}}$  value of 2.83BM for two unpaired electrons. The above experimental  $\mu_{\text{eff}}$  value is compatible with a high-spin Co(I) state ( $d^8$ ,  ${}^3F$  ground state) with substantial orbital contribution.<sup>31</sup> As evident from  ${}^1\text{H}$  NMR data of **3** in chapter II, the  $\text{NaBH}_4$  reduction process affords a 7,8-dihydro form of the pterin ligand residue ( $L^2 \rightarrow L^{2-}$ )(Scheme II-4). As a logical extension of this idea to the present system **3**, it can be inferred that an uncommon oxidation state of cobalt, e.g, Co(I) could be stabilized here in an environment of such a reduced pterin ligand and a  $\pi$ -acid ligand (phen). X-ray structural data could verify in another pterin system that the pyrazine ring (pterin) is the reaction locant of  $\text{NaBH}_4$  reduction.<sup>22,23</sup> Report exists about a tris Co(I) complex of 2, 2'-bipyridine, that is, enhanced stability of the low oxidation state of cobalt in presence of a  $\pi$ -acid ligand.<sup>79</sup> In other words,  $\text{NaBH}_4$  is a suitable reducing agent for achieving both metal-centred [ $\text{Co(II)} \rightarrow \text{Co(I)}$ ] and pterin-centred [oxidized/aromatic state  $\rightarrow$  7, 8-dihydro state] reductions of **2**; the resulting reduced compound (**3**) is of sufficient stability for isolation in the solid state and magnetic susceptibility measurement. The thermodynamic favorability ( $\Delta G^0 = -nFE^0$ ) of  $\text{NaBH}_4$  reduction is indicated below. Cyclic voltametry data of **2** indicates an  $E^{\circ'}$  value of -0.6 v for the  $\text{Co(II)} \rightarrow \text{Co(I)}$  reduction; now using an  $E^{\circ'}$  value of -0.75V for  $\text{NaBH}_4$  in neutral medium,<sup>56-58</sup> an  $E_{\text{cell}}$  value[  $E_{\text{cell}} = E_1 - E_2 = -0.6 - (-0.75)$ ] 0.15 is obtained which is associated with a free energy

change [ $\Delta G^\circ$ ] of 4.6 kcal mol<sup>-1</sup>. This is consistent with relevant Frost diagram, indicating a small free energy change for the Co(II)  $\rightarrow$  Co(I) reduction.

A simultaneous pterin-centred reduction is also achieved. The reverse step, that is, the oxidation of **3** with a mixture of bromobenzene/O<sub>2</sub> mixture, as discussed later, will highlight the functional modeling aspect for PAH activity associated with small free energy barriers for such conversions.



A Frost diagram for the first series of d-block elements in acidic solution (pH = 0). The broken line connects species in their group oxidation states.

## IR Spectroscopy

The IR spectra (KBr pellets) of **1** and **2** are shown in Figure III-6 and III-7 respectively. For **1**, the free pterin ligand (Scheme III-1; Figure III-6) an intense broad band over the region 3250 – 3050  $\text{cm}^{-1}$  corresponds to the  $\nu(\text{OH})$  and  $\nu(\text{NH})$  stretching vibrations of the hydrogen bonded lattice water molecules, the  $-\text{COOH}(6)$ ,  $\text{NH}(3)$  and  $\text{NH}_2(2)$  groups. The  $\nu(\text{C-H})$  stretching vibrations of the  $\text{CH}_3(7)$  group appear at 2851  $\text{cm}^{-1}$  and 2757  $\text{cm}^{-1}$  respectively.<sup>21</sup> An intense broad band centered around 1684  $\text{cm}^{-1}$  and extending over the region 1718 to 1636  $\text{cm}^{-1}$ , characterizes the  $\nu(\text{C=O})$  modes of the  $\text{C=O}(4)$  group as well as that of the  $\text{COOH}(6)$  group (Scheme III-1). Some of the  $\nu(\text{C=C})$  and  $\nu(\text{C=N})$  modes of pterin ring could be identified around 1560-1539  $\text{cm}^{-1}$ .<sup>25,28</sup> Two broad bands at 1383  $\text{cm}^{-1}$  and 1294  $\text{cm}^{-1}$  characterize the  $\delta(\text{O-H})$  and  $\nu(\text{C-O}) + \delta(\text{O-H})$  modes respectively, of the  $-\text{COOH}$  group.<sup>21</sup> A series of bands observed over the region 860-650  $\text{cm}^{-1}$ , are assigned to skeletal vibration of the pterin ligand. A prominent peak at 567  $\text{cm}^{-1}$ , is assigned to rocking vibration of the  $\text{NH}_2(2)$  group.

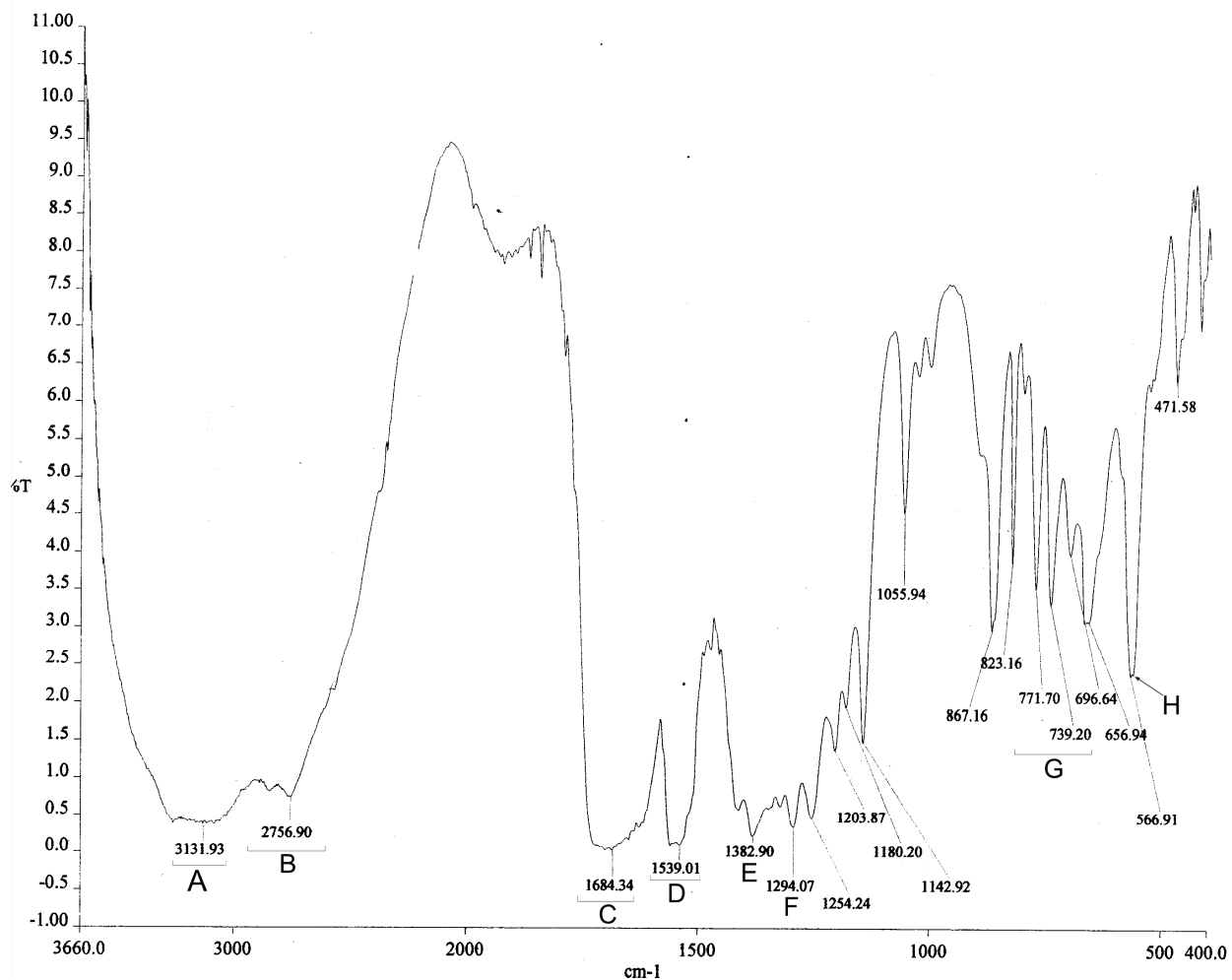


**Figure III-6:** FTIR spectrum (KBr) of the pterin ligand (H<sub>2</sub>L )(1).

- A: the broad band over the region 3250-3050 cm<sup>-1</sup> due to the  $\nu(\text{OH})$  and  $\nu(\text{NH})$  stretching vibrations of the hydrogen bonded H<sub>2</sub>O, -COOH(6), NH(3) and NH<sub>2</sub>(2) groups, Scheme III-1;
- B: the  $\nu(\text{CH})$  stretching vibrations of the CH<sub>3</sub>(7) group are observed at 2851 cm<sup>-1</sup> and 2757 cm<sup>-1</sup> respectively;

- C: an intense broad band centred at  $1684\text{ cm}^{-1}$  and spread over the region  $1718\text{-}1636\text{ cm}^{-1}$  is due to the  $\nu(\text{C}=\text{O})$  modes of the  $\text{C}=\text{O}(4)$  and  $\text{COOH}(6)$  groups, (Scheme III-1); the N-H bending vibrations at the  $\text{NH}_2(2)$  group are occluded under this band;
- D: the  $\nu(\text{C}=\text{C})$  and  $\nu(\text{C}=\text{N})$  modes at the pterin ring appears around  $1560\text{-}1539\text{ cm}^{-1}$ ;
- E&F: the  $\delta(\text{O-H})$  and  $\nu(\text{C-O}) + \delta(\text{O-H})$  modes of the  $\text{COOH}(6)$  group appear at  $1382\text{ cm}^{-1}$  and  $1294\text{ cm}^{-1}$  respectively;
- G: different types of skeletal bending vibrations of the pterin ring appear over the region  $860\text{-}650\text{ cm}^{-1}$ ;
- H: rocking vibrations of the  $\text{NH}_2(2)$  group appears around  $567\text{ cm}^{-1}$ .
- 

Most of these assignments could be checked theoretically by simulating the IR spectrum of **1** using Gaussian 09 software program and viewing the result with the help of Gauss view 5.0

Figure III-7 shows the IR spectrum (KBr) of the cobalt complex **2**. Most of the above-mentioned broad IR bands of **1** (Figure III-6) undergo considerable modification through complex formation with the  $\text{Co(II)}$  ion, as evident from a comparative study of Figure III-6 and III-7 respectively. For **2** (Figure III-7) the  $\nu(\text{O-H})$  and  $\nu(\text{N-H})$  modes of  $\text{H}_2\text{O}$  molecule and  $\text{NH}_2(2)$  group appear at  $3404$  and  $3338\text{ cm}^{-1}$  respectively. The  $\nu(\text{C-H})$  modes of phen moiety appear at  $3209$  and  $3066\text{ cm}^{-1}$  respectively. The  $\nu_{\text{as}}$  and  $\nu_{\text{s}}$  stretching vibrations of the carboxylate group (6) appear at  $1594.8$  and  $1369.7\text{ cm}^{-1}$  respectively.<sup>21</sup> The  $\Delta\nu$  value ( $\nu_{\text{as}} - \nu_{\text{s}}$ ) of  $224\text{ cm}^{-1}$  is consistent with monodentate carboxylate coordination.<sup>87,88</sup> The  $\nu(\text{C-O})$  mode of the coordinated (keto-enol tautomerism and deprotonation)  $\text{C}=\text{O}(4)$  group (pterin) appears at  $1296.5\text{ cm}^{-1}$ . The

vibrations of the pterin ring are observed over the region  $1518 - 1426 \text{ cm}^{-1}$ .<sup>25-28</sup> The out-of-plane bending vibrations of the phen moiety (at  $850$  and  $727 \text{ cm}^{-1}$ ) are also observed.<sup>21</sup>

Such data are consistent with tridentate pterin coordination involving the O(4), N(5) and  $\text{CO}_2^-$  (6) functional groups (Scheme III-1 and III-3) and supplement the x-ray structural data presented earlier (Figure III-1).

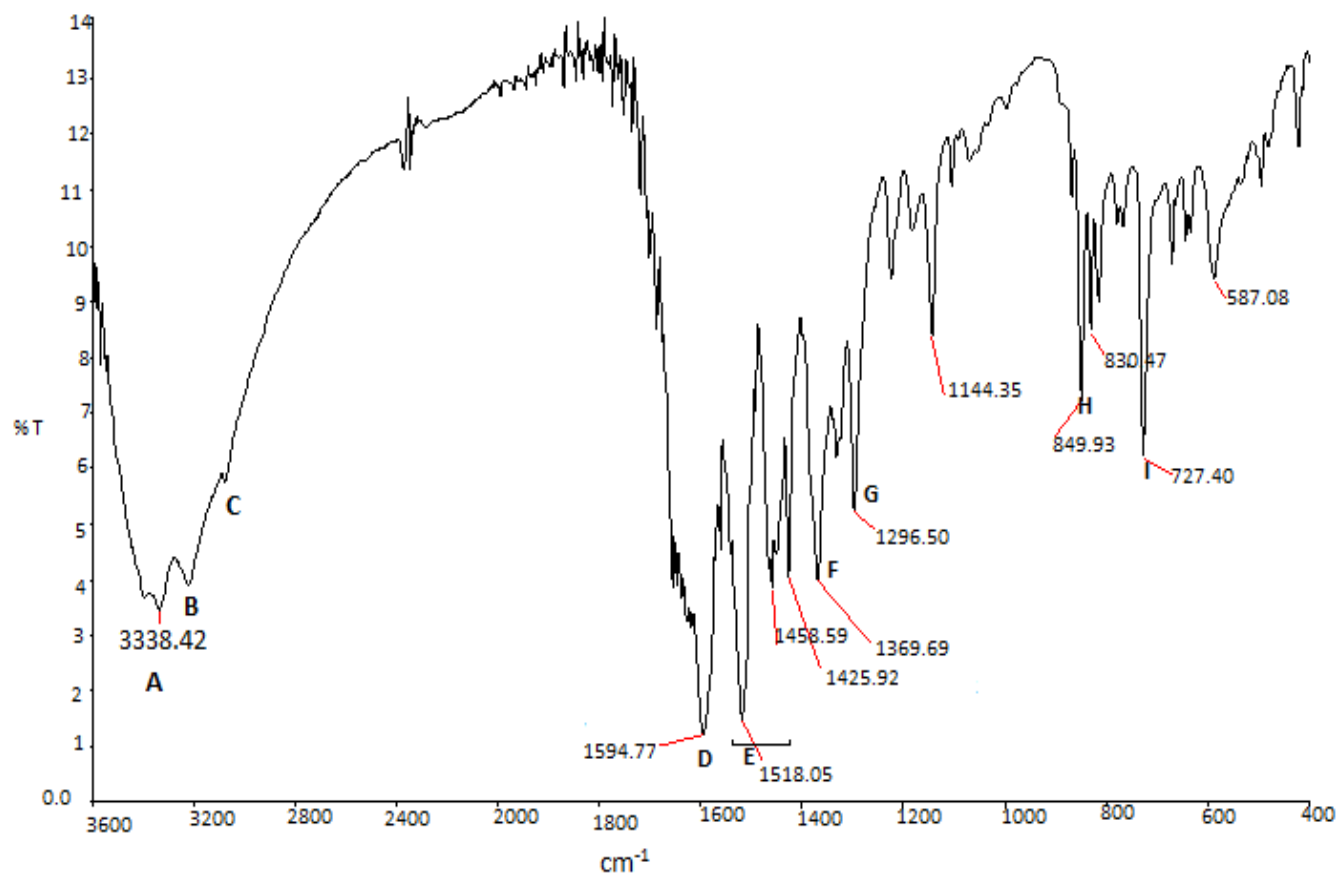


**Figure III-7.** IR spectra of compound **2** on KBr pellets

A: the  $\nu(\text{NH})$  vibration of the  $\text{NH}_2(2)$  group appear at  $3338.4 \text{ cm}^{-1}$ ; hydrogen bonded  $\nu(\text{OH})$  modes contributes to its broadness;

B&C: the  $\nu(\text{CH})$  vibration of the phen moiety appear at  $3209.5$  and  $3066.6 \text{ cm}^{-1}$  respectively;

- D: the  $\nu_{\text{as}}(\text{CO}_2)'$  vibration;
- E:  $\nu(\text{C}=\text{C})$ ,  $\nu(\text{C}=\text{N})$  vibration of the pterin ring;
- F:  $\nu_{\text{s}}(\text{CO}_2')$  vibration;
- G:  $\nu(\text{C}-\text{O})$  of pterin phenoxide (4) group;
- H&I: the out-of-plane C-H bending vibrations of the phen ring.
- 

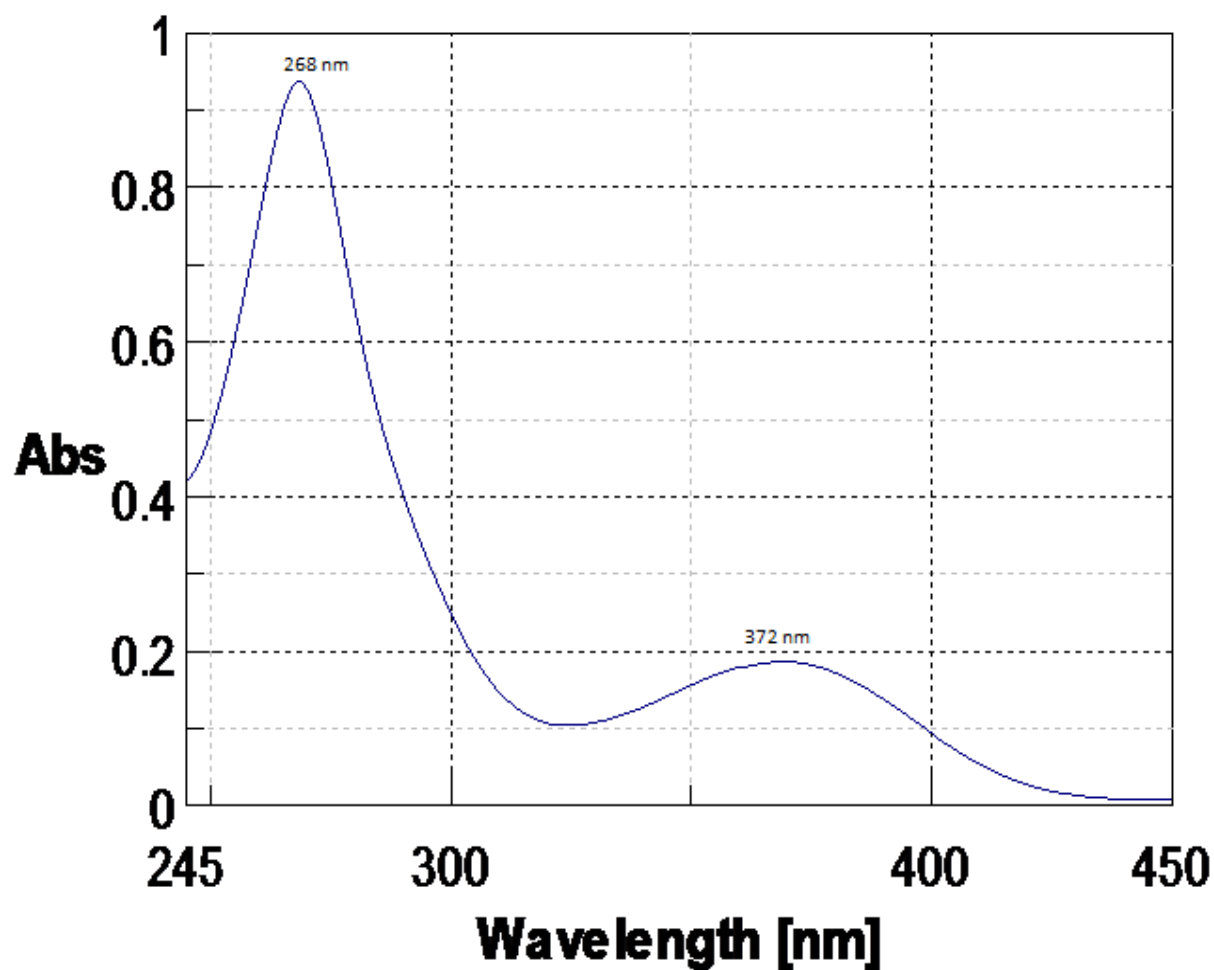


**Figure III-8(a).** Absorbance spectrum of **2** in CH<sub>3</sub>OH ( $4.15 \times 10^{-5}\text{M}$ )

---

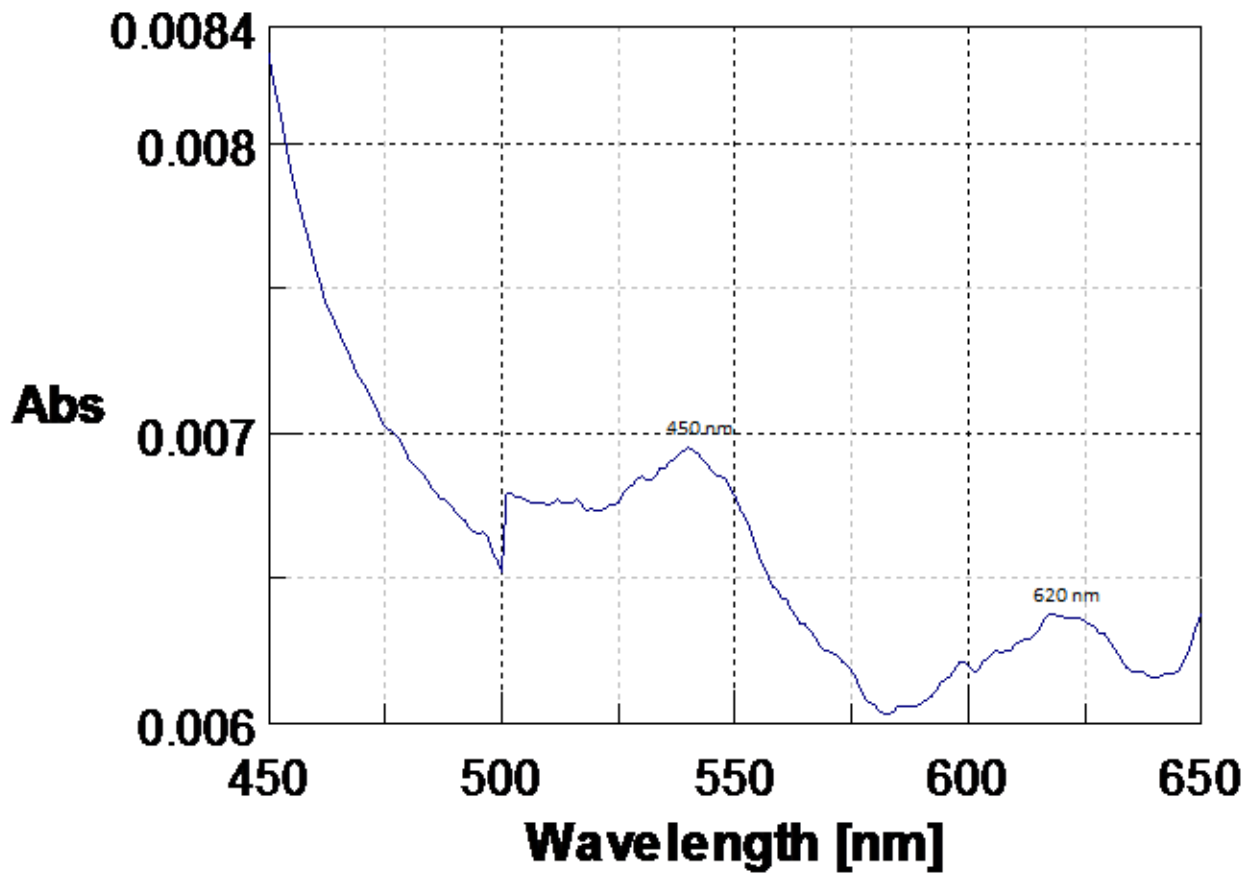


Figure III-8(b).

---

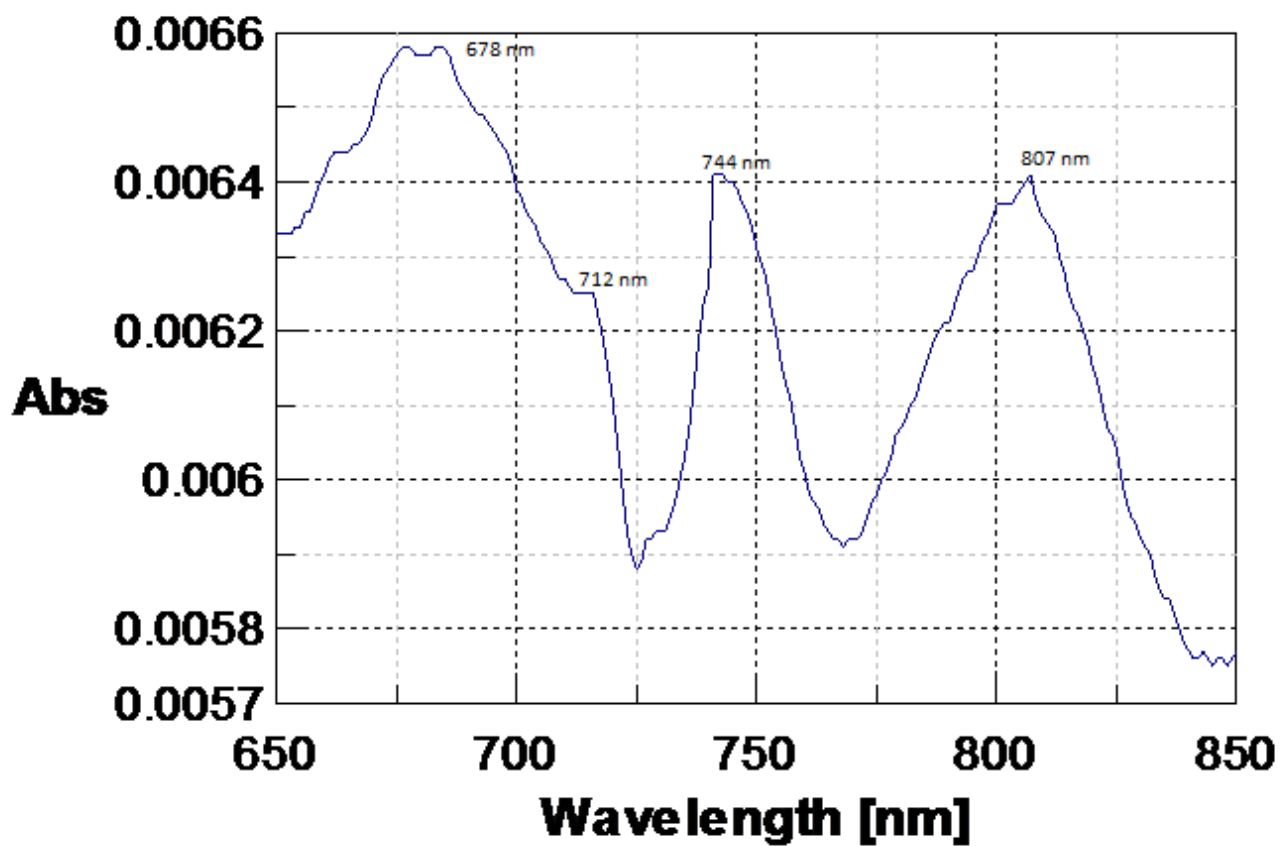


Figure III-8(c).

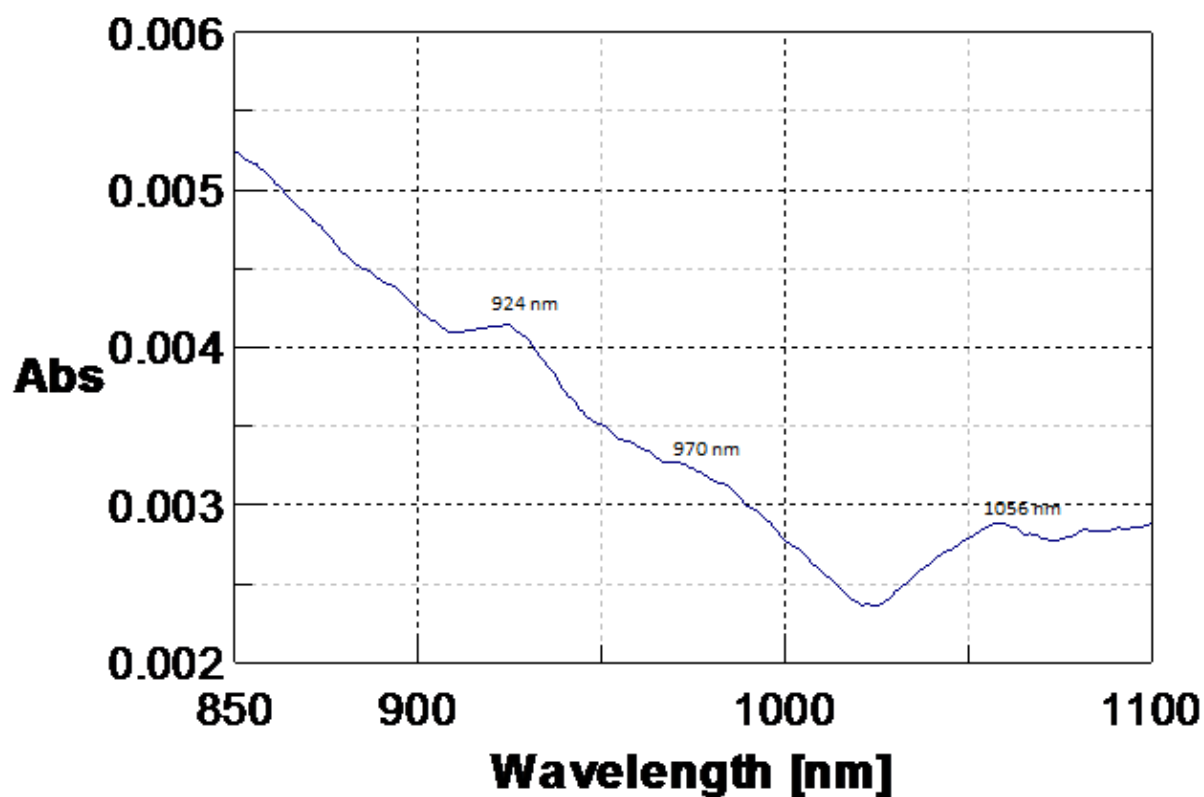


Figure III-8(d).

Table III-4. Electronic spectral data of **2** in CH<sub>3</sub>OH

Sl.No	Compound (solvent)	$\lambda_{\max}$ nm (log $\epsilon$ )
.		

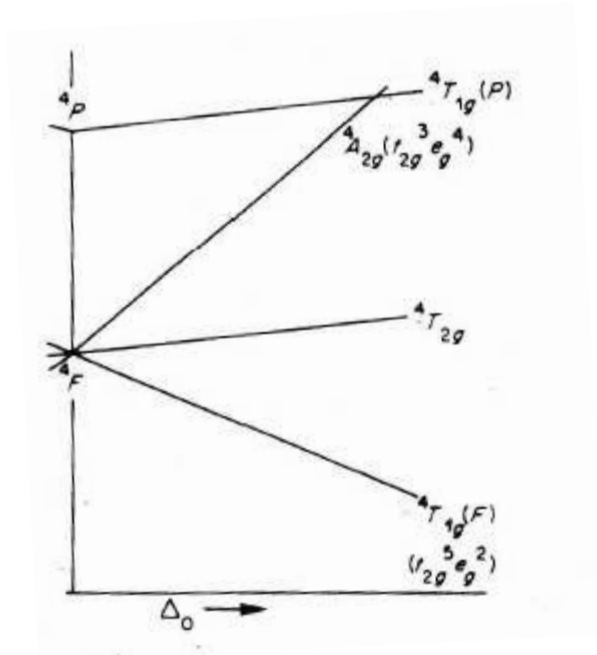
1.	<b>2</b> (CH <sub>3</sub> OH)	268(4.35), 372(3.65), 540br(2.22), 620br(2.19), 678(2.20), 712sh(2.17), 744(2.18), 807(2.18), 924sh(2.00), 970sh(1.90), 1056br(1.83)
----	-------------------------------	---

### Electronic spectroscopy

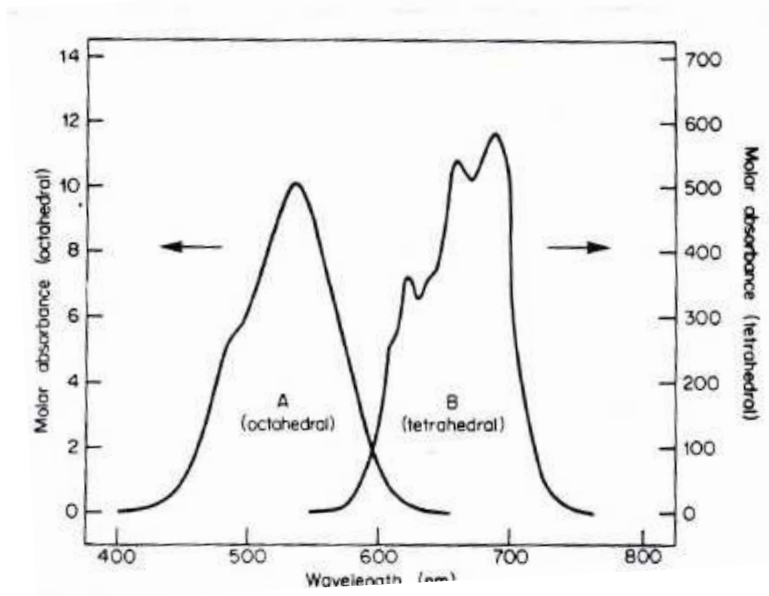
The absorption spectral data of compound **2** ( orange pink) are summarized in Table III-4 and the relevant absorption spectra in CH<sub>3</sub>OH are shown in Figure III-8(a)-(d): Apart from the two prominent bands at 268 nm and 372 nm [Figure III-8(a)] a large number of bands are observed in the longer wavelength region (540-1056 nm) Figure III-8(b)-(d). The intense peak at 268 nm is due to an intra ligand  $\pi \rightarrow \pi^*$  transition. The absorption band at 372 nm is assigned to a ligand-to-metal charge transfer transition (LMCT). The relevant lower intensity bands (with  $\epsilon$  values in the range 166 – 68) in the longer wavelength region may be understood in terms of the following Schemes III- 5 – III-7.

#### Scheme III-5

Configuration	Terms (Russell-Saunders states)
<b>d<sup>7</sup></b>	<sup>4</sup> F, <sup>4</sup> P, <sup>2</sup> H, <sup>2</sup> G, <sup>2</sup> F, <sup>2</sup> D(2), <sup>2</sup> P



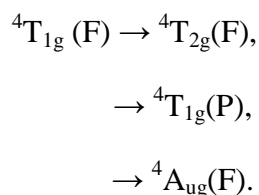
**Scheme III-6** Schematic energy level diagram for quartet states of a  $d^7$  ion in octahedral ligand field.<sup>79</sup>



**Scheme III-7** The visible spectra of  $[\text{Co}(\text{H}_2\text{O})_6]^{2+}$  (curve A) and  $[\text{CoCl}_4]^{2-}$  (curve B).<sup>79</sup>

Although in Scheme III-6<sup>79</sup>, only the crystal field states in an octahedral field, originating from the quartet states ( $^4F$ ,  $^4P$ ) are shown, there is also possibility of transitions to the higher

dublet states ( $^2H$ ,  $^2G$ ,  $^2F$  etc.) shown in Scheme III-5. As the complex **2** lacks a centre of symmetry (Figure III-1), the relevant electronic transitions should be Laporte-allowed/vibronically allowed. The absorption spectrum of  $[Co(H_2O)_6]^{2+}$  ion<sup>79</sup> is shown in Scheme III-7; it has a centre of symmetry and the visible region is dominated by the spin-allowed transition  $^4T_{1g}(F) \rightarrow ^4T_{1g}(P)$ . For **2** the absorption bands at 540 nm, 620 nm and 678 nm are assigned to the following spin-allowed transitions:-



The other absorption bands in the longer wave length region (712 – 1056 nm) are assigned to the spin-forbidden transitions to the higher dublet states (originating from the  $^2H$ ,  $^2G$ , etc. states, Scheme III-5). They acquire some intensity through spin-orbit coupling; beside these, they are all Laporte-allowed.

### **Circular dichroism spectroscopy**

The CD spectral response of **2** in  $CH_3OH$  is shown in Figure III-9. It reflects several positive cotton effects, e.g. the peak at 307.5 nm is a ligand- based transition, most likely  $\pi \rightarrow \pi^*$  transition of the 1, 10- phenanthroline (phen) moiety. The broad CD band centred around 477 nm is due to an optically active ligand field transition associated with the asymmetric/chiral Co(II) center of **2**. Three other weak CD signals could be detected at 679 nm, 779 nm and 823 nm respectively, corresponding to the other different ligand field transitions of **2**. They correspond to some of the electronic spectral data recorded in Table III-4.

The above CD data confirm the absence of a centre of symmetry for **2**, as evident from x-ray structural data as well (Figure III-1).

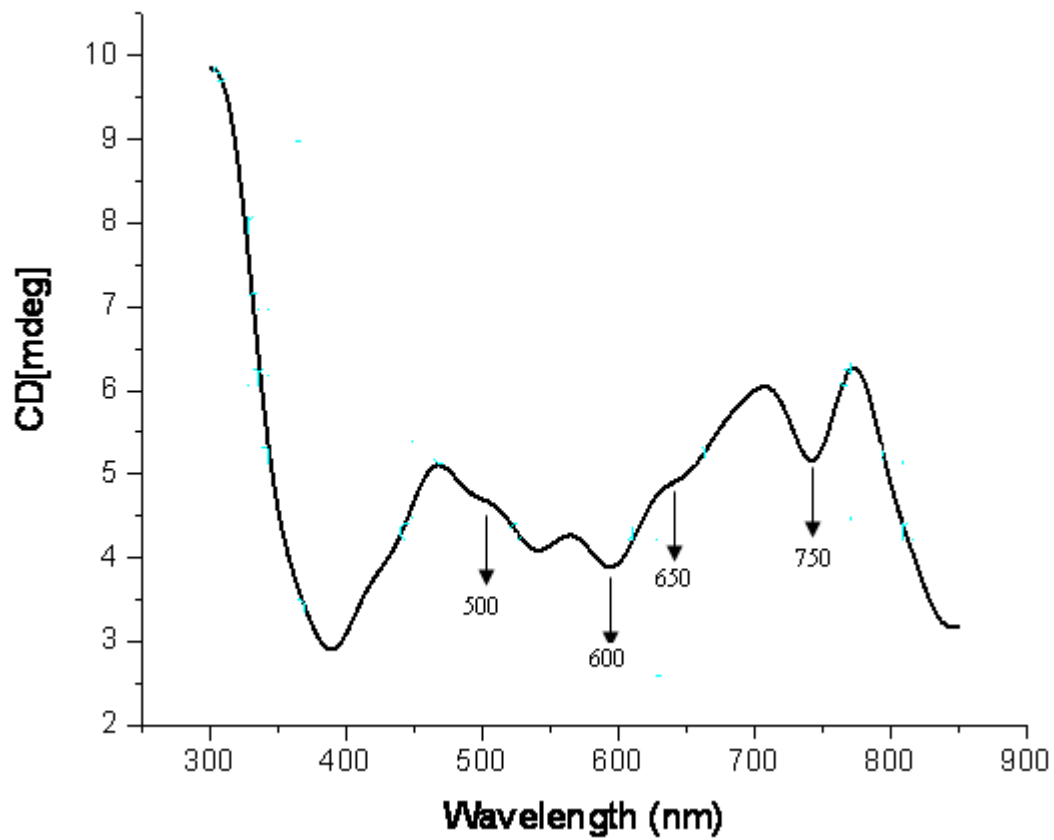


**Figure III-9.** CD spectral response in CH<sub>3</sub>OH of (a) **2** ( $4.7 \times 10^{-4} \text{M}$ ).

---

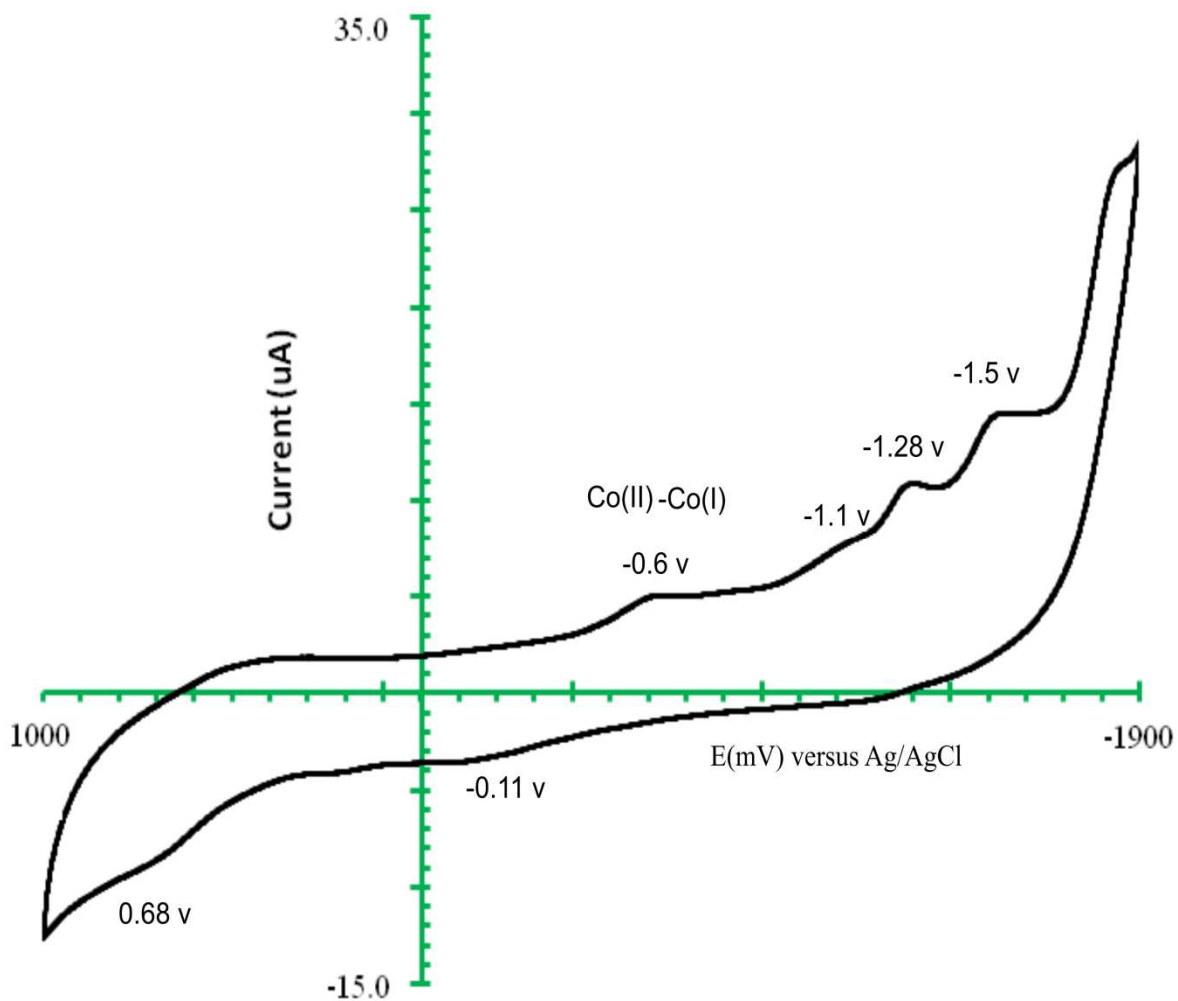


**Figure III-10.** Cyclic voltammetry data of **2** in DMSO (0.1mM; 0.1M TBAP; GCE) at a scan rate,  $100 \text{ mVs}^{-1}$ ; the potential scan starts from  $-1900 \text{ mV}$  and terminates here.

## Cyclic voltammetric studies

Cyclic voltammetric data of **2** is shown in Figure III-10. The present ligand (**1**) characterized by a single irreversible reduction peak ( $E_{PC}$ ) at -418 mV (ca.  $1 \times 10^{-3}$  mol dm<sup>-3</sup> in aqueous NaOH medium, pH ca. 10 with 0.1M dm<sup>-3</sup> KNO<sub>3</sub>; scan rate, 100 mV s<sup>-1</sup>). Figure III-10 shows several irreversible reduction as well as reoxidation steps. The peak at -0.6 v is a metal-centred process, reflecting the reduction Co(II)→Co(I). In terms of the frontier orbitals of **2** (Figure III-17), the LUMO and LUMO +1 levels are characterized by a small band gap (0.03 eV) and making this reduction step feasible. Actually, the Co(I), d<sup>8</sup> state is characterized by several well-defined compounds with  $\pi$ -acid type ligands like CO, 2,2-bipyridile, etc.<sup>79</sup> Besides this, the Frost diagram for the cobalt system over the oxidation states +2 and +1 is quite flat, almost parallel to the x-axis i.e. a small change in free energy ( $\Delta G^{\circ}_{\infty}$  NE°/V) can achieve interconversion between the two oxidation states.<sup>80</sup> As evident from the irreversible nature of this reduction (Figure III-10), the present ligand environment (phen and pterin) is unable to cope with the change associated with the above electron transfer, leading to decomposition of the reduced complex through solvent attack. The corresponding bipy-containing complex, [Co(L)(bipy)(H<sub>2</sub>O)]. 3H<sub>2</sub>O (chapter VI) shows a quasi-reversible behavior (Figure VI- 27) because of the better adaptability of bipy ligand to the present situation.<sup>79</sup>

Figure III-10 indicates three ligand-centered reductions of **2** at -1.1V, -1.2V and -1.5V respectively. Besides these, two reoxidation peaks appear at -0.11V and 0.68V respectively. At least some of the above-mentioned metal-and ligand-centred reductions of **2**, could be achieved on a preparative/scale by treating it with NaBH<sub>4</sub> in CH<sub>3</sub>OH medium and the resulting compound **3** could be isolated in the solid state (vide the experimental section).

**Fluorescence emission spectra.** The fluorescence emission spectra of **2** and **3** in CH<sub>3</sub>OH are shown in Figure III-11; their emission maxima appear at 450 nm and 455 nm respectively. Such emission maximum of the pterin ligand (**1**) (in aqueous NaOH solution) appears at 449 nm (Figure II-10).

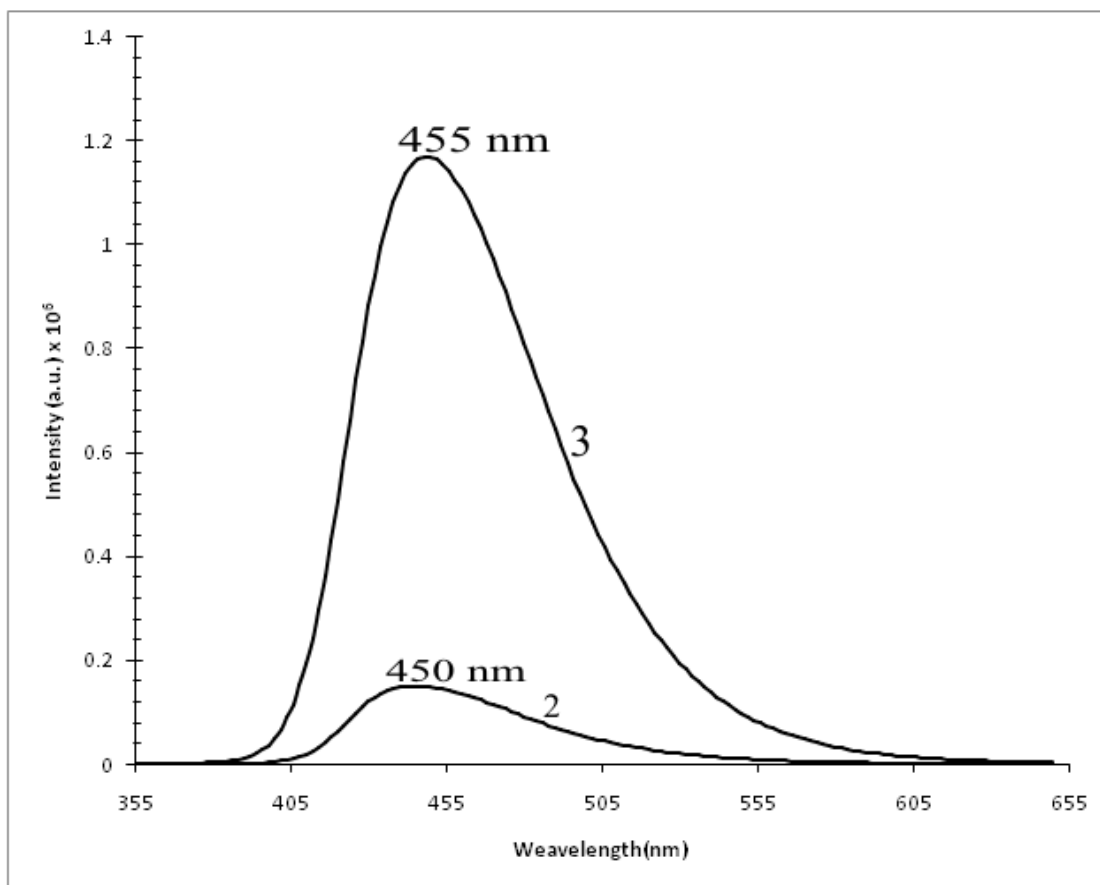


**Figure III-11.** Fluorescence emission spectra of **2**(CH<sub>3</sub>OH, 1.4 x 10<sup>-4</sup> M), **3** (CH<sub>3</sub>OH, 4.6 x 10<sup>-5</sup> M).

---

In terms of the intensity scale (a.u.) there is a drop in fluorescence intensity on complex formation process [ $\text{H}_2\text{L}(\mathbf{1}) \rightarrow \mathbf{2}$ ], but on reduction with  $\text{NaBH}_4$  [ $\mathbf{2} \rightarrow \mathbf{3}$ ] there is a considerable increase in intensity. This modification of intensity values (au) can be related to the change in electron density on the pterin ligand center as well as the metal center, during the above transformations [ $\mathbf{1} \rightarrow \mathbf{2} \rightarrow \mathbf{3}$ ].

Fluorescence data constitute an important property of pterin compounds, e.g., such data provided with the initial evidence about the pterin component of the molybdenum cofactor.<sup>33 - 34</sup> The pH dependence of fluorescence property is also interesting, e.g., no fluorescence is observed for the protonated form of biopterin but the anion is strongly fluorescent.<sup>35</sup> Most organic fluorescent molecules contain conjugated system of double bonds with extended  $\pi$ -orbitals in a planar cyclic/rigid structure and not many loosely coupled substituents through which the vibronic energy can dissipate.<sup>36</sup> The common fluorophores include aromatic / heteroaromatic rings as well as functional groups like  $\text{C} = \text{C}$ ,  $\text{C} = \text{O}$ ,  $\text{C} = \text{N}$ , etc., while fluorochromes (usually electron donors) like  $-\text{OH}$ ,  $-\text{NH}_2$ , etc., enhance the transition probability or fluorescence intensity. The enhanced fluorescence intensity of  $\mathbf{3}$  (Figure III-11) which is obtained by the  $\text{NaBH}_4$  reduction of  $\mathbf{2}$  in  $\text{CH}_3\text{OH}$ , may be understood in the light of greater electronic circulation in  $\mathbf{3}$  due to  $\text{Co}(\text{I})(\text{d}^7) \rightarrow$  phen type charge transfer transition;<sup>32</sup> the reduced pterin ring (7,8-dihydro form) also assists this process.

## Reactivity of $\mathbf{2}$

As evident from the molecular structure of  $\mathbf{2}$  (Figure III-1), it possesses an aquo group as well as two redox centers, e.g., the  $\text{Co}(\text{II})$  atom and the redox non-innocent pterin ligand residue.

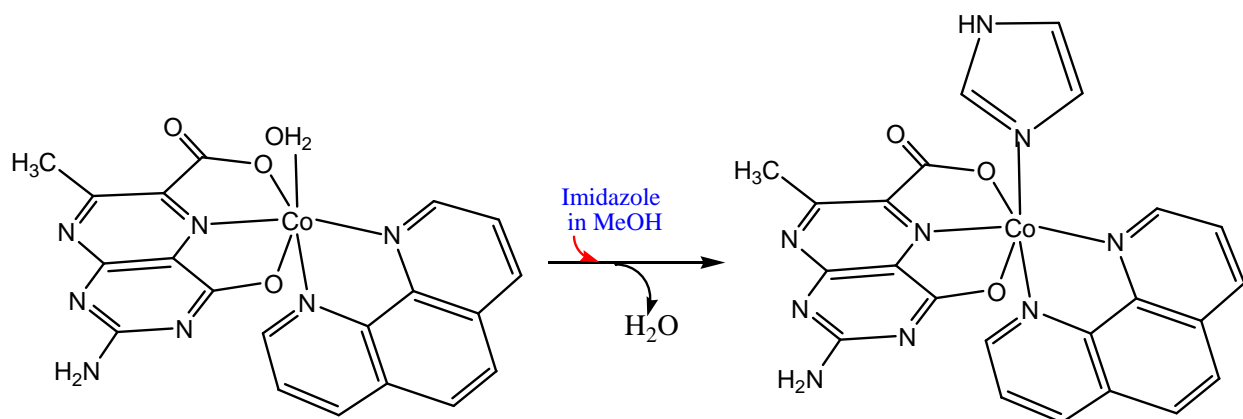
Its reactivity towards suitable reagents have been studied for exploring the group transfer (aquo group) and redox reactivities.

### Reactivity with imidazole

Figure III-12 represents the absorption spectral changes associated with the reaction of **2** with imidazole in CH<sub>3</sub>OH at 328K. Imidazole is related to the histidine residue of many protein chains and is well-known for its affinity towards the first transition metals in the biological systems. Kinetics of this reaction was followed at 372 nm and four different temperatures in the range 308-328K under pseudo-first order conditions (approx. 100 times excess of imidazole ligand). Observed rate constants were determined by least square method from the plots of  $\log(A_t - A_\infty)$  versus time, which were linear for three half-life.<sup>49,50</sup> The relevant data are as below:

$$k_{\text{obs}} = 2.6 \times 10^{-2} \text{ s}^{-1} ; \Delta S^\ddagger = -256.0 \text{ J mol}^{-1} \text{ deg}^{-1} .$$

They are consistent with a ligand substitution process (Scheme III-8) through an associative path way.



Scheme III-8

Scheme III-8 summarizes the above reactivity, indicating the formation of a imidazole substituted compound. Stoichiometry of the above process could be established x-ray crystallographically for the corresponding Ni(II) system containing an imidazole ligand in its coordination sphere.<sup>17c</sup>

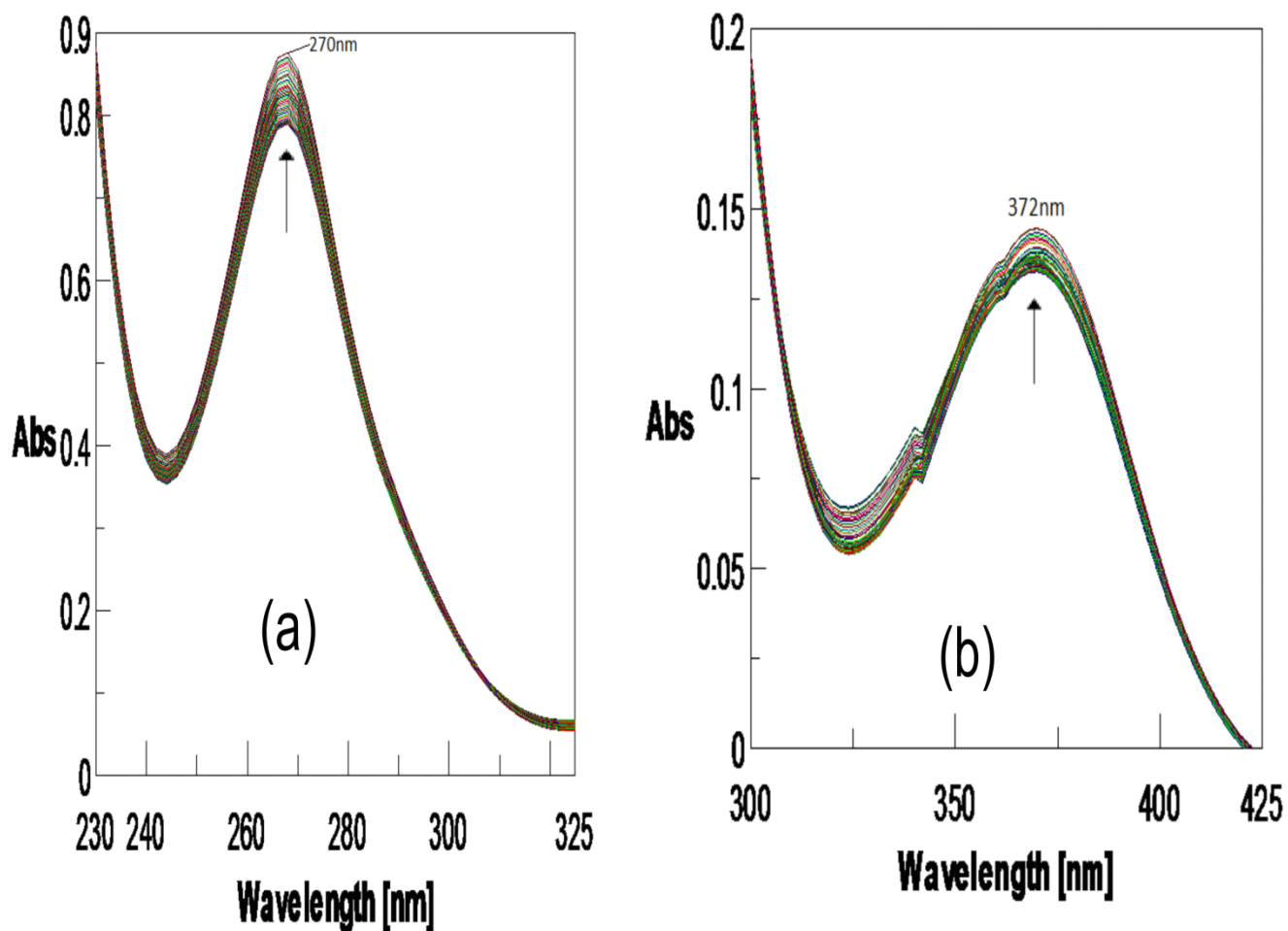


**Figure III-12.** Absorption spectral changes recorded at 6 minute interval during the reaction of **2** ( $1.42 \times 10^{-5}$  M) with imidazole (Im) ( $3.6 \times 10^{-2}$  M) in  $\text{CH}_3\text{OH}$  at 328K; (a) over the range 230- 325 nm; (b) over the range 300-425 nm.

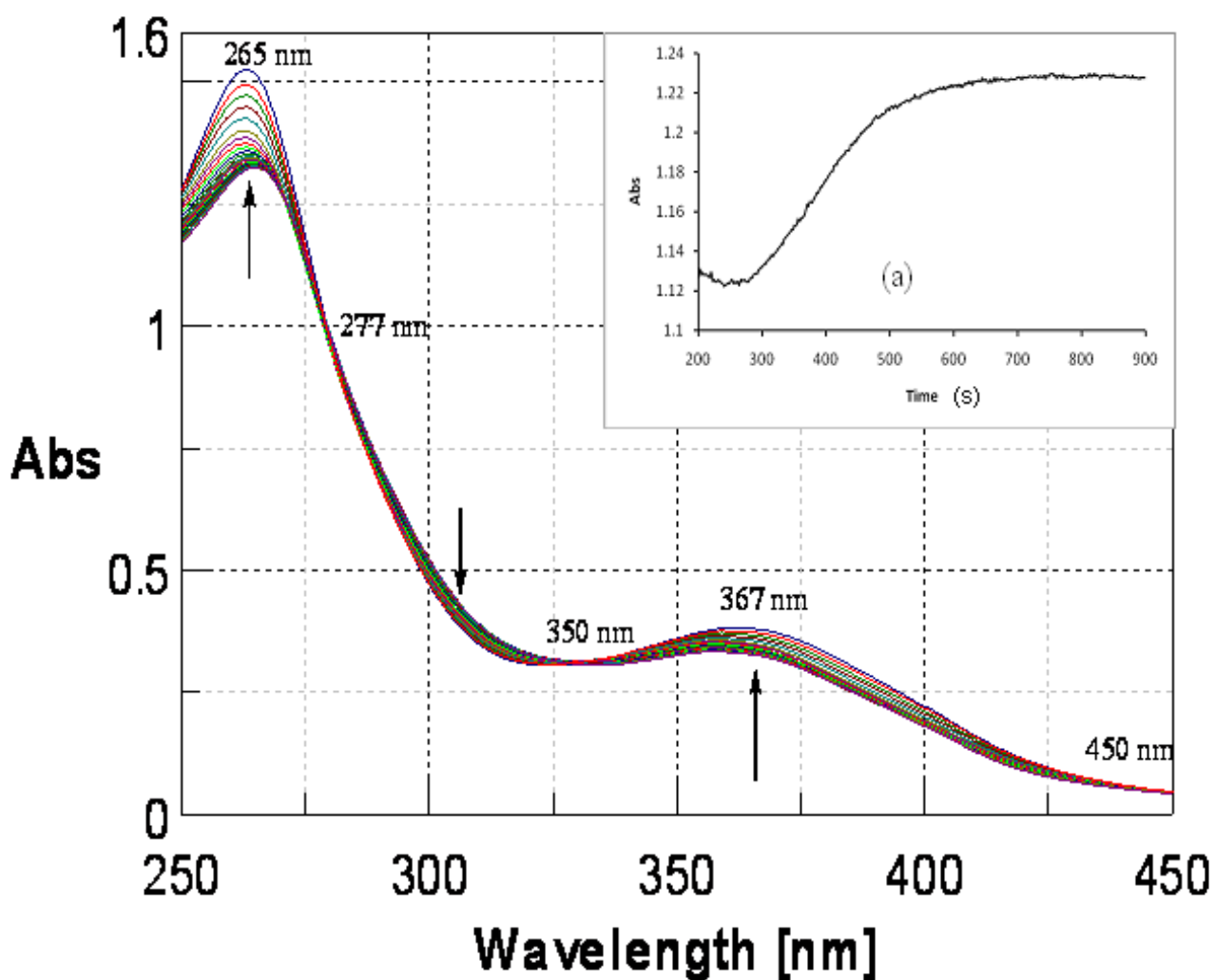


**Figure III-13.** Absorption spectral changes recorded at 2 min interval during the reaction of **2** ( $8.9 \times 10^{-5} \text{M}$ ) with  $\text{NaBH}_4$  ( $6.9 \times 10^{-2} \text{M}$ ) in  $\text{CH}_3\text{OH}$  at 298K showing three isosbestic points (at 277, 350 and 450 nm). The inset (a) shows the kinetic trace at 367 nm.

**Reactivity of 2 towards sodium borohydride ( $\text{NaBH}_4$ )**

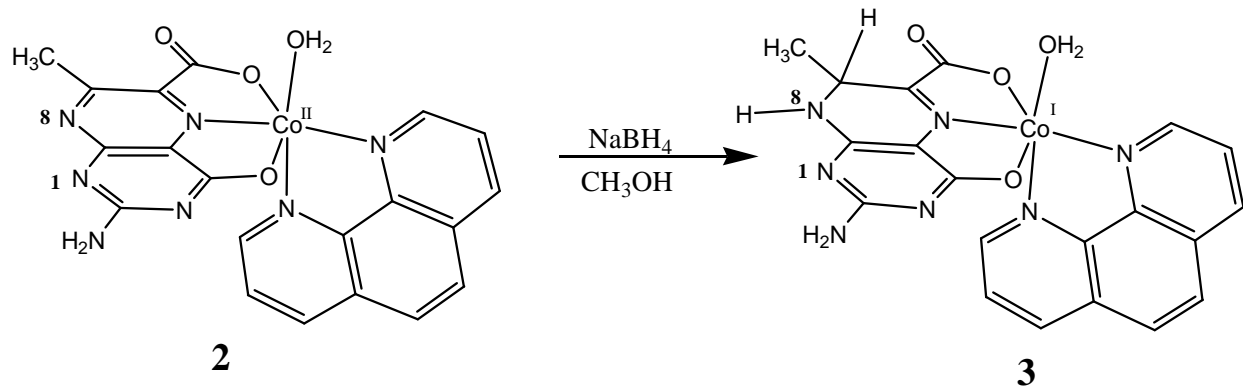
It is worthwhile to explore the reactivity of **2** towards NaBH<sub>4</sub> to find out its ability of accepting reducing equivalents at both the metal and pterin ligand centers (Figure III-13). Literature data indicate an E°' value of -0.75 V for NaBH<sub>4</sub> in neutral medium.<sup>56-58</sup> In terms of the cyclic voltammetry data of **2** (Figure III-10), the metal center [Co(II)] and at least the pyrazine ring of the pterin ligand residue, should be susceptible to NaBH<sub>4</sub> reduction. Figure III-13 shows the absorption spectral changes recorded during the reaction of **2** with NaBH<sub>4</sub> in CH<sub>3</sub>OH at 298K. Distinct changes in absorbance values are observed at 265 nm and 367 nm respectively, affecting both the ligand-centered ( $\pi \rightarrow \pi^*$  type) and metal-centered (LMCT type) transition regions. The presence of isosbestic points at 277 nm, 350 nm and 450 nm respectively, indicate a clean conversion (reduction) during reaction with NaBH<sub>4</sub>, without major structural change. Kinetics of this reaction with NaBH<sub>4</sub>, was followed at 367 nm and four different temperatures in the range 300-330K in CH<sub>3</sub>OH under pseudo-first order condition (with a **2** : NaBH<sub>4</sub> ratio of 1 :140). The following kinetic parameters were evaluated:

$$k_{\text{obs}} = 2.68 \times 10^{-3} \text{ s}^{-1}; \Delta S^{\ddagger} = -198.0 \text{ J mol}^{-1} \text{ deg}^{-1}.$$

The above results point towards a group transfer reaction involving an associative step. Stoichiometric study of this reaction was carried out by isolating the relevant reduction product **3**, as already discussed under the heading of experimental section, cyclic voltammetry and fluorescence spectroscopy.

Scheme III-9 shows the reaction between **2** and NaBH<sub>4</sub>, leading to the formation of the 7, 8-dihydro form of the pterin ligand and the reduction of the metal center [Co(II)  $\rightarrow$  Co(I)] in **3**, in conformity with the cyclic voltammetry data of **2** (Figure III-10). Of the different possible dihydro forms of pterin, 7, 8- dihydro form is the most stable one<sup>10</sup> due to overall planarity of

this partly reduced pterin ring, as verified x-ray structurally by Viscontini and coworkers.<sup>81</sup> The fluorescence spectral



**Scheme III-9.**

---

data (Figure III-11) reflect this increase in electron density in the pterin ring. Besides this, the steric/stereo-electronic factors of the ligand environment of **3**, helps to assimilate these reducing equivalents from NaBH<sub>4</sub> without much structural rearrangement.

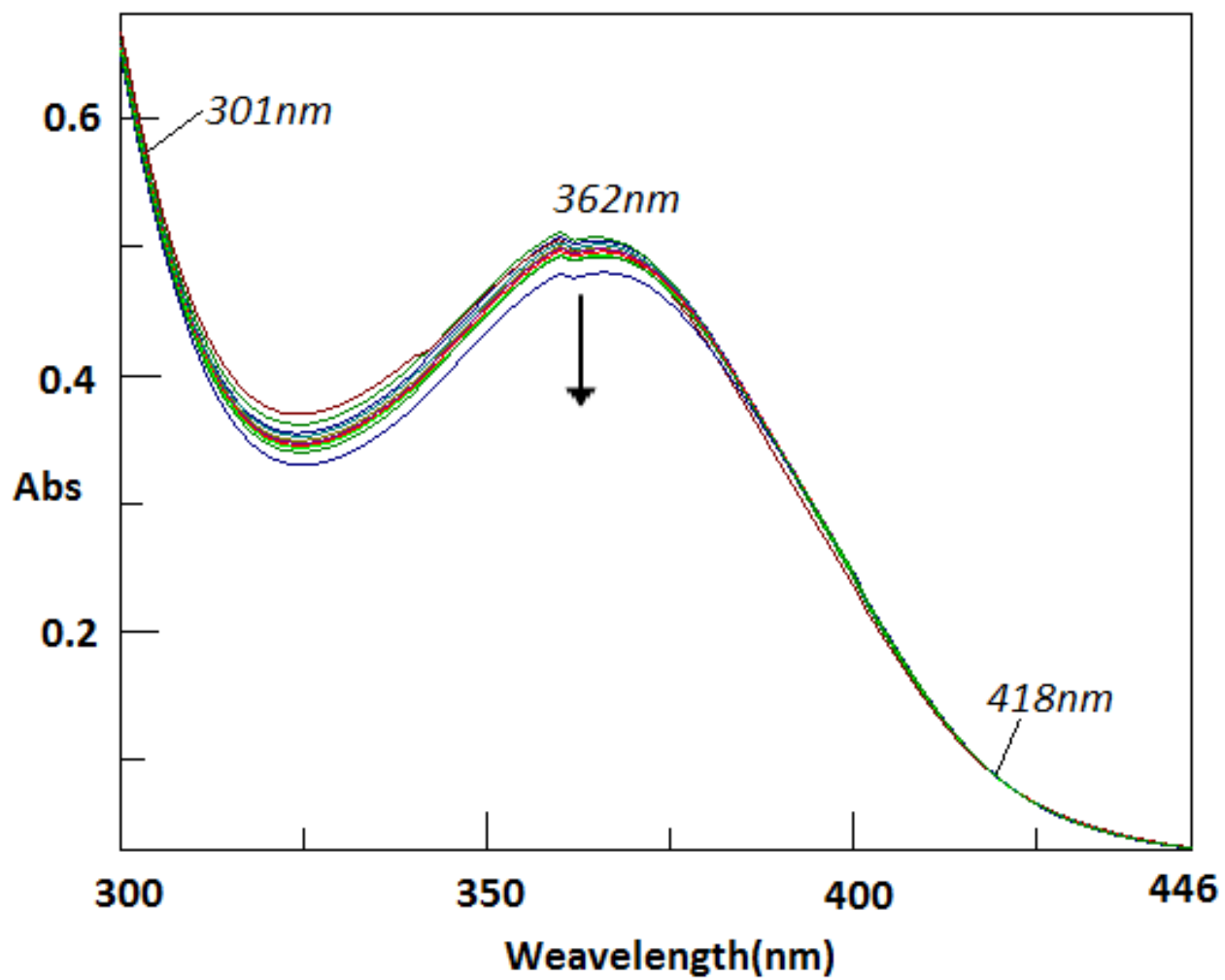


**Figure III-14.** Absorption spectral changes recorded at 5 min interval during the reaction of **3** ( $1.0 \times 10^{-4}\text{M}$ ) with bromobenzene ( $1.9 \times 10^{-2}\text{M}$ ) in  $\text{CH}_3\text{OH}$  saturated with  $\text{O}_2$  at 300K.

### Reactivity of **3** with bromobenzene (model substrate) in presence of O<sub>2</sub>

Figure III-14 explores the reactivity of the NaBH<sub>4</sub> reduced compound **3** with bromobenzene in presence of dioxygen in CH<sub>3</sub>OH. A distinct change in absorbance values occur at 362 nm (LMCT region) with a clean isosbestic point at 418 nm and a close approach to such an attribute at 301 nm. Nature of such changes is opposite to that in Figure III-13. Kinetics of this reaction (Figure III-14) was followed at 362 nm and four different temperatures (range 300-330K) in CH<sub>3</sub>OH saturated with O<sub>2</sub> under pseudo-first order conditions (with a **3**: bromobenzene ratio of 1 : 140) and the relevant data are indicated below:

$$k_{\text{obs}} = 2.86 \times 10^{-2} \text{ s}^{-1} ; \Delta S^{\ddagger} = -186.0 \text{ J mol}^{-1} \text{ deg}^{-1}.$$

In terms of  $k_{\text{obs}}$  values, the transfer of reducing equivalent from **3** to bromobenzene is approximately 10 times faster than the transfer of reducing equivalent from NaBH<sub>4</sub> to **2**. Figure III-15 and III-16 show the reactivity of NaBH<sub>4</sub> in CH<sub>3</sub>OH medium with 1, 10-phenanthroline and the pterin ligand **1** respectively. While 1, 10-phenanthroline remains essentially unaffected over the relevant spectral region (362 nm), the

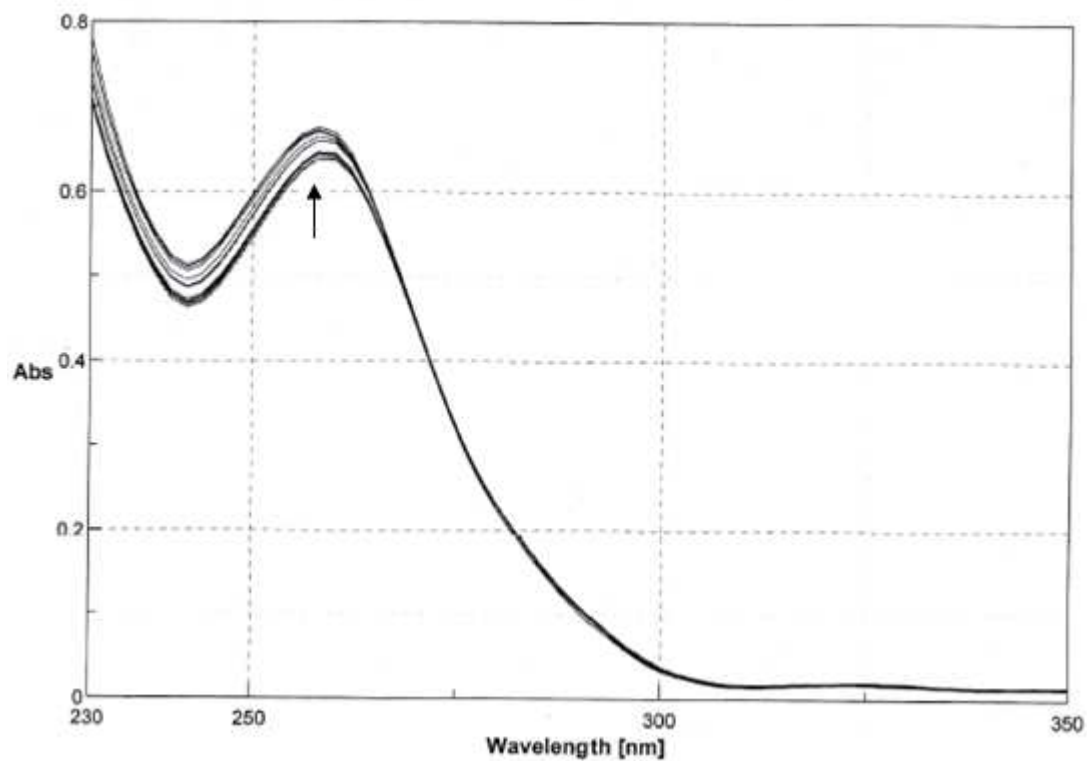


**Figure III-15.** Absorption spectral changes recorded at 2 min interval during the reaction of 1, 10-phenanthroline monohydrate (phen) ( $1.25 \times 10^{-3} \text{M}$ ) in  $\text{CH}_3\text{OH}$  at 303K with  $\text{NaBH}_4$  ( $1.35 \times 10^{-2} \text{M}$ ).

---

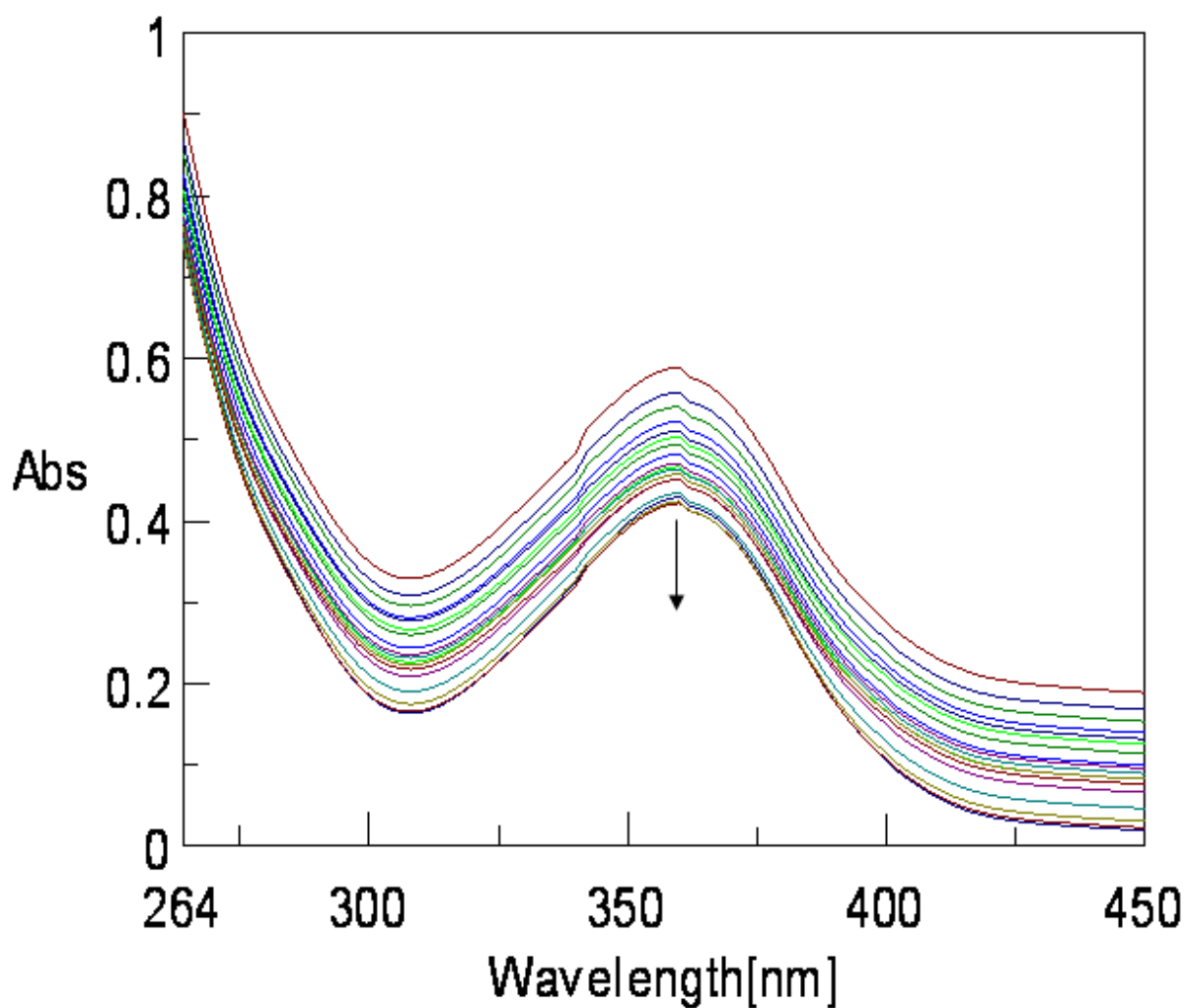


**Figure III-16.** absorption spectral changes recorded at 2 min interval during the reaction of **1** ( $1.34 \times 10^{-3}$  M) in aqueous NaOH solution ( $1.25 \times 10^{-2}$  M) with NaBH<sub>4</sub> ( $1.35 \times 10^{-2}$  M) at 303K.

pterin ligand undergoes reduction over same spectral region. This indicates that the pterin ligand is the reaction locant of **2** during reaction with NaBH<sub>4</sub> (Figure III-13).<sup>22, 23</sup> However, the nature of the absorption spectral change in Figure III-16 is different ( absence of isosbestic points) from

those in Figure III-13, indicating considerable modification of the pterin ligand moiety through complex formation with the Co(II) center in **2**.

In view of the reactivity data as evident from the above discussions on Figure III-13 to Figure III-16, **2** serves as an excellent mediator of reducing equivalents from NaBH<sub>4</sub> to bromobenzene in presence of dioxygen (O<sub>2</sub>), leading to the formation of 4-bromophenol; this aspect has been verified from reaction stoichiometric studies as outlined in chapter II. Mechanistic details of this process are outlined in the next section.

### **Electronic structure of 2**

The electronic structure of **2** was obtained by DFT calculations, performed using the Gaussian 09 package. Molecular orbitals were visualized using “Gauss View 5.0”. The method used was B3LYP hybrid-exchange functional and 6-31g basis set; the x-ray refined structure parameters were used as the input parameters. Since the x-ray refined structure parameters were used, optimization of the structure was not carried out here and the ground state energy minimization calculation gives the frontier orbitals diagram as shown in the Figure III-17. along with their energies and the compositions (%). The most remarkable aspect of Figure III-17 is the small band gap (0.3 – 0.5 eV) between the adjacent levels of the frontier orbitals, which is as low as 0.03 eV between the LUMO and LUMO+1 levels. The molecules with low HOMO/LUMO gaps are of particular importance due to their ability to easily donate (from HOMO) or accept (on LUMO) an electron, which is the basic process in all organic electronic devices. From chemical point of view such molecules can possess electrochemical/redox amphoteric behavior due to low barrier to thermo-excited electron transfer in either direction.<sup>82</sup> The present electrochemical and redox reactivities of **2**, as presented in Figure III-10, III-11, III-13, III-14 throw light on this

aspect . For example, cyclic voltametric data of **2** can be interpreted on the basis of reduction of both the metal and pterin ligand centers as well as reoxidation of the reduced pterin ligand. Again , the reaction of **2** with NaBH<sub>4</sub> and further reaction of the reduced complex **3** with bromobenzene/O<sub>2</sub> mixture, involves input of electron density into the LUMO/LUMO+1 levels as well as transfer of reducing equivalents out of them.

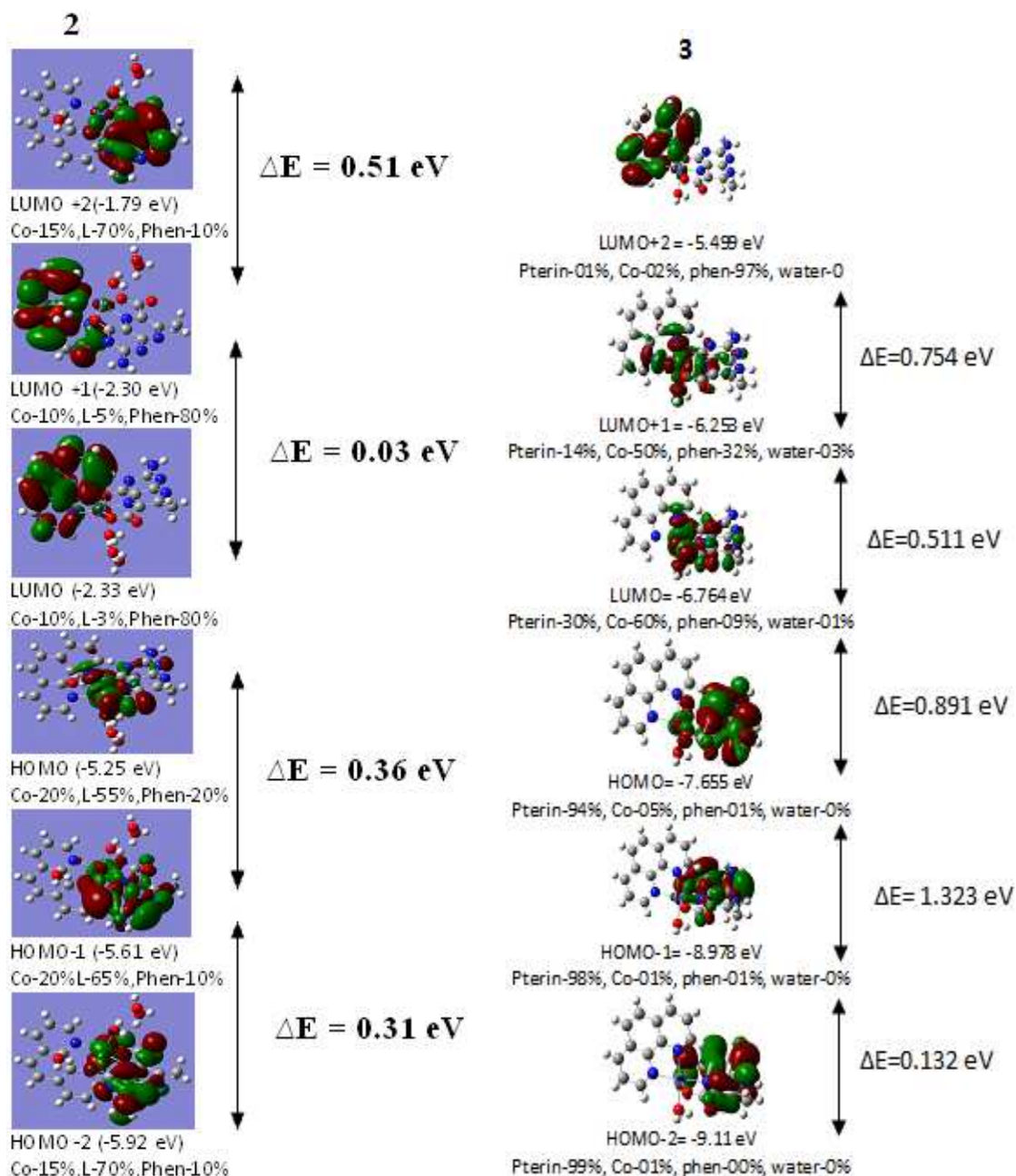
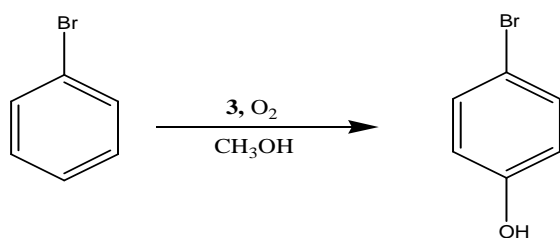


**Figure III-17.** Frontier molecular orbitals of **2** and **3**, showing their energies (eV) and compositions (%).

This redox amphoteric behavior of **2** is the high light of this work and it correlates well with the above-mentioned low energy band gaps (Figure III-17). Besides this, the compositions (%) of the

HOMO/LUMO levels give some hint regarding the nature of the electron transfer involved here. In this region, percentage contribution of the Co(II) center changes from 20% → 10%; the pterin ligand contribution changes over the region 55% → 3/5%, whereas phen contribution varies from 20 % → 80%. Thus the difference between the LUMO and LUMO+1 level, is controlled by a change over in pterin contribution from 3% →5%. In practical terms, LUMO and LUMO+1 levels are almost identical in terms of energies and compositions.

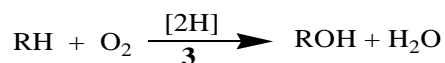


**Scheme III-10**

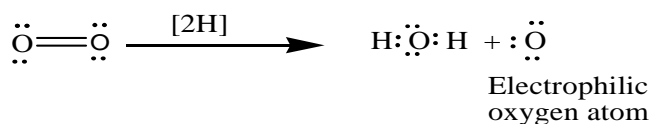
---

### Electrophilic oxygen addition to the substrate, RH

Monooxygenase type activity of **3** using O<sub>2</sub> as the source of oxygen atom transferred:



[2H]: reducing equivalents transferred by **3**



**Scheme III-11**

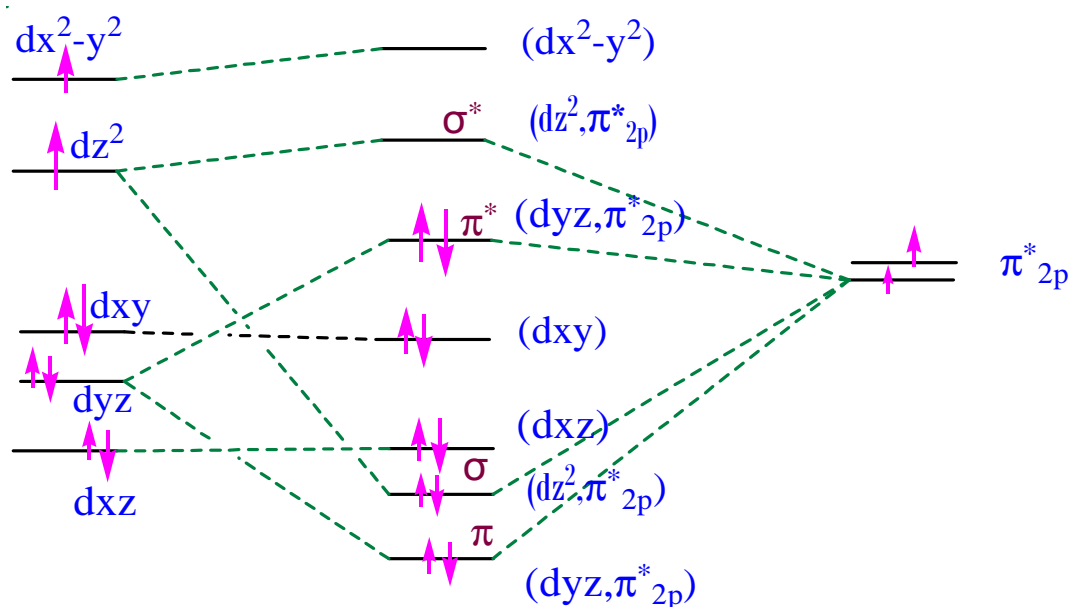
---

This aspects helps to rationalize the reactivity of **2** as shown in Scheme III-9. Obviously, the reduced complex **3** is of leaser stability and is correctly poised to react with the bromobenzene/O<sub>2</sub> reaction system (Scheme III-10). The reducing equivalents stored in **3** play a

decisive role in activating the dioxygen molecule ( $O_2$ ), producing the incipient electrophilic oxygen atom (Scheme III-11), which is transferred to the substrate RH, producing ROH, in other words, this is the basis of monooxygenase type activity of **3**.<sup>100,101</sup>

## Conclusion

This chapter presents the synthesis, characterization and reactivity aspects of a new mixed ligand Co(II) complex. Its spectroscopic, cyclic voltammetric and redox reactivity data could be rationalized in terms of the electronic structure (DFT) as well as the Frost diagram. The corresponding  $NaBH_4$  reduced complex **3** could be characterized to be a Co(I) species, a rare event in pterin chemistry. During its reaction with the bromobenzene/ $O_2$  reaction mixture, most likely a  $Co(I) \rightarrow O_2$  electron transfer step activates the dioxygen molecule;<sup>99</sup> Scheme III-12 shows the possible pathway through MO formation,<sup>30,31,90,102</sup> through replacement of the aquo group from the z-axis by  $O_2$  (Scheme III-9). Finally, the reduced pterin ring of **3** (Schemes III-9, to III-11) completes the process of reduction of one of the oxygen atoms to the level of water and the other oxygen atom is incorporated into the substrate (bromobenzene), thereby completing the monooxygenase type activity.



**3** **3(O<sub>2</sub>)Complex : a** **O<sub>2</sub>**  
**Hypothetical intermediate**  
**step involved in Scheme III-10 & III-11**

**Scheme III-12** This MO picture is based on Scheme III-9 whereby the aquo group of **3** is replaced by O<sub>2</sub> along the Z-axis as well as participation from the dz<sup>2</sup> (σ-type) and dyz(π-type) orbitals. The other d orbitals (d<sub>xz</sub>, d<sub>xy</sub> and d<sub>x<sup>2</sup>-y<sup>2</sup>) remain nonbonding.</sub>

This model monooxygenase type activity is the result of joint participation by both the redox active metal centre and the redox non-innocent pterin ligand centre of **2**.<sup>10,52-55,99-101</sup>

## **Chapter IV**

**Nickel (II)-pterin coordination chemistry in presence of 1, 2-diaminoethane as the ancillary ligand: synthesis, structural and comparative reactivity studies for aqua and imidazole substituted complexes in the light of DFT**

## Abstract

A 6-substituted pterin ligand 7-methylpterin-6-carboxylic acid ( $H_2L$ ) plays a pivotal role for the present study; it is complemented by a typical ligand like  $\sigma$ - donor ancillary ligand like 1,2-diaminoethane(en). Solubility of  $H_2L$  in aqueous alkali permits the synthesis of a mononuclear nickel(II) complex  $[Ni^{II}(L)(en)(H_2O)] \cdot 2H_2O$  (**1**) from this medium in the crystalline form and its x-ray structural characterization. Again, the use of imidazole (Im) as an additional supporting ligand, permits the synthesis and x-ray structural characterization of another new complex  $[Ni(L)(en)(Im)] \cdot 2H_2O$  (**2**). Their microanalytical, spectroscopic, magnetic susceptibility, cyclic voltammetric and reactivity data are quite valuable for characterization purpose. Both of them are chiral; their longer wavelength (755 -769 nm) positive cotton effect may be correlated with the  $\delta$ -conformation of the 'en' chelate ring. Reactivity of **1** towards imidazole (Im) is characterized by substrate saturation kinetics as well as a negative  $\Delta S^\ddagger$  value ( $-178.5 \text{ J mol}^{-1} \text{ deg}^{-1}$ ), indicating an associative pathway. The  $\mu_{\text{eff}}$  values (BM) are consistent with the presence of Ni(II) centres in these complexes, while cyclic voltammetric data point towards a metal-centred  $[Ni(II) \rightarrow Ni(I)]$  reaction process around -0.7 V. Their response towards redox reagents is almost unique. While the reactivity of **1** towards  $NaBH_4$  is characterized by a substrate saturation process [ $k_{\text{obs}} = 8.4 \times 10^{-3} \text{ s}^{-1}$ ;  $\Delta S^\ddagger = -198.5 \text{ J mol}^{-1} \text{ deg}^{-1}$ ], the corresponding reactivity profile of **2** is essentially a one-step process, associated with essentially three isosbestic points [ $k_{\text{obs}} = 9.0 \times 10^{-3} \text{ s}^{-1}$ ;  $\Delta S^\ddagger = -186.0 \text{ J mol}^{-1} \text{ deg}^{-1}$ ]. The related  $NaBH_4$  reduced complexes [**1R** and **2R**] could be isolated in the solid state as dark-colored, hygroscopic compounds and characterized to be Ni(I) complexes with 7, 8-dihydro form of the pterin ligand residue. **1R** and **2R** respond differently towards a reaction mixture of bromobenzene/ $O_2$ ; reaction profile of the latter is characterized by two isosbestic points. Their  $k_{\text{obs}}$  and  $\Delta S^\ddagger$  values are in the range  $1.4 \times$

$10^{-2}$  to  $8.8 \times 10^{-3} \text{ s}^{-1}$  and  $-191.6$  to  $-178.0 \text{ J mol}^{-1} \text{ deg}^{-1}$ , respectively, consistent with a group transfer process, involving associative pathway. Stoichiometric studies could establish the isolation of 4-bromophenol in each case, indicating activation of the aromatic ring. The above reactivity data highlight the change over in reaction profile brought about by substituting the aquo group of **1** with an imidazole group in **2**, that is, the fine tuning of both metal and pterin-centred redox reactivities. No less interesting is the oxidation of **2R** by  $\text{K}_3[\text{Fe}(\text{CN})_6]$ , where the relatively better resolved reaction profile is marked by three isosbestic points [ $k_{\text{obs}} = 3.6 \times 10^{-2}$ ;  $\Delta S^\ddagger = -184.0 \text{ J mol}^{-1} \text{ deg}^{-1}$ ]. The above ability of facile reactions with either a reducing agent ( $\text{NaBH}_4$ ) or an oxidizing agent [bromobenzene/ $\text{O}_2$  mixture or  $\text{K}_3[\text{Fe}(\text{CN})_6]$ ], may be considered as redox amphoteric behavior; electronic structures (DFT) provide with the necessary framework for rationalizing this property.

## Introduction

Nickel (relative atomic mass = 58.69) is a first-row transition metal in group VIII B of the periodic table. It can exist in oxidation states from 0 to +4 and all but the +4 state have been observed in biology. As per the relevant Frost diagram, only small free energy barriers could separate the lower oxidation states (0, +1 and +2) and thereby allowing their facile change over. The nickel enzymes can be divided into two groups: redox enzymes and hydrolases. The five nickel redox enzymes are hydrogenase, CO dehydrogenase (CODH), acetyl-CoA synthase (ACS), methyl-coenzyme M reductase (MCR) and superoxide dismutase (SOD). Glyoxalase –I and urease are Ni hydrolases. Ni proteins that are not enzymes, are also known.<sup>103,104</sup> These include regulatory proteins (NikR) and chaperonin and metal uptake proteins (CooJ, CooE, UreE and ABC transporters).

Although the 2+ state ( $3d^8$ ) is most common, the Ni redox enzymes appear to access either the 2+/1+ and/ or the 3+/2+ redox couples. It has been proposed that the 0 state is important during catalysis by acetyl-CoA synthase. The hydrolases appear to only use  $Ni^{2+}$ , which is a Lewis acid. Since  $Ni^+$  and  $Ni^{3+}$  are paramagnetic, EPR spectroscopy is a valuable probe for studying Ni redox enzymes. Some Ni enzymes have rather strong UV-visible and magnetic circular dichroism (MCD) bands that are redox- and coordination-dependent.

The present redox non-innocent pterin ligand 7-methylpterin-6-carboxylic acid ( $H_2L$ ) provides with an opportunity to explore the coordination chemistry of nickel, in at least a couple of its biologically relevant oxidation states. A  $\sigma$ -donor ancillary ligand like 1, 2-diaminoethane (en) helps to quench the Lewis acidity of the  $Ni^{2+}$  centre at least partly, so that the coordinating influence of the pterin ligand can prevail here. The imidazole ligand provides with further modulation of the nickel-pterin-en coordination environment. The above ligand combinations allow to grow x-ray quality crystals of the relevant complexes from the aqueous alkaline medium. Such complexes with redox active metal and pterin centres are excellent candidates for redox reactions with well-chosen reagents. Some of the bench mark data may be regarded as biomimetic chemistry.

## **Experimental**

**Materials:** Reagent grade chemicals were used as received. Solvents were purified before use following literature procedures<sup>20</sup>. Kinetic and electro-chemical studies were performed in spectroscopy grade SRL, Mumbai  $CH_3OH$  and DMSO respectively;  $Bu_4NClO_4$  (TBAP) was obtained by published methods<sup>72</sup>. Imidazole was obtained from E.Marck, Mumbai. CD spectra were recorded on a Jasco CD spectrometer (model J-815). 7-methylpterin-6-carboxylic acid was

prepared as per the published methods<sup>19</sup>; it was characterized through different physico-chemical methods including elemental analysis, ESIMS, IR, UV – VIS, and <sup>1</sup>H NMR data .

**Methods :** Most of the physico-chemical methods of characterization were the same as that discussed in Chapters II and III. IR spectra (KBr) were recorded on a Perkin Elmer FTIR Rx1. Magnetic susceptibilities were checked with a Sherwood magnetic susceptibility balance (MSB Mk1), using Hg[Co(SCN)<sub>4</sub>] as the calibrant.

**X-ray data collection:** Apex2 (Bruker , 2007); cell refinement: Apex2 (Bruker , 2007); data reduction: USER DEFINED DATA REDUCTION; program(s) used to solve structure: *SHELXS* 86 (Sheldrick, 2008); program(s) used to refine structure: *CRYSTALS* (Betteridge *et al.*, 2003); molecular graphics: *CAMERON* (Watkin *et al.*, 1996); software used to prepare material for publication: *CRYSTALS* (Betteridge *et al.*, 2003).

## Synthesis of the complexes

### [Ni(C<sub>8</sub>H<sub>5</sub>N<sub>5</sub>O<sub>3</sub>)(C<sub>2</sub>H<sub>8</sub>N<sub>2</sub>)(H<sub>2</sub>O)]. 2H<sub>2</sub>O (1)

The title complex was prepared by the slow addition of an aqueous alkaline solution (NaOH: 44mg, 1.1 mmol) of the pterin ligand H<sub>2</sub>L (C<sub>8</sub>H<sub>7</sub>N<sub>5</sub>O<sub>3</sub> 1.5 H<sub>2</sub>O; MW 248) (124mg, 0.5mmol) to a well-stirred warm (323K; paraffin oil bath) aqueous reaction mixture containing NiSO<sub>4</sub> . 7H<sub>2</sub>O (140mg, 0.5mmol) and 1, 2 – diaminoethane (36mg, 0.6mmol) under subdued light; final volume was 35 ml. The pH was adjusted to 9.2 and the stirring was continued for 3h. Upon standing, the reaction medium deposited yellow-brown crystals after 2 days, which were suitable for single crystal x-ray diffraction; yield, 30%. Analytically pure compound could be obtained by filtration, repeated washing with small quantities of water and drying in vacuo over silica gel. Analysis, calculated for C<sub>10</sub>H<sub>19</sub>N<sub>7</sub>O<sub>6</sub>Ni: C 30.70, H 4.89, N 25.06 %; found: C 30.51, H 5.11, N 24.55 %.

UV – VIS absorption bands [CH<sub>3</sub>OH, λ<sub>max</sub><sup>nm</sup>(logε)]: 205(4.91), 233sh(4.35), 277(4.44),

349(4.21), 734(1.24), 893(1.90)

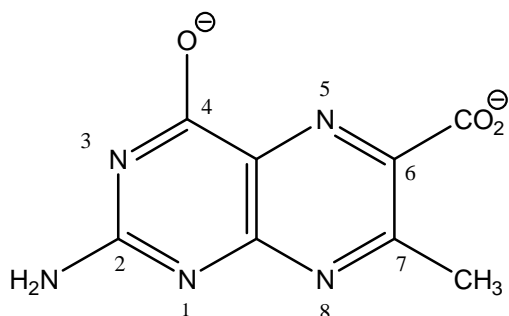
**[Ni(C<sub>8</sub>H<sub>5</sub>N<sub>5</sub>O<sub>3</sub>)(C<sub>2</sub>H<sub>8</sub>N<sub>2</sub>)(C<sub>3</sub>N<sub>2</sub>H<sub>4</sub>)] · 2H<sub>2</sub>O (2)**

The title complex was synthesized by the dropwise addition of an aqueous alkaline solution (NaOH: 11mg, 0.275 mmol) of the pterin ligand (31mg, 0.125mmol) to a warm (311K; paraffin oil bath) aqueous reaction mixture containing NiSO<sub>4</sub> · 7 H<sub>2</sub>O (35mg, 0.125mmol), 1,2 – diaminoethane (7.5mg, 0.125mmol) and 1H – imidazole (14mg, 0.2mmol); final volume was 45ml. The pH was adjusted to 10.3 and the mixture was stirred for 3h; final pH was 9.3. The orange coloured solution was transferred to a 100ml beaker and allowed to stand at room temperature. Orange crystal appeared after 4 days which were suitable for single crystal x-ray diffraction; yield, 40%. Sample for analytical purpose could be obtained by filtration, repeated washing with small quantities of water and drying in vacuo over silica gel. Analysis, calculated for C<sub>13</sub>H<sub>21</sub>N<sub>9</sub>O<sub>5</sub>Ni : C 35.31, H 4.80, N 28.52%; found: C 35.72, H 4.70, N 28.07%. UV – VIS absorption bands [CH<sub>3</sub>OH, λ<sub>max</sub><sup>nm</sup>(logε)]: 270(4.26), 369(3.88), 542br(1.12), 620br(0.96), 698(1.21), 748(1.24), 812(1.43), 921br(0.88), 1063sh(1.32)

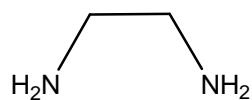
**Synthesis of Na[Ni<sup>I</sup>(L')(en)(H<sub>2</sub>O)] · 2H<sub>2</sub>O · CH<sub>3</sub>OH (1R)**, where (L')<sup>2-</sup> is the 7,8-dihydro form (Scheme II-4) of the pterin ligand anion (Scheme II-1), as established on the basis of microanalytical and spectroscopic data (vide infra). A methanolic solution (50 mL) of **1** (19.6 mg, 0.05 mmol) was treated with NaBH<sub>4</sub> (11.3 mg, 0.3 mmol) and the reaction was allowed to continue for 45 min at 301-303K under subdued light in a chlenk flask attached to a paraffin oil bubbler. The reaction mixture passed through a sequence of color changes e.g., yellow green → dark brown colour . It was then rotavapped and a dark brown solid was recovered. It was washed quickly (decantation ) with dinitrogen purged CH<sub>3</sub>OH ( 3 X 4 mL) and dried in vacuo over silica

gel for 48h. Yield: 40%. Anal. Calcd for  $\text{NaNiC}_{11}\text{H}_{25}\text{N}_7\text{O}_6$ : C, 31.98; H, 6.05; N, 23.74. Found: C, 30.29; H, 5.65; N, 24.15.

**Synthesis of  $\text{Na}[\text{Ni}^{\text{I}}(\text{L}')(\text{en})] \cdot 3\text{H}_2\text{O}$  (**2R**).** A methanolic solution (50 mL) of **1** (22.10 mg, 0.05 mmol) was treated with  $\text{NaBH}_4$  (11.3 mg, 0.3 mmol) and the reaction was allowed to continue for 45 min at 301-303K under subdued light in a Schlenk flask attached to a paraffin oil bubbler. The reaction mixture passed through a sequence of color changes e.g., yellow green  $\rightarrow$  dark brown colour. It was then rotavapped and a dark brown solid was recovered. It was washed quickly (decantation) with dinitrogen purged  $\text{CH}_3\text{OH}$  (3 X 4 mL) and dried in vacuo over silica gel for 48h. Yield: 38%. Anal. Calcd for  $\text{NaNiC}_{13}\text{H}_{25}\text{N}_9\text{O}_6$ : C, 32.18; H, 5.15; N, 25.99. Found: C, 31.45; H, 4.65; N, 24.23.

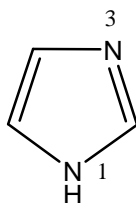


The pterin ligand ( $\text{H}_2\text{L}$ ) anion ( $\text{L}^{2-}$ ,  $\text{C}_8\text{H}_5\text{N}_5\text{O}_3$ )



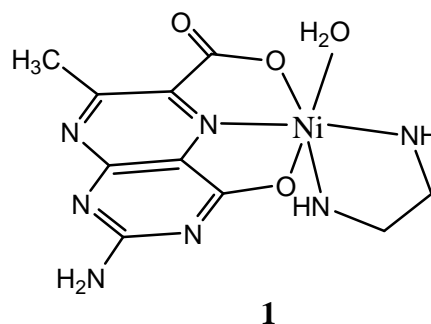
1, 2-diaminoethane (en,  $\text{C}_2\text{H}_8\text{N}_2$ )

#### Scheme IV-1



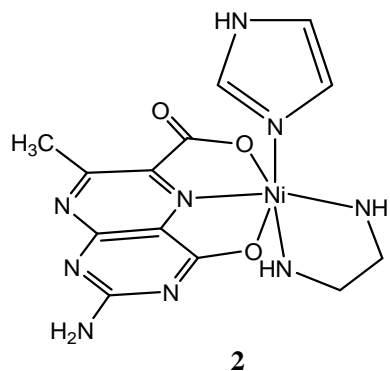
1H-imidazole (Im,  $\text{C}_3\text{N}_2\text{H}_4$ )

#### Scheme IV-2

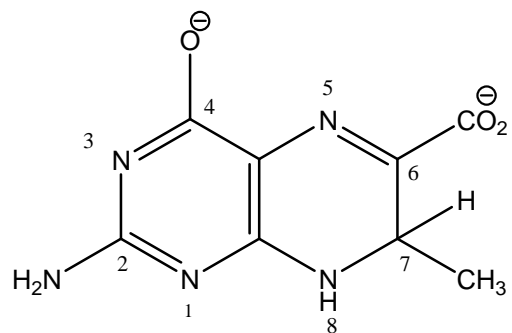


**1**

**Scheme IV-3**

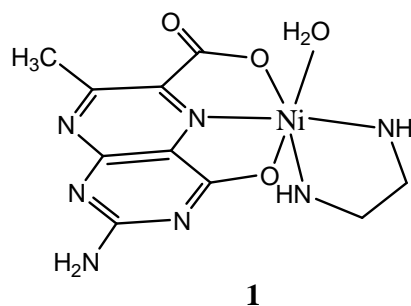


**Scheme IV-4**

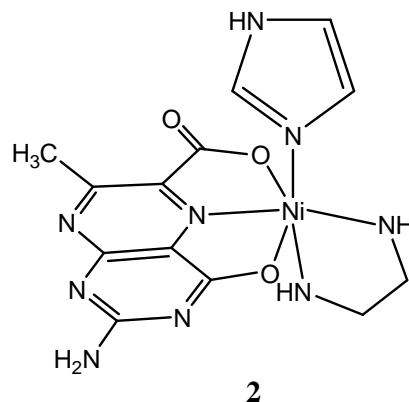


7, 8-dihydro pterin anion (L' 2-)

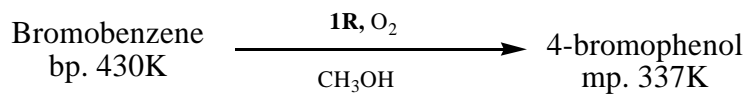
**Scheme IV-5**



**Scheme IV-6**



**Scheme IV-7**



**Scheme IV-8**

## Results and discussion

The two Ni(II) mixed ligand complexes of the pterin ligand (Scheme: IV-1) could be synthesized and crystallized out of the aqueous alkaline medium. The reaction conditions were

carefully controlled, including heating on a paraffin oil bath. In each case, x-ray quality crystals were deposited from the reaction medium. After proper washing and drying such crystals, analytically pure samples could be obtained giving correct microanalytical data as well as electrospray ionization mass spectral data (ESIMS). Successful use of aqueous medium for the above purpose, lends credibility to the present complexes for studies as model systems. Examples of quaternary complexes like **2**, are still rare in pterin coordination chemistry. Schemes IV-1 to IV-5 represent the present ligands and the new Ni(II) complexes.

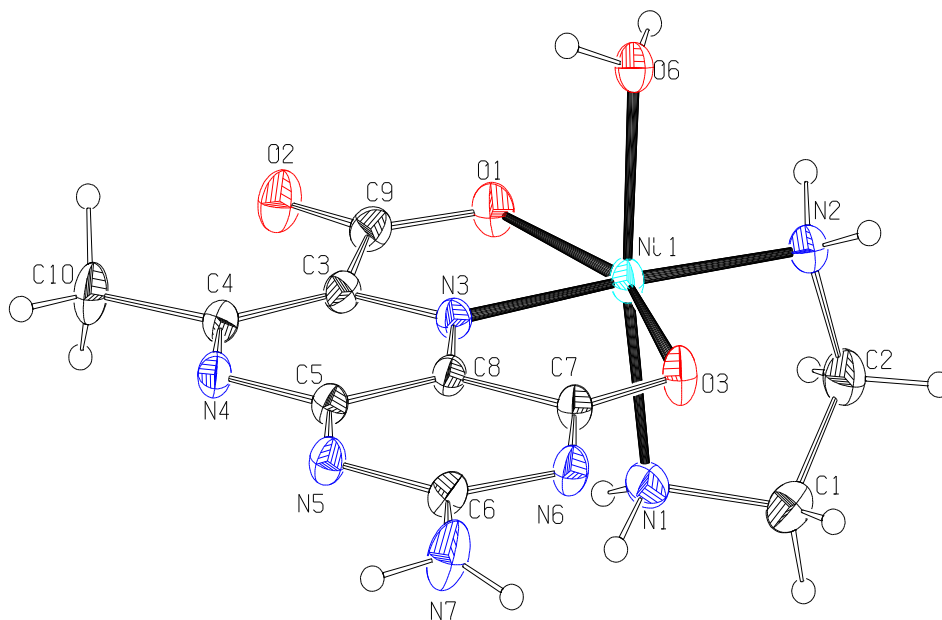


**Figure IV-1.** ORTEP diagram of the complex **1** with atom numbering scheme (40% probability factor for the thermal ellipsoids); lattice water molecules are omitted for clarity.

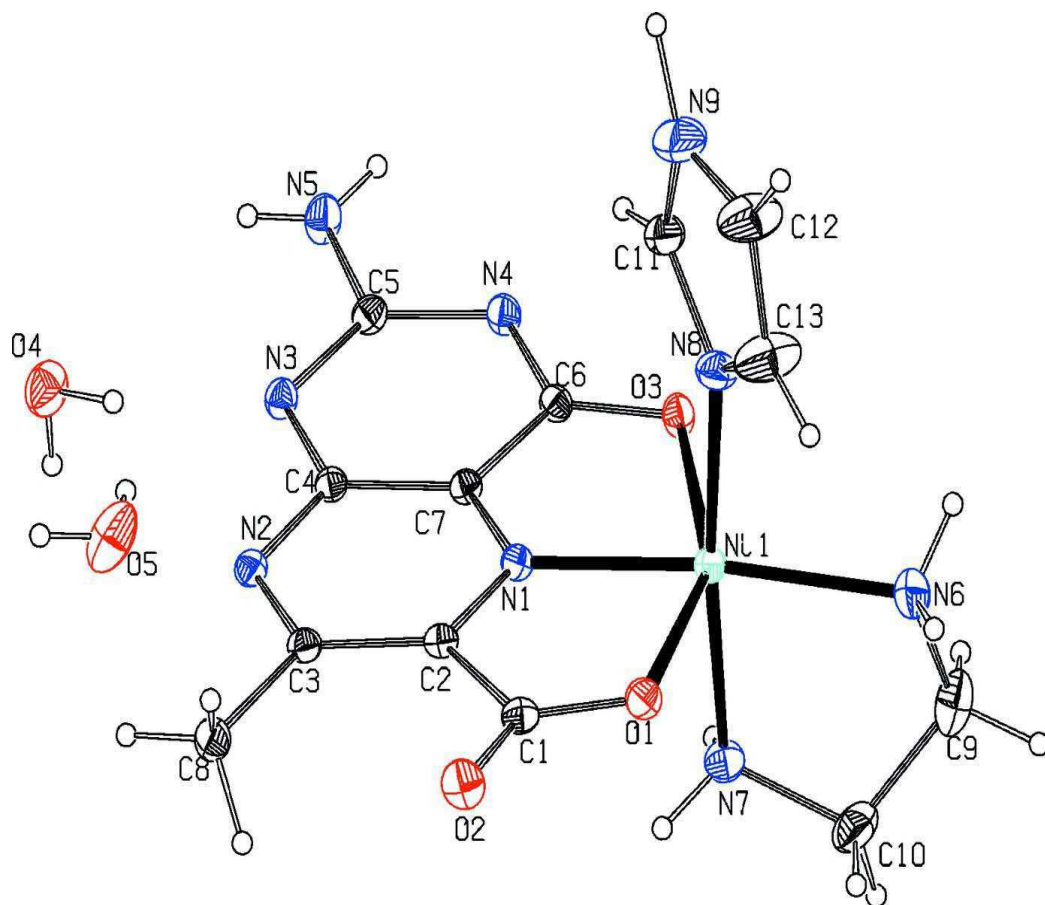


**Figure IV-2.** ORTEP diagram of the complex **2** with atom numbering scheme( 40% probability factor for the thermal ellipsoids).

---

**Table IV-1. Crystallographic data and structure refinement for 1 and 2**

Identification code	<b>1</b>	<b>2</b>
Empirical formula	$C_{10}H_{19}N_7NiO_6$	$C_{13}H_{21}N_9NiO_5$
Formula weight	392.01	442.08
Temperature/K	293	293
Crystal system	Monoclinic	orthorhombic
Space group	$P2_1/c$	Pbcn
a/Å	10.406(4)	13.484(2)
b/Å	14.323(5)	8.8741(15)
c/Å	10.450(4)	29.959(5)
$\alpha/^\circ$	90	90
$\beta/^\circ$	93.294(6)	90
$\gamma/^\circ$	90	90
Volume/Å <sup>3</sup>	1554.9(10)	3584.8(10)
Z	4	8
$\rho_{calc}/cm^3$	1.675	1.638
$\mu/mm^{-1}$	1.294	1.132
F(000)	816.0	1840.0
Crystal size/mm <sup>3</sup>	0.490 × 0.380 × 0.280	0.240 × 0.240 × 0.030
Radiation	Mo K $\alpha$ ( $\lambda = 0.71073$ )	Mo K $\alpha$ ( $\lambda = 0.71073$ )

2 $\theta$ range for data collection/ $^{\circ}$	3.92 to 56.382	2.718 to 56.6 $^{\circ}$
Index ranges	-13 $\leq$ h $\leq$ 13, -18 $\leq$ k $\leq$ 15, -11 $\leq$ l $\leq$ 13	-17 $\leq$ h $\leq$ 17, -11 $\leq$ k $\leq$ 11, -24 $\leq$ l $\leq$ 38
Reflections collected	8393	19640
Independent reflections	3488 [R <sub>int</sub> = 0.035]	4245[R(int) = 0.030]
Data/restraints/parameters	3488/0/217	4245/0/253
Goodness-of-fit on F <sup>2</sup>	0.914	0.945
Final R indexes [I $\geq$ 2 $\sigma$ (I)]	R <sub>1</sub> = 0.0499, wR <sub>2</sub> = 0.1255	R <sub>1</sub> = 0.0365, wR <sub>2</sub> = 0.0887
Final R indexes [all data]	R <sub>1</sub> = 0.0638, wR <sub>2</sub> = 0.1347	R <sub>1</sub> = 0.0442, wR <sub>2</sub> = 0.0921
Largest diff. peak/hole / e $\text{\AA}^{-3}$	1.10/-0.84	0.62/-0.32

**Table IV- 2. Geometric parameters for (1)**

**Bond lengths**

Atom	Atom	Length/ $\text{\AA}$	Atom	Atom	Length/ $\text{\AA}$
Ni1	O1	2.120(2)	C8	C7	1.460(4)
Ni1	N3	1.977(3)	C5	N4	1.362(4)
Ni1	O3	2.325(2)	C5	N5	1.358(4)
Ni1	O6	2.125(2)	N4	C4	1.349(4)
Ni1	N1	2.074(3)	C4	C10	1.501(4)

Ni1	N2	2.065(3)	N5	C6	1.360(4)
O1	C9	1.288(4)	C6	N6	1.381(4)
C9	O2	1.239(4)	C6	N7	1.347(4)
C9	C3	1.526(4)	N6	C7	1.338(4)
C3	N3	1.339(4)	C7	O3	1.274(4)
C3	C4	1.416(4)	N1	C1	1.479(5)
N3	C8	1.325(4)	C1	C2	1.501(5)
C8	C5	1.401(4)	C2	N2	1.481(5)

### **Bond angles**

<b>Atom</b>	<b>Atom</b>	<b>Atom</b>	<b>Angle/°</b>	<b>Atom</b>	<b>Atom</b>	<b>Atom</b>	<b>Angle/°</b>
O1	Ni1	N3	77.20(10)	Ni1	N3	C8	119.14(19)
O1	Ni1	O3	153.50(8)	N3	C8	C5	121.5(3)
N3	Ni1	O3	76.31(9)	N3	C8	C7	117.4(3)
O1	Ni1	O6	88.63(9)	C5	C8	C7	121.0(3)
N3	Ni1	O6	93.13(10)	C8	C5	N4	119.9(3)
O3	Ni1	O6	92.06(9)	C8	C5	N5	120.5(3)
O1	Ni1	N1	95.49(11)	N4	C5	N5	119.6(3)
N3	Ni1	N1	94.14(11)	C5	N4	C4	117.9(3)
O3	Ni1	N1	87.16(10)	C3	C4	N4	121.6(3)
O6	Ni1	N1	172.29(10)	C3	C4	C10	122.5(3)
O1	Ni1	N2	103.49(11)	N4	C4	C10	115.9(3)

N3	Ni1	N2	177.56(11)	C5	N5	C6	114.6(2)
O3	Ni1	N2	103.02(10)	N5	C6	N6	129.2(3)
O6	Ni1	N2	89.23(10)	N5	C6	N7	116.3(3)
N1	Ni1	N2	83.47(11)	N6	C6	N7	114.4(3)
Ni1	O1	C9	115.51(19)	C6	N6	C7	116.6(2)
O1	C9	O2	124.2(3)	C8	C7	N6	117.8(3)
O1	C9	C3	115.2(3)	C8	C7	O3	118.1(3)
O2	C9	C3	120.6(3)	N6	C7	O3	124.1(3)
C9	C3	N3	111.1(3)	Ni1	O3	C7	108.99(19)
C9	C3	C4	129.8(3)	Ni1	N1	C1	106.5(2)
N3	C3	C4	119.1(3)	N1	C1	C2	108.5(3)
C3	N3	Ni1	120.9(2)	C1	C2	N2	109.2(3)
C3	N3	C8	120.0(3)	C2	N2	Ni1	109.3(2)

**Table IV- 3. Hydrogen Bonds Geometry for 1**

D	H	A	D-H-A <sup>o</sup>	d(D-H)/Å	d(H-A)/Å	d(D-A)/Å
N7	H172	O5 <sup>1</sup>	130.79(11)	0.871	2.588	3.226(5)
N7	H171	O2 <sup>2</sup>	120.55(12)	0.847	2.370	2.894(5)
O6	H182	N5 <sup>1</sup>	147.64(10)	0.838	2.061	2.805(5)
O6	H181	O4	170.64(11)	0.821	1.962	2.775(5)
N2	H221	O4	137.51(11)	0.872	2.401	3.100(5)

N2	H222	O6 <sup>3</sup>	175.94(9)	0.847	2.218	3.064(5)
N1	H192	O1 <sup>4</sup>	146.50(8)	0.892	2.391	3.173(5)
N1	H192	O2 <sup>4</sup>	154.36(9)	0.892	2.416	3.242(5)
O4	H231	O3 <sup>3</sup>	160.21(11)	0.828	1.891	2.684(5)
O4	H232	O5 <sup>5</sup>	170.85(13)	0.821	2.043	2.857(5)
O5	H242	O1	160.40(10)	0.833	2.213	3.010(5)

**Table IV- 4. Geometric parameters for 2**

**Bond Lengths**

Atom	Atom	Length/Å	Atom	Atom	Length/Å
Ni1	N1	1.9790(16)	N7	C10	1.468(3)
Ni1	N6	2.0801(19)	N8	C11	1.337(3)
Ni1	N7	2.0956(17)	N8	C13	1.339(3)
Ni1	N8	2.0640(17)	N9	C11	1.343(3)
Ni1	O1	2.1522(14)	N9	C12	1.352(4)
Ni1	O3	2.2725(14)	O1	C1	1.270(2)
N1	C2	1.324(2)	O2	C1	1.243(2)
N1	C7	1.320(2)	O3	C6	1.270(2)
N2	C3	1.338(2)	C1	C2	1.522(3)
N2	C4	1.358(2)	C2	C3	1.418(3)
N3	C4	1.349(2)	C3	C8	1.498(3)

N3	C5	1.351(2)	C4	C7	1.396(2)
N4	C5	1.373(2)	C6	C7	1.453(2)
N4	C6	1.332(2)	C9	C10	1.491(4)
N5	C5	1.332(3)	C12	C13	1.329(4)
N6	C9	1.467(3)			

### **Bond Angles**

Atom	Atom	Atom	Angle/°	Atom	Atom	Atom	Angle/°
N1	Ni1	N6	173.25(7)	Ni1	O3	C6	108.71(11)
N1	Ni1	N7	91.67(7)	O1	C1	O2	125.26(18)
N1	Ni1	N8	94.18(7)	O1	C1	C2	114.90(16)
N1	Ni1	O1	75.91(6)	O2	C1	C2	119.82(17)
N1	Ni1	O3	77.49(6)	N1	C2	C3	118.47(16)
N6	Ni1	N7	82.05(8)	C1	C2	N1	111.47(16)
N6	Ni1	N8	92.13(8)	C1	C2	C3	130.06(16)
N6	Ni1	O1	101.53(7)	N2	C3	C8	116.27(17)
N6	Ni1	O3	105.07(7)	C2	C3	N2	121.72(16)
N7	Ni1	N8	174.12(7)	C2	C3	C8	122.00(17)
N7	Ni1	O1	90.31(7)	N2	C4	N3	120.48(16)
N7	Ni1	O3	91.93(6)	N2	C4	C7	119.28(16)
N8	Ni1	O1	91.64(7)	N3	C4	C7	120.24(16)
N8	Ni1	O3	88.81(7)	N3	C5	N5	116.89(17)

O1	Ni1	O3	153.36(5)	N4	C5	N3	128.64(17)
Ni1	N1	C2	121.70(13)	N4	C5	N5	114.46(17)
Ni1	N1	C7	117.63(12)	N4	C6	O3	123.89(16)
C2	N1	C7	120.57(16)	N4	C6	C7	117.18(16)
C3	N2	C4	118.22(16)	O3	C6	C7	118.90(16)
C4	N3	C5	115.13(16)	C4	C7	N1	121.64(16)
C5	N4	C6	117.22(16)	C6	C7	N1	117.14(16)
Ni1	N6	C9	109.21(15)	C6	C7	C4	121.22(16)
Ni1	N7	C10	108.07(14)	N6	C9	C10	108.2(2)
Ni1	N8	C11	128.23(15)	C9	C10	N7	109.3(2)
Ni1	N8	C13	126.84(17)	N9	C11	N8	111.0(2)
C11	N8	C13	104.8(2)	N9	C12	C13	107.4(2)
C11	N9	C12	105.9(2)	N8	C13	C12	110.7(2)
Ni1	O1	C1	115.81(12)				

**Table IV- 5. Hydrogen Bonds Geometry for 2**

<b>D</b>	<b>H</b>	<b>A</b>	<b>D-H-A/°</b>	<b>d(D-H)/Å</b>	<b>d(H-A)/Å</b>	<b>d(D-A)/Å</b>
N6	H62	O5 <sup>1</sup>	151.75(7)	0.900	2.276	3.099(3)
N7	H72	N2 <sup>2</sup>	176.41(5)	0.899	2.400	3.298(3)
N7	H71	O4 <sup>2</sup>	135.18(6)	0.899	2.509	3.211(3)
N5	H51	N4 <sup>3</sup>	177.50(15)	0.848	2.136	2.983(3)

O5	H51	O2 <sup>4</sup>	175.53(8)	0.857	1.967	2.822(3)
N5	H52	O4	140.01(15)	0.778	2.559	3.194(3)
O5	H52	O1 <sup>5</sup>	146.29(7)	0.737	2.148	2.791(3)
N9	H91	O5 <sup>6</sup>	160.29(15)	1.055	2.003	3.017(3)
C12	H121	O2 <sup>6</sup>	137.67(9)	0.931	2.186	2.941(3)
O4	H42	N3	169.81(7)	0.852	1.994	2.837(3)
O4	H41	O3 <sup>7</sup>	163.23(6)	0.866	2.018	2.858(3)

**Molecular structures of [Ni(C<sub>8</sub>H<sub>5</sub>N<sub>5</sub>O<sub>3</sub>)(C<sub>2</sub>H<sub>8</sub>N<sub>2</sub>)(H<sub>2</sub>O)]. 2H<sub>2</sub>O (1) and [Ni(C<sub>8</sub>H<sub>5</sub>N<sub>5</sub>O<sub>3</sub>)(C<sub>2</sub>H<sub>8</sub>N<sub>2</sub>)(C<sub>3</sub>N<sub>2</sub>H<sub>4</sub>)]. 2H<sub>2</sub>O (2)**

Figure IV-1 and Figure IV-2 represent the molecular structures of the above complex compounds. Their crystallographic data and structure refinements are shown in Table IV-1. The geometric parameters and hydrogen bonding data of **1** are presented in Table IV-2 and Table IV-3 respectively. Table IV-4 and Table IV-5 represent the geometric parameters and hydrogen bonds data of compound **2**. For complex **1** the six – coordinated Ni (II) atom shows departure from a regular octahedral geometry with respect to both bond lengths and bond angles (Figure IV-1, Table IV-2 ). The basal plane is formed by the two nitrogen atoms (N1, N2) of en, the pyrazine ring nitrogen atom (N3) of the pterin ligand and the aqua group oxygen atom (O6). The axial positions are occupied by the two pterin oxygen atoms O1 and O3, with the latter one forming the longest axial bond [2.325 (2) Å]. One important factor causing distortion from regular octahedral geometry is that this pterin ligand forms two five-membered chelate rings with small bite angles (76.31<sup>0</sup> and 77.14<sup>0</sup>), instead of only one per pterin ligand for the earlier case (Crispini *et al.*, 2005)<sup>83</sup>. A perusal of the charge balance of this complex, indicates that this

pterin ligand acts as a bidentate tridentate ONO donor. An orthogonal disposition of the en and pterin chelate rings is observed which helps to minimize the steric repulsion. Of the three axes, least deviation from linearity is observed in the N3 – Ni1 – N2 direction ( $177.52^\circ$ ) where the highest electron density is concentrated [Ni1 – N3: 1.977 (2) Å; Ni1 – N2: 2.065 (3) Å]. It represents the unique combination of a  $\sigma$  – donor atom N2 (en) and the N3 atom of the redox noninnocent pterin ligand from the opposite directions of the Ni (II) centre ( $d^8$ ), with possible assistance from the  $\pi$  – donating phenolate and carboxylate oxygen atoms (Kohzuma *et al.*, 1988)<sup>18a</sup>. Again, location of the pyrazine ring nitrogen atom (N3) in the basal plane is consistent with the earlier observations on related copper complexes (Odani *et al.*, 1992).<sup>84</sup>

Although the exocyclic bond length data of the pyrazine ring, e.g., C3 – C9 [1.527 (4)Å] and C4 – C10 [1.503 (4)Å] reflect only limited conjugation with the pyrazine ring  $\pi$  system, the corresponding bond length data of the pyrimidine ring, e.g., C7 – O3 [1.267 (3)Å] and C6 – N7 [1.349 (4)Å] merit attention. Small deviations, e.g.,  $2.02^\circ$  and  $1.37^\circ$  of the C7/N6/C6 and C5/N5/C6 segments respectively, with respect to the C – N7 multiple bond, indicate near planarity for the pyrimidine ring. So it can participate in the electron shuffling process by the pterin moiety from the pyrazine ring N4 to the C7 – carbonyl group, as suggested by Joule and coworker (Beddoes *et al.*, 1993; Russell *et al.*, 1992).<sup>22,23</sup> Formation of the Ni1 – O3 bond assists this process. In the crystal, the complex molecules and lattice water molecules are linked by inter-molecular N – H...O, O – H...N and O – H...O hydrogen bonds ( Table IV-3 ). The lattice water molecules are decisive for the crystal packing (Figure IV-3)

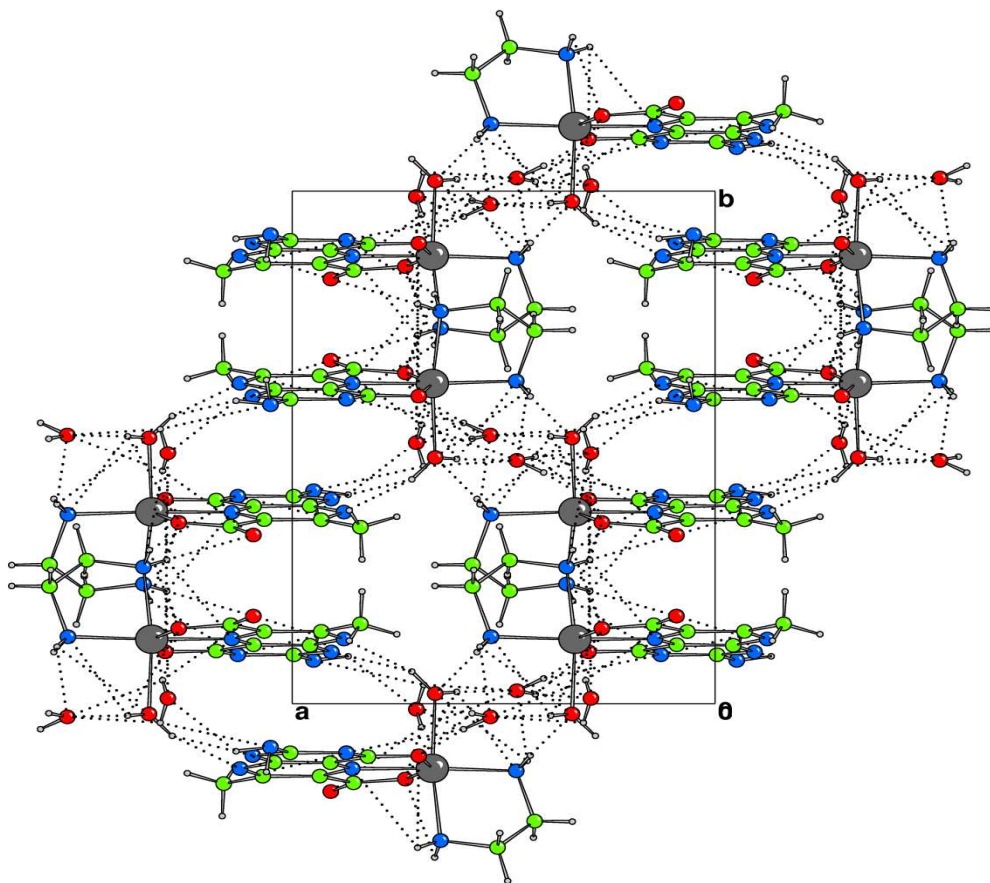


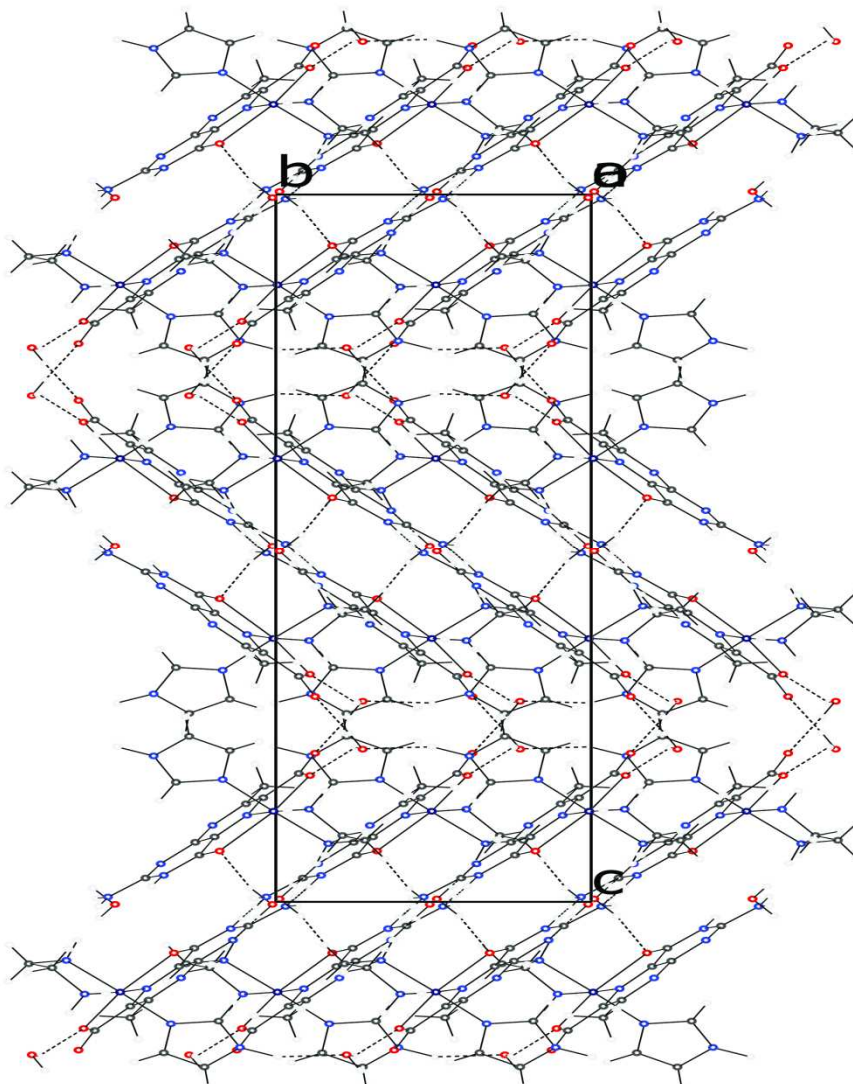
**Figure IV-3.** Crystal packing diagram of **1** and H-bonding network viewed along c axis.

The molecular structure of complex **2** is shown in Figure IV-2. Here a tridentate 2-amino-7-methyl-4-oxidopteridine-6-carboxylate ligand, a bidentate ancillary ethane-1,2-diamine (en) ligand and a monodentate 1H-imidazole (im) ligand complete a distorted octahedral geometry around the Ni(II) atom. The two N atoms (N6 and N7) of en, a pyrazine ring N atom (N1) of the pterin ligand and an imidazole ring N atom (N8) forming the equatorial plane. The two pterin O atoms (O1 and O3) occupy the longer axial positions, with the phenolate O3 constituting the longest axial bond [2.2725(14) Å]. As compared to complex **1**, an unique situation is presented by complex **2** (Figure IV-2) where the equatorial plane is formed by four

nitrogen atoms. The pterin ligand forms two five-membered chelate rings having small bite angles [75.91(6)<sup>0</sup> and 77.50(6)<sup>0</sup>], instead of only one per pterin ligand for an earlier case (Crispini et al., 2005)<sup>83</sup>. This factor is responsible to a large extent for the observed distortion here from regular octahedral geometry. Accordingly, the O1 – Ni1 – O3 axis shows maximum deviation (153.37<sup>0</sup>) from linearity. Again, closest approach to linearity (174.10<sup>0</sup>) is observed for the N7 – Ni1 – N8 axis which is associated with both the imidazole and en ligands. Here each such ligand tries to achieve near orthogonality [angle between the imidazole ring N atom (N8) and the mean plane of the pterin ring = 91.55<sup>0</sup>; dihedral angle between the mean plane of the en moiety and the pterin ring = 90.49<sup>0</sup>], with respect to the pterin ligand, for minimizing the steric repulsion. . In accordance with the earlier observations on related copper complexes, the pyrazine ring N atom (N1) is located in the equatorial plane.<sup>84</sup> The associated short metal-ligand distance (Ni1-N1=1.9790Å) indicates dπ – π interaction between the pterin ring and the Ni(II) centre (d<sup>8</sup>), with further assistance from the nearby π-donating phenolate and carboxylate O atoms<sup>18a</sup> The pterin ligand is coordinated in its binegative form as a ONO donor, as evident from the charge balance of this Ni(II) complex.

The significantly shorter nature of the O3 – C6 [1.271(2) Å] and N5 – C5 [1.332(2)Å] bonds could be rationalized in terms of electron – shuffling ability of the pterin ring , as discussed earlier for complex **1**.<sup>17c, 17d, 22, 23</sup> In the crystal, intermolecular N – H ...N, N – H ...O, O – H...N, O – H ...O hydrogen bonds (Table IV-5 ) link the complex molecules and lattice water molecules into layers along the a axis (Figure IV-4 ). The lattice water molecules play a decisive role for the crystal packing. Presence of the imidazole ligand in the coordination sphere for **2**, leads to a denser crystal packing with Z= 8, as compared to Z= 4 for **1**. This is the

highest Z value for the present series of x-ray structurally characterized pterin coordination complexes.<sup>17a-17e</sup>



**FigureIV- 4.** Crystal packing diagram of **2** with H-bonding network viewed along a axis

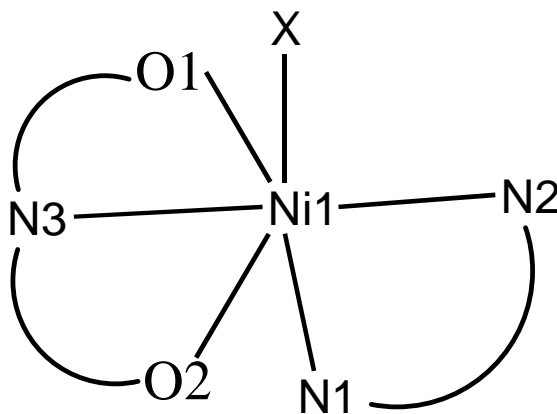
---

Table IV-6 shows the effect of imidazole substitution on selected bond length data in terms of  $\Delta = (\mathbf{1} - \mathbf{2})$  values ( $\text{\AA}$ ); in a couple of cases, the change over in bond length data fall in the range of  $0.05 - 0.06 \text{ \AA}$ . As evident from literature data such change over in dimension can affect ( Table

IV-8) redox reactivity to a large extent.<sup>79</sup> Significance of this observation in the present context ( reactivity) is elucidated later.

**Table IV- 6. Effect of imidazole substitution on selected bond length data.**

Sl No.	Bond	Bond length on <b>1</b> (Å)	Bond length on <b>2</b> (Å)	$\Delta=(1 - 2)$ value (Å)
1	Ni1 – O1	2.120(2)	2.1522(14)	-0.0322
2	Ni1 – O2	2.325(2)	2.2725(14)	0.0525
3	Ni1 – N1	2.074(3)	2.0956(17)	-0.0216
4	Ni1 – N2	2.065(3)	2.0801(19)	-0.0151
5	Ni1 – N3	1.977(3)	1.9790(16)	-0.002
6	Ni1 - X	2.125(2)	2.0640(17)	0.061



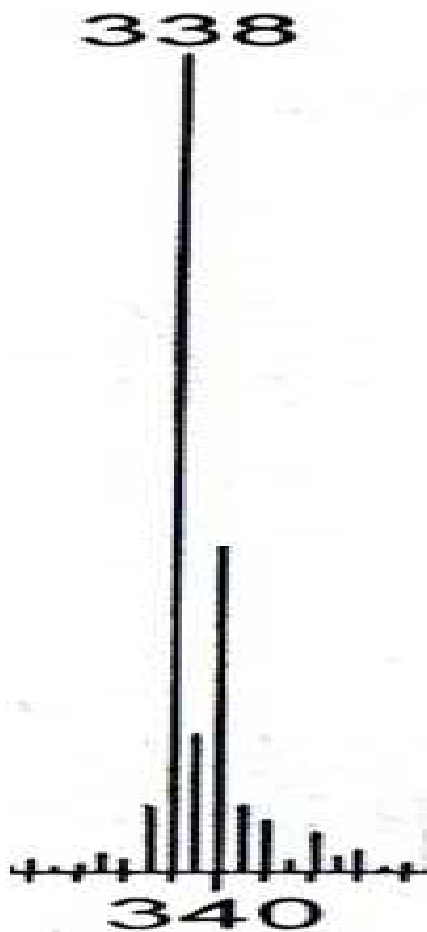
**1** (X=H<sub>2</sub>O) [Figure IV-1.]

**2** (X = Im) [Figure IV-2.]

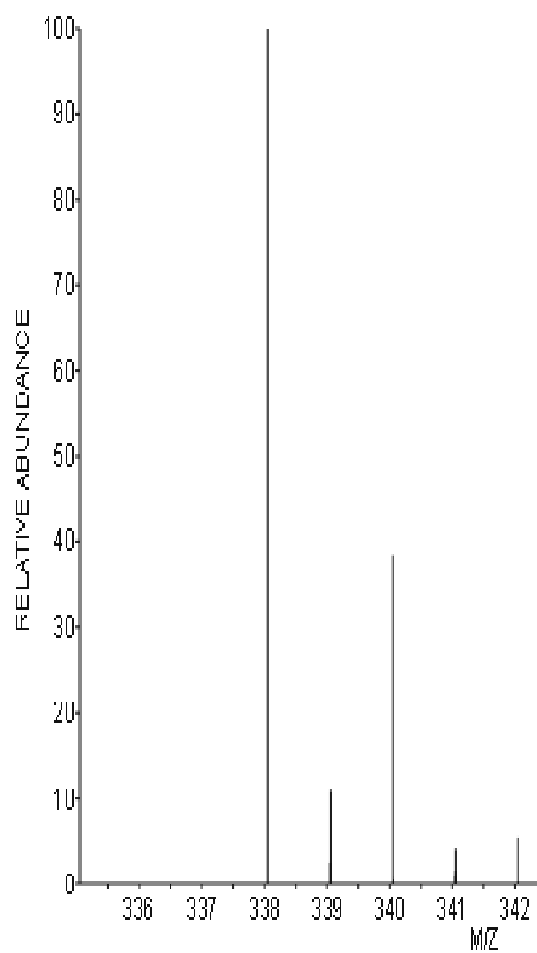
**N.B.** O1, N3 and O2 as shown above, correspond to O6, N5 and O4 donor atoms of the pterin ring (Scheme IV-1)

## ESIMS Data

Electrospray ionization mass spectrometry has been utilized as a soft ionization technique for the characterization of different types of inorganic and coordination compound including metal clusters;<sup>77</sup> the assignment of molecular formula ( or any definite fragment resulting from it) is confirmed by the experimental value of  $m/z$  (most abundant isotopic mass) as well as matching between the experimental and simulated (calculated) isotopic distribution profile.<sup>24,78</sup> Characterization of the desolvated species from a coordination compound in the mass spectrum is well established; even the presence of a fragmentation peak associated with loss of one of the ligand is taken as evidence in favour of a molecular ion peak.<sup>86</sup> Sometimes, isotope peak may be more intense than the calculated value because of ion-molecule interactions that vary with the sample concentration or with the class of compound involved e.g., the transfer of a hydrogen atom from the excess of the compound to the molecular ion in some cases.<sup>21</sup> Figure IV-5 shows the ESIMS data of **1** where the peak at  $m/z$  338 corresponds to the dehydrated species  $[\text{Ni}(\text{L})(\text{en})]^+$ ; the  $m/z$  value (most abundant isotopic mass) and the isotope distribution profile agreed with the corresponding theoretical value, thereby supporting the chemical composition of **1**, in conjunction with the elemental analysis and x-ray structural data.<sup>24</sup> Figure IV-6(a) shows another fragment peak at  $m/z = 278$  corresponding to the species  $[\text{Ni}(\text{L})]^+$ , obtained through loss of the ancillary ligand (en) as well as the intra/extra spheric water molecules; Figure IV-6(b) shows the corresponding calculated isotope distribution profile.<sup>24</sup>



(a)



(b)

**Figure IV-5.** (a) ESIMS data of **1**; (b) the calculated isotope pattern for the base peak at  $m/z = 338$  corresponding to the fragment  $[\text{Ni}(\text{L})(\text{en})]^+$

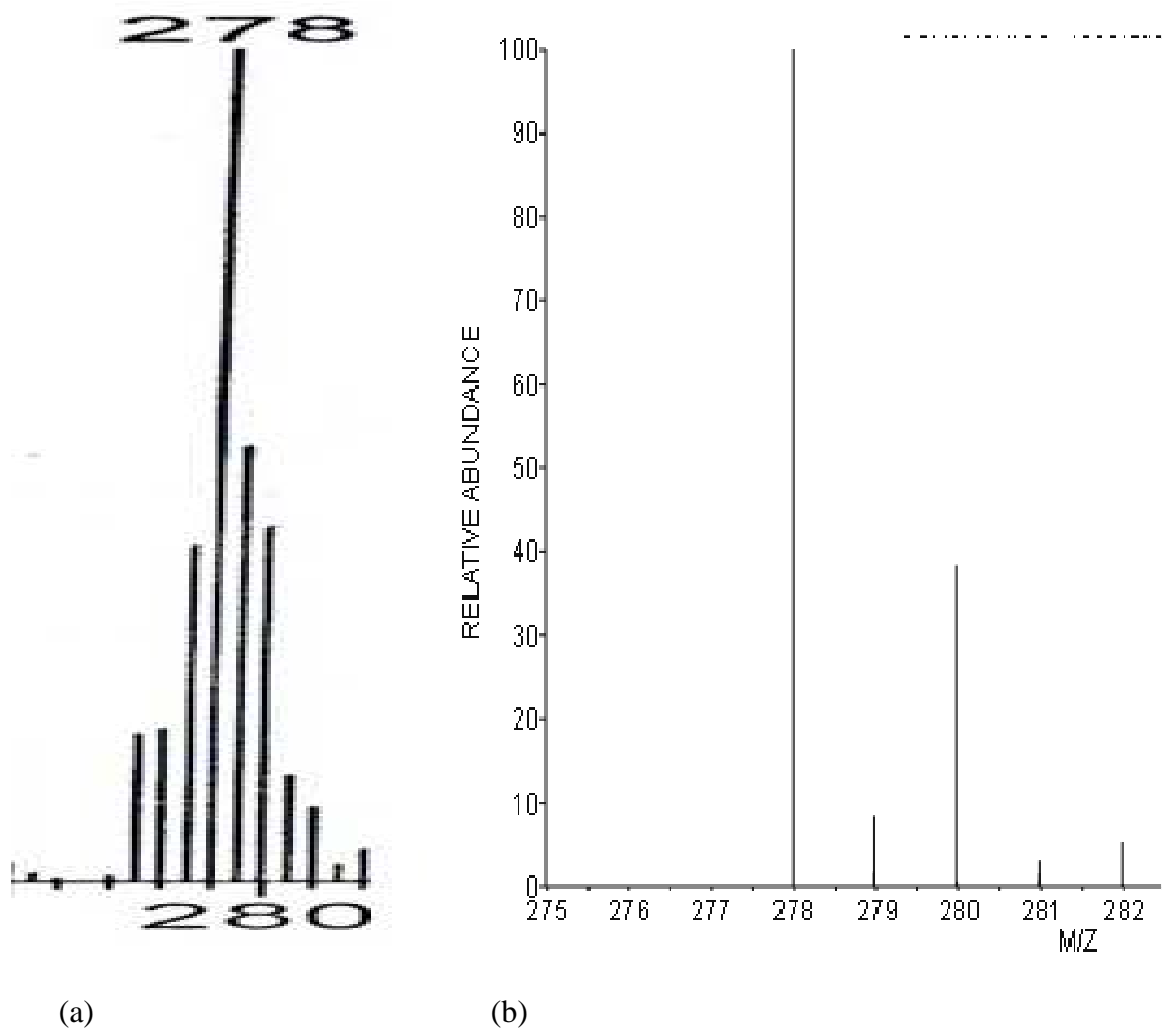


**Figure IV- 6.** (a) ESIMS data of **1**; (b) the calculated isotope pattern for the base peak at  $m/z = 278$  corresponding to the fragment  $[\text{Ni}(\text{L})]^+$  .

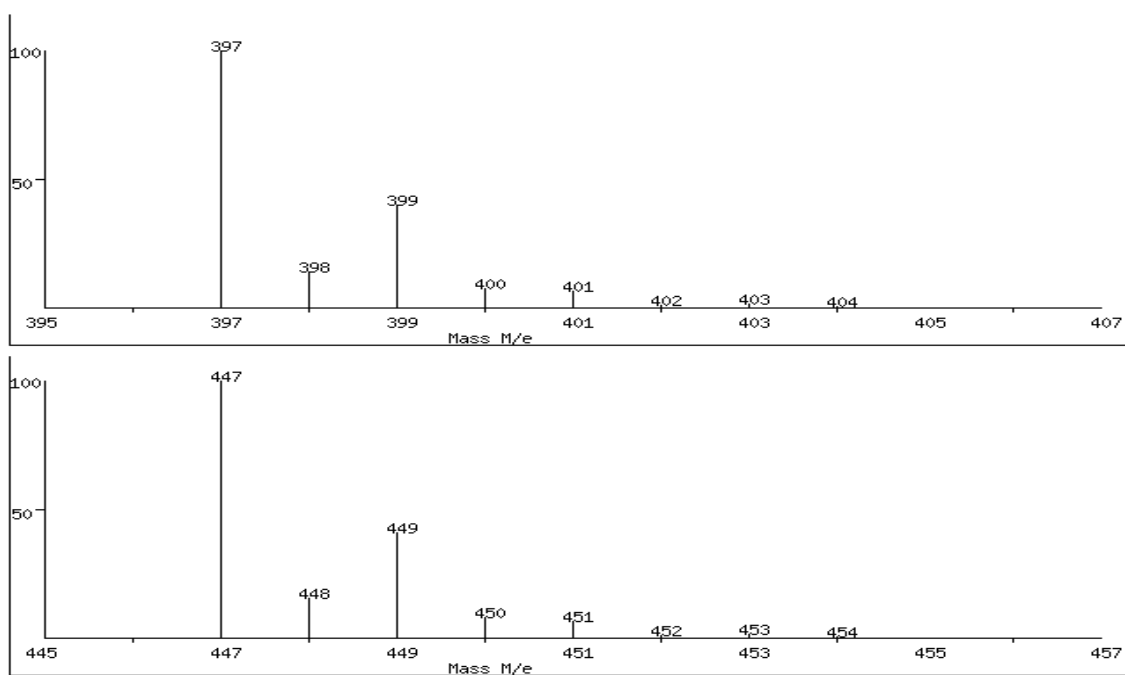
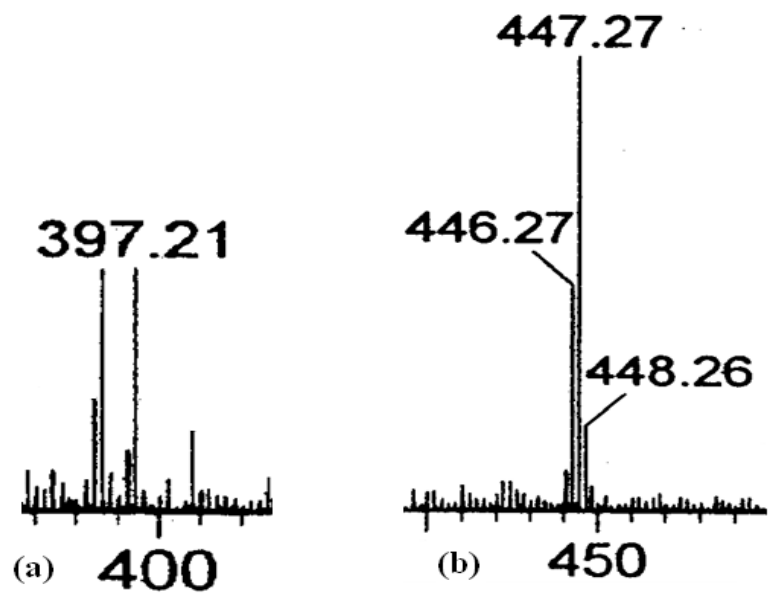


**Figure IV- 6a.** (a) ESIMS data of **1R**; the calculated isotope pattern for the base peak at  $m/z = 447.27$  and  $397.1$ .

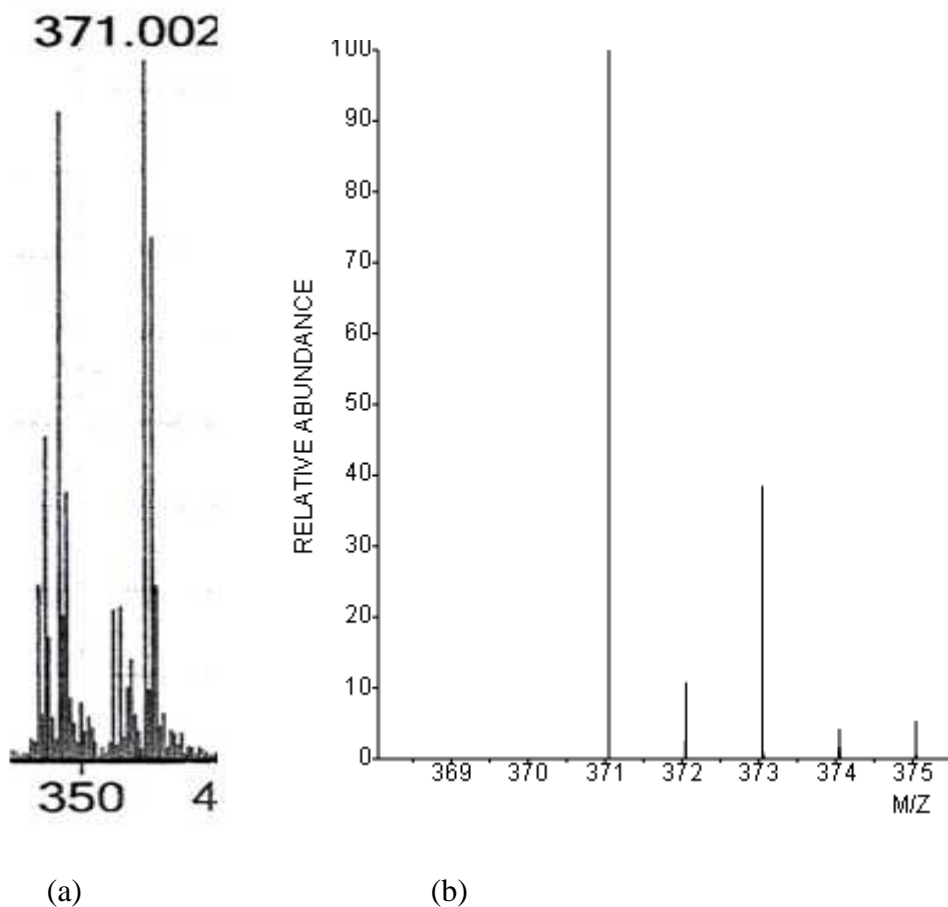


**Figure IV-7.** (a) ESIMS data of **2**; (b) the calculated isotope pattern for the base peak at  $m/z = 371$  corresponding to the fragment  $[M-Im-3H]^+$ , where M is the molecular formula of **2**.

The above mass spectral data verify the architectural stability of this mononuclear mixed ligand Ni(II) complex as well as the strength of the Ni(II)-pterin bonding.<sup>77,78</sup> Figure IV-7(a) shows the ESIMS data of **2** indicating a peak at  $m/z$  371, corresponding to the fragment  $[M-Im-3H]^+$ ; its isotope distribution pattern could be calculated [Figure IV-7(b)]. Once again the stability of the Ni(II) – pterin as well as the Ni(II) – en bonding is demonstrated, along with the affinity of the

extraspheric H<sub>2</sub>O molecule, as evident from the crystal packing diagram ( Figure IV-4). In other words, the neutral monodentate ligand (Im) can be lost from this quaternary complex **2**, without affecting its overall stability.

### ESIMS data of **1R**

The ESIMS data of **1R** is shown in Figure IV-6a . The molecular ion peak  $[M - 1]^+$  is observed at  $m/z$  447.27 where M is the molecular formula of **1R** with its full complement of extraspheric solvent molecules. It verifies the architectural stability of **1R** possessing the 7, 8-dihydro form of the pterin ligand residue ( $L'^{2-}$ , Scheme IV- 6) along with a Ni(I) centre and a balancing Na<sup>+</sup> counter ion. Another peak is observed at  $m/z$  397.1 which corresponds to the fragment  $[M - CH_3OH - H_2O - 1]^+$ , once again verifying the stability of the complex core. The isotopic distribution patterns of both these two peaks could be simulated [Figure IV-6a].

### IR spectroscopy

The IR spectra (KBr pellet) of **1** and **2** are shown in Figure IV-8 and IV-9 respectively along with assignments for the latter. IR spectra of the ancillary ligands 1, 2- diaminoethane (en) and imidazole (Im) are shown in Figure IV-10 and Figure IV-11 respectively. Some of the broad IR bands of the free pterin ligand (H<sub>2</sub>L, Scheme IV-1, Figure III-6) around 3131 cm<sup>-1</sup>, 1684 cm<sup>-1</sup> and 1382 – 1254 cm<sup>-1</sup> are modified on complex formation due to deprotonation of the –COOH(6) and NH(3) groups. For both complexes **1** and **2**, the  $\nu_{as}$  and  $\nu_s$  vibrations of the –CO<sub>2</sub>'(6) group appear around 1597 – 1590 cm<sup>-1</sup> and 1326 cm<sup>-1</sup> respectively; the  $\Delta$  values ( $\nu_{as} - \nu_s = 263 - 271$  cm<sup>-1</sup>), are well within the range for monodentate carboxylate coordination.<sup>87,88</sup> The  $\nu(C-O)$  mode of the pterin phenoxide(4) groups could be located around 1298 – 1305 cm<sup>-1</sup> in these complexes. Tridentate pterin coordination involving the O(4), N(5) and CO<sub>2</sub>'(6) functional

groups (Schemes IV-1 and IV-4) is indicated for both **1** and **2**. This is consistent with their x-ray structural data (Figures IV-1 and IV-2).

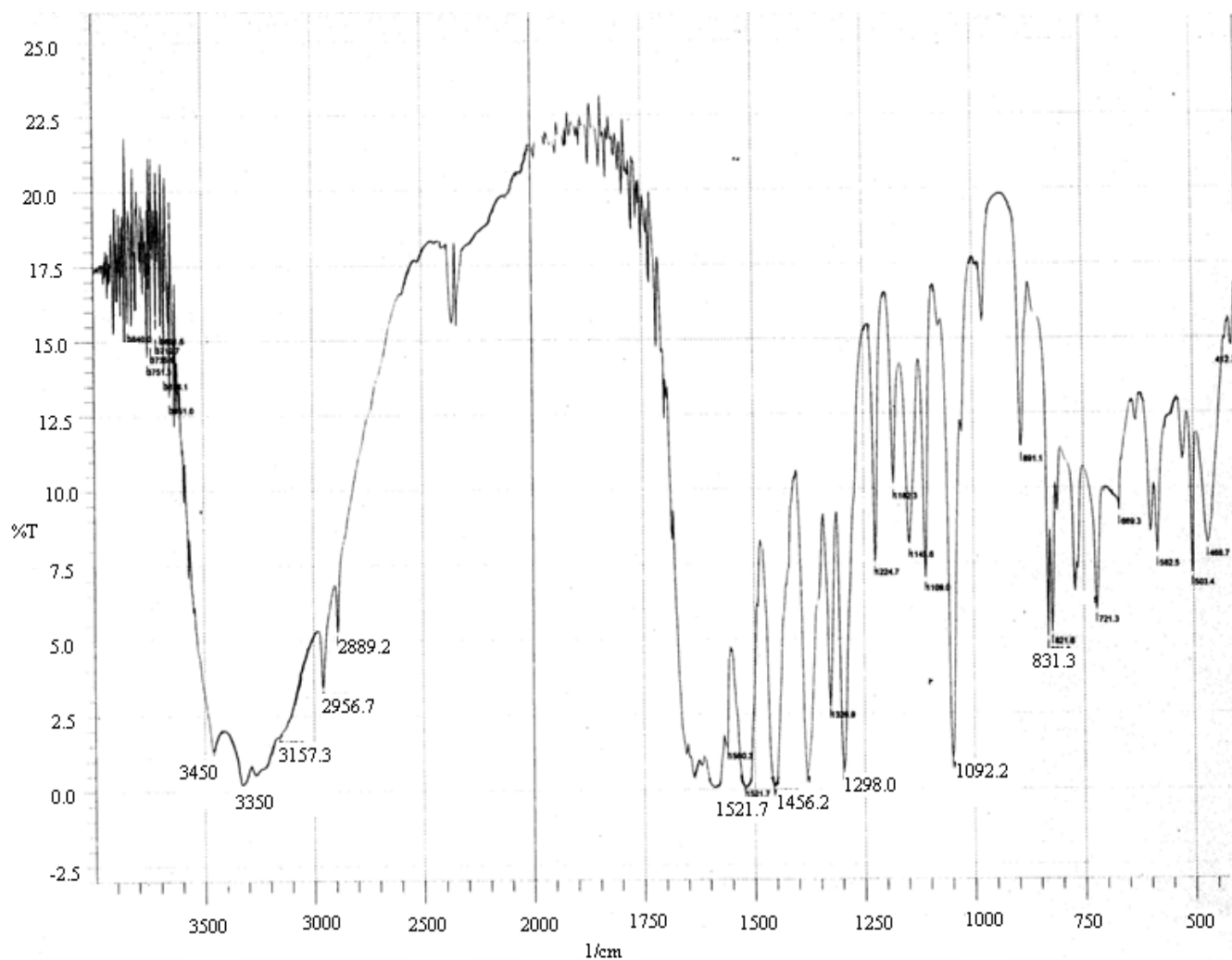


**Figure IV-8.** IR spectrum of **1** (KBr pellet)

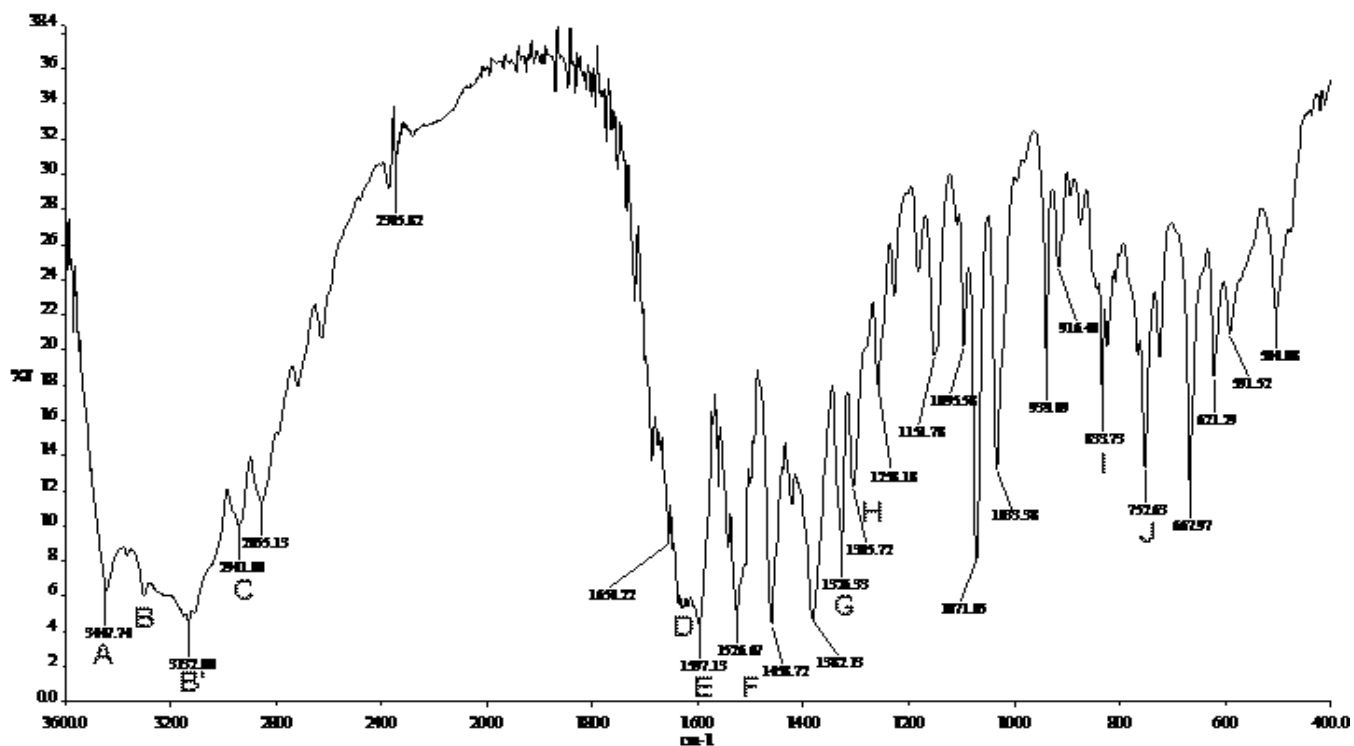
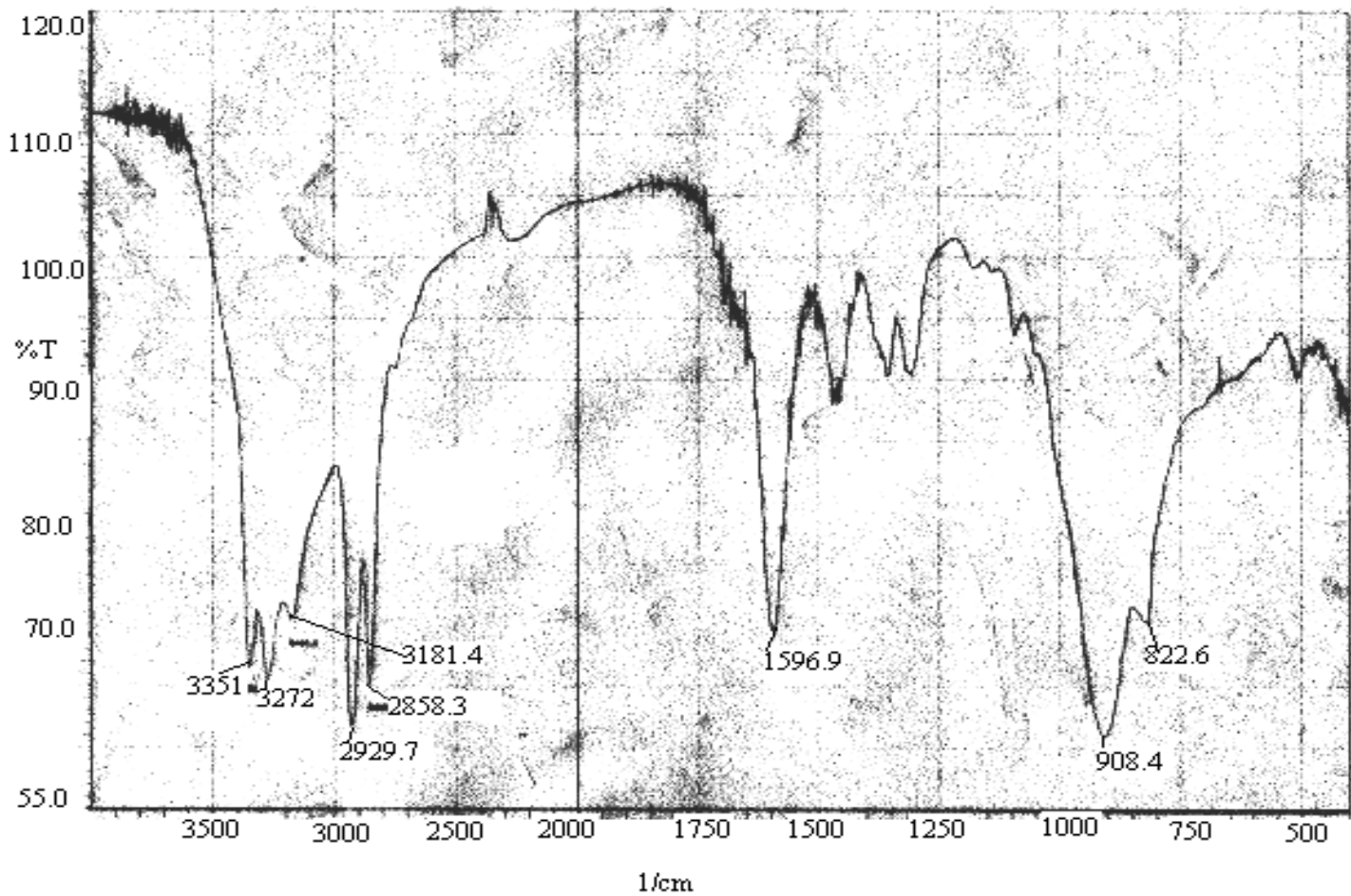


Figure IV-9. IR spectrum of compound 2 (KBr pellet)

- 
- A: Hydrogen bonded  $\nu(\text{OH})$  vibration;
  - B,B':  $\nu(\text{NH})$  vibration of  $\text{NH}_2(2)$  of pterin and 'en' ligands;
  - C:  $\nu(\text{CH})$  vibrations;
  - D,F:  $\nu(\text{C}=\text{C})$  and  $\nu(\text{C}=\text{N})$  vibrations;
  - E:  $\nu_{\text{as}}(\text{CO}_2')$ , (N – H) bending vibrations;
  - G:  $\nu_{\text{s}}(\text{CO}_2')$ ;
  - H:  $\nu(\text{C} - \text{O})$  of pterin phenoxide(4) group;
  - I,J: out- of- plane C – H bending vibration.
-



**Figure IV-10.** IR spectrum of 1, 2-diaminoethane (en)

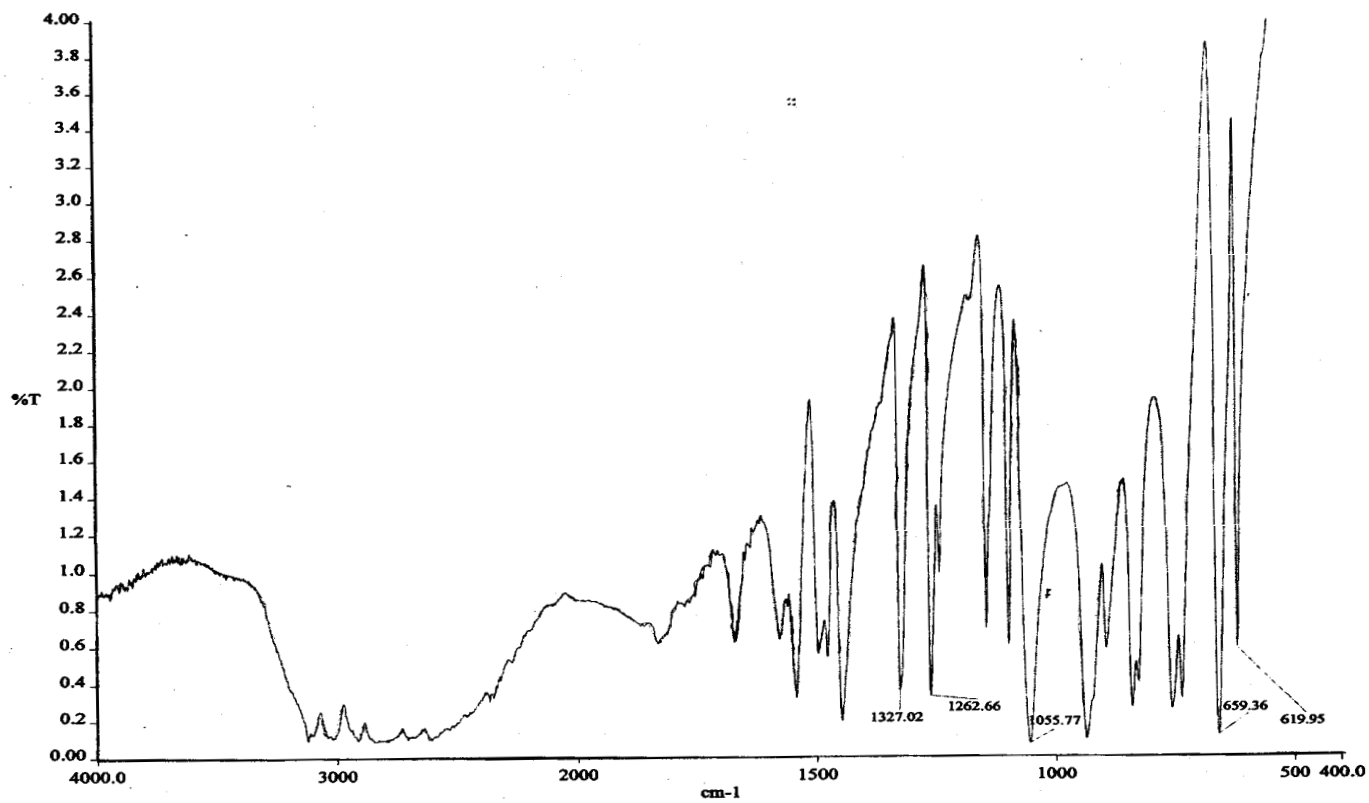


Figure IV-11. Spectrum of imidazole (Im) (KBr pellet)

## UV-VIS spectroscopy

**Table IV-7.** Electronic spectral data of **1** in H<sub>2</sub>O and **2** in CH<sub>3</sub>OH

Sl. No.	Compound	$\lambda_{\max}$ nm (log $\epsilon$ )
1.	<b>1</b>	258sh(3.97), 270(4.09), 341sh(3.51), 370(3.75), 401sh(3.41), 408sh(3.21), 946sh(2.74), 1004sh(2.745), 1057sh(2.76)
2.	<b>2</b>	270(4.26), 369(3.88), 542br(1.12), 620br(0.96), 698(1.21), 748(1.24), 812(1.43), 921br(0.88), 1063sh(1.32)

Electronic spectra (H<sub>2</sub>O) of **1** and (CH<sub>3</sub>OH) **2** are shown in Figure IV-12 and IV-13 respectively with Table IV-7 summarizing their essential features. Both of these two spectra are dominated by two intense bands at 270 nm and 369 – 370 nm, assignable to ligand  $\pi \rightarrow \pi^*$  and LMCT bands respectively. Besides these, at high resolution a few broad, longer wavelength bands of lower intensity could be identified; they are usually associated with vibronic fine structures. Such spectral features may be elucidated in the light of energy level diagram of the Ni(II) d<sup>8</sup> system and symmetry considerations. Scheme IV-7 shows the partial Orgel diagram diagram of the d<sup>8</sup> system in an octahedral environment along with two specific examples including their band assignments.<sup>90</sup> Splitting of the middle

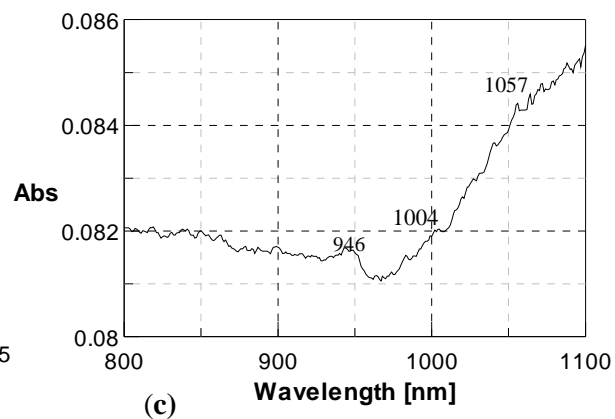
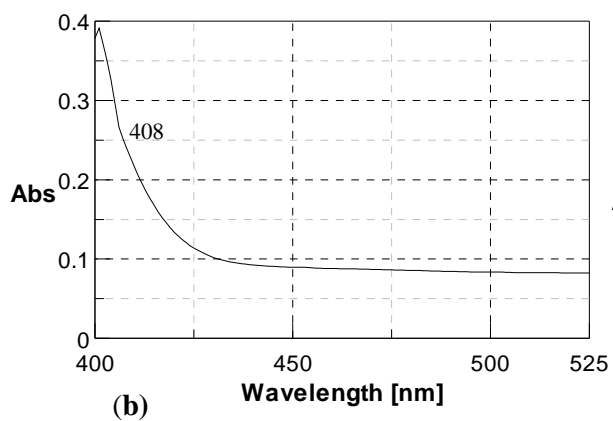
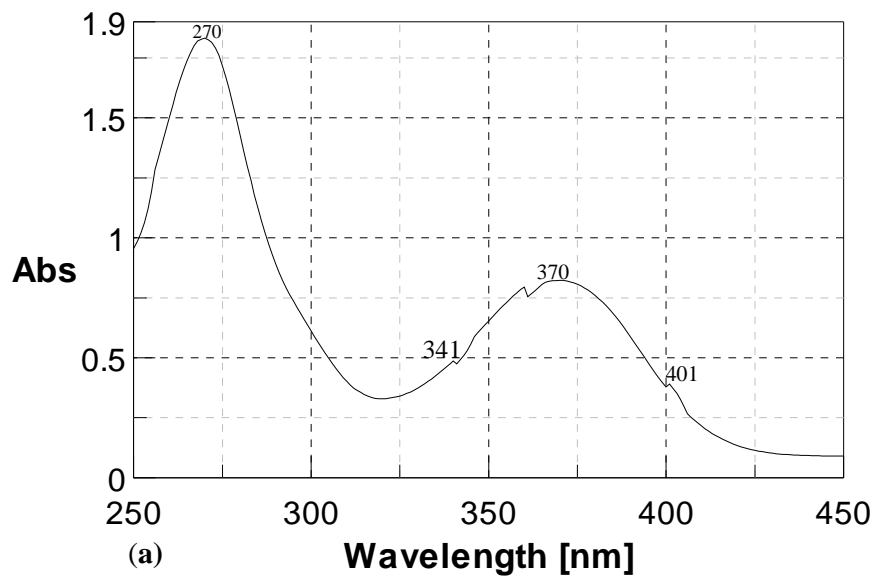


**Figure IV-12.** Electronic spectra of **1** in H<sub>2</sub>O ( $1.48 \times 10^{-4}$  mol dm<sup>-3</sup>)

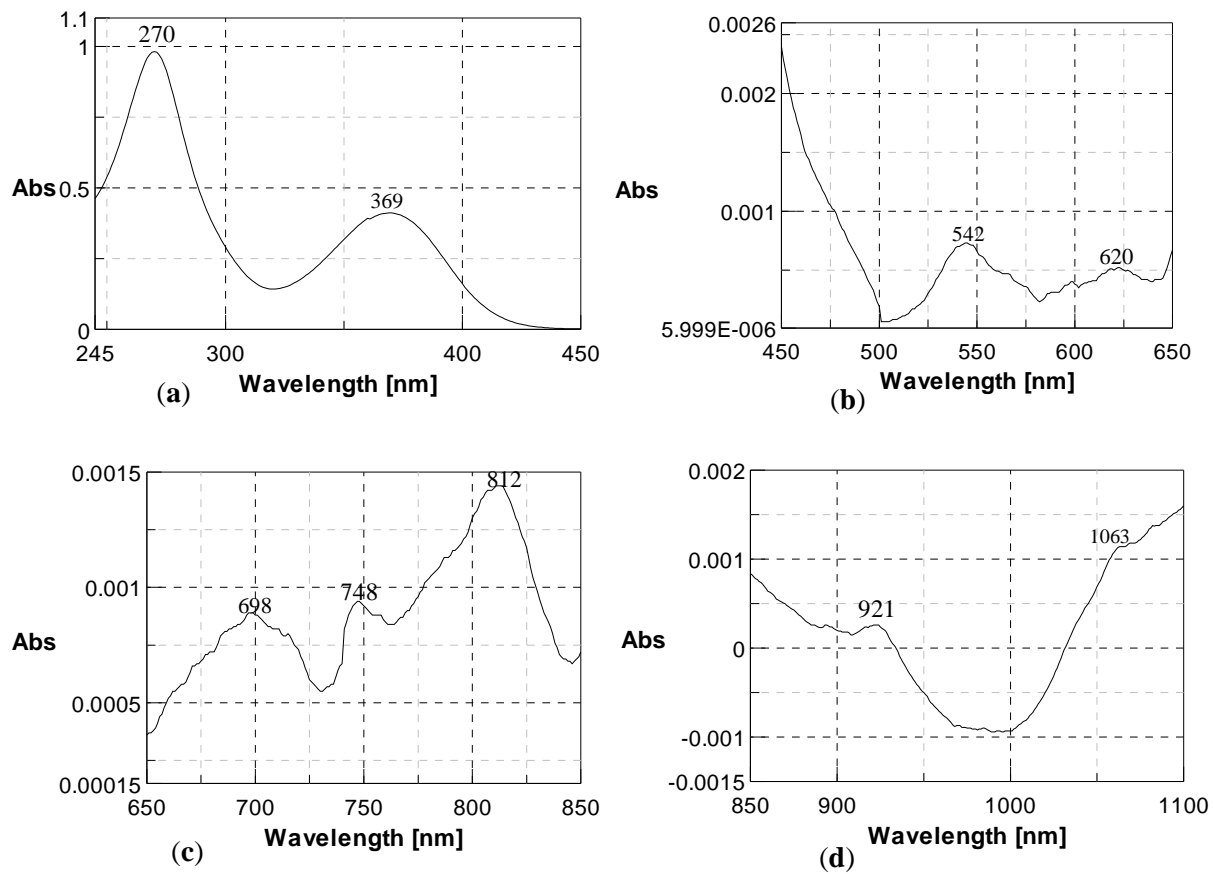
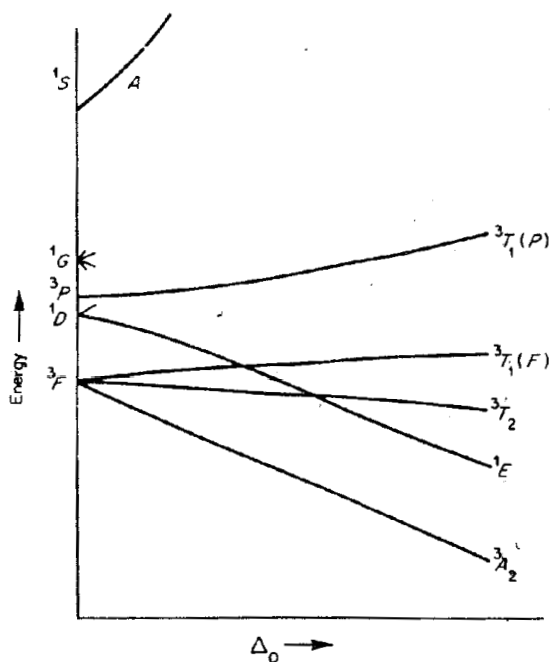
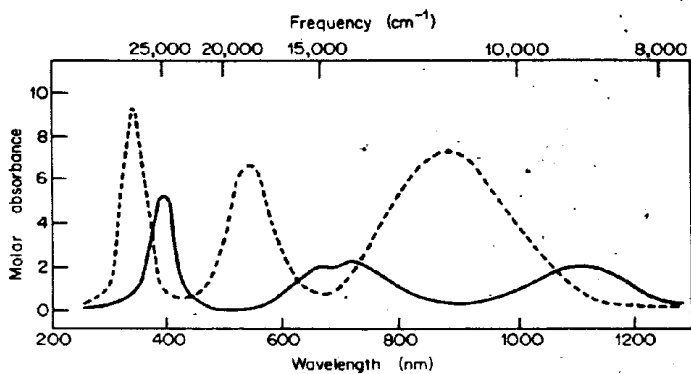


**Figure IV-13.** Electronic spectra of **2** in  $\text{CH}_3\text{OH}$



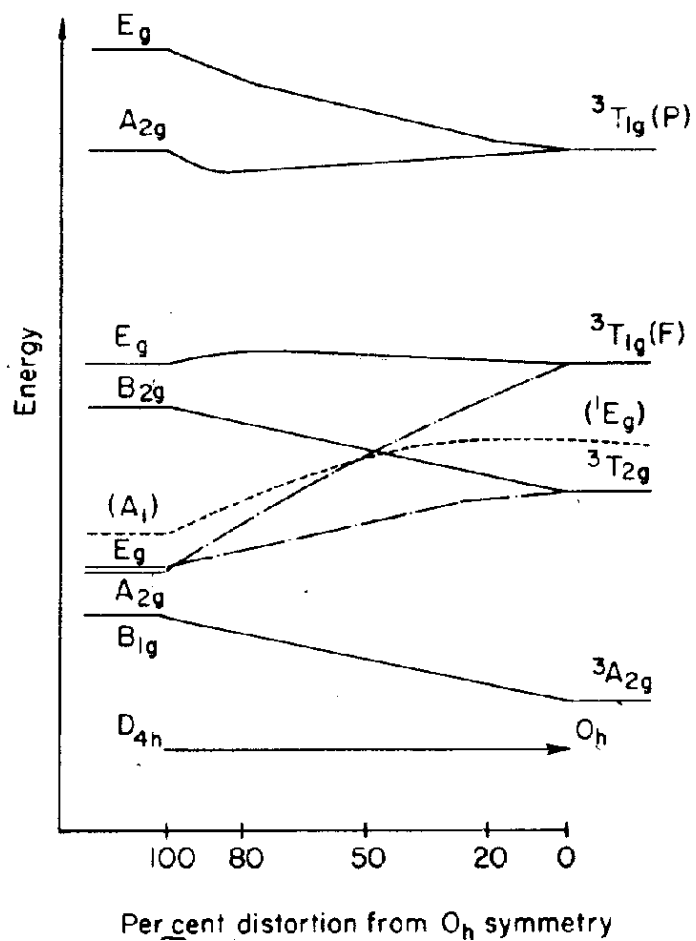
Partial energy-level diagram for a  $d^8$  ion in an octahedral field, showing the triplet states and only the lowest singlet state.



Absorption spectra of  $[\text{Ni}(\text{H}_2\text{O})_6]^{2+}$  (solid curve) and  $[\text{Ni}(\text{en})_3]^{2+}$  (dashed curve).

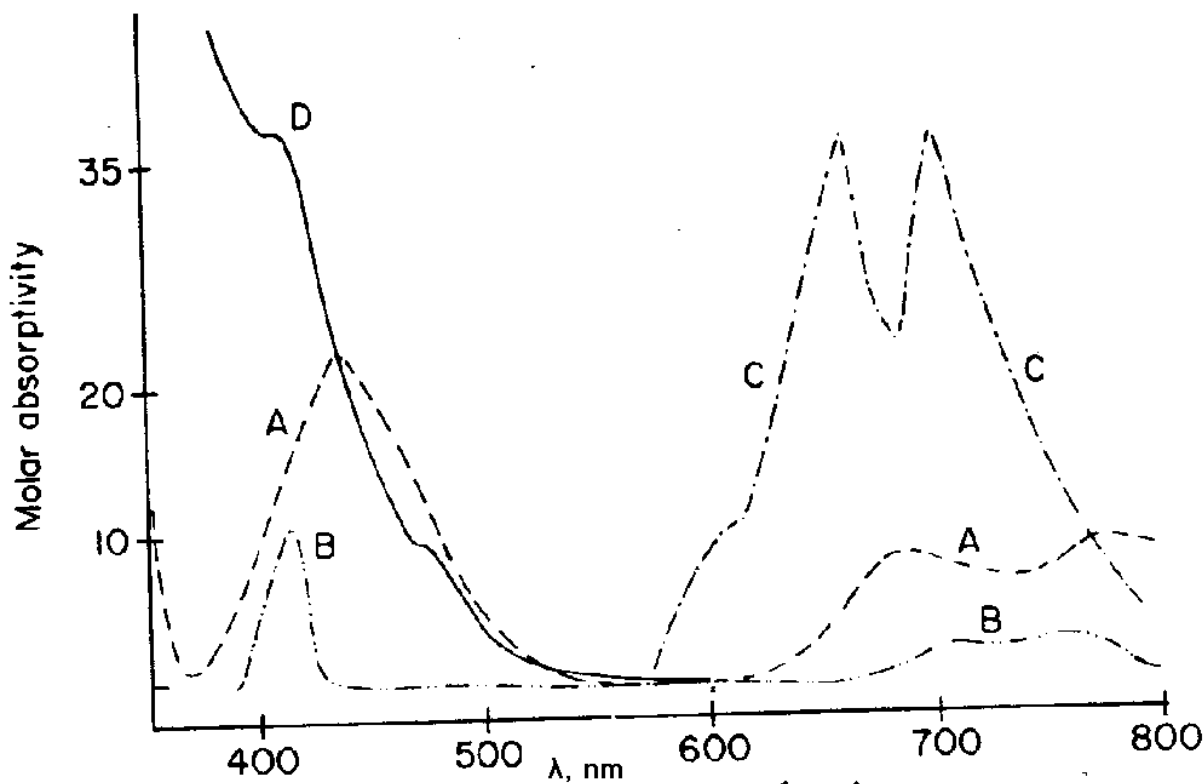
Transition	Approximate band positions ( $\text{cm}^{-1}$ )	
	$[\text{Ni}(\text{H}_2\text{O})_6]^{2+}$	$[\text{Ni}(\text{en})_3]^{2+}$
${}^3A_{2g} \rightarrow {}^3T_{2g}$	9,000	11,000
${}^3A_{2g} \rightarrow {}^3T_{1g}(F)$	14,000	18,500
${}^3A_{2g} \rightarrow {}^3T_{1g}(P)$	25,000	30,000

### Scheme IV-7



**Scheme IV-8** Effects of tetragonal distortion on the energy levels of Ni(II). Reference: C.

Furlani, and G. Sartori, *J. Inorg. Nucl. Chem.*, **8**, 126 (1958).



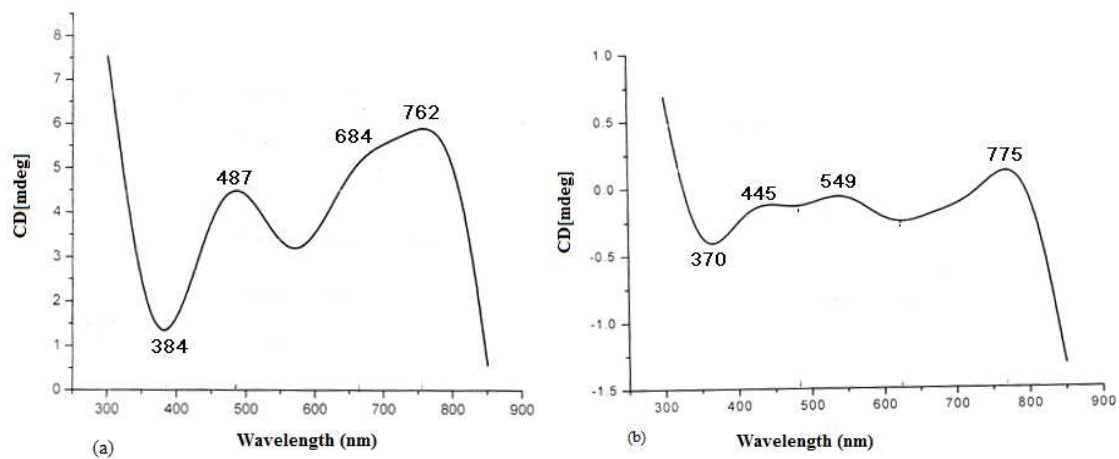
**Scheme IV -9** Electronic absorption spectra of some nickel complexes. A.  $\text{Ni}(\Phi_3\text{PO})_4(\text{ClO}_4)_2$  in  $\text{CH}_3\text{NO}_2(D_{2d})$ ; B,  $\text{Ni}[(\text{CH}_3)_2\text{SO}]_6(\text{ClO}_4)_2$  in  $(\text{CH}_3)_2\text{SO}(O_h)$ ; C,  $\text{NiCl}_4^{2-}$  in  $\text{CH}_3\text{NO}_2(T_d)$ ; D,  $\text{Ni(II)(dimethylglyoxinate)}_2$  in  $\text{CHCl}_3(D_{4h})$ . Curve C is a plot of  $\epsilon/5$ .

band in the  $[\text{Ni}(\text{H}_2\text{O})]^{2+}$  spectrum is due to spin-orbit coupling which mixes the  ${}^3T_{1g}(F)$  and  ${}^1E_g$  states which are quite close in energy at the  $\Delta_0$  value provided by  $6\text{H}_2\text{O}$ , while in the stronger crystal field of the  $3en$  they are far apart so that no significant mixing occurs. Scheme IV-8 shows the effect of lowering of symmetry from  $O_h \rightarrow D_{4h}$  on the electronic energy levels of the  $d^8$  system.<sup>89</sup> As evident from the x-ray structural data of both **1** and **2**, there is considerable

departure from regular octahedral geometry associated with additional splitting of the energy levels, some of them being even raised in energy (Scheme IV-8). The more numerous signals in the LMCT region [325 – 425 nm; Figure IV-12(b) and Figure IV-13(b)] of **1**, may be ascribed to its lower symmetry as compared to that of **2**. Scheme IV-9 illustrates the effect of changes in symmetry on the electronic spectra of Ni(II) complexes; for a square planar complex ( $D_{4h}$ ), there is little absorption in the longer wavelength region (600 – 800 nm).<sup>89</sup> In the light of Scheme IV-7 to IV-9 the broad, longer wavelength bands for **1** and **2** are assigned to spin-allowed as well as spin-forbidden ‘d-d’ transitions with considerable intensity stealing from the LMCT band (369 – 370 nm).<sup>31</sup>

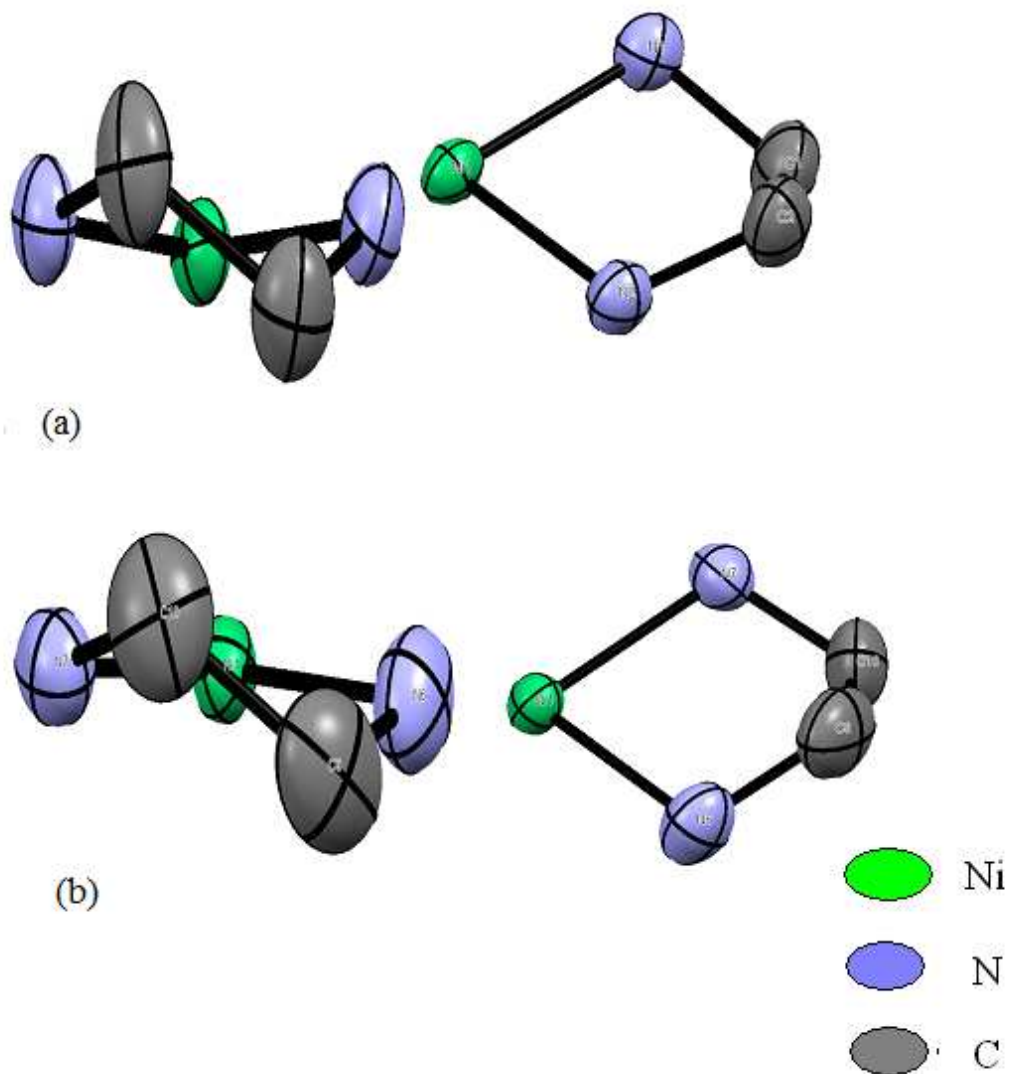
### **Circular dichroism spectroscopy**

Figure IV-14 shows the CD spectra of **1** and **2** in H<sub>2</sub>O indicating their low symmetry environments. Both signs and magnitudes of the associated Cotton effects need attention. The negative Cotton effects around 370-384 nm may be assigned to LMCT transition. For **1** [Figure IV-14(a)] three positive Cotton effects could be identified at 487 nm, 684 nm and 762 nm respectively. In case of **2** [Figure IV-14(b)] such Cotton effects are observed at 445 nm, 549 nm and 775 nm, respectively. But the magnitudes of the Cotton effects are larger for **1** as compared to those of **2**. This is due to greater distortion from regular octahedral geometry for **1**. The  $\delta$ -conformation of the ‘en’ chelate ring as observed from x-ray structural data, most likely decides the sign of the Cotton effects around 400-850 nm which correspond to some of the electronic transitions enlisted in Table IV-7.

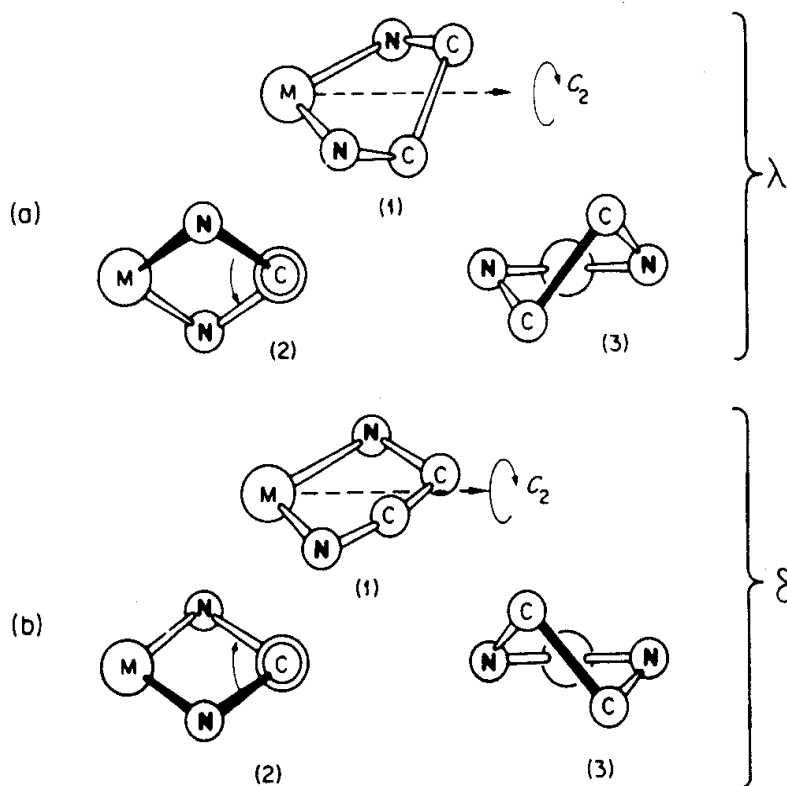


**Figure IV-14.** CD spectra in H<sub>2</sub>O: (a) **1** ( $2.55 \times 10^{-3}$  M); (b) **2** ( $2.26 \times 10^{-3}$  M).

---



**Figure IV-15.**  $\delta$  – conformation of the ethylenediamine chelate ring for (a) **1** and (b) **2**, as obtained from their x-ray structural data; other donor atoms [Figure IV-1 and IV-2] are omitted for enhancing the effect chelate ring pucker.



**Scheme IV-10** Different way of viewing the puckering of ethylenediamine chelate rings. The absolute configurations  $\lambda$  and  $\delta$  are defined.<sup>79</sup>

Scheme IV-10 shows the  $\lambda$ -/ $\delta$ -puckering of ethylene diamine (en) chelate ring. Projections of the x-ray structural data of **1** and **2** for viewing the puckering of the 'en' chelate ring in each case, are shown in Figure IV-15. A comparison with Scheme IV-10 indicates  $\delta$ -conformation of the 'en' ring in each case. Now the most important inference of this chiroptical study is that steric repulsion of the two chelate rings associated with the pterin ligand residue ( $L^{2-}$ ) could be minimised only for the  $\delta$ -conformation, as above.

## Fluorescence Emission Spectra

The fluorescence emission spectra (CH<sub>3</sub>OH) of **1**, **1R**, **2**, and **2R** are shown in Figure IV-16 and IV-17 respectively. In all these cases the emission maximum appears at 450 nm. For the pterin ligand (in aqueous NaOH solution) such emission maximum appears (Figure II-11) at 449 nm. It is apparent that on mixed ligand complex formation in **1** and **2**, there is considerable drop in fluorescence intensity, with the emission maximum position remaining essentially unchanged. Apparently there is some pathway through which the vibronic energy can dissipate, associated with this drop in fluorescence intensity. Again, the enhanced fluorescence intensity of the NaBH<sub>4</sub> reduced compounds (**1R** and **2R**) can be correlated with the greater electronic circulation in the 7, 8-dihydro form of the pterin ligand residue. (L<sup>2-</sup>; Scheme IV-6). Existence of the 7, 8-dihydro form in **1R** and **2R** could be inferred from the <sup>1</sup>H NMR spectral data of a Cu(I) complex in chapter II. Most organic fluorescence molecules contain conjugated system of double bonds with extended  $\pi$  orbitals in a planar cyclic/rigid structure and not many loosely coupled substituents through which the electronic energy can dissipate. Even the pH dependence fluorescence property is interesting, e.g. no fluorescence is observed for the protonated form of biopterin but the anion is strongly fluorescent.<sup>35-37</sup>

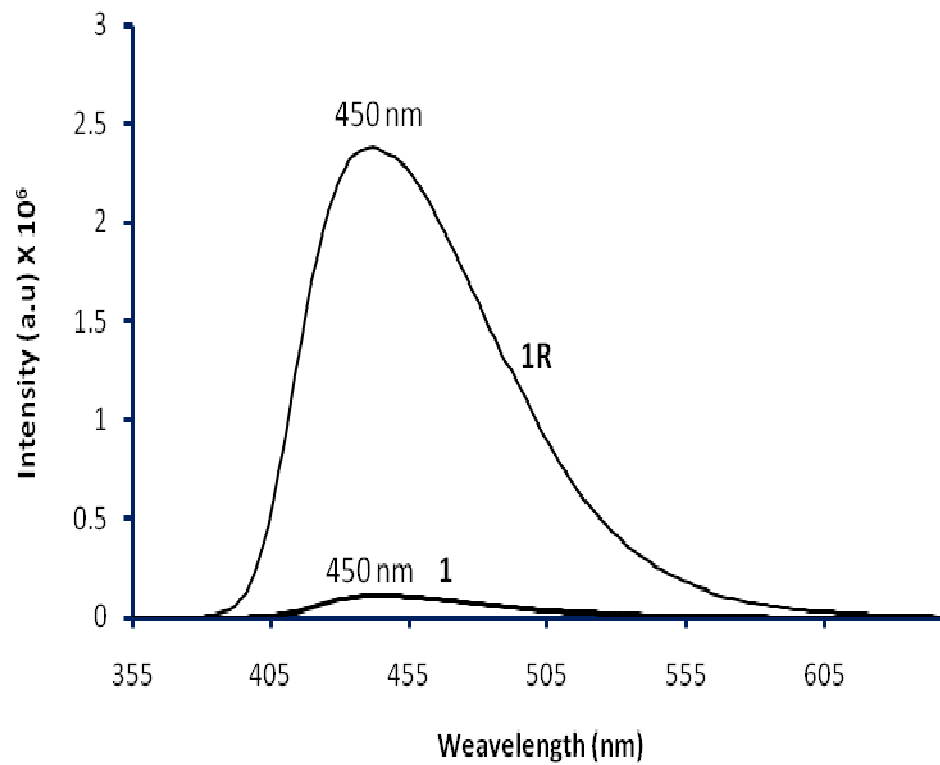


**Figure IV-16.** Fluorescence emission spectra of **1** (CH<sub>3</sub>OH, 1.4 x 10<sup>-4</sup> M), **1R** (CH<sub>3</sub>OH, 1.4x10<sup>-4</sup> M).

---

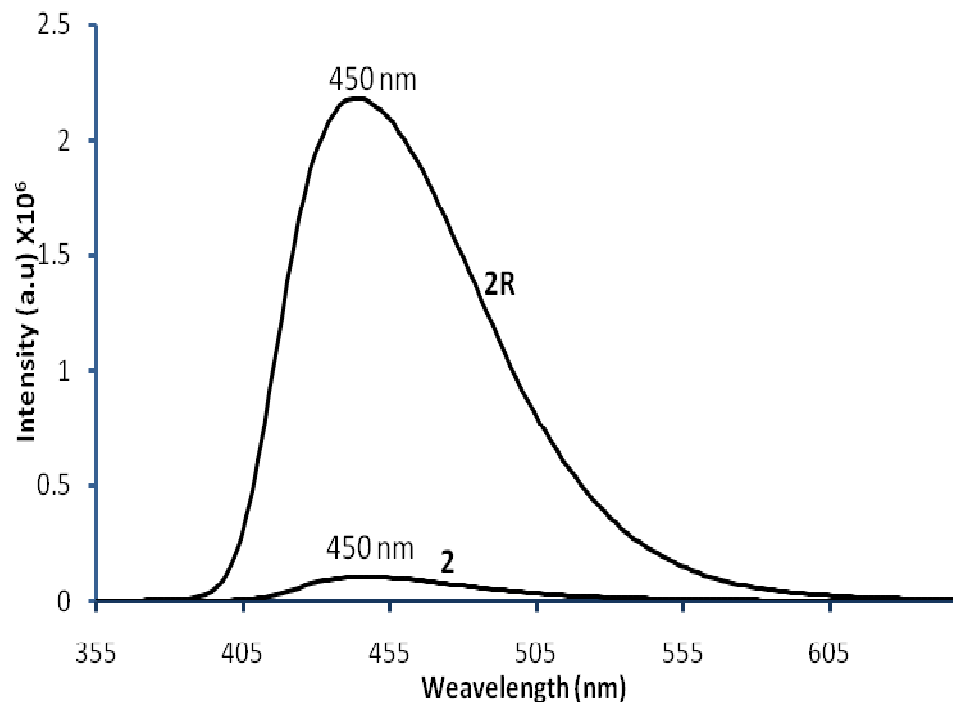


**Figure IV-17.** Fluorescence emission spectra of **2** (CH<sub>3</sub>OH, 1.4 x 10<sup>-4</sup> M), **2R** (CH<sub>3</sub>OH, 1.4 x 10<sup>-4</sup> M).

---

### EPR spectroscopy and magnetic susceptibility data

Magnetic susceptibility data ( $\mu_{\text{eff}}$ , 299K) of complexes **1** and **2** are 2.90 BM and 2.89 BM respectively. Both these values are close to the spin-only value (2.83 BM) for two unpaired electrons, with small orbital contribution. However, their EPR spectral data could not be recorded properly due to the problem of line broadening. For d<sup>8</sup> ion [e.g. Ni(II)] in distorted octahedral fields, the zero-field splitting becomes larger and EPR signals are quite difficult to observe. As an example, the EPR spectral response of **2** is shown in Figure IV-18 and it is inconclusive. Here the  $\mu_{\text{eff}}$  values provide the necessary guide lines about electronic structures here.

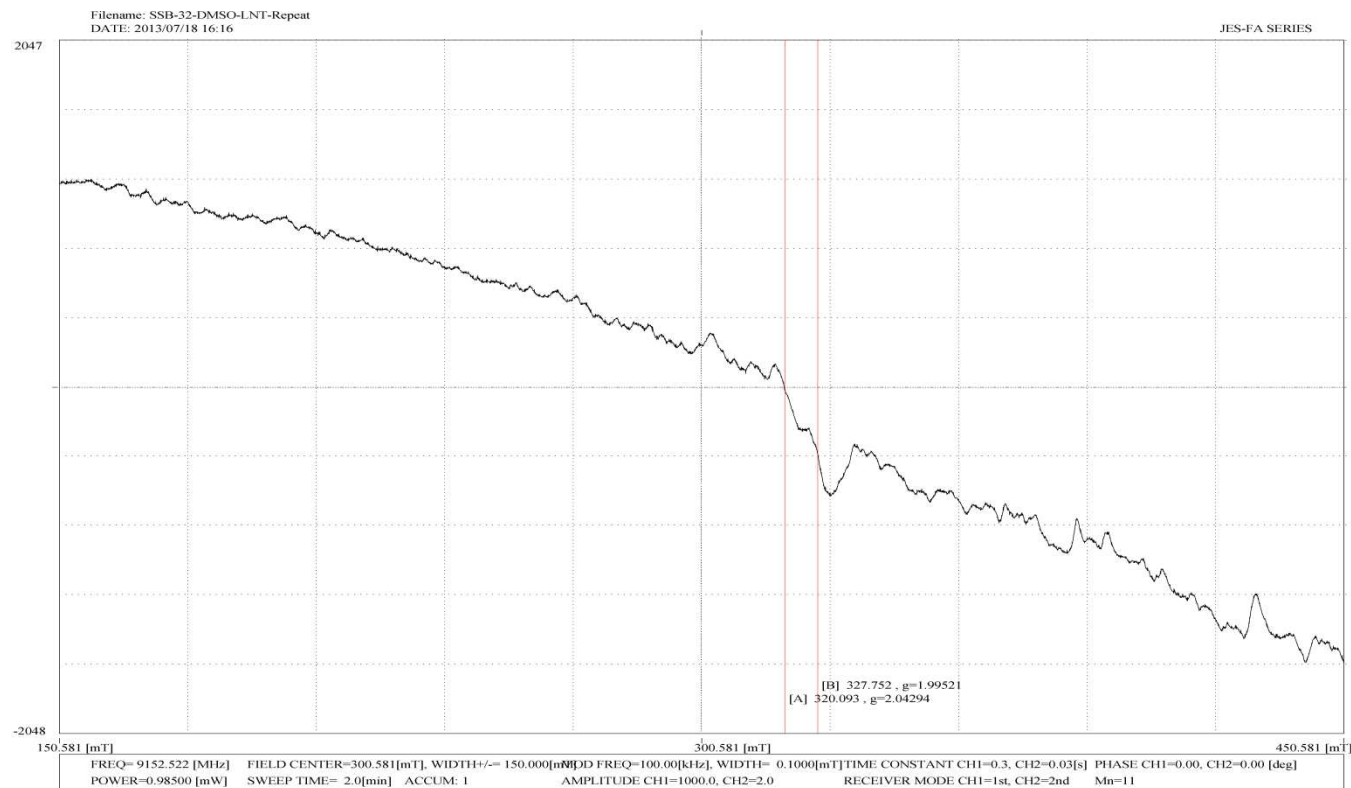


**Figure IV-18.** X-band EPR spectrum of **2** in DMSO at 77K.

## Cyclic voltammetry

Figure IV-19 shows the cyclic voltammetry data of **2** in DMSO. A metal-centred reduction occurs at -0.744 V; the corresponding re oxidation peak could be located at -0.669 V. The  $\Delta E_p$  value (75 mV) indicates the quasi-reversible nature of this redox process; besides this, a ligand reduction peak occurs at - 1.651 V. Here the quasi-reversible process can be assigned as follows –



This facile change over between the two oxidation states of nickel can be justified in terms of the relevant Frost diagram (Scheme IV-11). It is evident that the change over between the +1 and +2 oxidation states of nickel can be achieved with small change in free energy ( $\Delta G^\circ = -nFE^\circ$ ). Significance of this information obtained in the time scale of cyclic voltammetry, is further clarified during the reactivity study with  $\text{NaBH}_4$  (shown later) as well as isolation of a dark coloured compound (**2R**) through  $\text{NaBH}_4$  reduction where both the metal and pterin ligand centers are in the reduced forms [Ni(I) and 7, 8-dihydro state of pterin].

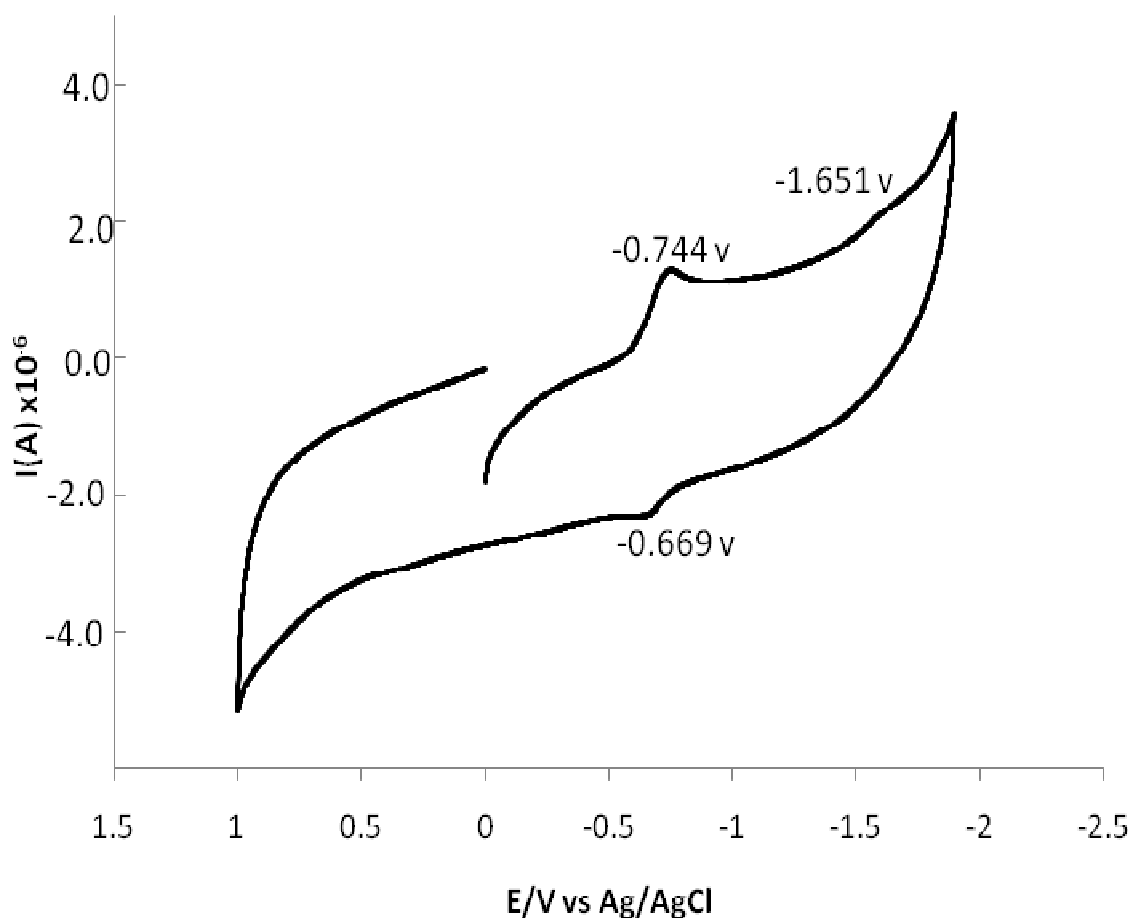


**Figure IV-19.** Cyclic voltammogram of **2** in DMSO (0.1 mM, 0.1M TBAP, GCE,  $100 \text{ mVs}^{-1}$ )

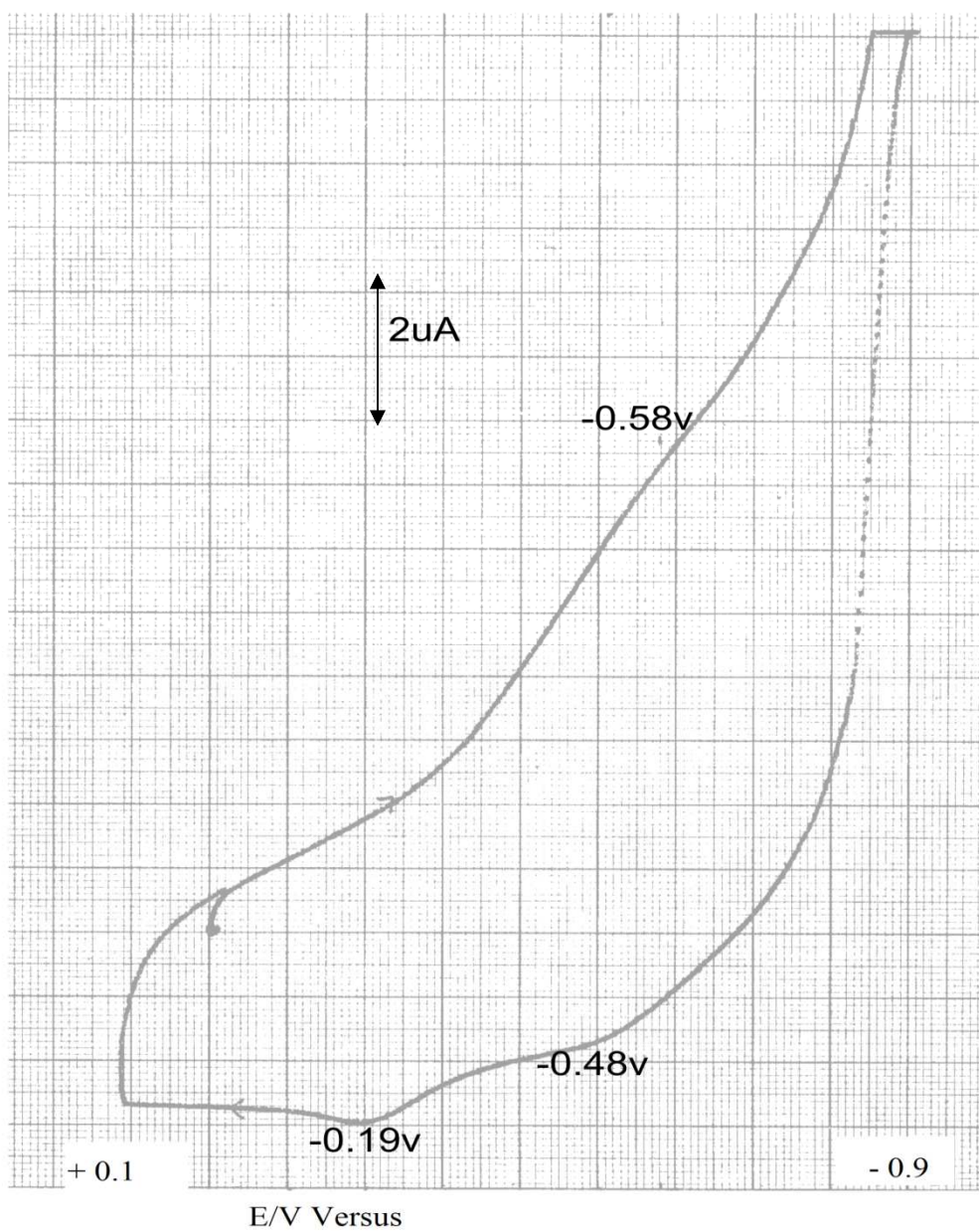


**Figure IV-20.** Cyclic voltammogram of **1** in H<sub>2</sub>O (1 mM, 0.1 M KNO<sub>3</sub>, GCE, 250 mVs<sup>-1</sup>)

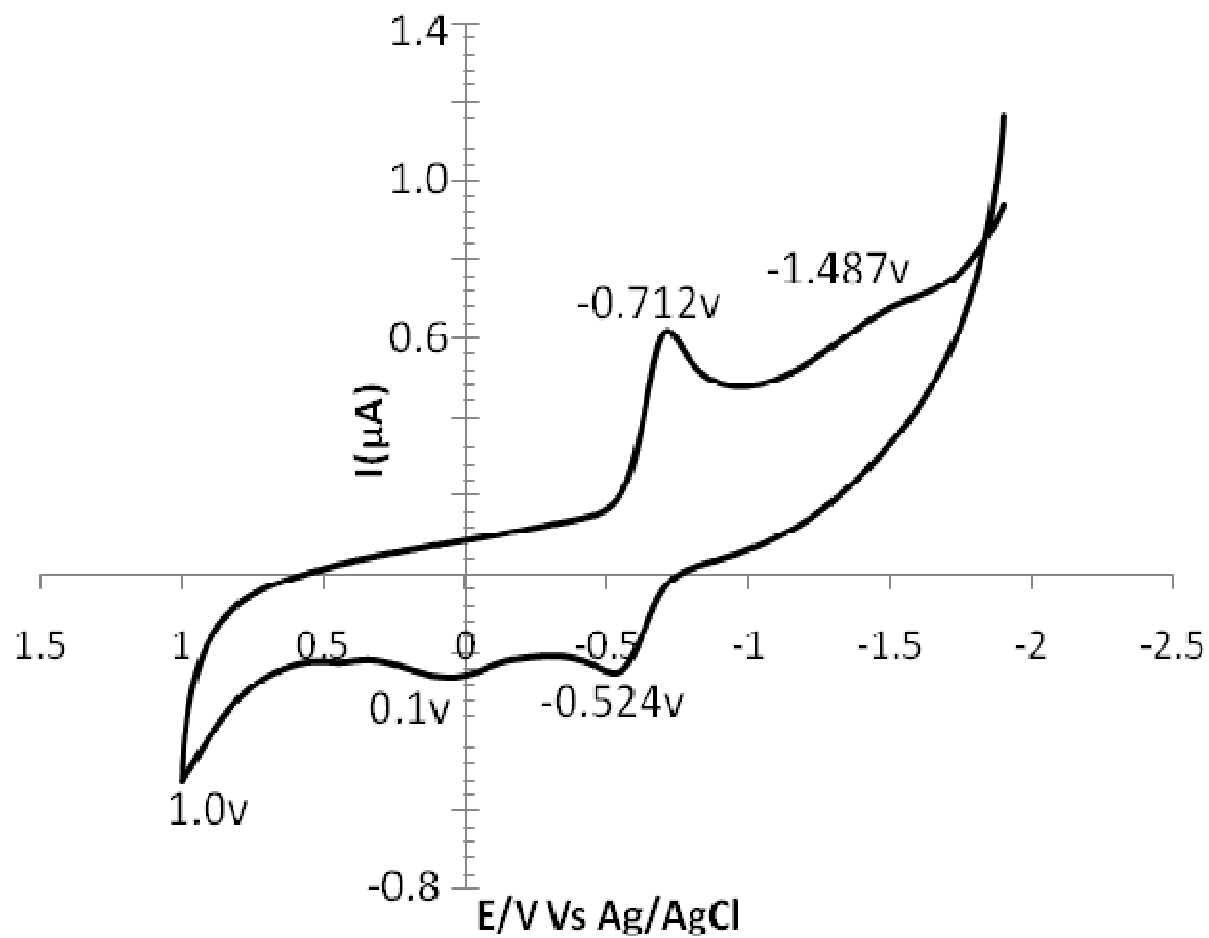
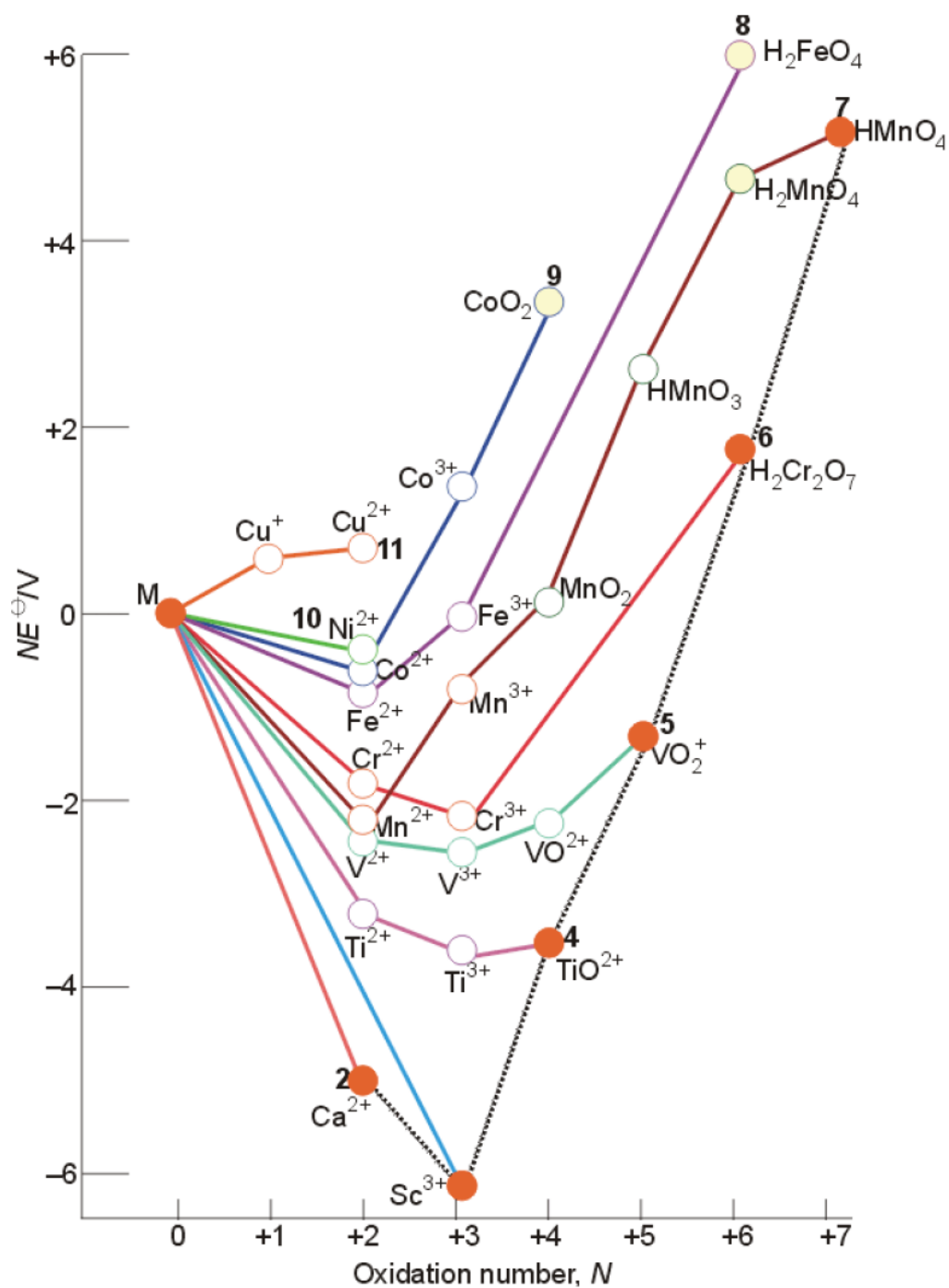


**Figure IV -21.** Cyclic voltammety data of **1** in DMSO ( 1mM, 0.1M TBAP, GCE,  $100 \text{ mVs}^{-1}$ )

---



**Scheme IV-11** Frost diagram of the first transition series in acidic solution ( $\text{pH} = 0$ )<sup>91</sup>

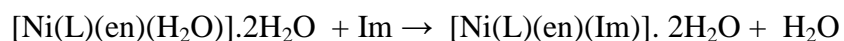
Elucidation of these metal- and pterin-centred reductions is provided later in the light of Frontier orbital energies (DFT).

Cyclic voltammetry data of **1** in H<sub>2</sub>O is shown in Figure IV-20. Here the metal-centred reduction process [Ni(II) → Ni(I)] could be located at – 0.58 V; the reduction product is quite unstable in aqueous medium, leading to essentially irreversible behavior. Two reoxidation peaks appear at -0.48 V and -0.19 V respectively.

Cyclic voltammetry data of **1** in DMSO is depicted in Figure IV-21. The metal-centred reduction and reoxidation peaks appear at -0.712 V and -0.524 V respectively ( $\Delta E_p = 188$  mV). Obviously, in DMSO the reduced species has a longer life time as compared to that in H<sub>2</sub>O. A ligand reduction peak appears at -1.487 V.

### **Reactivity of 1 towards imidazole**

**1** possesses an aquo group [Figure IV-1] and provides with an opportunity for exploring its group substitution reaction using imidazole (Im) as the reagent. The ubiquitous nature of the histidine residue in metalloproteins, makes this study all the more significant as imidazole is a model of histidine. Kinetics of the following reaction is presented here:



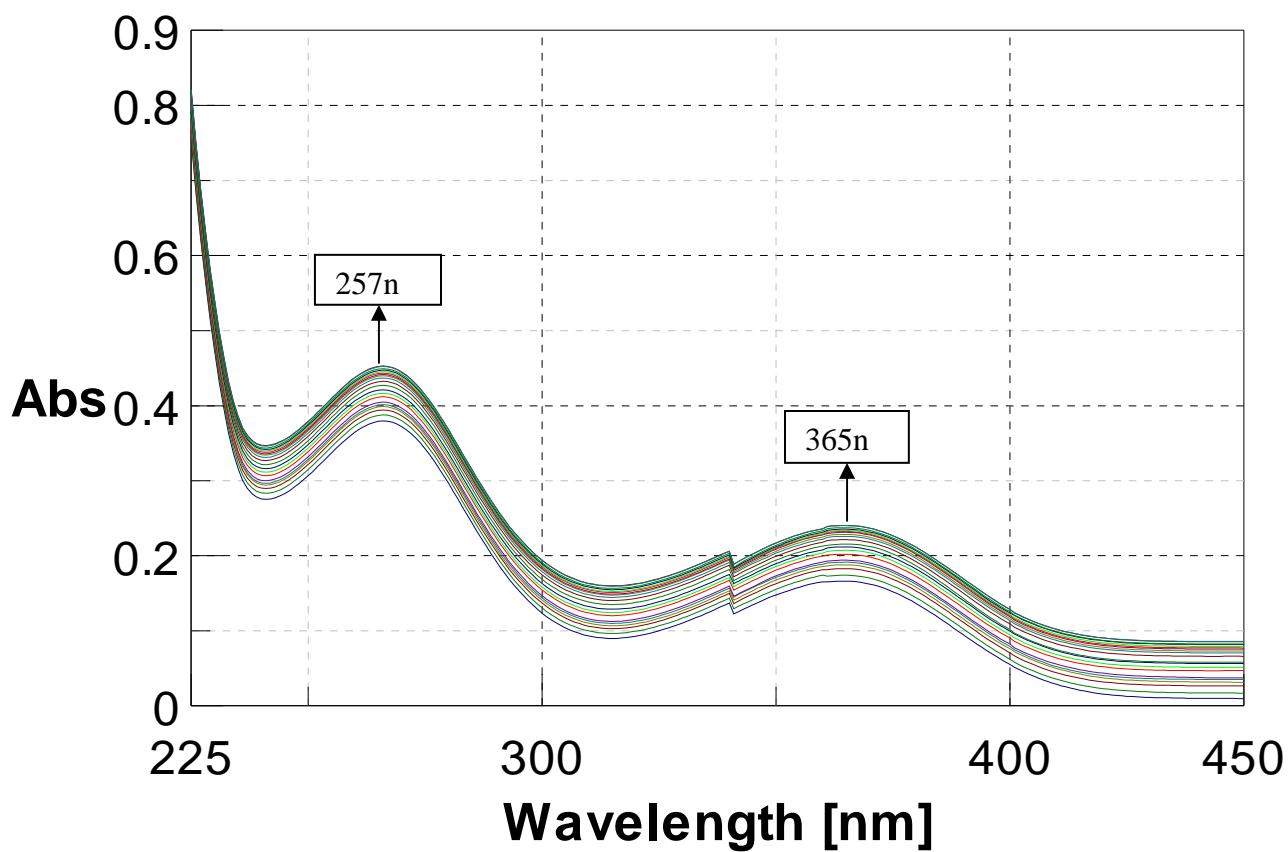


**Figure IV-22.** Absorption spectral changes recorded at 2 min interval during the reaction of (1) ( $5.8 \times 10^{-5} \text{M}$ ) with imidazole (Im) ( $4.8 \times 10^{-3} \text{M}$ ) in  $\text{CH}_3\text{OH}$  at 311K. The break at 340 nm in the spectral curve is due to lamp change over inside the instrument.

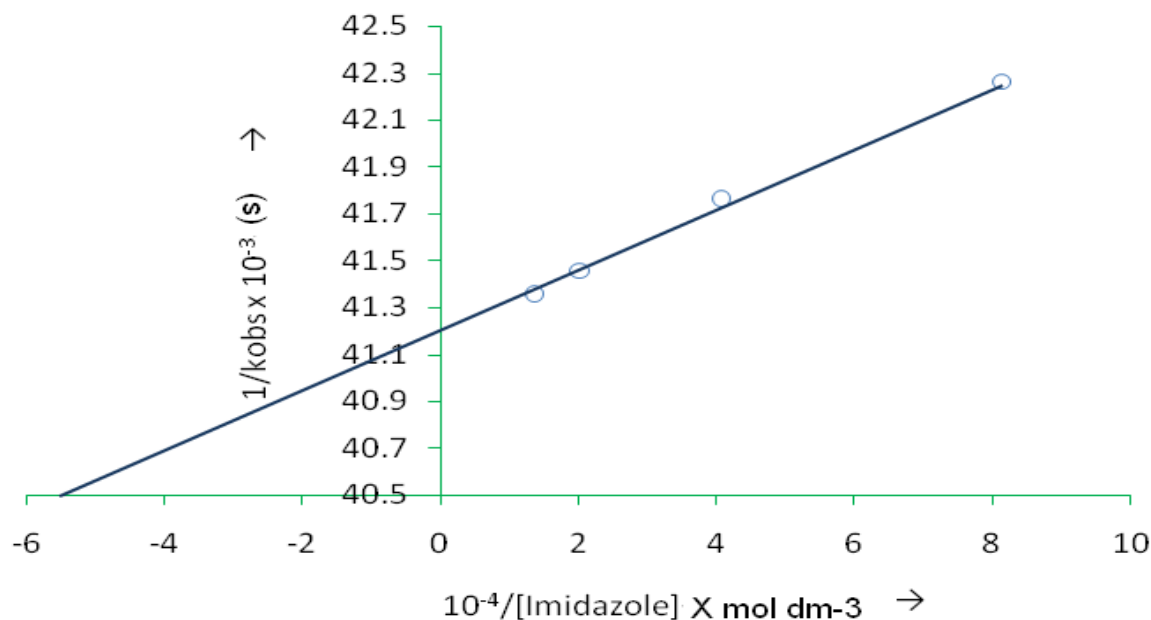
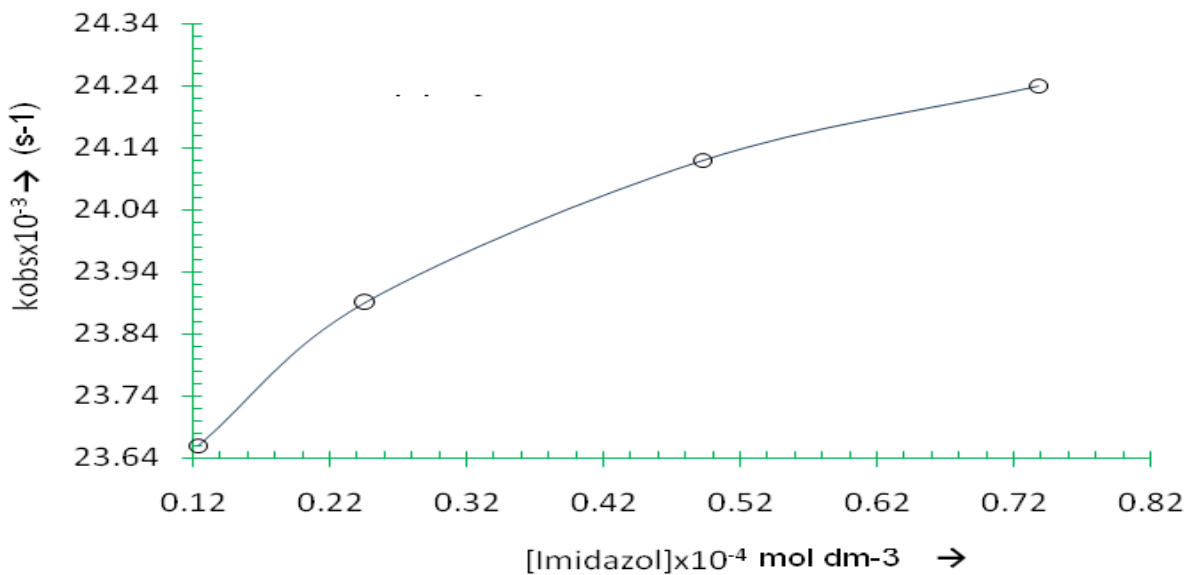
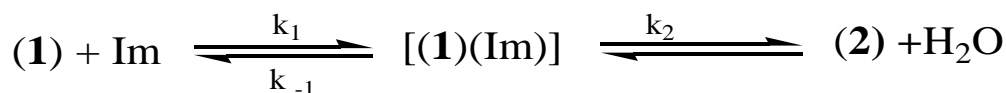


**Figure IV-23.** (a) Dependence of the rate of reaction of (1) ( $5.8 \times 10^{-5} \text{ M}$ ) with 20-100 times Im in  $\text{CH}_3\text{OH}$  at 334K on Im; (b) the corresponding double reciprocal plot.

Stoichiometry of the above reaction has been established x-ray structurally (Figure IV-2), for characterizing the imidazole substituted product 2. For obtaining a reasonable reaction rate, a

higher temperature range (308 – 328K) has been utilized here. Figure IV-22 represents the absorption spectral changes during the reaction of **1** with imidazole in CH<sub>3</sub>OH. Kinetics of this reaction was followed at 365 nm under pseudo first order conditions (using ca. 20-100 times excess of imidazole) and four different temperatures (range 308 – 328K). From the Eyring plot the entropy of activation  $\Delta S^\ddagger$  was found to be -178.5 J mol<sup>-1</sup> deg<sup>-1</sup>; the negative  $\Delta S^\ddagger$  value indicates the associative nature of this substitution process. Absence of any isosbestic point in the overlay scans, suggests that the reactant aquo complex **1** is not converted directly into the imidazole substituted product **2**, but an intermediate step is involved. The negative  $\Delta S^\ddagger$  value points towards the formation of a 7-coordinated intermediate with imidazole, which is ultimately converted to **2** along with the loss of the aquo group.

Observed rate constants were determined by least square method from the plots of  $\log(A_\infty - A_t)$ , versus time, which were linear for almost 3 half-lives.<sup>92</sup> The average  $k_{\text{obs}}$  value of  $2.4 \times 10^{-2} \text{ s}^{-1}$  is consistent with a group substitution process.<sup>92,97,98</sup> Figure IV-23(a) shows the plot of observed rate constant ( $k_{\text{obs}}$ , sec<sup>-1</sup>) versus [Imidazole]. The reaction system exhibits saturation kinetics at high substrate (Im) concentration, indicating applicability of Scheme IV – 12.




---

**Scheme IV-12**

In terms of Scheme IV-12 the observed rate constant ( $k_{\text{obs}}$ ) can be represented as follows,<sup>93</sup> where [S] represents the concentrations of the substrate (Im):

$$k_{\text{obs}} = (k_2[S]/K_m + [S]), \quad (1)$$

where  $K_m = (k_2 + k_{-1})/k_1$  or

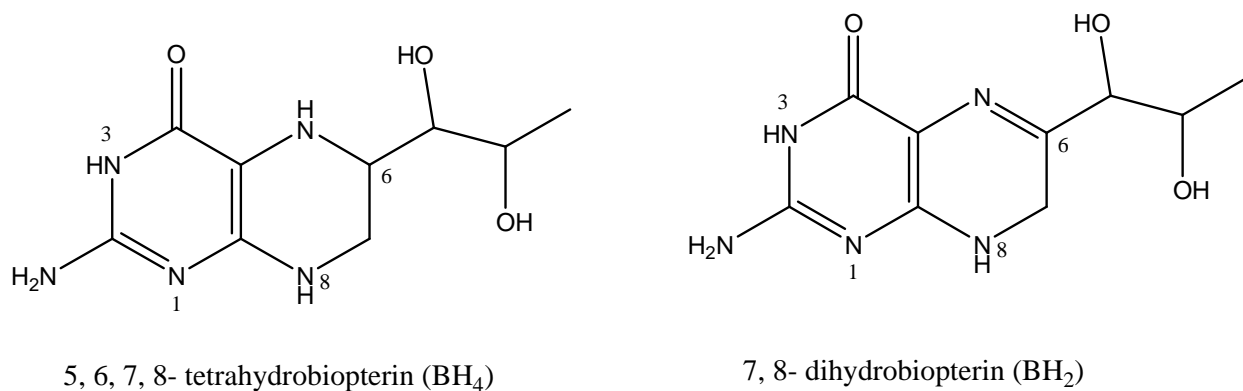
$$1/k_{\text{obs}} = 1/k_2 + K_m/k_2[S] \quad (2)$$

Where  $S = \text{Im}$

The plot of  $1/k_{\text{obs}}$  versus  $[1/\text{Im}]$  should give a straight line with  $1/k_2$  as the intercept and  $K_m/k_2$  as the slope. The x-axis intercept equals  $1/K_m$ . From the double reciprocal plot of  $1/k_{\text{obs}}$  versus  $[1/\text{Im}]$  [(Figure IV-23(b)),  $k_2$  and  $K_m$  were calculated as  $2.4 \times 10^{-2} \text{ s}^{-1}$  and  $1.82 \times 10^{-4} \text{ mol dm}^{-3}$  respectively at 308 K.

### Reactivity of **1** towards $\text{NaBH}_4$

Taking hints from the cyclic voltammetry data [Figure IV-21] of **1** as well as the Frost diagram of the Ni(I)/Ni(II) couple (Scheme IV-11), reactivity of **1** is explored towards a typical reducing agent like  $\text{NaBH}_4$ .  $\text{NaBH}_4$  is quite useful in pterin chemistry for its ability to reduce the pyrazine part of the pterin ring.<sup>22,23</sup> This aspect is relevant to the dihydro and tetrahydro states of biopterin (Scheme IV-13:  $\text{BH}_2/\text{BH}_4$ ), which is the essential cofactor for phenylalanine hydroxylase (PAH) type metalloenzymes.<sup>7,8,52-55</sup>



**Scheme IV-12**

---

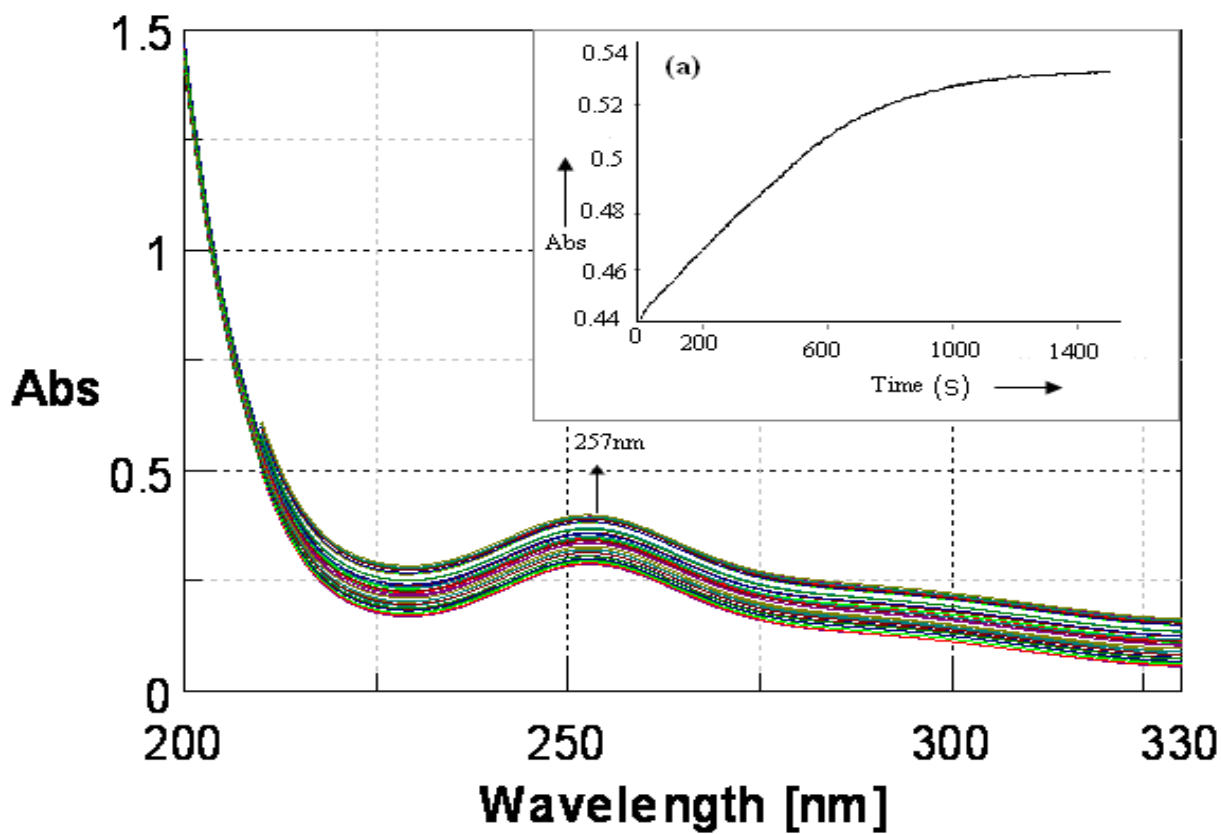
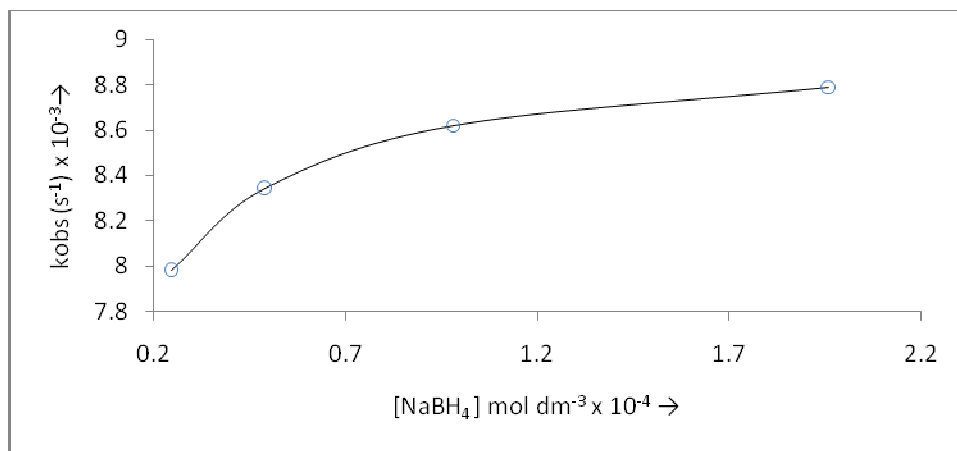
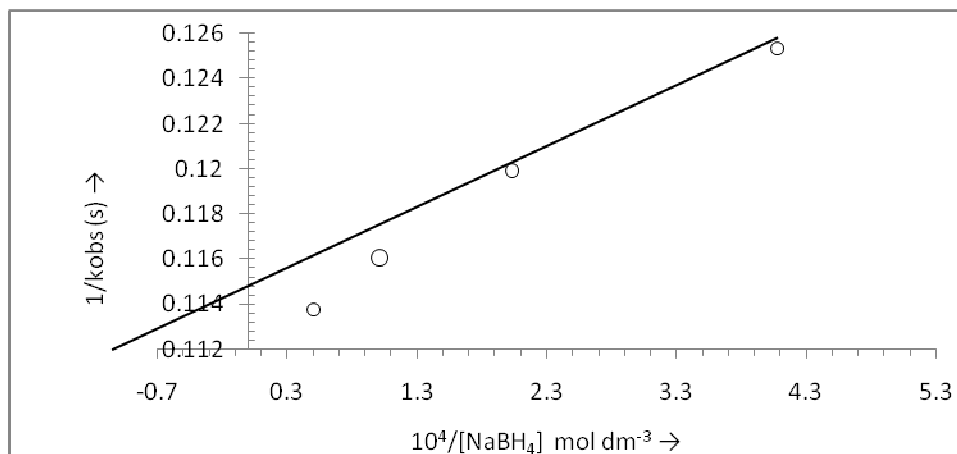


**Figure IV-24.** Absorption spectral changes recorded at 1.5 min interval during the reaction of **1** ( $5.8 \times 10^{-5} \text{M}$ ) with NaBH<sub>4</sub> ( $4.59 \times 10^{-3} \text{M}$ ) in CH<sub>3</sub>OH; (a) absorption spectral changes recorded at 257 nm represent the absorbance versus time curve at 311K



(a)

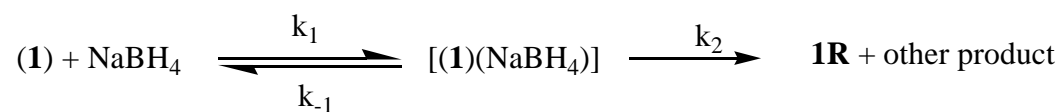


(b)

**Figure IV-25.** (a) Dependence of the rate of reaction of **1** ( $5.8 \times 10^{-5} \text{M}$ ) and 20-100 times of  $\text{NaBH}_4$  in  $\text{CH}_3\text{OH}$  at 311K on  $\text{NaBH}_4$ ; (b) the corresponding double reciprocal plot.

Thus we have the opportunity of exploring the metal-centered and pterin-centered redox reactivities of **1** with  $\text{NaBH}_4$ . Figure IV-24 shows the relevant overlay scans, highlighting the reaction between **1** and  $\text{NaBH}_4$  in  $\text{CH}_3\text{OH}$ . The reaction levels off after ca. 20 min. kinetics of this reaction was followed at 257 nm and four different temperatures (rang 300 -330K) under pseudo-first order conditions (using 10 – 140 times excess of  $\text{NaBH}_4$ ). From the plots of  $\log(A_\infty -$

A<sub>t</sub>) versus time, which were linear for ca. 3 half-lives,  $k_{\text{obs}}$  values were obtained by least square method. An average  $k_{\text{obs}}$  value of  $8.4 \times 10^{-3} \text{ s}^{-1}$  was found as well as an entropy of activation ( $\Delta S^\ddagger$ ) parameter of  $-198.5 \text{ J mol}^{-1} \text{ deg}^{-1}$ , respectively. The negative sign of the latter parameter indicates an overall associative pathway.



**Scheme IV-13**

---

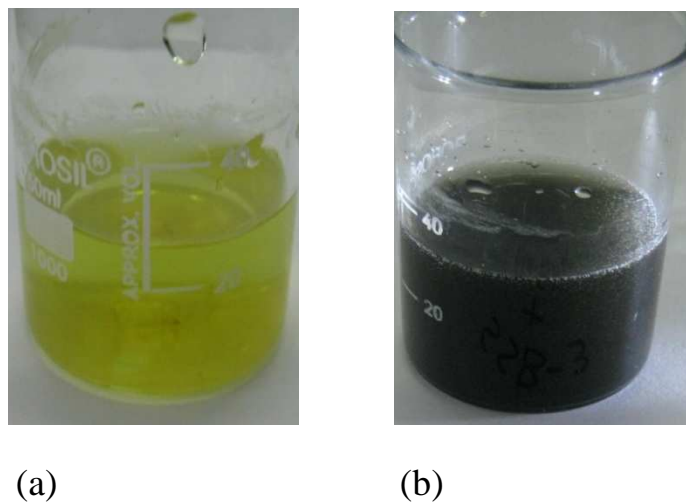


**Figure IV-26.** (a) Colour of the Ni(II) complex **1**: it is dark brown in the solid state

but is yellow-green in aqueous solution;

- (b) colour of the corresponding  $\text{NaBH}_4$  reduced compound, **1R** which is dark coloured.
-

As evident from the Figure IV-25(a) the system exhibits substrate saturation kinetics at high substrate ( $\text{NaBH}_4$ ) concentration, so that Scheme IV-13 may be applied. Now the observed rate constants ( $k_{\text{obs}}$ ) can be represented as follows.<sup>92,93</sup>

$$k_{\text{obs}} = (k_2[\text{S}]/K_m + [\text{S}]), \quad (3)$$

where  $K_m = (k_2 + k_{-1})/k_1$  or

$$1/k_{\text{obs}} = 1/k_2 + K_m/k_2[\text{S}] \quad (4)$$

where  $\text{S} = \text{NaBH}_4$

The plot of  $1/k_{\text{obs}}$  versus  $[1/\text{NaBH}_4]$  should give a straight line with  $1/k_2$  as the intercept and  $K_m/k_2$  as the slope. The intercept on the x-axis gives  $1/K_m$ . Accordingly Figure IV-26(b) yields the following data:

$$k_2 = 8.8 \times 10^{-3} \text{ s}^{-1}$$

$$K_m = 1.4 \times 10^{-3} \text{ mol dm}^{-3}.$$

The above experimental data may be assessed in the light of the following facts:

- (1) Figure III-16 depicts the reactivity of the free pterin ligand towards  $\text{NaBH}_4$ , where the absorption spectral change behavior is quite different from that of the **1** versus  $\text{NaBH}_4$ , (Figure IV-24) e.g. the  $\lambda_{\text{max}}$  value undergoes a change from 355 nm to 257 nm in **1**.
- (2) The  $\text{NaBH}_4$  reduction product (**1R**) from **1** has been isolated and characterized to be a Ni(I) – 7, 8,- dihydropterin complex. It is a dark colored moisture sensitive product. The color changes associated with  $\text{NaBH}_4$  reduction ( yellow-green  $\rightarrow$  dark color) is shown in Figure IV – 26.

(3) In chapter II it has been pointed out that the Cu(II)-pterin-phen mixed ligand complex, on NaBH<sub>4</sub> reduction provides with a Cu(I) complex, where the pterin ligand is in the 7,8-dihydro state.

It is worthwhile to explore the ability of **1R** to activate dioxygen for hydroxylation purpose towards a typical aromatic substrate like bromobenzene.<sup>55</sup>

Next section describes such an endeavor for modeling the PAH type activity.<sup>7,8,52-55</sup>

(4) Last but not the least **1** is the only member of the present series of examples discussed here [e.g. the corresponding Cu(II) and Co(II) – systems have been presented in chapters II and III respectively] which is able to exhibit substrate saturation kinetics with respect to both group transfer [Figure IV-23] and redox reagents [Figure IV-25] respectively.

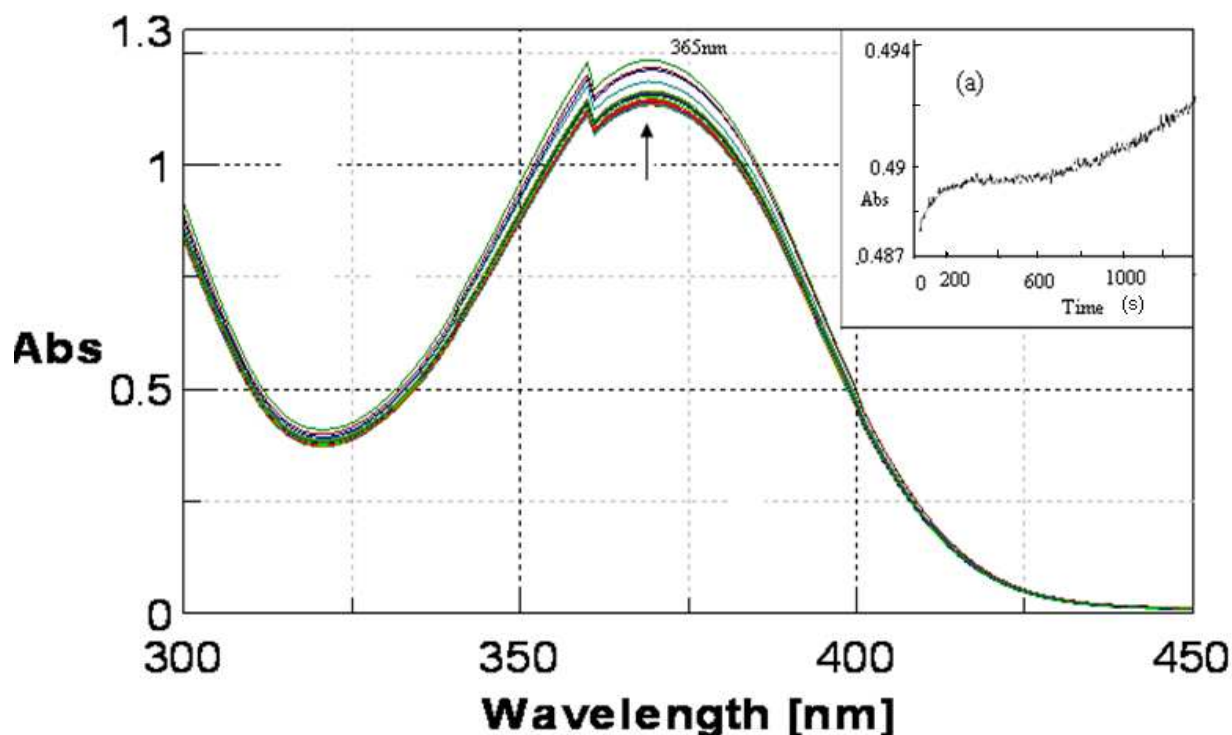
### **Reactivity of 1R with bromobenzene and dioxygen.**

Figure IV-27 shows the absorption spectral changes during reaction of **1R** ( obtained by NaBH<sub>4</sub> reduction of **1**) with bromobenzene in CH<sub>3</sub>OH medium saturated with dioxygen. Hardly any isosbestic point could be observed in the relevant spectral change behavior, which can be taken as an indication for the presence of an intermediate step, during conversion of the substrate (bromobenzene) to the product. A closer scrutiny of Figure IV-27(a) indicates that the initial fast step (upto ca. 200s), is followed by a brief pause (ca. 200 – 300 s region) and then the gradual conversion to the final product continues (beyond 1000 s). Kinetics of this reaction was followed at 365 nm and four different temperatures (range: 300 – 330K) in CH<sub>3</sub>OH saturated with O<sub>2</sub> under pseudo-first-order conditions (using a **1R** : bromobenzene ratio of 1 : 140); the entropy of

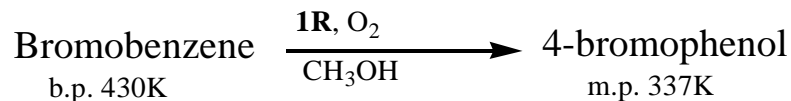
activation parameter ( $\Delta S^\ddagger$ ) was evaluated from the Eyring plot. The relevant data are indicated below:

$$k_{\text{obs}} = 1.4 \times 10^{-2} \text{ s}^{-1}; \quad \Delta S^\ddagger = -191.6 \text{ J mol}^{-1} \text{ deg}^{-1}.$$

The negative  $\Delta S^\ddagger$  value indicates an associative pathway, while the  $k_{\text{obs}}$  value is consistent with a group transfer process.<sup>92</sup> As suggested from DFT studies on the mechanistic pathway of PAH activity using the x-ray structural data of a PAH enzyme,<sup>99</sup> formation of an initial dioxygen – **1R** complex is quite likely whereby the dioxygen entity is activated through Ni(I)→O<sub>2</sub> electron transfer, leading to subsequent hydroxylation of bromobenzene.



**Figure IV-27.** Absorption spectral changes recorded at 1.5 min interval during the reaction of **1R** ( $5.8 \times 10^{-5} \text{ M}$ ) with bromobenzene ( $4.59 \times 10^{-3} \text{ M}$ ) in  $\text{CH}_3\text{OH}$ , saturated with  $\text{O}_2$  (a) Absorption spectral changes recorded at 365 nm represent the absorbance versus time curve at 311K.

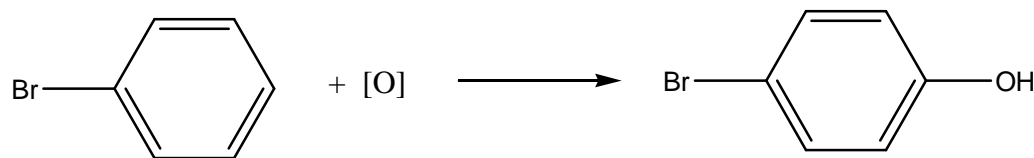


Stoichiometry of this reaction was established by repeating it on the preparative scale and recovering 4-bromophenol as a white solid (m.p.337K) from the reaction medium. Here the initial step is concerned with the formation of  $\text{O}_2 - \mathbf{1R}$  intermediate complex, activation of the  $\text{O}_2$  moiety through transfer of reducing equivalents from the Ni(I) centre/ 7, 8-dihydro pterin ring of  $\mathbf{1R}$  and the release of an electrophilic oxygen atom. The latter completes the formal hydroxylation step.

### 1st step



### 2nd step



The most crucial step is the activation of the dioxygen entity.

Further light is thrown on the above mechanistic pathway by  $\mathbf{2}$  and its  $\text{NaBH}_4$  reduction product  $\mathbf{2R}$ , as presented below.

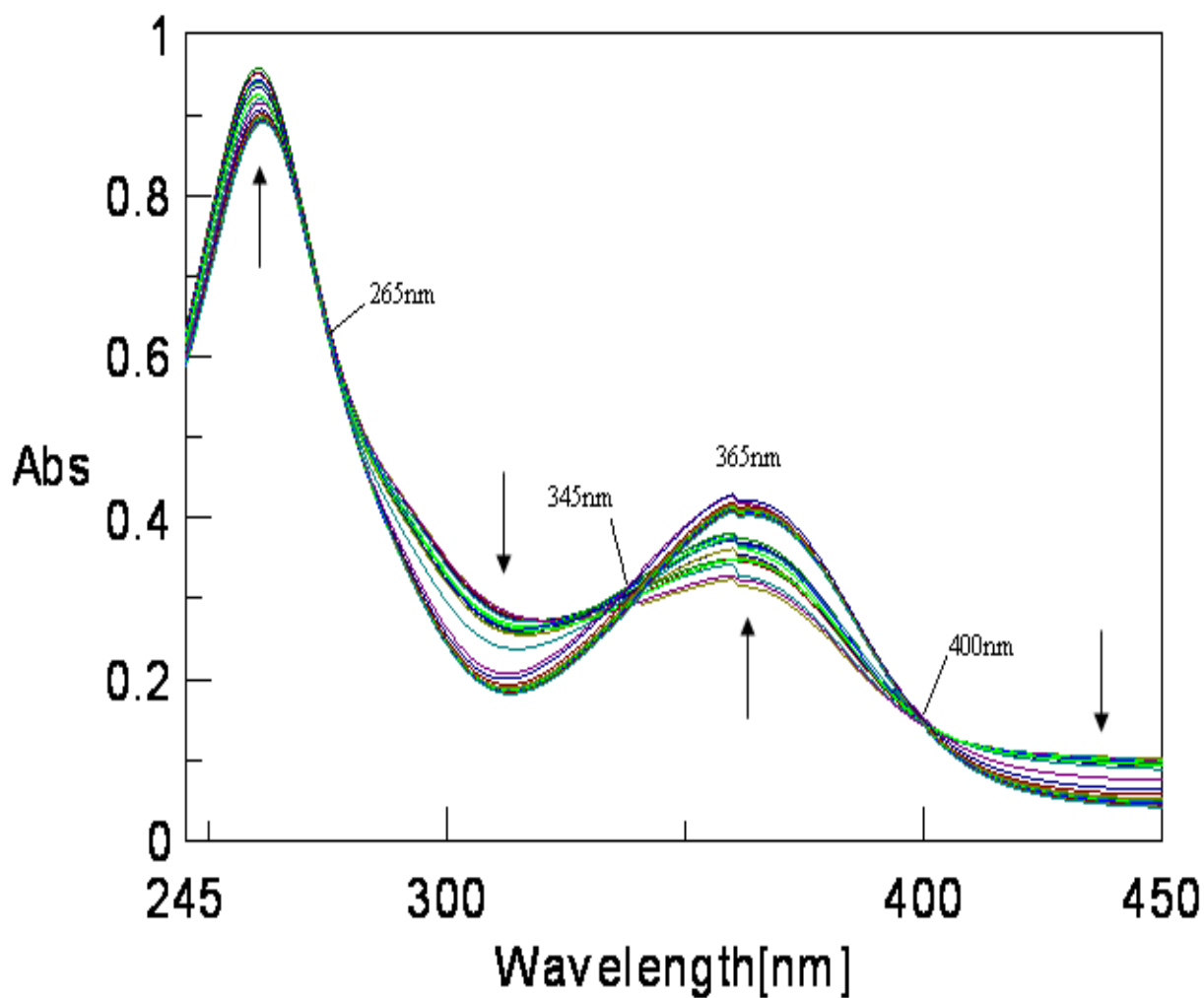
### Reactivity of $\mathbf{2}$ towards $\text{NaBH}_4$

Figure IV-28 shows the reaction profile for the interaction of  $\mathbf{2}$  with  $\text{NaBH}_4$  in  $\text{CH}_3\text{OH}$ . Unlike for the corresponding reaction between  $\mathbf{1}$  and  $\text{NaBH}_4$  (Figure IV-24), we find the appearance of two isosbestic points at 265 nm and 400 nm respectively; close approach to such a behavior is observed at 345 nm. This drastic change over in reactivity behavior towards  $\text{NaBH}_4$  could be achieved simply by substituting the aquo group of  $\mathbf{1}$  by an imidazole (Im) group in  $\mathbf{2}$ . [Figure IV-1 and IV-2]. Table IV-6 shows the effect of imidazole substitution on the relevant

geometric parameters together with the  $\Delta(= \mathbf{1} - \mathbf{2})$  values ( $\text{\AA}$ ). Although the magnitudes of most of the  $\Delta$  values are small, few of them are sufficient to affect the reactivity behavior. Table IV-8 shows few classic parameters on the electron transfer rate constants.<sup>79</sup> A change over in size by around  $0.04 - 0.09 \text{ \AA}$  could affect the rate constants by an order of  $10^3 - 10^5$ . This is essentially the Franck-Condon barrier to electron transfer reactions.<sup>79</sup> Besides this, the reactivity behavior of **1** towards  $\text{NaBH}_4$  conforms to substrate saturation kinetics [Figure IV – 25] which presupposes the formation of an intermediate like  $[(\mathbf{1})\text{NaBH}_4]$  (Scheme IV-13). But for **2**, the Figure IV -28 indicates an almost clean conversion  $\mathbf{2} \rightarrow \mathbf{2R}$ . Most likely the absence of an aquo group in **2** prevents the formation of an intermediate complex with  $\text{NaBH}_4$ , as indicated above for **1**. The relevant kinetic parameters are shown below.

$$k_{\text{obs}} = 9.0 \times 10^{-3} \text{ s}^{-1}; \Delta S^\ddagger = - 186.0 \text{ J K}^{-1} \text{ mol}^{-1}.$$

The negative  $\Delta S^\ddagger$  value is consistent with an associative pathway involving both group (hydride ion) and electron transfer process. This  $k_{\text{obs}}$  value is quite close for that of the reaction between **1** and  $\text{NaBH}_4$  (Figure IV-24;  $k_{\text{obs}} = 8.8 \times 10^{-3} \text{ s}^{-1}$ ), but the reaction pathway is different, as indicated above.



**Figure IV-28.** Absorption spectral changes recorded at 1.5 min interval during the reaction of (2) ( $5.8 \times 10^{-5} \text{M}$ ) with  $\text{NaBH}_4$  ( $4.59 \times 10^{-3} \text{M}$ ) in  $\text{CH}_3\text{OH}$  at 311K

**Table IV-8.** Some outer-sphere electron-exchange reaction.

Reacting pair	Electron configuration	Rate (L mol <sup>-1</sup> s <sup>-1</sup> at 25°C)	Difference in M—L bond lengths (Å)
[Fe(bipy) <sub>3</sub> ] <sup>2+/3+</sup>	$t_{2g}^6/t_{2g}^5$	>10 <sup>6</sup>	0.00 ± 0.01
[Mn(CN) <sub>6</sub> ] <sup>4-/3-</sup>	$t_{2g}^5/t_{2g}^4$		
[Mo(CN) <sub>8</sub> ] <sup>4-/3-</sup>	<i>a</i>		
[W(CN) <sub>8</sub> ] <sup>4-/3-</sup>	<i>a</i>		
[IrCl <sub>6</sub> ] <sup>3-/2-</sup>	$t_{2g}^6/t_{2g}^5$		
[Os(bipy) <sub>3</sub> ] <sup>2+/3+</sup>	$t_{2g}^6/t_{2g}^5$	~10 <sup>5</sup>	Very small
[Fe(CN) <sub>6</sub> ] <sup>4-/3-</sup>	$t_{2g}^6/t_{2g}^5$		
[Ru(en) <sub>3</sub> ] <sup>2+/3+</sup>	$t_{2g}^6/t_{2g}^5$	4 × 10 <sup>4</sup>	0.04 ± 0.01 <sup>b</sup>
[Ru(NH <sub>3</sub> ) <sub>6</sub> ] <sup>2+/3+</sup>	$t_{2g}^6/t_{2g}^5$	4 × 10 <sup>3</sup>	
[Ru(H <sub>2</sub> O) <sub>6</sub> ] <sup>2+/3+</sup>	$t_{2g}^6/t_{2g}^5$	20 <sup>c</sup>	
[Fe(H <sub>2</sub> O) <sub>6</sub> ] <sup>2+/3+</sup>	$t_{2g}^4 e_g^2 / t_{2g}^3 e_g^2$	4	0.09 ± 0.02 <sup>b</sup>
[MnO <sub>4</sub> ] <sup>2-/1-</sup>	<i>a</i>	>10 <sup>3</sup>	0.14 ± 0.02 <sup>b</sup>
[Co(en) <sub>3</sub> ] <sup>2+/3+</sup>	$t_{2g}^3 e_g^2 / t_{2g}^6$	~10 <sup>-4</sup>	
[Co(NH <sub>3</sub> ) <sub>6</sub> ] <sup>2+/3+</sup>			
[Co(C <sub>2</sub> O <sub>4</sub> ) <sub>3</sub> ] <sup>4-/3-</sup>			

Ref. 79, F.A. Cotton and G. Wilkinson, Advanced Inorganic Chemistry, 5<sup>th</sup> ed (1988). p1308.

John Wiley & Sons, New York.

### Reactivity of 2R with bromobenzene/ O<sub>2</sub> reaction mixture

Reactivity of **2R** with bromobenzene in presence of dioxygen was studied and the relevant reaction profile is shown in Figure IV-29. Two isosbestic points at 265 nm and 400 nm respectively, characterized this reaction process, whereas reaction stoichiometric study afforded the isolation of 4-bromophenol from the reaction medium. Almost a clean conversion to the hydroxylated product is indicated. This reaction profile is completely different from that of **1R**

with bromobenzene/O<sub>2</sub> mixture [Figure IV-27]. Once again the imidazole substitution at the metal centre could achieved this change over in kinetic behavior (Tables IV-6 and IV-8). The following kinetic data are obtained for the above process [Figure IV-29]:

$$k_{\text{obs}} = 8.8 \times 10^{-3} \text{ s}^{-1}; \Delta S^{\ddagger} = -178.0 \text{ J K}^{-1} \text{ mol}^{-1}.$$

Once again, an associative pathway is indicated, for the following process, which takes place in

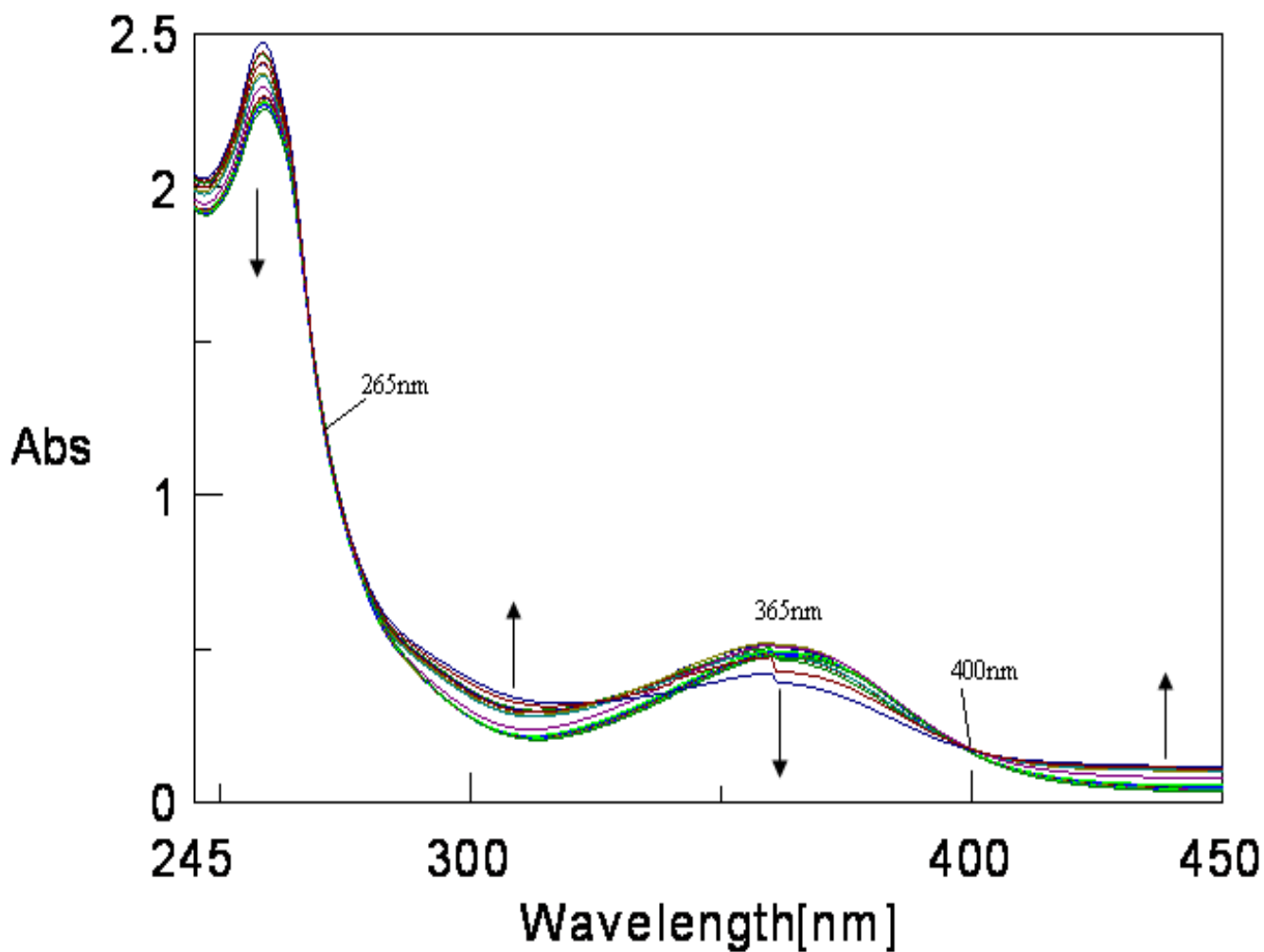
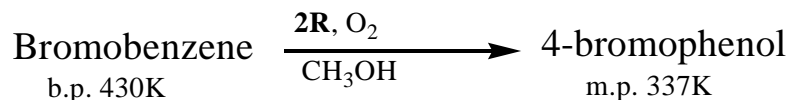


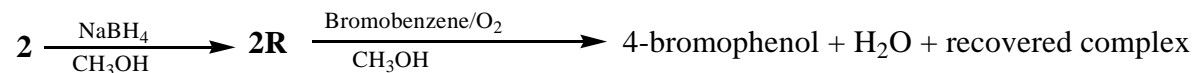
**Figure IV-29.** Absorption spectral changes recorded at 1 min interval during the reaction of (**2R**) ( $5.8 \times 10^{-5} \text{M}$ ) with bromobenzene ( $4.59 \times 10^{-3} \text{M}$ ) in  $\text{CH}_3\text{OH}$  saturated with dioxygen ( $\text{O}_2$ ) at 311K.

---



essentially one step.

Now a comparison of Figure IV-28 and IV-29, together with the corresponding  $k_{\text{obs}}$  values of  $9.0 \times 10^{-3} \text{ s}^{-1}$  and  $8.8 \times 10^{-3} \text{ s}^{-1}$  respectively, indicates that the transfer of reducing equivalents (from  $\text{NaBH}_4$ ) to **2** and the onwards transformation of the same (from **2R**) to the bromobenzene/ $\text{O}_2$  reaction mixture, take place in one step in either case, at almost same rate.



Only difference between the above two spectra is the movement of the arrows indicating the spectral change behavior; even the positions of the isosbestic points remain unchanged. The above reactivity steps highlight the ability of the present nickel (II)-pterin complexes to assimilate reducing equivalents from  $\text{NaBH}_4$  and further to activate the aromatic ring of bromobenzene towards hydroxylation; in other words, they may be treated as functional models of phenylalanine hydroxylase (PAH).<sup>7,52-55,99-101</sup>

**The most interesting aspect of this study is that fine tuning of the metal centre through substitution of an imidazole group could achieve an enormous change over in kinetic behavior from a substrate saturation process to another involving essentially one step conversion.**

### Reactivity of **2R** with $\text{K}_3[\text{Fe}(\text{CN})_6]$

The relevant reaction profile is shown in Figure IV-30 indicating an almost clean oxidation reaction with isosbestic points at 265 nm and 400 nm respectively. Apart from the positions of the isosbestic points, the directions of movement of the spectral curves are quite similar to that in Figure IV- 29. In either case the reaction profile highlights the transfer of reducing equivalent away from **2R**, as mentioned earlier such reducing equivalents were transferred to **2** [**2**+  $\text{NaBH}_4 \rightarrow \text{2R}$ ] by  $\text{NaBH}_4$  (Figure IV-28). The spectral change behavior is quite well-defined for the reaction with  $\text{K}_3[\text{Fe}(\text{CN})_6]$  (Figure IV-30). Kinetics of the reaction was followed at 360 nm under pseudo-first-order condition [using a **2R** :  $\text{K}_3[\text{Fe}(\text{CN})_6]$  ratio of 1: 100] and four different temperatures (300 – 330K) in  $\text{CH}_3\text{OH}-\text{H}_2\text{O}$  (3: 1 v/v).

The following kinetic parameters were evaluated:

$$k_{\text{obs}} = 3.6 \times 10^{-2} \text{ s}^{-1} ; \Delta S^\ddagger = - 184.0 \text{ J K}^{-1} \text{ mol}^{-1}.$$

A comparison of the  $k_{\text{obs}}$  data with that of **2R** with bromobenzene/ $\text{O}_2$  mixture, indicates an almost 4 times increase in reaction rate with  $\text{K}_3[\text{Fe}(\text{CN})_6]$ .

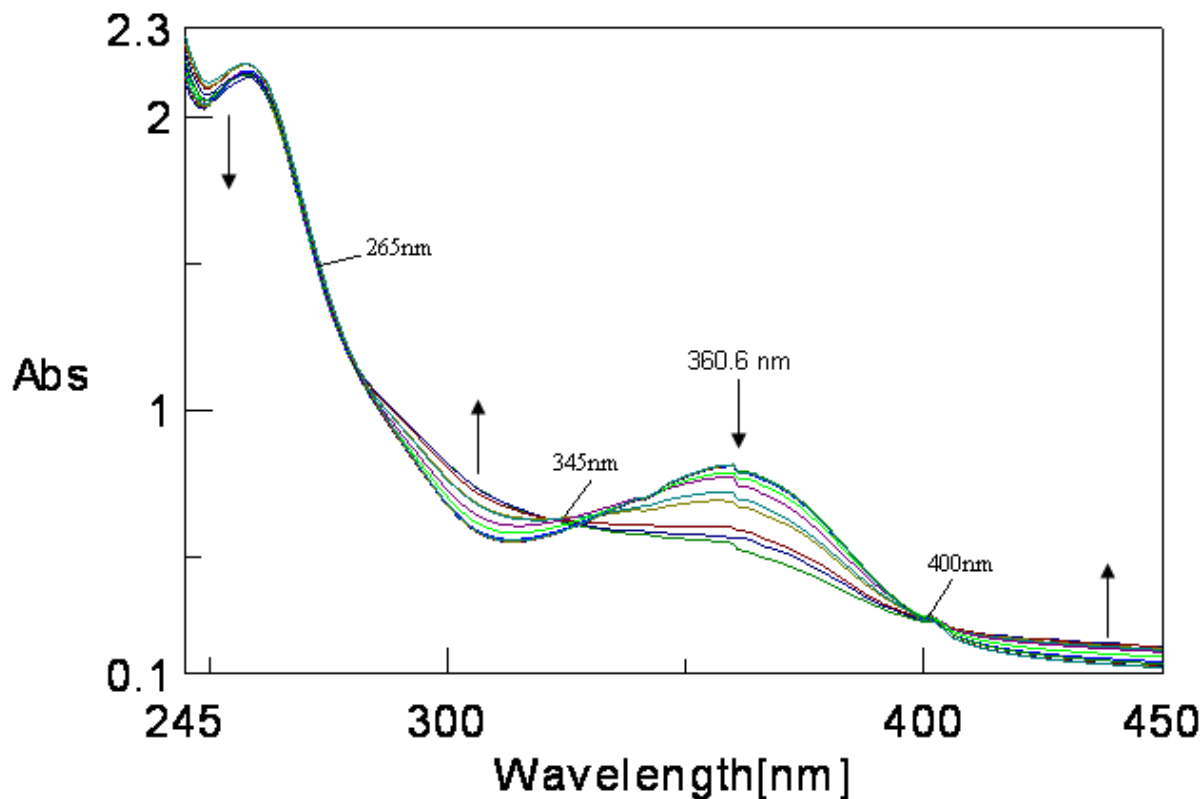


**Figure IV-30.** Absorption spectral changes recorded at 15 second interval during the reaction of (**2R**) ( $5.8 \times 10^{-5} \text{M}$ ) with  $\text{K}_3[\text{Fe}(\text{CN})_6]$  ( $4.59 \times 10^{-3} \text{M}$ ) in  $\text{CH}_3\text{OH} - \text{H}_2\text{O}$  (3:1 v/v) at 298K.

---

Figure IV -31 shows an attempt for exploring reactivity between  $\text{NaBH}_4$  and  $\text{K}_3[\text{Fe}(\text{CN})_6]$  in  $\text{CH}_3\text{OH} - \text{H}_2\text{O}$  (3:1 v/v) medium at 320K. Hardly any reactivity is observed in this case, indicating no direct transfer of reducing equivalents from  $\text{NaBH}_4$  towards  $\text{K}_3[\text{Fe}(\text{CN})_6]$ . As evident from the above discussion, this Ni(II)-pterin complex serves as an excellent mediator for

transferring reducing equivalents from  $\text{NaBH}_4$  to either a model substrate like bromobenzene in presence of  $\text{O}_2$  or a biochemically relevant oxidizing agent like  $\text{K}_3[\text{Fe}(\text{CN})_6]$  [ $E^\circ = 0.36 \text{ V}$ ]. It may be stated in this connection that  $\text{NAD}^+$  and  $\text{NADPH}^+$  can be reduced nonenzymatically by reducing agents like sodium dithionite or sodium borohydride.  $\text{NADH}$  and  $\text{NADPH}$  can in turn be nonenzymatically reoxidized with ferrocyanide, but they are not oxidized directly by molecular oxygen at pH 7.4.<sup>94</sup> Activation of dioxygen through  $\text{Ni}(\text{I}) \rightarrow \text{O}_2$  electron transfer, is most possibly responsible for above ability of **2R**, which in turn is obtained through the  $\text{NaBH}_4$  reduction of **2**.<sup>99</sup> It has already been pointed out that **2R** is a  $\text{Ni}(\text{I})$ -7,8-dihydro pterin complex. The dihydro pterin ring could supply the reducing equivalents needed to reduce one of oxygen atoms of  $\text{O}_2$  to the level of  $\text{H}_2\text{O}$  and releasing the other oxygen atom required for the conversion bromobenzene  $\rightarrow$  4-bromophenol

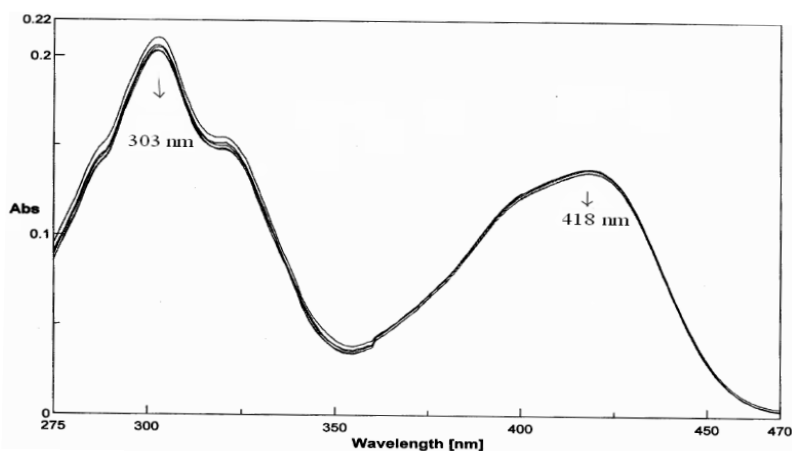
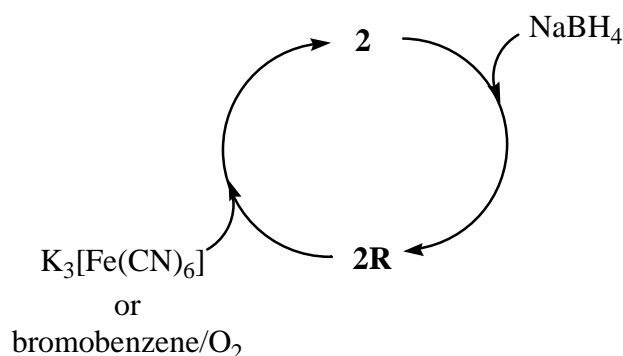


**Figure IV- 31.** Absorption spectral data recorded at 10 min interval for exploring the reactivity between  $\text{NaBH}_4$  ( $1.2 \times 10^{-4} \text{ M}$ ) and  $\text{K}_3[\text{Fe}(\text{CN})_6]$  ( $1.2 \times 10^{-4} \text{ M}$ ) in  $\text{CH}_3\text{OH}-\text{H}_2\text{O}$  (3:1 v/v) at 320 K.

In other words, dioxygen is activated here for performing the tusk of hydroxylating an aromatic ring. The above conversions can be summarized in terms of the following scheme:



**Scheme IV-14**

---

In terms of Figures IV-28 – IV-30, the above transfer of two reducing equivalents [ $\text{O}_2 + [2\text{H}] \rightarrow \text{H}_2\text{O} + \text{incipient oxygen atom (O)}$ ] takes place simultaneously.<sup>94</sup>

### **Electronic structures of 1 and 2 : Correlation with reactivity**

DFT calculations were performed with the Gaussian 09 package using the B3LYP hybrid functional and the 6-31g basis set.<sup>95,96</sup> Starting parameters for complex **1** and **2** were taken from their refined crystal structure parameters.<sup>17c,d</sup> Geometry optimization was not carried out separately as here the structures were obtained from the refined crystal parameters. The ground state energy minimization was carried out and the energy level diagrams of the selected frontier molecular orbitals were obtained (figure IV-32). This diagram also indicates information about the compositions of the relevant frontier orbitals. Few relevant band gaps (eV) are also indicated in Figure IV-32. For several cases the energy band gap between adjacent levels is quite low (0.11 – 0.3 eV). In recent years synthetic molecules with exceptionally small (< 0.5 eV) band gaps are receiving considerable attention due to their interesting electrochemical/redox amphoteric behavior.<sup>64,66</sup> Usually in such cases the HOMO – LUMO orbitals are located in different

covalently linked centers within the same molecule. Thermo-excited intermolecular electron transfer can

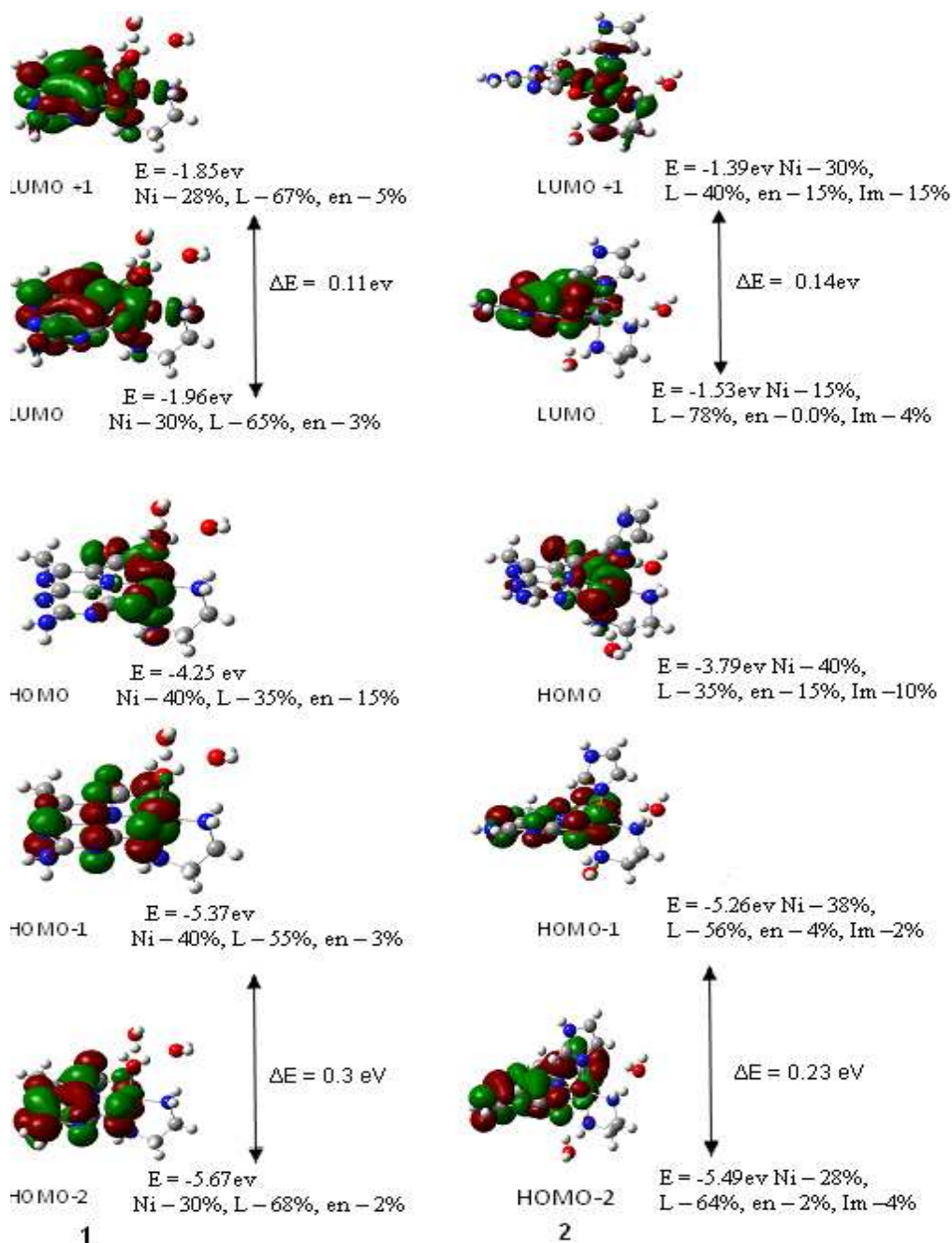


**Figure IV-32.** Frontier molecular orbitals of **1** and **2**, showing their energies (eV) and compositions (%).

take place between two such centers in solution. The combination of the redox non-innocent pterin ligand residue with the redox active metal centre [Ni(II)  $\rightarrow$  Ni(I)] in complexes **1** and **2**, leads to such a situation here, associated with distinct redox activities.<sup>9-11,53</sup> For **2** additional stereoelectronic factor comes into play due to the presence of  $\pi$ -acidic imidazole ligand, with a definite contribution (10-15%) to the HOMO and LUMO +1 levels respectively. For both **1** and **2** the HOMO-1 and HOMO-2 levels are characterized small band gaps (0.23 – 0.3 eV). Such gaps are still smaller (0.11 – 0.14 eV) for the corresponding LUMO and LUMO+1 levels. The latter aspect may be taken as reason for the facile reaction of **1** and **2** with NaBH<sub>4</sub>, leading to the transfer of reducing equivalents to the aforesaid vacant energy levels. Now a closer look may be taken at the compositions of the frontier orbitals. For example, in case of **1** the pterin (65-67%) and Ni(II) centres (28-30%) make major contributions to the LUMO and LUMO+1 levels. For **2** the LUMO+1 level is composed of almost equal shares of Ni(II), pterin and the ancillary ligands. That is, there is a substantial lowering of contribution to the LUMO+1 level from pterin in case of **2**. This aspect may be as one of the reasons for the different reactions profiles of **1** and **2** (Figure IV-24 & IV-28; IV-27 & IV-29). Besides this, the steric factors as per Tables IV-6 and IV-8, may be partly responsible for the above reactivity differences.

Now a closer look may be taken at the cyclic voltammetry data of **1** and **2** (Figure IV-19 – IV-21) in the light of Figure IV-32 as well as Scheme IV -11, showing the Frost diagram of the Ni(II) – Ni(I) centres. For both **1** and **2** there is a small band gap between the LUMO and LUMO +1 levels, indicating the easy reduction of the Ni(II) centre. Besides this, the small energy change over (Scheme IV-11), associated with Ni(II)  $\rightarrow$  Ni(I) transformation, may be responsible for the appearance of the above metal-centered reduction peak in cyclic voltammetry. The Ni(I) species has a lower life time in aqueous medium (Figure IV-20).

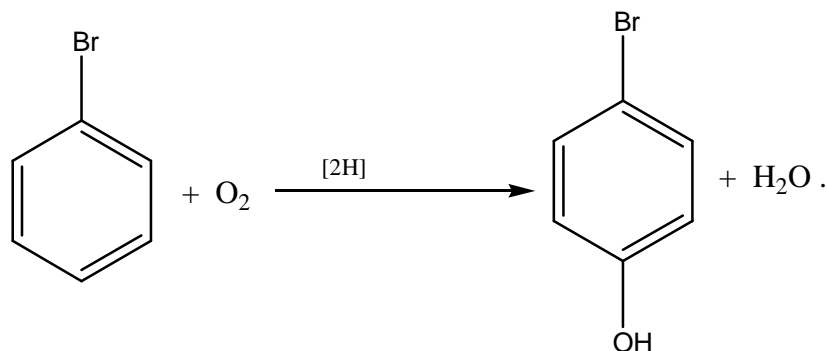
## Conclusion

This chapter is concerned with detailed studies on two new nickel(II)-pterin complexes. They could be synthesized and crystallized out of the aqueous medium, a reasonable synthetic achievement, as non aqueous medium is usually needed for such synthesis. These x-ray structurally characterized complexes, permit the recording of a wide variety of physico-chemical and reactivity data and their meaningful interpretation. The ESIMS, IR, UV-VIS data are consistent with their chemical compositions. Their CD spectral data throw light on the conformation of the chelate ring of the ancillary ligand “en”. Hence the positive cotton effect around 755-769 nm, is correlated with the  $\delta$ -conformation of “en” ring. NaBH<sub>4</sub> reduction of both these complexes could be achieved and such reductions are associated with a substantial increase in fluorescence emission intensity, indicating increase in electron density in the resulting reduced complexes. Cyclic voltammetric data of **1** and **2** indicate the formation of the corresponding Ni(I) species on the time scale of cyclic voltammetry; this reduced species has a longer life time in DMSO as compared to that in the aqueous medium. Reactivity of **1** with both imidazole and NaBH<sub>4</sub>, follow substrate saturation kinetic path way. No other compound of this treatise possess this attribute. The NaBH<sub>4</sub> reduced complex **1R** (Figure IV-26) could be isolated in the solid state and characterized to be a Ni(I) complex of the 7,8-dihydro form of the pterin ligand.<sup>22,23</sup> In other words, reducing equivalents are transferred to both the metal and pterin ligand centers of **1** → **1R**. Reactivity of **1R** towards a reaction mixture of bromobenzene/O<sub>2</sub> could be followed both kinetically and stoichiometrically. Here bromobenzene has been utilized as a model substrate for following the phenylalanine hydroxylase (PAH) type activity of **1R**; isolation of 4-bromophenol from the reaction medium reveals the ability of **1** to act as a functional model here in transferring reducing equivalents from NaBH<sub>4</sub> to the bromobenzene/O<sub>2</sub> reaction mixture through the **1R**

stage. Most likely, a Ni(I)→ O<sub>2</sub> electron transfer initiates the process of dioxygen activation, followed by hydroxylation of the aromatic ring of bromobenzene.

From consideration of kinetic application of crystal field theory to the substitution process of octahedral complexes involving the associative pathway, it appears that the crystal field contribution to the total activation energy ( $E_{\text{CFAE}}$ ), makes definite contribution to d<sup>3</sup>, spin paired d<sup>6</sup> and d<sup>8</sup> systems, predicting slower reaction rates.<sup>97,98</sup> In any mechanism the most important single factor is the strength of the bond between the central atom and the leaving group. Only a small part of this bond energy is related to crystal field effects. Changes in metal-ligand attractions, ligand-ligand repulsion, etc., make large contribution to the activation energy. For **1** the positive  $E_{\text{CFAE}}$  value and the presence of the aquo group make it suitable for substrate saturation kinetics (Figure IV-22 to IV-25 as well as IV-27). Literature data for Ni(II) complexes indicate lability for a  $\sigma$ -donor ligand like H<sub>2</sub>O/en, but inertness for a  $\pi$ -acceptor ligand like phen/bipy.<sup>63</sup> In **2** an imidazole group ( $\pi$ -acceptor type ligand) replaces the aquo group and could achieve a complete change over in kinetic behavior (Figure IV-28 and IV-29) to one-step process. Even the oxidation of **2R** by an essentially transfer agent like K<sub>3</sub>[Fe(CN)<sub>6</sub>] (Figure IV-30) is an one-step process, with the change over point at 345 nm (LMCT region) being more clearly defined. On the other hand, for reactions with group transfer agent like NaBH<sub>4</sub> or bromobenzene/O<sub>2</sub> mixture (Figure IV-29), the LMCT region ( $\approx$  345 nm) is quite spread out, indicating the participation of at least a couple of species differing in their oxidation state of the pterin ring (7, 8- dihydro state → oxidized/aromatic state) as well as Ni(I)-pterin → Ni(II)-pterin bonding change over. The frontier orbital energy level diagram (Figure IV-32) is helpful for rationalizing some of the unique redox activity aspects, in terms of small energy band gaps as well as composition of such energy levels. The Frost diagram (SchemeIV-11) is able to justify

the isolation of the Ni(I) – 7, 8-dihydropterin complexes (**1R,2R**) in the solid state. On the basis of the above deliberations, it is reasonable to consider **1** and **2** as functional models for PAH-type activity with bromobenzene as the model substrate and NaBH<sub>4</sub> as a model of NADH/NADPH in transferring reducing equivalents to the model active sites of **1** and **2**, needed for the following purpose:<sup>22,23,53</sup>



Most likely, the Ni(I)→O<sub>2</sub> electron transfer step initiates the process of dioxygen activation, with the 7, 8 – dihydro form of the pterin ring. ( of **1R, 2R**) completing the process of reducing equivalent, [2H] transfer. For **1R**, it is a two- step process (Figure IV-27), while **2R** completes this process in essentially a single step (Figure I-29).

## **Chapter V**

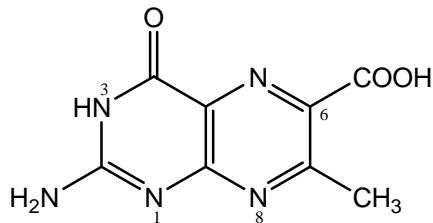
**Conformational control of pterin- and nickel- centred  
redox reactions of mixed ligand nickel-pterin  
complexes: synthesis, structural, chiroptical and  
reactivity studies.**

## Abstract

Two new nickel(II) complexes having the identical chemical composition  $[\text{Ni}(\text{L})(\text{pn})(\text{H}_2\text{O})] \cdot 5\text{H}_2\text{O}$  have been synthesized and characterized, where  $\text{L}^{2-}$  is the anion of 7-methylpterin-6-carboxylic acid and 'pn' represents R-(+)-pn or S-(-)-pn. Circular dichroism spectroscopy establish their chiral nature which can be traced to the conformation of their 'pn' chelate rings. Reactivities of these two complex have been studied using both group and group/electron transfer reagents. For group and group/electron transfer reagents (imidazole,  $\text{NaBH}_4$ , bromobenzene/ $\text{O}_2$ ) the  $k_{\text{obs}}$  values are of the order of  $10^{-3}\text{s}^{-1}$ ; for an electron transfer agent like  $\text{K}_3[\text{Fe}(\text{CN})_6]$ , the  $k_{\text{obs}}$  value has an order of  $10^{-2}\text{s}^{-1}$ . In all these cases the  $\Delta S^\ddagger$  value is negative, indicating the associative nature of such reactions. The reaction profiles of these two chiral complexes towards each of the above reagents are different highlighting the conformational control of the 'pn' chelate ring in such cases. The small band gaps between some of their frontier orbitals are partly responsible for such unique redox activities.

## Introduction

In pursuance of our continued interest in redox chemistry of nickel [Ni(I) and Ni(II) states] with the redox non-innocent pterin ligand 7-methylpterin-6-carboxylic acid ( $\text{H}_2\text{L}$ , **1**), we present here our studies on two new nickel(II) complexes, with the chiral ancillary ligands R-(+)-1, 2 – diaminopropane and S-(-)-1, 2 – diaminopropane.



The pterin ligand (**1**, H<sub>2</sub>L)

The ancillary ligands have been chosen purposefully for exploring the chelate ring conformational control of redox activity of the resulting complexes. Once again, the methods and reagents have been chosen carefully for this purpose.

Finally, the molecular properties have been analyzed on the basis of electronic structures obtained by DFT method.

## Experimental

**Materials:** Reagent grade chemicals were used as received. Solvents were purified before use following literature procedures<sup>20</sup>. Kinetic and electro-chemical studies were performed in spectroscopy grade methanol and DMSO respectively (SRL, Mumbai); Bu<sub>4</sub>NClO<sub>4</sub> (TBAP) were obtained from published methods<sup>72</sup>. R- (+)- 1, 2- diaminopropane [R-(+)-pn] and S -(-) – 1, 2 – diaminopropane [S-(-)-pn] were obtained from Sigma Aldrich. NiSO<sub>4</sub>, 7H<sub>2</sub>O, K<sub>3</sub>Fe(CN)<sub>6</sub>, imidazole (Im) and NaBH<sub>4</sub> were obtained from SRL, Mumbai. H<sub>2</sub>L was prepared by published procedure.<sup>19</sup>

**Method:** The two new complexes characterized x-ray crystallographically and also by different physico-chemical methods including elemental analysis, ESIMS, IR, UV-Vis and <sup>1</sup>H NMR data. Details about the instrumental measurements have been presented in earlier chapters, especially chapter III.

## Synthesis of the complexes

### **2-amino-4-hydroxy-7-methylpteridine-6-carboxylic acid sesquihydrate (C<sub>8</sub>H<sub>7</sub>N<sub>5</sub>O<sub>3</sub> · 1.5H<sub>2</sub>O)**

**(1)**

The above pterin ligand (H<sub>2</sub>L · 1.5 H<sub>2</sub>O) was obtained by published procedure.<sup>19</sup>

### **[Ni(C<sub>8</sub>H<sub>5</sub>N<sub>5</sub>O<sub>3</sub>)(R- (+) -C<sub>3</sub>H<sub>10</sub>N<sub>2</sub>)(H<sub>2</sub>O)]. 5H<sub>2</sub>O (2)**

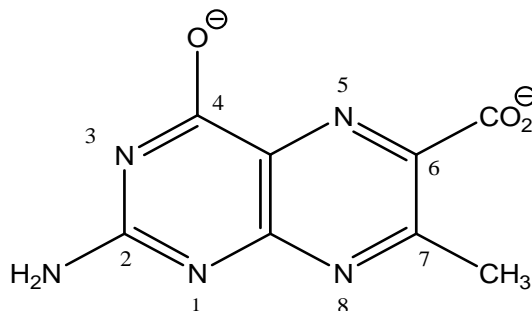
The complex was prepared by the slow addition of an aqueous alkaline solution (NaOH: 44mg, 1.1 mmol) of the pterin ligand (124mg, 0.5mmol) to a well-stirred warm (323K; paraffin oil bath) aqueous reaction mixture containing NiSO<sub>4</sub> · 7H<sub>2</sub>O (140mg, 0.5mmol) and R- (+)-pn (39mg, 0.6mmol) under subdued light; final volume was 35 ml. The pH was adjusted to 9.2 and the stirring was continued for 3h. Upon standing, the reaction medium deposited golden-yellow crystals after 2 days, which were suitable for single crystal x-ray diffraction yield, 30%.

Analytically pure compound could be obtained by filtration, repeated washing with small quantities of water and drying in vacuo over silica gel. Analysis, calculated for C<sub>11</sub>H<sub>28</sub>N<sub>7</sub>O<sub>9</sub>Ni: C 28.65, H 6.07, N 21.27 %; found: C 28.91, H 5.74, N 20.94 %. UV – VIS absorption bands [CH<sub>3</sub>OH, λ<sub>max</sub><sup>nm</sup>(logε)]: 211(4.51), 243sh(4.15), 272(4.13), 277(4.54), 349(4.31), 365(3.89), 764(1.24), 895(1.93)

### **[Ni(C<sub>8</sub>H<sub>5</sub>N<sub>5</sub>O<sub>3</sub>)(S-(-)- C<sub>3</sub>H<sub>10</sub>N<sub>2</sub>)(H<sub>2</sub>O)]. 5H<sub>2</sub>O (3)**

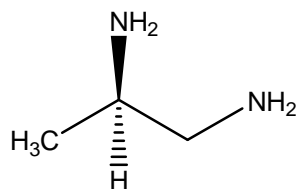
The complex was prepared by the slow addition of an aqueous alkaline solution (NaOH: 44mg, 1.1 mmol) of the pterin ligand (124mg, 0.5mmol) to a well-stirred warm (323K; paraffin oil bath) aqueous reaction mixture containing NiSO<sub>4</sub> · 7H<sub>2</sub>O (140mg, 0.5mmol) and S -(-)-pn (39mg, 0.6mmol) under subdued light; final volume was 35 ml. The pH was adjusted to 9.2 and the stirring was continued for 3h. Upon standing, the reaction medium deposited golden-yellow crystals after 2 days, which were suitable for single crystal x-ray diffraction yield, 30%.

Analytically pure compound could be obtained by filtration, repeated washing with small quantities of water and drying in vacuo over silica gel. Analysis, calculated for  $C_{11}H_{28}N_7O_9Ni$ : C 28.65, H 6.07, N 21.27 %; found: C 29.34, H 5.82, N 21.16 %. UV – VIS absorption bands [ $CH_3OH$ ,  $\lambda_{max}^{nm}(\log\epsilon)$ ]: 273(4.36), 365(3.98), 512sh(1.02), 640sh(1.06), 707(1.22), 728(1.44), 802(1.53), 911sh(0.78), 1053sh(1.35)



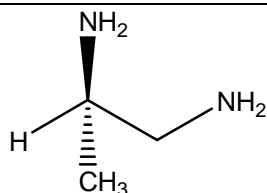
The pterin ligand ( $H_2L$ ) anion ( $L^{2-}$ ,  $C_8H_5N_5O_3$ )

**Scheme V- 1**



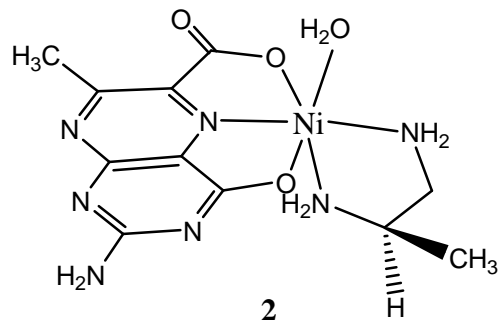
R-(+)- 1, 2- diaminopropane[R-(+)-pn]

**Scheme V-2**

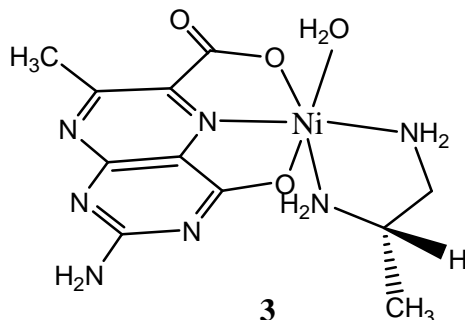


S-(-)- 1, 2- diaminopropane[S-(-)-pn]

**Scheme V-3**



**Scheme V-4**



**Scheme V-5**

## Results and Discussion

These two new Ni(II) mixed ligand complexes (Scheme V-4 and Scheme V-5) could be crystallized out of the aqueous alkaline medium. Careful control of the reaction conditions led to their isolation in the chiral form, using the chiral ancillary ligands R-(+)-pn and S-(-)-pn respectively [Scheme V-2 and Scheme V-3]. Analytically pure samples could be obtained through washing the crystals with water and drying in vacuo; such that samples are suitable for microanalytical purpose as well as electrospray ionisation mass spectral data (ESIMS) collection.

These chiral compounds afford valuable chiroptical, electrochemical and redox reactivity data, as discussed below.

### **Molecular structure of [Ni(C<sub>8</sub>H<sub>5</sub>N<sub>5</sub>O<sub>3</sub>)(R-(+)-C<sub>3</sub>H<sub>10</sub>N<sub>2</sub>)(H<sub>2</sub>O)]. 5H<sub>2</sub>O (2) and [Ni(C<sub>8</sub>H<sub>5</sub>N<sub>5</sub>O<sub>3</sub>)(S-(-)-C<sub>3</sub>H<sub>10</sub>N<sub>2</sub>)(H<sub>2</sub>O)]. 5H<sub>2</sub>O (3)**

Figure V-1 and V-2 represent the molecular structures of the two new Ni(II) complexes. Table V-1 shows their crystallographic data and structure refinements. Their geometry parameters, hydrogen atom coordinates are presented in Table V-2, V-3, V-4 and V-5

respectively. The crystal packing diagrams and unit cells of **2** and **3** are represented in Figure V-3, V – 4, V – 5 and V – 6, respectively.

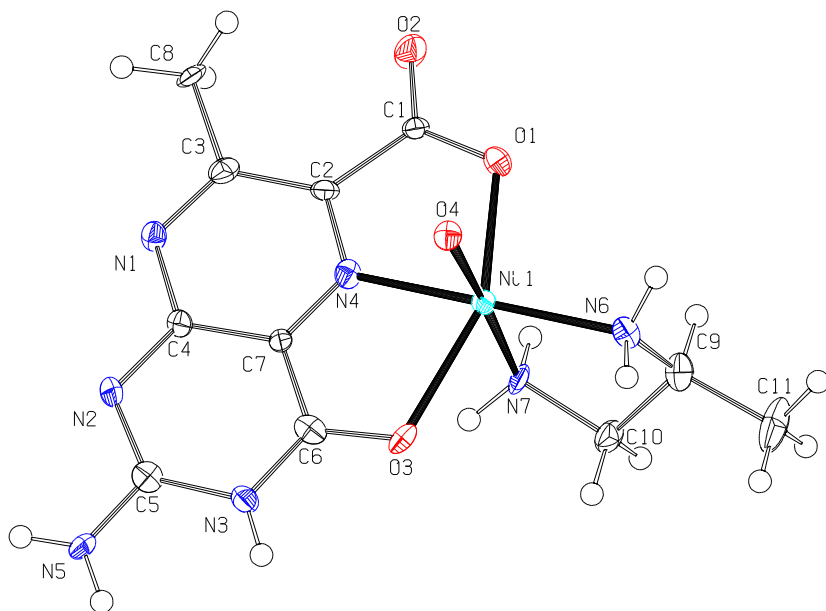


**Figure V-1.** ORTEP diagram of **2** probability at 50% thermal ellipsoide; lattice water molecules are omitted for clarity.

---

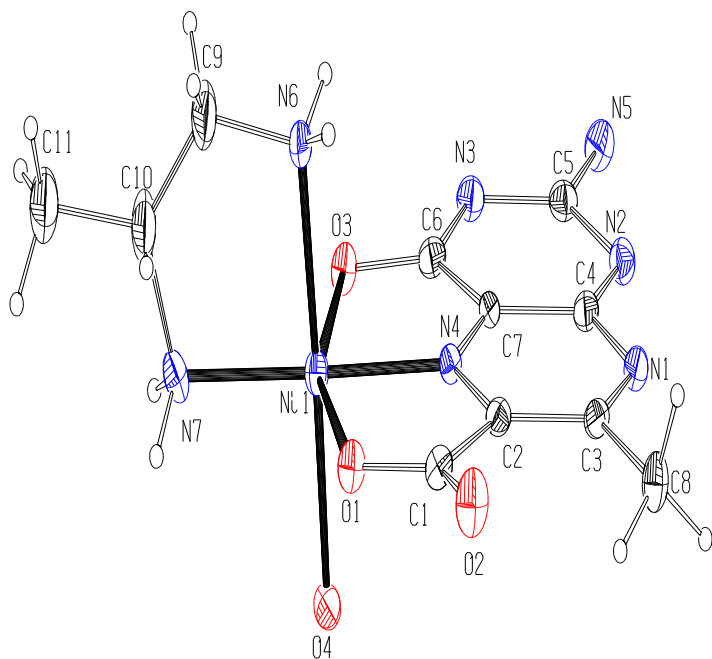


**Figure V- 2.** ORTEP diagram of **3** probability at 50% thermal ellipsoide; lattice water molecules are omitted for clarity.

---

**Table V-1. Crystal data and structure refinement for 2 and 3**

<b>Identification code</b>	<b>2</b>	<b>3</b>
<b>Empirical formula</b>	C <sub>22</sub> H <sub>32</sub> N <sub>14</sub> Ni <sub>2</sub> O <sub>18</sub>	C <sub>11</sub> H <sub>13</sub> N <sub>7</sub> NiO <sub>9</sub>
<b>Formula weight</b>	898.04	445.99
<b>Temperature/K</b>	110(2)	293(2)
<b>Crystal system</b>	Monoclinic	Monoclinic
<b>Space group</b>	P2 <sub>1</sub>	P2 <sub>1</sub> /c
<b>a/Å</b>	10.4777(14)	14.47(2)
<b>b/Å</b>	13.3994(17)	13.59(2)
<b>c/Å</b>	14.2435(18)	10.632(17)
<b>α/°</b>	90.00	90.00
<b>β/°</b>	102.434(2)	102.04(2)
<b>γ/°</b>	90.00	90.00
<b>Volume/Å<sup>3</sup></b>	1952.8(4)	2045(5)
<b>Z</b>	2	4
<b>ρ<sub>calc</sub>/cm<sup>3</sup></b>	1.527	1.449
<b>μ/mm<sup>-1</sup></b>	1.052	1.004
<b>F(000)</b>	924.0	912.0
<b>Crystal size/mm<sup>3</sup></b>	0.33 × 0.20 × 0.06	0.21 × 0.12 × 0.03
<b>Radiation</b>	MoKα (λ = 0.71073)	MoKα (λ = 0.71073)
<b>2θ range for data collection/°</b>	2.92 to 56.52	4.16 to 49.98

<b>Index ranges</b>	-13 ≤ h ≤ 13, -17 ≤ k ≤ 14, -18 ≤ l ≤ 15	-17 ≤ h ≤ 17, -16 ≤ k ≤ 14, -12 ≤ l ≤ 11
<b>Reflections collected</b>	11475	9416
<b>Independent reflections</b>	7004 [R <sub>int</sub> = 0.0280]	3545 [R <sub>int</sub> = 0.0664]
<b>Data/restraints/parameters</b>	7004/1/494	3545/0/255
<b>Goodness-of-fit on F<sup>2</sup></b>	1.063	1.175
<b>Final R indexes [I ≥ 2σ (I)]</b>	R <sub>1</sub> = 0.0596, wR <sub>2</sub> = 0.1635	R <sub>1</sub> = 0.1327, wR <sub>2</sub> = 0.3704
<b>Final R indexes [all data]</b>	R <sub>1</sub> = 0.0634, wR <sub>2</sub> = 0.1670	R <sub>1</sub> = 0.1455, wR <sub>2</sub> = 0.3800
<b>Largest diff. peak/hole / e Å<sup>-3</sup></b>	2.90/-0.66	1.73/-1.06

**Table V – 2. Geometric parameters of 2**

<b>Atom</b>	<b>Atom</b>	<b>Length/Å</b>	<b>Atom</b>	<b>Atom</b>	<b>Length/Å</b>
Ni1	N4	1.959(4)	N6	C9	1.498(9)
Ni1	N6	2.044(4)	N7	C10	1.479(5)
Ni1	N7	2.080(3)	N8	C14	1.336(5)
Ni1	O1	2.129(4)	N8	C15	1.353(5)

Ni1	O4	2.145(5)	N9	C15	1.343(5)
Ni1	O3	2.249(4)	N9	C16	1.374(6)
Ni2	N11	1.961(2)	N10	C17	1.339(5)
Ni2	N13	2.048(4)	N10	C16	1.363(6)
Ni2	N14	2.060(5)	N11	C13	1.294(5)
Ni2	O5	2.133(4)	N11	C18	1.338(5)
Ni2	O8	2.157(5)	N12	C16	1.336(5)
Ni2	O7	2.245(4)	N13	C20	1.471(8)
O1	C1	1.298(6)	N14	C21	1.479(6)
O2	C1	1.239(6)	C1	C2	1.509(7)
O3	C6	1.289(7)	C2	C3	1.418(8)
O5	C12	1.294(7)	C3	C8	1.496(7)
O6	C12	1.233(7)	C4	C7	1.414(7)
O7	C17	1.283(6)	C6	C7	1.433(7)
N1	C3	1.334(6)	C9	C11	1.511(9)
N1	C4	1.356(7)	C9	C10	1.512(7)
N2	C4	1.356(6)	C12	C13	1.510(6)
N2	C5	1.359(7)	C13	C14	1.450(7)
N3	C6	1.325(6)	C14	C19	1.489(7)
N3	C5	1.389(7)	C15	C18	1.405(7)
N4	C7	1.308(6)	C17	C18	1.445(7)
N4	C2	1.328(6)	C20	C21	1.514(8)

N5 C5 1.319(7) C20 C22 1.534(9)

Atom	Atom	Atom	Angle/°	Atom	Atom	Atom	Angle/°
N4	Ni1	N6	179.1(3)	O2	C1	O1	123.6(5)
N4	Ni1	N7	94.12(16)	O2	C1	C2	120.8(5)
N6	Ni1	N7	85.0(2)	O1	C1	C2	115.6(4)
N4	Ni1	O1	77.40(16)	N4	C2	C3	118.3(4)
N6	Ni1	O1	102.44(16)	N4	C2	C1	111.5(4)
N7	Ni1	O1	94.25(15)	C3	C2	C1	130.1(5)
N4	Ni1	O4	87.53(18)	N1	C3	C2	121.0(5)
N6	Ni1	O4	93.4(2)	N1	C3	C8	117.3(5)
N7	Ni1	O4	174.81(12)	C2	C3	C8	121.7(4)
O1	Ni1	O4	90.91(18)	N1	C4	N2	122.2(5)
N4	Ni1	O3	77.82(16)	N1	C4	C7	118.4(4)
N6	Ni1	O3	102.32(15)	N2	C4	C7	119.2(5)
N7	Ni1	O3	86.41(14)	N5	C5	N2	116.7(4)
O1	Ni1	O3	155.19(14)	N5	C5	N3	115.2(5)
O4	Ni1	O3	89.13(17)	N2	C5	N3	128.1(5)
N11	Ni2	N13	177.5(2)	O3	C6	N3	122.2(5)
N11	Ni2	N14	93.16(14)	O3	C6	C7	117.4(4)
N13	Ni2	N14	84.4(2)	N3	C6	C7	120.3(5)
N11	Ni2	O5	76.27(11)	N4	C7	C4	121.0(5)
N13	Ni2	O5	104.14(16)	N4	C7	C6	118.6(4)

N14	Ni2	O5	90.9(2)	C4	C7	C6	120.3(4)
N11	Ni2	O8	88.60(14)	N6	C9	C11	113.7(6)
N13	Ni2	O8	93.8(2)	N6	C9	C10	108.7(5)
N14	Ni2	O8	177.88(17)	C11	C9	C10	111.8(6)
O5	Ni2	O8	90.62(19)	N7	C10	C9	108.7(4)
N11	Ni2	O7	79.38(11)	O6	C12	O5	124.0(5)
N13	Ni2	O7	100.19(16)	O6	C12	C13	122.3(5)
N14	Ni2	O7	90.30(18)	O5	C12	C13	113.8(4)
O5	Ni2	O7	155.65(14)	N11	C13	C14	118.6(4)
O8	Ni2	O7	88.87(17)	N11	C13	C12	112.4(4)
C1	O1	Ni1	114.1(3)	C14	C13	C12	128.9(5)
C6	O3	Ni1	108.9(3)	N8	C14	C13	119.9(4)
C12	O5	Ni2	115.0(3)	N8	C14	C19	117.7(4)
C17	O7	Ni2	107.7(3)	C13	C14	C19	122.4(4)
C3	N1	C4	119.6(4)	N9	C15	N8	121.2(4)
C4	N2	C5	116.1(4)	N9	C15	C18	120.2(4)
C6	N3	C5	115.5(5)	N8	C15	C18	118.6(4)
C7	N4	C2	121.5(4)	N12	C16	N10	114.1(4)
C7	N4	Ni1	117.3(3)	N12	C16	N9	117.8(4)
C2	N4	Ni1	121.2(3)	N10	C16	N9	128.2(4)
C9	N6	Ni1	107.8(4)	O7	C17	N10	123.9(4)
C10	N7	Ni1	106.1(3)	O7	C17	C18	119.3(4)

C14	N8	C15	120.3(3)	N10	C17	C18	116.8(4)
C15	N9	C16	115.0(3)	N11	C18	C15	120.7(4)
C17	N10	C16	117.9(3)	N11	C18	C17	117.6(4)
C13	N11	C18	121.9(3)	C15	C18	C17	121.7(4)
C13	N11	Ni2	121.9(2)	N13	C20	C21	108.6(4)
C18	N11	Ni2	115.8(2)	N13	C20	C22	112.3(6)
C20	N13	Ni2	108.4(4)	C21	C20	C22	111.8(6)
C21	N14	Ni2	106.8(3)	N14	C21	C20	108.4(5)

**Table V – 3. Hydrogen Atom Coordinates ( $\text{\AA}\times 10^4$ ) and Isotropic Displacement Parameters ( $\text{\AA}^2\times 10^3$ ) for 2**

Atom	x	y	z	U(eq)
H3	4429	2726	8579	19
H5A	4471	2700	10910	22
H5B	3631	2758	9925	22
H6A	8463	2140	5706	19
H6B	7068	2278	5658	19
H7A	7558	4381	7572	19
H7B	8827	4413	7302	19
H10	10675	10169	1337	16
H12B	11475	10167	37	21

H12C	10648	10189	-954	21
H13A	8023	10794	4296	19
H13B	6660	10575	4300	19
H14A	6329	8491	2404	19
H14B	7752	8534	2712	19
H8A	11206	2378	11580	26
H8B	11651	3262	11005	26
H8C	11818	2157	10690	26
H9	8886	3740	5625	26
H10A	7488	4964	5976	23
H10B	6444	4152	6078	23
H11A	7749	3261	4109	55
H11B	7459	4382	4296	55
H11C	6424	3559	4375	55
H19A	3895	10176	-1623	30
H19B	3419	10876	-885	30
H19C	3307	9715	-798	30
H20	8647	9243	4415	23
H21A	7181	7931	4012	24
H21B	5989	8671	3876	24
H22A	8248	9696	5905	63
H22B	7884	8568	5722	63

**Table V – 4. Geometric parameters of 3**

Atom	Atom	Length/Å	Atom	Atom	Length/Å		
Ni1	N4	1.982(8)	N5	C5	1.347(15)		
Ni1	N6	2.081(10)	N6	C9	1.460(16)		
Ni1	N7	2.085(9)	N7	C10	1.460(19)		
Ni1	O1	2.154(8)	O1	C1	1.324(12)		
Ni1	O4	2.183(8)	O2	C1	1.247(13)		
Ni1	O3	2.256(7)	O3	C6	1.318(13)		
N1	C3	1.320(15)	C1	C2	1.494(15)		
N1	C4	1.385(14)	C2	C3	1.461(14)		
N2	C4	1.343(14)	C3	C8	1.521(14)		
N2	C5	1.389(14)	C4	C7	1.436(14)		
N3	C6	1.338(14)	C6	C7	1.466(14)		
N3	C5	1.374(14)	C9	C10	1.33(2)		
N4	C7	1.320(14)	C10	C11	1.49(2)		
N4	C2	1.355(13)					
Atom	Atom	Atom	Angle/°	Atom	Atom	Atom	Angle/°
N4	Ni1	N6	94.4(3)	O2	C1	O1	124.7(10)
N4	Ni1	N7	178.0(4)	O2	C1	C2	120.4(9)

N6	Ni1	N7	83.8(4)	O1	C1	C2	114.8(8)
N4	Ni1	O1	76.5(3)	N4	C2	C3	117.2(9)
N6	Ni1	O1	93.0(4)	N4	C2	C1	112.1(8)
N7	Ni1	O1	102.6(3)	C3	C2	C1	130.7(9)
N4	Ni1	O4	88.0(3)	N1	C3	C2	120.7(9)
N6	Ni1	O4	175.4(3)	N1	C3	C8	118.8(9)
N7	Ni1	O4	93.8(3)	C2	C3	C8	120.4(10)
O1	Ni1	O4	91.4(3)	N2	C4	N1	123.8(9)
N4	Ni1	O3	79.3(3)	N2	C4	C7	118.9(9)
N6	Ni1	O3	88.7(4)	N1	C4	C7	117.3(9)
N7	Ni1	O3	101.5(3)	N5	C5	N3	114.6(9)
O1	Ni1	O3	155.8(3)	N5	C5	N2	117.3(9)
O4	Ni1	O3	87.9(3)	N3	C5	N2	128.0(10)
C3	N1	C4	121.4(9)	O3	C6	N3	122.8(9)
C4	N2	C5	116.8(9)	O3	C6	C7	117.9(9)
C6	N3	C5	116.2(9)	N3	C6	C7	119.3(9)
C7	N4	C2	122.3(8)	N4	C7	C4	121.1(9)
C7	N4	Ni1	116.4(6)	N4	C7	C6	118.5(8)
C2	N4	Ni1	121.3(6)	C4	C7	C6	120.2(10)
C9	N6	Ni1	107.7(8)	C10	C9	N6	121.0(14)
C10	N7	Ni1	108.7(8)	C9	C10	N7	118.6(13)
C1	O1	Ni1	114.9(6)	C9	C10	C11	124.4(16)

C6 O3 Ni1 107.9(6) N7 C10 C11 116.9(14)

**Table V- 5. Hydrogen Atom Coordinates ( $\text{\AA}\times 10^4$ ) and Isotropic Displacement Parameters ( $\text{\AA}^2\times 10^3$ ) for 3**

Atom	<i>x</i>	<i>y</i>	<i>z</i>	U(eq)
H6A	7571	2101	5123	55
H6B	7525	2062	3738	55
H7A	9268	4238	4070	54
H7B	9303	4240	5451	54
H8A	3825	3159	1022	69
H8B	4396	4063	676	69
H8C	3508	4231	1278	69
H9A	8995	1799	5507	181
H9B	8943	1742	4031	181
H10	9405	2893	3870	203
H11A	10639	2160	4742	174
H11B	10740	2836	5958	174
H11C	10756	3300	4613	174

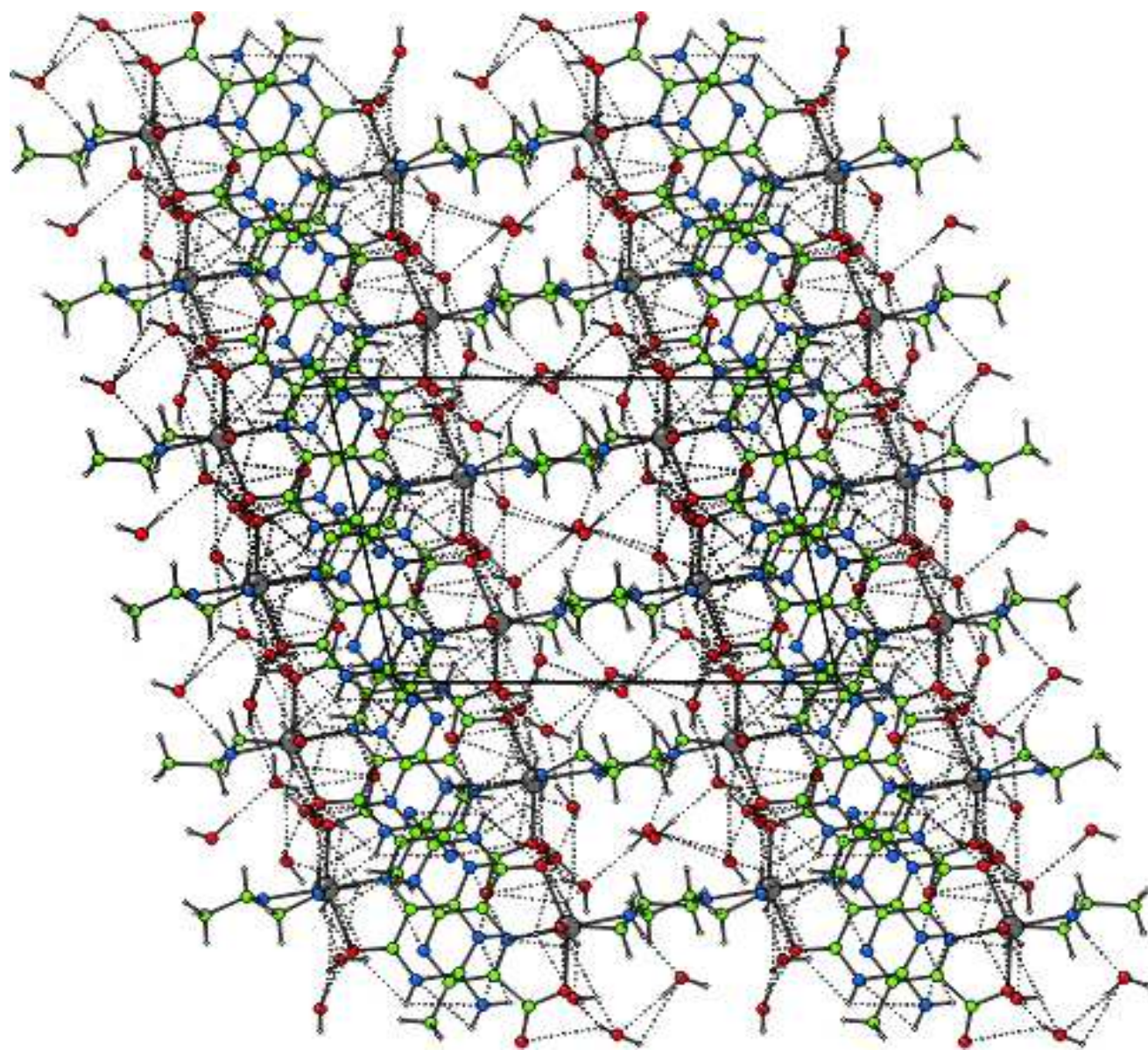


**Figure V-3.** Crystal packing diagram of **2** and H-bonding network viewed along b axis.

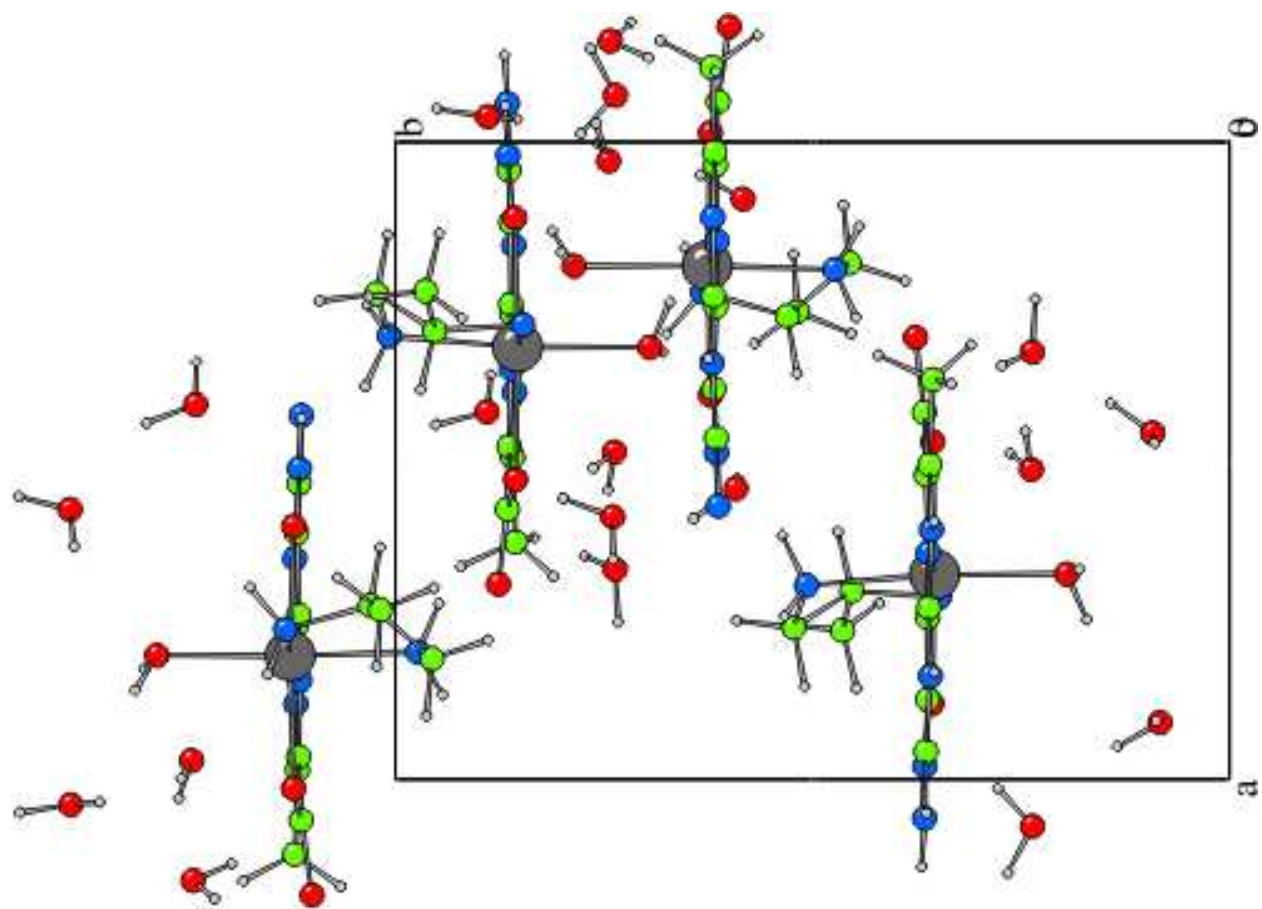


**Figure V – 4.** Unit cell of the complex 2 along c axis

---

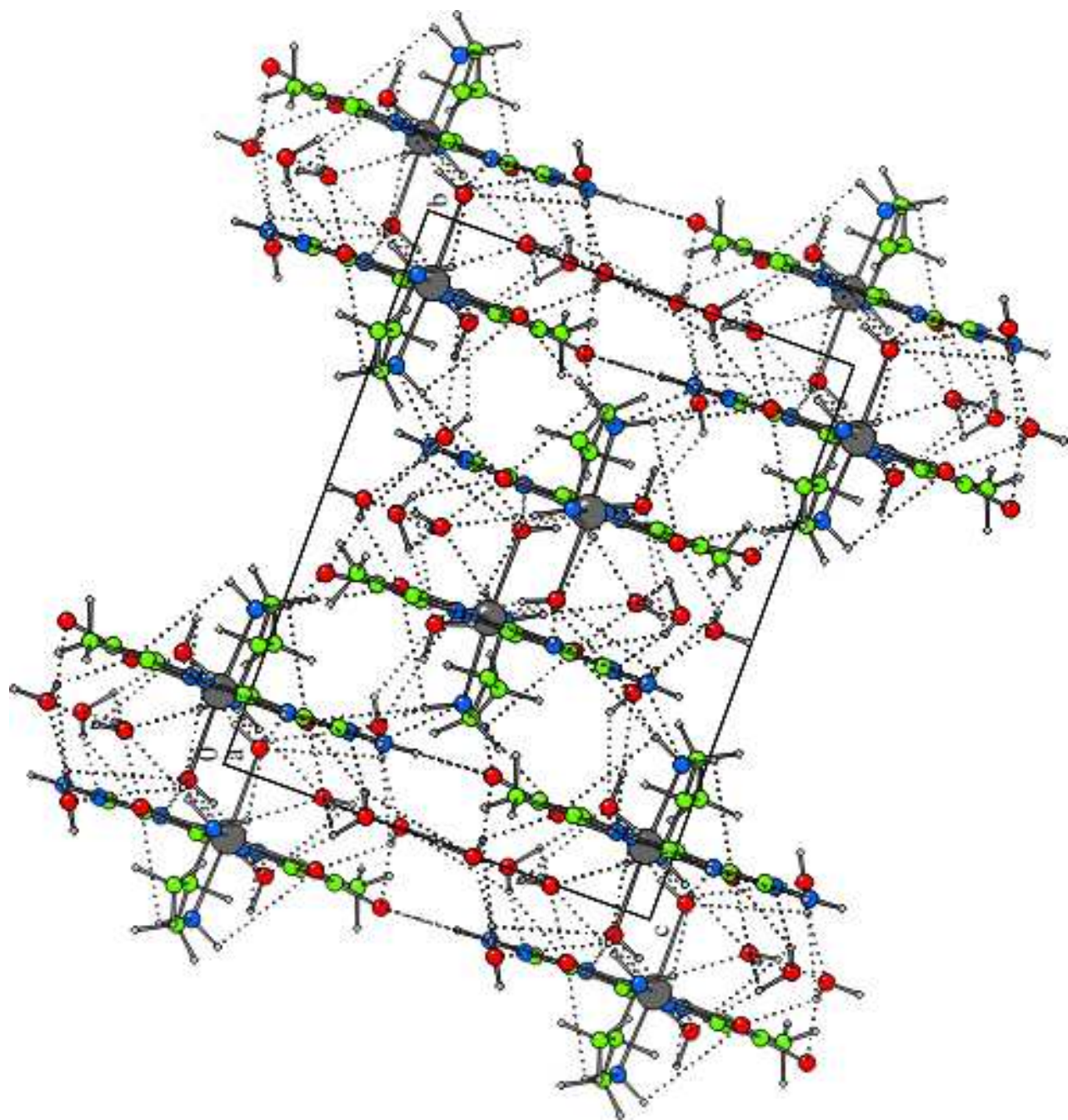


**Figure V – 5.** Crystal packing diagram of **3** and H-bonding network viewed along a axis.

---

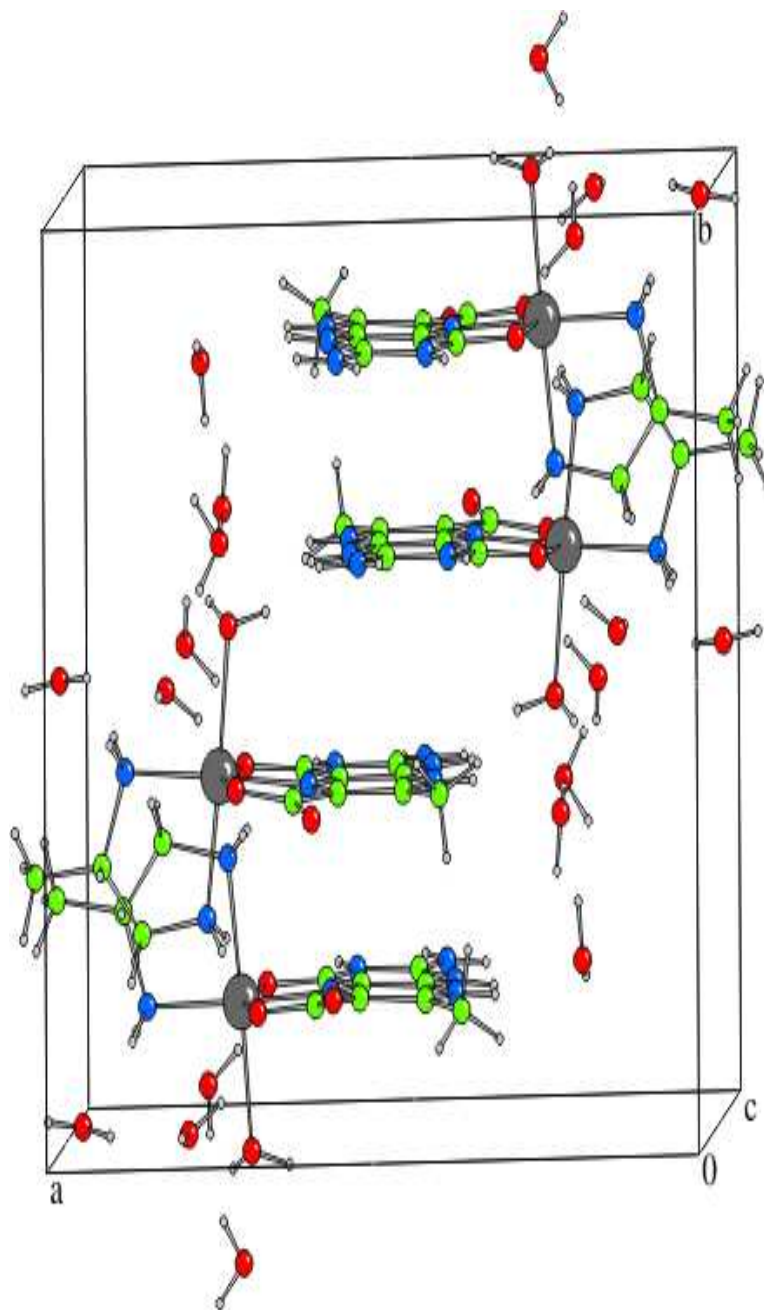


**Figure V – 6.** Unit cell of the complex **3** along *c* axis

---

The Ni(II) atom in **2** is located in a distorted octahedron, where it is coordinated by the tridentate pterin ligand, the bidentate ancillary ligand R-(+)-pn and a water molecule. The pterin ligand forms two five membered chelate rings. The R-(+)-pn chelate ring is arranged orthogonally with

respect to the pterin ligand, for minimising the steric repulsion Figure V-4.<sup>17,18</sup> Geometric parameters of **2** (Table V-2) revealed the extent of departure from octahedral geometry in this case. The basal plane is formed by the two nitrogen atoms (N6, N7) of R-(+)-pn, the pyrazine ring nitrogen atom (N4) and the aquo group atom (O4). The axial positions are occupied by the two pterin oxygen atoms (O1 and O3) with the latter one forming the longest axial bond [2.249(4)Å]. Considering the charge balance of this complex, it is apparent that the pterin ligand is acting as a bidentate O – N – O donor. Of the three axes, least deviation from linearity is observed for the N4 – Ni1 – N6 axis [179.1(3)°], where the highest electron density is concentrated [Ni – N4: 1.959(4)Å; Ni – N6 : 2.044(4)Å]. This situation represents contributions from the  $\sigma$ -donor atom N6 (pn) and the N4 atom of the redox non-innocent pterin ligand from the opposite directions of the Ni(II) centre ( $d^8$ ), with possible assistance from the  $\pi$ -donating phenolate and carboxylate oxygen atoms<sup>18</sup>.

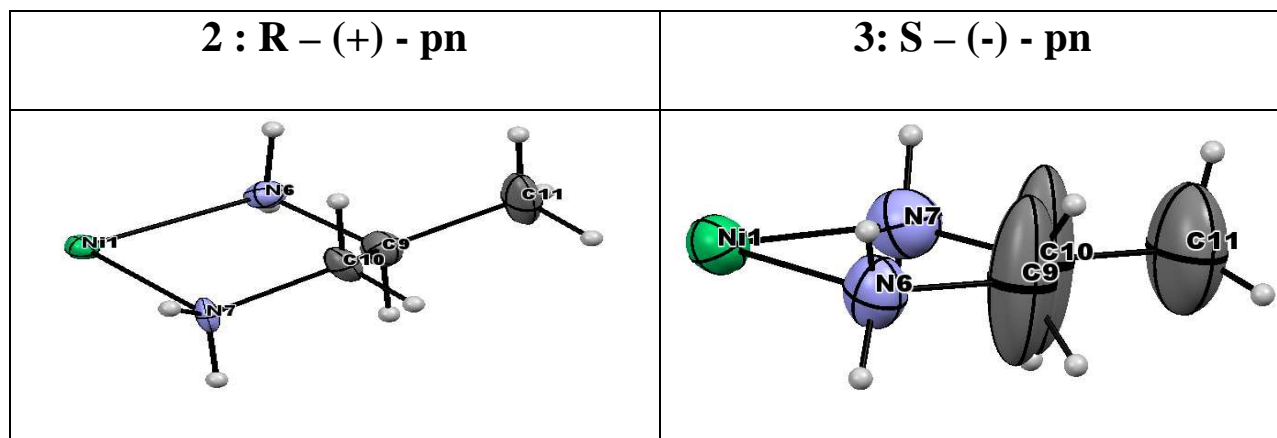
The exocyclic bond length data of the pyrimidine ring, e.g., C6 – O3 [1.289(7)Å] and C5 – N5 [1.319(7)Å] merit attention. Their near double bond character is ascribed to the electron shuffling process by the pterin moiety, from the pyrazine ring nitrogen atom (N1) to the C6-carbonyl group, during formation of the Ni1 – O3 bond.<sup>22,23</sup> In the crystal N – H...O, O – H ...N and O – H ...O hydrogen bonds link the complex molecule and lattice water molecule into layers along the b axis (Figure V-3). The lattice water molecules are decisive for crystal packing.

The molecular structure of **3** (Figure V-2) also conform to a distorted octahedral geometry, as evident from the geometric parameters in Table V-4. A major cause of such distortion from regular geometry is mainly due to the formation of two five membered chelate rings by the pterin ligand with small bite angles [87.9° and 76.5°(3)] for minimising the steric repulsion. The pterin ring and the pn ring are arranged orthogonally (Figure V-6). As earlier,

least deviation [ $178.0(4)^\circ$ ] from linearity is observed along the N4 – Ni – N7 axis. The exocyclic bonds of the pyrimidine ring namely C6 – O3 [ $1.318(13)\text{\AA}$ ] and C5 – N5 [ $1.347(15)\text{\AA}$ ] show near double bond character as well. The crystal packing diagram of **3** is shown in Figure V-5.

A persual of Figure V-3 and V-5 shows extensive differences in H-bonding pattern between them; this may be traced partly to the conformational difference associated with the R-(+)-pn and S-(-)-pn chelate rings as summarised below.

Figure V-7 shows the conformational differences with respect to the “pn” chelate rings, between **2** and **3**. A comparison of the projections with that in Scheme IV-10, indicates  $\delta$ -conformation in each case.<sup>79,90,149</sup> But their extent of puckering of the ‘pn’ chelate ring is different, with that for **3** [S-(-)-pn] approaching near planarity. Achieving equatorial disposition of the CH<sub>3</sub> – group (of ‘pn’ chelate ring) appears to be the main driving force behind such an observation.<sup>79,90</sup> Such conformational differences gives rise to subtle difference in the CD spectra of **2** and **3** as discussed later.



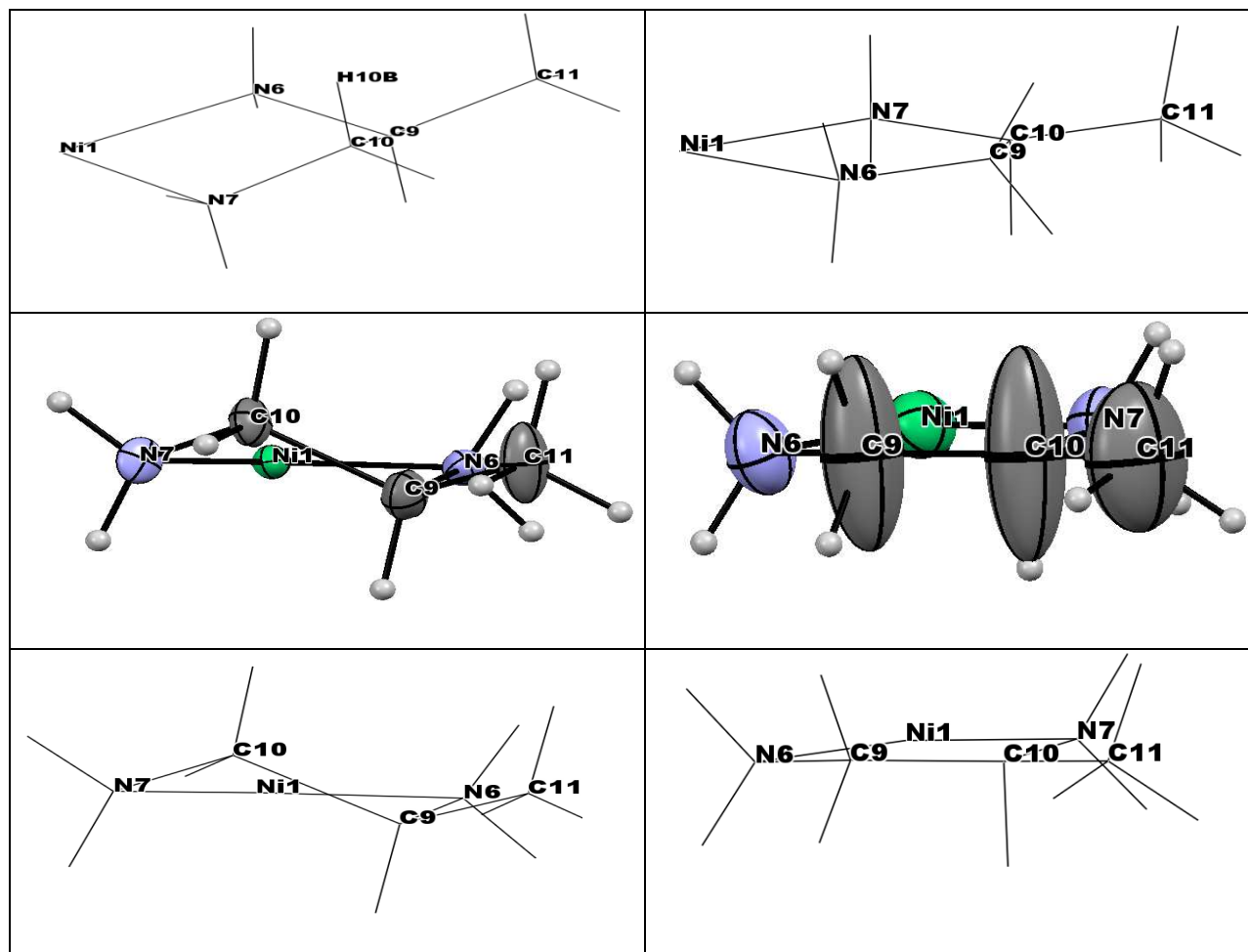


**Figure V-7.** Projections of x-ray structural data of **2** and **3** for viewing the puckering of R-(+)-pn/S-(-)-pn [pn = 1,2-diaminopropane] chelate rings respectively, from different angles.<sup>79,90</sup> For **2** [with R-(+)-pn] a  $\delta$ -conformation is observed, while in case of **3** [with S-(-)-pn], the chelate ring approach planarity for achieving the equatorial disposition of the CH<sub>3</sub> group.

## ESIMS DATA of **2**

The molecular ion peak at m/z 458 corresponds to the species  $[M-2H]^+$ , relative abundance=20%; the peak at m/z 352 corresponds to the dehydrated species  $[M-6H_2O]^+$ , relative abundance=65% and that m/z 702 is due to the dimer of the dehydrated species  $2[M-6H_2O-H]$ , relative abundance=100% ; all the isotope distribution patterns could be simulated, where M represents to the corresponding molecular formula of **2** ( $NiC_{11}H_{27}N_7O_9$ , FW 459.71)

The above data indicate stability of the Ni(II) – pterin as well as the Ni(II) – pn bonds, which remains intact during the above mass spectral process. Figures V-8 and V-10 show the relevant data.

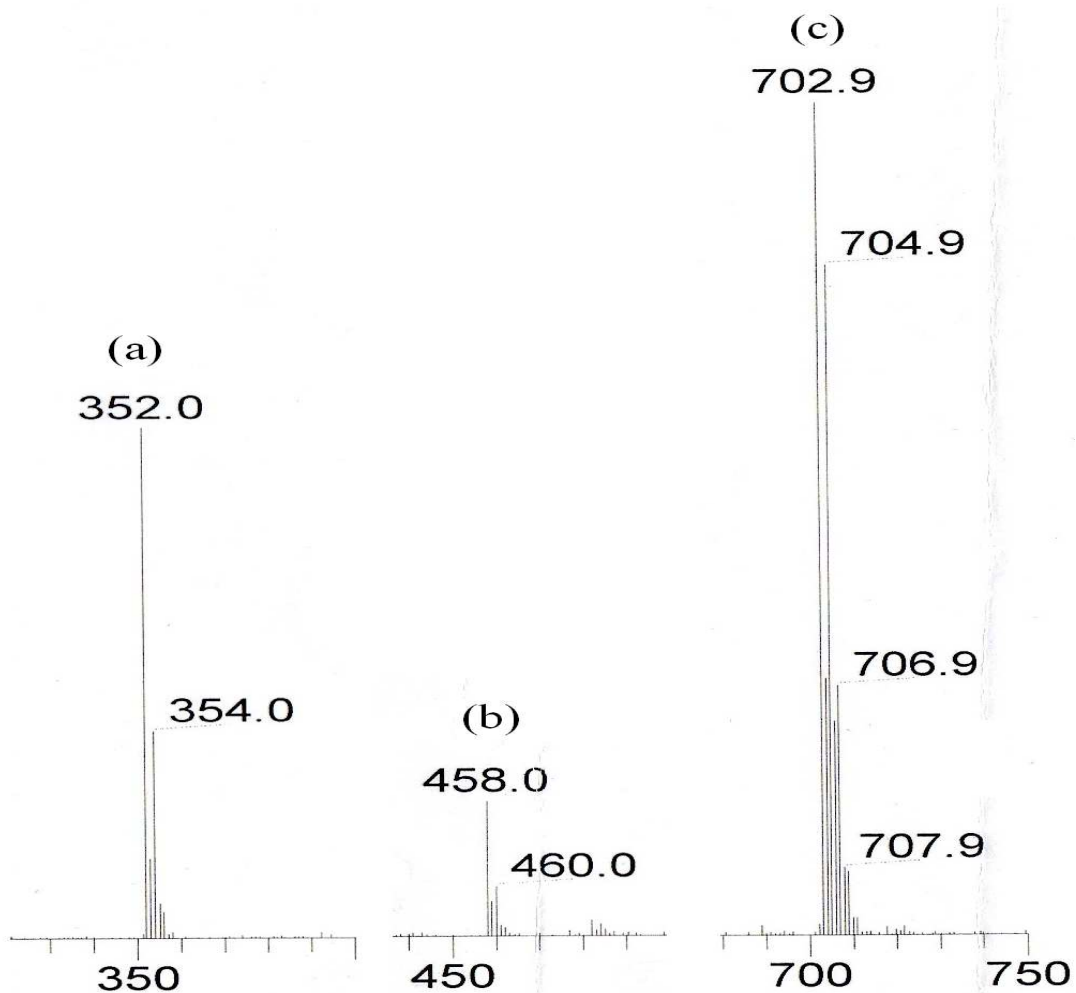


**Figure V-8.** ESIMS data of **2**: (a) for the peak at  $m/z = 352$  corresponding to the fragment  $[M-6H_2O]^+$ , relative abundance=65%; (b)  $m/z = 458$  for the peak corresponding to the fragment  $[M-2H]^+$ , relative abundance=20%; (c)  $m/z = 702$  for the peak corresponding to the fragment  $2[M-6H_2O-H]^+$ , relative abundance=100%. Here M is the molecular formula of **2**.

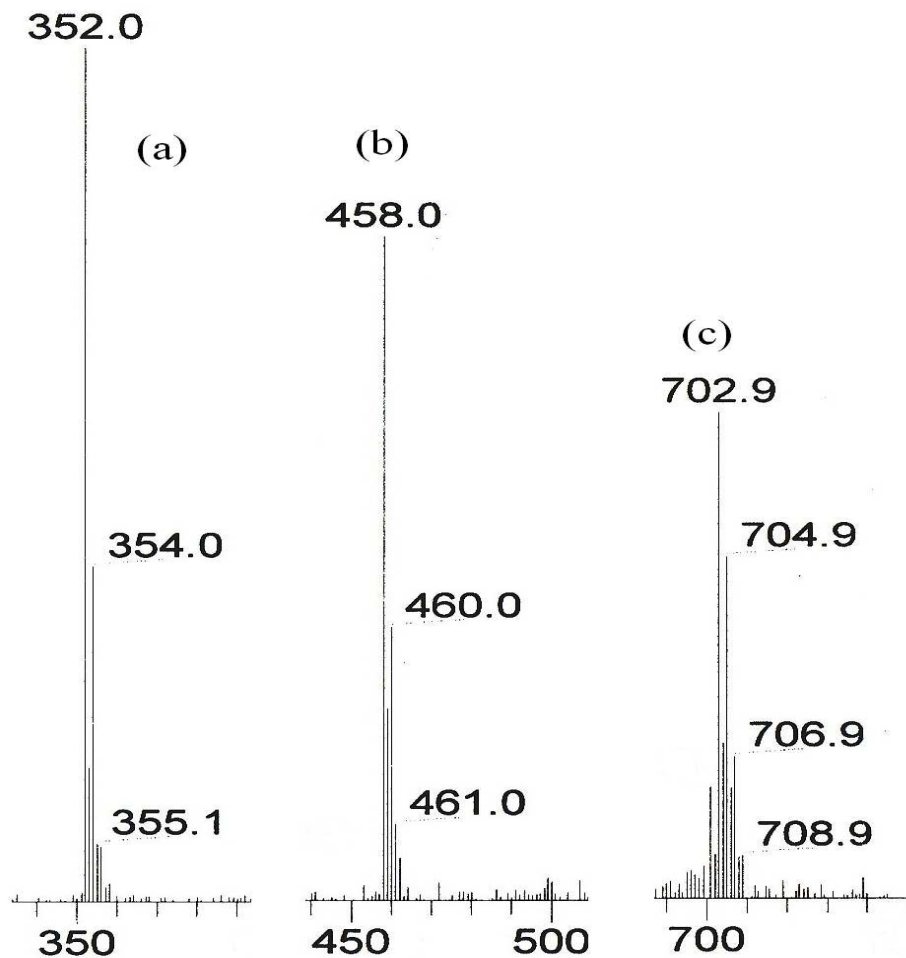


**Figure V-9.** ESIMS data of **3**: (a) for the peak at  $m/z = 352$  corresponding to the fragment  $[M-6H_2O]^+$ , relative abundance= 100%; (b)  $m/z = 458$  for the peak corresponding to the fragment  $[M-2H]^+$ , relative abundance= 83%; (c)  $m/z = 702$  for the peak corresponding to the fragment  $2[M-6H_2O-H]^+$ , relative abundance= 62%. Here M represents the formula of **3**.

---

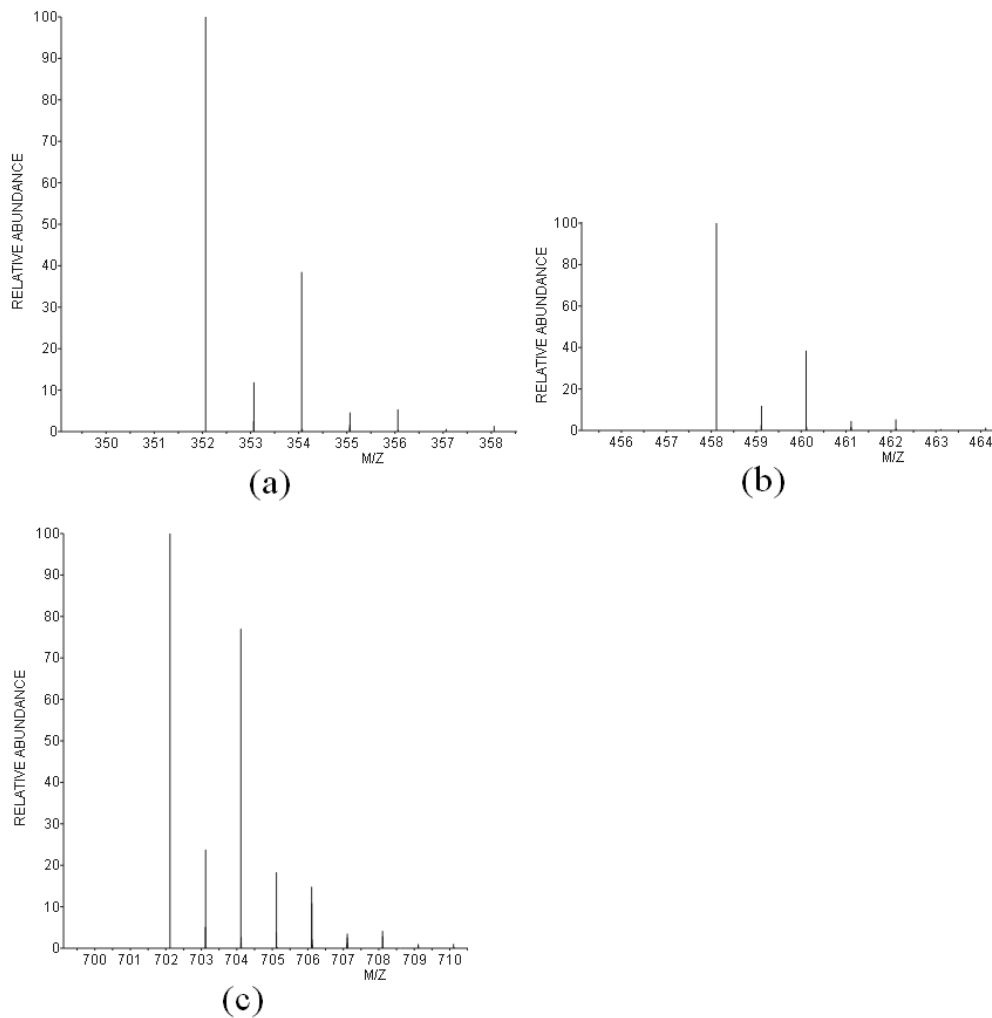


**Figure V-10.** The calculated isotope patterns of **2** & **3**: (a) for the peak at  $m/z = 352$  corresponding to the fragment  $[M-6H_2O]^+$  ; (b)  $m/z = 458$  for the peak corresponding to the fragment  $[M-2H]^+$  ; (c)  $m/z = 702$  for the peak corresponding to the fragment  $2[M-6H_2O-H]^+$  . Here M has the usual meaning.

### ESIMS DATA of **3**

The molecular ion peak at  $m/z$  458 corresponds to the species  $[M-2H]^+$ , relative abundance= 83%; the peak at  $m/z$  352 corresponds to the dehydrated species  $[M-6H_2O]^+$ , relative abundance= 100% and that at  $m/z$  702.9 is due to the dimer of the dehydrated species  $2[M-6H_2O-H]$ , relative abundance= 62%; all the isotope distribution patterns could be simulated, where M represents the corresponding molecular formula of **3** (same as that of **2**; Figure V-9 and V-10). Once again the stability of metal-ligand bonds of **3** is indicated, remaining essentially intact during the mass spectral process.

Taken together with the microanalytical and x-ray structural data, such ESIMS data affirm the chemical compositions of **2** and **3**, as spelt out in the earlier sections as well as their purity. Finally, a comparison of Figures V-8 and V-9 underlines an interesting aspect; although the three above-mentioned peaks are similar with respect to their positions ( $m/z$  values), their relative intensities (relative abundance) are different, most likely originating from the differences in the unit cell structures of **2** and **3** as well as their H-bonding patterns (Table V-1; Figure V-3 to V-6).

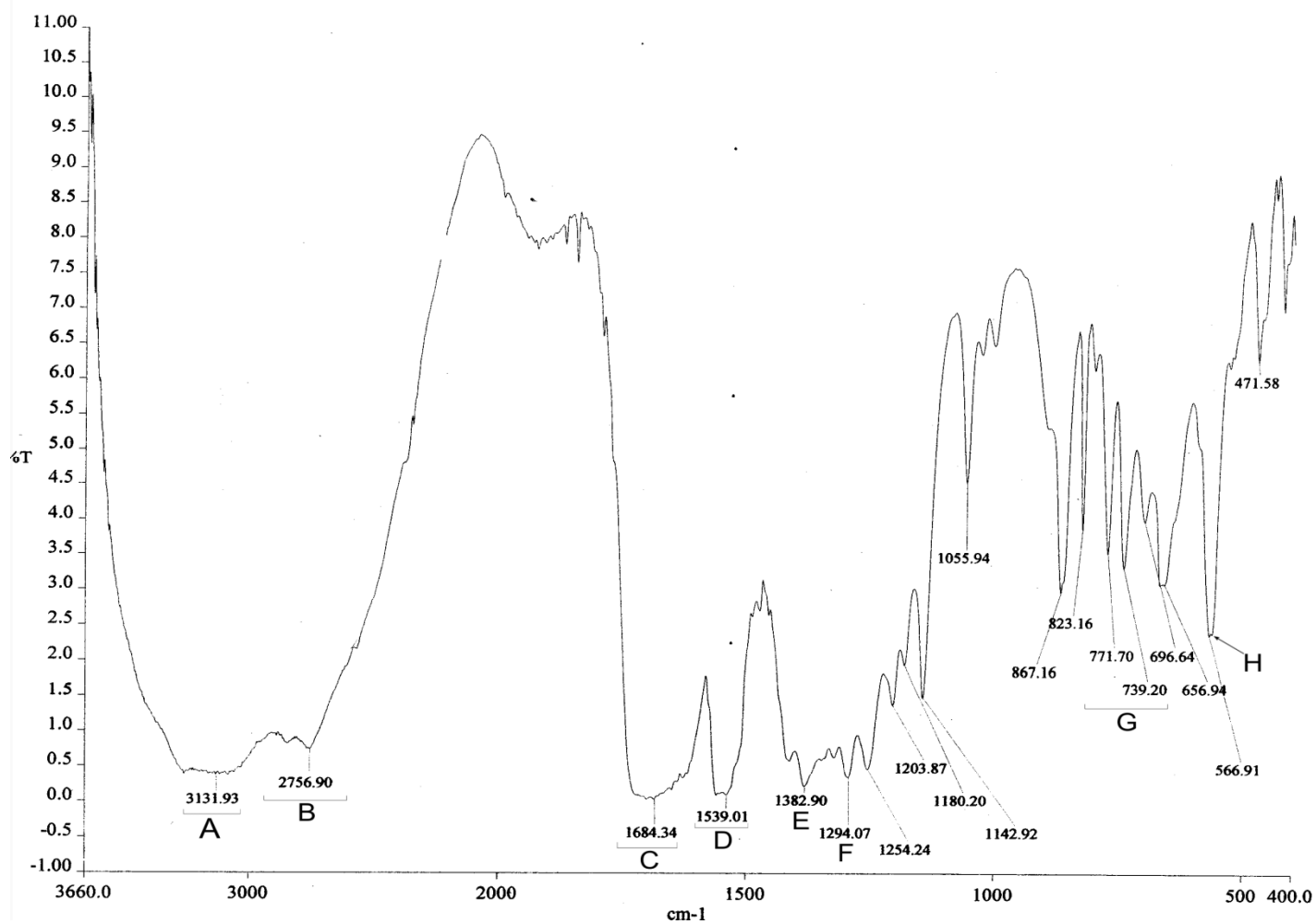


**Figure V-11.** IR spectrum (KBr) of H<sub>2</sub>L · 1.5H<sub>2</sub>O (**1**)

- A: the broad band over the region 3250-3050 cm<sup>-1</sup> due to the ν(OH) and ν(NH) stretching vibrations of the hydrogen bonded H<sub>2</sub>O, -COOH(6), NH(3) and NH<sub>2</sub>(2) groups, Scheme III-1;
- B: the ν(CH) stretching vibrations of the CH<sub>3</sub>(7) group are observed at 2851 cm<sup>-1</sup> and 2757 cm<sup>-1</sup> respectively;

- C: an intense broad band centred at  $1684\text{ cm}^{-1}$  and spread over the region  $1718\text{-}1636\text{ cm}^{-1}$  is due to the  $\nu(\text{C}=\text{O})$  modes of the  $\text{C}=\text{O}(4)$  and  $\text{COOH}(6)$  groups, (Scheme III-1); the N-H bending vibrations of the  $\text{NH}_2(2)$  group are occluded under this band;
- D: the  $\nu(\text{C}=\text{C})$  and  $\nu(\text{C}=\text{N})$  modes at the pterin ring appears around  $1560\text{-}1539\text{ cm}^{-1}$ ;
- E&F: the  $\delta(\text{O-H})$  and  $\nu(\text{C-O}) + \delta(\text{O-H})$  modes of the  $\text{COOH}(6)$  group appear at  $1382\text{ cm}^{-1}$  and  $1294\text{ cm}^{-1}$  respectively;
- G: different types of skeletal bending vibrations of the pterin ring appear over the region  $860\text{-}650\text{ cm}^{-1}$ ;
- H: rocking vibrations of the  $\text{NH}_2(2)$  group appears around  $567\text{ cm}^{-1}$ .
-

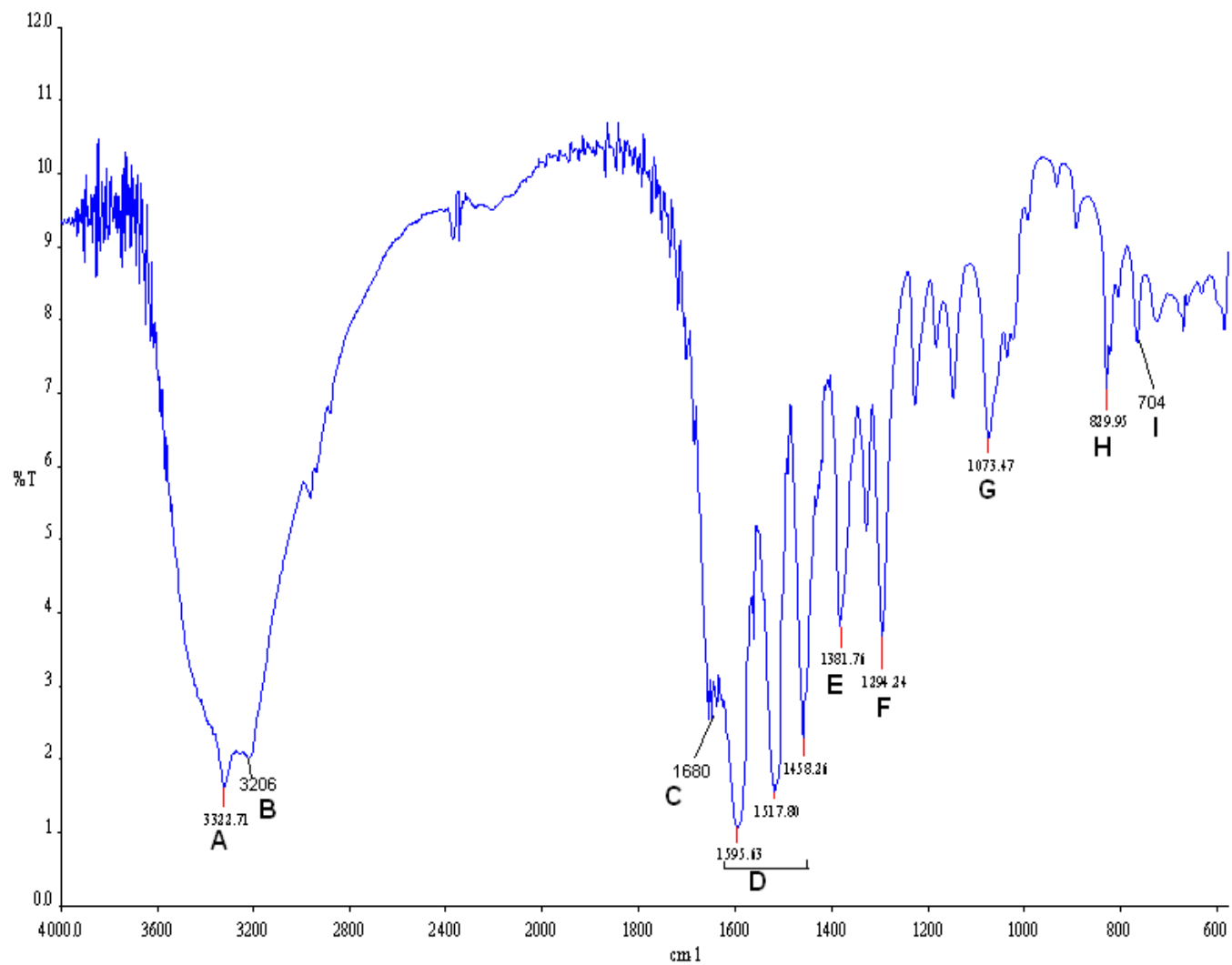
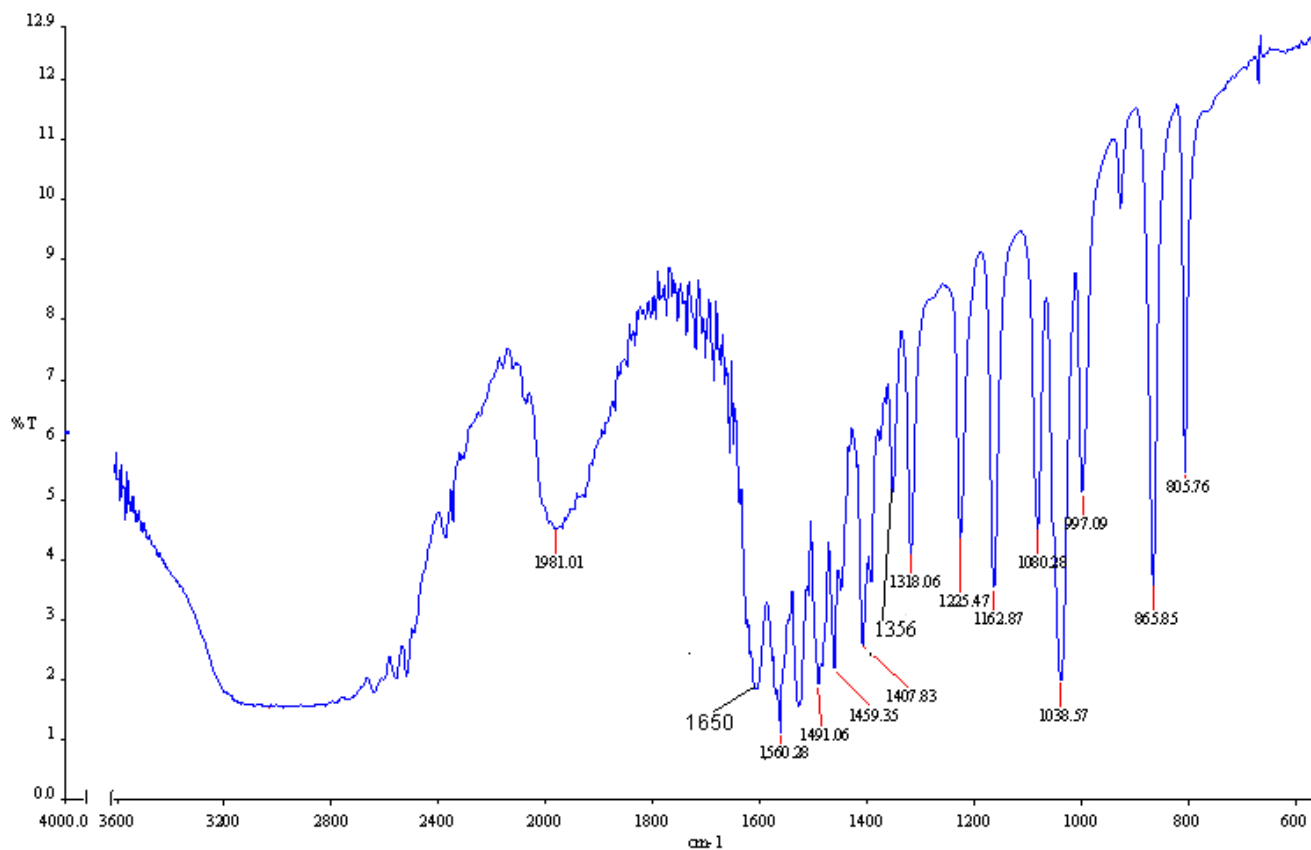


**Figure V-12.** IR spectrum (KBr) of **2**



. **Figure V-13.** IR spectrum (KBr) of **3**

**IR Spectroscopy.** The IR spectrum of the pterin ligand ( $\text{H}_2\text{L} \cdot 1.5\text{H}_2\text{O}$ , **1**) is shown in Figure V-11, while those of **2** and **3** are shown in Figure V-12 and V-13 respectively. As pointed out in the earlier chapters, the intense broad band over the region  $3300 - 2500 \text{ cm}^{-1}$  (Figure V-11) originate from the  $\nu(\text{OH})$ ,  $\nu(\text{NH})$ ,  $\nu(\text{CH})$  stretching vibrations of the different functional groups of **1** as well as its lattice water molecules; another intense broad band centred around  $1684 \text{ cm}^{-1}$  corresponds to the  $\nu(\text{C}=\text{O})$  modes of the  $\text{C}=\text{O}(4)$  group as well as that of the  $\text{COOH}(6)$  functional groups of **1**.<sup>21,148</sup> Few  $\nu(\text{C}=\text{C})$  and  $\nu(\text{C}=\text{N})$  vibrations of the pterin ring appear around  $1560\text{-}1539 \text{ cm}^{-1}$ . Two other broad bands at  $1383 \text{ cm}^{-1}$  and  $1294 \text{ cm}^{-1}$  characterize the  $\delta(\text{O}-$

H) and  $\nu(\text{C-O}) + \delta(\text{O-H})$  modes of the  $\text{COOH}(6)$  group.<sup>21</sup> It is evident from Figures V-12 and V-13 that most of the above-mentioned IR bands are modified on complex formation with the Ni(II) centre in **2** and **3**, through deprotonation of the  $\text{COOH}(6)$  and  $\text{NH}(3)$  groups (Scheme V-1); their broad bands centred around  $3300 - 3200 \text{ cm}^{-1}$  correspond to the extra- and intraspheric water molecules [ $\nu(\text{OH})$ ] and the  $\text{NH}_2(2)$  group [ $\nu(\text{NH})$ ]. The  $\nu_{\text{as}}$  and  $\nu_{\text{s}}$  stretching vibrations of the  $\text{CO}_2'$  group appear at  $1659 - 1650 \text{ cm}^{-1}$  and  $1382 - 1356 \text{ cm}^{-1}$  respectively; the  $\Delta\nu$  values ( $294 - 278 \text{ cm}^{-1}$ ) indicate unidentate carboxylate coordination, in accordance with their x-ray structural data (Figure V-1 and V-2).<sup>87,88</sup> The  $\text{NH}_2$  deformation vibrations (of the 'pn' chelate ring) contribute to the broad nature of the IR bands around  $1600 \text{ cm}^{-1}$  for both **2** and **3**. Finally, a comment is necessary about the difference in relative intensity of peaks around  $1700 - 750 \text{ cm}^{-1}$  region of **2** and **3**, although their numbers are almost the same. One likely reason is their difference in hydrogen bonding patterns (Figure V-3 and V-5); the more intense bands at  $865 \text{ cm}^{-1}$  for **3** (Figure V-13) arise most likely from the out-of-plane C - H deformation vibrations of the  $\text{CH}_3$  group [of the S(-)-pn ring].<sup>21,148</sup> The greater distortion of the aforesaid 'pn' ring [Figure V-7] is another possible reason of such an observation.

**Fluorescence emission spectra.** Fluorescence emission spectra of **2** and **3** in  $\text{CH}_3\text{OH}$  are shown in Figure V-14 and V-15 respectively. The reduced forms of these complexes (**2R** and **3R**) were also studied by the addition of requisite quantity of  $\text{NaBH}_4$  to the methanolic solutions of **2** and

3. As discussed in chapter IV, such reduced forms are the corresponding Ni(I) complex with the 7,8-dihydro forms of the pterin ligand ( $L^{2-}$ , Scheme IV-6).

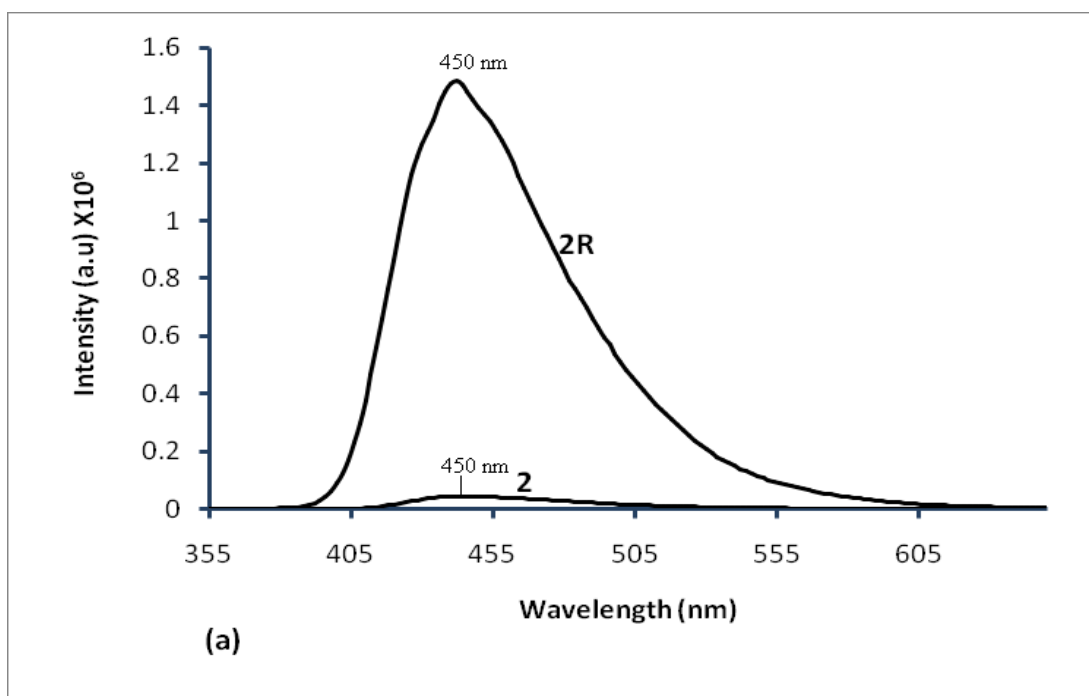


**Figure V-14.** Fluorescence emission spectra of **2** ( $\text{CH}_3\text{OH}$ ,  $1.1 \times 10^{-3}$  M), **2R** ( $\text{CH}_3\text{OH}$ ,  $1.4 \times 10^{-3}$  M).

---

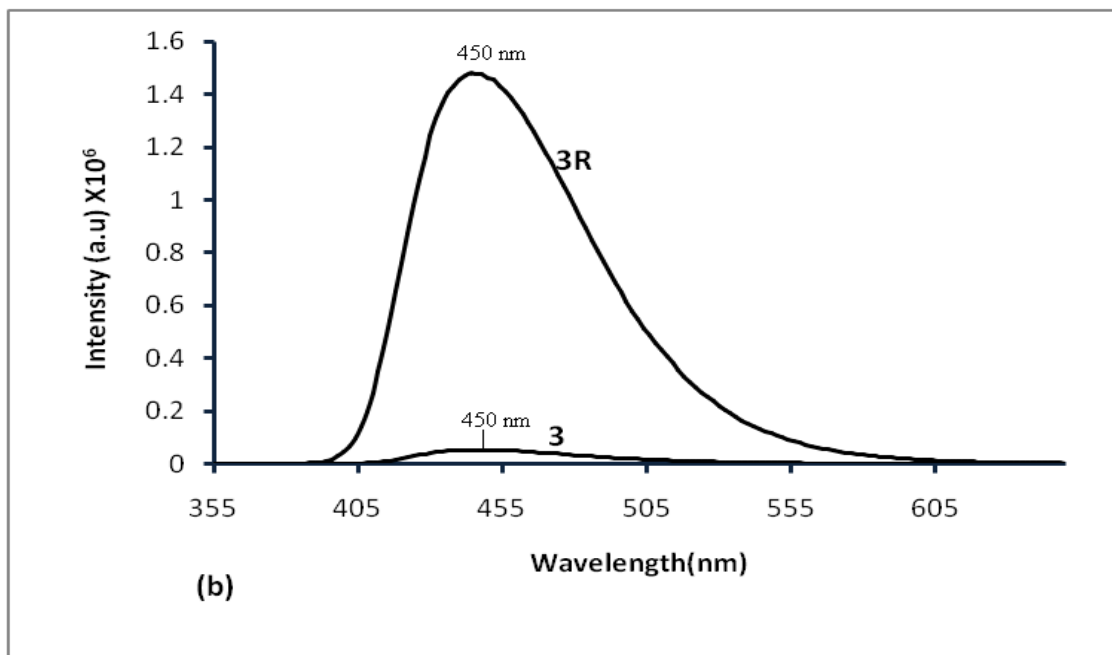
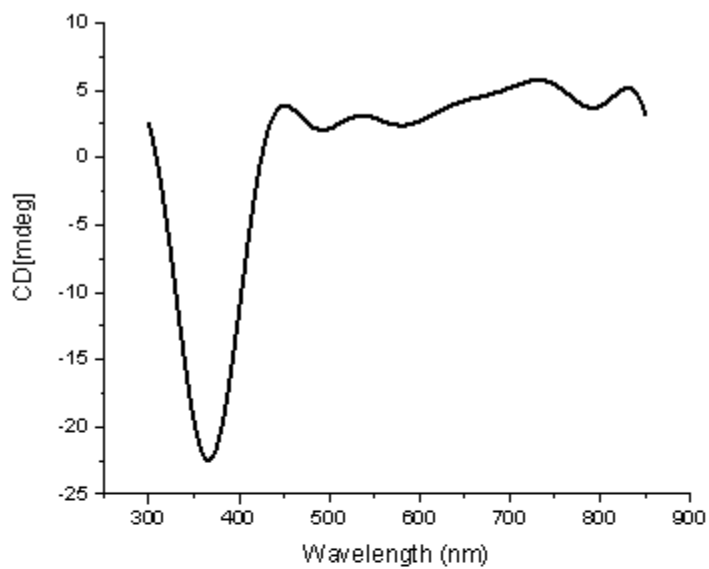
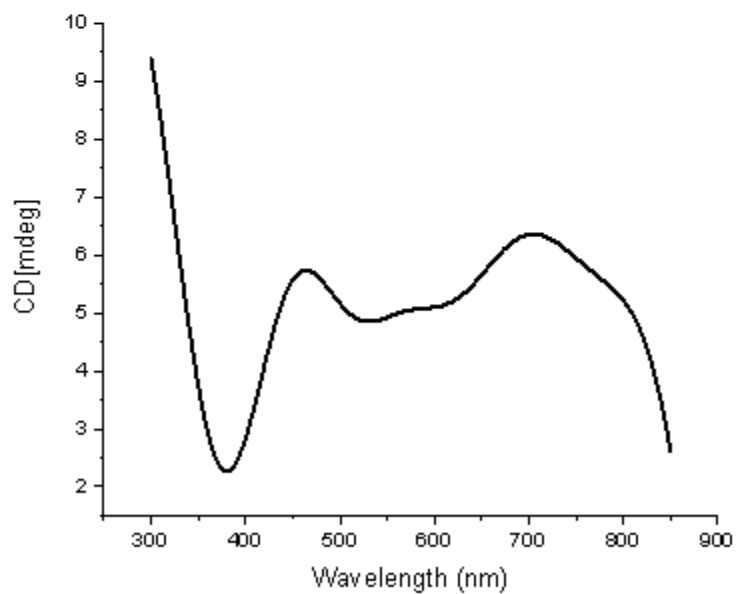


**Figure V-15.** Fluorescence emission spectra of **3** ( $\text{CH}_3\text{OH}$ ,  $5.8 \times 10^{-4}$  M), **3R** ( $\text{CH}_3\text{OH}$ ,  $5.8 \times 10^{-4}$  M).

Although the emission maximum appears consistently at 450 nm in all these cases, a considerable enhancement of fluorescence intensity is observed upon  $\text{NaBH}_4$  reduction. This can be associated with the greater electronic circulation in the rigid reduced complex molecules, involving the extended  $\pi$  orbitals (pterin) and Ni(I) ( $d^9$ ) orbitals; there appears to be less scope for the loss of the vibronic energy.<sup>36</sup> MLCT type transitions [ $\text{Ni(I)}e_g^* \rightarrow \pi^*$ , pterin] are also possible.<sup>32</sup>



(a)



(b)

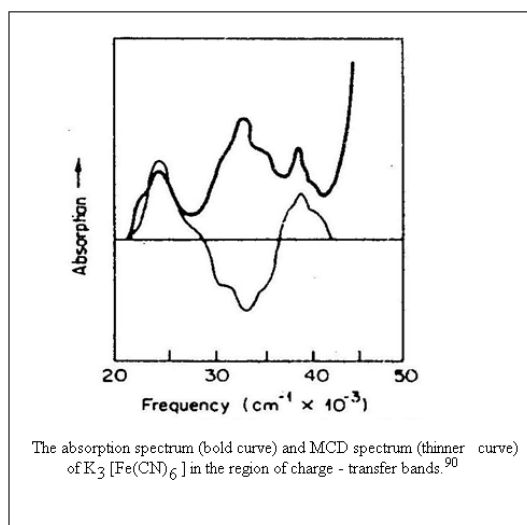
**Figure V-16.** CD spectral data in CH<sub>3</sub>OH of (a) **2** ( $1.3 \times 10^{-3}$  M); (b) **3** ( $1.1 \times 10^{-3}$  M).

## Circular Dichroism Spectroscopy

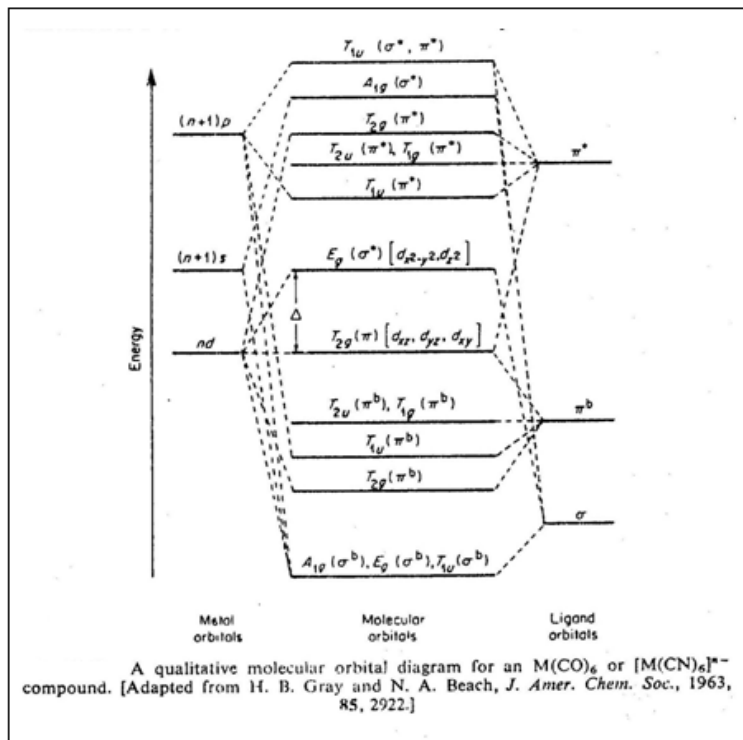
The CD spectral data of **2** and **3** are shown in Figure V-16. The two above spectra can be subdivided into two distinct regions:

1. 300 – 450 nm region, where the LMCT type transition occurs, characterized by a distinct negative Cotton effect; on the basis of MCD spectral study of  $K_3[Fe(CN)_6]$ , such a negative CD band is assigned to a  $t_{2u}$  (ligand  $\pi$  orbital)  $\rightarrow$   $t_{2g}$  (metal) transition (Scheme V-6);<sup>90, 150-152</sup>
2. 450 – 850 nm region where a series of weak positive Cotton effects are observed, corresponding to the different spin-allowed and spin-forbidden transitions of the Ni(II) centre (Scheme IV-7 and IV-8).

The  $\delta$ -conformation of the 'pn' chelate ring (Figure V-7), decides the positive nature of the Cotton effects of the second type.<sup>149</sup> The greater puckering of the 'pn' chelate ring is possibly responsible for the higher intensity of such bands for **3**.



**Scheme V-6(a)**



Scheme V – 6(b)

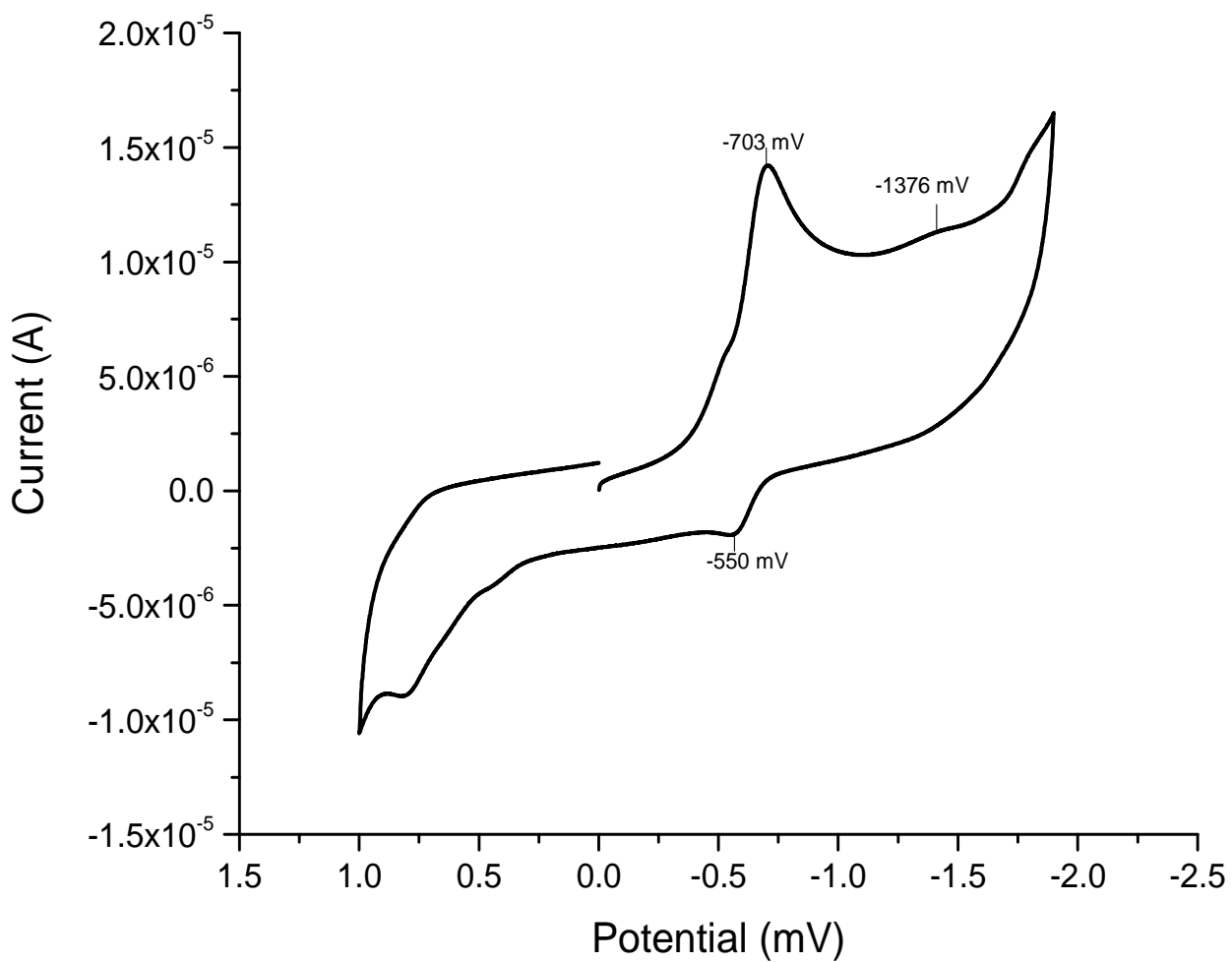


**Figure V- 17.** Cyclic voltammetry data of **2** in DMSO ( 0.1M TBAP; scan rate, 100mV s<sup>-1</sup>).

---

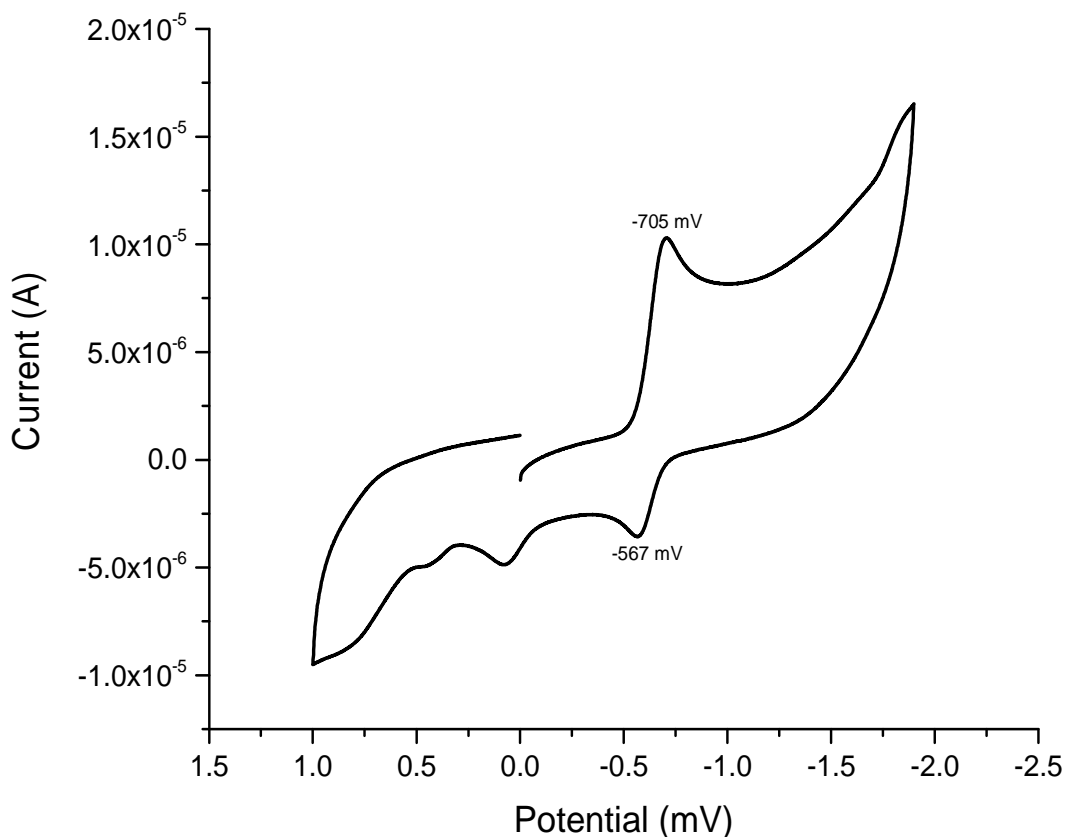


**Figure V - 18.** Cyclic voltammetry data of **3** in DMSO ( 0.1M TBAP; scan rate, 100mV s<sup>-1</sup>).

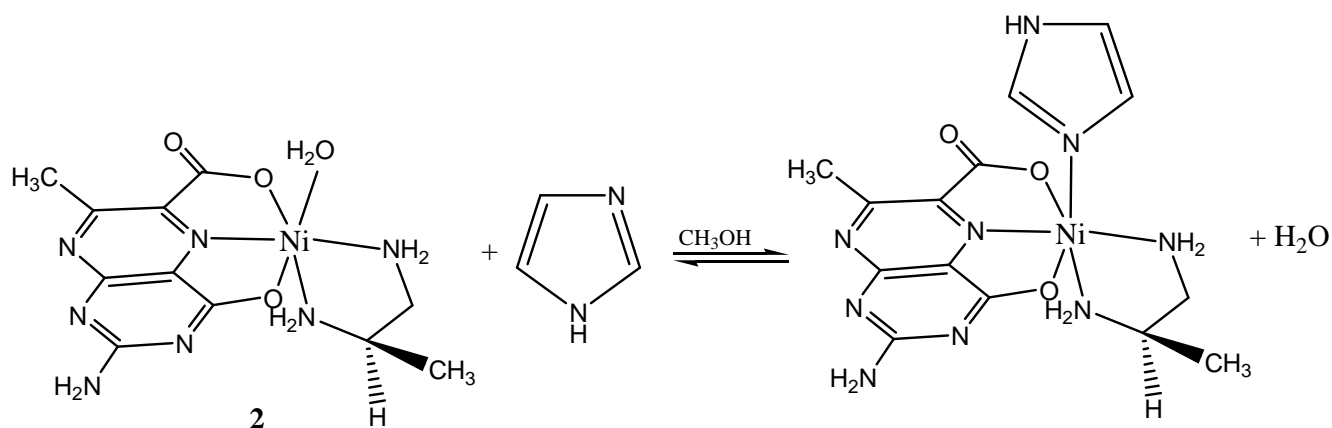
### Cyclic Voltammetric Studies.

Cyclic voltammetry data of **2** and **3** are shown in Figure V-17 and V-18 respectively. In each case a prominent reduction peak is observed around -703 to -707 mV region corresponding to the metal-centred reduction Ni(II)(d<sup>8</sup>) → Ni(I)(d<sup>9</sup>); this process involves a small change in free energy as evident from the corresponding Frost diagram [Scheme IV-11]. This has been verified in chapter IV through isolation (NaBH<sub>4</sub> reduction) and characterization of the relevant Ni(I) complexes. A ligand-centred reduction peak is observed around -1376 mV to 1403 mV region. A

few reoxidation peaks can also be identified. In case of **2** such peaks appear at -550 mV and 822 mV respectively. For **3** such reoxidation peaks appears at -567 mV and 75 mV, respectively. A closer look at Figure V-18 indicates a near approach to quasi-reversible behavior for the metal-centred reduction-reoxidation couple ( $\Delta E_p = 138$  mV). The almost planar 'pn' chelate ring of **3** (Figure V-7) is possibly more effective in protecting the electrogenerated Ni(I) species from solvent attack. The extent of puckering of the 'pn' chelate ring (of **2** and **3**) in controlling the kinetic properties, is further illustrated by the kinetic data (UV-Vis spectroscopy), presented in the next section.

### Reactivity of **2** and **3** towards imidazole

Each of **2** and **3** possesses an aquo group and the group transfer reaction of the aquo group by imidazole (Im) will be interesting. As pointed out earlier imidazole is linked with histidine, which is a versatile coordinating agent towards the first transition metal in the biological systems. A typical reaction scheme e.g., for **2** (Scheme V-7) is shown below.



**Scheme V-7**

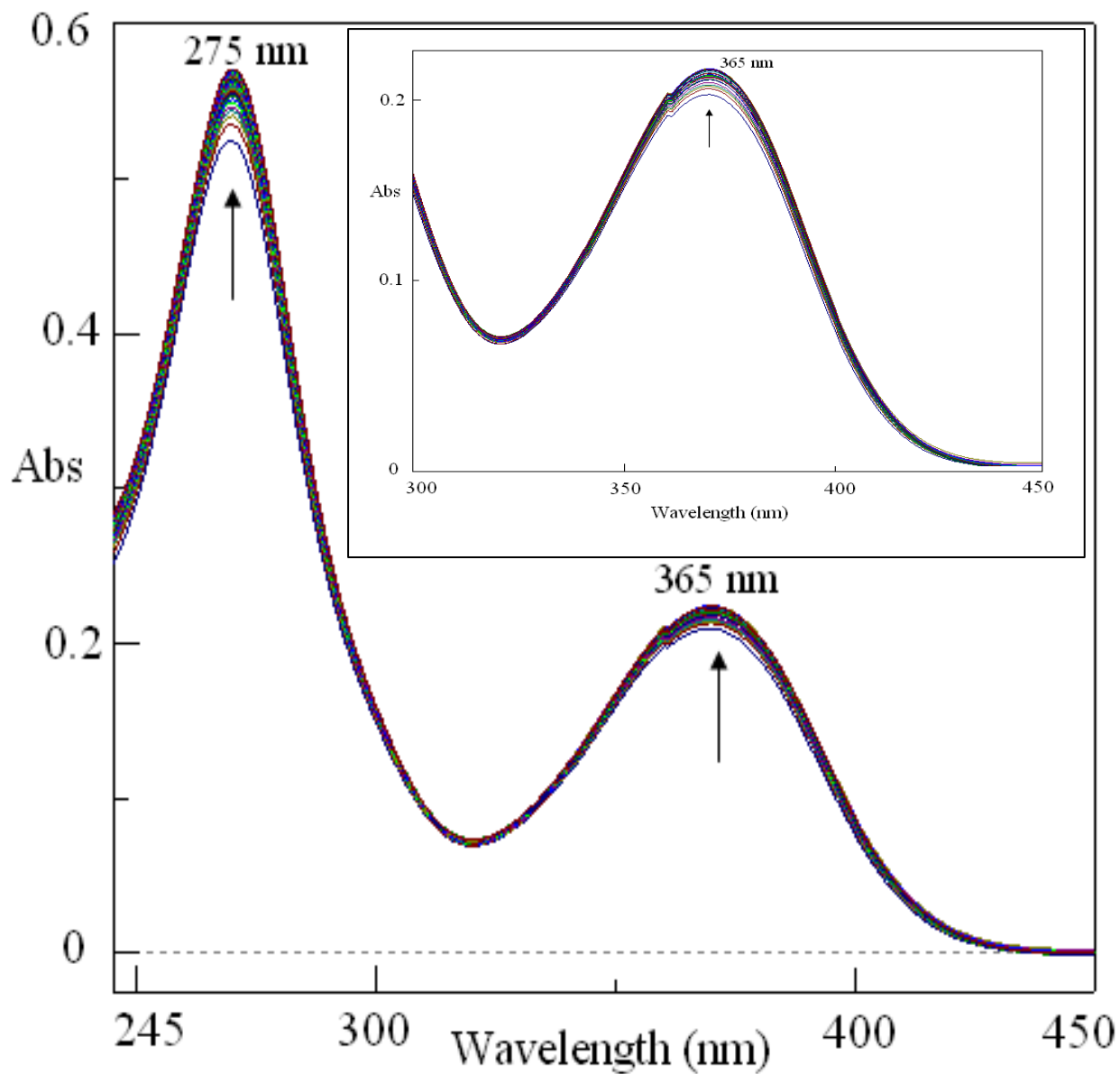


**Figure V-19.** Absorption spectral changes recorded at 2 min interval during the reaction of (2) ( $5.8 \times 10^{-5} \text{M}$ ) with Im ( $4.8 \times 10^{-3} \text{M}$ ) in  $\text{CH}_3\text{OH}$  at 311K

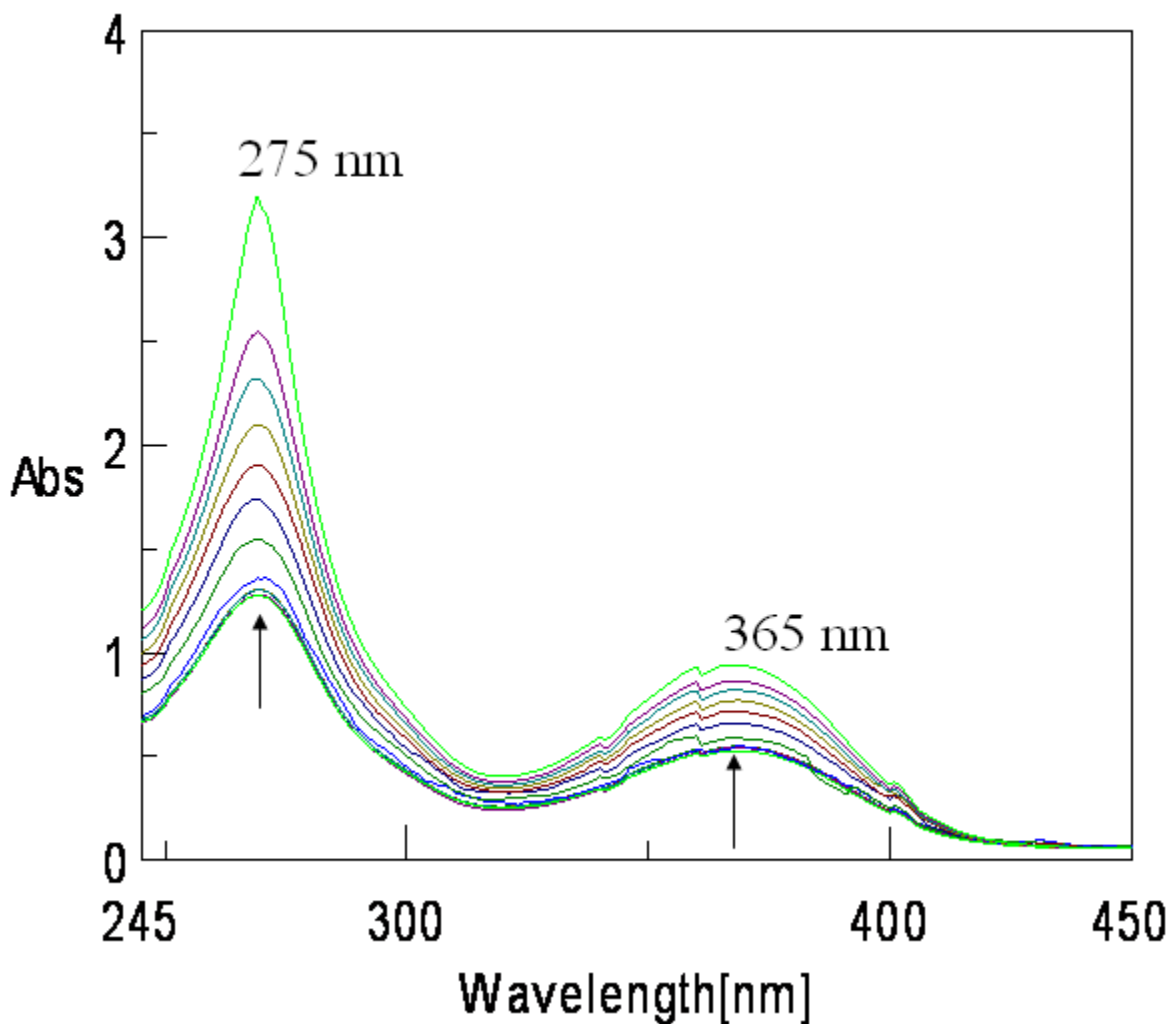


**Figure V-20.** Absorption spectral changes recorded at 4.5 min interval during the reaction of (3) ( $4.8 \times 10^{-5} \text{M}$ ) with Im ( $4.68 \times 10^{-3} \text{M}$ ) in  $\text{CH}_3\text{OH}$  at 313K

---

Stoichiometry of this reaction has been established in one case through the isolation and x-ray structural characterization of the corresponding imidazole substituted Ni(II) complex (Figure IV-1 and IV-2). The reaction profiles (overlay scans) are shown in Figure V-19 and V-20 respectively. Kinetics of these reactions were followed at 365 nm and four different temperatures in the range 308 – 328K under pseudo-first-order conditions (keeping ca. 100 times excess of the imidazole ligand). Observed rate constants were determined least square method

from the plots of  $\log(A_t - A_\infty)$  versus time, which were linear for 3 half-lives.<sup>49,50,92</sup> The relevant data are indicated below:

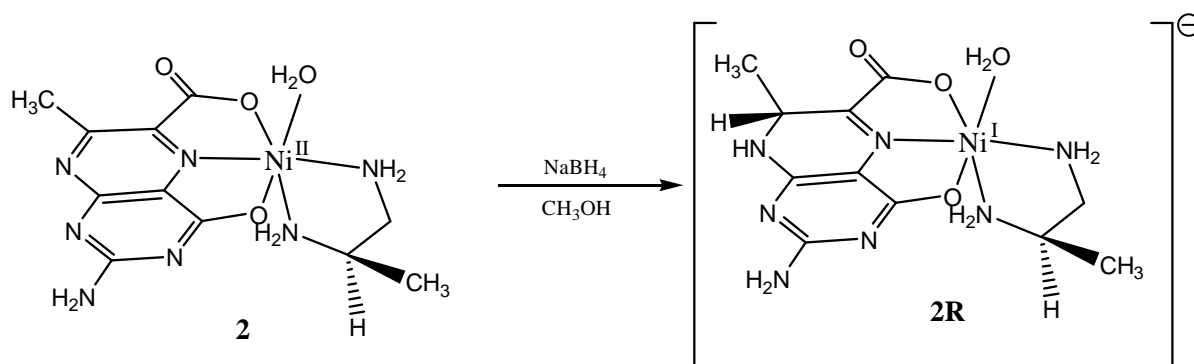
$$\text{For } \mathbf{2}: k_{\text{obs}} = 3.4 \times 10^{-3} \text{ s}^{-1}; \quad \Delta S^\ddagger = -198 \text{ J mol}^{-1} \text{ deg}^{-1};$$

$$\text{For } \mathbf{3}: k_{\text{obs}} = 3.9 \times 10^{-3} \text{ s}^{-1}; \quad \Delta S^\ddagger = -218 \text{ J mol}^{-1} \text{ deg}^{-1}.$$

The above data are commensurable with a ligand substitution process involving an associative pathway.<sup>97,98</sup> Such data together with Figure V-19 and V-20 illustrate the 'pn' chelate ring conformational control (Figure V-7) of the ligand substitution process here.

### Redox reactions of **2** and **3** with $\text{NaBH}_4$

It has been presented in chapter IV that treatment of a Ni(II) complex in  $\text{CH}_3\text{OH}$  medium with a slight excess of  $\text{NaBH}_4$  affords a dark-colored compound; physico-chemical studies pointed towards the formation of a Ni(I) complex with the 7, 8- dihydro form ( $\text{L}^{2-}$ ) of the pterin ligand residue, that is  $\text{NaBH}_4$  reduction affects only the pyrazine part of the pterin ring. In the present case, such reduced forms are termed as **2R** and **3R** respectively. The reaction profile (Scheme V-8) leading to the formation of **2R** and **3R** from **2** and **3** are shown in Figure V-21 and V-22, respectively.



**Scheme V-8**

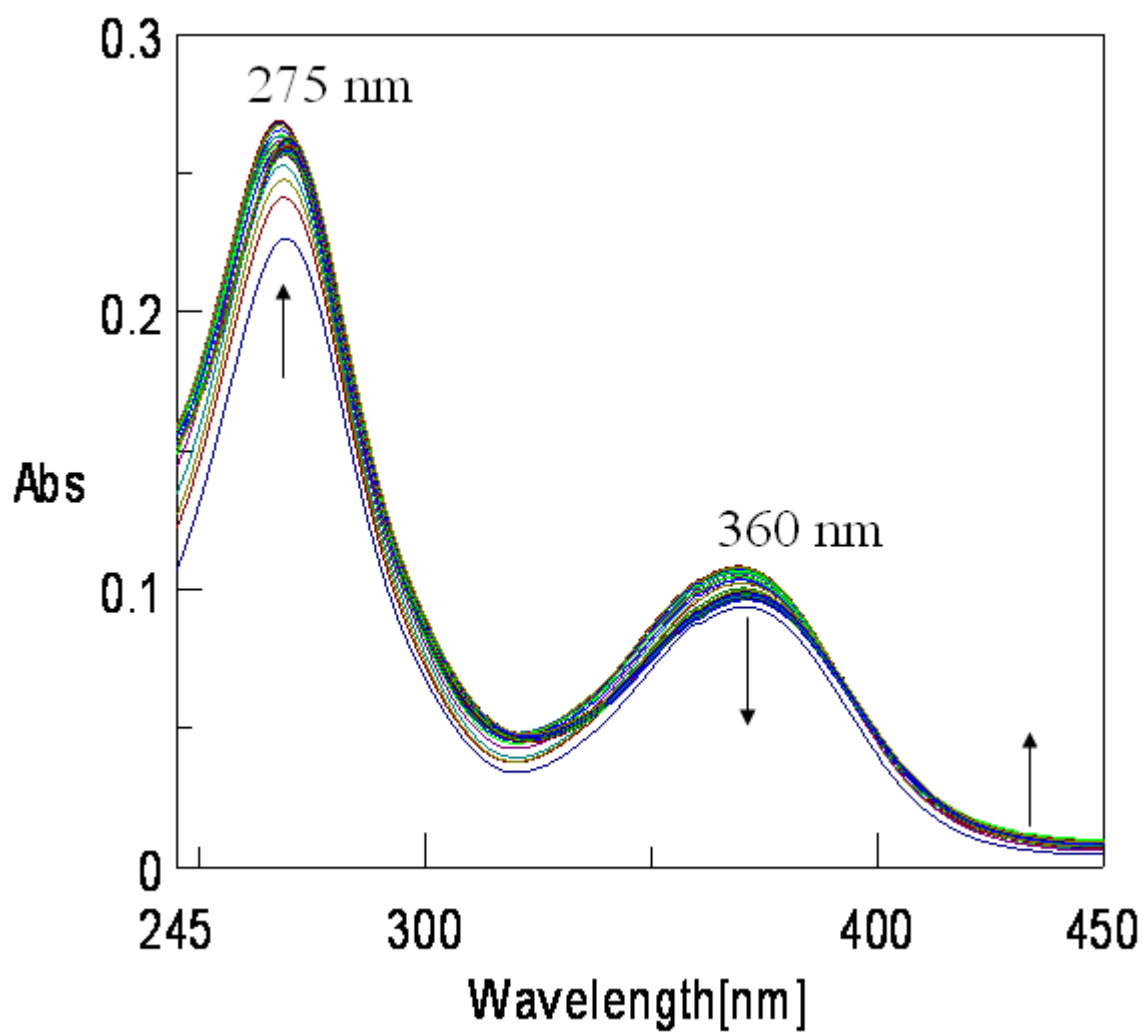


**Figure V-21.** Absorption spectral changes recorded at 1.5 min interval during the reaction of (2) ( $3.5 \times 10^{-5} \text{M}$ ) with  $\text{NaBH}_4$  ( $2.35 \times 10^{-3} \text{M}$ ) in  $\text{CH}_3\text{OH}$

---

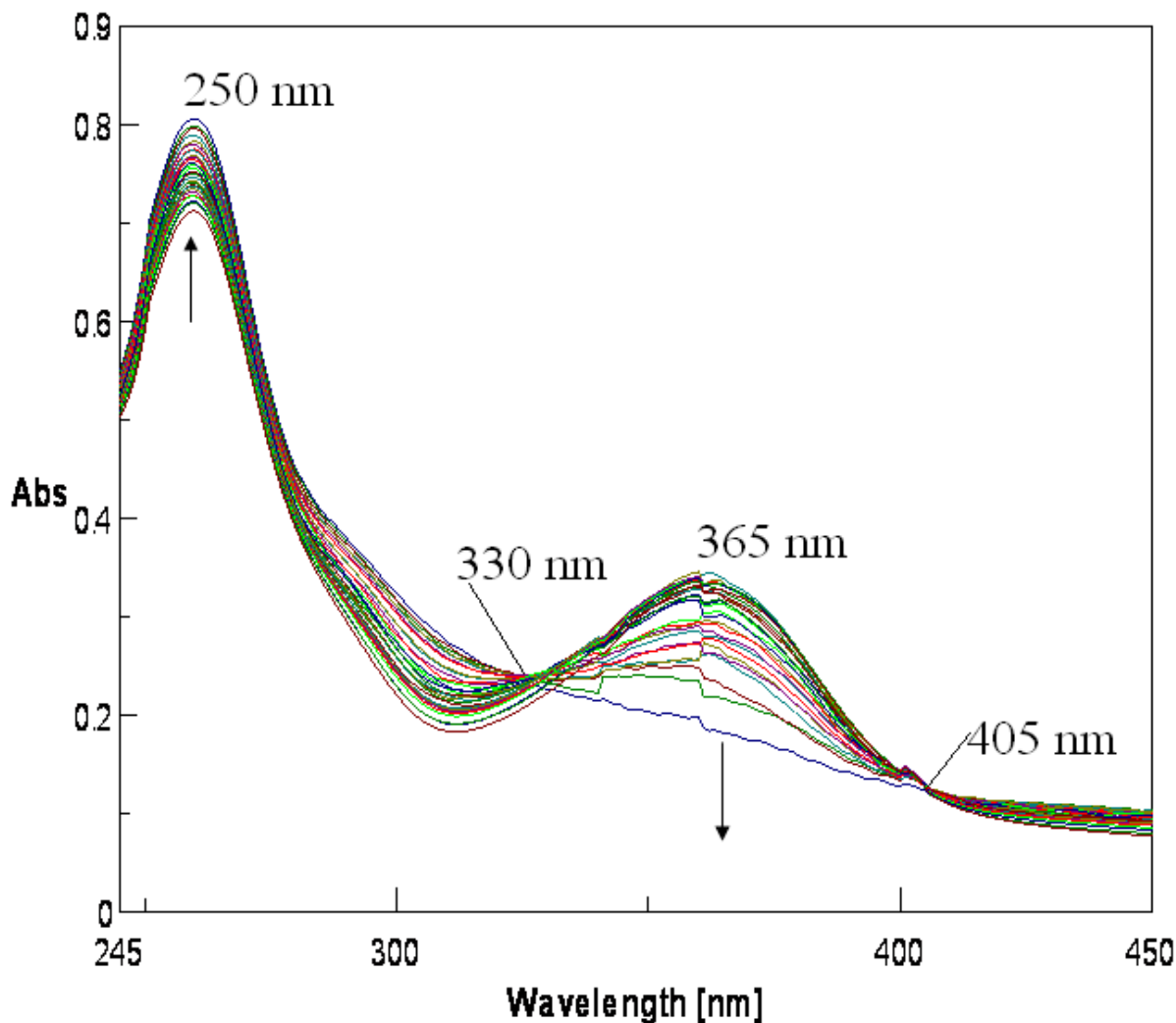


**Figure V-22.** Absorption spectral changes recorded at 1.5 min interval during the reaction of **3** ( $4.8 \times 10^{-5} \text{M}$ ) with  $\text{NaBH}_4$  ( $2.55 \times 10^{-3} \text{M}$ ) in  $\text{CH}_3\text{OH}$

They involve simultaneous reductions of the metal [ $\text{Ni(II)} \rightarrow \text{Ni(I)}$ ] and pterin [aromatic/oxidized state  $\rightarrow$  7, 8- dihydro state] ligand centres. The two  $\lambda_{\text{max}}$  values around 250 – 275 nm and 360 – 365 nm [ Figure V-21 and V-22] correspond to the  $\pi \rightarrow \pi^*$  (pterin) and LMCT (pterin  $\rightarrow$  metal) transitions. While Figure V-21 is devoid of any isosbestic point, Figure V-22 possesses such an attribute at 405 nm and close approach such a property around 330 nm; most likely the change over in oxidation state of the pterin ring is responsible for this observation, that

is, the spread out at 330 nm. For **3** the NaBH<sub>4</sub> reduction leading to the formation of **3R**, is essentially a one-step process. Kinetics of this reaction (Scheme V-8) were followed at 360 nm (365 nm for **3**) and four different temperatures in the range 300 – 330K in CH<sub>3</sub>OH under pseudo-first-order conditions ( with a **2/3** : NaBH<sub>4</sub> ratio of 1 : 140) and the pertinent kinetic parameters are stated below:

$$\text{For } \mathbf{2}: k_{\text{obs}} = 3.4 \times 10^{-3} \text{ s}^{-1}; \quad \Delta S^{\ddagger} = -208 \text{ Jmol}^{-1} \text{ deg}^{-1};$$

$$\text{For } \mathbf{3} \quad k_{\text{obs}} = 3.8 \times 10^{-3} \text{ s}^{-1}; \quad \Delta S^{\ddagger} = -228 \text{ Jmol}^{-1} \text{ deg}^{-1}.$$

The simultaneous group and electron transfer steps take place through associative pathway and once again highlight the ‘pn’ chelat ring conformational control of such reactions. The following redox reactions verify the reduced nature of **2R** and **3R**.

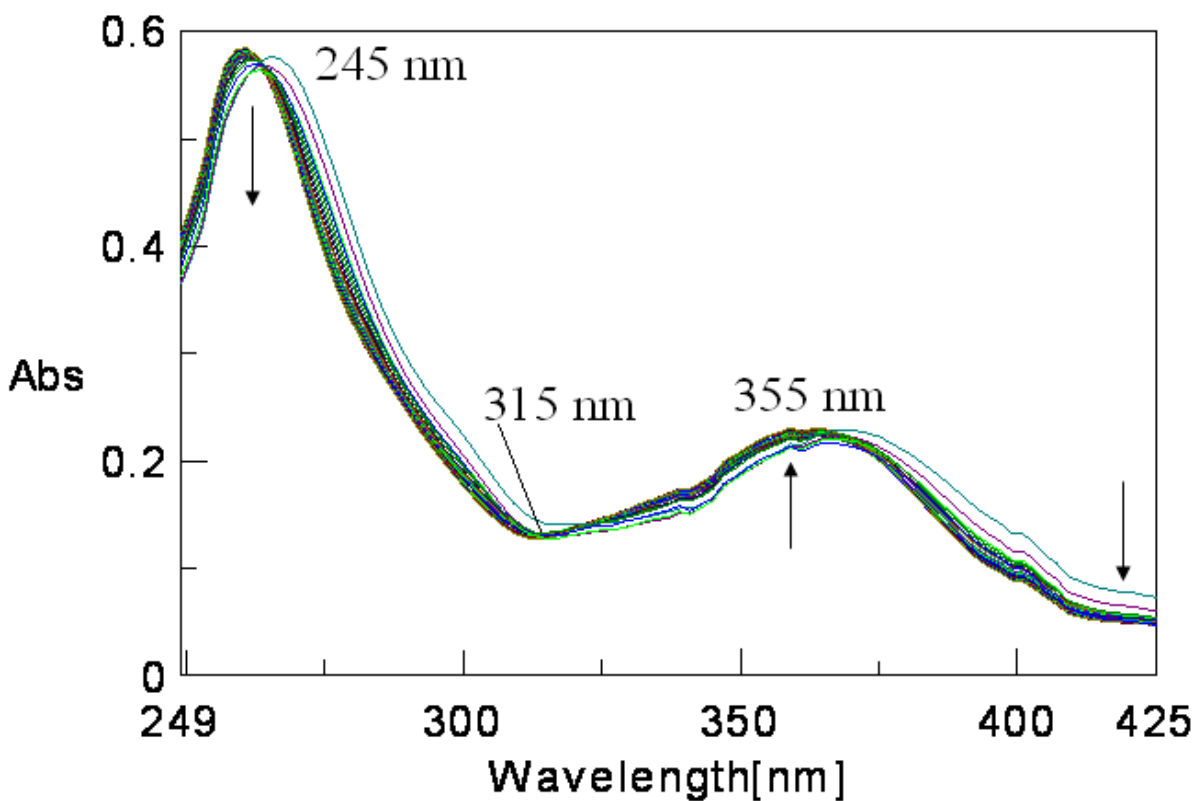


**Figure V-23.** Absorption spectral changes recorded at 15 second interval during the reaction of **2R** ( $3.5 \times 10^{-5} \text{M}$ ) with  $\text{K}_3\text{Fe}(\text{CN})_6$  ( $3.68 \times 10^{-3} \text{M}$ ) in  $\text{CH}_3\text{OH}$  at 298K

---

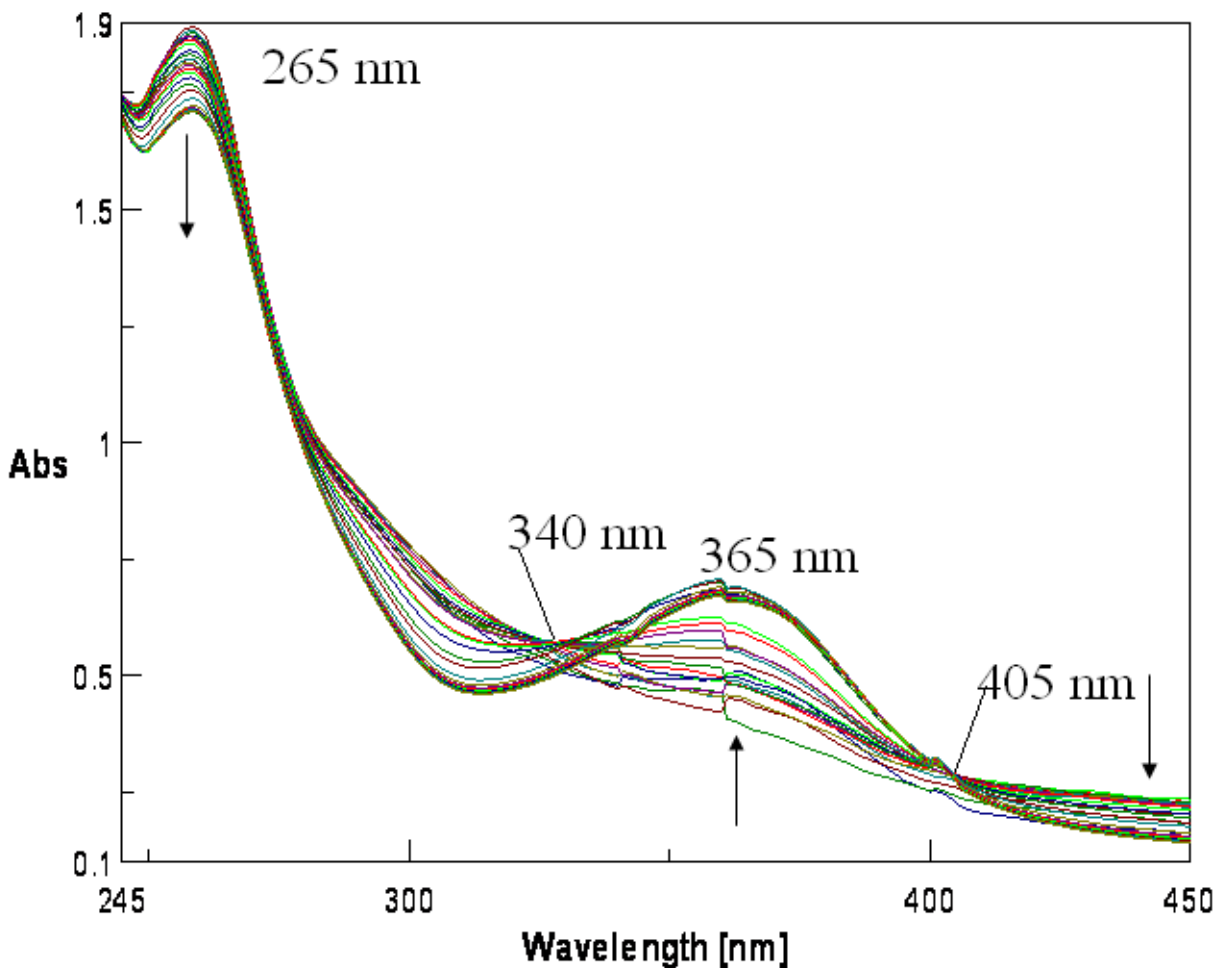


**Figure V-24.** Absorption spectral changes recorded at 15 second interval during the reaction of **3R** ( $4.8 \times 10^{-5} \text{M}$ ) with  $\text{K}_3\text{Fe}(\text{CN})_6$  ( $2.68 \times 10^{-3} \text{M}$ ) in  $\text{CH}_3\text{OH}$  at 298K

---

#### Reactions of **2R** and **3R** with $\text{K}_3[\text{Fe}(\text{CN})_6]$

The one-electron oxidant  $\text{K}_3[\text{Fe}(\text{CN})_6]$  is widely used for probing biochemical redox systems.<sup>94</sup> Its reaction profiles with **2R** and **3R** are shown in Figure V-23 and V-24

respectively; of them only Figure V-23 is characterized by an isosbestic point at 315 nm. Kinetics of this reaction was followed at 355 nm (365 nm for **3**) and four different temperatures (range 300 – 330K) in CH<sub>3</sub>OH under pseudo-first-order conditions (with a **2R/3R** : K<sub>3</sub>[Fe(CN)<sub>6</sub>] ratio of 1 : 140) and the relevant data are presented below:

$$\text{For } \mathbf{2R}: \quad k_{\text{obs}} = 1.7 \times 10^{-2} \text{ s}^{-1}; \quad \Delta S^{\ddagger} = -179 \text{ J mol}^{-1} \text{ deg}^{-1};$$

$$\text{For } \mathbf{3R} \quad k_{\text{obs}} = 2.2 \times 10^{-2} \text{ s}^{-1}; \quad \Delta S^{\ddagger} = -189 \text{ J mol}^{-1} \text{ deg}^{-1}.$$

The above  $k_{\text{obs}}$  data are faster by a power of ten than the previous results, most likely due to the pure electron transfer nature of K<sub>3</sub>[Fe(CN)<sub>6</sub>]. The initial oxidized species may undergo further reactions as evident from the reaction profile of **3R** (Figure V-24), lacking any isosbestic point.

Again, the absorption spectral studies indicate (Figure IV-26) that NaBH<sub>4</sub> is unable to react with K<sub>3</sub>[Fe(CN)<sub>6</sub>], but both **2R** and **3R** do as the present data indicate. In other words, **2** and **3** are able to mediate the transfer of reducing equivalents from NaBH<sub>4</sub> to K<sub>3</sub>[Fe(CN)<sub>6</sub>] through **2R** and **3R**. An analogy may be drawn (of **2/2R** as well as **3/3R**) with the NAD<sup>+</sup>/NADH couple, which is a typical biochemical mediator.<sup>94</sup> NAD<sup>+</sup> can be reduced nonenzymatically by NaBH<sub>4</sub>, whereas NADH can in turn be nonenzymatically reoxidized with K<sub>3</sub>[Fe(CN)<sub>6</sub>], but not by molecular O<sub>2</sub>. A major factor responsible for such unique redox property of **2** and **3** (as well as of **2R** and **3R**) is the presence of the redox non-innocent pterin ring (its pyrazine part) which can exist in a couple of oxidation states. This aspect is accentuated by the redox active metal centre and further such redox property of the same metal-pterin entity can be fine tuned by the chiral ancillary ligand as evident from Figure V-21 to V-24. This has direct bearing on the pterin-containing metalloenzymes where such fine tuning of property of the metal-pterin unit is possible by the donor atom of the protein backbone.<sup>103</sup>

### **Reactivity of 2R and with bromobenzene and dioxygen.**

For exploring the ability of **2R** to model phenylalanine hydroxylase type (PAH) activity, its reactivity towards a reaction mixture of bromobenzene and dioxygen has been studied. Here bromobenzene is used as a model substrate (instead of phenylalanine) for its ease of handling, facilitating the recovery of the corresponding product (i.e., 4-bromophenol) and its characterization. Figure V-25 shows the relevant reaction profile; here the arrows showing the movements of

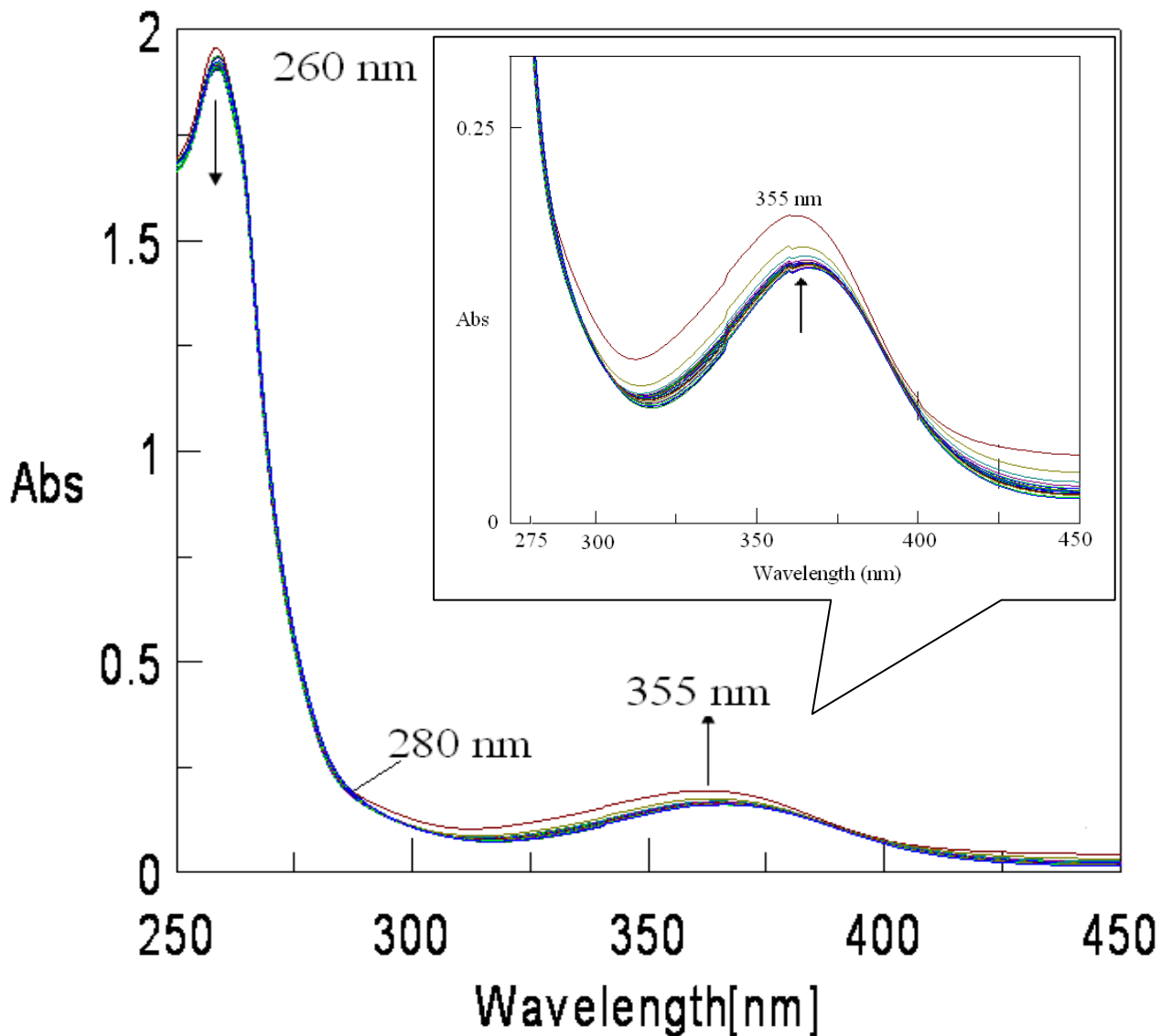
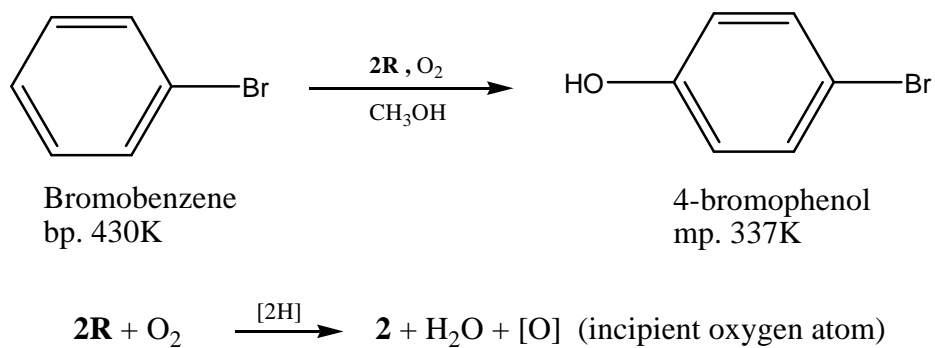


**Figure V-25.** Absorption spectral changes recorded at 2 min interval at 303K during the reaction of (**2R**) ( $3.5 \times 10^{-5} \text{M}$ ) with bromobenzene ( $3.54 \times 10^{-3} \text{M}$ ) in  $\text{CH}_3\text{OH}$  saturated with  $\text{O}_2$ .

the absorption spectral curves represent an opposite behavior to those in Figure V-21, (reflecting the  $\text{NaBH}_4$  reduction of **2** to **2R**). Scheme V-9 summarizes the above-mentioned redox reaction leading to the hydroxylation of the aromatic ring of bromobenzene (a model of PAH reaction);



**Scheme V-9**

the role of **2R** (or specifically its 7, 8-dihydro form of the pterin ligand residue, L<sup>2-</sup>) in supplying two reducing equivalents, [2H] to O<sub>2</sub> is apparent. Kinetics of this reaction (Figure V-25) was followed at 355 nm and four different temperatures (range 300 – 330 K) in CH<sub>3</sub>OH saturated with O<sub>2</sub> under pseudo-first-order conditions (with a **2R** : bromobenzene ratio 1 :140) and the kinetic parameters are shown below:

For **2R**:  $k_{\text{obs}} = 2.6 \times 10^{-3} \text{ s}^{-1}$ ;  $\Delta S^\ddagger = -228 \text{ Jmol}^{-1} \text{ deg}^{-1}$ ;

For **3R**:  $k_{\text{obs}} = 2.1 \times 10^{-3} \text{ s}^{-1}$ ;  $\Delta S^\ddagger = -238 \text{ Jmol}^{-1} \text{ deg}^{-1}$ .

The above kinetic parameters are summarized in Table V-6.

**Table V-6.** Comparison of kinetic parameters for the reactions of **2**, **2R** & **3**, **3R** with different substrates

Compound	Kinetic parameters	Reaction with Imidazole (2/3)	Reaction with bromobenzene (2R/3R)	Reaction with K <sub>3</sub> [Fe(CN) <sub>6</sub> ] in CH <sub>3</sub> OH-H <sub>2</sub> O 3:1 v/v (2R/3R)	Reaction with NaBH <sub>4</sub> in CH <sub>3</sub> OH (2/3)
<b>2</b>	k <sub>obs</sub> <sup>(a)</sup> (s <sup>-1</sup> )	3.4x10 <sup>-3</sup>	2.6 x10 <sup>-3</sup>	1.7x10 <sup>-2</sup>	3.4 x10 <sup>-3</sup>
	ΔS <sup>‡</sup> (JK <sup>-1</sup> mol <sup>-1</sup> )	-198	-228	-178	-208
<b>3</b>	k <sub>obs</sub> <sup>(a)</sup> (s <sup>-1</sup> )	3.9x10 <sup>-3</sup>	2.1 x 10 <sup>-3</sup>	2.2 x10 <sup>-2</sup>	3.8 x10 <sup>-3</sup>
	ΔS <sup>‡</sup> (JK <sup>-1</sup> mol <sup>-1</sup> )	-218	-238	-189	-228

### Electronic structures of 2 and 3 : Correlation with reactivity

The electronic structures of **2** and **3** have been obtained by DFT calculations, using their x-ray structural data as input parameters for the Gaussian 09 program. The energies (eV) and composition(%) of few frontier MOs are shown in Figure V-26. A small band gap (ΔE = 0.19 eV) is observed between the HOMO and HOMO-1 levels of **2**; again an energy difference of 0.56 eV exists between the LUMO and LUMO +1 levels. On the other hand for **3** LUMO and LUMO+1 levels have an energy gap of 0.19eV. As stated earlier synthetic molecules with

exceptionally small (0.5 eV) HOMO – LUMO gaps are receiving attention due to their interesting electrochemical / redox amphoteric behavior.<sup>64,66</sup> Usually in such cases the HOMO – LUMO orbitals are located in different covalently linked centers in a single molecule. Thermoexcited intramolecular electron transfer may occur between two such centers in solution. Most likely the combination of the redox non-innocent pterin ligand residue with the redox active metal centre [Ni(II)/Ni(I)] in complexes **2** and **3**, lead to such a situation here associated with distinct redox activities.<sup>9-11,53</sup> For example, reducing equivalents can be transferred with ease into the LUMO, LUMO + 1 levels of **2** and **3**, during reaction with NaBH<sub>4</sub>. On the other hand, the HOMO and HOMO-1 levels of **2** are associated with a small band gap, a property not shared by **3**. As a result the release of reducing equivalents from **2R** and **3R** [during reactions with K<sub>3</sub>[Fe(CN)<sub>6</sub>] and bromobenzene/O<sub>2</sub>] should be different kinetically. Figure V-23 to V-25 illustrate this aspect.

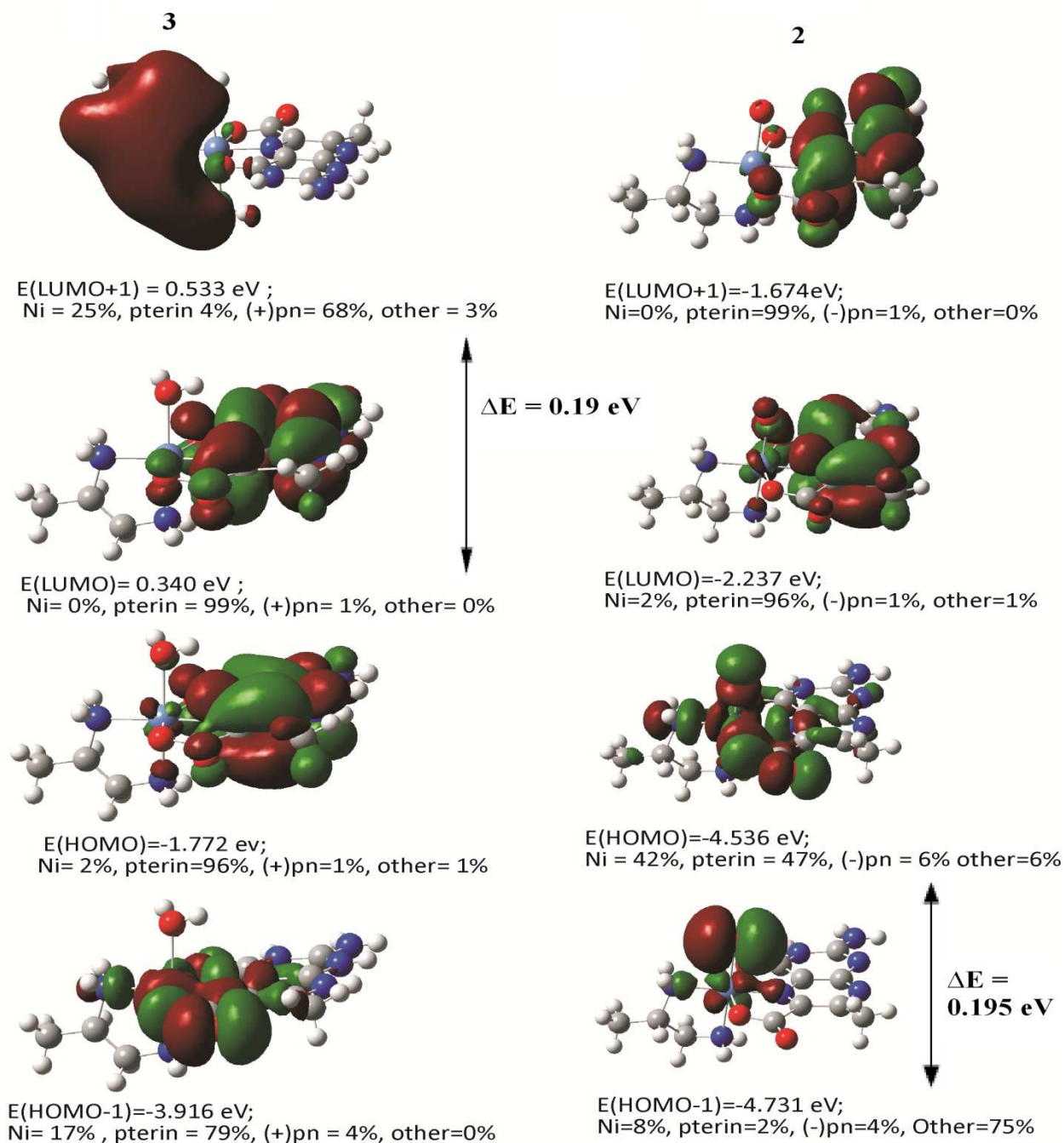


**Figure V-26.** Frontier molecular orbitals of **2** and **3**, showing their energies (eV) and compositions (%).

## Conclusion

This chapter is centered on two chiral mixed ligand Ni(II)-pterin complexes. They possess identical chemical composition and the ancillary ligands (pn) confers chirality on them through conformational contribution ( $\delta/+$ ). Their cyclic voltammetric data as well as reactivities towards imidazole,  $\text{NaBH}_4$  and also of their reduced forms (**2R** & **3R**) towards  $\text{K}_3[\text{Fe}(\text{CN})_6]$  and bromobenzene/ $\text{O}_2$ , highlight the conformational control of metal and pterin based group and / electron transfer reactions. The above aspect is significant in understanding the reactions catalysed by pterin-containing metalloenzymes, where donor atoms from the protein back bone play a significant role in controlling the redox properties of the metal centre.

## **Chapter VI**

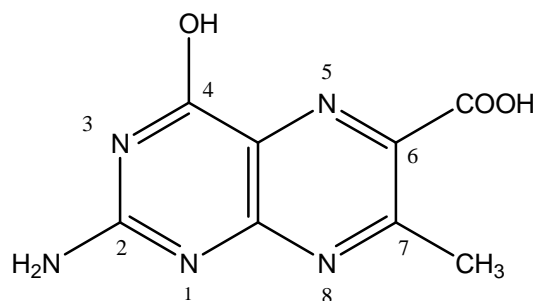
**Internal redox process in metal-pterin complexes:  
synthesis, characterization, physico-chemical and DFT  
studies on new pterin complexes of  $d^7 - d^{10}$  bivalent  
transition metal ions.**

## Abstract

Four new mononuclear mixed ligand complexes  $[M(L)(B)(H_2O)] \cdot xH_2O$  [ $M = Co(II)$ ,  $Ni(II)$ ,  $Cu(II)$  and  $Zn(II)$ ;  $B = bipy$ ,  $phen$ ;  $x = 2$  or  $3$ ] have been synthesized using 7-methylpterin-6-carboxylic acid ( $H_2L$ ). They have been characterized by elemental analysis, electrospray ionization mass spectrometry, different spectroscopic techniques and cyclic voltammetry. For the  $Zn(II)$  complex (**1**) x-ray structural data could be recorded. The DFT optimized molecular structures and related geometric parameters of all these complexes are consistent with the x-ray structural data of **1**. The EPR spectral data for **2** and **4** are of the axial type, indicating elongation along the z-axis. Most of the UV-Vis MLCT bands in the longer wavelength region, could be assigned to pterin  $\rightarrow$  phen/bipy charge transfer across the metal centre, on the basis of their electronic structures.  $^1H$  NMR spectrum of **1** verify such charge transfer in terms of shielding of the phen proton signals. Redox reactivities with  $NaBH_4$  and  $K_3[Fe(CN)_6]$  further highlight the redox non-innocent property of the pterin ligand residue here.

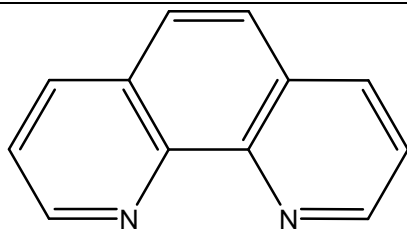
## Introduction

This chapter is concerned mainly with further exploration of the coordination property of the pterin ligand 7-methylpterin – 6 – carboxylic acid ( $H_2L$ , Scheme VI-1) using the  $Zn(II)d^{10}$  ion, possessing a fixed oxidation state of +2. 1, 10-phenanthroline ( $phen$ , Scheme VI-2) and 2, 2'-bipyridyl ( $bipy$ , Scheme VI-3) play the role of suitable  $\pi$ -acid ligands.



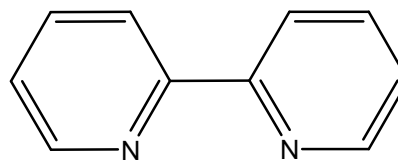
The pterin ligand (**1**,H<sub>2</sub>L)

**Scheme VI-1**



1, 10 - phenanthroline

**Scheme VI-2**



2, 2' - bipyridine

**Scheme VI-3**

An important purpose of this work is to examine the result of <sup>1</sup>H NMR spectral study for a mononuclear/ diamagnetic M(II) – pterin complex; the related compounds presented in earlier chapters are all paramagnetic, except for a binuclear diamagnetic Cu(I)d<sup>10</sup> complex stated in chapter II. Just like phen, 2, - 2'-bipyridyl acts here as a good ancillary ligand as well. Rationalizing physico-chemical properties in the light of electronic structures is an important aspect of this study. Few related Co(II), Ni(II) and Cu(II) complexes assists in bringing this work to a satisfactory level.

## Experimental

**Materials and Methods:** Reagent grade chemicals were used as received. Solvents were purified, prior to use, following literature procedure <sup>20</sup>. ZnSO<sub>4</sub>. 7H<sub>2</sub>O, NiSO<sub>4</sub>.7H<sub>2</sub>O, CoSO<sub>4</sub>. 7H<sub>2</sub>O and CuSO<sub>4</sub>. 3H<sub>2</sub>O were obtained from E. Merck, Mumbai. NaOH was obtained from SRL, Mumbai and 1, 10-phenanthroline and 2, 2'- bipyridine were procured from E. Merck, Mumbai. Kinetic and electrochemical measurements were performed in spectroscopic grade CH<sub>3</sub>OH and DMSO (SRL, Mumbai) respectively . Bu<sub>4</sub>NClO<sub>4</sub> (TBAP) for CV measurements was obtained by published methods <sup>72</sup>.

**Methods.** Most of the physico-chemical methods of characterization were the same as those discussed in Chapters II and III. IR spectra (KBr) were recorded on a Perkin Elmayer FTIR RX1. Magnetic susceptibilities were checked with a Sherwood magnetic susceptibility balance (MSB Mk1), using Hg[Co(SCN)<sub>4</sub>] as the calibrant.

### Synthesis of the complex

#### [Zn(C<sub>8</sub>H<sub>5</sub>N<sub>5</sub>O<sub>3</sub>)(C<sub>12</sub>H<sub>8</sub>N<sub>2</sub>)(H<sub>2</sub>O)]. 3H<sub>2</sub>O/ [Zn(L)(phen)(H<sub>2</sub>O)]. 3H<sub>2</sub>O (1)

The title complex was prepared by the dropwise addition of a solution (15 ml) of ZnSO<sub>4</sub>. 7H<sub>2</sub>O (35.9 mg, 0.125 mmol) containing 1, 10 – phenanthroline monohydrate (25 mg, 0.125 mmol) to a warm (312K) aqueous alkaline solution (NaOH : 11 mg, 0.275 mmol) of the pterin ligand H<sub>2</sub>L (31 mg, 0.125 mmol). The pH value was maintained around 9.9 – 10.0 and the final volume was 60 ml. The reaction mixture was transferred to a 100 ml beaker and allowed to stand at room temperature. Light brown shining crystals suitable for single crystal x-ray diffraction appeared after 10 days (yield: 30%). UV-VIS absorption bands [CH<sub>3</sub>OH, λ<sub>max</sub>nm (logε)]: 326s(4.835), 376br(5.057), 733(4.086).

#### [Co(C<sub>8</sub>H<sub>5</sub>N<sub>5</sub>O<sub>3</sub>)(C<sub>10</sub>H<sub>8</sub>N<sub>2</sub>)(H<sub>2</sub>O)]. CH<sub>3</sub>OH/[Co(L)(bipy)(H<sub>2</sub>O)],CH<sub>3</sub>OH (2)

A solution of  $\text{CoSO}_4 \cdot 7\text{H}_2\text{O}$  (0.1405gm, 0.5mmol) in  $\text{CH}_3\text{OH}$  (50ml) was mixed with bipy (0.1015gm, 0.65mmol); to this solution of  $\text{H}_2\text{L}$  (0.115gm, 0.5mmol) dissolved in methanolic  $\text{Bu}_4\text{NOH}$  (1.1mmol) was added dropwise. Total volume of the mixture was 155ml and pH was ca.7.5. The mixture was warmed on a paraffin oil bath ( $50^\circ - 55^\circ\text{C}$ ) for 3h maintaining darkness. The orange coloured solution was evaporated to minimize the volume and the deep orange solution was kept in a silica gel desiccator for crystallization. After few days orange coloured microcrystals separated from the reaction mixture. Yield 35%. Its purity was checked through TLC ( UV lamp ) and characterized by CHN and ESIMS data. Analytically pure compound for this purpose could be obtained by filtration, repeated washing with small quantities of  $\text{CH}_3\text{OH}$  and drying in vacuo over silica gel. Analysis, calculated for  $\text{C}_{19}\text{H}_{19}\text{N}_7\text{O}_5\text{Co}$ : C 47.11, H 3.93, N 20.25 %; found: C 46.67, H 2.56, N 20.99 %. UV-VIS absorption bands [ $\text{CH}_3\text{OH}$ ,  $\lambda_{\text{max}}\text{nm}$  ( $\log\epsilon$ ): 280(4.23), 307sh (3.686), 380br(3.156), 460sh(2.48), 894(2.35).

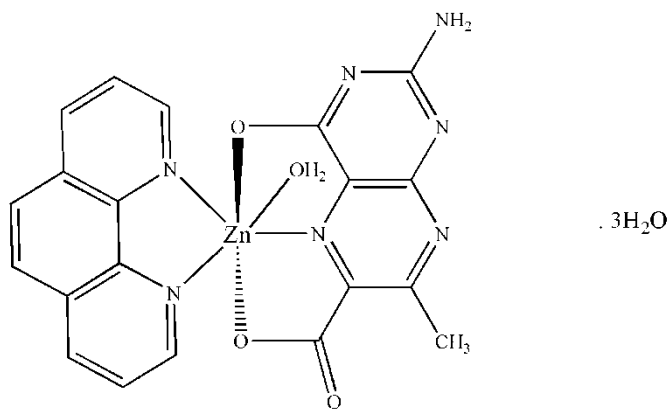
**$[\text{Ni}(\text{C}_8\text{H}_5\text{N}_5\text{O}_3)(\text{C}_{10}\text{H}_8\text{N}_2)(\text{H}_2\text{O})] \cdot 2\text{H}_2\text{O} / [\text{Ni}(\text{L})(\text{bipy})(\text{H}_2\text{O})] \cdot 4\text{H}_2\text{O}$  (3)**

A solution of  $\text{NiSO}_4 \cdot 7\text{H}_2\text{O}$  (0.035gm, 0.125mmol) in  $\text{CH}_3\text{OH}$  (50ml) was mixed with bipy (0.0195gm, 0.125mmol); to this solution of  $\text{H}_2\text{L}$  (0.029gm, 0.125mmol) dissolved in methanolic  $\text{Bu}_4\text{NOH}$  (0.28mmol) was added dropwise. Total volume of the mixture was 50ml and pH was ca. 8.5. The mixture was warmed on a paraffin oil bath ( $50^\circ - 55^\circ\text{C}$ ) for 3h under subdued light. Upon standing the reaction mixture deposited light green micro crystals after 24 hours. It was then separated by suction filter and washed with methanol and dried on vacuo over silica gel. Yield 38%. Its purity was checked through TLC ( UV lamp ) and characterized by CHN and ESIMS data. Analysis, calculated for  $\text{C}_{18}\text{H}_{19}\text{N}_7\text{O}_6\text{Ni}$ : C 44.29, H 3.89, N 20.09 %; found: C 43.94, H 4.15, N 19.86 %. UV-VIS absorption bands [ $\text{CH}_3\text{OH}$ ,  $\lambda_{\text{max}}\text{nm}$  ( $\log\epsilon$ ): 285(4.083), 309sh(3.818), 391br(3.576).

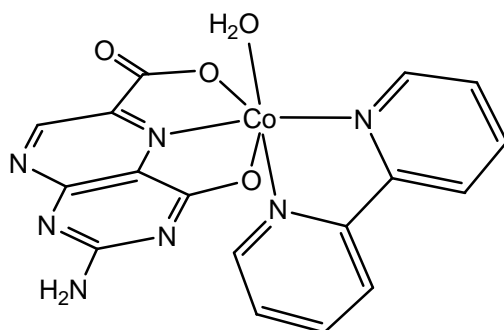
**[Cu(C<sub>8</sub>H<sub>5</sub>N<sub>5</sub>O<sub>3</sub>)(C<sub>10</sub>H<sub>8</sub>N<sub>2</sub>)(H<sub>2</sub>O)]. 4H<sub>2</sub>O/[Cu(L)(bipy)(H<sub>2</sub>O)]. 4H<sub>2</sub>O (4)**

A solution of CuSO<sub>4</sub>·3H<sub>2</sub>O (0.030gm, 0.125mmol) in CH<sub>3</sub>OH (50ml) was mixed with bipy (0.0195gm, 0.125mmol); to this solution of H<sub>2</sub>L (0.029gm, 0.125mmol) dissolved in methanolic Bu<sub>4</sub>NOH (0.28mmol) was added dropwise. Total volume of the mixture was 65ml and pH was ca. 7.5. The mixture was warmed on a paraffin oil bath (50<sup>0</sup> – 55<sup>0</sup>C) for 2.5h, maintaining O<sub>2</sub> flow and darkness. The greenish yellow coloured solution was filtrated (Whatman – 42) and the clear solution was kept for crystallization. After seven days green coloured crystals appeared at the bottom of the beaker. They were separated by suction filter, washed with methanol and dried in vacuo over silica gel. Yield 32%. Its purity was checked through TLC( UV lamp ) and characterized by CHN and ESIMS data. Analysis, calculated for C<sub>18</sub>H<sub>23</sub>N<sub>7</sub>O<sub>8</sub>Cu: C40.84, H4.35, N 18.53%; found: C41.79, H3.50, N 18.28%. UV-VIS absorption bands [CH<sub>3</sub>OH, λ<sub>max</sub>nm (logε)]:

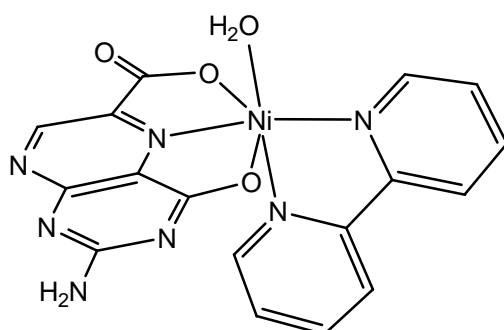
250sh(4.48),	276(4.498),	303sh(4.43),
375(4.09),	692(2.4),	744(2.36),
779(2.35),	808(2.35),	919(2.13),
1069(2.10).		



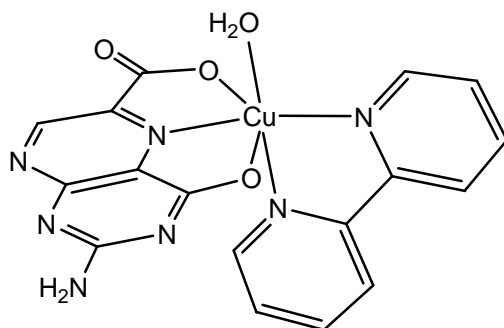
**Scheme VI-4**



**Scheme VI-5**



**Scheme VI-6**



**Scheme VI-7**

---

## Results and discussion

The Zn(II), Co(II), Ni(II) and Cu(II) mixed ligand complexes (**1 – 4**; Schemes VI-4 to VI-7) of the pterin ligand (Scheme: VI-1) could be synthesized and crystallized out of the



**Table VI-1. Crystallographic data and structure refinement for 1**

Identification code	1
Empirical formula	C <sub>20</sub> H <sub>21</sub> N <sub>7</sub> O <sub>7</sub> Zn
Formula weight	536.81
Temperature/K	293
Crystal system	Triclinic
Space group	P-1
a/Å	8.4819(7)
b/Å	9.9573(9)
c/Å	13.7257(12)
α/°	97.6670(10)
β/°	95.2430(10)
γ/°	110.7160(10)
Volume/Å <sup>3</sup>	1062.51(9)
Z	2
ρ <sub>calc</sub> /cm <sup>3</sup>	1.678
μ/mm <sup>-1</sup>	1.217
F(000)	552.0

Crystal size/mm <sup>3</sup>	0.240 × 0.190 × 0.040
Radiation	Mo K $\alpha$ ( $\lambda$ = 0.71073)
2 $\Theta$ range for data collection/°	3.028 to 56.518
Index ranges	-11 ≤ h ≤ 11, -13 ≤ k ≤ 13, -17 ≤ l ≤ 18
Reflections collected	9149
Independent reflections	4794 [R <sub>int</sub> = 0.018, R <sub>sigma</sub> = N/A]
Data/restraints/parameters	4794/12/346
Goodness-of-fit on F <sup>2</sup>	0.942
Final R indexes [I ≥ 2 $\sigma$ (I)]	R <sub>1</sub> = 0.0393, wR <sub>2</sub> = 0.0882
Final R indexes [all data]	R <sub>1</sub> = 0.0421, wR <sub>2</sub> = 0.0894
Largest diff. peak/hole / e Å <sup>-3</sup>	0.64/-0.33

**Table VI-2. Selected geometric parameters for 1(Å, °)**

Atom	Atom	Length/Å
Zn1	O2	2.1373(15)
Zn1	N6	2.0303(17)
Zn1	O16	2.3727(15)
Zn1	O18	2.1128(16)

Zn1	N19	2.0684(17)
Zn1	N26	2.1627(18)

<b>Atom</b>	<b>Atom</b>	<b>Atom</b>	<b>Angle/°</b>
O2	Zn1	N6	76.37(6)
O2	Zn1	O16	150.97(6)
N6	Zn1	O16	74.60(6)
O2	Zn1	O18	90.05(6)
N6	Zn1	O18	91.77(7)
O16	Zn1	O18	91.21(6)
O2	Zn1	N19	121.85(6)
N6	Zn1	N19	160.68(7)
O16	Zn1	N19	86.96(6)
O18	Zn1	N19	94.39(7)
O2	Zn1	N26	92.53(6)
N6	Zn1	N26	94.76(7)
O16	Zn1	N26	89.49(6)
O18	Zn1	N26	173.38(6)
N19	Zn1	N26	79.07(7)
Zn1	O2	C3	115.97(13)

### Molecular structure of [Zn(L)(phen)(H<sub>2</sub>O)]. 3H<sub>2</sub>O (**1**)

Figure VI-1 represents the molecular structure of the above complex compound **1**. Its crystallographic data and structure refinements are shown in Table VI-1. The selected geometric parameters of **1** are presented in Table VI-2. For complex **1** the six – coordinated Zn(II) atom shows departure from a regular octahedral geometry with respect to both bond lengths and bond angles (Figure VI-1, Table VI-2 ). The complex possesses both a tridentate pterin ligand and a  $\pi$  – acceptor ancillary ligand like 1, 10 – phenanthroline (phen). The equatorial plane is formed by the two N atoms (N19, N26) of phen, the pyrazine ring N atom (N6) of the pterin ligand and the aqua O atom (O18). The axial positions are occupied by the two pterin O atoms (O2 and O16), with the latter one forming the longest axial bond [2.3724(16) Å]. One important reason causing distortion from regular octahedral geometry is that this pterin ligand forms two five-membered chelate rings with small bite angles 76.28(7) and 74.66(6)°, instead of only one per pterin ligand for an earlier case (Mitsumi et al., 1995).<sup>154</sup> A consideration of the charge balance of this complex indicates that this pterin ligand acts as a binegative tridentate ONO donor. A near orthogonal disposition of the phen ligand and pterin chelate ring is observed, which affords minimum steric repulsion. Of the three axes, least deviation from linearity is observed in the O18 – Zn1 – N26 direction [173.36(7)°].

The exocyclic bond length data of the pyrimidine ring, e.g., C15 – O16 [1.257(3)Å] and C13 – N17 [1.335(3)Å] merit attention. Participation of the pterin unit in the electron – shuffling process, from the pyrazine ring N9 to the C15 – carbonyl group is indicated, as suggested in the literature (Baisya & Roy, 2014; Beddoes et al., 1993; Kohzuma et al., 1988; Miyazaki et al., 2008; Russell et al., 1992).<sup>17,18,22,23,115</sup> Formation of the Zn1 – O16 bond assists this process.

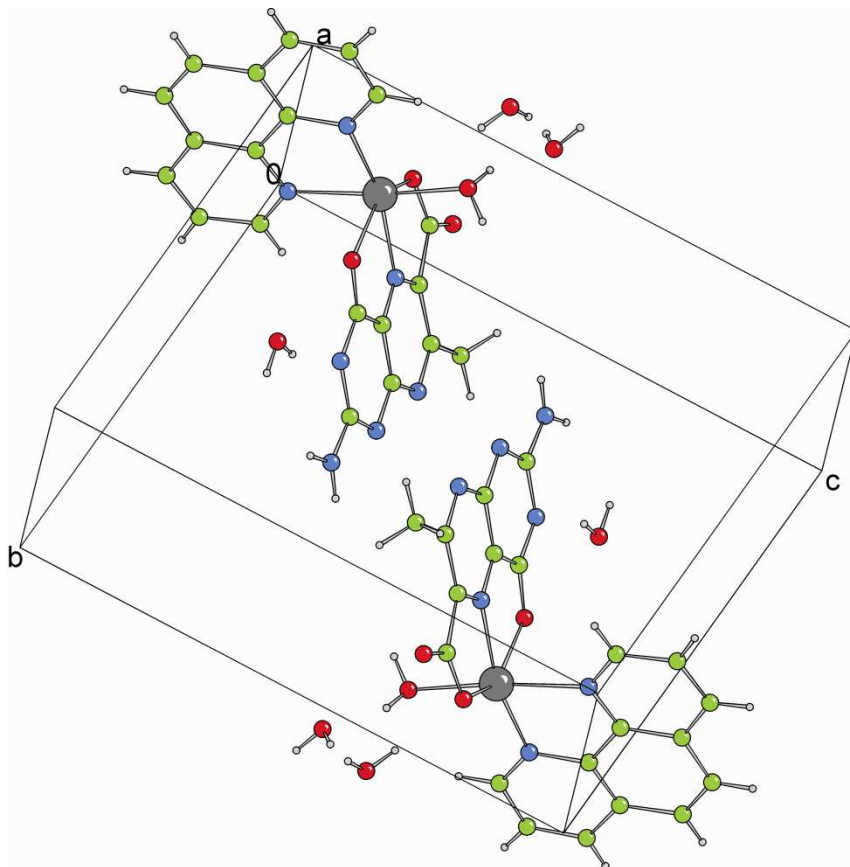


**Figure VI-2.** Unit cell packing diagram of **1** viewed along plane 1 0 0.

In the crystal, the complex molecules and lattice water molecules are linked by intermolecular N – H ...O, O – H ...N and O – H ...O hydrogen bonds into a three-dimensional network. The lattice water molecules play a decisive role in the crystal packing process. Figure VI-2 indicates  $\pi$ - $\pi$  stacking interactions involving two parallel, inversion-related pterin rings within the same unit cell and showing face – to – face distance of 3.442 Å. Besides this, the nearly parallel phen rings of adjacent molecules also display  $\pi$  –  $\pi$  stacking interactions with centroid distance of 3.568, 3.701 and 3.664 Å.

#### **DFT optimized molecular structures of 1 – 4**

The DFT calculations have been utilized for the present pterin complexes for getting the DFT optimized molecular structures of **1** to **4** (Figure VI-3 to VI-6). For this purpose Gaussian 09 software package was used with the B3LYP hybrid functional and 6-31g basic set.<sup>155,156</sup> In selected cases, the bulk solvent effects were considered through the polarization continuum model (PCM), e.g., compound **2** in CH<sub>3</sub>OH.<sup>157-159</sup> The atom numbering scheme of the above figures is obtained from the DFT calculations.

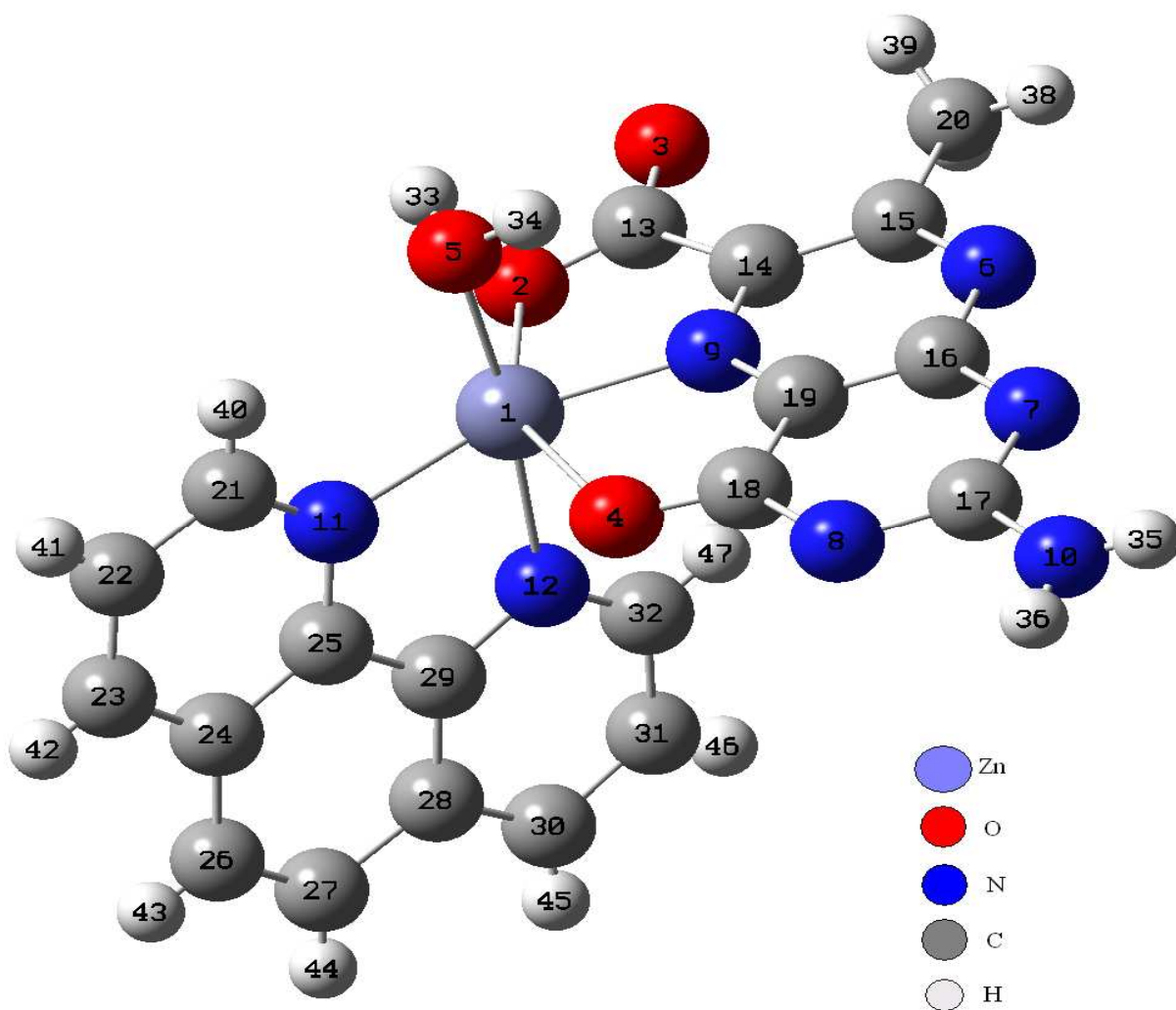


**Figure VI-3.** DFT optimized molecular structure of the compound **1**

As per the above figures each of these compounds consists of octahedrally coordinated mononuclear metal centers, with tridentate ONO pterin coordination and bidentate NN coordination from bipy/phen; the H<sub>2</sub>O ligand completes the coordination octahedron. The relevant optimized geometric parameters are presented in Table VI-3 to VI-6; they are in good agreement with the x-ray structural data of related metal complexes of the same pterin ligand.<sup>17</sup> These optimized molecular structures provides with reliable frame works for interpreting the

spectroscopic and physico-chemical data.

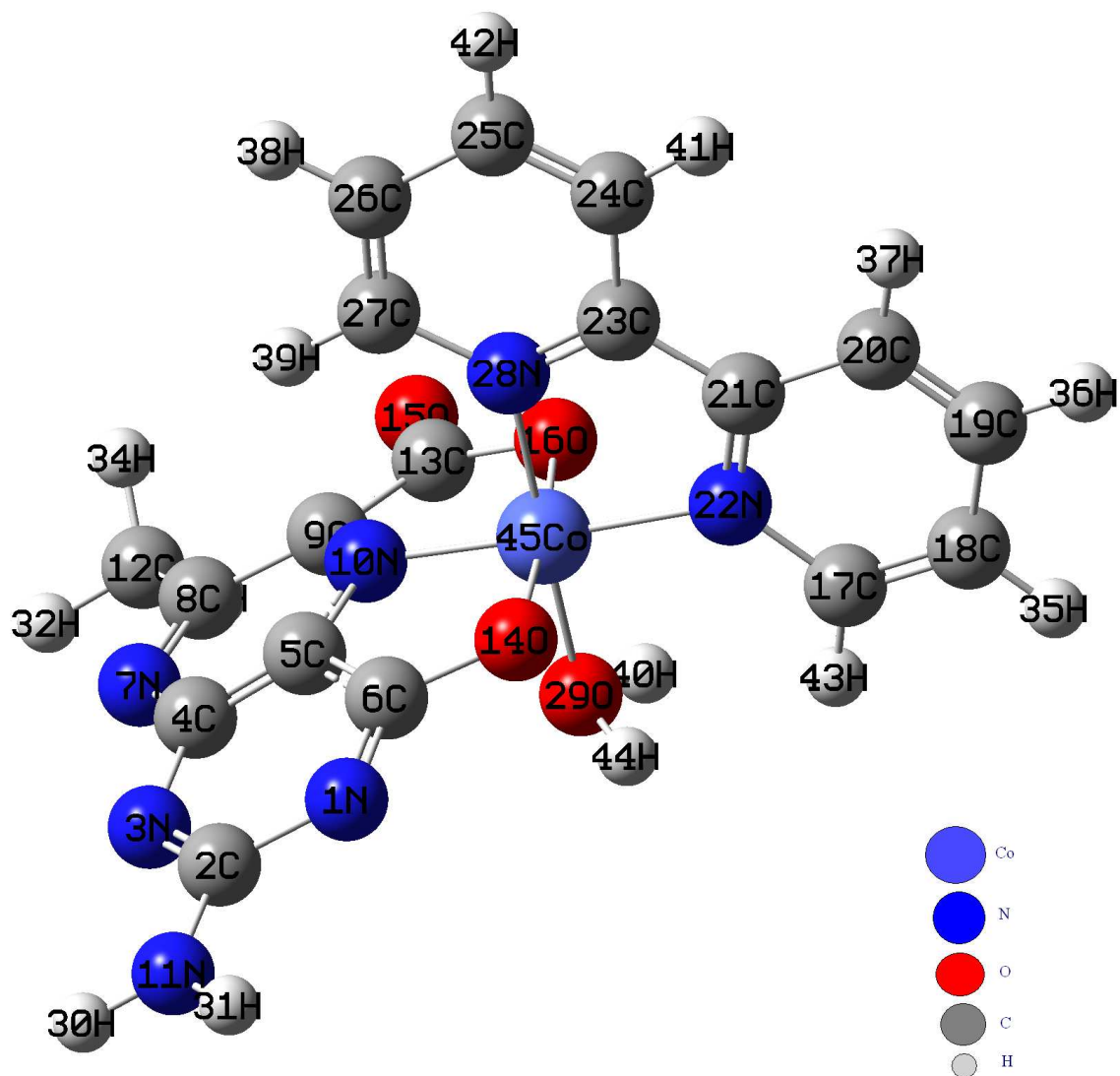


**Figure VI-4.** DFT optimized molecular structure of the compound 2

---

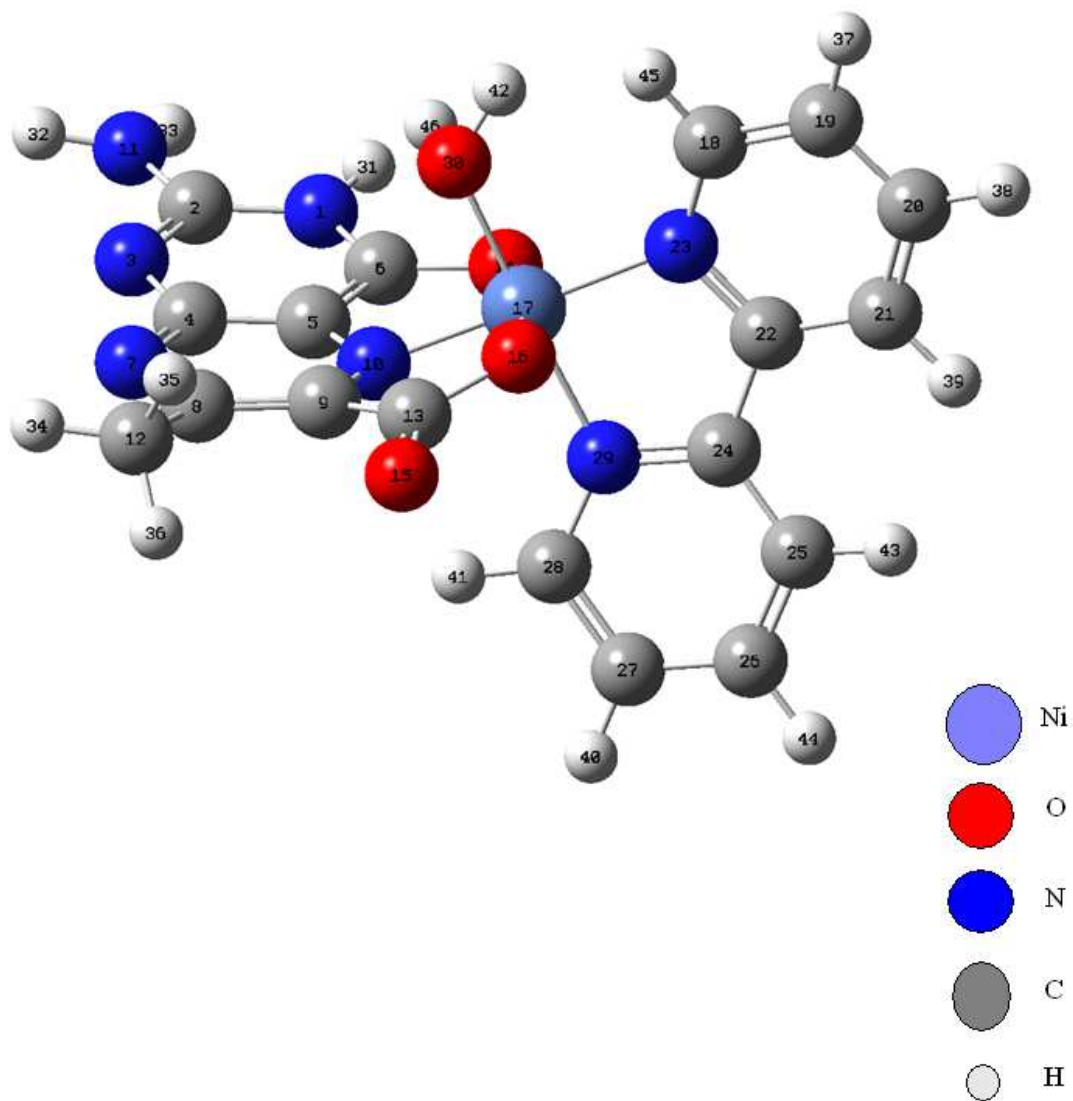


**Figure VI-5.** DFT optimized molecular structure of the compound **3**

---

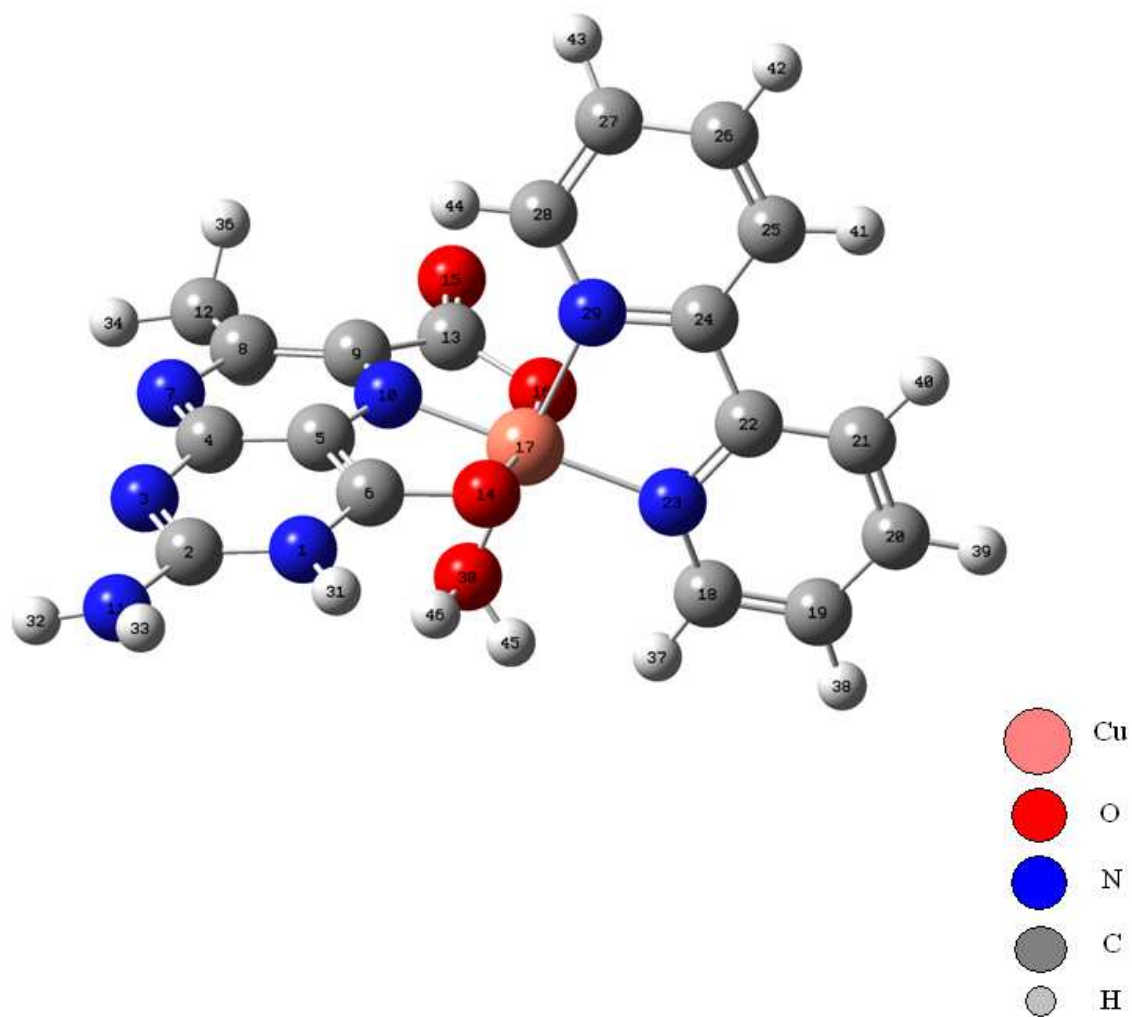


**Figure VI-6.** DFT optimized molecular structure of the compound **4**

---

**Table VI-3. Selected optimized geometric parameters (Å, °) of 1<sup>155-160</sup> and their comparison with the related x-ray structural data (Table VI-2)<sup>17a</sup>**

<b>Bond lengths (Å)</b>	<b>x-ray data of 1<sup>17a</sup></b>	<b>DFT Optimized data of 1<sup>155-160*</sup></b>
Zn(1) – O(2)	2.1373(15)	2.3135
Zn(1) – N(9)	2.0303(17)	2.0492
Zn(1) – O(4)	2.3727(15)	2.1386
Zn(1) – O(5)	2.1128(16)	2.2083
Zn(1) – N(11)	2.0684(17)	2.1045
Zn(1) – N(12)	2.1627(18)	2.1876
<b>Bond Angles (°)</b>	<b>x-ray data of 1<sup>17a</sup></b>	<b>DFT Optimized data of 1<sup>155-160</sup></b>
O(2) – Zn(1) – N(9)	76.37(6)	72.2569
O(2) – Zn(1) – O(4)	150.97(6)	150.3077
N(9) – Zn(1) – O(4)	74.60(6)	79.4508
O(2) – Zn(1) – O(5)	90.05(6)	67.1668
N(9) – Zn(1) – O(5)	91.77(7)	96.9843
O(4) – Zn(1) – O(5)	91.21(6)	108.501
O(2) – Zn(1) – N(11)	121.85(6)	108.4855
N(9) – Zn(1) – N(11)	160.68(7)	177.0695
O(4) – Zn(1) – N(11)	86.96(6)	100.2285

O(5) – Zn(1) – N(11)	94.39(7)	85.8868
O(2) – Zn(1) – N(12)	92.53(6)	94.3437
N(9) – Zn(1) – N(12)	94.76(7)	99.0196
O(4) – Zn(1) – N(12)	89.49(6)	98.8631
O(5) – Zn(1) – N(12)	173.38(6)	150.3723
N(11) – Zn(1) – N(12)	79.07(7)	78.1308
Zn(1) – O(2) – C(13)	115.97(13)	115.2433

\*Vacume

**Table VI-4. Selected optimized geometric parameters ( $\text{\AA}$ ,  $^{\circ}$ ) of  $2^{155-160}$  and their comparison with the related x-ray structural data (Table III-2)<sup>17e</sup>**

<b>Bond lengths (<math>\text{\AA}</math>)</b>	<b>DFT optimized data of 2*</b>	<b>Related x-ray data From Table III-2<sup>17e</sup></b>
Co(45) – N(28)	1.9217	2.079(3)
Co(45) – N(22)	1.9322	2.016(3)
Co(45) – N10)	1.8344	2.123(3)
Co(45) – O(16)	1.8918	2.140(2)
Co(45) – O(14)	1.918	2.270(2)
Co(45) – O(29)	1.8555	2.120(2)

<b>Bond angles (<math>^{\circ}</math>)</b>	<b>DFT optimized data of 2*</b>	<b>Related x-ray data From Table III-2<sup>17e</sup></b>
--	---------------------------------	--

O(16) – Co(45)– N(10)	86.2948	75.10(10)
N(10) – Co(45) – O(14)	88.5126	76.26(9)
O(14) – Co(45) – N(22)	92.2199	89.46(9)
N(22) – Co(45) – O(16)	90.5287	90.99(10)
N(28) – Co(45) – N(10)	92.5645	164.48(10)
N(10) – Co(45) – O(29)	88.2612	90.23(10)
O(29) – Co(45) – N(22)	93.793	173.29(10)
N(22) – Co(45) – N(28)	85.3814	79.12(10)
N(10) – Co(45) – N(22)	177.8243	96.45(10)
O(14) – Co(45) – O(16)	174.739	151.22(8)
O(14) – Co(45) – N(28)	90.5423	88.76(9)
O(14) – Co(45) – O(29)	89.4652	92.74(9)
O(29) – Co(45) – O(16)	89.5331	93.13(9)

\*PCM (methanol)

**Table VI-5. Selected optimized geometric parameters ( $\text{\AA}$ ,  $^\circ$ ) of 3 and their comparison with the x-ray structural data of a related compound (Table IV-2)<sup>17d</sup>**

<b>Bond lengths (<math>\text{\AA}</math>)</b>	<b>DFT optimized data of 3*</b>	<b>Related x-ray data (Table IV-</b>	<b>MM2 optimized data ( Chem 3D Ultra 2004)</b>

		<b>2)</b>	
O(14)-Ni(17)	1.8483	2.325(2)	1.848
O(16)-Ni(17)	1.8035	2.120(2)	1.804
Ni(17)-N(23)	1.9194	2.065(3)	1.919
Ni(17)-N(29)	1.9447	2.074(3)	1.945
Ni(17)-O(30)	1.8481	2.125(2)	1.848
N(10)-Ni(17)	1.7884	1.977(3)	1.788

<b>Bond angles ( ° )</b>	<b>DFT optimized data of 3*</b>	<b>Related x-ray data (Table IV- 2)</b>	<b>MM2 optimized data ( Chem 3D Ultra 2004)</b>
N(10)-Ni(17)-O(14)	85.7925	76.31(9)	85.793
N(10)-Ni(17)-O(16)	85.5661	77.20(10)	85.566
N(10)-Ni(17)-N(23)	172.4891	177.56(11)	172.489
N(10)-Ni(17)-N(29)	96.625	94.14(11)	96.625
N(10)-Ni(17)-O(30)	85.950	93.13(10)	85.950
O(14)-Ni(17)-O(16)	171.358	153.50(8)	171.358
O(14)-Ni(17)-N(23)	101.189	103.02(10)	101.189
O(14)-Ni(17)-N(29)	92.898	87.16(10)	92.898
O(14)-Ni(17)-O(30)	87.700	92.06(9)	87.700
O(16)-Ni(17)-N(23)	87.439	103.49(11)	87.439
O(16)-Ni(17)-N(29)	88.177	95.49(11)	88.177
O(16)-Ni(17)-O(30)	91.612	88.63(9)	91.612

N(23)-Ni(17)-N(29)	85.870	83.47(11)	85.870
N(23)-Ni(17)-O(30)	91.522	89.23(10)	91.522
N(29)-Ni(17)-O(30)	177.390	172.29(10)	177.390

\*calculated at the DFT/B3LYP level in PCM (methanol)

**Table VI-6. Selected optimized geometric parameters ( $\text{\AA}$ ,  $^\circ$ ) of 4 and their comparison with the x-ray structural data of a related compound (Table II-2)<sup>17b</sup>**

<b>Bond lengths ( <math>\text{\AA}</math> )</b>	<b>DFT optimized data of 4*</b>	<b>Related x-ray data (Table II- 2)<sup>17b</sup></b>	<b>MM2 optimized data ( Chem 3D Ultra 2004)</b>
Cu(17) – O(14)	1.8484	2.384(3)	1.848
Cu(17) – O(16)	2.0509	2.304(3)	1.804
Cu(17) – O(30)	1.8483	2.019(3)	1.848
Cu(17) – N(10)	1.9334	1.999(3)	1.788
Cu(17) – N(23)	1.991	2.002(3)	1.919
Cu(17) – N(29)	1.9849	2.037(3)	1.945

<b>Bond angles( <math>^\circ</math> )</b>	<b>DFT optimized data of 4*</b>	<b>Related x-ray data (Table II-</b>	<b>MM2 optimized data ( Chem 3D Ultra 2004)</b>
---	-------------------------------------	--	---

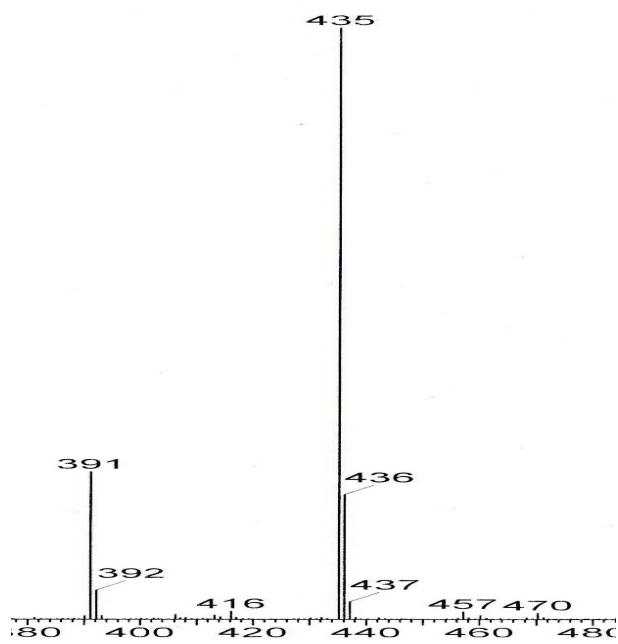
		<b>2</b> <sup>17b</sup>	
N(10) – Cu(17) – O(30)	73.68	91.01(12)	85.950
O(14) – Cu(17) – O(30)	87.6997	93.07(12)	87.700
O(16) – Cu(17) – O(30)	98.35	88.62(13)	92.261
N(23) – Cu(17) – O(30)	75.36	93.79(13)	91.522
N(10) - Cu(17) – N(23)	148.16	165.66(13)	172.489
N(29) – Cu(17) – N(23)	83.16	82.20(13)	85.870
N(29) – Cu(17) – O(16)	122.24	89.98(12)	87.531
N(29) – Cu(17) – O(14)	91.14	90.74(12)	92.898
N(10) – Cu(17) – N(29)	116.18	93.79(13)	96.625

\*Calculated at the DFT/B3LYP level in PCM (methanol)

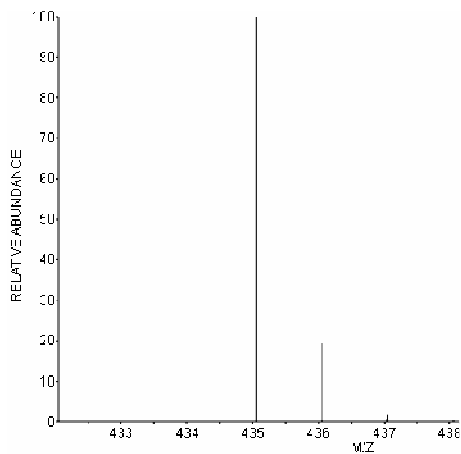
### ESIMS Data

Figure VI-7 (a) shows the ESIMS data of **2** where the peak at  $m/z$  435 corresponds to the dehydrated species  $[\text{Co}(\text{L})(\text{bipy})]^+$ ; the simulated  $m/z$  value (most abundant isotopic mass) and the isotope distribution profile in Figure VI-7(b) agreed well with the corresponding experimental value, thereby supporting the chemical composition of **2**, in conjunction with the elemental analysis data.<sup>24</sup> Figure VI-7(a) shows another fragment peak at  $m/z = 391$  corresponding to the species  $[\text{Co}(\text{L})(\text{bipy}) - \text{CO}_2]^+$ , obtained through the loss of  $\text{CO}_2$  from the

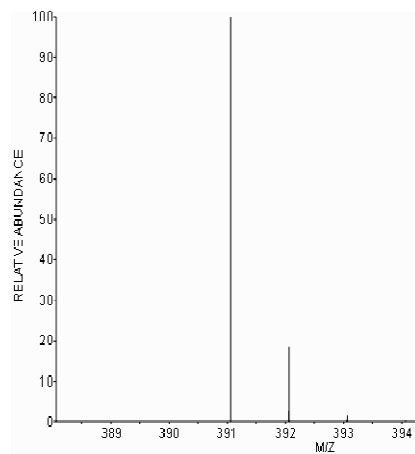
carboxylate group of pterin ligand as well as the intra/extra spheric water/methanol molecules; Figure VI-7(c) shows the corresponding calculated isotope distribution profile.<sup>24</sup>



(a)



(b)



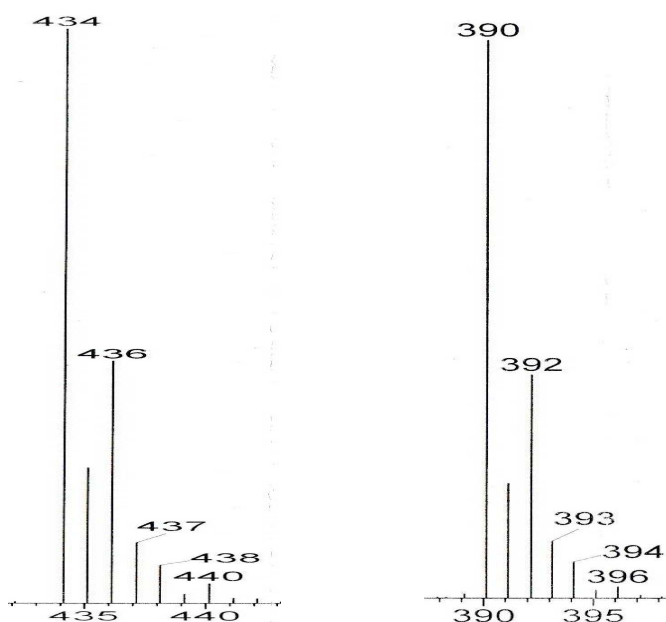
(c)

**Figure VI-7.** (a) ESIMS data of **2**; (b) the calculated isotope pattern for the base peak at  $m/z = 435$  corresponding to the fragment  $[\text{Co(L)(bipy)}]^+$  and (c) for the peak  $m/z = 391$  corresponding to the fragment  $[\text{Co(L)(bipy)} - \text{CO}_2]^+$ .

---

Figure VI-8 (a) and (b) shows the ESIMS data of **3** where the peak at  $m/z$  434 corresponds to the dehydrated species  $[\text{Ni(L)(bipy)}]^+$  and that at  $m/z = 390$  represents the species  $[\text{Ni(L)(bipy)} - \text{CO}_2]^+$ . The simulated isotope distribution profile are shown in Figure VI-8(c) and (d) respectively. Again, good agreements between the experimental and simulated data verify the assigned chemical composition, in conjunction with these mass spectral data.

Figure VI-9(a) shows the ESIMS data of **4** where the peak at  $m/z$  438.9 corresponds to the dehydrated species  $[\text{Cu(L)(bipy)}]^+$ ; its isotope distribution profile agreed with the corresponding calculated spectrum [Figure VI-9 (b)], thereby verifying the assigned chemical composition of **4**.<sup>24</sup>



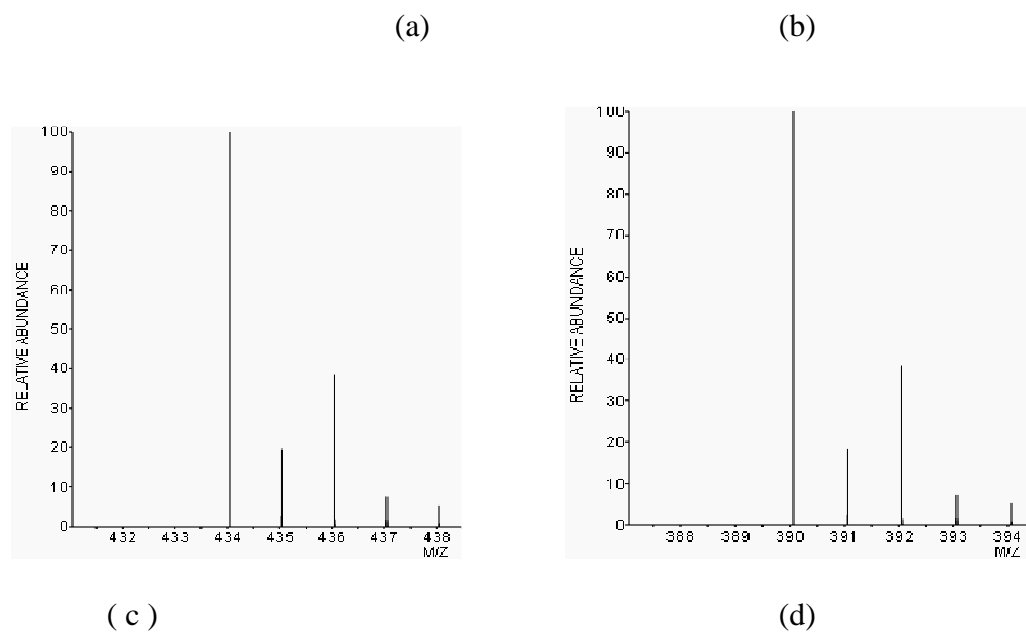
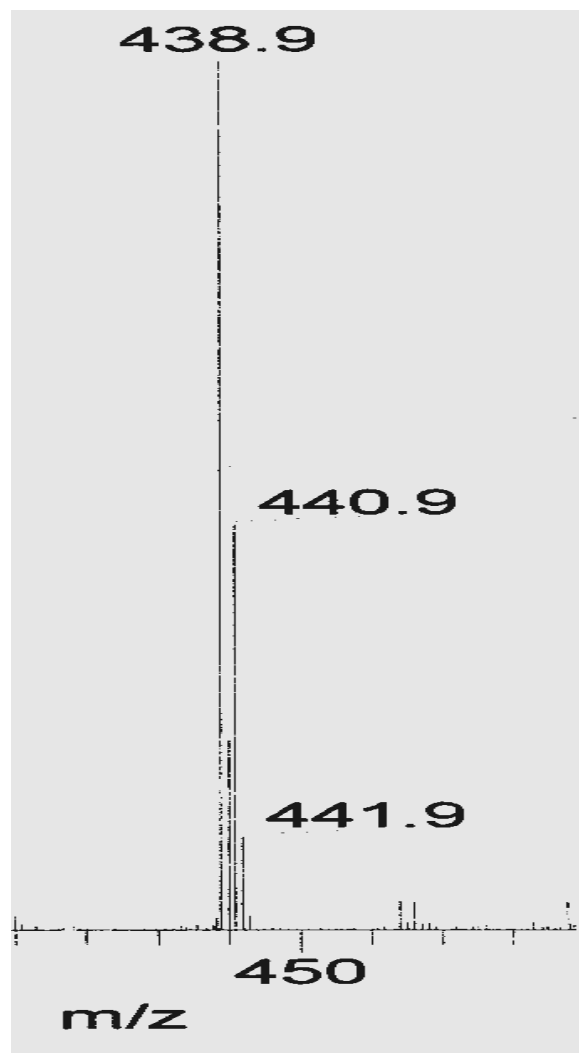
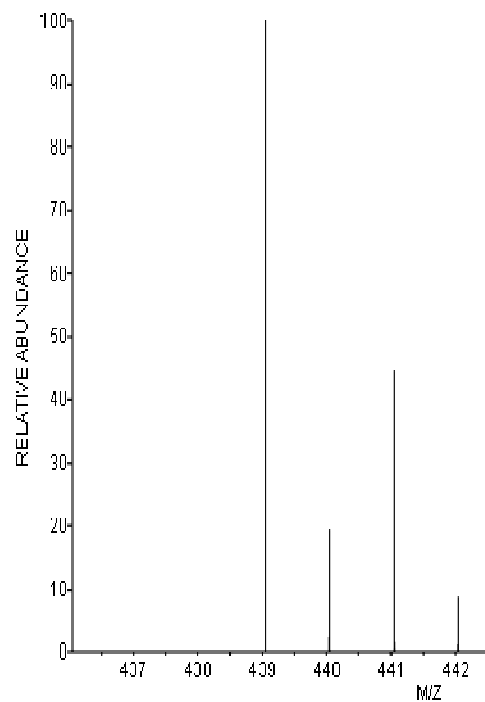


**Figure VI-8.** (a) and (b) ESIMS data of **3**; (c) the calculated isotope pattern for the base peak at  $m/z = 434$  corresponds to the fragment  $[\text{Ni}(\text{L})(\text{bipy})]^+$  and (d) for the calculated peak  $m/z = 390$  corresponding to the fragment  $[\text{Ni}(\text{L})(\text{bipy}) - \text{CO}_2]^+$ .

---



(a)



(b)

**Figure VI-9.** (a) ESIMS data of **4**; (b) the calculated isotope pattern for the base peak at  $m/z = 438.9$  corresponding to the fragment  $[\text{Cu}(\text{L})(\text{bipy})]^+$ .

## IR spectroscopy

Figure VI-10 to VI-13 represent the IR spectral data of compounds **1** – **4** along with the assignments of the major IR bands. IR spectrum of the free pterin ligand is shown in Figures II-9(a) and II-10; its broad IR bands centered around  $1684\text{ cm}^{-1}$ ,  $1383\text{ cm}^{-1}$  and  $1294\text{ cm}^{-1}$  are absent in the above- mentioned spectra,

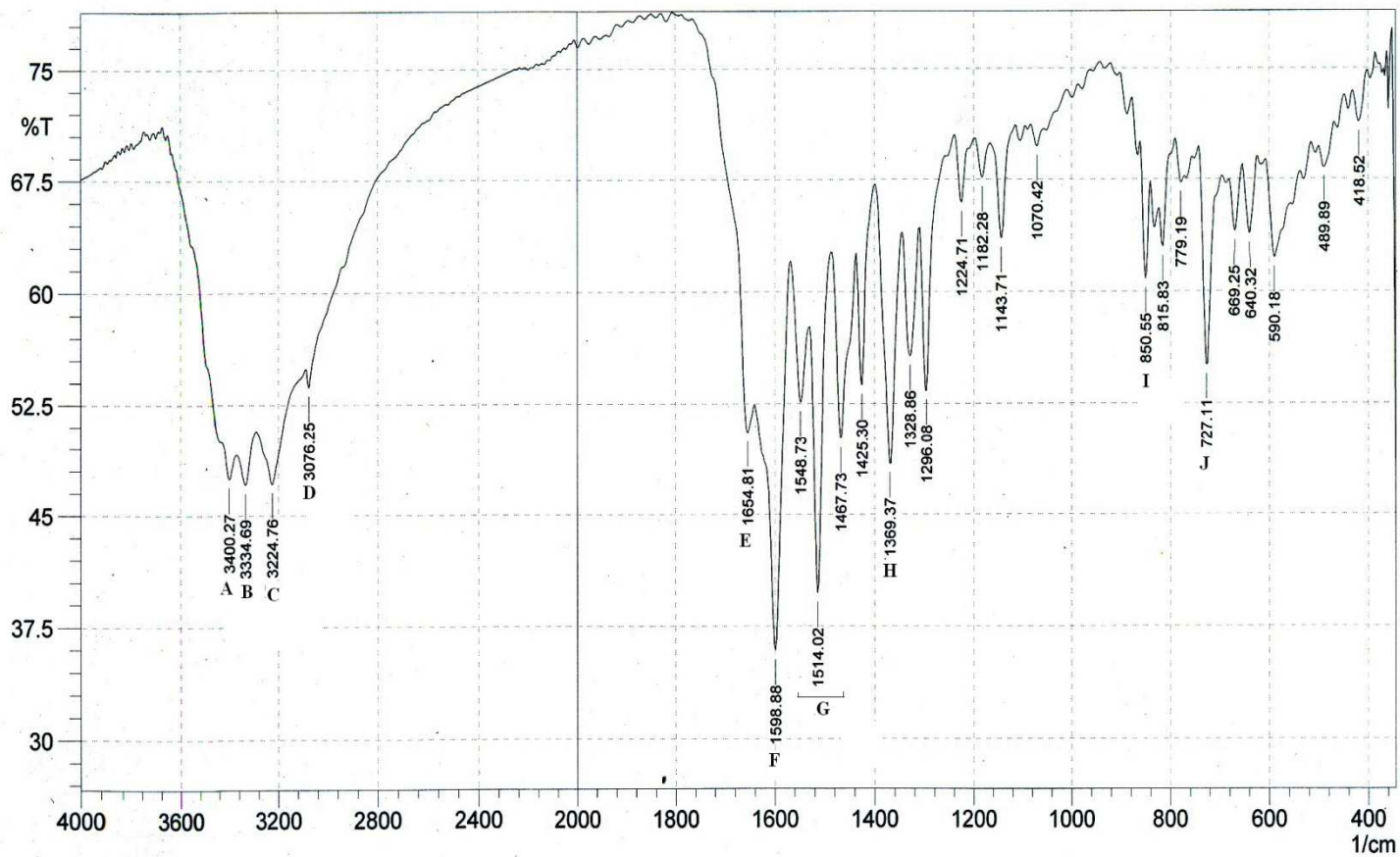


**Figure VI-10.** IR spectrum of compound **1** (KBr pellet).

- A: Hydrogen bonded  $\nu(\text{OH})$  vibration;
- B:  $\nu(\text{NH})$  vibration of  $\text{NH}_2(2)$  of the pterin ligands;
- C,D:  $\nu(\text{CH})$  vibrations (pterin / phen);
- E:  $\nu(\text{C}=\text{O})$  of the coordinated  $\text{C}=\text{O}$  group;
- F:  $\nu_{\text{as}}(\text{CO}_2')$  along with the  $(\text{N}-\text{H})$  bending vibration;

- G :  $\nu(\text{C}=\text{C})$  and  $\nu(\text{C}=\text{N})$  vibrations (pterin / phen);
- H:  $\nu_s(\text{CO}_2')$ ;
- I, J: out- of- plane C – H bending vibrations of the phen ligand.

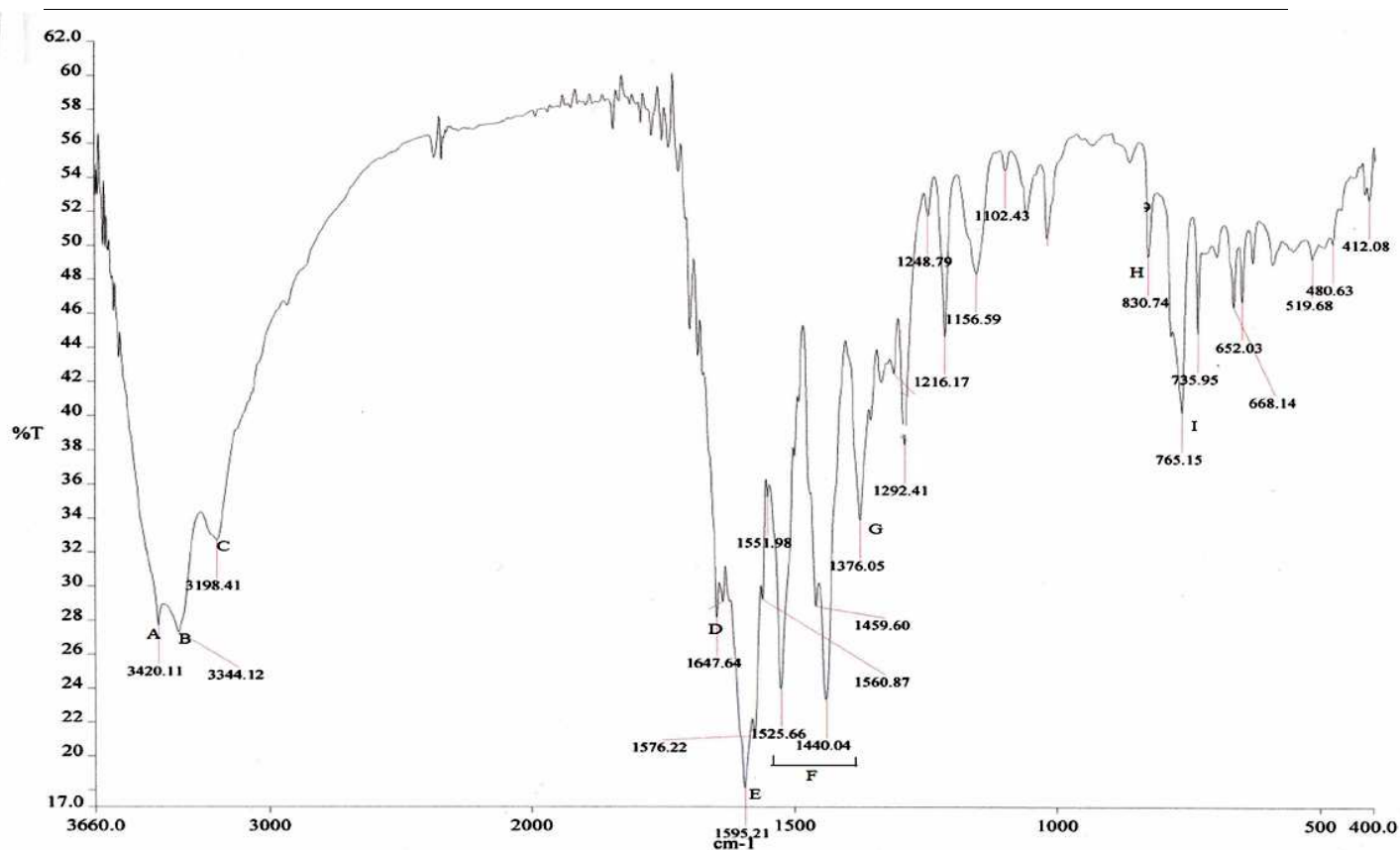


**Figure VI-11.** IR spectrum of compound **2** (KBr pellet).

- A: Hydrogen bonded  $\nu(\text{OH})$  vibration;
- B:  $\nu(\text{NH})$  vibration of  $\text{NH}_2(2)$  of the pterin ligands;
- C:  $\nu(\text{CH})$  vibrations (phen/pterin);
- D:  $\nu(\text{C}=\text{O})(4)$  vibrations;
- E:  $\nu_{\text{as}}(\text{CO}_2')$  along (N – H) bending vibration;
- F :  $\nu(\text{C} = \text{C})$  and  $\nu(\text{C} = \text{N})$  vibration (pterin/phen);
- G:  $\nu_s(\text{CO}_2')$ ;

H,I: out- of- plane C – H bending vibrations of the bipy ligand.

---

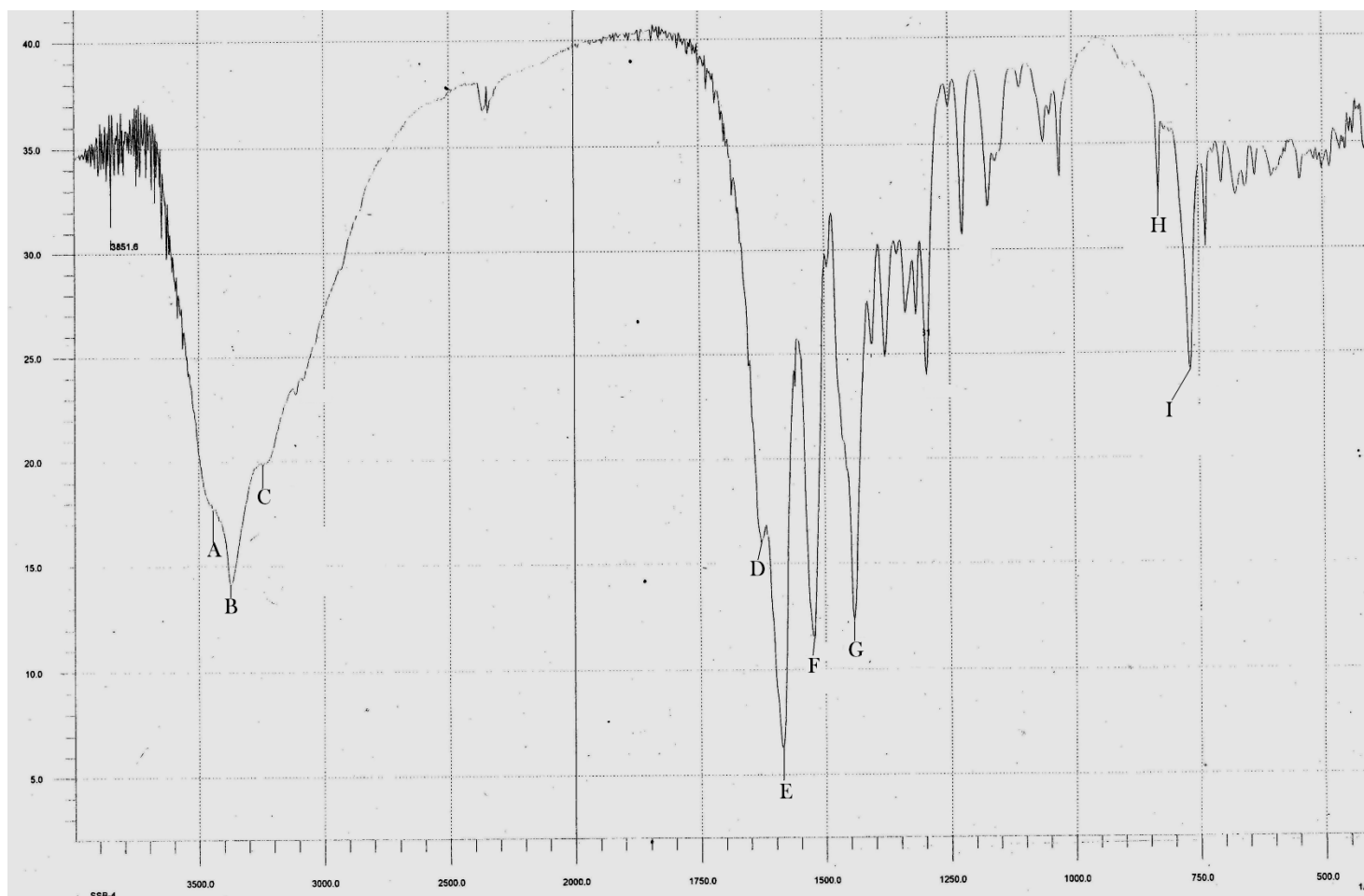


**Figure VI-12.** IR spectrum of compound **3** (KBr pellet).

- A: Hydrogen bonded  $\nu(\text{OH})$  vibration ( $3412\text{ cm}^{-1}$ );
- B:  $\nu(\text{NH})$  vibration of  $\text{NH}_2(2)$  of pterin ligands ( $3373.3\text{ cm}^{-1}$ );
- C:  $\nu(\text{CH})$  vibrations (pterin/bipy) ( $3232.5\text{ cm}^{-1}$ );
- D:  $\nu(\text{C}=\text{O})(4)$  of the coordinated  $\text{C}=\text{O}(4)$  group ( $1645\text{ cm}^{-1}$ );
- E:  $\nu_{\text{as}}(\text{CO}_2')$  along with the (N – H) bending vibration ( $1585\text{ cm}^{-1}$ );
- F:  $\nu(\text{C}=\text{C})$  and  $\nu(\text{C}=\text{N})$  of pterin/bipy ( $1521.7\text{ cm}^{-1}$ );

G:  $\nu_s(\text{CO}_2')$  ( $1442.7 \text{ cm}^{-1}$ );

H,I: out- of- plane C – H bending vibrations of bipy( $825 \text{ cm}^{-1}$  and  $767.6 \text{ cm}^{-1}$ ).

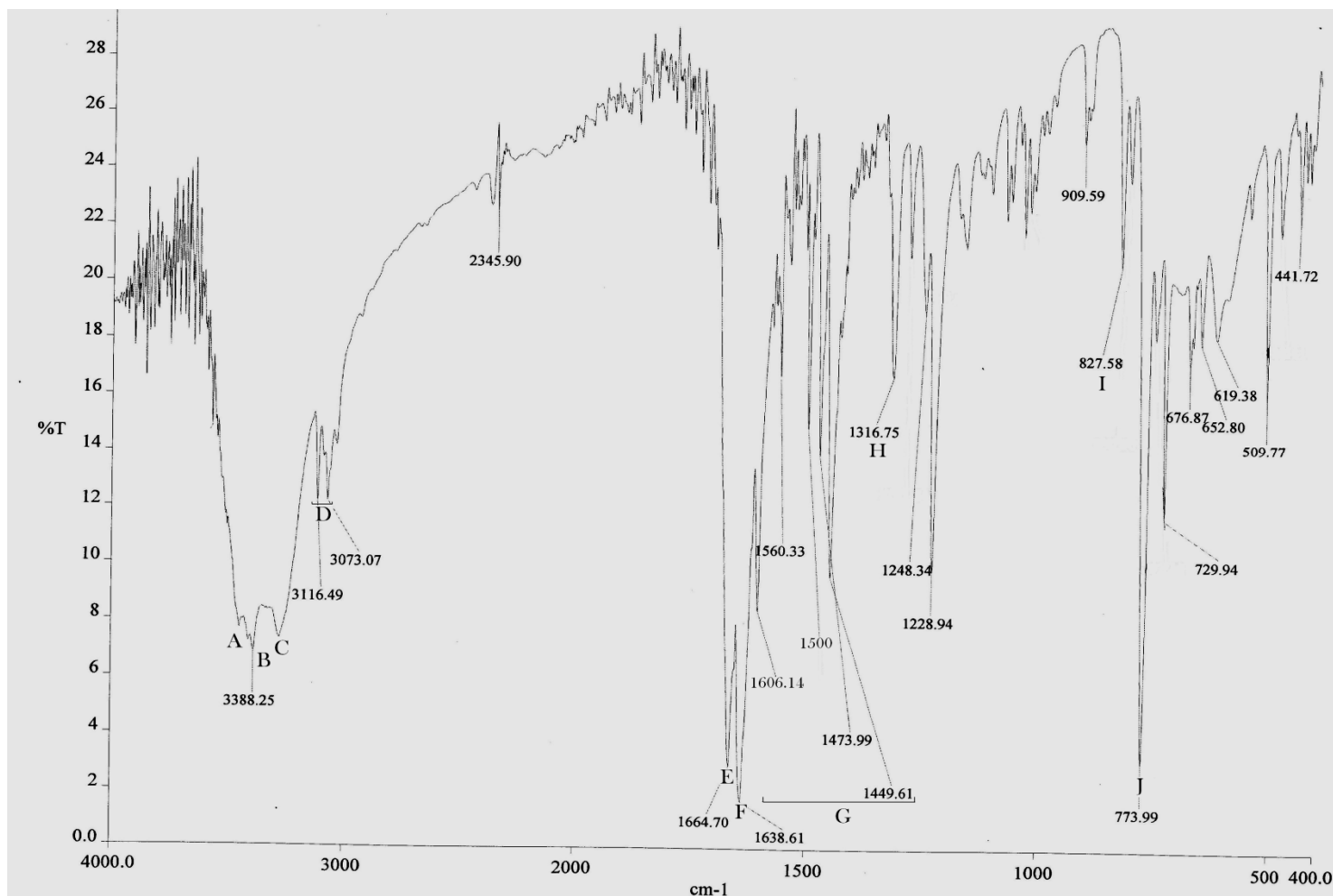


**Figure VI-13.** IR spectrum of compound 4 (KBr pellet).

A: Hydrogen bonded  $\nu(\text{OH})$  vibration;

B,C:  $\nu(\text{NH})$  vibration of  $\text{NH}_2(2)$  of pterin ligands;

D:  $\nu(\text{CH})$  vibrations (pterin/bipy);

E:  $\nu(\text{C=O})(4)$  of the coordinated  $\text{C=O}(4)$  group;

F:  $\nu_{\text{as}}(\text{CO}_2')$  along with the (N – H) bending vibration of  $\text{NH}_2(2)$  group;

G:  $\nu(\text{C=C})$  and  $\nu(\text{C=N})$  vibration (pterin/bipy);

H:  $\nu_s(\text{CO}_2')$ ;

I,J: out- of- plane C – H bending vibrations of bipy.

---

signifying deprotonation of the COOH(6) and NH(3) groups. The  $\Delta\nu$  value ( $\nu_{\text{as}} - \nu_s$ ) for the carboxylate group,  $\text{CO}_2'(6)$  varies around 219 -290  $\text{cm}^{-1}$  for **1** to **4**, indicating unidentate carboxylate coordination.<sup>87,88</sup> The  $\nu(\text{C}=\text{O})$  mode of the coordinated C=O(4) phenoxide group is assigned at 1655  $\text{cm}^{-1}$  for compound **1** (Figure VI-10); this is in agreement with the multiple bond character of the C15 – O16 bond with a bond length of 1.257(3)Å (Figure VI-1).<sup>17a</sup> In other cases (Figure VI-11 to VI-13), this  $\nu(\text{C}=\text{O})$  mode is observed around 1648 – 1665  $\text{cm}^{-1}$ . From the above, tridentate pterin coordination involving O(4), N(5) and O(6) donor atoms is inferred which is consistent with the x-ray structural data of **1** (Figure VI-1). The C-H out of plane bending vibrations of bipy/phen ligands are also observed (850-727  $\text{cm}^{-1}$ )<sup>21</sup>.

### UV-VIS spectroscopy

The electronic spectra of the compounds **1** – **4** are shown in Figure VI-14 to VI-17; the relevant data are summarized in Table VI-7. In some of these cases, the intraligand  $\pi \rightarrow \pi^*$  transitions are observed in the region 250 nm to 309 nm. Besides these, a LMCT transition is observed around 375 nm – 391 nm. For **1**- **4** (Table VI-7) at least one or numerous bands are also observed in the visible region; their  $\epsilon$  values are much higher than those which could be assigned to 'd – d' transitions.<sup>31</sup> Such electronic transitions could be assigned to MLCT bands from metal  $e_g^*$  level to ligand  $\pi^*$  levels (phen/bipy/pterin). According to Scheme II-9 this is quite feasible for these  $\text{M}^{2+}$  ions with 7-10 electrons in the 3d levels [ $\text{Co(II)d}^7$ ,  $\text{Ni(II)d}^8$ ,  $\text{Cu(II)d}^9$  and  $\text{Zn(II)d}^{10}$ ]. The best exponent of such MLCT bands is observed for the  $\text{Zn(II)d}^{10}$  complex **1**, with a log  $\epsilon$  value of 4.086 at 733 nm; this is responsible for its light brown color.

**Table VI-7.** Electronic spectral data of **1**, **2**, **3** and **4** in CH<sub>3</sub>OH

Compound	$\lambda(\log\epsilon)$
<b>1</b>	326s(4.835), 376br(5.057), 733(4.086)
<b>2</b>	280(4.23), 307sh(3.686), 380br(3.156), 460sh(2.48), 894(2.35)
<b>3</b>	285(4.083), 309sh(3.818), 391br(3.576)
<b>4</b>	250sh(4.48), 276(4.498), 303sh(4.43), 375(4.09),692(2.4),744(2.36),779(2.35),808(2.35),919(2.13), 1069(2.10)

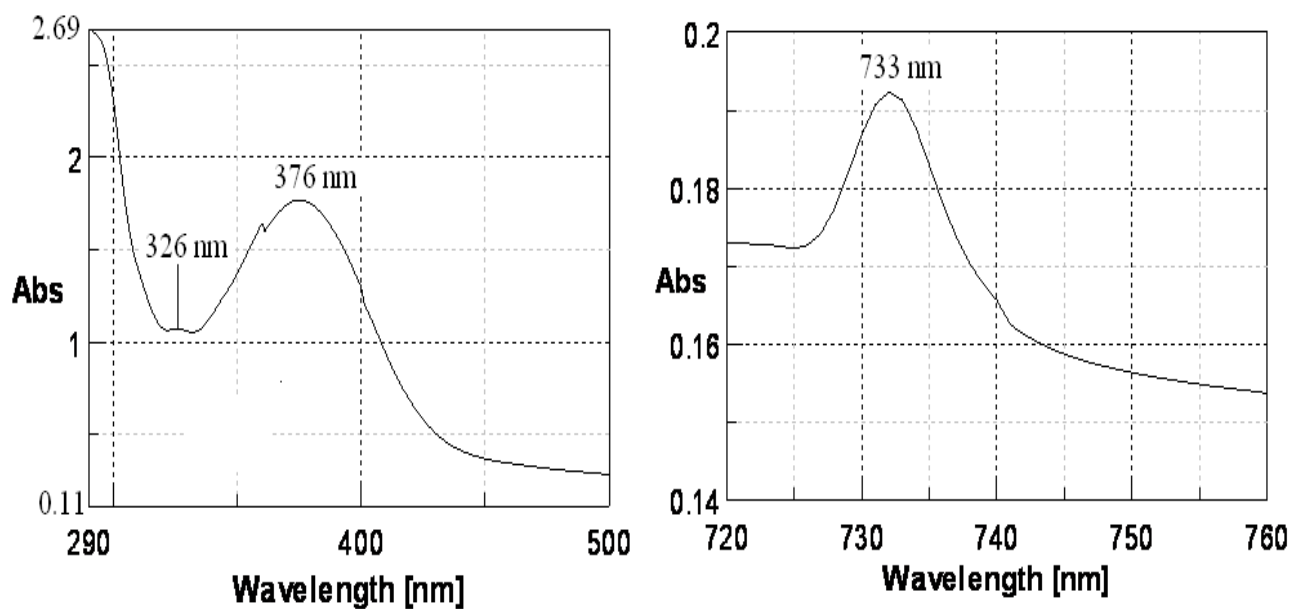


**Figure VI-14.** Electronic spectra of **1** in H<sub>2</sub>O ( $1.58 \times 10^{-5}$  mol dm<sup>-3</sup>).

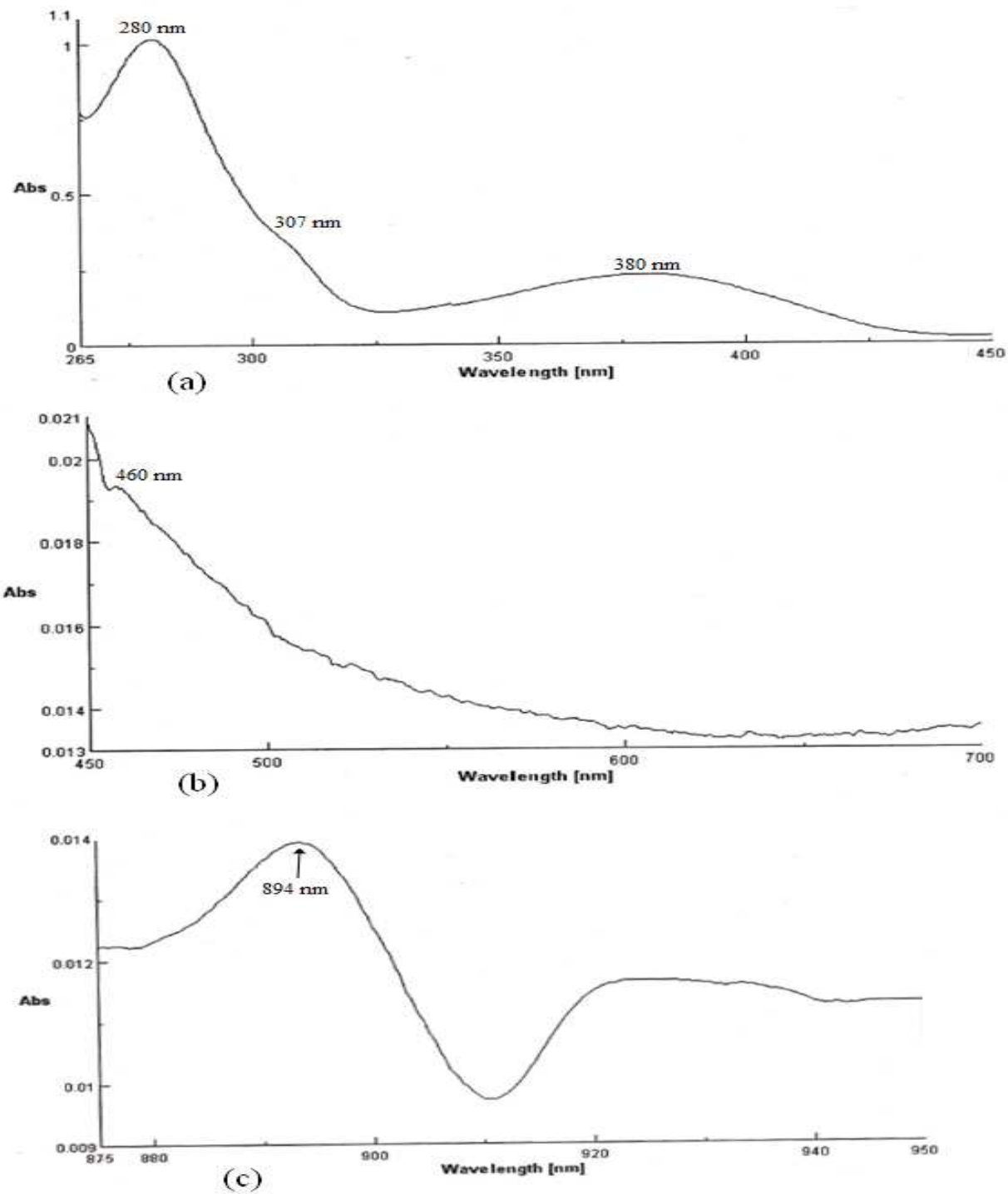
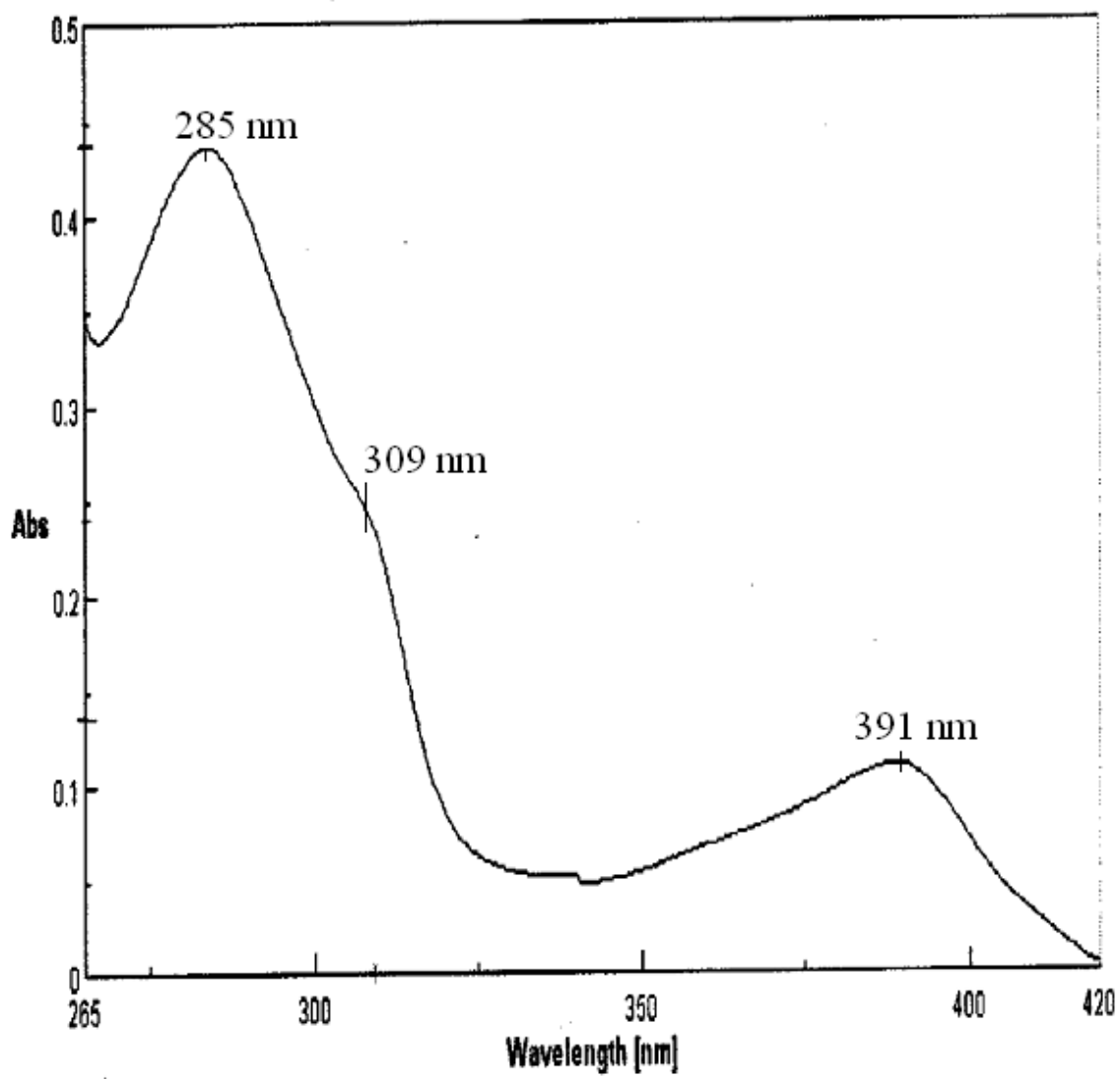
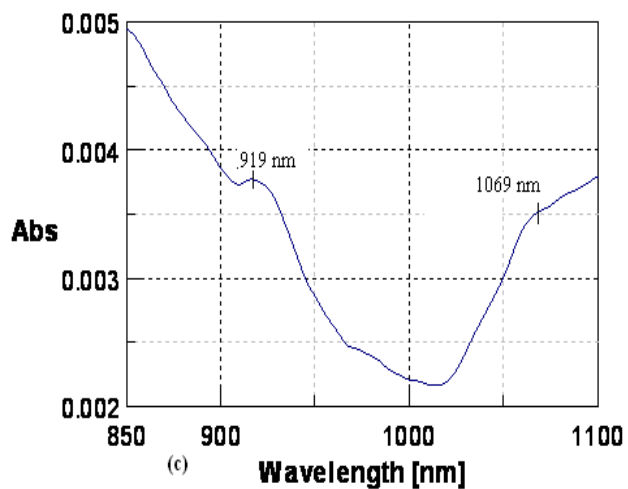
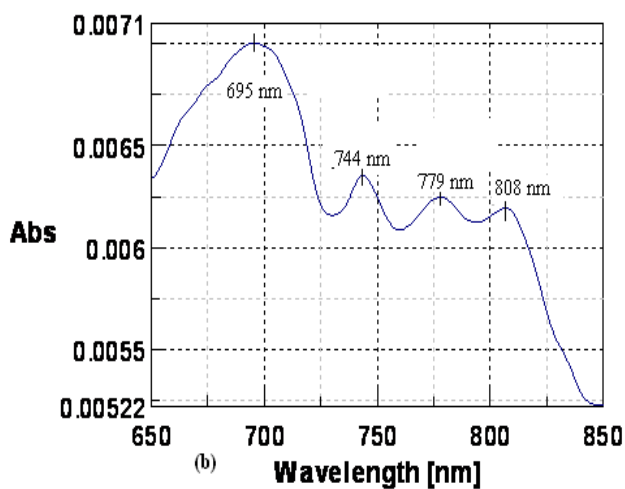
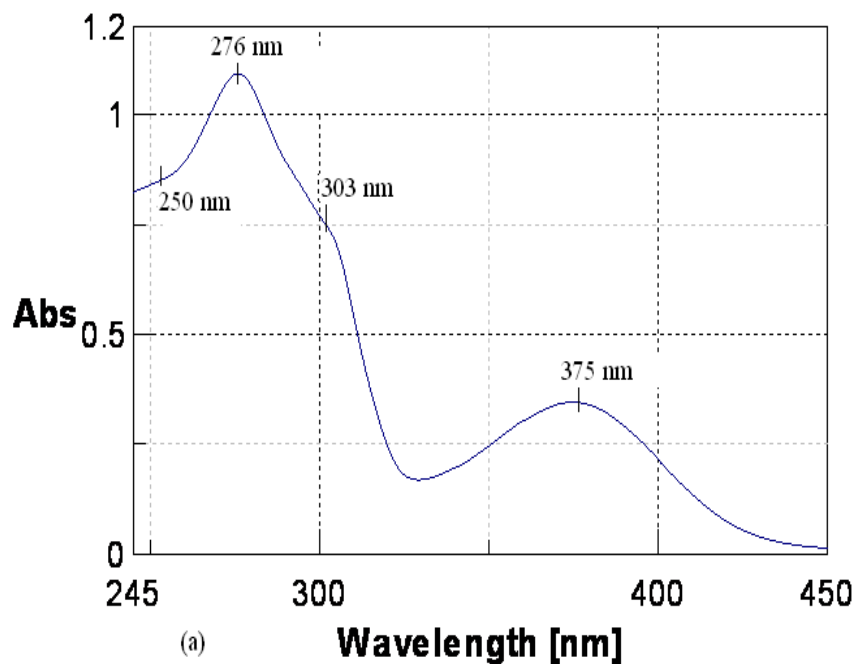


Figure VI-15. Electronic spectra of **2** in DMSO ( $0.62 \times 10^{-4} \text{ mol dm}^{-3}$ ).



**Figure VI-16.** Electronic spectra of **3** in DMSO ( $3.6 \times 10^{-5} \text{ mol dm}^{-3}$ ).



**Figure VI-17.** Electronic spectra of **4** in H<sub>2</sub>O ( $2.78 \times 10^{-5}$  mol dm<sup>-3</sup>).

### Fluorescence Spectra

Fluorescence spectral data of **2**, **3** and **4** are shown in Figure VI-18, VI-19 and VI-20 respectively. Their emission maxima appear around 450-453 nm. Additional transitions are also

observed in the longer wavelength region 550-600 nm. As observed in earlier chapters, reduction with  $\text{NaBH}_4$  of such complexes is associated with considerable increase in fluorescence. For **4R** [Figure VI-20] there is considerable fluorescence intensity increase at 453 nm over **4** [4 treated with  $\text{NaBH}_4$  in  $\text{H}_2\text{O} \rightarrow \mathbf{4R}$ ] for this reason. The **4** $\rightarrow$ **4R** conversion is associated with two simultaneous reduction steps, e.g., oxidized/aromatic pterin  $\rightarrow$  7, 8-dihydro pterin and  $\text{Cu(II)} \rightarrow \text{Cu(I)}$  conversion. The increased electron density in **4R** causes such fluorescence intensity increase and also due to greater electronic circulation in this  $\text{Cu(I)} d^{10}$  complex (Scheme II-9).

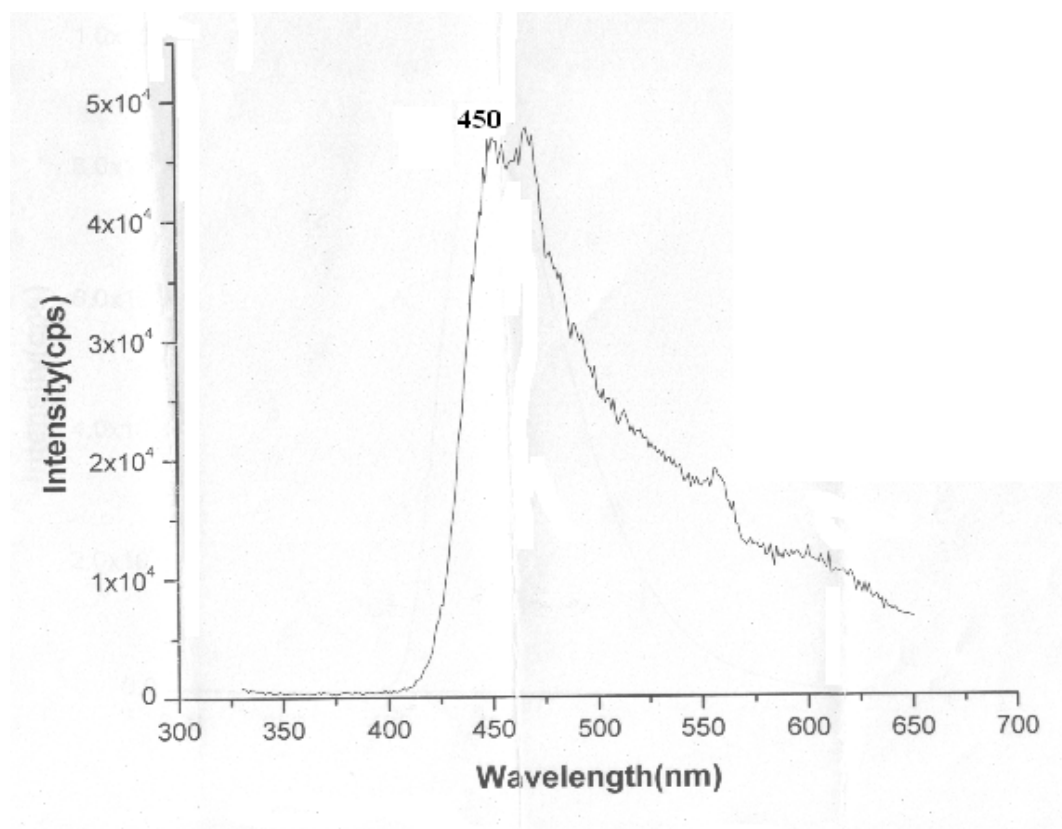


**Figure VI-18.** Fluorescence emission spectra of **2** in DMSO.

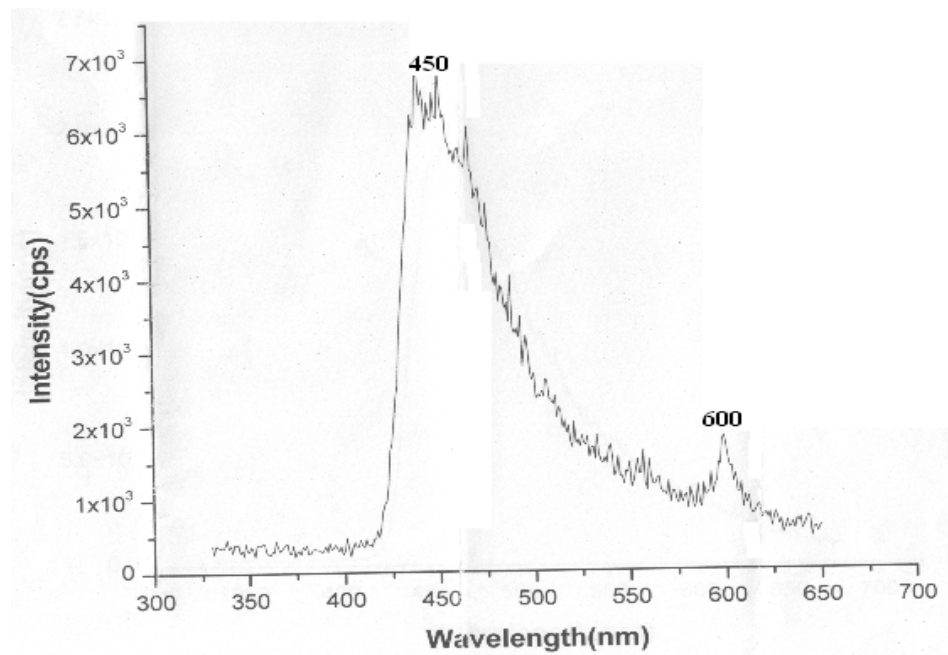


**Figure VI-19.** Fluorescence emission spectra of **3** in DMSO.

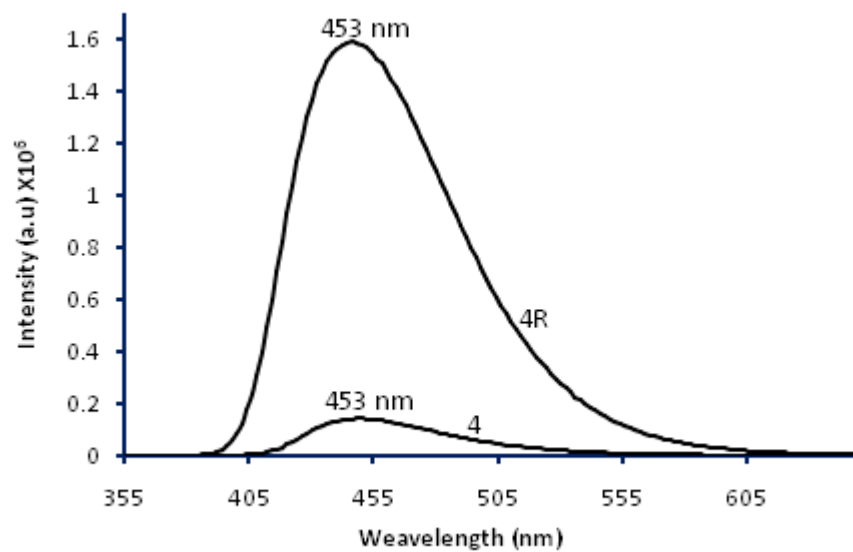


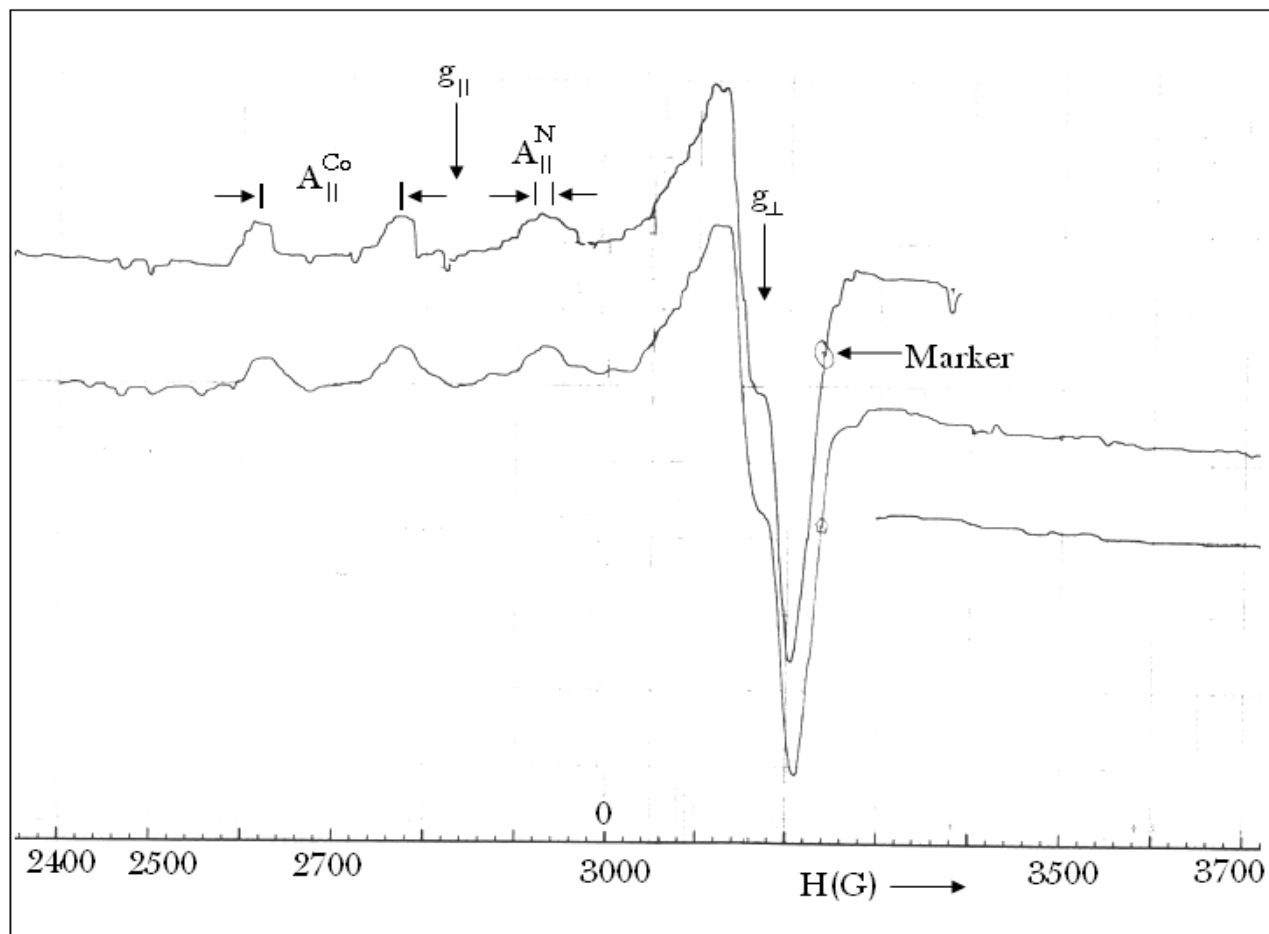
**Figure VI-20.** Fluorescence emission spectra of **4** and **4R** in  $H_2O$ .

## EPR spectroscopy

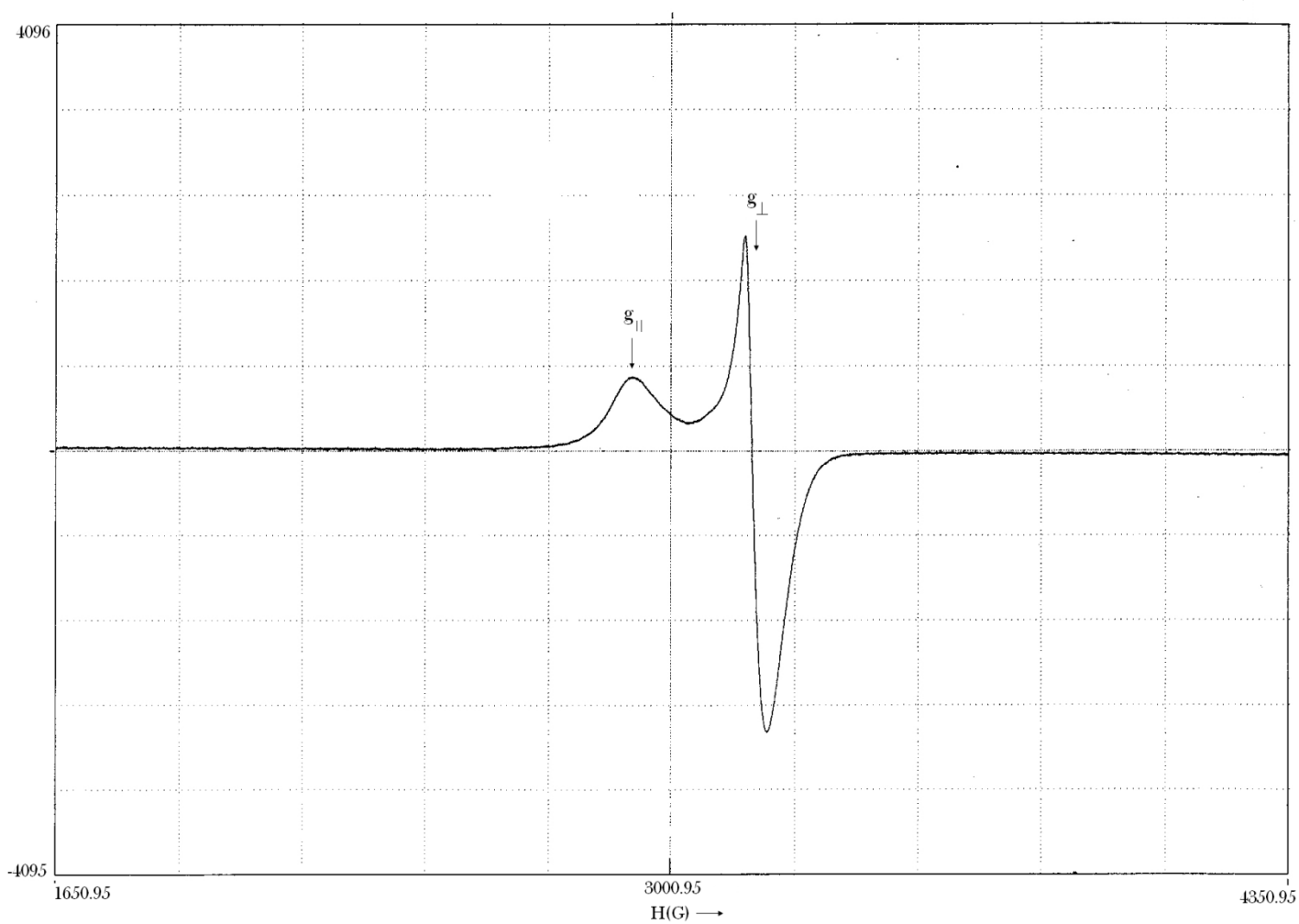
EPR spectra of **2** and **4** are presented in Figure VI-21 and VI-22 respectively. For **3** unusual line broadening prevented its EPR spectral study. The two above Figures represent axial type of EPR spectra, indicating elongation along the z axis for both **2** and **4**. Such an inference is consistent with the x-ray structural data of related Co(II) and Cu(II) complexes of the same pterin ligand(H<sub>2</sub>L).<sup>17</sup>

Figure VI-21 yields the characteristic EPR spectral parameters for **2**, e. g.,  $g_{\parallel} = 2.30$  and  $g_{\perp} = 2.05$ . Here the basic signal is split (hyperfine interaction) by the Co(II) atom ( $I = 7/2$ ) into eight bands, out of which four could be identified on  $g_{\parallel}$ . Each of such bands is further split (superfine splitting) by the three nitrogen atoms ( $I = 1$ ) of **2** with the CoN<sub>3</sub>O<sub>3</sub> coordination environment. Few equispaced lines could be assigned:  $A_{\parallel}^{\text{Co}}(152 \times 10^{-4} \text{cm}^{-1})$  and  $A_{\parallel}^{\text{N}}(11 \times 10^{-4} \text{cm}^{-1})$ .<sup>37,38</sup>

From Figure VI-22, the  $g_{\parallel} = 2.24$  and  $g_{\perp} = 2.05$  values for **4** can be evaluated. Here the hyperfine/superfine lines due to splitting by the Cu(II) atom ( $I = 3/2$ ) and the three nitrogen atom ( $I = 1$ ) from the CuH<sub>3</sub>O<sub>3</sub> coordination geometry, are absent.



**Figure VI-21.** X-band EPR spectrum of **2** in DMSO at 77K versus TCNE marker. The lower curve is a repetition of the upper one, showing the scan result on the higher field (H) side. This spectrum has been recorded by SAIF, IIT Bombay, using a Varian E-112 ESR spectrometer.



**Figure VI-22.** X-band EPR spectrum of **4** in DMSO at 77K. This spectrum has been recorded by SAIF, IIT Bombay using a Jeol JES-FA200 ESR spectrometer.

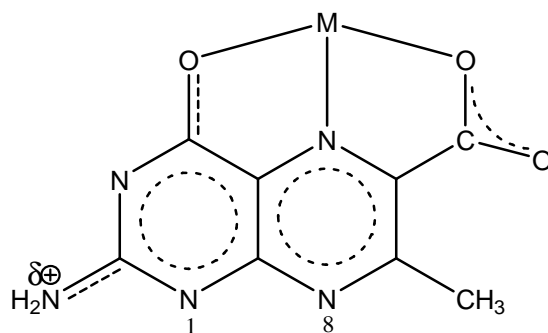
---

## NMR spectroscopy

Here **1**, a Zn(II)d<sup>10</sup> diamagnetic complex provides with the opportunity of recording the <sup>1</sup>H NMR spectral data in DMSO-d<sub>6</sub> and ascertaining the electronic environments of its pterin and the ancillary (phen) ligands. No other complex of this affords such NMR data because they are all paramagnetic substances; in chapter II the <sup>1</sup>H NMR data of a binuclear Cu(I) complex has been reported.

Figure VI-23 to VI-25 reports the NMR data of **1** along with assignments. Scheme VI-8 shows the <sup>1</sup>H NMR spectra of the pterin ligand (H<sub>2</sub>L) in NaOD/D<sub>2</sub>O (a) and **1**, 10-phenanthroline monohydrate in CDCl<sub>3</sub>(b). It may be stated here that such spectra have already been discussed in chapter II. In DMSO solution **1** exist in three forms the major form is shown in Figure VI-23, while the pterin proton signals [CH<sub>3</sub>(7) and NH<sub>2</sub>(2)] of the two minor forms are shown in Figure VI-24. A coordinated DMSO signal is observed at δ2.27; its sharp quintuplet nature verifies the assignments.<sup>21</sup> <sup>1</sup>H-<sup>1</sup>H COSY data of **1** (Figure VI-25) verified the proton signal assignments of Figure VI-23. The CH<sub>3</sub>(7) signal (pterin) appears at δ2.38 for the free pterin ligand (H<sub>2</sub>L) and at δ2.88 for **1**, i.e., deshielded by δ0.5 through complex formation. This is in agreement with the x-ray structural data **1** with the C15 – C16 bond showing multiple bond character [1.257(3)Å] (Figure VI-1)<sup>17</sup>; electron density withdrawn from the pyrazine and pyrimidine rings contributes to this observed bond length data. On the other hand, most of the <sup>1</sup>H NMR signals of the ‘phen’ moiety are shielded to a significant extent (δ1.1 to δ0.5), indicating increase in electron density on coordination. A reasonable interpretation may be given to this observation in the light of the UV-Vis spectrum of **1** (Figure VI-14; Table VI-7) showing a MLCT band at 733 nm. Obviously a Zn(II)d<sup>10</sup>→phen transition (Scheme II-9) contributed to the observed electron density increase in the ‘phen’ moiety through coordination.

For the free pterin ligand ( $H_2L$ ), the weak/ broad signal due to the  $NH_2(2)$  group appears at  $\delta 2.418$  (Scheme VI-8). In **1**, this signal is located around  $\delta 9.2 - 8.3$ , along with the  $H'_2, H'_9$  signal (phen); the concerned protonic integration value of 1.0 supports this inference, taking a value of 0.25 per proton in terms of the protonic integration value of 0.75 for the  $CH_3(7)$  signal (figure VI-23). This deshielding of the  $NH_2(2)$  signal (by ca.  $\delta 6.3$ ) through complex formation, may be elucidated in the light of the x-ray structural data of **1**, showing a multiple bond character [ a bond length value of  $1.335(3)\text{\AA}$  is observed for the C13 – N17 bond, Figure V-1] for the  $NH_2(2) - C(2)$  bond.<sup>17</sup> For a Lewis structure of the following type, the partial positive charge



on the nitrogen atom [ $NH_2(2)$ ] is responsible for the observed deshielding of the above protons.

Redox non-innocent behavior of the pterin residue ( $L^{2-}$ ) in **1**, is responsible for this observation.

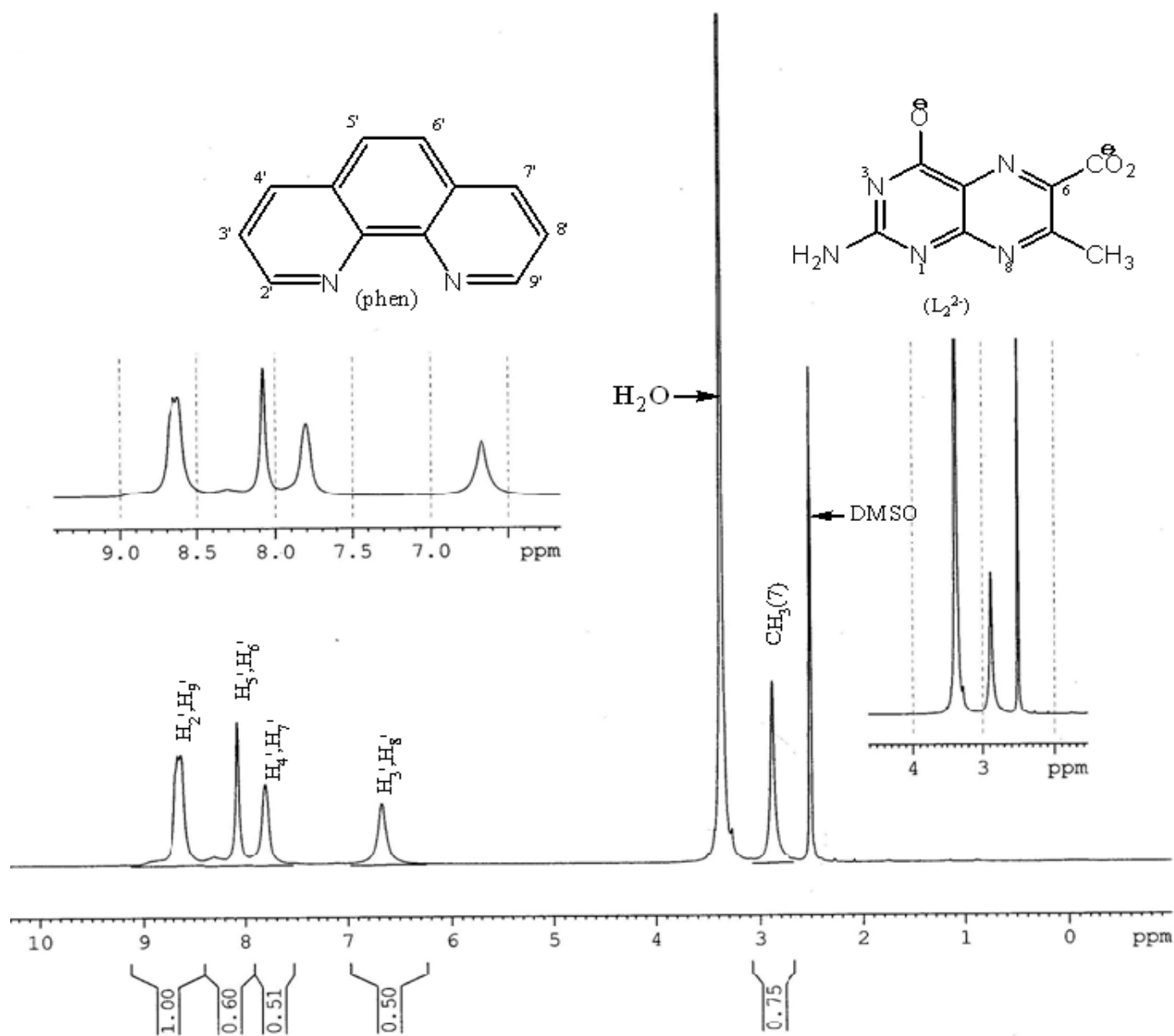


**Figure VI-23.** 300 MHz  $^1\text{H}$  NMR spectrum of **1** in  $\text{DMSO-d}_6$ . The expanded regions are shown in the inset. Expansion of the region  $\delta 2.5\text{-}0.7$  is shown in Figure VI-24. Figure VI-25 shows the corresponding 2D NMR spectrum.

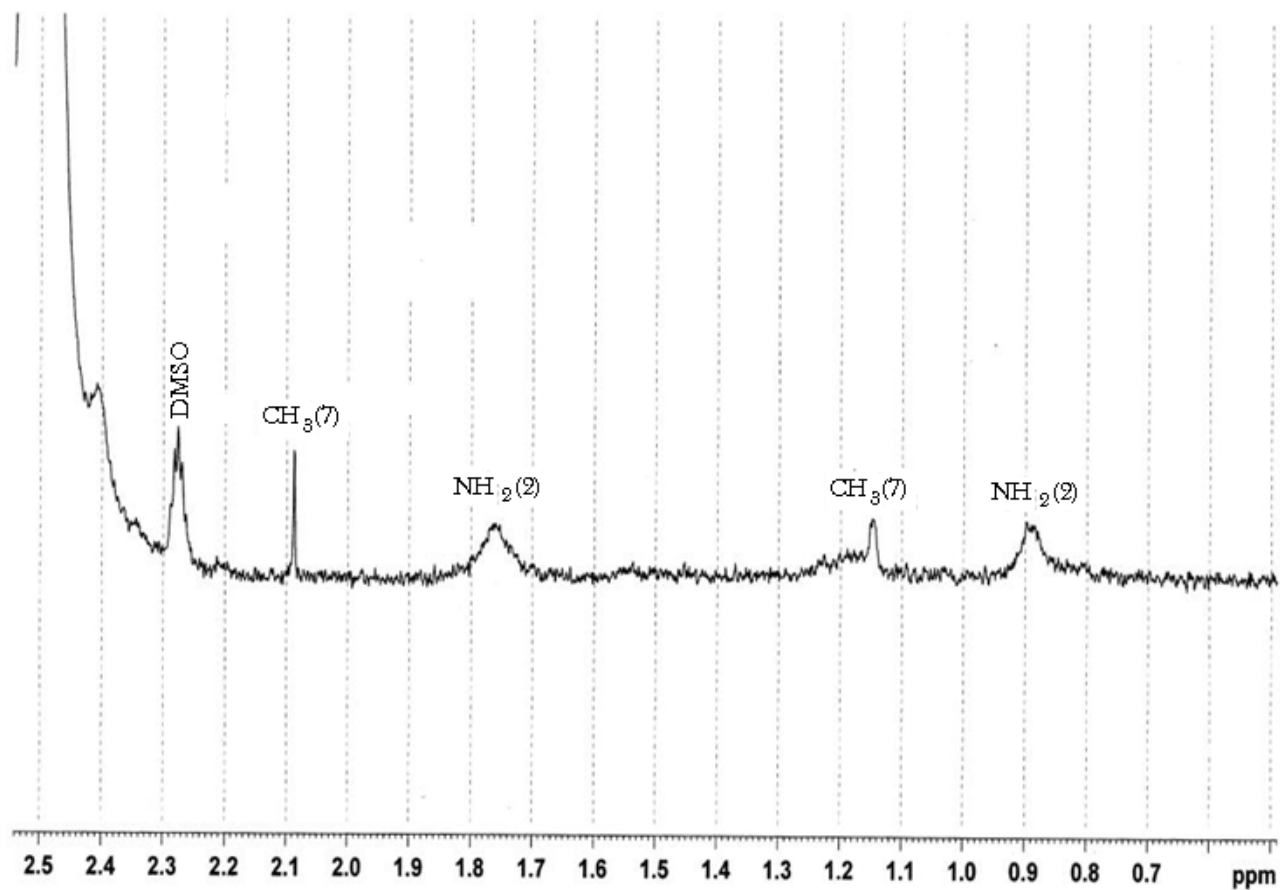


**Figure VI-24.** 300 MHz  $^1\text{H}$  NMR spectrum of **1** in  $\text{DMSO-d}_6$ . Expansion of the region  $\delta 2.5\text{-}0.7$  of Figure VI - 23 is shown here, indicating the presence of two minor forms of the pterin ligand and a coordinated DMSO molecule.

---

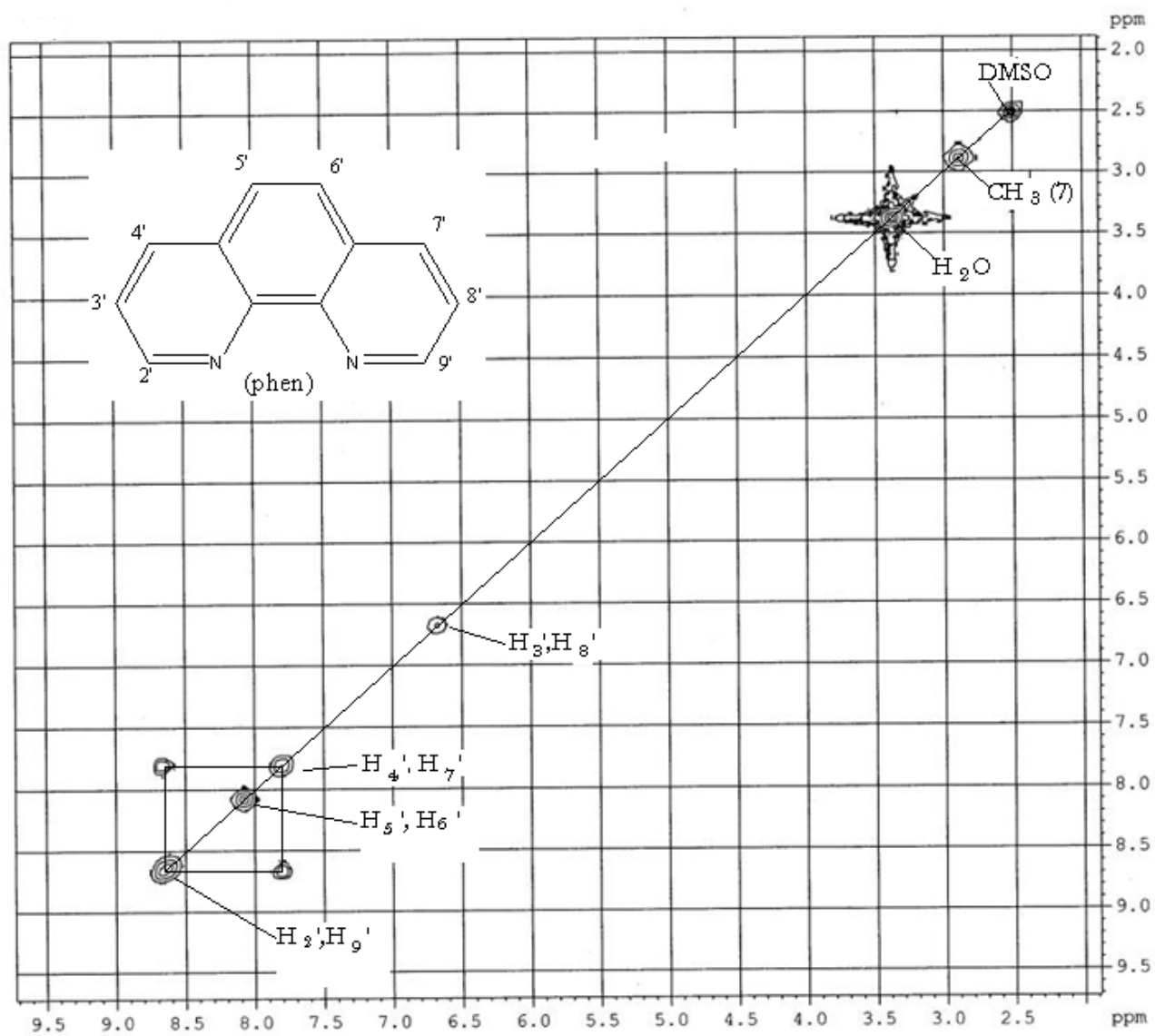
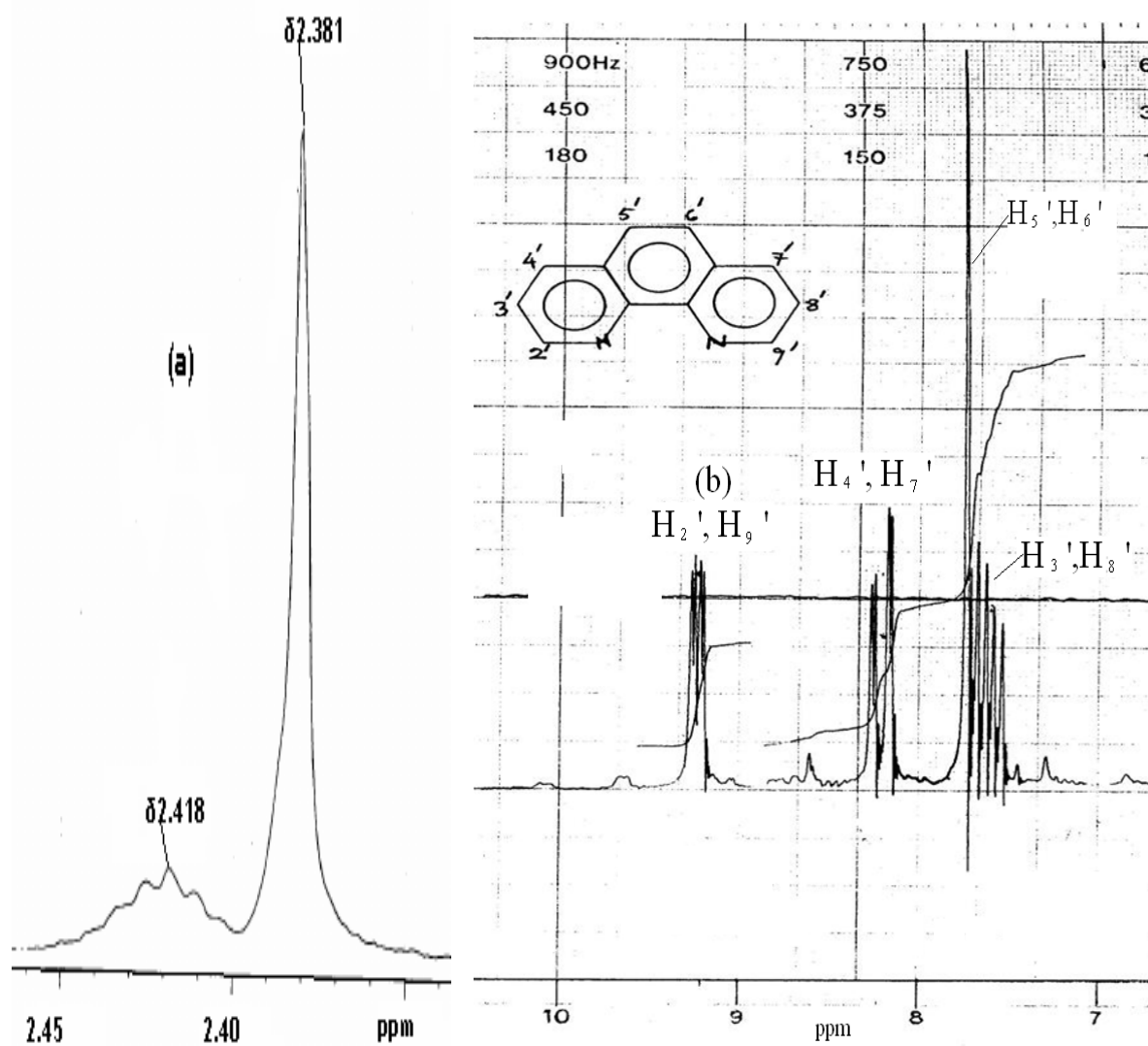


**Figure VI-25.** 300 MHz <sup>1</sup>H - <sup>1</sup>H cosy spectrum of **1** in DMSO-d<sub>6</sub>.



**Scheme VI-8**

**Table VI-8.**  $^1\text{H}$  NMR signals ( $\delta$ , ppm) of **1**, 10-phenanthroline monohydrate (ancillary ligand) and the 'phen' moiety in **1**, along with  $\Delta(\delta_{\text{complex}} - \delta_{\text{ligand}})$  values (ppm)

Compound	H <sub>2</sub> ,H <sub>9</sub>	H <sub>4</sub> , H <sub>7</sub>	H <sub>5</sub> , H <sub>6</sub>	H <sub>3</sub> ,H <sub>8</sub>
Free ancillary ligand, phen (DMSO)*+	9.15(q)	8.51(q)	8.02(s)	7.78(q)
'phen' moiety in <b>1</b> (DMSO – d <sub>6</sub> )	8.65(br,d) Δ = -0.5	7.8(s) Δ = -0.7	8.09(s) Δ = 0.07	6.68(s) Δ = -1.1

\*Miller, J.D.; Prince, R. H. J. Chem. Soc., 4706 (1965)

+The corresponding spectrum in CDCl<sub>3</sub> is shown in Scheme VI-8.

### Cyclic voltammetry

The cyclic voltammetry data of **1** and **2** are shown in Figure VI-26 and VI-27 respectively. For **1**, a Zn(II) (d<sup>10</sup>) species, no metal-centred reduction peak is observed; only a few ligand-centred reductions (-0.94 to -1.57v) and reoxidations (-0.56v and 0.25v) are observed. For **2**, the cyclic voltammetric data is dominated by a metal-centred reduction (-0.82v) and a reoxidation (-0.67v) peak; the ΔE<sub>p</sub> value (-150 mv) indicates a close approach to quasi-reversible behavior involving the redox couple:



As per the Frost diagram of the first transition metals (Scheme IV-11), the Co(II) → Co(I) reduction involves little free energy change and is quite feasible here. Besides this,

feasibility of  $\text{NaBH}_4$  reduction of this and other compounds (e.g., **4**) of this series is also indicated.

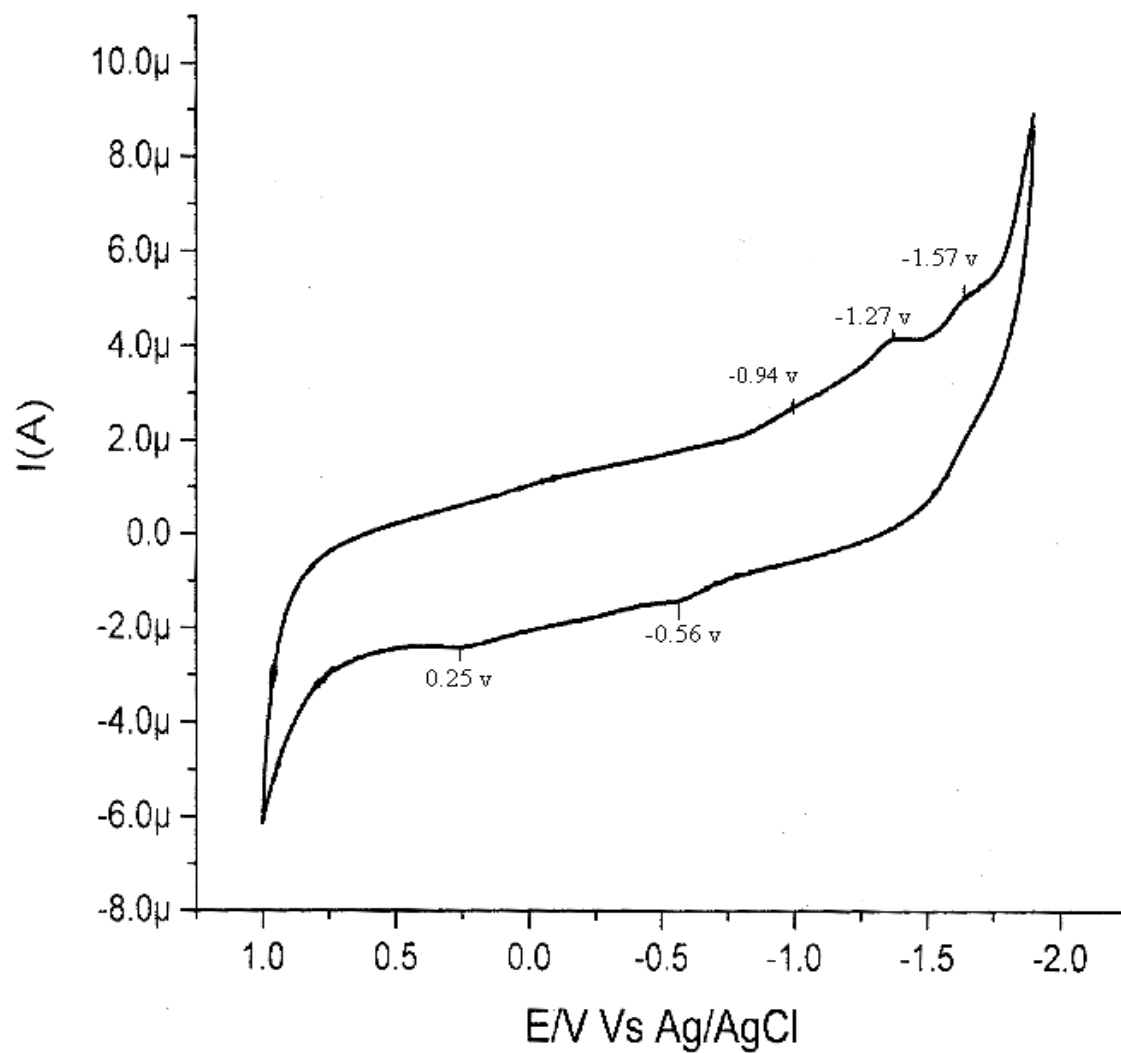


**Figure VI -26.** Cyclic voltammetry data of **1** in DMSO (  $1\text{mM}$ ,  $0.1\text{M}$  TBAP, GCE,  $100\text{ mVs}^{-1}$ )

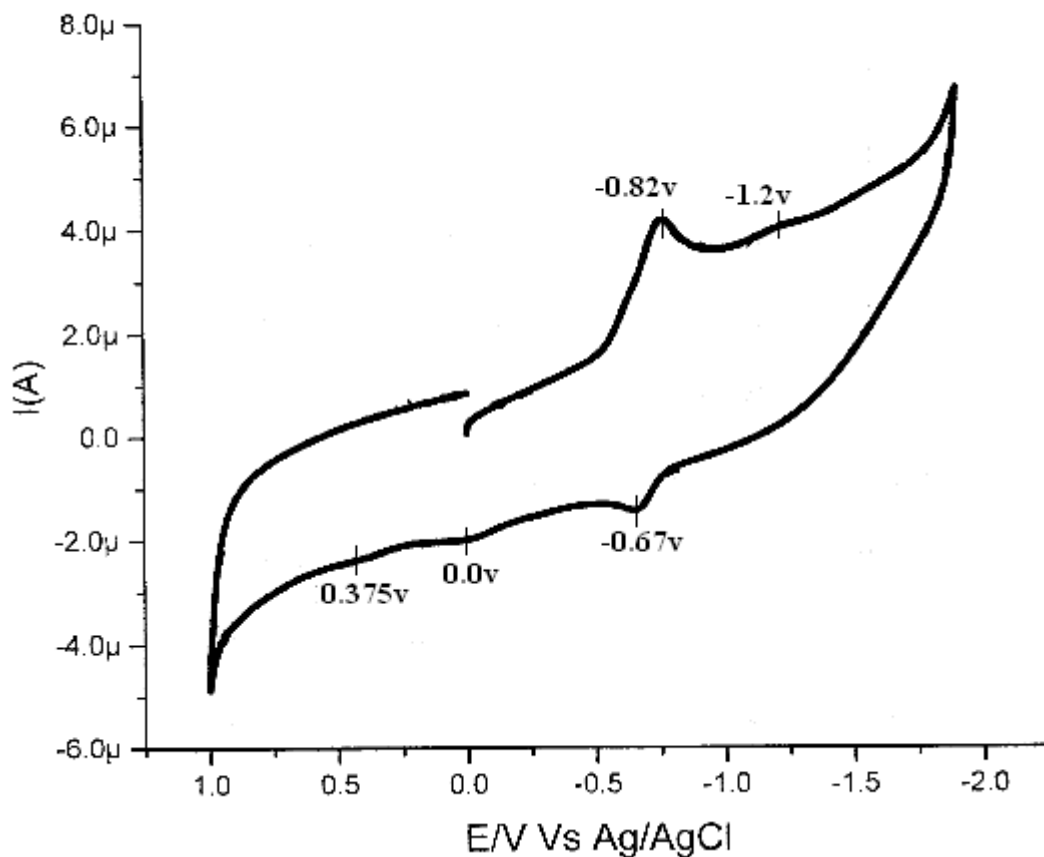
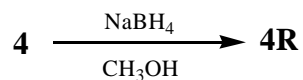


**Figure VI -27.** Cyclic voltammetry data of **2** in DMSO ( 1mM, 0.1M TBAP, GCE, 100 mVs<sup>-1</sup>)

#### Reactivity studies of **4**: UV-Vis spectroscopy

Reactivities of **4** with group transfer as well as electron transfer agents are shown in Figure VI-28 to VI-30. Figure VI-28 shows the reaction profile of **4** with imidazole (Im), signifying the replacement of its aquo group by imidazole; absence of any isosbestic point indicates a multistep reaction. Figure VI-29 is corresponds with the following reaction:-



The NaBH<sub>4</sub> reduction affects both the metal and pterin ligand centers:

(i) oxidized/aromatic pterin  $\rightarrow$  7, 8-dihydro pterin conversion;

(ii) Cu(II)  $\rightarrow$  C(I) reduction.

In view of the relevant discussions in earlier chapters, presence of such reduced metal and ligand centers in **4R** is quite likely. Figure VI-30 reflects the reactivity of **4R** towards an oxidizing agent like  $K_3[Fe(CN)_6]$ , indicating the presence of reduced centers in **4R**, as above.<sup>94</sup>

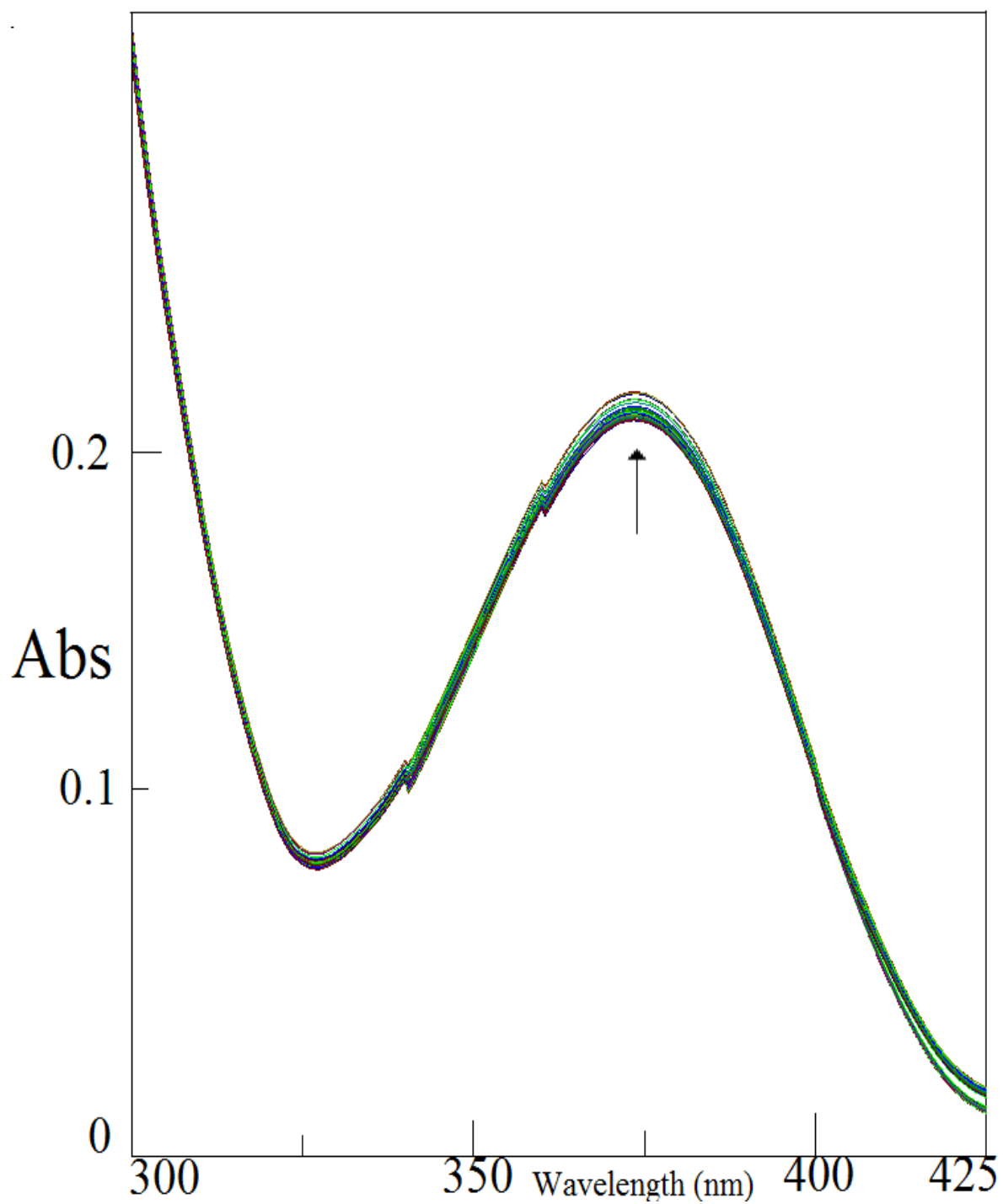


**Figure VI-28.** Absorption spectral changes recorded at 2 min interval during the reaction of (4) ( $2.76 \times 10^{-5} \text{M}$ ) with Im ( $3.78 \times 10^{-3} \text{M}$ ) in  $\text{CH}_3\text{OH}$  at 300K

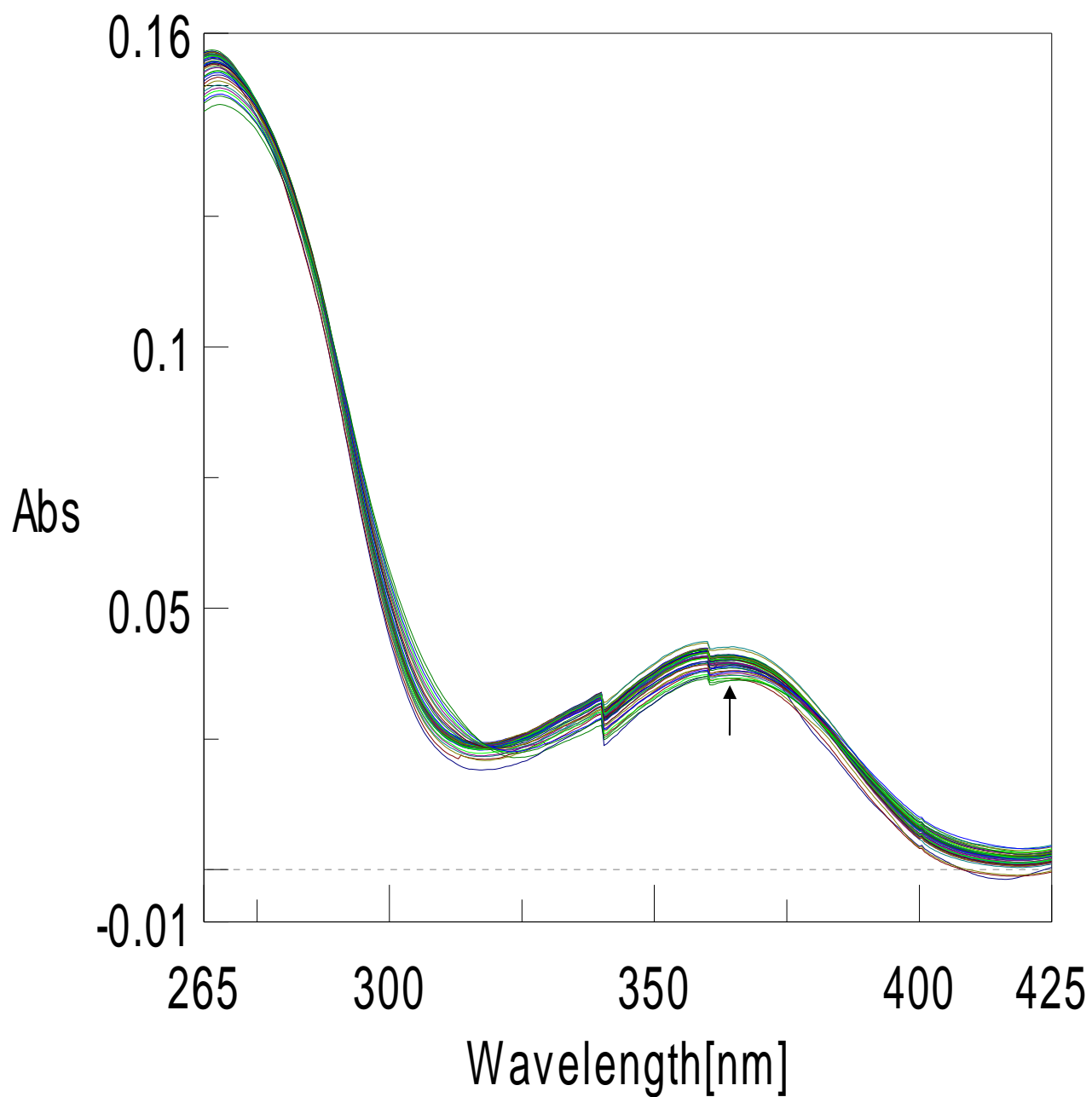


**Figure VI-29:** Absorption spectral changes recorded at 1.0 min interval during the reaction of (4) ( $2.78 \times 10^{-5} \text{M}$ ) with  $\text{NaBH}_4$  ( $3.56 \times 10^{-3} \text{M}$ ) in  $\text{CH}_3\text{OH}$

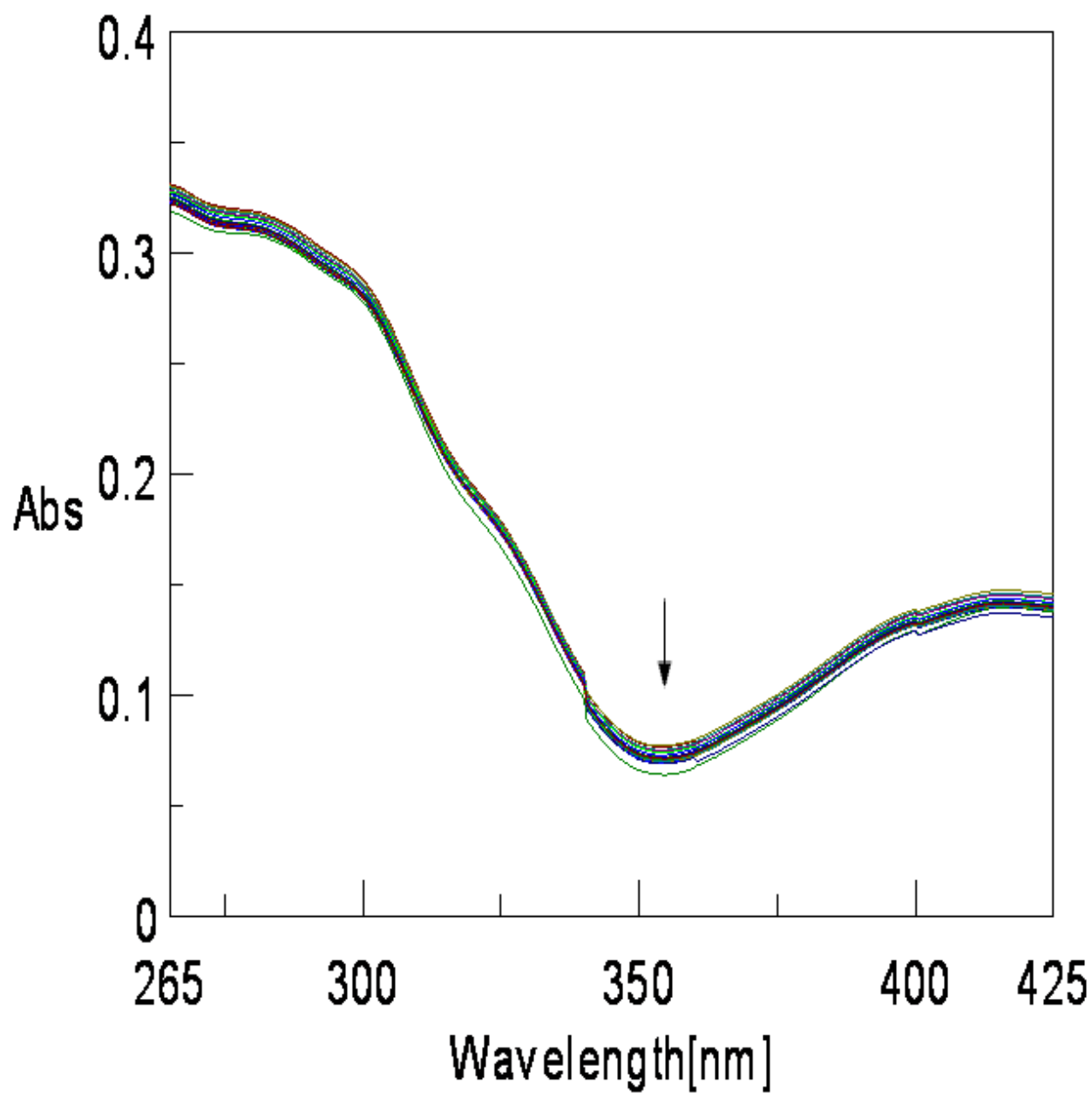
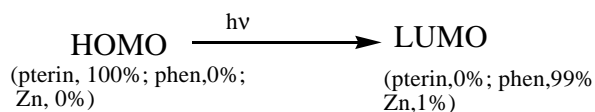


**Figure VI-30:** Absorption spectral changes recorded at 20 second interval during the reaction of (**4R**) ( $3.86 \times 10^{-5} \text{M}$ ) with  $\text{K}_3\text{Fe}(\text{CN})_6$  ( $4.68 \times 10^{-3} \text{M}$ ) in  $\text{CH}_3\text{OH}$  at 298K

---

Electronic structures of **1 – 4**

The relevant electronic structures have been obtained by DFT methods and are shown in Figure VI-31 and VI-32.<sup>155-159</sup> A noteworthy feature of the frontier orbitals of these complexes (**1** – **4**) is that in each case at least a couple of energy levels are present with energy band gaps less than 0.5 eV. As detailed out in earlier chapters, such compounds possess unusual redox properties including redox amphoteric behavior.<sup>64-66</sup> For example, in case of **1**, the lowest energy transition can be assigned (Figure VI-31) as follows.



In UV-Vis spectroscopy, this transition could be detected above 700 nm as a MLCT band with large  $\epsilon$  value. As par the above information about compositions (%) of the concerned energy levels, it is essentially a charge migration across the entire complex molecule from pterin to phen, through the Zn(II) centre. In other words, it represents an internal redox process involving the redox non-innocent pterin ligand and the  $\pi$ -acidic phen ligand. Such high-intensity MLCT bands in the visible region are also observed for the other complexes (**2** to **4**) with  $d^7 - d^9$  transition metal [M(II)] ions. Presence of energy levels with small band gaps ( $\leq 0.5$  eV) in all these cases (Figure VI-31 and VI-32) accounts for such observations.

Reactivities of **4** towards  $\text{NaBH}_4$  and that of **4R** towards  $\text{K}_3[\text{Fe}(\text{CN})_6]$ , highlight the redox amphoteric behavior here.<sup>64-66</sup> The redox non-innocent pterin ligand plays a definite role in this process.

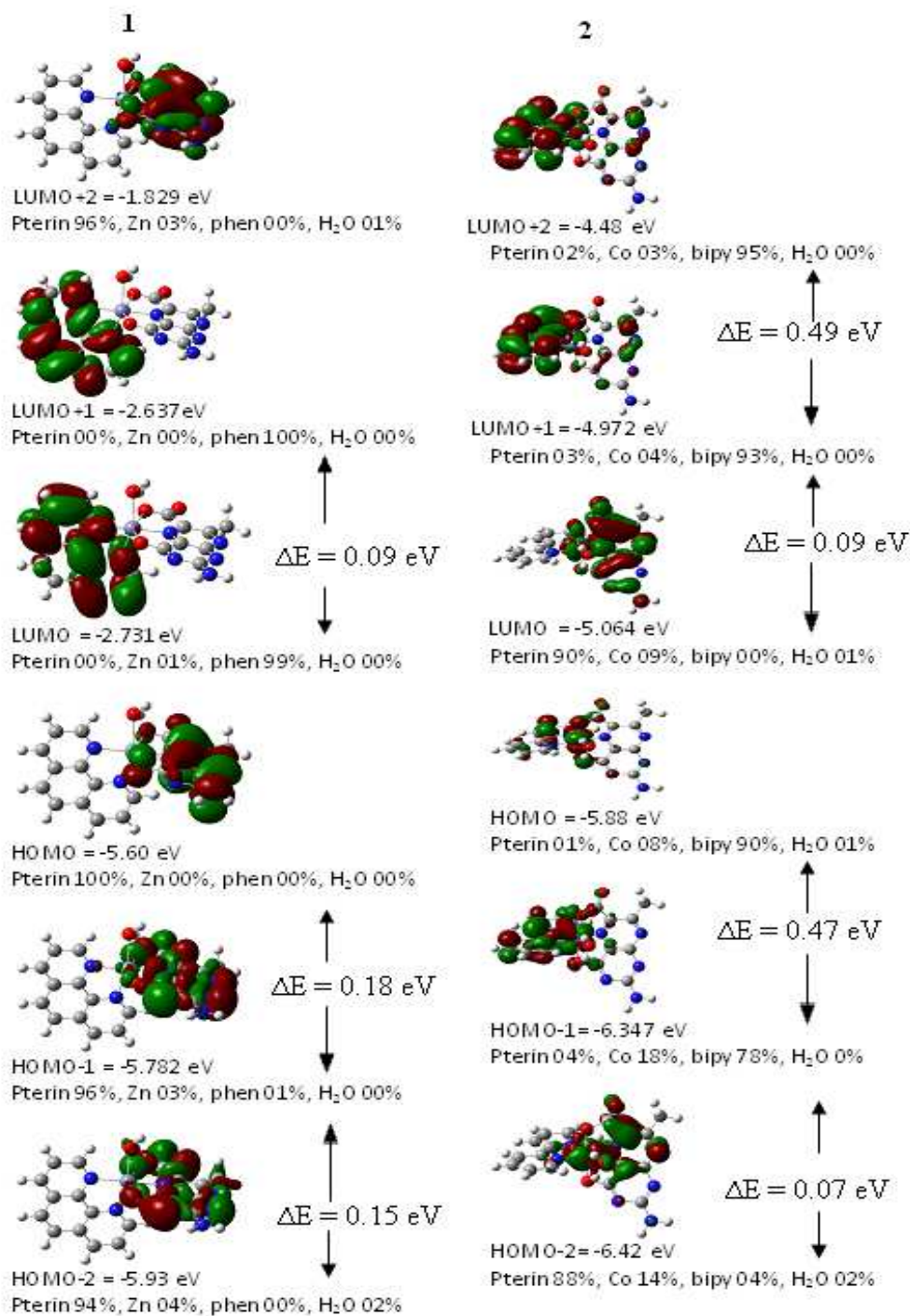


**Figure VI-31.** Frontier molecular orbitals of **1** and **2**, showing their energies (eV) and compositions (%); the  $|\Delta E|$  (eV) values ( $\leq 0.5$  eV) are also indicated.<sup>64-66</sup>

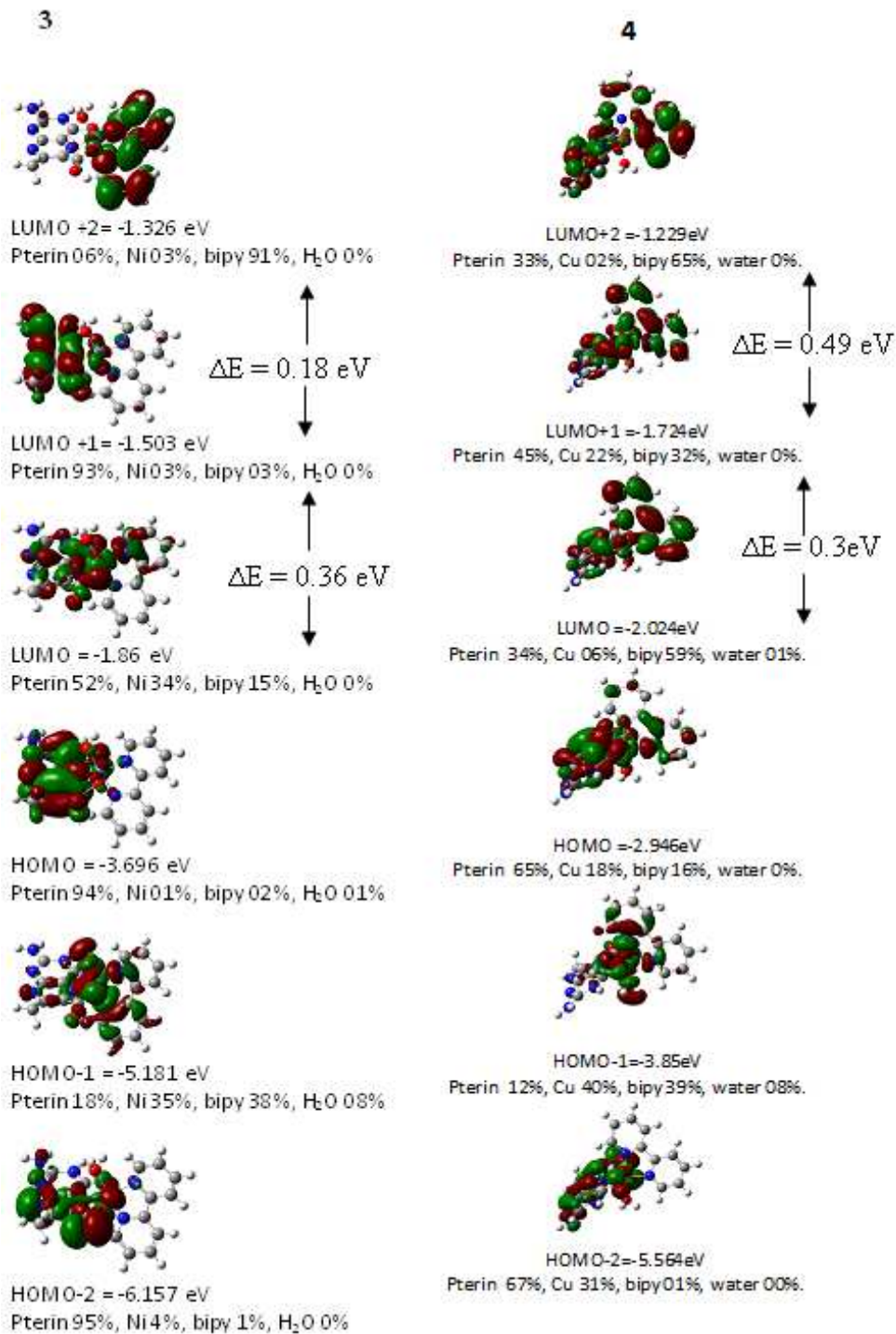


**Figure VI-32.** Frontier molecular orbitals of **3** and **4**, showing their energies (eV) and compositions (%); the  $|\Delta E|$  values ( $\leq 0.5 \text{ eV}$ ) are also indicated.<sup>64-66</sup>

## Conclusion

This chapter is concerned with four new mixed ligand complexes of the pterin ligand ( $H_2L$ , Scheme VI-1), along with phen and bipy (Scheme VI-2 and VI-3) acting as the ancillary ligands. The concerned metal ions [M(II) ions with  $d^7$  and  $d^{10}$  configurations] are all biologically relevant. The Zn(II) complex (**1**) has been characterized x-ray structurally. A vital outcome of this structural work is the multiple nature of the  $NH_2(2) - C(2)$  bond of the pterin moiety [in Figure VI-1, the  $N17 - C17$  bond possess a bond length of  $1.335(3)\text{\AA}$ ]. This observation is consistent with similar data of earlier chapters, centred on  $d^7$ - $d^9$  M(II) ions like Co(II), Ni(II) and Cu(II), with redox capability. From the above, it can be inferred that the redox non-innocent nature of the pterin ligand is responsible for such electronic redistribution associated with the multiple nature of the above bond. For all these complexes (**1** – **4**) satisfactory elemental analysis (carbon-hydrogen-nitrogen) data and ESIMS data have been obtained. They have been synthesized from aqueous alkaline medium; in view of the poor solubility of pterins, the synthetic protocols are reliable. Their UV-Vis spectral data are remarkable in the sense that in the visible region they show high intensity bands (with large  $\log \epsilon$  values). According to their electronic structures, such long wavelength bands can be assigned to MLCT transitions between energy levels with low energy band gaps. As par the compositions (%) of such energy level, **the charge migration** takes places across the entire molecule or **an internal redox process**. For complex **1**, such a MLCT process from pterin  $\rightarrow$  phen involves deshielding of the pterin protons and shielding of the phen protons. This is clearly reflected in the  $^1H$  NMR spectrum of this diamagnetic ( $d^{10}$ ) species. The EPR spectra of **2** and **4** are of the axial type and this inference is in line with the x-ray structural data of **1** showing an axially elongated octahedron. The DFT optimized molecular structures and associated electronic structures provide with a good frame

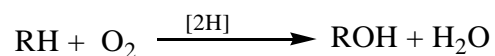
work for elucidation of physico-chemical properties, including redox reactivities. These compounds are all fluorescent, a property inherent in the pterin moiety.  $\text{NaBH}_4$  reduction enhances this attribute

## Concluding remarks

The importance of 6-substituted pterins, especially their reduced forms for the functioning of different classes of redox metalloenzymes, is well-known. Nature has achieved optimum synchronization among the changes in oxidation levels of the substrate, the concerned metal centre and the pterin/pyrazine ring in such cases. With this view in mind the coordination chemistry of a 6-substituted pterin ligand has been pursued here with the bivalent transition metal ions like Co(II), Ni(II), Cu(II) and Zn(II). Bench mark data (characterization, spectroscopic, physico-chemical and reactivity) have been recorded for the new coordination compounds. Although a significant portion of the data is concerned with compounds involving the oxidized (aromatic) form of the pterin ligand with a bivalent metal centre, attempts have been made to access the lower oxidation state of the metal ion in suitable cases [e.g., Co(I), Ni(I), Cu(I)] in presence of a partly reduced form (e.g., the 7, 8-dihydro state,  $L^{2-}$ ) of the ligand. The concerned Frost diagram (Scheme IV-11) predicts only a small thermodynamic barrier ( $\Delta G^\circ = -NFE^\circ$ ) for the transformation  $M(II) \rightarrow M(I)$  ( $M = \text{Co, Ni, Cu}$ ), with the associated kinetic step being achieved here without much difficulty. The pyrazine ring of the pterin ligand, is the locant of reducing equivalent storage/transfer; pure compounds containing both a M(I) metal centre and a reduced form (7, 8-dihydro pterin) of the ligand, could be obtained using  $\text{NaBH}_4$  reduction. Some of the labile intermediates in between the above two extremes (i.e., the fully oxidized and fully reduced forms of these complexes) could be visualized on the time scales of cyclic voltammetry and also from the reaction profiles followed using UV-VIS spectroscopy; the relative intensities of fluorescence spectral bands are a good measure of the electron densities (oxidation states) of the pterin rings in the new complexes. Interesting results have been obtained from the reactivity studies on the reduced forms of these compounds as well as their formation

from the corresponding oxidized forms. They throw light not only on the different facets of redox chemistry of pterin compounds but also helpful in understanding the reaction catalyzed by phenylalanine hydroxylase (PAH).

Scheme I-13 summarizes the PAH catalytic cycle where the tetrahydrobiopterin cofactor (BH<sub>4</sub>) plays a decisive role in transferring reducing equivalents to the phenylalanine/O<sub>2</sub> reaction system, itself being oxidized to BH<sub>2</sub> during this step; NADH restores the reduced state (BH<sub>4</sub>) once again. Two chemically significant steps associated with this process are: (i) the activation of the dioxygen (O<sub>2</sub>) molecule and (ii) the activation of the aromatic ring (of the substrate) towards hydroxylation.

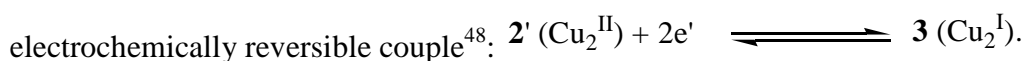


The present new compounds provide with a scope for understanding some of the above aspects.

Copper-pterin chemistry has been explored in chapter II which has several important features.

The fact that [Cu<sup>II</sup>(L)(phen)(H<sub>2</sub>O)]. 3H<sub>2</sub>O (**2**) could be synthesized by three different routes, is a sufficient indication of its chemical/ thermodynamic stability. Formation of **3** from **2** by NaBH<sub>4</sub> reduction as well as its characterized by different methods including 2D NMR (<sup>1</sup>H-<sup>1</sup>H COSY) is interesting; the latter step verifies **3** to be a Cu(I) complex with a reduced form [(L<sup>2-</sup>), 7, 8-dihydro pterin] of the pterin ligand (Scheme II-5 and II-6). From the kinetic data (Figure II-23) as well as thermodynamic considerations, it is evident that the formation of **3** is a two-step process (Scheme II-6); but **3** is able to transfer its reducing equivalents to the bromobenzene/O<sub>2</sub> reaction mixture in a single step (Figure II-25; Scheme II-7 and II-8).

For the quasi-reversible cyclic voltammetric data of **3** [Figure II-20(b)], the cathodic (E<sub>pc</sub>) and anodic (E<sub>pa</sub>) responses can be interpreted in terms of the forms **3** and **2'** as shown in Scheme II-6; the  $i_{pc}/i_{pa}$  ratio (0.97; Table II-6) indicates sufficient kinetic stability for the intermediate binuclear species **2'** on the cyclic voltammetric time scale as well as the existence of the



The above cathodic and anodic steps can be correlated with the chemical redox processes as shown in Figure II-23(b) (NaBH<sub>4</sub> reduction) and Figure II-25 (oxidation by O<sub>2</sub>/bromobenzene reaction mixture) respectively. Presence of isosbestic points is a common feature of these two chemical steps, indicating single-step conversions.

Figure II-27 summarizes the above aspects and at the same time throws light on the mechanism of hydroxylation of bromobenzene by **3** in presence of O<sub>2</sub>. Possibly, the formation of a **3**(O<sub>2</sub>) complex initiates the process, followed by concerted electron transfer **3**→O<sub>2</sub> and reducing equivalent transfer from the 7, 8-dihydro form of the pterin ligand (L') to the reaction system; sufficient stability of **2** ensures completion of the last step. The exceptionally small band gaps (0.5 eV) for some of the frontier orbitals of **2** and **3**, play a vital role in controlling such electron/reducing equivalent transfers. As the direct transfer of reducing equivalents from NaBH<sub>4</sub> to the bromobenzene/O<sub>2</sub> reaction mixture is not possible, the **2/3** combination may be regarded as a model mediator for this purpose.

Chapter III is concerned with cobalt-pterin chemistry where the mixed ligand compound [Co<sup>II</sup>(L)(phen)(H<sub>2</sub>O)]. 3H<sub>2</sub>O (**2**) plays a vital role in elucidating redox properties. On reduction with NaBH<sub>4</sub> in CH<sub>3</sub>OH it affords Na[Co<sup>I</sup>(L')(phen)(H<sub>2</sub>O)]. 2H<sub>2</sub>O.CH<sub>3</sub>OH (**3**), where (L')<sup>2-</sup> = 7, 8-dihydro form of the pterin ligand (L)<sup>2-</sup>. Magnetic susceptibility and other physico-chemical data indicate **2** and **3** to be high-spin Co(II) and Co(I) complexes, respectively. Frost diagram

(Scheme IV-11) predicts a facile  $\text{Co(II)} \rightarrow \text{Co(I)}$  conversion which could be visualized in cyclic voltammetry as an irreversible reduction peak at  $-0.6\text{V}$ . Such reduction process is accompanied by a considerable increase in fluorescence emission intensity. The corresponding chemical reduction process by  $\text{NaBH}_4$  can be followed UV-VIS spectroscopically (Figure III-13) where the presence of isosbestic points indicates the conversion  $\mathbf{2} \rightarrow \mathbf{3}$  to be a one-step process. Such data are consistent with the chemical composition of  $\mathbf{3}$ , indicating a mononuclear species with  $\text{Co(I)}$  centre and a reduced form ( $\text{L}'$ ) of the pterin ligand. On the other hand, the reaction profile (Figure III- 14) representing the transfer of reducing equivalents from  $\mathbf{3}$  towards the  $\text{O}_2/\text{bromobenzene}$  reaction mixture, is devoid of any isosbestic point. It provides with a much-needed information about the mechanism of hydroxylation of bromobenzene here. Formation of a dioxygen complex  $\mathbf{3}(\text{O}_2)$  most likely initiates this reaction which is followed by sequential transfer of electron ( $\text{Co}^{\text{I}} \rightarrow \text{Co}^{\text{II}} + \text{e}'$ ) to  $\text{O}_2$  and reducing equivalents from the 7, 8-dihydro pterin ligand moiety ( $\text{L}'$ ) to the reaction system, achieving bromobenzene  $\rightarrow$  4-bromophenol conversion. The remarkably small band gaps ( $<0.5\text{eV}$ ) for the frontier orbitals of  $\mathbf{2}$  and also for a few of  $\mathbf{3}$  (Figure III-17) are helpful in controlling such facile electron/reducing equivalent transfers towards  $\mathbf{2}$  or out of  $\mathbf{3}$  respectively.

Chapter IV focuses its attention on the two new mixed ligand  $\text{Ni(II)}$  complexes, e.g.,  $[\text{Ni}^{\text{II}}(\text{L})(\text{en})(\text{H}_2\text{O})] \cdot 2\text{H}_2\text{O}$  ( $\mathbf{1}$ ) and  $[\text{Ni}^{\text{II}}(\text{L})(\text{en})(\text{Im})] \cdot 2\text{H}_2\text{O}$  ( $\mathbf{2}$ ), for pursuing nickel-pterin chemistry. In terms of chemical compositions and molecular structures, only an imidazole ligand distinguishes  $\mathbf{2}$  from  $\mathbf{1}$ ; but it has a profound effect on the redox reactivity profiles. Here the 'en' chelate ring possesses a  $\delta$ -conformation and the extent of such puckering may be assessed from the CD spectral data of  $\mathbf{1}$  and  $\mathbf{2}$ .

Only a small thermodynamic barrier (Frost diagram, Scheme IV-11) is associated with the conversion Ni(II)  $\rightarrow$  Ni(I) and NaBH<sub>4</sub> reduction in CH<sub>3</sub>OH helps to achieve it, providing **1R** and **2R** from **1** and **2** respectively, accompanied by a significant fluorescent emission intensity increase. Both **1R** and **2R** have been characterized as mononuclear mixed ligand Ni(I) complexes of 7, 8-dihydro form of the pterin ligand (L'), with 'en' as the ancillary ligand. The quasi-reversible ( $\Delta E_p = 75 - 188$  mV) cyclic voltammetric responses of both **1** and **2**, are helpful in visualizing the Ni(II)/Ni(I) states here.

A comparison of reaction profiles (Figure IV-30 and IV-31) for the interaction of K<sub>3</sub>[Fe(CN)<sub>6</sub>] with NaBH<sub>4</sub> and **2R** respectively, is quite interesting. While K<sub>3</sub>[Fe(CN)<sub>6</sub>] is essentially unable to accept reducing equivalents from NaBH<sub>4</sub> directly, the reverse is true for **2R**; presence of isosbestic point for the latter process indicates a single-step conversion. In other words, the **2/2R** combination serves here as an excellent mediator (Scheme IV-14) of reducing equivalents between NaBH<sub>4</sub> and K<sub>3</sub>[Fe(CN)<sub>6</sub>].<sup>94</sup> The same property is manifested during the reactions of **1** and **2** with NaBH<sub>4</sub> and those of **1R** and **2R** with the bromobenzene/O<sub>2</sub> reaction mixture. The reaction profiles (Figure IV-24 and IV-27) representing the reduction **1**  $\rightarrow$  **1R** and the transfer of reducing equivalents from **1R** to the bromobenzene/O<sub>2</sub> mixture, are devoid of any isosbestic points, hinting at multistep processes. But those for **2** and **2R** (Figure IV-28 and IV-29) possess such an attribute, indicating single-step conversions, commensurate with the chemical composition of **2R** (i.e., a mononuclear species). Such flexible redox behavior of **1** and **2** can be traced to the small band gaps (<0.5 eV) for some of their frontier orbitals (Figure IV-32).<sup>64-66</sup>

The most-interesting aspect of this study is that the control of reducing equivalent mediator property of a nickel-pterin centre by a donor atom from an ancillary ligand; viewed in

the context of a metalloprotein or metalloenzyme, such control of function of a metal-centred cofactor, is achieved by donor atoms from the anchoring protein chain.

Chapter V delves deeper into nickel-pterin chemistry using two new chiral Ni(II) complexes (**2** and **3**) with the identical chemical composition  $[\text{Ni}^{\text{II}}(\text{L})(\text{pn})(\text{H}_2\text{O})] \cdot 5\text{H}_2\text{O}$ ; here 'pn' stands for the two chiral ancillary ligands R-(+)-1,2-diaminopropane [R-(+)-pn] and S-(-)-1,2-diaminopropane [S-(-)-pn] respectively. X-ray structural data establish  $\delta$ -conformation for the 'pn' chelate ring in each case, but for **3** the extent of such distortion is more significant, approaching near planarity. Such conformational difference between **2** and **3** induced by the R-(+)-pn and S-(-)-pn chelate rings, affect their reactivities considerably; even their crystal packing diagrams/H-bonding networks are different (Figure V-3 and V-5). The effect of H-bonding on the redox properties of biomolecules is well-known<sup>162</sup>.

The Ni(I) state of both **2** and **3** could be accessed in terms of their quasi-reversible cyclic voltammetric responses ( $\Delta E_p = 138 - 153 \text{ mV}$ ) (Figure V-17 and V-18).  $\text{NaBH}_4$  reduction in  $\text{CH}_3\text{OH}$  affords the reduced forms of **2** and **3**, i.e., **2R** and **3R** respectively; analytical data indicate them to be mononuclear Ni(I) complexes with the 7, 8-dihydro form of the pterin ligand ( $\text{L}'$ ). The reaction profiles representing the interactions of  $\text{NaBH}_4$  with **2** and **3** (Figure V-21 and V-22) highlight the conformational control of redox reactions in terms of the absence or presence of isosbestic points, affecting both the metal and pterin ligand centres. The products of such reactions, i.e., **2R** and **3R** transfer their reducing equivalents to a typical electron acceptor like  $\text{K}_3[\text{Fe}(\text{CN})_6]$  through pathways having subtle differences (Figure V-23 and V-24). Difference in kinetic parameters (Table V-6) are also observed for the transfer of reducing equivalents from **2R** and **3R** to the bromobenzene/ $\text{O}_2$  reaction mixture.

The 'pn' chelate ring conformational differences affect the electronic structures of **2** and **3** as well. For example, a small band gap ( $< 0.5$  eV) exists between the HOMO and (HOMO-1) levels of **2**; on the other hand such a small band gap is observed for **3** between the (LUMO+1) and LUMO levels (Figure V-26). In other words, the conformational and electronic structural differences act synergistically, for achieving such reactivity differences between **2** and **3**.

The implicit bioinorganic significance (vis-à-vis the metalloenzymes) of the above conformational control of redox properties (or reducing equivalent transfer properties) of nickel-pterin centres by the ancillary ligand chelate rings, may be understood<sup>100</sup>.

Finally, chapter VI focuses its attention on four mononuclear mixed ligand complexes (**1** – **4**) of bivalent transition metal ions [Co(II), Ni(II), Cu(II) and Zn(II)], with 2,2'-bipyridyl acting as the ancillary ligand in three cases. The x-ray structural, spectroscopic and electrochemical data of the complex compound with redox silent Zn(II) centre (**1**), play a crucial role here in substantiating some of the interpretations presented in earlier chapters. For example, the multiple nature of the NH<sub>2</sub>(2) – C(2) and C(4) – O(4) bonds [C13 – N17, 1.335(3)Å and C15 – O16, 1.257(3)Å in Figure VI-1] verifies that the electron-shuffling of the pterin ring (L<sup>2-</sup>) is essentially responsible for such observations, with little participation from the metal centre.

This Zn(II) complex (**1**) possesses an intense ( $\log \epsilon = 4.086$ ) electronic spectral band at 733 nm (Figure VI-14) which can only be ascribed to a MLCT band Zn(II)(d<sup>10</sup>) e<sub>g</sub>\*  $\rightarrow$   $\pi^*$ (phen). Such long wavelength intense bands are common features of the Co(II), Ni(II), Cu(II) complexes discussed earlier and they could be interpreted using suitable MO diagrams. The frontier orbitals (Figure VI-31 and VI-32) of **1** – **4** are characterized by at least a couple of band gaps which are remarkably small ( $< 0.5$  eV), conferring unique redox properties on them.<sup>64-66</sup> For **1** the HOMO  $\rightarrow$  LUMO transition is essentially a pterin  $\rightarrow$  phen electron transfer through the Zn(II)(d<sup>10</sup>) centre

(Figure VI-31) or an internal redox process covering the entire molecule. This is consistent with the  $\pi$ -acidic nature of the 'phen' ligand; it is further verified by the  $^1\text{H}$  NMR spectrum (Figure VI-23 and Scheme VI-8) of **1** where the 'phen' protons undergo shielding through coordination with the Zn(II) centre. The cyclic voltammograph of **1** (Figure VI-26) lacks any cathodic reduction peak (Epc) over the range -0.6V to -0.8V; this observation may be linked to the redox silent nature of the concerned metal centre [Zn(II)]. The fluorescence and EPR spectral data as well as the reactivity studies presented here, augment the inferences of earlier chapters.

Active site of the heme proteins/enzymes like Hb/Mb, cytP-450 and cyt c describe almost graphically how the same cofactor (iron-porphyrin) can be modulated for different purposes (ranging from oxygen carrier to electron carrier as well as monooxygenase activity) through selective coordination by donor atoms from the anchoring protein chain.

Such level of understanding about the structural control of function is yet to be achieved for the pterin-containing metalloenzymes.

Synthetic, physico-chemical and reactivity studies on new model coordination compounds, provide with suitable pathways for achieving such research goals. The present work is a sincere attempt in that direction.

## References

- (1) Hille, R. *Chem. Rev.* **1996**, *96*, 2757 – 2816.
- (2) Johnson, M. K.; Rees, D. C.; Adams, M. W. W. *Chem. Rev.* **1996**, *96* 2817 – 2840.
- (3) Enemark, J. H. ; Cooney, J. J. A. ; Wang, J. J. ; Holm, R. H. *Chem. Rev.* **2004**, *104*, 1175 – 1200.

- (4) Moura, J. J. G.; Bernhardt, P.V.; Maia, L. B.; Gonzalez, P. J. *J. Biol. Inorg. Chem.* **2015**, *20*, 181 – 182.
- (5) Holm, R.H.; Solomon, E. I.; Majumdar, A. Tenderholt, A. *Coord. Chem. Rev.* **2011**, *255*, 993 – 1015.
- (6) Majumdar A. ; Sarkar, S. *Coord. Chem. Rev.* **2011**, *255*, 1039 – 1054.
- (7) (a)Kappock, T. J.; Caradonna, J. P. *Chem. Rev.* **1996**, *96*, 2659 – 2756. (b)Fitzpatrick, P. *F. Biochemistry*, **2003**, *42*, 14083 -14091.
- (8) (a)Aoyagi, M.; Arvai, A. S.; Ghosh, S.; Stuehr, D. J.; Tainer J. A.; Getzoff, E. D. *Biochemistry*, **2001**, *40*, 12826-12832. (b)Wei, C-C.; Crane, B.R.; Stuehr, D. J. *Chem. Rev.* **2003**, *103*, 2365-2383.
- (9) Kaim, W. *Rev. Chem. Intermediates*, **1987**, *8*, 247-286.
- (10) Burgmayer, S. J. N. *Struct. Bond.* **1998**, *92*, 67-119.
- (11) Miyazaki, S.; Kojima, T.; Sakamoto, T.; Matsumoto, T.; Ohkubo, K.; Fukuzumi, S. *Inorg. Chem.* **2008**, *47*, 333-343.
- (12) (a)Jimenez-Pulido, S. B.; Linares-Ordonez, F. M.; Moreno-Carretero, M. N.; Quiros-Olozabal, M. *Inorg. Chem.* **2008**, *47*, 1096-1106. (b)Jimenez- Pulido, S. B.; Illan-Cabeza, N. A.; Hueso-Urena, F.; Moreno- Carretero, M. N. *Polyhedron*, **2013**, *50*, 10-15.
- (13) (a)Jana,R.; Lissner, F.; Kaim, W. *Z. Anorg. Allg. Chem.* **2015**, *641*, 261-265. (b)Kaim, W.; Schwederski, B. *Coord. Chem. Rev.* **2010**, *254*, 1580-1588. (c)Kaim, W.; Schwederski, B.; Heilmann, O.; Hornung, F. M. *Coord. Chem. Rev.* **1999**, *182*, 323-342.
- (14) Lee, D-H.; Murthy, N. N.; Lin, Y.; Nasir, N. S.; Karlin, K. D. *Inorg. Chem.* **1997**, *36*, 6328-6334.

- (15) Funahashi, Y.; Hara, Y.; Masuda, H.; Yamauchi, O. *Inorg. Chem.* **1997**, *36*, 3869-3875.
- (16) **Note:** References (10) to (15) present a good overview of the available literature on the coordination chemistry of the pteridine/pterin ligands.
- (17) (a)Baisya, S. S.; Ghosh, B.; Roy, P. S. *Acta Cryst.* **2015**, *E71*, m162-m163. (b)Baisya, S. S.; Roy, P. S. *Acta Cryst.* **2014**, *E70*, 348-351. (c)Baisya, S. S.; Roy, P. S. *Acta Cryst.* **2013**, *E69*, m193-m194. (d)Baisya, S. S.; Roy, P. S. *Acta Cryst.* **2013**, *E69*, m99-m100. (e)Baisya S. S.; Sen, S.; Roy, P. S. *Acta Cryst.* **2013**, *E69*, m70-m71. (f)Ghosh, B.; Roy, P. S. *Indian J Chem*, **2007**, *46A*, 1585-1593. (g)Sen, S.; Ghosh, B.; Roy, P. S. *Transition Met. Chem.* **2007**, *32*, 737-745. (h)Sen, S.; Roy, P. S. *Transition Met. Chem.* **2005**, *30*, 797-803. (i) Ali, M. A.; Roy, P. S. *Transition Met. Chem.* **2002**, *27*, 366-371. (j)Ali, M. A.; Roy, P. S. *Proc. Indian Acad. Sci. (Chem. Sci.)*. **2001**, *113*, 77 -87.
- (18) (a)Kohzuma, T.; Odani, A.; Morita, Y.; Takani, M.; Yamauchi, O. *Inorg. Chem.* **1988**, *27*, 3854-3858. (b)Kohzuma, T.; Masuda, H.; Yamauchi, O. *J. Am. Chem. Soc.* **1989**, *111*, 3431-3433. (c)Odani, A.; Masuda, H.; Inukai, K.; Yamauchi, O. *J. Am. Chem. Soc.* **1992**, *114*, 6294-6300.
- (19) Wittle, E. L.; O'Dell, B. L.; Vandenberg, J. M. ; Pfiffner, J. J. *J. Am. Chem. Soc.*, **1947**, *69*, 1786-1792.
- (20) Perrin, D.D.; Armarego, W.L.F. *Purification of Laboratory Chemicals*, Pergamon Press, Oxford, 3<sup>rd</sup> ed., **1988**, pp 105.
- (21) Silverstein, R. M.; Webster, F. X. *Spectrometric Identification of Organic Compounds*, John Wiley & Sons, Inc., New York, 6<sup>th</sup> ed, **1998**, Chapters 2-4 and 5.
- (22) Beddoes, R. L.; Russell, J. R.; Garner, C. D. ; Joule, J. A. *Acta Cryst.* **1993**, *C49*, 1649-1652.

- (23) Russell, J. R.; Garner, C. D. ; Joule, J. A. *J. Chem. Soc. Perkin Trans.1* **1992**, 1245-1249.
- (24) Yan, J. *Isotope Pattern Calculator*, **2001**, V4.0.
- (25) Burgmayer, S. J. N.; Stiefel, E.I. *Inorg. Chem.*, **1988**, 27, 4059-4065.
- (26) Perkinson, J.; Brodie, S.; Yoon, K.; Mosny, K. ; Carroll, P. J.; Morgan, T. V. ;  
Burgmayr, S. J. N. *Inorg. Chem*, **1991**, 30, 719-727.
- (27) Burgmayer, S. J. N.; Arkin, M. R.; Bostick, L.; Dempster, S.; Everett, K. M.; Layton, H.L.; Paul, K. E.; Rogge, C.; Rheingold, A. L. *J. Am. Chem. Soc.*, **1995**, 117, 5812-5823.
- (28) Fischer, B.; Schmale, H.; Dubler, E.; Schäfer, A.; Viscontini, M. *Inorg. Chem.*, **1995**, 34, 5726-5734.
- (29) Prasad, M.V.S.; Udaya Sri, N. ; Veeraiah, A.; Veeraiah ,V. ; Chaitanya, K. J. *At. Mol. Sci.*, **2013**, 4, 1-17.
- (30) Breda, S.; Reva, I. D.; Lapinski, L.; Nowak, M. J.; Fausto, R. *J. Mol. Struc.* **2006**, 786, 193-206.
- (31) Day , M. C. ; Selbin, J. *Theoretical Inorganic Chemistry*, Affiliated East-West Press Pvt. Ltd., New Delhi **1971**, pp495-502.
- (32) Huheey, J. E.; Keiter, E. A. ; Keiter, R. L. *Inorganic Chemistry*, Addison-Wesley Publishing Co., New York, 4<sup>th</sup> ed, **1993**, pp 455 – 459.
- (33) Pitterle, D.M.; Johnson, J.L.; Rajagopalon, K.V. *J. Biol. Chem.*, **1993**, 268,13506-13509.
- (34) Burgmayer, S.J.N. ; Stiefel, E.I. *J. Chem. Educ.* **1985**, 62, 943-953.
- (35) Mengel, R.; Pfeleiderer, W. ; Knappe , W.R. *Tetrahedron letters*, **1977**, 18, 2817-2820.

- (36) Rohatgi-Mukherjee, K.K. *Fundamentals of Photochemistry*, New Age International (P)Ltd., Publishers, New Delhi, **1986**, pp 99 -103, pp 137-144.
- (37) Palmer, G. *Methods for Determining Metal Ion Environments in Proteins: Structure and Function of Metalloproteins*, Ed. Darnall ,D.W. ; Wilkins, R.G. Elsevier, New York **1980**, Vol. 2, Chapter 6.
- (38) Dutta, R.L. Syamal, A. *Elements of Magnetochemistry*, Affiliated East-West Press Pvt.Ltd., New Delhi, 2<sup>nd</sup> ed., **1993**, Chapter 12.
- (39) Miller, J. D. ; Prince, R. H. *J. Chem. Soc.*, **1965**, 4706-4709.
- (40) Dyer, J. R. *Applications of Absorption Spectroscopy of Organic Compounds*, Prentice – Hall of India Pvt. Ltd. New Delhi, **1989**, pp 97-113.
- (41) Patterson, B. T. ; Keene, F. R. *Inorg. Chem.*, **1998**, 37, 645 – 650.
- (42) Panchanan, S.; Hämäläinen, R.; Roy, P. S. *J. Chem. Soc. Dalton Trans.* **1994**, 2381-2390.
- (43) Naganagowda, G. A.; Ramanathan, K. V.; Gayathri, V. ; Gowda, N. M. N. *Magn. Reson. Chem.* **2000**, 38, 223 – 228.
- (44) Gorren, A.C.F.; Kungl, A.J.; Schmidt, K.; Werner, E.R.; Mayer, B. *Nitric Oxide : Biology and Chemistry*, **2001**, 5, 176-186.
- (45) Patterson, G.S.; Holm, R.H. *Bioinorganic Chemistry*, **1975**, 4, 257-275.
- (46) James, B.R. ; Williams, R.J.P. *J. Chem. Soc.*, **1961**, 2007-2019.
- (47) Hawkins, C.J.; Perrin, D.D. *J.Chem. Soc.*, **1963**, 2996 – 3002.
- (48) Fenton, D.E. ; Lintvedt, R.L. *J. Am. Chem. Soc.*, **1978**, 100, 6367-6375.
- (49) Craig, J.A. ; Holm, R.H. *J. Am. Chem. Soc.*, **1989**, 111, 2111-2115.
- (50) Schultz, B.E. ; Holm, R.H. *Inorg. Chem.*, **1993**, 32, 4244-4248.

- (51) Flydal, M.I. ; Martinez, A. *IUBMB Life*, **2013**, *65*, 314-349.
- (52) Fitzpatrick, P.F. *Biochemistry*, **2003**, *42*, 14083 – 14091.
- (53) Erlandsen, H.; Bjørge, E.; Flatmark, T.; Stevens, R.C. *Biochemistry*, **2000**, *39*, 2208-2217.
- (54) Carr, R.T.; Benkovic, S.J. *Biochemistry* **1993**, *32*, 14132 – 14138.
- (55) Dix, T.A. ; Benkovic, S.J. *Acc. Chem. Res.* **1988**, *21*, 101-107.
- (56) Gomez-Lahoz, C.; Garcia-Herruzo, F.; Rodriguez-Maroto, J.M. ; Rodriguez, J.J. *Water Research*, **1993**, *27*, 985-992.
- (57) Chatenet, M.; Micoud, F.; Roche, I. ; Chainet, E. *Electrochimica Acta.* **2006**, *51*, 5459-5467.
- (58) Schaeffer, G.W.; Waller, M.C. ; Hohn-Stedt, L.F. *Anal. Chem.* **1961**, *33*, 1719-1722.
- (59) Segel, I.H. *Biochemical Calculations*, John Wiley & Sons, New York, 2<sup>nd</sup> ed., **1976**, pp172-179,
- (60) Chen, D. ; Frey, P.A. *J. Biol. Chem.*, **1998**, *273*, 25594-25601.
- (61) Hagedoorn, P-L.; Schmidt, P.P.; Andersson, K.K.; Hagen, W.R.; Flatmark, T. ; Martinez, A. *J. Biol. Chem.*, **2001**, *276*, 22850-22856.
- (62) Jocelyn, P.C. *European J. Biochem.*, **1967**, *2*, 327-331.
- (63) Shriver, D.F. ; Atkins, P.W. *Inorganic Chemistry*, Oxford University Press, Oxford, 3<sup>rd</sup> ed., **1999**, pp 193-203.
- (64) Perepichka, D. F. ; Bryce, M. R. *Angew. Chem. Int. Ed.* **2005**, *44*, 5370-5373.
- (65) Perepichka, D.F. ; Bryce, M.R. ; Pearson, C. ; Petty, M.C.; McInnes, E.J.L. ; Zhao, J.P. *Angew. Chem.* **2003**, *115*,4784-4787.
- (66) Bendikov, M.; Wudl, F. ; Perepichka, D.F. *Chem. Rev.*, **2004**, *104*, 4891-4945.

- (67) Holm, R.H.; Kennepohl, P.; Solomon, E.I. *Chem. Rev.* **1996**, *96*, 2239-2314.
- (68) Karlin, K.D. ; Gultneh, Y. J. *Chem. Educ.*, **1985**, *62*, 983-990.
- (69) Solomon, E.I.; Chen. P.; Metz, M.; Lee, S-K. ; Palmer, A.E. *Angew. Chem. Int. Ed.* **2001**, *40*, 4570-4590.
- (70) Decker, H.; Schweikardt, T.; Nillius, D.; Salzbrunn, U.; Jaenicke, E. ;Tuczek, F. *Gene*, **2007**,*398*, 183-191.
- (71) Sendovski, M.; Kanteev, M.; Ben-Yosef, V.S.; Adir, N. ; Fishman, A. *J. Mol. Biol.* **2011**, *405*, 227-237.
- (72) Sawyer D. T.; Roberts J. L. *Experimental Electrochemistry for Chemists*, John Wiley & Sons, New York, **1974**, pp 212.
- (73) (a) Schireks B.; Bieri J. H. and Viscontini M. *Helv. Chim. Acta.* **1985**, *68*, 1639. (b) Russell J. R.; Garner C. D. and Joule J. A. *Synlett.* **1992**, 711.
- (74) (a) Pfeleiderer W., *J. Heterocyc. Chem.*, **1992**, *29*, 583. (b) Collison D.; Garner C. D. and Joule J. A. *Chem. Soc. Rev.*, **1996**, *25*, 25.
- (75) Pfeleiderer W., *Comprehensive Heterocyclic Chemistry*, ed. A. R. Katritzky and C. W. Rees, **1984**, Vol. 3, Paragon Press, Oxford, pp, 263-327.
- (76) Acuña-Cueva, E. R. ; Faure, R. ; Illan-Cabeza, N. A.; Jimenez-Pulido, S. B.; Moreno-Carretero, M. N. And Quiros-Olozabal, M. *Inorg. Chim. Acta*, **2003**, *342*, 209-218.
- (77) (a) Cotton, R. and Traeger, J. C. *Inorg. Chim. Acta*, **1992**, *201*, 153.(b) Curtis, J. M.; Derrick, P.J.; Schnell, A.; Constantin, E.; Gallagher, R. T. and Chapmen, J. R. *Inorg. Chim. Acta.* **1992**,*201*, 197. (c) Falaras, P. ; Mitsopoulan, C. A.; Argyropoulos, D.; Lyris, E. Psaroudakis, N.; Vrachnon, E. and Kotakis, D. *Inorg. Chem.*,**1995**, *34*,4536. (d) Basu, P.; Nemykin, V. N. and Sengar, R. S. *Inorg. Chem.*,**2003**, *42*, 7489. (e) Dessapt, R. ;

- Jegal, C. S.; Mallard, A.; Lavanant, H.; Marret, J. and Secheresse, F. *Inorg. Chem.* **2003**, *42*, 6425.
- (78) Ebsworth, E.A.V.; Rankin, D.W.H. and Craddock, S. *Structural Methods in Inorganic Chemistry*, **1987**, ch. 9. (ELBS/Black Well Scientific Publications, UK).
- (79) Cotton, F. A. ; Wilkinson, G. *Advance Inorganic Chemistry*, **1988**, John Wiley & Sons Inc., New York, 5<sup>th</sup> ed., pp – 725, 729-730, 1308.
- (80) Atkins, P. ; Overton, T. ; Rourke, J. ; Weller, M.; Armstrong, F. *Shriver & Atkins Inorganic Chemistry*, **2010**, Oxford University Press, UK, 5<sup>th</sup> ed., pp – 164, 454.
- (81) (a) Bieri, J. H. ; Viscontini, M., *Helv. Chim. Acta.*, **1977**, *60*, 1926. (b) Wei, C. C. ; Crave, B. R. ; Stvehr, D. J., *Chem. Rev.*, **2003**, *103*, 2365.
- (82) (a) Bendikov, M. and Wudl, F., *Chem. Rev.* **2004**, *104*, 4891-4945. (b) Peripichka, D. F. and Bryee M. R., *Angew. Chem. Int. Ed.*, **2005**, *44*, 5370-5373. (c) Peripichka D. F. ; Bryee, M. R. ; Pearson, C. ; Petty, M. C. ; McInnes, E. J. L. and Zhao, J. P. *Angew. Chem.*, **2003**, *115*, 4784-4787.
- (83) Crispini, A.; Pucci, D. ; Bellusci, A. ; Barberio, G. ; Deda, M. L. ; Cataldi, A.; Ghedini, M., *Cryst. Growth. Des.* **2005**, *5*, 1597-1601.
- (84) Odani, A. ; Masuda, H. Inukai, K. and Yamauchi, O. *J. Am. Chem. Soc.* **1992**, *114*, 6294-6300.
- (85) Craig J. A. ; Harlan E. W. ; Snyder, B. S. ; Whitener, M. A. and Holm, R.H. *Inorg. Chem.* **1989**, *28*, 2082.
- (86) Nemykin, V. N. ; Davie, S. R. ; Mondal, S.; Rubie, N.; Kirk, M. L. ; Somogyi, A. and Basu, P. *J. Am. Chem. Soc.*, **2002**, *124*, 756.

- (87) (a) Casellato, U. ; Vigato, P. A. and Vidali, M. *Coord. Chem. Rev.*, **1978**, 26, 85. (b) Deacan, G. B. and Phillips, R. J., *Coord. Chem.Rev.*, **1980**, 33, 227.
- (88) Nakamoto, K., *Infrared Spectra of Inorganic Coordination Compounds*, Wiley Interscience, New York, 2<sup>nd</sup> ed. **1970**.
- (89) Drago, R. S., *Physical Methods in Inorganic Chemistry*, Affiliated East-West Press Pvt., New Delhi, **1971**, pp 162 – 181.
- (90) Cotton, F. A. and Wilkinson, G., *Advance Inorganic Chemistry*, 3<sup>rd</sup> ed. **1972**, Wiley Eastern Ltd., New Delhi, 1978, pp 571 – 581, 893 – 894.
- (91) Atkins, P. ; Overton, T. ; Rourke, J. ; Weller, M.; Armstrong, F., *Shriver & Atkins Inorganic Chemistry*, **2010**, Oxford University Press, New Delhi., 5<sup>th</sup> ed., pp – 454.
- (92) (a) Craig, J. A. and Holm, R. H., *J. Am. Chem. Soc.* , **1989**, *111*, 2111. (b) Schultz, B. E. and Holm, R. H.; *Inorg. Chem.* **1993**, *32*, 4244. (c) Berg, J. M. and Holm, R. H., *J. Am. Chem. Soc.*, **1985**, *107*, 915, 925. (d) Caredona, J. P. ; Reddy, P. R. and Holm R. H., *J. Am. Chem. Soc.*, **1988**, *110*, 2139.
- (93) (a) Ochiai, E. I., *Bioinorganic Chemistry. Boston: Allyn and Bacon.*, **1977**, p 27 (b) Das, S, K. ; Chaudhury, P. K. ; Biswas, D. and Sarkar, S., *J. Am. Chem. Soc.* **1994**, *116*, 9061.
- (94) Lehninger, A. L., *Biochemistry*, Kalyani publishers, New Delhi, 2<sup>nd</sup> ed. **1984**, pp 482-487.
- (95) Gaussian 09, Gaussian, Inc. : Wallingford, CT, 2004.
- (96) (a) Becke, A. D. *Phy. Rev. A.* , **1988**, *38*, 3098-3100. (b) Lee, C. ; Yang, W. ; Parr, R. G. *Phy. Rev. B.*, **1988**, *37*, 785-789.

- (97) Basolo, F. and Pearson, R. G., *Mechanism of Inorganic Reactions*, Wiley Eastern Pvt. New Delhi, 2<sup>nd</sup> ed, **1967**, pp 145 – 158, 310-313.
- (98) Wilkins, R. G. *Kinetics and Mechanism of Reaction of Transition Metal Complexes*, VCH Publishers, Inc. New York, 2<sup>nd</sup> ed., **1991**, pp 408-410.
- (99) Williams, B.R.; Fu, Y.; Yap G.P.A. and Burgmayer S.J.N., *J.Am.Chem.Soc.*, **2012**, *134*, 19584-19587.
- (100) Rothery, R.A.; Stein, B.; Solomonson, M.; Kirk M.L. and Weiner J.H., *PNAS*, **2012**, *109*, 14773-14778.
- (101) Basu, P. and Burgmayer, S.J.N. *Coord.Chem.Rev.*, **2011**, *255*, 1016-1038.
- (102) Swedo, K.B. and Enemark, J.H. *J.Chem.Educ.*, **1979**, *56*, 70-76.
- (103) Stiefel, E.I., *Science*, **1996**, *272*, 1599-1600.
- (104) Stiefel, E.I. *J.Chem.Soc., Dalton Trans.*, **1997**, 3915-3923..
- (105) Kappock, T.J. and Caradonna, J.P. *Chem.Rev.*, **1996**, *96*, 2659-2756.
- (106) Enemark, J.H. and Garner, C.D. *J.Biol.Inorg.Chem.*, **1997**, *2*, 817-822.
- (107) Collison, D.; Garner, C.D. and Joule, J.A., *Chem.Soc.Rev.*, **1996**, *25*, 25-32.
- (108) Enemark, J.H. and Young, C.G. *Adv.Inorg.Chem.*, **1993**, *40*, 1-88.
- (109) Zhang, L.; Nelson, K.J.; Rajagopalan, K.V. and George, G.N. *Inorg.Chem.*, **2008**, *47*, 1074-1078.
- (110) Bugrmayer, S.J.N.; Kaufmann, H.L.; Fortunato, G.; Hug, P. and Fisher, B. *Inorg. Chem.*, **1999**, *38*, 2607-2613.
- (111) (a) Fischer, B.; Schmalle, H.; Dubler E.; Schafer, A. and Viscontini, M. *Inorg.Chem.*, **1995**,

- 34 ,5726-5734. (b) Burgmayer, S.J.N.; Kim, M.; Petit, R.; Rothkopf, A.; Kim, A.; Belhamdounia, S.; Hou, Y.; Somogyi, A.; Habel-Rodriguez, D.; Williams, A. and Kirk, M.L. *J.Inorg.Biochem.*, **2007**, *101* ,1601-1616.
- (112) Odani, A.; Masuda, H.; Inukai K. and Yamauchi, O. *J.Am.Chem.Soc.*, **1992**, *114* ,6294-6300.
- (113) Yamauchi, O. *Pure Appl.Chem.*, **1995**, *67* ,297-304.
- (114) (a) Nasir, M.S.; Karlin, K.D.; Chen Q. and Zubieta, J., *J.Am.Chem.Soc.*, **1992**, *114* ,2264-2265. (b) Chen, T.R.; Wu, Y.Y.; Wu C.P.; Chen, J.D.; Huang, C.W.; Keng T.C. and Wang, J.C. *Inorg.Chem.Commun.*, **2000**, *3*,231-233.
- (115) Miyazaki, S.; Kojima, T.; Sakamoto, T.; Matsumoto, T.; Ohkubo K. and Fukuzumi, S., *Inorg.Chem.*, **2008**, *47*, 333-343.
- (116) Fukuzumi, S. and Kojima, T. *J.Biol.Inorg.Chem.*, **2008**, *13* ,321-333.
- (117) Fitzpatrick, P.F., *Biochemistry*, **2003**, *42* ,14083-14091.
- (118) Basu, P. and Burgmayer, S.J.N. *J. Biol.Inorg.Chem.*, **2015**, *20* ,373-383.
- (119) Volner, A.; Zoidakis, J. and Abu-Omar, M.M. *J.Biol.Inorg.Chem.*, **2003**, *8* ,121-128.
- (120) Olsson, E.; Martinez, A.; Teigen K. and Jensen V.R. *Chem.Eur.J.*, **2011**, *17* ,3746-3758.
- (121) Fitzpatrick, P.F. *Current Opinion in Structural Biology*, **2015**, *35*, 1-6.
- (122) Hurshman, A.R.; Krebs, C.; Edmondson, D.E.; Huynh, B.H. and Marletta, *Biochemistry* **1999**, *38*, 15689-15696.
- (123) Presta, A.; Weber-Main, A.M.; Stankovich, M.T. and Stuehr, D.J. *J.Am.Chem.*

- Soc.*, **1998**, *120*, 9460-9465.
- (124) (a) Wei, C.C.; Crane B.R.; and Stuehr D.J. *Chem.Rev.*, **2003**, *103*, 2365-2383.
- (b) Aoyagi M.; Arvai, A.S.; Ghosh, S.; Stuehr, D.J.; Tainer, J.A. and Getzoff, E. *Biochemistry*, **2001**, *40*, 12826-12832.
- (125) Chreifi, G.; Li, H.; McInnes, C.R.; Gibson, C.L.; Suckling C.J. and Poulos, T.L. *Biochemistry*, **2014**, *53*, 4216-4223.
- (126) Breinlinger, E.; Niemz A. and Rotello, V.M. *J.Am.Chem.Soc.*, **1995**, *117*, 5379-5380.
- (127) Inui, Y.; Miyazaki, S.; Ohkubo, K.; Fukuzumi S. and Kojima, T. *Angew. Chem. Int. Ed.* **2012**, *51*, 4623-4627.
- (128) Jimenez-Pulido, S.B.; Linares-Ordóñez, F.M.; Moreno-Carretero, M.N. and Quiro's-Olozabal, M. *Inorg.Chem.*, **2008**, *47*, 1096-1106.
- (129) Miyazaki, S.; Kojima, T.; Mayer J.M. and Fukuzumi, S. *J.Am.Chem.Soc.*, **2009**, *131*, 11615-11624.
- (130) Md.Afsar Ali, Ph.D. thesis, University of North Bengal (2009), "Synthetic, physico-chemical and reactivity aspects of coordination compounds of molybdenum and dioxouranium(VI) with pterin and aldimine ligands".
- (131) Samir Sen, Ph.D. thesis, University of North Bengal (submitted in Dec., 2015), "Studies on coordination compounds of cobalt and tungsten, having biochemical relevance to pterin-containing metalloenzymes".
- (132) Baidyanath Ghosh, Ph.D. thesis, University of North Bengal (submitted in March, 2016), "Synthesis and physico-chemical studies on coordination compounds of molybdenum, copper, iron and zinc with 2-amino substituted pterins".
- (133) Hille, R. *TRENDS in Bioshchemical science*, **2002**, *27*, 360-367.

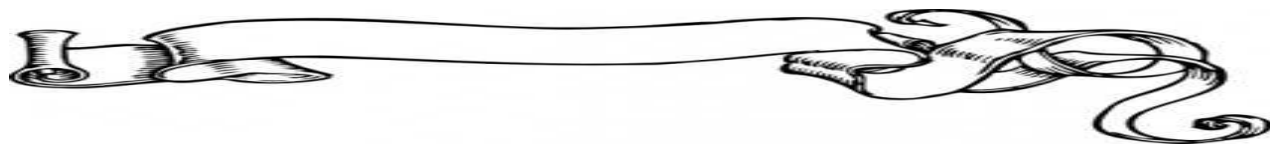
- (134) (a) Dewar, M. Bull. Soc. Chem. Fr. **1951**, 18, C79; (b) Chatt, J.; Duncanson, L. A. J. Chem. Soc., **1953**, 2939-2947. (c) Chatt, J.; Duncanson, L. A.; Venanzi, L. M. J. Chem. Soc., **1955**, 4456-4460.
- (135) (a) Carter, M. J. ; Engelhardt, L. M. ; Rillema and Basolo, F. J. Chem. Soc. , Chem. Commn., **1973**, 810. (b) Hoffman, B. M. ; Diement, D. L. ; Basolo, F. J. Am. Chem. Soc., **1970**, 92, 61-65. (c) Hoffman, B. M.; Petering, D. H. Proc. National Acad. Sci., **1970**, 67, 637-643. (d) Carter, M. J. ; Rillema, D. P. ; Basolo, F. J. Am.m. Soc., **1974**, 96, 392-400. (e) Basolo, F. ; Hoffman, B. M. ; Ibers, J. A. Acc. Chem. Res., **1975**, 8, 384 – 392. (f) Janes, R. D.; Summerville, D. A.; Basolo, F. Chem. Rev., **1979**, 79, 139-179. (g) Szymanski,T.; Cape, T. W.; Duyne, R. P. V.; Basolo, F. J. Chem. Soc. Chem. Commn., **1979**, 5. (h) Summerville, D. A.; Jones, R. D.; Hoffman, B. M.; Basolo, F. J. Chem. Educ., **1979**, 56, 157.
- (136) Shriver, D. F.; Atkins, P. W.; Langford, C. H. Inorganic Chemistry, **1990**, Oxford University Press, Oxford, pp610-615.
- (137) Hughes, M. N. The Inorganic Chemistry of Biological Processes, 2<sup>nd</sup> ed, **1981**, John Wiley & Sons, New York, Chapter one and seven.
- (138) Harrison, P. M. and Hoare, R. J. Metals in biochemistry, Chapmon & Hall, New York, **1980**, Chapter 3 and 4.
- (139) Hayaishi, O. (Ed) Molecular mechanism of oxygen activation, Academic Press, New York, **1974**, Chapter 7 and 8.
- (140) Das A. K. Bioinorganic Chemistry, Books and Allied (P)Ltd., Kolkata, **2007**, Chapter 5.

- (141) Banerjea, D. Inorganic Chemistry: Principles, Book Syndicate(P)Ltd., Kolkata, **2000**, 435-437.
- (142) Mitome, H.; Ishizuka, T.; Kotani, H.; Shiota, Y.; Yoshizawa, K.; Kojima, T. J. Am. Chem. Soc. **2016**, 138, 9508-9520.
- (143) Burgmayer, S.J.N.; Stiefel, E. I. J. Am. Chem. Soc., **1986**, 108, 8310.
- (144) Lippard, S.j.; Berg, J.M. Principles of Bioinorganic Chemistry, **1994**, University Science Books, California, Chapter 10.
- (145) White, A.; Handler, P.; Smith, E. L. Principles of Biochemistry, 5<sup>th</sup> ed, **1973**, McGraw-Hill Kogakusha, LTD., Tokyo, Chapter 14-16.
- (146) Kaufman, S. Proc. Nat. Acad. Sci. **1963**, 50,1085.
- (147) Kaufman, S. J. Biol. Chem. **1967**, 242, 3934.
- (148) Kamp, W. Organic Spectroscopy, 3<sup>rd</sup> ed. **1991**, Palgrave, New York, Chapter 2.
- (149) Mason, S.F. Molecular optical activity and the chiral discriminations, Cambridge University Press, Cambridge, **1982**, Chapter 7.
- (150) Day, P. Electronic Structure and Magnetism of Inorganic Compounds, Volume, I, Specialist Periodical Reports, The Chemical Society London, **1972**, pp 153-161.
- (151) Day, P. Electronic states of Inorganic Compounds: New Experimental Techniques, D. Reidel Publishing Co., Boston, **1974**, pp 177-240.
- (152) Harding, M. J; Mason, S. F.; Robbins, D. J.; Thomson, A. J. Chem. Phys. Letters, **1970**, 7, 70-72.
- (153) Karlin, K. D.; Itoh, S.(ed.) Copper-Oxygen Chemistry, Wiley, New Jersey, **2011**.
- (154) Mitsumi, M.; Toyoda, J.; Nakasuji, K. Inorg. Chem., **1995**, 34, 3367-3370.
- (155) Becke, A. D. J. Chem. Phys. **1993**, 98, 5648-5652.

- (156) Lee, C.; Yang, W.; Parr, R. G. *Phys. Rev. B: Condens. Matter*, **1988**, 37, 785-789.
- (157) Hay, P. J.; Wadt, W. R. J. *Chem. Phys.* **1985**, 82, 284-298.
- (158) Hay, P. J.; Wadt, W. R. J. *Chem. Phys.* **1985**, 82, 299-310.
- (159) Tomasi, J.; Mennucci, B.; Cammi, R. *Chem. Rev.* **2005**, 105, 2999-3093.
- (160) (a) Chem Office, Chem 3D Ultra, **2005** (Cambridge Soft Corp, 100 Cambridge Park Drive, Cambridge, MA 021409802, USA). (b) Zimmer, M. *Chem. Rev.* **1995**, 95, 2629.  
(c) Leach, A. R. *Molecular Modelling Principles and Applications*, 2<sup>nd</sup> ed., Pearson Education Ltd., UK, **2001**, Chapter 4.
- (161) Yanus, R. L.; Yardeni, G.; Mainon, E.; Saphier, M.; Zilbermann, I.; Meyerstein, D. *Eur. J. Inorg. Chem.* **2016**, Issue 8, 1161-1164.
- (162) (a) Ghachtouli, S.E.; Lassalle-Kaiser, B.; Guillot, R.; Aukauloo, A. *Eur. J. Inorg. Chem.* **2014**, 4750-4755. (b) Inui, Y.; Miyazaki, K.O.; Fukuzumi, S.; Kojima, T. *Angew. Chem. Int. Ed.* **2012**, 51, 4623-4627. (c) Breinlinger, E.; Niemz, A.; Rotello, V.M. *J. Am. Chem. Soc.*, **1995**, 117, 5379-5380.

## Appendix A

### List of Publications



- [1] Siddhartha S.Baisya, Baidyanath Ghosh and Parag S.Roy, "Crystal structure of (2-amino-7-methyl-4-oxidopteridine-6-carboxylato- $\kappa^3$ O<sup>4</sup>,N<sup>5</sup>,O<sup>6</sup>)aqua(1,10-phenanthroline- $\kappa^2$ N,N') zinc trihydrate", Acta Cryst. **E71**,m162-m163(2015).
- [2] S.S.Baisya and P.S.Roy, Crystal structure of (2-amino-7-methyl-4-oxidopteridine-6-carboxylato- $\kappa^3$ O<sup>4</sup>N<sup>5</sup>O<sup>6</sup>)aqua(1,10-phenanthroline- $\kappa^2$ N,N')copper(II) trihydrate, Acta Cryst.(2014),**E70**, 348-351.
- [3] S.Sen,S.S.Baisya and P.S.Roy, Synthesis,characterization of new tungsten(IV)-pterin complexe and their reactivity studies towards trimethylamine N-oxide,sodium borohydride and potassium ferricyanide, J. Chromatography Separation Techniques,Vol.4,Issue 8 (2013) 1000198.
- [4] S.S.Baisya and P.S.Roy, (2-Amino-7-methyl-4-oxidopteridine-6-carboxylato- $\kappa^3$ O<sup>4</sup>N<sup>5</sup>O<sup>6</sup>)(ethane-1,2-diamine - $\kappa^2$ N,N')(1H-imidazole- $\kappa$ N<sup>3</sup>)nickel(II)dehydrate, Acta Cryst. (2013). **E69**,m193-m194.

- [5] S.S.Baisya and P.S.Roy, (2-Amino-7-methyl-4-oxidopteridine-6-carboxylato- $\kappa^3\text{O}^4\text{N}^5\text{O}^6$ )aqua(ethane-1,2-diamine- $\kappa^2\text{N},\text{N}'$ )nickel(II)dehydrate, Acta Cryst. (2013). **E69**,m99-m100.
- [6] S.S.Baisya, S.Sen and P.S.Roy, (2-Amino-7-methyl-4-oxidopteridine-6-carboxylato- $\kappa^3\text{O}^4, \text{N}^5, \text{O}^6$ )aqua(1,10-phenanthroline- $\kappa^2\text{N}, \text{N}'$ )cobalt(II)trihydrate, Acta Cryst. (2013). **E69**,m70-71.

### Appendix B



1. 19<sup>TH</sup> CRSI NATIONAL SYMPOSIUM IN CHEMISTRY, July 14<sup>th</sup> – 16<sup>th</sup>, 2016.  
Organized by Department of Chemistry, University of North Bengal, Darjeeling 734013
2. Frontiers in Chemistry – 2016, March 7<sup>th</sup> & 8<sup>th</sup>, 2016. Organized by Department of Chemistry, University of North Bengal, Darjeeling 734013
3. National Seminar on FRONTIERS IN CHEMISTRY, March 11<sup>th</sup> & 12<sup>th</sup>, 2014.  
Organized by Department of Chemistry, University of North Bengal, Darjeeling 734013
4. Science Academies' Lecture Workshop on Recent Trends in Chemistry, November 11<sup>th</sup> & 12<sup>th</sup>, 2011. Organized by Department of Chemistry, University of North Bengal, Darjeeling 734013

5. Chemical Research Society of India Eastern Zonal Meeting, 2011 & Celebration of the International Year of Chemistry 2011, July 22<sup>nd</sup> – 24<sup>th</sup>, 2011. Organized by Department of Chemistry, University of North Bengal, Darjeeling 734013
  
6. SIXTH CRSI (KOLKATA CHAPTER) SYMPOSIUM, August 02, 2008. Organized by Department of Chemistry, University of North Bengal, Darjeeling 734013

## **Appendix C**

Published papers

(2-Amino-7-methyl-4-oxopteridine-6-carboxylato- $\kappa^3 O^4, N^5, O^6$ )aqua(1,10-phenanthroline- $\kappa^2 N, N'$ )cobalt(II) trihydrate

Siddhartha S. Baisya, Samir Sen and Parag S. Roy\*

Department of Chemistry, University of North Bengal, Siliguri 734 013, India  
Correspondence e-mail: psrbu@gmail.com

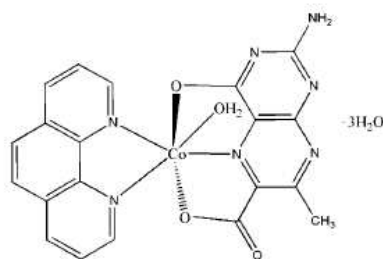
Received 10 December 2012; accepted 18 December 2012

Key indicators: single-crystal X-ray study;  $T = 110$  K; mean  $\sigma(C-C) = 0.005$  Å;  
R factor = 0.057; wR factor = 0.129; data-to-parameter ratio = 15.0.

In the title compound,  $[\text{Co}(\text{C}_8\text{H}_5\text{N}_5\text{O}_3)(\text{C}_{12}\text{H}_8\text{N}_2)(\text{H}_2\text{O})] \cdot 3\text{H}_2\text{O}$ , a tridentate 2-amino-7-methyl-4-oxopteridine-6-carboxylate ligand, a bidentate ancillary 1,10-phenanthroline (phen) ligand and a water molecule complete a distorted octahedral geometry around the  $\text{Co}^{\text{II}}$  atom. The pterin ligand forms two chelate rings. The phen and pterin ring systems are nearly perpendicular [dihedral angle =  $85.15$  ( $8^\circ$ )].  $\text{N}-\text{H} \cdots \text{O}$ ,  $\text{O}-\text{H} \cdots \text{N}$  and  $\text{O}-\text{H} \cdots \text{O}$  hydrogen bonds link the complex molecules and lattice water molecules into a layer parallel to (001).  $\pi-\pi$  stacking contacts (involving phen-phen and pteridine-pteridine) are also observed [centroid-centroid distances =  $3.670$  (2),  $3.547$  (2),  $3.698$  (2) and  $3.349$  (2) Å].

## Related literature

For background to the chemistry of pterins in metalloenzymes, see: Basu & Burgmayer (2011); Burgmayer (1998); Fitzpatrick (2003); Fukuzumi & Kojima (2008). For structures of related cobalt complexes, see: Acuña-Cueva *et al.* (2003); Beddoes *et al.* (1997); Burgmayer & Stiefel (1988); Funahashi *et al.* (1997). For structures of related copper complexes, see: Odani *et al.* (1992). For the electron-shuffling ability of the pterin unit as well as its donor groups and the effect on the geometric parameters of related complexes, see: Beddoes *et al.* (1993); Kohzuma *et al.* (1988); Russell *et al.* (1992). For the synthesis of the pterin ligand, see: Wittle *et al.* (1947).



## Experimental

## Crystal data

$[\text{Co}(\text{C}_8\text{H}_5\text{N}_5\text{O}_3)(\text{C}_{12}\text{H}_8\text{N}_2) \cdot (\text{H}_2\text{O})] \cdot 3\text{H}_2\text{O}$   
 $M_r = 530.36$   
Triclinic,  $P\bar{1}$   
 $a = 8.454$  (2) Å  
 $b = 9.934$  (3) Å  
 $c = 13.778$  (4) Å  
 $\alpha = 97.534$  ( $4^\circ$ )

$\beta = 95.281$  ( $4^\circ$ )  
 $\gamma = 110.603$  ( $4^\circ$ )  
 $V = 1061.8$  (5) Å<sup>3</sup>  
 $Z = 2$   
Mo  $K\alpha$  radiation  
 $\mu = 0.87$  mm<sup>-1</sup>  
 $T = 110$  K  
 $0.23 \times 0.11 \times 0.04$  mm

## Data collection

Bruker Kappa APEXII CCD diffractometer  
Absorption correction: multi-scan (SADABS; Sheldrick, 1996)  
 $T_{\text{min}} = 0.82$ ,  $T_{\text{max}} = 0.97$

8945 measured reflections  
4726 independent reflections  
4360 reflections with  $I > 2\sigma(I)$   
 $R_{\text{int}} = 0.030$

## Refinement

$R[F^2 > 2\sigma(F^2)] = 0.057$   
 $wR(F^2) = 0.129$   
 $S = 1.03$   
4726 reflections

316 parameters  
H-atom parameters constrained  
 $\Delta\rho_{\text{max}} = 0.99$  e Å<sup>-3</sup>  
 $\Delta\rho_{\text{min}} = -0.88$  e Å<sup>-3</sup>

Table 1

Hydrogen-bond geometry (Å, °).

$D-H \cdots A$	$D-H$	$H \cdots A$	$D \cdots A$	$D-H \cdots A$
$\text{N7}-\text{H141} \cdots \text{O2}^{\text{i}}$	0.85	2.12	2.942 (4)	163
$\text{N7}-\text{H142} \cdots \text{O6}^{\text{ii}}$	0.84	2.15	2.970 (4)	165
$\text{O4}-\text{H181} \cdots \text{O6}$	0.81	1.93	2.717 (3)	164
$\text{O4}-\text{H182} \cdots \text{N5}^{\text{ii}}$	0.80	2.25	3.051 (4)	176
$\text{O5}-\text{H341} \cdots \text{O1}$	0.82	2.34	3.079 (4)	151
$\text{O5}-\text{H341} \cdots \text{O2}$	0.82	2.23	2.896 (4)	139
$\text{O5}-\text{H342} \cdots \text{N4}^{\text{iii}}$	0.82	2.04	2.844 (4)	166
$\text{O6}-\text{H351} \cdots \text{O5}$	0.83	1.92	2.740 (4)	174
$\text{O6}-\text{H352} \cdots \text{N5}^{\text{iv}}$	0.82	2.05	2.871 (4)	176
$\text{O7}-\text{H331} \cdots \text{O5}^{\text{i}}$	0.80	2.25	2.941 (4)	145
$\text{O7}-\text{H332} \cdots \text{O3}$	0.81	2.23	2.962 (5)	151

Symmetry codes: (i)  $x+1, y+1, z$ ; (ii)  $-x+1, -y+1, -z+1$ ; (iii)  $x-1, y-1, z$ ; (iv)  $x, y-1, z$ .

Data collection: APEX2 (Bruker, 2007); cell refinement: SAINT (Bruker, 2007); data reduction: SAINT; program(s) used to solve structure: SHELXS97 (Sheldrick, 2008); program(s) used to refine structure: CRYSTALS (Betteridge *et al.*, 2003); molecular graphics: CAMERON (Watkin *et al.*, 1996); software used to prepare material for publication: CRYSTALS.

The authors express their gratitude to the UGC, New Delhi, for financial assistance (SAP-DRS program). Thanks are due to the CSMCRI, Bhavnagar, Gujrat, India, for the X-ray

structural data and the University of North Bengal for infrastructure.

Supplementary data and figures for this paper are available from the IUCr electronic archives (Reference: HY2609).

## References

- Acuña-Cueva, E. R., Faure, R., Illán-Cabeza, N. A., Jiménez-Pulido, S. B., Moreno-Carretero, M. N. & Quirós-Olozabal, M. (2003). *Inorg. Chim. Acta*, **342**, 209–218.
- Basu, P. & Burgmayer, S. J. N. (2011). *Coord. Chem. Rev.* **255**, 1016–1038.
- Beddoes, R. L., Dinsmore, A., Helliwell, M., Garner, C. D. & Joule, J. A. (1997). *Acta Cryst.* **C53**, 213–215.
- Beddoes, R. L., Russell, J. R., Garner, C. D. & Joule, J. A. (1993). *Acta Cryst.* **C49**, 1649–1652.
- Betteridge, P. W., Carruthers, J. R., Cooper, R. I., Prout, K. & Watkin, D. J. (2003). *J. Appl. Cryst.* **36**, 1487.
- Bruker (2007). *APEX2* and *SAINT*. Bruker AXS Inc., Madison, Wisconsin, USA.
- Burgmayer, S. J. N. (1998). *Struct. Bond.* **92**, 67–119.
- Burgmayer, S. J. N. & Stiefel, E. I. (1988). *Inorg. Chem.* **27**, 4059–4061.
- Fitzpatrick, P. F. (2003). *Biochemistry*, **42**, 14083–14091.
- Fukuzumi, S. & Kojima, T. (2008). *J. Biol. Inorg. Chem.* **13**, 321–333.
- Funahashi, Y., Hara, Y., Masuda, H. & Yamauchi, O. (1997). *Inorg. Chem.* **36**, 3869–3875.
- Kohzuma, T., Odani, A., Morita, Y., Takani, M. & Yamauchi, O. (1988). *Inorg. Chem.* **27**, 3854–3858.
- Odani, A., Masuda, H., Inukai, K. & Yamauchi, O. (1992). *J. Am. Chem. Soc.* **114**, 6294–6300.
- Russell, J. R., Garner, C. D. & Joule, J. A. (1992). *J. Chem. Soc. Perkin Trans. 1*, pp. 1245–1249.
- Sheldrick, G. M. (1996). *SADABS*. University of Göttingen, Germany.
- Sheldrick, G. M. (2008). *Acta Cryst.* **A64**, 112–122.
- Watkin, D. J., Prout, C. K. & Pearce, L. J. (1996). *CAMERON*. Chemical Crystallography Laboratory, Oxford, England.
- Wittle, E. L., O'Dell, B. L., Vandenbelt, J. M. & Pfiffner, J. J. (1947). *J. Am. Chem. Soc.* **69**, 1786–1792.

## supporting information

*Acta Cryst.* (2013). E69, m70–m71 [doi:10.1107/S1600536812051185]

**(2-Amino-7-methyl-4-oxidopteridine-6-carboxylato- $\kappa^3 O^4, N^5, O^6$ )aqua(1,10-phenanthroline- $\kappa^2 N, N'$ )cobalt(II) trihydrate**

Siddhartha S. Baisya, Samir Sen and Parag S. Roy

**S1. Comment**

The primary motivation for pursuing coordination chemistry of pterins is the ubiquitous presence of this heterocyclic system in nature including a substantial number of metalloenzymes (Basu & Burgmayer, 2011; Burgmayer, 1998; Fitzpatrick, 2003; Fukuzumi & Kojima, 2008). Literature survey reveals the existence of only a few X-ray structurally characterized cobalt-pterin/pteridine/lumazine complexes as well as one containing an organocobalt moiety (Acuña-Cueva *et al.*, 2003; Beddoes *et al.*, 1997; Burgmayer & Stiefel, 1988; Funahashi *et al.*, 1997). The concerned ligands usually act as bidentate O,N-donors and none of the above complexes possesses a typical  $\pi$ -acceptor ancillary ligand like 1,10-phenanthroline (phen). In this crystallographic study on the title cobalt(II) complex, possessing both a tridentate pterin ligand and a  $\pi$ -acidic ligand like phen, different aspects are considered, *e.g.* crystal, molecular and electronic structures.

In the title compound (Fig. 1), the stereochemistry around the Co<sup>II</sup> atom is essentially distorted octahedral with two N atoms of phen, a pyrazine ring N atom (N3) of the pterin ligand and an aqua O atom forming the equatorial plane; two pterin O atoms (O1 and O3) define the longer axial positions, with the phenolate O3 forming the longest axial bond [2.270 (2) Å]. Extent of distortion of this coordination octahedron is much more pronounced as compared to that of the Co(II)-pteridine complexes reported earlier (Acuña-Cueva *et al.*, 2003; Burgmayer & Stiefel, 1988; Funahashi *et al.*, 1997). A major cause of this departure from regular geometry is that the pterin ligand forms two five-membered chelate rings having small bite angles [75.10 (10) and 76.26 (9)°], instead of only one per pteridine ligand for the earlier cases. Location of the short Co1—N3 bond [2.016 (3) Å] in the equatorial plane is consistent with the literature, which suggests a strong cobalt-pterin interaction (Odani *et al.*, 1992). The pterin ligand is coordinated here as a binegative tridentate ONO donor, as evident from the charge balance of this complex. The phen and pterin rings are nearly perpendicular to each other for minimizing the steric repulsion. The Co1—N1 [2.079 (3) Å] and Co1—N2 [2.123 (3) Å] bond lengths are at par with that of the Co1—N3 bond [2.016 (3) Å] and indicate receipt of  $\pi$ -back donation to both phen and pterin rings from the Co(II) centre ( $d^7$ ) through  $d\pi$ - $p\pi$  interactions. This process is further strengthened by the presence of  $\pi$ -donating phenolate and carboxylate O atoms around the metal centre (Kohzuma *et al.*, 1988).

For rationalizing the near double bond nature of the O3—C18 [1.265 (4) Å] bond, a hypothesis of Joule (Beddoes *et al.*, 1993; Russell *et al.*, 1992) may be invoked, which suggests withdrawal of electron density from the pyrazine ring N6 by the pyrimidine ring C18-carbonyl group through mesomeric interaction. Formation of the O3—Co1 bond accentuates this electron withdrawal towards O3. The electron-rich N7—C17 [1.337 (4) Å] bond may also participate in this electron transfer. The pyrimidine ring is fairly planar and deviations of the C16/N5/C17 and C17/N4/C18 segments with respect to the N7—C17 multiple bonds are 2.6 and 0.7°, respectively.

In the crystal, intermolecular N—H $\cdots$ O, O—H $\cdots$ N and O—H $\cdots$ O hydrogen bonds (Table 1) link the complex molecules and lattice water molecules into a layer parallel to (001) (Fig. 2). The lattice water molecules are decisive for the crystal packing. Fig. 3 reveals  $\pi$ – $\pi$  stacking interactions involving two parallel, inversion-related pterin rings within the same unit cell and showing face-to-face distance of 3.283 (4) and 3.366 (4) Å. Again the phen rings display two types of  $\pi$ – $\pi$  stacking on either side of the unit cell. In one case, the adjacent phen rings are essentially parallel to each other with an average interplanar distance of 3.496 (4) Å; on the other side of the unit cell, the face-to-face separations between parallel phen rings are 3.578 (4) and 3.629 (5) Å.

## S2. Experimental

2-Amino-4-hydroxy-7-methylpteridine-6-carboxylic acid sesquihydrate (C<sub>8</sub>H<sub>7</sub>N<sub>5</sub>O<sub>5</sub>·1.5H<sub>2</sub>O) was obtained by published procedure (Wittle *et al.*, 1947). The title complex was prepared by the dropwise addition of an aqueous alkaline solution (NaOH: 11 mg, 0.275 mmol) of the pterin ligand (31 mg, 0.125 mmol) to a warm (311 K) aqueous reaction medium containing CoSO<sub>4</sub>·7H<sub>2</sub>O (35 mg, 0.125 mmol) and 1,10-phenanthroline monohydrate (25 mg, 0.125 mmol) in a total volume of 60 ml. The pH value was adjusted to 10.8 using aqueous NaOH solution and dioxygen was bubbled in for 48 h; final pH was 10.3. Initially a small amount of yellow-white precipitate came out and the reaction mixture ultimately assumed a reddish-pink tinge. It was transferred to a 100 ml beaker, requisite quantity of water was added to make up for the evaporation loss and allowed to stand at room temperature. Pink crystals suitable for single-crystal X-ray diffraction appeared after 15 days (yield: 30%).

## S3. Refinement

The H atoms were all located in a difference map, but those attached to C atoms were repositioned geometrically. The H atoms were initially refined with soft restraints on the bond lengths and angles to regularize their geometry (C—H = 0.93–0.98, N—H = 0.86–0.89, O—H = 0.82 Å) and with  $U_{iso}(H) = 1.2\text{--}1.5 U_{eq}(\text{parent atom})$ , after which the positions were refined with rigidifying constrains.

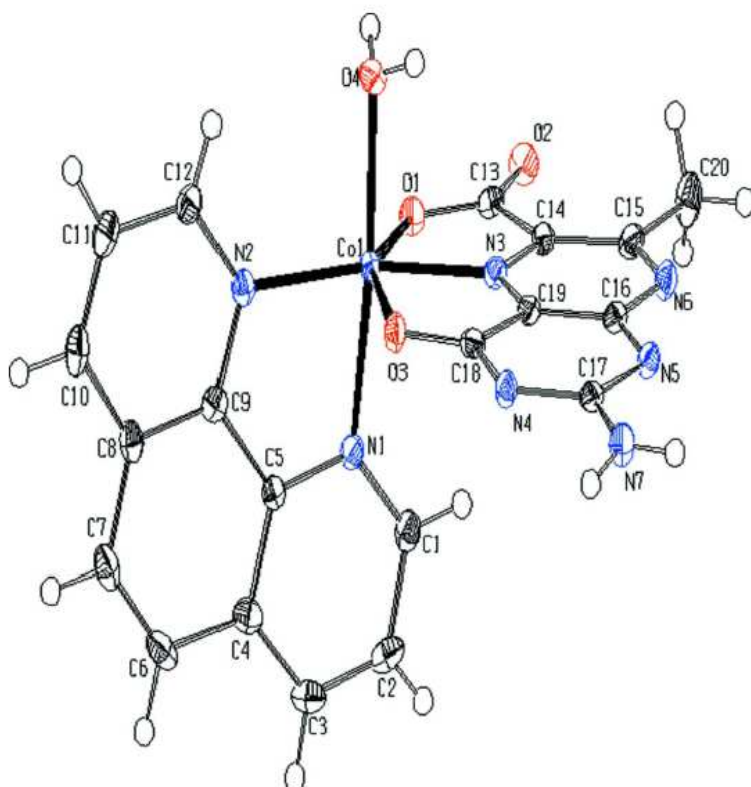


**Figure 1**

The molecular structure of the title compound. Displacement ellipsoids are drawn at the 50% probability level. Lattice water molecules are omitted for clarity.

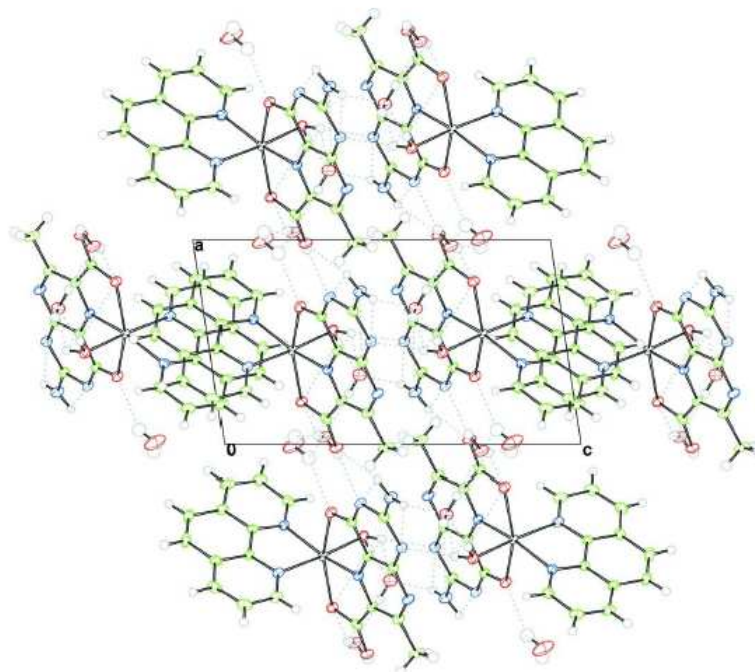


**Figure 2**

The crystal packing diagram of the title compound, viewed along the *b* axis. Dotted lines indicate hydrogen bonds, assisting the formation of a layer structure parallel to (001).

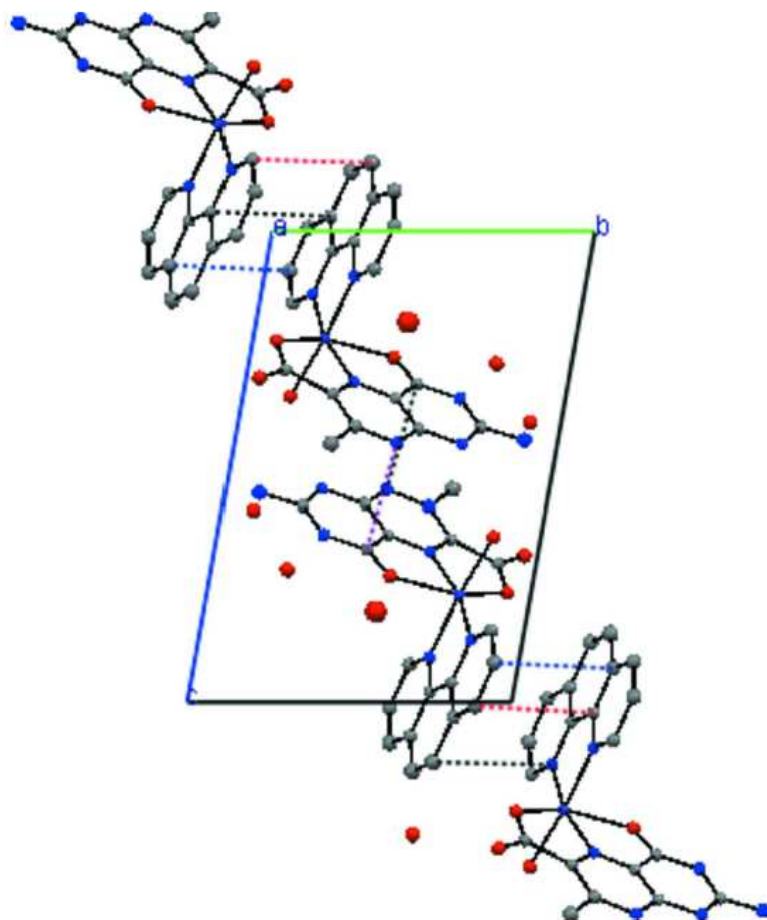


Figure 3

A molecular packing diagram highlighting  $\pi$ - $\pi$  stacking interactions between two neighbouring phen-phen and pterin-pterin rings, respectively.

(2-Amino-7-methyl-4-oxidopteridine-6-carboxylato- $\kappa^3O^4,N^5,O^6$ )aqua(1,10-phenanthroline- $\kappa^2N,N'$ )cobalt(II) trihydrate

*Crystal data*

$[\text{Co}(\text{C}_8\text{H}_5\text{N}_3\text{O}_3)(\text{C}_{12}\text{H}_8\text{N}_2)(\text{H}_2\text{O})] \cdot 3\text{H}_2\text{O}$

$M_r = 530.36$

Triclinic,  $P\bar{1}$

Hall symbol: -P 1

$a = 8.454$  (2) Å

$b = 9.934$  (3) Å

$c = 13.778$  (4) Å

$\alpha = 97.534$  (4)°

$\beta = 95.281$  (4)°

$\gamma = 110.603$  (4)°

$V = 1061.8$  (5) Å<sup>3</sup>

$Z = 2$

$F(000) = 546$

$D_x = 1.659$  Mg m<sup>-3</sup>

Mo  $K\alpha$  radiation,  $\lambda = 0.71073$  Å

Cell parameters from 8945 reflections

$\theta = 2$ -28°

$\mu = 0.87$  mm<sup>-1</sup>

## supporting information

$T = 110$  K  
Block, pink  $0.23 \times 0.11 \times 0.04$  mm

### Data collection

Bruker Kappa APEXII CCD diffractometer  
Graphite monochromator  
 $\varphi$  and  $\omega$  scans  
Absorption correction: multi-scan (SADABS; Sheldrick, 1996)  
 $T_{\min} = 0.82$ ,  $T_{\max} = 0.97$   
8945 measured reflections

4726 independent reflections  
4360 reflections with  $I > 2\sigma(I)$   
 $R_{\text{int}} = 0.030$   
 $\theta_{\max} = 28.2^\circ$ ,  $\theta_{\min} = 1.5^\circ$   
 $h = -11 \rightarrow 11$   
 $k = -12 \rightarrow 13$   
 $l = -18 \rightarrow 18$

### Refinement

Refinement on  $F^2$   
Least-squares matrix: full  
 $R[F^2 > 2\sigma(F^2)] = 0.057$   
 $wR(F^2) = 0.129$   
 $S = 1.03$   
4726 reflections  
316 parameters  
0 restraints

Primary atom site location: structure-invariant direct methods  
Hydrogen site location: difference Fourier map  
H-atom parameters constrained  
Method = Modified Sheldrick  $w = 1/[\sigma^2(F^2) + (0.04P)^2 + 3.34P]$ ,  
where  $P = (\max(F_o^2, 0) + 2F_c^2)/3$   
 $(\Delta/\sigma)_{\max} = 0.0001859$   
 $\Delta\rho_{\max} = 0.99 \text{ e } \text{\AA}^{-3}$   
 $\Delta\rho_{\min} = -0.88 \text{ e } \text{\AA}^{-3}$

### Fractional atomic coordinates and isotropic or equivalent isotropic displacement parameters ( $\text{\AA}^2$ )

	<i>x</i>	<i>y</i>	<i>z</i>	$U_{\text{iso}}^*/U_{\text{eq}}$
Co1	0.45982 (5)	0.22172 (4)	0.22887 (3)	0.0125
O1	0.2062 (3)	0.0747 (2)	0.23341 (17)	0.0176
C13	0.1224 (4)	0.1182 (3)	0.2948 (2)	0.0159
O2	-0.0205 (3)	0.0408 (2)	0.31159 (18)	0.0204
C14	0.2096 (4)	0.2762 (3)	0.3463 (2)	0.0150
N3	0.3618 (3)	0.3367 (3)	0.32052 (19)	0.0137
C19	0.4572 (4)	0.4746 (3)	0.3559 (2)	0.0137
C16	0.4012 (4)	0.5628 (3)	0.4205 (2)	0.0151
N5	0.4986 (3)	0.7057 (3)	0.4529 (2)	0.0154
C17	0.6493 (4)	0.7539 (3)	0.4170 (2)	0.0157
N4	0.7169 (3)	0.6739 (3)	0.3559 (2)	0.0161
C18	0.6243 (4)	0.5321 (3)	0.3254 (2)	0.0148
O3	0.6704 (3)	0.4463 (2)	0.26886 (17)	0.0174
N7	0.7460 (4)	0.8957 (3)	0.4440 (2)	0.0199
H141	0.8293	0.9343	0.4135	0.0223*
H142	0.7086	0.9522	0.4775	0.0228*
N6	0.2466 (3)	0.5028 (3)	0.4504 (2)	0.0176
C15	0.1508 (4)	0.3621 (3)	0.4146 (2)	0.0171
C20	-0.0163 (4)	0.2992 (4)	0.4506 (3)	0.0256
H172	-0.0359	0.3696	0.4963	0.0378*
H173	-0.0185	0.2188	0.4829	0.0383*
H171	-0.1061	0.2680	0.3985	0.0380*
O4	0.5538 (3)	0.1469 (2)	0.35063 (17)	0.0185
H181	0.4964	0.0663	0.3597	0.0272*

supporting information

H182	0.5418	0.1894	0.4013	0.0271*
N2	0.3758 (3)	0.2801 (3)	0.0963 (2)	0.0162
C12	0.2567 (4)	0.3370 (4)	0.0798 (3)	0.0196
C11	0.2191 (4)	0.3750 (4)	-0.0116 (3)	0.0230
C10	0.3071 (4)	0.3548 (4)	-0.0867 (3)	0.0220
C8	0.4354 (4)	0.2958 (4)	-0.0719 (2)	0.0183
C9	0.4634 (4)	0.2593 (3)	0.0218 (2)	0.0138
C5	0.5897 (4)	0.1963 (3)	0.0422 (2)	0.0147
N1	0.6075 (3)	0.1592 (3)	0.1330 (2)	0.0152
C1	0.7247 (4)	0.1018 (3)	0.1537 (2)	0.0178
C2	0.8260 (4)	0.0749 (4)	0.0839 (3)	0.0225
C3	0.8069 (4)	0.1096 (4)	-0.0079 (3)	0.0221
C4	0.6854 (4)	0.1721 (3)	-0.0323 (2)	0.0179
C6	0.6545 (4)	0.2115 (4)	-0.1271 (3)	0.0227
C7	0.5346 (5)	0.2690 (4)	-0.1461 (3)	0.0241
H321	0.5124	0.2898	-0.2083	0.0280*
H311	0.7136	0.1926	-0.1771	0.0268*
H291	0.8704	0.0898	-0.0554	0.0258*
H281	0.9086	0.0377	0.1020	0.0257*
H271	0.7401	0.0814	0.2171	0.0208*
H221	0.2815	0.3779	-0.1477	0.0263*
H211	0.1346	0.4115	-0.0211	0.0270*
H201	0.1976	0.3531	0.1304	0.0229*
O7	0.9931 (4)	0.4695 (3)	0.1919 (3)	0.0445
H331	1.0355	0.5568	0.1993	0.0644*
H332	0.9309	0.4819	0.2305	0.0648*
O5	0.0341 (3)	-0.2327 (3)	0.28207 (18)	0.0224
H341	0.0418	-0.1559	0.2637	0.0322*
H342	-0.0472	-0.2571	0.3124	0.0321*
O6	0.3374 (3)	-0.0951 (2)	0.40693 (18)	0.0204
H351	0.2468	-0.1420	0.3696	0.0287*
H352	0.3795	-0.1552	0.4182	0.0294*

Atomic displacement parameters ( $\text{\AA}^2$ )

	$U^{11}$	$U^{22}$	$U^{33}$	$U^{12}$	$U^{13}$	$U^{23}$
Co1	0.0135 (2)	0.0131 (2)	0.0129 (2)	0.00622 (16)	0.00458 (15)	0.00324 (15)
O1	0.0164 (11)	0.0142 (11)	0.0210 (12)	0.0040 (9)	0.0048 (9)	0.0026 (9)
C13	0.0156 (15)	0.0157 (15)	0.0168 (15)	0.0064 (12)	-0.0002 (12)	0.0050 (12)
O2	0.0143 (11)	0.0173 (11)	0.0269 (13)	0.0015 (9)	0.0059 (9)	0.0056 (10)
C14	0.0134 (14)	0.0150 (15)	0.0185 (15)	0.0062 (12)	0.0048 (12)	0.0053 (12)
N3	0.0134 (12)	0.0130 (12)	0.0153 (13)	0.0049 (10)	0.0035 (10)	0.0038 (10)
C19	0.0139 (14)	0.0141 (14)	0.0156 (15)	0.0062 (12)	0.0053 (12)	0.0057 (12)
C16	0.0158 (15)	0.0172 (15)	0.0152 (15)	0.0085 (12)	0.0029 (12)	0.0050 (12)
N5	0.0149 (13)	0.0129 (12)	0.0196 (14)	0.0060 (10)	0.0040 (10)	0.0030 (10)
C17	0.0157 (15)	0.0175 (15)	0.0167 (15)	0.0083 (12)	0.0030 (12)	0.0063 (12)
N4	0.0150 (13)	0.0148 (13)	0.0202 (14)	0.0057 (10)	0.0078 (11)	0.0047 (11)
C18	0.0144 (15)	0.0169 (15)	0.0150 (15)	0.0065 (12)	0.0036 (12)	0.0063 (12)

## supporting information

O3	0.0173 (11)	0.0170 (11)	0.0193 (12)	0.0073 (9)	0.0065 (9)	0.0028 (9)
N7	0.0188 (14)	0.0136 (13)	0.0264 (15)	0.0044 (11)	0.0081 (12)	0.0020 (11)
N6	0.0164 (13)	0.0169 (13)	0.0224 (14)	0.0083 (11)	0.0071 (11)	0.0041 (11)
C15	0.0148 (15)	0.0171 (15)	0.0226 (16)	0.0075 (12)	0.0065 (12)	0.0079 (13)
C20	0.0163 (16)	0.0207 (17)	0.040 (2)	0.0056 (14)	0.0126 (15)	0.0024 (15)
O4	0.0198 (12)	0.0193 (11)	0.0174 (11)	0.0069 (9)	0.0052 (9)	0.0063 (9)
N2	0.0151 (13)	0.0150 (13)	0.0203 (14)	0.0061 (10)	0.0063 (11)	0.0055 (11)
C12	0.0169 (16)	0.0171 (15)	0.0263 (18)	0.0064 (13)	0.0075 (13)	0.0055 (13)
C11	0.0193 (17)	0.0195 (16)	0.0319 (19)	0.0082 (14)	0.0003 (14)	0.0098 (14)
C10	0.0202 (17)	0.0232 (17)	0.0224 (17)	0.0061 (14)	-0.0007 (13)	0.0107 (14)
C8	0.0177 (16)	0.0168 (15)	0.0178 (16)	0.0030 (12)	0.0007 (12)	0.0044 (13)
C9	0.0133 (14)	0.0114 (14)	0.0153 (15)	0.0026 (11)	0.0032 (11)	0.0022 (11)
C5	0.0129 (14)	0.0113 (14)	0.0176 (15)	0.0020 (11)	0.0022 (12)	0.0015 (12)
N1	0.0152 (13)	0.0133 (12)	0.0158 (13)	0.0040 (10)	0.0034 (10)	0.0013 (10)
C1	0.0171 (15)	0.0150 (15)	0.0199 (16)	0.0058 (12)	0.0002 (12)	0.0005 (12)
C2	0.0169 (16)	0.0214 (17)	0.0312 (19)	0.0103 (14)	0.0035 (14)	0.0025 (14)
C3	0.0162 (16)	0.0190 (16)	0.0298 (19)	0.0059 (13)	0.0079 (14)	-0.0016 (14)
C4	0.0152 (15)	0.0162 (15)	0.0200 (16)	0.0032 (12)	0.0055 (13)	0.0009 (13)
C6	0.0241 (17)	0.0251 (17)	0.0181 (17)	0.0072 (14)	0.0093 (14)	0.0026 (14)
C7	0.0299 (19)	0.0254 (18)	0.0169 (16)	0.0070 (15)	0.0085 (14)	0.0086 (14)
O7	0.0352 (16)	0.0272 (15)	0.074 (2)	0.0127 (13)	0.0292 (16)	-0.0010 (15)
O5	0.0178 (11)	0.0184 (12)	0.0318 (14)	0.0057 (9)	0.0095 (10)	0.0059 (10)
O6	0.0192 (12)	0.0166 (11)	0.0266 (13)	0.0077 (9)	0.0020 (10)	0.0060 (10)

### Geometric parameters (Å, °)

Co1—O1	2.140 (2)	N2—C12	1.333 (4)
Co1—N3	2.016 (3)	N2—C9	1.355 (4)
Co1—O3	2.270 (2)	C12—C11	1.402 (5)
Co1—O4	2.120 (2)	C12—H201	0.923
Co1—N2	2.123 (3)	C11—C10	1.363 (5)
Co1—N1	2.079 (3)	C11—H211	0.914
O1—C13	1.279 (4)	C10—C8	1.414 (5)
C13—O2	1.244 (4)	C10—H221	0.926
C13—C14	1.519 (4)	C8—C9	1.408 (4)
C14—N3	1.319 (4)	C8—C7	1.435 (5)
C14—C15	1.426 (4)	C9—C5	1.439 (4)
N3—C19	1.319 (4)	C5—N1	1.359 (4)
C19—C16	1.397 (4)	C5—C4	1.411 (4)
C19—C18	1.450 (4)	N1—C1	1.333 (4)
C16—N5	1.354 (4)	C1—C2	1.406 (5)
C16—N6	1.360 (4)	C1—H271	0.930
N5—C17	1.360 (4)	C2—C3	1.363 (5)
C17—N4	1.378 (4)	C2—H281	0.928
C17—N7	1.337 (4)	C3—C4	1.412 (5)
N4—C18	1.335 (4)	C3—H291	0.928
C18—O3	1.265 (4)	C4—C6	1.439 (5)
N7—H141	0.852	C6—C7	1.349 (5)

## supporting information

N7—H142	0.843	C6—H311	0.925
N6—C15	1.342 (4)	C7—H321	0.926
C15—C20	1.491 (4)	O7—H331	0.800
C20—H172	0.947	O7—H332	0.810
C20—H173	0.960	O5—H341	0.811
C20—H171	0.930	O5—H342	0.820
O4—H181	0.810	O6—H351	0.830
O4—H182	0.801	O6—H352	0.820
O1—Co1—N3	75.10 (10)	H172—C20—H171	106.6
O1—Co1—O3	151.22 (8)	H173—C20—H171	109.7
N3—Co1—O3	76.26 (9)	Co1—O4—H181	116.6
O1—Co1—O4	90.13 (9)	Co1—O4—H182	109.7
N3—Co1—O4	90.23 (10)	H181—O4—H182	95.0
O3—Co1—O4	92.74 (9)	Co1—N2—C12	128.8 (2)
O1—Co1—N2	90.99 (10)	Co1—N2—C9	112.7 (2)
N3—Co1—N2	96.45 (10)	C12—N2—C9	118.5 (3)
O3—Co1—N2	89.46 (9)	N2—C12—C11	122.3 (3)
O4—Co1—N2	173.29 (10)	N2—C12—H201	119.1
O1—Co1—N1	119.55 (10)	C11—C12—H201	118.6
N3—Co1—N1	164.48 (10)	C12—C11—C10	119.6 (3)
O3—Co1—N1	88.76 (9)	C12—C11—H211	120.2
O4—Co1—N1	94.58 (10)	C10—C11—H211	120.2
N2—Co1—N1	79.12 (10)	C11—C10—C8	119.9 (3)
Co1—O1—C13	116.8 (2)	C11—C10—H221	120.1
O1—C13—O2	124.1 (3)	C8—C10—H221	120.0
O1—C13—C14	114.6 (3)	C10—C8—C9	116.7 (3)
O2—C13—C14	121.2 (3)	C10—C8—C7	124.4 (3)
C13—C14—N3	111.4 (3)	C9—C8—C7	118.9 (3)
C13—C14—C15	129.9 (3)	C8—C9—N2	123.1 (3)
N3—C14—C15	118.8 (3)	C8—C9—C5	120.1 (3)
Co1—N3—C14	121.6 (2)	N2—C9—C5	116.8 (3)
Co1—N3—C19	117.6 (2)	C9—C5—N1	117.5 (3)
C14—N3—C19	120.8 (3)	C9—C5—C4	119.5 (3)
N3—C19—C16	121.8 (3)	N1—C5—C4	123.0 (3)
N3—C19—C18	117.4 (3)	Co1—N1—C5	113.6 (2)
C16—C19—C18	120.7 (3)	Co1—N1—C1	127.6 (2)
C19—C16—N5	120.8 (3)	C5—N1—C1	118.5 (3)
C19—C16—N6	118.7 (3)	N1—C1—C2	122.0 (3)
N5—C16—N6	120.4 (3)	N1—C1—H271	118.0
C16—N5—C17	115.1 (3)	C2—C1—H271	120.0
N5—C17—N4	127.9 (3)	C1—C2—C3	119.8 (3)
N5—C17—N7	117.0 (3)	C1—C2—H281	119.3
N4—C17—N7	115.1 (3)	C3—C2—H281	120.9
C17—N4—C18	117.6 (3)	C2—C3—C4	119.9 (3)
C19—C18—N4	117.7 (3)	C2—C3—H291	120.7
C19—C18—O3	118.1 (3)	C4—C3—H291	119.4
N4—C18—O3	124.2 (3)	C3—C4—C5	116.8 (3)

supporting information

Co1—O3—C18	110.63 (19)	C3—C4—C6	124.2 (3)
C17—N7—H141	119.8	C5—C4—C6	119.0 (3)
C17—N7—H142	119.9	C4—C6—C7	121.2 (3)
H141—N7—H142	117.6	C4—C6—H311	119.5
C16—N6—C15	119.0 (3)	C7—C6—H311	119.2
C14—C15—N6	120.8 (3)	C8—C7—C6	121.3 (3)
C14—C15—C20	121.7 (3)	C8—C7—H321	118.4
N6—C15—C20	117.4 (3)	C6—C7—H321	120.3
C15—C20—H172	111.5	H331—O7—H332	86.2
C15—C20—H173	110.1	H341—O5—H342	108.7
H172—C20—H173	108.2	H351—O6—H352	105.5
C15—C20—H171	110.7		

Hydrogen-bond geometry ( $\text{\AA}$ ,  $^\circ$ )

<i>D</i> —H $\cdots$ <i>A</i>	<i>D</i> —H	H $\cdots$ <i>A</i>	<i>D</i> $\cdots$ <i>A</i>	<i>D</i> —H $\cdots$ <i>A</i>
N7—H141 $\cdots$ O2 <sup>i</sup>	0.85	2.12	2.942 (4)	163
N7—H142 $\cdots$ O6 <sup>ii</sup>	0.84	2.15	2.970 (4)	165
O4—H181 $\cdots$ O6	0.81	1.93	2.717 (3)	164
O4—H182 $\cdots$ N5 <sup>ii</sup>	0.80	2.25	3.051 (4)	176
O5—H341 $\cdots$ O1	0.82	2.34	3.079 (4)	151
O5—H341 $\cdots$ O2	0.82	2.23	2.896 (4)	139
O5—H342 $\cdots$ N4 <sup>iii</sup>	0.82	2.04	2.844 (4)	166
O6—H351 $\cdots$ O5	0.83	1.92	2.740 (4)	174
O6—H352 $\cdots$ N5 <sup>iv</sup>	0.82	2.05	2.871 (4)	176
O7—H331 $\cdots$ O5 <sup>i</sup>	0.80	2.25	2.941 (4)	145
O7—H332 $\cdots$ O3	0.81	2.23	2.962 (5)	151

Symmetry codes: (i)  $x+1, y+1, z$ ; (ii)  $-x+1, -y+1, -z+1$ ; (iii)  $x-1, y-1, z$ ; (iv)  $x, y-1, z$ .

# Crystal structure of (2-amino-7-methyl-4-oxido-pteridine-6-carboxylato- $\kappa^3 O^4, N^5, O^6$ )aqua(1,10-phenanthroline- $\kappa^2 N, N'$ )copper(II) trihydrate

Siddhartha S. Baisya and Parag S. Roy\*

Received 24 September 2014  
Accepted 9 October 2014

Department of Chemistry, University of North Bengal, Siliguri 734 013, India. \*Correspondence e-mail: psmbu@gmail.com

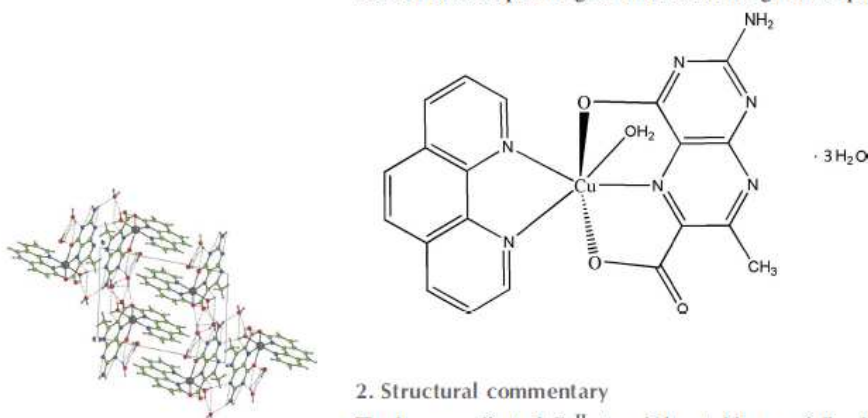
Edited by D.-J. Xu, Zhejiang University (Yuquan Campus), China

**Keywords:** pterin; copper;  $\pi$ - $\pi$  stacking; crystal structure.**CCDC reference:** 1028413**Supporting information:** this article has supporting information at journals.iucr.org/e

In the title compound,  $[\text{Cu}(\text{C}_8\text{H}_5\text{N}_5\text{O}_3)(\text{C}_{12}\text{H}_8\text{N}_2)(\text{H}_2\text{O})] \cdot 3\text{H}_2\text{O}$ , the  $\text{Cu}^{\text{II}}$  cation is  $O, N, O'$ -chelated by the 2-amino-7-methyl-4-oxidopteridine-6-carboxylate anion and  $N, N'$ -chelated by the 1,10-phenanthroline (phen) ligand. A water molecule further coordinates to the  $\text{Cu}^{\text{II}}$  cation to complete the elongated distorted octahedral coordination geometry. In the molecule, the pteridine ring system is essentially planar [maximum deviation = 0.055 (4) Å], and its mean plane is nearly perpendicular to the phen ring system [dihedral angle = 85.97 (3)°]. In the crystal,  $N-H \cdots O$ ,  $O-H \cdots N$  and  $O-H \cdots O$  hydrogen bonds, as well as weak  $C-H \cdots O$  hydrogen bonds and  $C-H \cdots \pi$  interactions, link the complex molecules and lattice water molecules into a three-dimensional supramolecular architecture. Extensive  $\pi$ - $\pi$  stacking between nearly parallel aromatic rings of adjacent molecules are also observed, the centroid-to-centroid distances being 3.352 (2), 3.546 (3), 3.706 (3) and 3.744 (3) Å.

## 1. Chemical context

The ubiquitous presence of pterins in nature including several classes of metalloenzymes, has catalysed developments of their coordination chemistry (Basu & Burgmayer, 2011; Burgmayer, 1998; Dix & Benkovic, 1988; Erlandsen *et al.*, 2000; Fitzpatrick, 2003). Literature survey reveals the paucity of structurally characterized  $\text{Cu}^{\text{II}}$  complexes involving tridentate pterin coordination (Kohzuma *et al.*, 1989). The present work is concerned with the title complex, possessing both a tridentate pterin ligand and a  $\pi$ -acidic ligand like phen.



## 2. Structural commentary

The hexacoordinated  $\text{Cu}^{\text{II}}$  atom is located in an axially elongated distorted octahedron (Fig. 1 and Table 1). The equatorial plane is formed by the two N atoms of phen, the pyrazine ring N atom of the pterin ligand and the aqua O atom. The axial positions are occupied by the two pterin O

OPEN ACCESS

Table 1  
Selected bond lengths (Å).

Cu1—N1	2.002 (3)	Cu1—O1	2.384 (3)
Cu1—N2	2.037 (3)	Cu1—O2	2.304 (3)
Cu1—N6	1.999 (3)	Cu1—O4	2.019 (3)

Table 2  
Hydrogen-bond geometry (Å, °).

*C<sub>g</sub>* is the centroid of the N3/N4/C13–C16 ring.

<i>D</i> — <i>H</i> ··· <i>A</i>	<i>D</i> — <i>H</i>	<i>H</i> ··· <i>A</i>	<i>D</i> ··· <i>A</i>	<i>D</i> — <i>H</i> ··· <i>A</i>
O4—H4C···O5	0.82 (3)	1.92 (3)	2.722 (4)	169 (5)
O4—H4D···N4 <sup>i</sup>	0.81 (3)	2.26 (3)	3.038 (4)	161 (5)
O5—H5C···O6	0.82 (3)	1.96 (4)	2.748 (5)	162 (4)
O5—H5D···N4 <sup>ii</sup>	0.82 (5)	2.07 (5)	2.891 (5)	176 (3)
O6—H6C···O2	0.82 (3)	2.23 (3)	2.921 (4)	141 (5)
O6—H6C···O3	0.82 (3)	2.25 (4)	3.029 (4)	158 (5)
O7—H7C···O6	0.82 (2)	2.24 (3)	2.965 (6)	148 (5)
O7—H7D···O1 <sup>iii</sup>	0.81 (5)	2.16 (4)	2.943 (6)	162 (5)
N7—H7E···O5 <sup>i</sup>	0.85 (5)	2.17 (4)	2.998 (6)	162 (4)
N7—H7F···O3 <sup>iv</sup>	0.86 (4)	2.14 (5)	2.908 (5)	148 (4)
C1—H1···O3 <sup>v</sup>	0.93	2.47	3.175 (6)	133
C10—H10···O1 <sup>vi</sup>	0.93	2.54	3.406 (5)	155
C12—H12···O7 <sup>vii</sup>	0.93	2.57	3.343 (7)	140
C6—H6··· <i>C<sub>g</sub></i> <sup>viii</sup>	0.93	2.82	3.740 (5)	173

Symmetry codes: (i)  $-x+2, -y+2, -z+2$ ; (ii)  $x, y-1, z$ ; (iii)  $x-1, y-1, z$ ; (iv)  $x+1, y+1, z$ ; (v)  $x+1, y, z$ ; (vi)  $-x+2, -y+2, -z+1$ ; (vii)  $x, y+1, z$ .

atoms, with the former one forming the longest axial bond [2.384 (3) Å]. Apart from the characteristic Jahn–Teller effect, another reason for distortion from a regular octahedral geometry is that the pterin ligand forms two five-membered chelate rings with small bite angles [76.47 (10) and 74.66 (11)°]. Consideration of the charge balance of this complex indicates that this pterin ligand acts as a binategative tridentate *O,N,O'*-donor. A near orthogonal disposition of the phen ligand and pterin chelate ring helps to minimize the steric repulsion. Of the three axes, the least deviation from

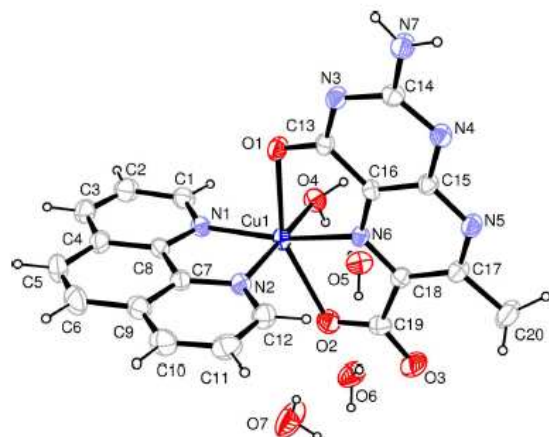


Figure 1  
The molecular structure of the title compound. Displacement ellipsoids are drawn at the 30% probability level.

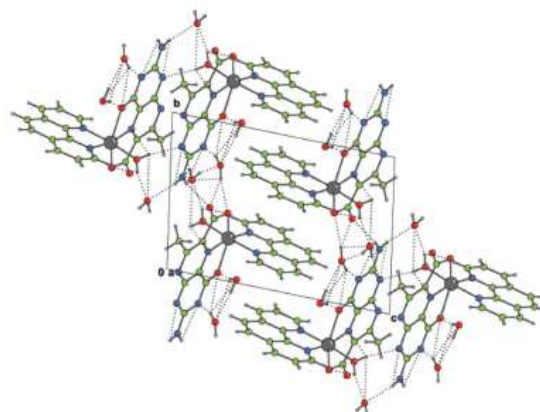


Figure 2  
The crystal packing diagram of the title compound, viewed along the *a* axis. Hydrogen bonds (dotted lines) assist the formation of a layer structure parallel to (001).

linearity is observed in the O4—Cu1—N2 direction [174.45 (13)°]. Location of the pyrazine ring N atom (N6) in the equatorial plane is in agreement with earlier observations on related copper and cobalt complexes (Baisya *et al.*, 2013; Odani *et al.*, 1992); the Cu1—N6 bond length [1.999 (3) Å] is the shortest one in this case.

The multiple bond character of the O1—C13 bond [1.237 (4) Å] may be elucidated in the light of Joule's hypothesis (Beddoes *et al.*, 1993; Russell *et al.*, 1992), suggesting electron-density withdrawal from the pyrazine ring N5 by the pyrimidine ring C13 carbonyl group through mesomeric interaction. Formation of the O1—Cu1 bond assists this electron flow towards atom O1, with possible participation of the electron-rich N7—C14 [1.327 (5) Å] bond in this process.

### 3. Supramolecular features

In the crystal, intermolecular N—H···O, O—H···N and O—H···O hydrogen bonds (Table 2) link the complex molecules and lattice water molecules into a layer parallel to (001) (Fig. 2). Intermolecular weak C—H···O hydrogen bonds and C—H··· $\pi$  interactions are also observed in the crystal. In addition,  $\pi$ – $\pi$  stacking between nearly parallel pterin ring systems of adjacent molecules occurs in the crystal structure, the centroid–centroid distance being 3.352 (2) Å (Fig. 3). Again, the nearly parallel phen rings of adjacent molecules also display  $\pi$ – $\pi$  stacking interactions with centroid distances of 3.546 (3), 3.706 (3) and 3.744 (3) Å. These intermolecular interactions link the molecules into a three-dimensional supramolecular architecture.

### 4. Database survey

The crystal structures of copper(II) complexes chelated by the pterin-6-carboxylate anion have been reported by Kohzuma *et*

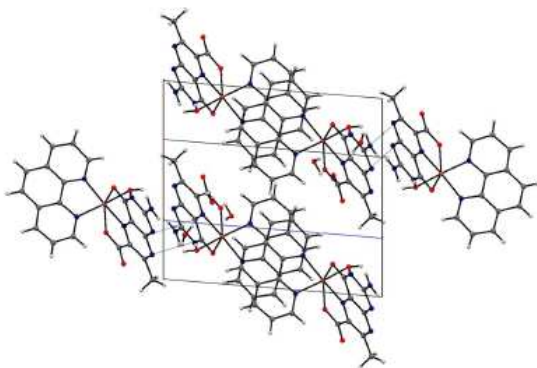


Figure 3  
A molecular packing diagram highlighting  $\pi$ - $\pi$  stacking interactions between neighbouring phen-phen and pterin-pterin rings.

*al.* (1989) and Funahashi *et al.* (1999). In both complexes, the  $\text{Cu}^{\text{II}}$  atom has the elongated distorted octahedral coordination geometry.

## 5. Synthesis and crystallization

2-Amino-4-hydroxy-7-methylpteridine-6-carboxylic acid sesquihydrate ( $\text{C}_8\text{H}_7\text{N}_5\text{O}_3 \cdot 1.5\text{H}_2\text{O}$ ) was obtained by a published procedure (Wittle *et al.*, 1947). The title complex could be obtained by two different methods; the crystals obtained by method B have been used for the present structural study. The X-ray structural data of the crystals synthesized by method A, are available from the Cambridge Crystallographic Data Center (CCDC deposition No. 985054).

**Method A.** The title complex was synthesized by bubbling oxygen into an aqueous reaction mixture (50 ml) containing  $\text{Cu}(\text{NO}_3)_2 \cdot 3\text{H}_2\text{O}$  (30 mg, 0.125 mmol), 1,10-phenanthroline monohydrate (25 mg, 0.125 mmol) and pterin (31 mg, 0.125 mmol) dissolved in NaOH (11 mg, 0.275 mmol) for 60 h at 310–312 K under subdued light; additional NaOH solution was added for adjusting the initial pH at 10.5. Within a short while the initial bright-green solution turned hazy blue due to the presence of a fine white precipitate which gradually disappeared substantially. The final blue solution was slightly hazy. Upon storage under aerobic conditions for one week the clear blue solution yielded green crystals, suitable for X-ray structure determination. Analysis calculated for  $\text{C}_{20}\text{H}_{21}\text{CuN}_7\text{O}_7$ : C 44.90, H 3.93, N 18.33%; found: C 44.38, H 4.06, N 17.65%. ESIMS data: the molecular ion peak  $[M + 2\text{H}]^+$  appeared at 536.4 (relative abundance = 41.2%); the  $[M - 4\text{H}_2\text{O} - 3\text{H}]^+$  peak was observed at 459.2 (relative abundance = 100%), indicating stability of the desolvated ternary species arising from the title complex.

**Method B.** Using  $\text{NaBH}_4$  reduction in equimolar proportion of the original complex (obtained by **Method A**) and subsequent aerial reoxidation of the reduced complex to the present crystals merits attention due to the involvement of intricate redox chemistry. The  $\text{NaBH}_4$  treatment (Beddoes *et al.*, 1993;

Table 3  
Experimental details.

Crystal data	
Chemical formula	$[\text{Cu}(\text{C}_8\text{H}_5\text{N}_3\text{O}_3)(\text{C}_{12}\text{H}_8\text{N}_2)(\text{H}_2\text{O})] \cdot 3\text{H}_2\text{O}$
$M_r$	534.98
Crystal system, space group	Triclinic, $P\bar{1}$
Temperature (K)	273
$a, b, c$ (Å)	8.5399 (17), 10.038 (2), 13.601 (3)
$\alpha, \beta, \gamma$ (°)	97.292 (3), 94.587 (3), 110.999 (3)
$V$ (Å <sup>3</sup> )	1069.8 (4)
$Z$	2
Radiation type	Mo $K\alpha$
$\mu$ (mm <sup>-1</sup> )	1.08
Crystal size (mm)	0.20 × 0.05 × 0.03
Data collection	
Diffractometer	Bruker Kappa APEXII
Absorption correction	Multi-scan (SADABS; Bruker, 2001)
$T_{\text{min}}, T_{\text{max}}$	0.813, 0.968
No. of measured, independent and observed [ $I > 2\sigma(I)$ ] reflections	8227, 4134, 3590
$R_{\text{int}}$	0.024
$(\sin \theta/\lambda)_{\text{max}}$ (Å <sup>-1</sup> )	0.617
Refinement	
$R[F^2 > 2\sigma(F^2)], wR(F^2), S$	0.051, 0.136, 1.15
No. of reflections	4134
No. of parameters	349
No. of restraints	10
H-atom treatment	H atoms treated by a mixture of independent and constrained refinement
$\Delta\rho_{\text{max}}, \Delta\rho_{\text{min}}$ (e Å <sup>-3</sup> )	0.66, -0.31

Computer programs: APEX2 and SAINT (Bruker, 2007), SHELXS97 (Sheldrick, 2008), CRYSTALS (Betteridge *et al.*, 2003) and CAMERON (Watkin *et al.*, 1996).

Russell *et al.*, 1992) leads to the formation of a dark-brown compound in solution, which could be isolated in the solid state and characterized (microanalysis, ESIMS, 2DNMR, *etc.*) to be  $\text{Na}_2[\text{Cu}_2(L')_2(\text{phen})(\text{H}_2\text{O})_4] \cdot 2\text{H}_2\text{O}$ , where  $L'$  is the 7,8-dihydro form of the present pterin ligand anion ( $\text{C}_8\text{H}_5\text{N}_3\text{O}_3$ ) (Burgmayer, 1998); it is able to convert bromobenzene into 4-bromophenol in the presence of oxygen (Baisya & Roy, unpublished results). However, in the absence of any substrate (*e.g.* bromobenzene; Dix & Benkovic, 1988), aerial oxidation reconverts the reduced compound to the title complex (**Method B**).

Although the title compound could be obtained by two alternative methods, the present structural data obtained using the crystals from **Method B**, represent better accuracy [ $R = 0.057$  and  $wR(F^2) = 0.135$ ] as compared to the other one [ $R = 0.113$  and  $wR(F^2) = 0.279$ ].

Cyclic voltammetry data of this complex indicate an  $E^{\text{oc}}$  value of -0.68 V; now using an  $E^{\text{oc}}$  value of -0.80 V for  $\text{NaBH}_4$  in neutral medium (Chatenet *et al.*, 2006; Celikkan *et al.*, 2007), an  $E_{\text{cell}}$  value ( $E_{\text{cell}} = E_1 - E_2$ ; Segel, 1976) of 0.12 V is obtained for the  $\text{Cu}^{\text{II}} \rightarrow \text{Cu}^{\text{I}}$  reduction in the title complex; it is within the range of  $E_{\text{cell}}$  value (0.033 V) for the  $\text{Fe}^{\text{III}}$ -tetrahydrobiopterin reduction in phenylalanine hydroxylase (Hagedoorn *et al.*, 2001; Gorren *et al.*, 2001). The dark-brown reduced complex (as above) shows an  $E^{\text{oc}}$  value of -0.67 V (cyclic voltammetry); using an  $E^{\text{oc}}$  value of 0.70 V for the

O<sub>2</sub>/H<sub>2</sub>O<sub>2</sub> couple, an  $E_{\text{cell}}$  value of 1.37 V is obtained, indicating facile aerial oxidation. Now using an  $E^{\circ'}$  value of 0.19 V for the chelated pterin ligand (oxidized/aromatic; Eberlein *et al.*, 1984), synchronization of its reduction or oxidation with the above redox process may be rationalized. Actually, for pterin-containing metalloenzymes the redox processes at the metal centres could be linked to the changes in the pterin ring oxidation level (Burgmayer, 1998; Erlandsen *et al.*, 2000).

## 6. Refinement

Crystal data, data collection and structure refinement details are summarized in Table 3. H atoms attached to N and O atoms were located in a difference Fourier map and refined with distance constraints of N–H = 0.86 (1) Å and O–H = 0.82 (1) Å. H atoms attached to C atoms were positioned geometrically, with C–H = 0.93–0.96 Å, and refined in riding mode. For all atoms,  $U_{\text{iso}}(\text{H}) = 1.2\text{--}1.5U_{\text{eq}}(\text{C,N,O})$ .

## Acknowledgements

The authors express their gratitude to UGC, New Delhi, for financial assistance (SAP–DRS program). Thanks are due to CSMCRI, Bhavnagar, India, for the X-ray structural and microanalytical data. ESIMS data have been obtained from the SAIF, CDRI, Lucknow. Infrastructural support of University of North Bengal is duly acknowledged. Cyclic voltammetric data have been recorded by Professor J. P. Naskar, Jadavpur University, Kolkata, India.

## References

- Baisya, S. S., Sen, S. & Roy, P. S. (2013). *Acta Cryst.* **E69**, m70–m71.
- Basu, P. & Burgmayer, S. J. N. (2011). *Coord. Chem. Rev.* **255**, 1016–1038.
- Beddoes, R. L., Russell, J. R., Garner, C. D. & Joule, J. A. (1993). *Acta Cryst.* **C49**, 1649–1652.
- Betteridge, P. W., Carruthers, J. R., Cooper, R. I., Prout, K. & Watkin, D. J. (2003). *J. Appl. Cryst.* **36**, 1487.
- Bruker (2001). *SADABS*. Bruker AXS Inc., Madison, Wisconsin, USA.
- Bruker (2007). *APEX2* and *SAINT*. Bruker AXS Inc., Madison, Wisconsin, USA.
- Burgmayer, S. J. N. (1998). *Struct. Bond.* **92**, 67–119.
- Celikkan, H., Sahin, M., Aksu, M. L. & Nejat Veziroglu, T. (2007). *Int. J. Hydrogen Energy*, **32**, 588–593.
- Chatenet, M., Micoud, F., Roche, I. & Chainet, E. (2006). *Electrochim. Acta*, **51**, 5459–5467.
- Dix, T. A. & Benkovic, S. J. (1988). *Acc. Chem. Res.* **21**, 101–107.
- Eberlein, G., Bruice, T. C., Lazarus, R. A., Henrie, R. & Benkovic, S. J. (1984). *J. Am. Chem. Soc.* **106**, 7916–7924.
- Erlandsen, H., Bjørge, E., Flatmark, T. & Stevens, R. C. (2000). *Biochemistry*, **39**, 2208–2217.
- Fitzpatrick, P. F. (2003). *Biochemistry*, **42**, 14083–14091.
- Funahashi, Y., Kato, C. & Yamauchi, O. (1999). *Bull. Chem. Soc. Jpn.* **72**, 415–424.
- Gorren, A. C. F., Kungl, A. J., Schmidt, K., Werner, E. R. & Mayer, B. (2001). *Nitric Oxide: Biol. Chem.* **5**, 176–186.
- Hagedoorn, P. L., Schmidt, P. P., Andersson, K. K., Hagen, W. R., Flatmark, T. & Martínez, A. (2001). *J. Biol. Chem.* **276**, 22850–22856.
- Kohzuma, T., Masuda, H. & Yamauchi, O. (1989). *J. Am. Chem. Soc.* **111**, 3431–3433.
- Odani, A., Masuda, H., Inukai, K. & Yamauchi, O. (1992). *J. Am. Chem. Soc.* **114**, 6294–6300.
- Russell, J. R., Garner, C. D. & Joule, J. A. (1992). *J. Chem. Soc. Perkin Trans. 1*, pp. 1245–1249.
- Segel, I. H. (1976). *Biochemical Calculations*, 2nd ed., pp. 172–179. New York: John Wiley & Sons.
- Sheldrick, G. M. (2008). *Acta Cryst.* **A64**, 112–122.
- Watkin, D. J., Prout, C. K. & Pearce, L. J. (1996). *CAMERON*. Chemical Crystallography Laboratory, Oxford, England.
- Wittle, E. L., O'Dell, B. L., Vandenbelt, J. M. & Pfiffner, J. J. (1947). *J. Am. Chem. Soc.* **69**, 1786–1792.

## supporting information

*Acta Cryst.* (2014). E70, 348–351 [doi:10.1107/S1600536814022302]

## Crystal structure of (2-amino-7-methyl-4-oxopteridine-6-carboxylato- $\kappa^3O^4, N^5, O^6$ )aqua(1,10-phenanthroline- $\kappa^2N, N'$ )copper(II) trihydrate

Siddhartha S. Baisya and Parag S. Roy

### Computing details

Data collection: *APEX2* (Bruker, 2007); cell refinement: *SAINT* (Bruker, 2007); data reduction: *SAINT* (Bruker, 2007); program(s) used to solve structure: *SHELXS97* (Sheldrick, 2008); program(s) used to refine structure: *CRYSTALS* (Betteridge *et al.*, 2003); molecular graphics: *CAMERON* (Watkin *et al.*, 1996); software used to prepare material for publication: *CRYSTALS* (Betteridge *et al.*, 2003).

(2-Amino-7-methyl-4-oxopteridine-6-carboxylato- $\kappa^3O^4, N^5, O^6$ )aqua(1,10-phenanthroline- $\kappa^2N, N'$ )copper(II) trihydrate

### Crystal data

[Cu(C<sub>8</sub>H<sub>5</sub>N<sub>5</sub>O<sub>3</sub>)(C<sub>12</sub>H<sub>8</sub>N<sub>2</sub>)(H<sub>2</sub>O)]·3H<sub>2</sub>O  
*M<sub>r</sub>* = 534.98  
 Triclinic, *P* $\bar{1}$   
 Hall symbol: -P 1  
*a* = 8.5399 (17) Å  
*b* = 10.038 (2) Å  
*c* = 13.601 (3) Å  
 $\alpha$  = 97.292 (3)°  
 $\beta$  = 94.587 (3)°  
 $\gamma$  = 110.999 (3)°  
*V* = 1069.8 (4) Å<sup>3</sup>

*Z* = 2  
*F*(000) = 550  
*D<sub>x</sub>* = 1.661 Mg m<sup>-3</sup>  
 Mo *K* $\alpha$  radiation,  $\lambda$  = 0.71073 Å  
 Cell parameters from 4804 reflections  
 $\theta$  = 3.0–29.0°  
 $\mu$  = 1.08 mm<sup>-1</sup>  
*T* = 273 K  
 Needle, green  
 0.20 × 0.05 × 0.03 mm

### Data collection

Bruker Kappa APEXII  
 diffractometer  
 Radiation source: fine-focus sealed tube  
 Graphite monochromator  
 $\varphi$  &  $\omega$  scans  
 Absorption correction: multi-scan  
 (*SADABS*; Bruker, 2001)  
*T<sub>min</sub>* = 0.813, *T<sub>max</sub>* = 0.968

8227 measured reflections  
 4134 independent reflections  
 3590 reflections with *I* > 2 $\sigma$ (*I*)  
*R<sub>int</sub>* = 0.024  
 $\theta_{\max}$  = 26.0°,  $\theta_{\min}$  = 1.5°  
*h* = -10→10  
*k* = -12→12  
*l* = -16→16

### Refinement

Refinement on *F*<sup>2</sup>  
 Least-squares matrix: full  
*R* [*F*<sup>2</sup> > 2 $\sigma$ (*F*<sup>2</sup>)] = 0.051  
*wR*(*F*<sup>2</sup>) = 0.136  
*S* = 1.15  
 4134 reflections  
 349 parameters

10 restraints  
 Primary atom site location: structure-invariant  
 direct methods  
 Secondary atom site location: difference Fourier  
 map  
 Hydrogen site location: inferred from  
 neighbouring sites

H atoms treated by a mixture of independent

and constrained refinement  
 $w = 1/[\sigma^2(F_o^2) + (0.052P)^2 + 1.8801P]$   
 where  $P = (F_o^2 + 2F_c^2)/3$

$(\Delta/\sigma)_{\max} = 0.001$

$\Delta\rho_{\max} = 0.66 \text{ e } \text{\AA}^{-3}$

$\Delta\rho_{\min} = -0.31 \text{ e } \text{\AA}^{-3}$

#### Special details

**Experimental.** The crystal was placed in the cold stream of an Oxford Cryosystems open-flow nitrogen cryostat (Cosier & Glazer, 1986) with a nominal stability of 0.1 K.

Cosier, J. & Glazer, A. M., 1986. *J. Appl. Cryst.* 105–107.

**Geometry.** All esds (except the esd in the dihedral angle between two l.s. planes) are estimated using the full covariance matrix. The cell esds are taken into account individually in the estimation of esds in distances, angles and torsion angles; correlations between esds in cell parameters are only used when they are defined by crystal symmetry. An approximate (isotropic) treatment of cell esds is used for estimating esds involving l.s. planes.

**Refinement.** Refinement of  $F^2$  against ALL reflections. The weighted R-factor wR and goodness of fit S are based on  $F^2$ , conventional R-factors R are based on F, with F set to zero for negative  $F^2$ . The threshold expression of  $F^2 > 2\text{sigma}(F^2)$  is used only for calculating R-factors(gt) etc. and is not relevant to the choice of reflections for refinement. R-factors based on  $F^2$  are statistically about twice as large as those based on F, and R- factors based on ALL data will be even larger.

#### Fractional atomic coordinates and isotropic or equivalent isotropic displacement parameters ( $\text{\AA}^2$ )

	x	y	z	$U_{\text{iso}}^*/U_{\text{eq}}$
Cu1	0.96752 (6)	0.72720 (5)	0.73038 (3)	0.02733 (16)
O1	1.1883 (3)	0.9602 (3)	0.7732 (2)	0.0353 (7)
O2	0.6970 (4)	0.5696 (3)	0.7379 (2)	0.0402 (7)
O3	0.4778 (4)	0.5558 (3)	0.8185 (3)	0.0463 (8)
O4	1.0500 (4)	0.6534 (3)	0.8475 (2)	0.0356 (7)
O5	0.8413 (4)	0.4056 (3)	0.9019 (3)	0.0425 (7)
O6	0.5380 (4)	0.2754 (3)	0.7786 (3)	0.0496 (8)
O7	0.5000 (6)	−0.0210 (5)	0.6878 (5)	0.0974 (17)
N1	1.1082 (4)	0.6636 (3)	0.6383 (2)	0.0288 (7)
N2	0.8823 (4)	0.7835 (4)	0.6039 (2)	0.0296 (7)
N3	1.2193 (4)	1.1811 (3)	0.8566 (2)	0.0309 (7)
N4	0.9983 (4)	1.2067 (3)	0.9516 (2)	0.0303 (7)
N5	0.7502 (4)	1.0056 (4)	0.9482 (3)	0.0330 (8)
N6	0.8684 (4)	0.8399 (3)	0.8203 (2)	0.0247 (7)
N7	1.2417 (5)	1.3974 (4)	0.9441 (3)	0.0410 (9)
C1	1.2221 (5)	0.6068 (5)	0.6587 (3)	0.0360 (9)
H1	1.2374	0.5846	0.7223	0.043*
C2	1.3205 (6)	0.5790 (5)	0.5872 (4)	0.0454 (11)
H2	1.4011	0.5403	0.6039	0.054*
C3	1.2988 (6)	0.6084 (5)	0.4932 (4)	0.0450 (11)
H3	1.3617	0.5871	0.4452	0.054*
C4	1.1804 (5)	0.6712 (5)	0.4691 (3)	0.0374 (10)
C5	1.1463 (6)	0.7074 (6)	0.3733 (3)	0.0502 (12)
H5	1.2072	0.6912	0.3224	0.060*
C6	1.0283 (7)	0.7643 (5)	0.3551 (3)	0.0485 (12)
H6	1.0084	0.7855	0.2918	0.058*
C7	0.9651 (5)	0.7606 (4)	0.5263 (3)	0.0291 (8)
C8	1.0885 (5)	0.6975 (4)	0.5453 (3)	0.0295 (8)

## supporting information

C9	0.9327 (6)	0.7929 (5)	0.4312 (3)	0.0384 (10)
C10	0.8072 (6)	0.8508 (5)	0.4183 (3)	0.0449 (11)
H10	0.7811	0.8741	0.3566	0.054*
C11	0.7228 (6)	0.8730 (5)	0.4962 (4)	0.0459 (11)
H11	0.6386	0.9106	0.4877	0.055*
C12	0.7642 (5)	0.8386 (5)	0.5887 (3)	0.0376 (10)
H12	0.7070	0.8550	0.6415	0.045*
C13	1.1328 (5)	1.0386 (4)	0.8256 (3)	0.0275 (8)
C14	1.1494 (5)	1.2573 (4)	0.9168 (3)	0.0298 (8)
C15	0.9039 (5)	1.0639 (4)	0.9189 (3)	0.0276 (8)
C16	0.9640 (5)	0.9774 (4)	0.8548 (3)	0.0245 (8)
C17	0.6568 (5)	0.8674 (4)	0.9142 (3)	0.0330 (9)
C18	0.7141 (5)	0.7807 (4)	0.8461 (3)	0.0274 (8)
C19	0.6205 (5)	0.6222 (4)	0.7984 (3)	0.0316 (9)
C20	0.4884 (6)	0.8090 (5)	0.9510 (4)	0.0537 (13)
H20A	0.4874	0.8722	1.0100	0.081*
H20B	0.4695	0.7143	0.9666	0.081*
H20C	0.4006	0.8032	0.9000	0.081*
H4C	0.984 (5)	0.575 (3)	0.856 (4)	0.050*
H4D	1.062 (6)	0.702 (5)	0.9021 (19)	0.050*
H5C	0.750 (3)	0.351 (4)	0.871 (3)	0.046 (15)*
H5D	0.882 (6)	0.346 (4)	0.915 (4)	0.054 (16)*
H6C	0.540 (6)	0.358 (2)	0.778 (4)	0.050*
H6D	0.448 (3)	0.215 (4)	0.750 (3)	0.050*
H7C	0.548 (6)	0.0668 (15)	0.705 (4)	0.050*
H7D	0.415 (4)	-0.043 (6)	0.715 (4)	0.050*
H7E	1.204 (6)	1.455 (4)	0.977 (3)	0.050*
H7F	1.338 (3)	1.442 (5)	0.926 (4)	0.050*

### Atomic displacement parameters ( $\text{\AA}^2$ )

	$U^{11}$	$U^{22}$	$U^{33}$	$U^{12}$	$U^{13}$	$U^{23}$
Cu1	0.0323 (3)	0.0302 (3)	0.0238 (3)	0.0159 (2)	0.00750 (18)	0.00499 (18)
O1	0.0324 (15)	0.0302 (15)	0.0431 (17)	0.0104 (12)	0.0163 (13)	0.0017 (12)
O2	0.0420 (17)	0.0321 (16)	0.0416 (17)	0.0097 (13)	0.0077 (14)	0.0001 (13)
O3	0.0329 (16)	0.0410 (18)	0.055 (2)	0.0011 (14)	0.0115 (14)	0.0083 (15)
O4	0.0413 (17)	0.0350 (17)	0.0323 (16)	0.0151 (14)	0.0047 (13)	0.0092 (13)
O5	0.0405 (19)	0.0339 (18)	0.053 (2)	0.0139 (15)	0.0021 (16)	0.0098 (15)
O6	0.0364 (17)	0.0333 (17)	0.076 (3)	0.0082 (14)	0.0124 (17)	0.0077 (17)
O7	0.073 (3)	0.065 (3)	0.155 (5)	0.025 (3)	0.057 (3)	-0.004 (3)
N1	0.0300 (17)	0.0279 (17)	0.0277 (17)	0.0113 (14)	0.0037 (13)	0.0000 (13)
N2	0.0300 (17)	0.0322 (18)	0.0267 (17)	0.0114 (14)	0.0043 (13)	0.0058 (13)
N3	0.0299 (17)	0.0273 (17)	0.0348 (18)	0.0083 (14)	0.0109 (14)	0.0058 (14)
N4	0.0328 (18)	0.0244 (16)	0.0339 (18)	0.0108 (14)	0.0080 (14)	0.0029 (13)
N5	0.0303 (18)	0.0308 (18)	0.040 (2)	0.0128 (15)	0.0123 (15)	0.0034 (15)
N6	0.0257 (16)	0.0248 (16)	0.0249 (16)	0.0090 (13)	0.0077 (13)	0.0069 (12)
N7	0.039 (2)	0.0264 (19)	0.050 (2)	0.0044 (16)	0.0169 (18)	-0.0010 (16)
C1	0.035 (2)	0.036 (2)	0.037 (2)	0.0165 (19)	0.0012 (18)	-0.0006 (18)

supporting information

C2	0.038 (2)	0.046 (3)	0.053 (3)	0.022 (2)	0.004 (2)	-0.005 (2)
C3	0.038 (2)	0.046 (3)	0.046 (3)	0.013 (2)	0.013 (2)	-0.006 (2)
C4	0.036 (2)	0.034 (2)	0.037 (2)	0.0077 (18)	0.0114 (18)	-0.0016 (17)
C5	0.054 (3)	0.060 (3)	0.033 (2)	0.016 (3)	0.018 (2)	0.002 (2)
C6	0.062 (3)	0.053 (3)	0.029 (2)	0.016 (2)	0.011 (2)	0.013 (2)
C7	0.029 (2)	0.0248 (19)	0.029 (2)	0.0055 (16)	0.0053 (16)	0.0025 (15)
C8	0.030 (2)	0.027 (2)	0.026 (2)	0.0059 (16)	0.0054 (16)	-0.0001 (15)
C9	0.041 (2)	0.036 (2)	0.032 (2)	0.0060 (19)	0.0026 (18)	0.0075 (18)
C10	0.048 (3)	0.050 (3)	0.035 (2)	0.014 (2)	0.000 (2)	0.018 (2)
C11	0.038 (2)	0.050 (3)	0.052 (3)	0.017 (2)	0.000 (2)	0.017 (2)
C12	0.038 (2)	0.040 (2)	0.039 (2)	0.019 (2)	0.0067 (19)	0.0082 (19)
C13	0.029 (2)	0.030 (2)	0.0250 (19)	0.0112 (16)	0.0066 (15)	0.0077 (15)
C14	0.032 (2)	0.0254 (19)	0.031 (2)	0.0090 (16)	0.0032 (16)	0.0052 (16)
C15	0.027 (2)	0.0265 (19)	0.029 (2)	0.0104 (16)	0.0052 (15)	0.0047 (15)
C16	0.0288 (19)	0.0242 (19)	0.0216 (18)	0.0105 (16)	0.0056 (15)	0.0044 (14)
C17	0.027 (2)	0.034 (2)	0.039 (2)	0.0114 (17)	0.0088 (17)	0.0074 (17)
C18	0.0260 (19)	0.029 (2)	0.028 (2)	0.0110 (16)	0.0049 (15)	0.0076 (15)
C19	0.031 (2)	0.031 (2)	0.031 (2)	0.0085 (17)	0.0003 (17)	0.0091 (16)
C20	0.036 (3)	0.045 (3)	0.076 (4)	0.009 (2)	0.026 (2)	-0.001 (2)

Geometric parameters (Å, °)

Cu1—N1	2.002 (3)	N7—H7E	0.856 (10)
Cu1—N2	2.037 (3)	N7—H7F	0.854 (11)
Cu1—N6	1.999 (3)	C1—C2	1.400 (6)
Cu1—O1	2.384 (3)	C1—H1	0.9300
Cu1—O2	2.304 (3)	C2—C3	1.361 (7)
Cu1—O4	2.019 (3)	C2—H2	0.9300
O1—C13	1.237 (5)	C3—C4	1.408 (7)
O2—C19	1.267 (5)	C3—H3	0.9300
O3—C19	1.234 (5)	C4—C8	1.404 (6)
O4—H4C	0.819 (10)	C4—C5	1.432 (7)
O4—H4D	0.812 (10)	C5—C6	1.346 (7)
O5—H5C	0.819 (10)	C5—H5	0.9300
O5—H5D	0.820 (10)	C6—C9	1.430 (7)
O6—H6C	0.823 (10)	C6—H6	0.9300
O6—H6D	0.817 (10)	C7—C9	1.403 (6)
O7—H7C	0.819 (10)	C7—C8	1.433 (6)
O7—H7D	0.815 (10)	C9—C10	1.400 (6)
N1—C1	1.321 (5)	C10—C11	1.367 (7)
N1—C8	1.363 (5)	C10—H10	0.9300
N2—C12	1.328 (5)	C11—C12	1.398 (6)
N2—C7	1.357 (5)	C11—H11	0.9300
N3—C13	1.345 (5)	C12—H12	0.9300
N3—C14	1.364 (5)	C13—C16	1.460 (5)
N4—C14	1.355 (5)	C15—C16	1.405 (5)
N4—C15	1.363 (5)	C17—C18	1.425 (6)
N5—C17	1.326 (5)	C17—C20	1.499 (6)

## supporting information

N5—C15	1.348 (5)	C18—C19	1.528 (5)
N6—C16	1.326 (5)	C20—H20A	0.9600
N6—C18	1.333 (5)	C20—H20B	0.9600
N7—C14	1.327 (5)	C20—H20C	0.9600
N6—Cu1—N1	165.66 (13)	C6—C5—H5	119.2
N6—Cu1—O4	91.01 (12)	C4—C5—H5	119.2
N1—Cu1—O4	93.79 (13)	C5—C6—C9	121.4 (4)
N6—Cu1—N2	93.79 (13)	C5—C6—H6	119.3
N1—Cu1—N2	82.20 (13)	C9—C6—H6	119.3
O4—Cu1—N2	174.45 (13)	N2—C7—C9	123.3 (4)
N6—Cu1—O2	74.74 (11)	N2—C7—C8	116.3 (3)
N1—Cu1—O2	118.84 (12)	C9—C7—C8	120.4 (4)
O4—Cu1—O2	88.62 (12)	N1—C8—C4	123.1 (4)
N2—Cu1—O2	89.98 (12)	N1—C8—C7	117.1 (3)
N6—Cu1—O1	76.45 (11)	C4—C8—C7	119.8 (4)
N1—Cu1—O1	89.79 (11)	C10—C9—C7	116.7 (4)
O4—Cu1—O1	93.07 (12)	C10—C9—C6	125.0 (4)
N2—Cu1—O1	90.74 (12)	C7—C9—C6	118.3 (4)
O2—Cu1—O1	151.17 (10)	C11—C10—C9	120.1 (4)
C13—O1—Cu1	107.2 (2)	C11—C10—H10	120.0
C19—O2—Cu1	113.0 (3)	C9—C10—H10	120.0
Cu1—O4—H4C	114 (4)	C10—C11—C12	119.4 (4)
Cu1—O4—H4D	116 (4)	C10—C11—H11	120.3
H4C—O4—H4D	101 (5)	C12—C11—H11	120.3
H5C—O5—H5D	100 (5)	N2—C12—C11	122.4 (4)
H6C—O6—H6D	111 (5)	N2—C12—H12	118.8
H7C—O7—H7D	106 (5)	C11—C12—H12	118.8
C1—N1—C8	118.7 (3)	O1—C13—N3	123.3 (3)
C1—N1—Cu1	128.8 (3)	O1—C13—C16	119.8 (3)
C8—N1—Cu1	112.3 (3)	N3—C13—C16	116.9 (3)
C12—N2—C7	118.2 (3)	N7—C14—N4	116.9 (4)
C12—N2—Cu1	129.9 (3)	N7—C14—N3	115.4 (4)
C7—N2—Cu1	111.9 (3)	N4—C14—N3	127.6 (3)
C13—N3—C14	118.8 (3)	N5—C15—N4	119.1 (3)
C14—N4—C15	115.3 (3)	N5—C15—C16	119.8 (3)
C17—N5—C15	119.0 (3)	N4—C15—C16	121.0 (3)
C16—N6—C18	120.8 (3)	N6—C16—C15	120.5 (3)
C16—N6—Cu1	117.0 (2)	N6—C16—C13	119.4 (3)
C18—N6—Cu1	122.2 (3)	C15—C16—C13	120.1 (3)
C14—N7—H7E	122 (4)	N5—C17—C18	121.4 (3)
C14—N7—H7F	125 (3)	N5—C17—C20	116.2 (4)
H7E—N7—H7F	112 (5)	C18—C17—C20	122.4 (4)
N1—C1—C2	121.7 (4)	N6—C18—C17	118.3 (3)
N1—C1—H1	119.2	N6—C18—C19	114.0 (3)
C2—C1—H1	119.2	C17—C18—C19	127.7 (3)
C3—C2—C1	120.3 (4)	O3—C19—O2	124.7 (4)
C3—C2—H2	119.9	O3—C19—C18	119.5 (4)

## supporting information

C1—C2—H2	119.9	O2—C19—C18	115.8 (3)
C2—C3—C4	119.6 (4)	C17—C20—H20A	109.5
C2—C3—H3	120.2	C17—C20—H20B	109.5
C4—C3—H3	120.2	H20A—C20—H20B	109.5
C8—C4—C3	116.6 (4)	C17—C20—H20C	109.5
C8—C4—C5	118.5 (4)	H20A—C20—H20C	109.5
C3—C4—C5	124.9 (4)	H20B—C20—H20C	109.5
C6—C5—C4	121.6 (4)		

### Hydrogen-bond geometry (Å, °)

Cg is the centroid of the N3/N4/C13–C16 ring.

<i>D</i> —H··· <i>A</i>	<i>D</i> —H	H··· <i>A</i>	<i>D</i> ··· <i>A</i>	<i>D</i> —H··· <i>A</i>
O4—H4C···O5	0.82 (3)	1.92 (3)	2.722 (4)	169 (5)
O4—H4D···N4 <sup>i</sup>	0.81 (3)	2.26 (3)	3.038 (4)	161 (5)
O5—H5C···O6	0.82 (3)	1.96 (4)	2.748 (5)	162 (4)
O5—H5D···N4 <sup>ii</sup>	0.82 (5)	2.07 (5)	2.891 (5)	176 (3)
O6—H6C···O2	0.82 (3)	2.23 (3)	2.921 (4)	141 (5)
O6—H6C···O3	0.82 (3)	2.25 (4)	3.029 (4)	158 (5)
O7—H7C···O6	0.82 (2)	2.24 (3)	2.965 (6)	148 (5)
O7—H7D···O1 <sup>iii</sup>	0.81 (5)	2.16 (4)	2.943 (6)	162 (5)
N7—H7E···O5 <sup>i</sup>	0.85 (5)	2.17 (4)	2.998 (6)	162 (4)
N7—H7F···O3 <sup>iv</sup>	0.86 (4)	2.14 (5)	2.908 (5)	148 (4)
C1—H1···O3 <sup>v</sup>	0.93	2.47	3.175 (6)	133
C10—H10···O1 <sup>vi</sup>	0.93	2.54	3.406 (5)	155
C12—H12···O7 <sup>vii</sup>	0.93	2.57	3.343 (7)	140
C6—H6···Cg <sup>vi</sup>	0.93	2.82	3.740 (5)	173

Symmetry codes: (i)  $-x+2, -y+2, -z+2$ ; (ii)  $x, y-1, z$ ; (iii)  $x-1, y-1, z$ ; (iv)  $x+1, y+1, z$ ; (v)  $x+1, y, z$ ; (vi)  $-x+2, -y+2, -z+1$ ; (vii)  $x, y+1, z$ .

